Michael Mains   *Editor*

Topics in Modal Analysis & Testing, Volume 10

Proceedings of the 34th IMAC, A Conference and Exposition on Structural Dynamics 2016

SEM

Springer

Conference Proceedings of the Society for Experimental Mechanics Series

More information about this series at http://www.springer.com/series/8922

Michael Mains
Editor

Topics in Modal Analysis & Testing, Volume 10

Proceedings of the 34th IMAC, A Conference and Exposition on Structural Dynamics 2016

Springer

Editor
Michael Mains
Suite 310, Brüel & Kjær North America
Cincinnati, OH, USA

Preface

Topics in Modal Analysis & Testing represents one of ten volumes of technical papers presented at the 34th IMAC, A Conference and Exposition on Structural Dynamics, organized by the Society for Experimental Mechanics and held in Orlando, Florida, January 25–28, 2016. The full proceedings also include volumes on nonlinear dynamics; dynamics of civil structures; model validation and uncertainty quantification; dynamics of coupled structures; sensors and instrumentation; special topics in structural dynamics; structural health monitoring, damage detection, and mechatronics; and rotating machinery, hybrid test methods, vibro-acoustics and laser vibrometry, shock and vibration, aircraft/aerospace, energy harvesting, acoustics and optics.

Each collection presents early findings from experimental and computational investigations on an important area within structural dynamics. Topics in modal analysis represent papers on enabling technologies for modal analysis measurements and applications of modal analysis in specific application areas.

The organizers would like to thank the authors, presenters, session organizers, and session chairs for their participation in this track.

Cincinnati, OH, USA   M. Mains

Contents

Chapter 1
Comparison of Various Modal Vector Estimation Methods Used in Modal Parameter Estimation

R.J. Allemang and A.W. Phillips

Abstract Modal vectors can be estimated in a number of different ways in modern modal parameter estimation (MPE) algorithms. At the very least, when using single frequency response function (FRF), single degree of freedom (SDOF) methods, the modal vectors are estimated from a least squares estimate of the residues of a partial fraction model in the frequency domain, with or without various residuals, or an equivalent model in the time domain. Once the MPE methods involve multiple input, multiple output (MIMO) FRFs, many options exist. These MIMO MPE methods often involve a matrix polynomial equation that is solved using eigenvalue-eigenvector methods. Depending on the spatial dimensionality of the MIMO FRF matrix, these methods estimate an eigenvector that can be used as an estimate of the modal vector directly or an estimate of a portion (subset) of the modal vector. Alternately, these eigenvectors can be used as weighting in a MIMO version of estimating the residues of the partial fraction model using a weighted least squares method, with or without residuals. These weighting vectors can be normalized to remove arbitrary rotations in the eigenvectors and/or real normalized to influence the potential nature of complex-valued modal vectors. This paper reviews all of the approaches using MIMO FRF data on a simple structure where the modal vectors can be expected to be nearly normal modes. Both modal vectors and the associated modal scaling and mean phase correlation (MPC) are evaluated to document the similarities and differences.

Keywords Modal vector estimation • Residue estimation • Modal vector contamination • Modal participation vectors • Modal vectors

Nomenclature

N_i	No. of input DOFs
N_o	No. of output DOFs
N_L	Long dimension
N_S	Short dimension
N_f	No. of frequencies
N_e	No. of effective modal frequencies.
$N, 2N$	No. of modal frequencies
ω_i	Frequency (rad/s)
λ_r	Complex modal frequency
$[\psi]$	Modal vector matrix
$[L]$	Modal participation matrix
A_{pqr}	Residue, output DOF p, input DOF q, mode r
$R_{I_{pq}}$	Residual inertia, output DOF p, input DOF q
$R_{F_{pq}}$	Residual flexibility, output DOF p, input DOF q
$[C]$	Companion matrix
$[H(\omega_i)]$	Frequency response function matrix
$[U]$	Left singular vector matrix
$[\Sigma]$	Singular value matrix (diagonal)
$[V]$	Right singular vector, or eigenvector, matrix

R.J. Allemang (✉) • A.W. Phillips
Structural Dynamics Research Laboratory, Mechanical and Materials Engineering, University of Cincinnati, Cincinnati, OH 45221-0072 USA
e-mail: Randall.Allemang@uc.edu

1.1 Introduction

As modal parameter estimation (MPE) has evolved over the last 40 years or so, the way that modal vectors are estimated from experimental data has changed as well. Although the technological advances from single measurement and single reference modal parameter estimation to autonomous multiple input, multiple output (MIMO) modal parameter estimation has resulted in improved estimates, the recent developments in autonomous parameter estimation methods have revealed that, while the random errors are reduced, these estimates may still contain small amounts of bias contamination from nearby modes. The results of this contamination are slightly complex-valued estimates of the modal vectors when normal (real-valued) modal vectors are anticipated. The contamination may be due to random or bias errors in measurements, utilizing data from physical systems that do not match the limitations (assumptions) associated with modal analysis or from problems associated with the modal parameter estimation process. The challenge for the test engineer is how to deal with this contamination and uncertainty.

In testing situations where modal vectors show some contamination, the problem is often ignored or eliminated through a real normalization procedure of the final modal vectors. Frequently, this process is justified because the contamination appears to be dominantly random. However, when the contamination is biased, this justification becomes uncertain. Even with the most sophisticated modal parameter estimation algorithms and numerical procedures, the form of the contamination can be a bias error that arises from another mode that is nearby in frequency. This indicates that, while the estimated modal vectors may satisfy whatever algorithm and numerical procedures are being utilized, the estimated modal vectors still contain characteristics that might be perceived as non-physical. Ideally, through a thorough understanding of the modal parameter estimation process, some of these random and bias errors can be minimized.

1.2 Background

The estimation of modal vectors in modern modal parameter estimation algorithms normally involves a two-step process. In the first step (MPE-1), the modal frequencies, λ_r, and the modal participation vectors, $[L]$, are estimated from the eigenvalues and eigenvectors of a companion matrix formed from the experimental data. The participation vectors are formulated on the basis of either the short dimension, N_S, or the long dimension, N_L, of the measured FRF data matrix depending upon the modal parameter estimation algorithm. Then in a second step (MPE-2), the corresponding modal vectors, $[\psi]$, are found from a weighted least squares set of linear equations involving the selected (known) modal frequencies (from the eigenvalues of the companion matrix) [1] and associated modal participation vectors (from the eigenvectors of the companion matrix). In modern algorithms, due to the available speed and memory of modern computers used in testing and data analysis, these two steps are often combined, in what appears to the user, as a single step.

In a recent paper [2], the authors noted that the normalization of the modal participation vectors had an important affect on the final estimation of the modal vectors. This issue is represented in the following Fig. 1.1. Both figures are color-plots
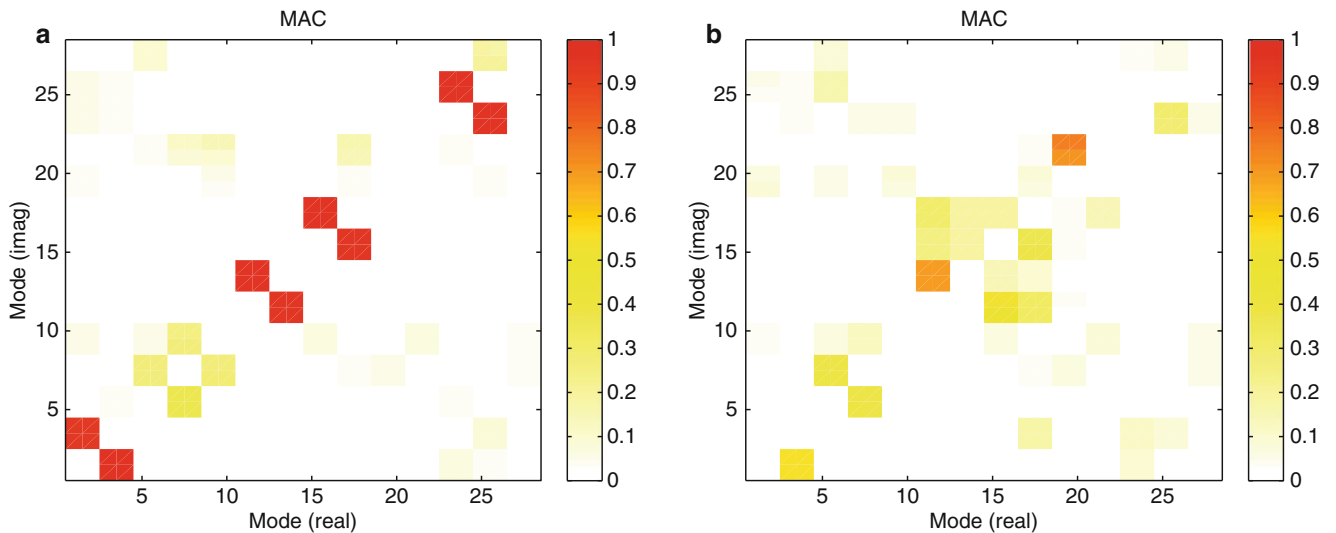
Fig. 1.1 riMAC Plot - C-Plate example. (**a**) riMAC: complex participations. (**b**) riMAC: real participations

of the riMAC [3] matrix for a set of modal vectors. The riMAC compares the real part of each modal vector to the imaginary part of each modal vector. For this set of data, taken from the same circular plate that will be used in the case studies later in this paper, many of the modal vectors are associated with pseudo-repeated modal frequencies. The plot on the left shows that the imaginary part of one vector is linearly related to the real part of the modal vector that is nearby in frequency. Upon inspection, this linear correlation occurs for every pseudo-repeated root pair of modal vectors. The figure on the right shows that the linear correlation is greatly reduced when real normalization is applied to the modal participation vectors.

The following sections review the relevant theoretical concepts and equations required for discussing the estimation of final, scaled modal vectors. The final scaled modal vectors are often derived from the residues of the partial fraction model of the MIMO FRF data matrix [4]. Alternatively, the final, scaled modal vectors can be presented as a vector proportional to the residue vector with associated modal scaling, such as Modal A (M_{A_r}). Finally, a procedure will be presented that can be used to define the process of modal vector estimation for most situations. This procedure will have several optional steps that can effect the characteristics of the final modal vector estimates and the procedure will then be followed in the cases presented to compare and contrast the solutions.

In the following discussion, the use of notation involving the number of input degrees-of-freedom (DOFs), (N_i), and the number of output DOFs, (N_o), is replaced by an alternate notation. Since the FRF matrix is always assumed to be reciprocal, it is more important to note the smaller and larger of the number of DOFs with respect to the inputs and outputs when the data is utilized by modern MIMO modal parameter estimation algorithms. For this reason, the dimension that is larger is referred to as the long dimension, (N_L) and the dimension that is smaller is referred to as the short dimension, (N_S). The short dimension is often referred to as the *number of references* and the long dimension is often referred to as the *number of responses*.

1.2.1 Modal Vectors from Residues: Single Reference FRFs

The equations that relate the complex modal frequencies, complex-valued residues, and complex-valued modal vectors to the single reference FRF data are well-known and are restated in the following equations for discussion purposes [4, 5]:

$$H_{pq}(\omega) = \sum_{r=1}^{N} \frac{A_{pqr}}{j\omega - \lambda_r} + \frac{A_{pqr}^*}{j\omega - \lambda_r^*} \tag{1.1}$$

$$\{H_{pq}(\omega)\}_{N_L \times 1} = \sum_{r=1}^{N} \frac{\{A_{pqr}\}_{N_L \times 1}}{j\omega - \lambda_r} + \frac{\{A_{pqr}^*\}_{N_L \times 1}}{j\omega - \lambda_r^*} \tag{1.2}$$

The above equations represent a partial fraction, residue model for the displacement-force FRF relationships. At the point where modal vectors are estimated, the FRF measurements, the measured frequencies and the complex-valued modal frequencies, λ_r, are known. The above model assumes that the residues (the numerator terms) occur in complex conjugate pairs. This model is often generalized as follows:

$$H_{pq}(\omega) = \sum_{r=1}^{2N} \frac{A_{pqr}}{j\omega - \lambda_r} \tag{1.3}$$

$$\{H_{pq}(\omega)\}_{N_L \times 1} = \sum_{r=1}^{2N} \frac{\{A_{pqr}\}_{N_L \times 1}}{j\omega - \lambda_r} \tag{1.4}$$

In the above equations, no assumption is made regarding the complex conjugate pair relationship among the residues. Once the residues are estimated, the estimates are evaluated to determine if there are complex conjugate pairs as a measure of quality.

Note that the modal vector is determined from the residue vector via a user choice of vector normalization as follows:

$$\{\psi_r\}_{N_L \times 1} = \frac{\{A_{pqr}\}_{N_L \times 1}}{max(A_{pqr})} \qquad A_{pqr} = \frac{\psi_{pr}\, \psi_{qr}}{M_{A_r}} \tag{1.5}$$

In the above equation, the residue vector is divided by the residue with the largest complex magnitude, mode by mode. This yields a modal vector that will generally be dominantly real-valued and limited in magnitude to plus/minus unity. The modal A scaling term (M_{A_r}) can then be found to provide the absolute scaling associated with the modal vector normalization.

1.2.2 Modal Vectors from Residues: Multiple Reference FRFs

Likewise, the equations that relate the complex modal frequencies, complex-valued modal participation vectors, complex-valued modal vectors and complex-valued residues in the multiple reference, multi-input, multi-output (MIMO) FRF data situation are well-known and are restated in the following equations for discussion purposes [4, 6]:

$$[\, H(\omega)\,]_{N_S \times N_L} \;=\; \sum_{r=1}^{2N} \frac{[\,A_r\,]_{N_S \times N_L}}{j\omega - \lambda_r} \tag{1.6}$$

The above equation is the natural extension of the single reference, partial fraction residue model in the previous section. When this equation is applied to the estimation of modal vectors, the relationships between the references (known as the modal participation vectors), $[L]$, and the complex-valued modal frequencies, λ_r, are already known. This allows the equation to be rearranged to take this *a-priori* information into account.

$$[\![\, H(\omega)\,]\!]_{N_S \times N_L \times N_f} \;=\; [\,L\,]_{N_S \times 2N} \, [\![\, \Lambda(\omega)\,]\!]_{2N \times 2N \times N_f} \, [\,\psi\,]^T_{2N \times N_L} \tag{1.7}$$

Noting that:

$$A_{pqr} \;=\; L_{pr}\psi_{qr} \;=\; \frac{\psi_{pr}\,\psi_{qr}}{M_{A_r}} \tag{1.8}$$

In the above equation, note that an unconventional format is used to clarify the structure of the equation. The double bracket notation $[\![\;]\!]$ is used to note that the term within the brackets is repeated across all frequencies (N_f). This makes the matrix products ambiguous since a matrix product between a 2D and a 3D matrix is not uniquely defined. This will be explained further in the next section and in the Appendix.

Also in the above equations note that the columns of the $[\![\, H(\omega)\,]\!]$ matrix are uncoupled as are the columns of the $[\,\psi\,]$ matrix. This allows this equation to be implemented for N_S FRFs, associated with one response DOF. This solution then proceeds for each of the N_L response DOFs, one at a time as in the single reference situation.

In all equations to this point in the paper, it should be noted that the residues should be purely imaginary for a normal mode case (proportional damping) utilizing displacement over force FRF data. For the anticipated normal mode situation, there is no constraint on the numerical characteristics of either the modal participation coefficient or the modal vector coefficient individually as long as the product of these two terms yields the correct residue characteristic.

1.2.3 Modal Vector Estimation: Numerical Solutions

For all practical cases where single reference or multiple reference FRF models are utilized to estimate modal vectors, the solution involves a linear equation that is over-determined since the number of frequencies involved in the solution is much greater than the number of unknowns. This results in a least-squares (LS) solution for the single reference FRF case and a weighted least-squares (WLS) solution for the multiple reference case. The structure of the equations is explained further in the following two sections.

1.2.3.1 Least Squares Solution: Single Reference FRFs

While a number of formulations are possible, the most common least squares solution method for a single reference set of FRF data (column or row) is to solve for the residues, measurement by measurement. Once all of the measurements have

been processed, the modal vectors can be found by conditioning the residue vectors, mode by mode. Note that the number of frequencies, (N_f), must be greater than or equal to the number of unknowns, $(2N)$.

$$\{H_{pq}(\omega)\}_{N_f \times 1} = \left[\frac{1}{j\omega - \lambda_r}\right]_{N_f \times 2N} \{A_{pqr}\}_{2N \times 1} \tag{1.9}$$

$$\{H_{pq}(\omega)\} = \begin{Bmatrix} H_{pq}(\omega_1) \\ H_{pq}(\omega_2) \\ H_{pq}(\omega_3) \\ \cdots \\ H_{pq}(\omega_{N_f}) \end{Bmatrix} \qquad \{A_{pqr}\} = \begin{Bmatrix} A_{pq1} \\ A_{pq2} \\ A_{pq3} \\ \cdots \\ A_{pq2N} \end{Bmatrix} \tag{1.10}$$

$$\left[\frac{1}{j\omega - \lambda_r}\right] = \begin{bmatrix} \dfrac{1}{j\omega_1 - \lambda_1} & \dfrac{1}{j\omega_1 - \lambda_2} & \dfrac{1}{j\omega_1 - \lambda_3} & \cdots & \dfrac{1}{j\omega_1 - \lambda_{2N}} \\ \dfrac{1}{j\omega_2 - \lambda_1} & \dfrac{1}{j\omega_2 - \lambda_2} & \dfrac{1}{j\omega_2 - \lambda_3} & \cdots & \dfrac{1}{j\omega_2 - \lambda_{2N}} \\ \dfrac{1}{j\omega_3 - \lambda_1} & \dfrac{1}{j\omega_3 - \lambda_2} & \dfrac{1}{j\omega_3 - \lambda_3} & \cdots & \dfrac{1}{j\omega_3 - \lambda_{2N}} \\ \cdots & \cdots & \cdots & \cdots & \cdots \\ \dfrac{1}{j\omega_{N_f} - \lambda_1} & \dfrac{1}{j\omega_{N_f} - \lambda_2} & \dfrac{1}{j\omega_{N_f} - \lambda_3} & \cdots & \dfrac{1}{j\omega_{N_F} - \lambda_{2N}} \end{bmatrix} \tag{1.11}$$

The residues in Eq. (1.9) can be solved by pre-multiplying both sides of Eq. (1.9) by the pseudo-inverse of the matrix described in Eq. (1.10). The above equations are utilized for each of the N_L measurements sequentially. Note that the matrix in Eq. (1.10) only needs to be formulated once and is reused for each FRF measurement.

1.2.3.2 Least Squares Solution: Multiple Reference MIMO FRFs

For the multiple reference FRF model, essentially the same least-squares process is used but more information is known that can be utilized in a weighted least-squares process. The modal participation vectors are found when the complex modal frequencies are estimated (via an eigenvalue-eigenvector problem). The physical interpretation of the modal participation vectors is that, for each mode, this vector represents how a particular mode is excited by a particular reference. Each modal participation vector is in general complex-valued but can be normalized so that the largest value is unity. This means that, for a particular mode, the modal participation coefficient that is unity is the best reference that excites that mode. For a multiple reference set of data, the best reference may be different from mode to mode. For this reason, rather than choosing only the single best reference for each mode, all of the participation coefficients are used to weight the least-squares process.

In the following equation, the modal participation vectors, $([L])$ are utilized in this fashion, as a weighting matrix in the least squares solution.

$$[\![H(\omega)]\!]_{N_S \times N_L \times N_f} = [L]_{N_S \times 2N} [\![\Lambda(\omega)]\!]_{2N \times 2N \times N_f} [\psi]^T_{2N \times N_L} \tag{1.12}$$

where:

$$[\![H(\omega)]\!] = \begin{bmatrix} [H(\omega_1)] \\ [H(\omega_2)] \\ [H(\omega_3)] \\ \cdots \\ [H(\omega_{N_f})] \end{bmatrix}_{N_S N_f \times N_L} \qquad [L] [\![\Lambda(\omega)]\!] = \begin{bmatrix} [L] [\Lambda(\omega_1)] \\ [L] [\Lambda(\omega_2)] \\ [L] [\Lambda(\omega_3)] \\ \cdots \\ [L] [\Lambda(\omega_{N_f})] \end{bmatrix}_{N_S N_f \times 2N} \tag{1.13}$$

$$A_{pqr} = L_{pr} \psi_{qr} = \frac{\psi_{pr} \psi_{qr}}{M_{A_r}} \tag{1.14}$$

In the above equations, the weighted least-squares solution is used to estimate the transpose of the modal vector matrix, $([\psi]^T)$ since all other information in the equation is known. The transpose of the modal vector matrix $([\psi]^T)$ in Eq. (1.12)

can be solved by pre-multiplying both sides of Eq. (1.12) by the pseudo-inverse of the matrix described in Eq. (1.13) (the combined $[L]$ and $[\Lambda]$ matrices). The solution proceeds, FRF measurement set by FRF measurement set. Each FRF measurement set contains N_S FRF measurements for each response DOF in the N_L dimension of the FRF matrix. Note again that there are many more frequencies (N_f) than unknowns ($2N$) for each FRF measurement set.

Complete details of the structure of these equations to more clearly show the individual matrices is given in the Appendix.

1.2.4 Residuals

The above models do not show additional mathematical terms, referred to as residuals, that account for the influence of modes with modal frequencies outside of the range of the frequencies used in the modal parameter estimation, or even outside the frequency range of the FRF measurements. The oldest and simplest approach is to include two frequency domain terms to account for the inertia effect of lower frequency modes of vibration, below the minimum frequency, and the stiffness effect of higher frequency modes of vibration, above the maximum frequency. These two terms are referred to as residual inertia $R_{I_{pq}}$ and residual flexibility $R_{F_{pq}}$.

$$R_{I_{pq}} \;=\; R_1 \times \omega_i^0 \qquad R_{F_{pq}} \;=\; \frac{R_2}{\omega_i^2} \tag{1.15}$$

This approach can be generalized to a set of five or more frequency domain, polynomial terms that are mathematical in structure but simply an extension of the residual inertia and flexibility concept. This approach better accounts for modes with frequencies above and below the maximum and minimum frequency of interest for cases where the modal frequencies are close to the frequency boundaries.

The above two approaches to estimating residuals are most often a part of the LS and WLS solutions. The concept is that the addition of residuals reduces the contamination of the modal vectors that are estimated from the modes with frequencies outside the frequency band of interest.

Another form of residuals is to allow extra computational poles (terms that have the same form as complex modal frequencies) to augment the physical complex modal frequencies that have been identified. These additional terms are of similar mathematical structure to the physical complex modal frequencies and are easy to implement in the solution procedure. Again the concept is that these additional computational terms allow the modal vectors to be estimated with less influence or contamination from modes that are nearby in frequency or even noise within the frequency band of interest. These computational poles may take on any complex-valued frequency value and are found from the modal parameter estimation process. In normal situations, these poles are not included as physical, complex modal frequencies since they do not satisfy requirements of complex modal frequencies (consistency of estimates, realistic damping or frequency, etc.).

In all cases, the value of the residuals are of little practical value except to improve the estimates of the modal vectors as part of the MPE-2 solution procedure. The information is generally not retained after the modal vectors have been estimated and is not generally useful in the modal model.

In the following case study, two different forms of residuals will be used. Computational poles will be used as residuals in the first stage of modal parameter estimation (MPE-1) and two residuals, residual inertia and residual flexibility, are used in the second stage of modal parameter estimation (MPE-2).

1.3 Vector Conditioning

Vector conditioning generally applies to the three vectors (modal participation vectors, residue vectors and modal vectors) that are estimated as part of any modal parameter estimation method. Vector conditioning involves methods that are designed to improve the final modal vector estimates and may vary from user to user and may be available at different levels in commercial software. In general, vector conditioning, first and foremost, is designed to remove potential contamination from the final modal vector estimates.

Vector conditioning begins with the recognition that the modal participation vector is the result of an eigenvalue problem where the eigenvectors are arbitrarily scaled and even a normal mode might be represented as a set of real-valued numbers modified by a complex-valued scalar. This means that some sort of normalization is needed to remove the complex-valued scalar. Furthermore, if some sort of real normalization is desirable (to match up well with an undamped, analytical model,

for example), the understanding of the contamination that is being removed is a prerequisite to any procedure. Random contamination may simply be ignored, smoothed or averaged out, but if the contamination is related to a bias from nearby modes, it may indicate that the modal parameter estimation may need further evaluation or that more data from additional reference DOFs is required.

1.3.1 Vector Normalization

Vector conditioning begins with some form of normalization. Normalization simply means that each vector will be normalized with respect to one element within the vector. This is often done as is shown in Eq. (1.5) where the residue vector is divided by the largest element within the residue vector. The meaning of largest in this sense is that the magnitude of the complex-valued element of the vector is the maximum absolute value found within the vector but the division occurs on a complex-valued basis. This means that the largest element of the normalized vector will be unity. In general, though, the normalized vector will still be complex-valued at all other positions in the normalized vector. Other normalization choices are possible (unity vector length, etc.) but dividing by the maximum provides a simple and reliable method. This approach will also yield modal scaling values that can be more directly related to the physical properties of the system.

Normalization as defined above can be applied to either the modal participation vectors or the modal vectors. Since the residue vectors have physical meaning and units, normalization is generally not applied except to estimate the modal vector from the residue vector.

1.3.1.1 Real Normalization

Once a vector has been normalized to be dominantly real-valued, the vector can be limited to only real values if desired. This limitation can be a simple truncation (delete imaginary parts) or some other procedure that preserves the complex magnitude with the appropriate zero or 180° phase. The complex-valued vectors should always be evaluated, visually or numerically, before any real normalization is performed to be certain the process does not have unintended consequences.

In the case of modal participation vectors, while these vectors are theoretically proportional to the final modal vectors at the included DOFs, their function in the modal parameter estimation process is one of weighting the least-squares solution in the second stage of modal parameter estimation (MPE-2). Performing a real normalization of the modal participation vectors has been found to be beneficial always and does not affect the final modal vector estimates adversely [2].

1.3.2 Central Axis Rotation

The normalization described in the previous section guarantees that one element in the vector will become unity but the vector itself may statistically not be best aligned with the real axis. A statistical estimate of the central axis of the vector can be performed to make sure that the mean phase of the vector is along the real axis. This is in addition to making sure that the largest magnitude in this statistical solution is unity (in a complex magnitude sense).

In order to establish a uniform procedure for normalizing vectors that are related to modal vectors (modal vectors, modal participation vectors, residue vectors), each potentially complex-valued vector must first be rotated to an orientation where the dominant information of the vector in complex space is aligned with the real axis. This is required since the complex-valued vector is generally the result of the solution of an eigenvalue-eigenvector problem involving the complex-valued MIMO FRF data as stated above.

Given an original modal vector for mode r, a central axis rotation method is utilized to determine the dominant axes. These dominant axes can be identified via the singular value decomposition of the relationship between the real part, $\{\psi_R\}_r$, and the imaginary part, $\{\psi_I\}_r$, of the vector for mode r as follows:

$$[U, \Sigma, V] = SVD\left([\{\psi_I\}_r \ \{\psi_R\}_r]^T [\{\psi_I\}_r \ \{\psi_R\}_r]\right) \tag{1.16}$$

Recognize that this decomposition is an attempt to locate the two dominant axes of a 2-D ellipse that encompasses the modal vector data in the complex plane. Following the decomposition, the central axis angle is estimated using the true (four quadrant) arctangent of the right singular vector relationship. Note that, regardless of the number of DOF positions

represented in the modal vector, the right singular vector matrix will always be two by two in dimension representing the 2-D characteristics of the ellipse.

$$\bar{\phi}_r \; = \; \tan^{-1} \left(\frac{V_{22}}{-V_{12}} \right) \tag{1.17}$$

After identifying the central axis angle, the original complex-valued modal vector is rotated by multiplying by the complex rotational phasor.

$$\left\{ \hat{\psi} \right\}_r \; = \; \left(\cos\left(\bar{\phi}_r \right) \; - \; j \, \sin\left(\bar{\phi}_r \right) \right) \, \{\psi\}_r \tag{1.18}$$

This rotation, followed by a normalization by the maximum element in the resulting vector, results in a normalization procedure that assures that the resulting vector is dominantly real, with a maximum value of unity, based upon all of the vector information, rather than a single DOF that is chosen arbitrarily (for example, rather than selecting the DOF associated with the largest modal vector coefficient).

1.3.3 Vector Complexity

Vector complexity is often defined in terms of mean phase deviation as an indication of how the phase deviates from zero and/or 180°. This definition allows some ambiguity in what is meant by a *complex mode*. It may simply mean that the elements of the estimated modal vector contain complex values. For this case, the elements of the modal vector may be rotated by an angle in the complex plane, but are otherwise co-linear. Or it may mean that the modal vector contains complex values that cannot be made real by a simple complex phasor rotation. For this case, the modal coefficients are not all co-linear in the complex plane. For this development, it is the second definition that is used. Note that if the central axis rotation procedure is performed, the mean phase will always be 0°.

The *mean phase deviation* (MPD_r) for modal vector r has been defined historically as a number between zero and unity where zero represents a real-valued modal vector (normal mode) and where unity represents a complex-valued modal vector with no recognizable dominant real or imaginary characteristic, once an attempt has been made to rotate the vector to a dominant central axis position. This fraction is often multiplied by 100 to represent the percentage of complex-valued modal vector characteristics. In terms of the definitions utilized in the previous section, assuming that the modal vector has already been rotated to its most dominant real orientation, the MPD_r is defined as the norm of the imaginary part of the rotated vector divided by the norm of the real part of the rotated vector, as shown in Eq. (1.17). Thus, the MPD_r gives a dispersion ratio around the central axis of the rotated modal vector bounded between zero and one.

Mean Phase Deviation (MPD_r):

$$MPD_r \; = \; \frac{\left\| \left\{ \hat{\psi}_I \right\}_r \right\|}{\left\| \left\{ \hat{\psi}_R \right\}_r \right\|} \tag{1.19}$$

Once the MPD_r is defined in terms of the fraction between zero and unity, the associated *mean phase correlation* for modal vector r is defined as in Eq. (1.18).

Mean Phase Correlation (MPC_r):

$$MPC_r \; = \; 1 \; - \; MPD_r \tag{1.20}$$

The mean phase correlation can then be interpreted as an indicator of normalcy; from a purely normal mode (1.0) to a purely complex mode (0.0).

A *modal vector complexity plot* is often used to represent the characteristics of modal vectors with respect to MPC and vector complexity. The vectors in this presentation are always scaled to a maximum value of unity. Figure 1.2 is an example of such a plot and these plots will be used to describe the results of the case studies.

Modal Vector Complexity Plots

362.4 Hz	363.6 Hz	557.0 Hz	761.2 Hz	764.2 Hz
MPC 99.4%	MPC 99.2%	MPC 99.4%	MPC 99.0%	MPC 99.1%
M_A1.10e+04$\langle$−88.5°$\rangle$	M_A1.53e+04$\langle$−89.8°$\rangle$	M_A4.13e+04$\langle$−89.0°$\rangle$	M_A2.10e+04$\langle$−90.1°$\rangle$	M_A2.06e+04$\langle$−91.4°$\rangle$

1223.0 Hz	1224.1 Hz	1328.0 Hz	1328.7 Hz	2019.1 Hz
MPC 97.4%	MPC 97.3%	MPC 96.0%	MPC 97.6%	MPC 98.0%
M_A5.30e+04$\langle$−89.6°$\rangle$	M_A5.84e+04$\langle$−90.2°$\rangle$	M_A3.51e+04$\langle$−87.7°$\rangle$	M_A3.43e+04$\langle$−91.1°$\rangle$	M_A4.51e+04$\langle$−87.7°$\rangle$

2024.0 Hz	2321.6 Hz	2322.8 Hz	2337.5 Hz
MPC 95.2%	MPC 94.7%	MPC 66.1%	MPC 81.2%
M_A4.47e+04$\langle$−86.2°$\rangle$	M_A5.89e+04$\langle$−85.1°$\rangle$	M_A2.32e+05$\langle$−59.3°$\rangle$	M_A1.84e+05$\langle$−99.7°$\rangle$

Fig. 1.2 Case 6: Modal vector complexity plot, multiple references, all DOFs, ERA method

1.3.4 Procedure for Modal Vector Estimation

In the following modal vector estimation procedure, an autonomous modal parameter estimation method, referred to as CSSAMI [7–9]) is used to minimize the sensitivity of the complex modal frequency and modal participation vectors to user interaction. Two different modal parameter estimation methods are used to evaluate the effects of long dimension based methods versus short dimension based methods. Complete details concerning this thought process can be found in Reference [4].

The long dimension method that will be used is an implementation of the second order time domain method known as the eigensystem realization algorithm (ERA) [10, 11]. The notable characteristic of this method is that the modal participation vectors found during the MPE-1 phase of modal parameter estimation are of length N_L. The short dimension method that will be used is an implementation of a rational fraction polynomial method with Z mapping (RFP-Z). This method is the same as the polyreference least squares complex frequency method (PLSCF) [12–14] which is the basis of the commercial PolyMAX algorithm. The notable characteristic of this method is that the modal participation vectors found during the MPE-1 phase of modal parameter estimation are of length N_S. Complete details on the implementation of these and other modal parameter estimation algorithms can be found in Reference [4].

The following list is a summary of the basic vector estimation procedure. The modal parameter estimation procedure consists of two stages. In the first stage, the complex modal frequencies and the modal participation vectors are estimated. The modal participation vectors can be of length N_S or N_L depending upon the MPE algorithm used. These modal participation vectors can optionally be conditioned. In the second stage, the residue vectors and the modal vectors are estimated. The second stage uses the modal participation vectors from the first stage as weighting factors in the WLS solution for residue vectors. For consistency, modal participation vectors for this exercise are always limited to vectors of length N_S for all cases studied. The modal participation vectors can optionally be conditioned. The final modal vectors can optionally be conditioned before any modal scaling is estimated.

Modal Parameter Estimation, Stage 1 (MPE-1):

- **[Modal Frequency and Participation Vector Solution]:** Solve the characteristic equation for modal frequencies and modal participation vectors for varying model orders (or subspace). If a short dimension MPE algorithm is used, then the resulting vectors will span the short (reference) space. If a long dimension MPE algorithm is used, then the resulting vectors will span the long space. This step forms the consistency diagram.
- *Optional:* **[Participation Vector Normalization]:** Normalize the vectors via a central axis rotation (or division by largest coefficient.)
  - *Optional:* Truncate the resulting participation vectors to their real component.
  - *Optional:* Normalize the coefficients by dividing each vector by its largest component magnitude.

- *Optional:* **[Residue Solution]:** Solve for residues using the complete set of pole/vector solutions identified (including all the computational poles and vectors as residuals) from each model order variation through a partial fraction solution (Eqs. (1.12)–(1.14)). If the basis is short, the resulting residue vectors will span the long basis space. If the basis is long, then the resulting residues will span the short space.
  - *Optional:* For long basis algorithms, the resulting residue vector spans the short basis. Repeat the **[Participation Vector Normalization]** and **[Residue Solution]** steps using the short basis residue vector as the participation vector. The result will be a full length residue vector.

- **[Parameter Selection]:** Apply the CSSAMI (pole wizard) (or manual user interaction) to the complete sets of solutions from all model order variations to identify the probable realistic and *best* estimate of each pole/vector pair.

Modal Parameter Estimation, Stage 2 (MPE-2):

- *Optional:* **[Participation Vector Normalization]:** Normalize the vectors via a central axis rotation (or division by largest coefficient.)
  - *Optional:* Truncate the resulting participation vectors to their real component.
  - *Optional:* Normalize the coefficients by dividing each vector by its largest component magnitude.

- **[Residue Solution]:** Solve for residues using the set of identified pole/vector pairs through a partial fraction solution (Eqs. (1.12)–(1.14)). If the basis of the participation is long, subset the participation vectors to the common short basis DOFs.
  - *Optional:* Include selected residuals in the partial fraction solution.

- *Optional:* **[Residue Vector Normalization]:** Estimate the final modal vectors by performing the central axis rotation and maximally real normalization

In the above procedure template, there are numerous options that can be included in the process. To a lesser or greater degree, these optional choices affect the final modal vector estimates.

1.4   C-Plate Example

The data used for the following case study is MIMO FRF data taken from an impact test of a steel disc supported in a pseudo free-free boundary condition. The steel disc is approximately 2 cm. thick and 86 cm. in diameter with several small holes through the disc. The center area of the disc (diameter of approximately 25 cm.) has a thickness of approximately 6 cm. There are seven reference accelerometers and measured force inputs from an impact hammer are applied to thirty-six locations,

Table 1.1 Modal vector estimation cases

	MPE-1					MPE-2		
	MPE Method	Vector Scaling	Real L	MRNV	Reference DOFs [L]	Real L	MRNV	Reference DOFs [L]
Case 1	RFP-Z	Residue	on	on	all	on	on	DOF 1
Case 2	RFP-Z	Residue	on	on	all	on	on	DOF 6
Case 3	RFP-Z	Residue	on	on	all	on	on	DOFs 1,6
Case 4	RFP-Z	Residue	on	on	all	on	on	–
Case 5	ERA	Participation	–	on	all	–	–	–
Case 6	ERA	Participation	–	on	all	on	on	all DOFs
Case 7	ERA	Residue	on	on	all	–	–	–
Case 8	ERA	Residue	on	on	all	on	on	all DOFs
Case 9	RFP-Z	Participation	–	on	all	–	–	–
Case 10	RFP-Z	Participation	–	on	all	on	on	all DOFs
Case 11	ERA	Participation	–	on	all	off	on	all DOFs

including next to the seven reference accelerometers. The frequency resolution of the data is 5 Hz. Based upon the coherence functions associated with the FRF data, the quality of the data is quite good but there are obvious time truncation errors (leakage) identifiable at the peak frequencies.

While the disc is not as challenging as some industrial data situations that contain more noise or other complicating factors like small nonlinearities, the disc has a number of pseudo-repeated roots spaced well within the 5 Hz frequency resolution and a mix of close modes involving repeated and non-repeated roots which are very challenging. Based upon the construction of the disc, real-valued, normal modes can be expected and the inability to resolve these modes can be instructive relative to modal parameter estimation algorithm, autonomous procedure performance and, particularly in this set of case studies, the expected performance of the modal vector estimation part of the modal parameter estimation.

Eleven case studies, which is a subset of a larger number that were evaluated, will be summarized in the following section and in the Appendix (Table 1.1). With all of the optional choices, a complete study would involve many more cases and include other structures of varying degree of difficulty.

In the above table, the acronym *MRNV* stands for *maximally real normalized vector* which means the vector has been rotated using the central axis rotation to a zero mean phase and the largest coefficient for each vector is scaled to unity. The acronym *Real L* indicates whether the participation vector has been truncated to the real part only.

For these case studies, the entire frequency range from 220 to 2500 Hz was fit by the RFP-Z algorithm and the ERA algorithm using traditional complex-valued participation vector weighting as well as real-valued participation vector weighting. For most cases, the complete set of modal participation vectors was utilized although two cases show the deficiencies of single reference approaches. One case with two references shows the power of multiple reference modal parameter estimation. The CSSAMI autonomous modal parameter estimation procedure [7] was utilized to remove user bias from the selected results.

1.4.1 Case 6:

Case 6 demonstrates that, while most of the modes appear to have been fit for residues in the MPE-2 stage reasonably well, simply converting the complex-valued participation to real does not guarantee the quality of fit. The three modes between 2320 and 2340 Hz represent a repeated root pair and an additional close mode. The MPC shows that the fit for two of the modes retains significant modal complexity that is not anticipated in this structure. The details for the first three modes and the last three modes for all case evaluated are included in Table 1.2. The plots for all the cases evaluated, but not presented in the main body of the text, are presented in Appendix 2 (Figs. 1.3, 1.4, 1.5, 1.6, 1.7, 1.8, 1.9, 1.10, 1.11, and 1.12).

Table 1.2 Modal vector estimation cases—(combined table) results

Summary of modal vector estimation case study

	Frequency (Hz)	Modal A Mag. (Phase)	MPC %	Frequency (Hz)	Modal A Mag. (Phase)	MPC percent	Frequency (Hz)	Modal A Mag. (Phase)	MPC %
Case 1	362.6	9.02e+03⟨−83.0o⟩	93.8	363.9	4.23e+04⟨+137.9o⟩	69.0	557.1	4.12e+04⟨−88.5o⟩	99.4
Case 2	362.6	1.17e+04⟨−73.7o⟩	93.2	363.9	1.57e+04⟨−80.5o⟩	84.8	557.1	4.08e+04⟨−88.4o⟩	99.4
Case 3	362.6	1.07e+04⟨−86.6o⟩	99.3	363.9	1.51e+04⟨−86.9o⟩	98.9	557.1	4.13e+04⟨−88.5o⟩	99.5
Case 4	362.6	1.11e+04⟨−87.1o⟩	99.4	363.9	1.52e+04⟨−87.7o⟩	98.8	557.1	4.19e+04⟨−88.9o⟩	99.4
Case 5	362.4	Not Applicable	88.4	363.6		89.5	557.0		99.5
Case 6	362.4	1.10e+04⟨−88.5o⟩	99.4	363.6	1.53e+04⟨−89.8o⟩	99.2	557.0	4.13e+04⟨−89.0o⟩	99.4
Case 7	362.4	1.07e+04⟨−88.8o⟩	99.0	363.6	1.43e+04⟨−89.6o⟩	98.8	557.0	4.06e+04⟨−88.7o⟩	99.4
Case 8	362.4	1.10e+04⟨−88.5o⟩	99.4	363.6	1.54e+04⟨−89.9o⟩	99.2	557.0	4.14e+04⟨−89.0o⟩	99.4
Case 9	362.6	Not Applicable	94.6	363.9		92.5	557.1		99.3
Case 10	362.6	1.08e+04⟨−87.2o⟩	98.8	363.9	1.45e+04⟨−87.5o⟩	99.2	557.1	4.10e+04⟨−88.7o⟩	99.5
Case 11	362.4	1.09e+04⟨−88.3o⟩	90.8	363.6	1.49e+04⟨−90.6o⟩	88.1	557.0	4.13e+04⟨−88.9o⟩	99.4
Case 1	2322.0	9.13e+04⟨−56.0o⟩	40.1	2322.5	1.06e+05⟨−94.0o⟩	55.9	2338.1	1.95e+05⟨−86.8o⟩	96.0
Case 2	2322.0	3.71e+04⟨−71.5o⟩	58.0	2322.5	8.18e+04⟨+4.9o⟩	37.0	2338.1	1.92e+05⟨−91.8o⟩	95.7
Case 3	2322.0	8.69e+04⟨−89.4o⟩	97.5	2322.5	1.07e+05⟨−87.4o⟩	95.9	2338.1	2.07e+05⟨−90.5o⟩	97.1
Case 4	2322.0	9.39e+04⟨−86.3o⟩	97.5	2322.5	1.12e+05⟨−90.5o⟩	97.3	2338.1	2.03e+05⟨−94.4o⟩	94.9
Case 5	2321.6	Not Applicable	31.2	2322.8		83.0	2337.5		84.2
Case 6	2321.6	5.89e+04⟨−85.1o⟩	94.7	2322.8	2.32e+05⟨−59.3o⟩	66.1	2337.5	1.84e+05⟨−99.7o⟩	81.2
Case 7	2322.2	9.41e+04⟨−89.4o⟩	95.3	2322.3	1.72e+05⟨−86.1o⟩	97.3	2337.5	2.29e+05⟨−92.8o⟩	96.2
Case 8	2322.2	4.72e+04⟨−85.9o⟩	97.3	2322.3	6.32e+04⟨−86.3o⟩	94.8	2337.5	2.19e+05⟨−99.2o⟩	94.9
Case 9	2322.0	Not Applicable	70.1	2322.5		74.9	2338.2		96.0
Case 10	2322.0	8.61e+04⟨−90.3o⟩	97.4	2322.5	9.75e+04⟨−91.9o⟩	97.5	2338.2	1.98e+05⟨−89.8o⟩	97.0
Case 11	2321.6	7.95e+04⟨+161.0o⟩	59.9	2322.8	1.36e+05⟨+28.5o⟩	32.9	2337.5	2.02e+05⟨−114.0o⟩	84.3

Modal Vector Complexity Plots

362.4 Hz	363.6 Hz	557.0 Hz	761.2 Hz	764.2 Hz
MPC 99.4%	MPC 99.2%	MPC 99.4%	MPC 99.0%	MPC 99.2%
$M_A 1.10e+04\langle-88.5°\rangle$	$M_A 1.54e+04\langle-89.9°\rangle$	$M_A 4.14e+04\langle-89.0°\rangle$	$M_A 2.11e+04\langle-90.2°\rangle$	$M_A 2.06e+04\langle-91.4°\rangle$

1223.0 Hz	1224.1 Hz	1328.0 Hz	1328.7 Hz	2019.1 Hz
MPC 97.3%	MPC 97.3%	MPC 95.9%	MPC 97.7%	MPC 98.4%
$M_A 5.30e+04\langle-89.6°\rangle$	$M_A 5.87e+04\langle-90.2°\rangle$	$M_A 3.39e+04\langle-87.7°\rangle$	$M_A 3.43e+04\langle-91.2°\rangle$	$M_A 4.47e+04\langle-88.0°\rangle$

2024.0 Hz	2322.2 Hz	2322.3 Hz	2337.5 Hz
MPC 95.8%	MPC 97.3%	MPC 94.8%	MPC 94.9%
$M_A 4.25e+04\langle-86.3°\rangle$	$M_A 4.72e+04\langle-85.9°\rangle$	$M_A 6.32e+04\langle-86.3°\rangle$	$M_A 2.19e+05\langle-99.2°\rangle$

Fig. 1.3 Case 8: Modal vector complexity plot, multiple references, all DOFs, ERA method

1.4.2 Case 8:

Case 8 is identical to Case 6 with the addition of reprocessing the normalized eigenvector from the ERA method to residue scaling and then performing the central axis rotation, and decimation of the long dimension N_L vectors to the short dimension N_S followed by real normalization of the short dimension participation vectors ($[L]$) yields a very physical, realistic result. The improvement on the estimation can be noted for the last two modes.

1.4.3 Case 10:

Case 10 shows a comparable result to Case 8 even though a short dimension MPE algorithm is utilized. Case 10 shows that reprocessing the normalized eigenvector from the RFP-Z method to residue scaling and then performing the central axis rotation, followed by real normalization of the short dimension participation vectors ($[L]$) yields a very physical, realistic result with even a slight additional improvement in the MPC value for the last two modes.

Modal Vector Complexity Plots
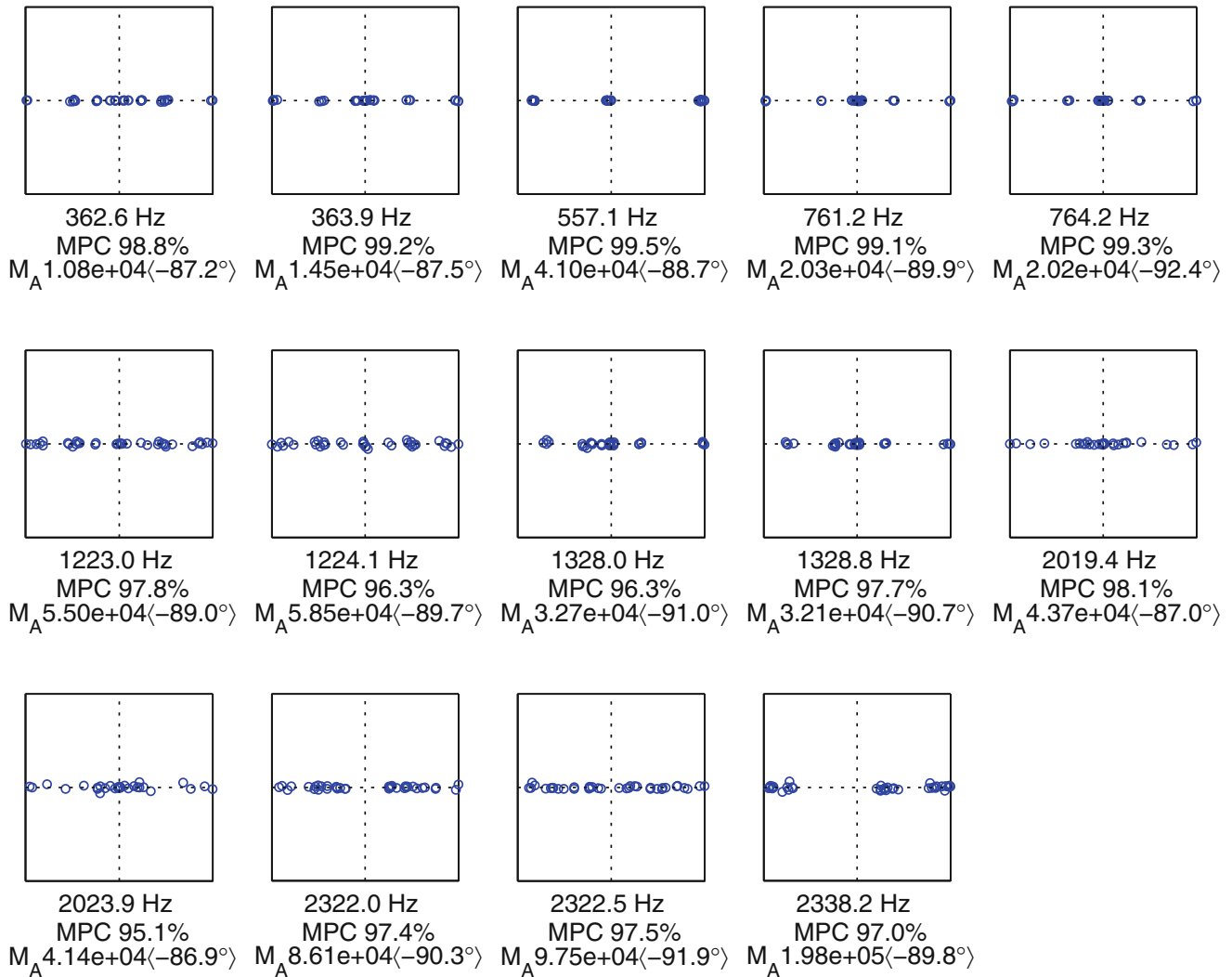
Fig. 1.4 Case 10: Modal vector complexity plot, multiple references, all DOFs, RFP-Z method

1.5 Discussion

In Table 1.2, the quality of the results when comparing different cases can be summarized by the Modal A and MPC values for each mode compared from case to case. Since there is an expectation for this test article that the modal vectors should represent real-valued modal vectors, cases where the Modal A is closest to minus 90° along with MPC value close to 100 % would represent the *best* result.

In Cases 1 and 2 where only single references were used to estimate the modal vectors, the results were unacceptable even though the complex modal frequencies were selected from a multiple reference method during MPE-1.

In the three cases featured (Case 6, Case 8 and Case 10), both the long dimension MPE algorithm (ERA) utilized and the short dimension MPE algorithm (RFP-Z) give very acceptable and comparable results. If anything, the short dimension MPE algorithm (RFP-Z) appears to estimate slightly improved estimates of the modal vectors for this structure.

Case 11 is included as it is a typical procedure utilized in the past when a long dimension MPE algorithm like ERA was utilized to estimate modal vectors. Despite the availability of more spatial information, the modal vectors show some uncertainty when the participation vectors are not truncated to real values.

1.6   Summary and Future Work

While there is no best procedure for the estimation of modal vectors, there are a number of general characteristics that can be summarized based upon the cases evaluated for this particular structure where normal modes were anticipated.

- Multiple references always improve the estimation of the modal vectors. Even the addition of a second reference provides substantial improvement. It is unlikely that using one reference at a time, when multiple references are available, will result in the same level of improvement.
- Real normalization of the modal participation vectors $[L]$ always improves the modal vector estimation. The role of the modal participation vectors as weighting in the WLS procedure is only complicated by allowing the modal participation vectors to be complex-valued.
- The initial eigenvector solution always has more uncertainty when compared to the modal vector found by fitting the residue model and then normalizing to get the modal vector. This appears to be true whether the participation vectors are normalized and truncated to real values or not.

A relatively small change to the modal vector estimation procedure shows dramatically improved results with little to no observable negative effects. For the examples chosen, the use of central vector rotation and real normalization of the modal participation vectors appears to improve the quality and characteristics of the final, scaled modal vectors (and residues) significantly.

Future work will involve a review of the eigenvalue-eigenvector procedure that is used to get the initial estimates of the modal participation vectors. This solution is based upon a well-known companion matrix solution that stems from the same physical model (but in rational fraction polynomial form) that is used in the residue estimation of the partial fraction model. A more complete understanding of why the eigenvalue-eigenvector solution appears to result in more uncertainty, DOF by DOF in the eigenvector, is still needed.

Appendix 1: Multiple Reference Model Details

The details of how the data is positioned into the MIMO FRF model for the estimation of modal vectors often requires a little manipulation to see the matrix conformal relationships. The following development expands each term so that the over-determined linear equation is easier to visualize.

The primary equation used for multiple reference, modal vector estimation can be restated as:

$$\llbracket H(\omega) \rrbracket_{N_S \times N_L \times N_f} = [L]_{N_S \times 2N} \llbracket \Lambda(\omega) \rrbracket_{2N \times 2N \times N_f} [\psi]^T_{2N \times N_L} \tag{1.21}$$

where:

$$\llbracket H(\omega) \rrbracket = \begin{bmatrix} [H(\omega_1)] \\ [H(\omega_2)] \\ [H(\omega_3)] \\ \cdots \\ [H(\omega_{N_f})] \end{bmatrix}_{N_S N_f \times N_L} \qquad [L] \llbracket \Lambda(\omega) \rrbracket = \begin{bmatrix} [L][\Lambda(\omega_1)] \\ [L][\Lambda(\omega_2)] \\ [L][\Lambda(\omega_3)] \\ \cdots \\ [L][\Lambda(\omega_{N_f})] \end{bmatrix}_{N_S N_f \times 2N} \tag{1.22}$$

The modal participation matrix $[L]$ is of the following form:

$$[L] = \begin{bmatrix} L_{1,1} & L_{2,1} & L_{3,1} & \dots & L_{2N,1} \\ L_{1,2} & L_{2,2} & L_{3,2} & \dots & L_{2N,2} \\ L_{1,3} & L_{2,3} & L_{3,3} & \dots & L_{2N,3} \\ \dots & \dots & \dots & \dots & \dots \\ L_{1,N_S} & L_{2,N_S} & L_{3,N_S} & \dots & L_{2N,N_S} \end{bmatrix} \tag{1.23}$$

Note that in the above notation, the modal participation vectors span the row space with each column representing the participation information for another mode. The modal vector matrix $[\psi]$ is of the following form:

$$[\psi]^T = \begin{bmatrix} \psi_{1,1} & \psi_{1,2} & \psi_{1,3} & \dots & \psi_{1,N_L} \\ \psi_{2,1} & \psi_{2,2} & \psi_{2,3} & \dots & \psi_{2,N_L} \\ \psi_{3,1} & \psi_{3,2} & \psi_{3,3} & \dots & \psi_{3,N_L} \\ \dots & \dots & \dots & \dots & \dots \\ \psi_{2N,1} & \psi_{2N,2} & \psi_{2N,3} & \dots & \psi_{2N,N_L} \end{bmatrix} \tag{1.24}$$

Note that in the above notation, the transpose of the modal vector matrix span the column space with each row representing another mode. Note that the notation for both the $[L]$ and the $[\psi]$ matrices is consistent with the academic definition of a modal matrix but the solution method is actually finding the $[\psi]^T$ matrix.

The diagonal $[\Lambda(\omega_i)]$, at each frequency, is of the following form:

$$\lceil \Lambda(\omega_i) \rfloor = \begin{bmatrix} \dfrac{1}{j\omega_i - \lambda_1} & & & & \\ & \dfrac{1}{j\omega_i - \lambda_2} & & & \\ & & \dfrac{1}{j\omega_i - \lambda_3} & & \\ & & & \ddots & \\ & & & & \dfrac{1}{j\omega_i - \lambda_{2N}} \end{bmatrix} \tag{1.25}$$

Finally, the combined matrix of the $[L]$ matrix and the $[\Lambda]$ matrix can be formed at each frequency:

$$[L][\Lambda(\omega_i)] = \begin{bmatrix} \dfrac{L_{1,1}}{j\omega_i - \lambda_1} & \dfrac{L_{2,1}}{j\omega_i - \lambda_1} & \dfrac{L_{3,1}}{j\omega_i - \lambda_1} & \dots & \dfrac{L_{2N,1}}{j\omega_i - \lambda_1} \\ \dfrac{L_{1,2}}{j\omega_i - \lambda_2} & \dfrac{L_{2,2}}{j\omega_i - \lambda_2} & \dfrac{L_{3,2}}{j\omega_i - \lambda_2} & \dots & \dfrac{L_{2N,2}}{j\omega_i - \lambda_2} \\ \dfrac{L_{1,3}}{j\omega_i - \lambda_3} & \dfrac{L_{2,3}}{j\omega_i - \lambda_3} & \dfrac{L_{3,3}}{j\omega_i - \lambda_3} & \dots & \dfrac{L_{2N,3}}{j\omega_i - \lambda_3} \\ \dots & \dots & \dots & \dots & \dots \\ \dfrac{L_{1,2N}}{j\omega_i - \lambda_{2N}} & \dfrac{L_{2,2N}}{j\omega_i - \lambda_{2N}} & \dfrac{L_{3,2N}}{j\omega_i - \lambda_{2N}} & \dots & \dfrac{L_{2N,2N}}{j\omega_i - \lambda_{2N}} \end{bmatrix} \tag{1.26}$$

This combined matrix can now be stacked vertically so that the row space matches the row space of the $[\![H(\omega)]\!]$ matrix, as in Eqs. (1.21) and (1.22). Now the solution for the modal vectors can be found by multiplying both sides of Eq. (1.21) by the pseudo-inverse of the $[L][\![\Lambda(\omega)]\!]$ matrix.

Note that in the above development, if the short dimension, N_S, of the FRF matrix is one, the matrix in Eq. (1.26) will be the same as the matrix in Eq. (1.10).

Appendix 2: Modal Vector Complexity Plots: Other Case Studies

Case 1:

Modal Vector Complexity Plots

362.6 Hz	363.9 Hz	557.1 Hz	761.2 Hz	764.2 Hz
MPC 93.8%	MPC 69.0%	MPC 99.4%	MPC 98.5%	MPC 55.1%
M_A9.02e+03⟨−83.0°⟩	M_A4.23e+04⟨+137.9°⟩	M_A4.12e+04⟨−88.5°⟩	M_A2.04e+04⟨−92.7°⟩	M_A4.26e+05⟨+19.5°⟩

1223.0 Hz	1224.1 Hz	1328.0 Hz	1328.8 Hz	2019.3 Hz
MPC 85.7%	MPC 84.6%	MPC 84.3%	MPC 75.9%	MPC 95.0%
M_A4.98e+04⟨−89.0°⟩	M_A4.42e+04⟨−82.1°⟩	M_A2.80e+04⟨−89.8°⟩	M_A5.02e+04⟨−89.3°⟩	M_A4.18e+04⟨−89.2°⟩

2023.8 Hz	2322.0 Hz	2322.5 Hz	2338.1 Hz
MPC 65.7%	MPC 40.1%	MPC 55.9%	MPC 96.0%
M_A1.22e+05⟨+14.4°⟩	M_A9.13e+04⟨−56.0°⟩	M_A1.06e+05⟨−94.0°⟩	M_A1.95e+05⟨−86.8°⟩

Fig. 1.5 Case 1: Modal vector complexity plot, single reference, DOF 1

Case 2:

Modal Vector Complexity Plots

362.6 Hz
MPC 93.2%
M_A1.17e+04⟨−73.7°⟩

363.9 Hz
MPC 84.8%
M_A1.57e+04⟨−80.5°⟩

557.1 Hz
MPC 99.4%
M_A4.08e+04⟨−88.4°⟩

761.2 Hz
MPC 58.1%
M_A6.08e+05⟨−57.0°⟩

764.2 Hz
MPC 98.7%
M_A1.97e+04⟨−91.5°⟩

1223.0 Hz
MPC 86.1%
M_A4.37e+04⟨−86.5°⟩

1224.1 Hz
MPC 75.9%
M_A8.92e+04⟨+41.3°⟩

1328.0 Hz
MPC 77.4%
M_A2.81e+04⟨−83.7°⟩

1328.8 Hz
MPC 85.0%
M_A2.82e+04⟨−83.7°⟩

2019.3 Hz
MPC 94.1%
M_A4.16e+04⟨−88.2°⟩

2023.8 Hz
MPC 86.2%
M_A3.37e+04⟨−75.7°⟩

2322.0 Hz
MPC 58.0%
M_A3.71e+04⟨−71.5°⟩

2322.5 Hz
MPC 37.0%
M_A8.18e+04⟨ +4.9°⟩

2338.1 Hz
MPC 95.7%
M_A1.92e+05⟨−91.8°⟩

Fig. 1.6 Case 2: Modal vector complexity plot, single reference, DOF 6

Case 3:

Modal Vector Complexity Plots

362.6 Hz	363.9 Hz	557.1 Hz	761.2 Hz	764.2 Hz
MPC 99.3%	MPC 98.9%	MPC 99.5%	MPC 98.6%	MPC 99.0%
M_A1.07e+04⟨−86.6°⟩	M_A1.51e+04⟨−86.9°⟩	M_A4.13e+04⟨−88.5°⟩	M_A2.03e+04⟨−90.0°⟩	M_A2.02e+04⟨−91.2°⟩

1223.0 Hz	1224.1 Hz	1328.0 Hz	1328.8 Hz	2019.3 Hz
MPC 96.4%	MPC 96.5%	MPC 97.2%	MPC 96.5%	MPC 98.1%
M_A4.92e+04⟨−88.8°⟩	M_A4.94e+04⟨−82.5°⟩	M_A3.24e+04⟨−87.4°⟩	M_A3.15e+04⟨−89.1°⟩	M_A4.39e+04⟨−86.6°⟩

2023.8 Hz	2322.0 Hz	2322.5 Hz	2338.1 Hz
MPC 97.1%	MPC 97.5%	MPC 95.9%	MPC 97.1%
M_A4.74e+04⟨−85.4°⟩	M_A8.69e+04⟨−89.4°⟩	M_A1.07e+05⟨−87.4°⟩	M_A2.07e+05⟨−90.5°⟩

Fig. 1.7 Case 3: Modal vector complexity plot, multiple references, DOFs 1,6

Case 4:

Modal Vector Complexity Plots

362.6 Hz	363.9 Hz	557.1 Hz	761.2 Hz	764.2 Hz
MPC 99.4%	MPC 98.8%	MPC 99.4%	MPC 98.8%	MPC 99.3%
M_A1.11e+04⟨−87.1°⟩	M_A1.52e+04⟨−87.7°⟩	M_A4.19e+04⟨−88.9°⟩	M_A2.07e+04⟨−90.0°⟩	M_A2.09e+04⟨−91.9°⟩

1223.0 Hz	1224.1 Hz	1328.0 Hz	1328.8 Hz	2019.3 Hz
MPC 97.2%	MPC 97.8%	MPC 96.0%	MPC 98.0%	MPC 98.5%
M_A5.30e+04⟨−89.6°⟩	M_A6.02e+04⟨−90.6°⟩	M_A3.19e+04⟨−87.4°⟩	M_A3.14e+04⟨−90.6°⟩	M_A4.47e+04⟨−87.4°⟩

2023.8 Hz	2322.0 Hz	2322.5 Hz	2338.1 Hz
MPC 96.1%	MPC 97.5%	MPC 97.3%	MPC 94.9%
M_A4.43e+04⟨−87.5°⟩	M_A9.39e+04⟨−86.3°⟩	M_A1.12e+05⟨−90.5°⟩	M_A2.03e+05⟨−94.4°⟩

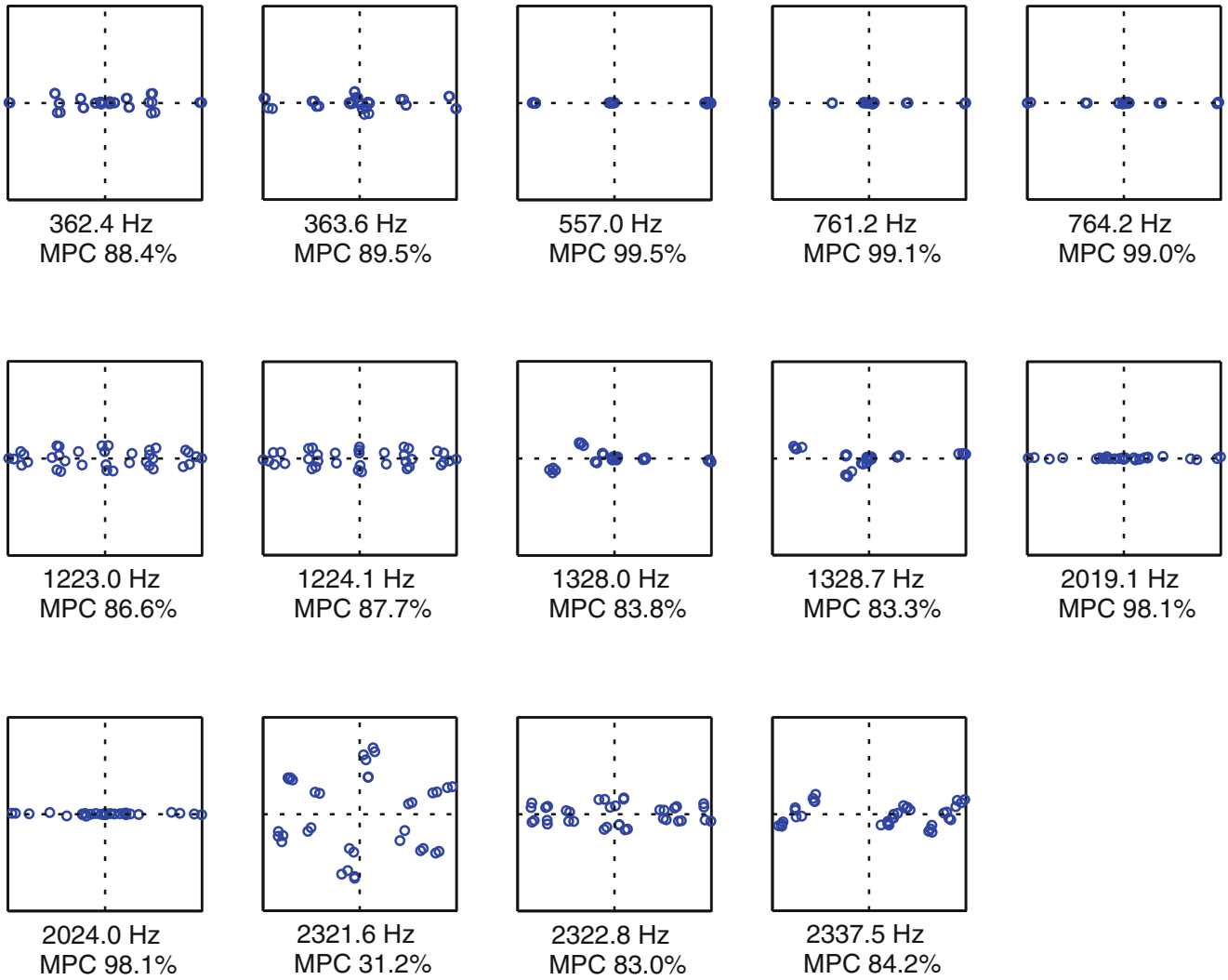**Fig. 1.8** Case 4: Modal vector complexity plot, multiple references, all DOFs

Case 5:

Modal Vector Complexity Plots

| 362.4 Hz | 363.6 Hz | 557.0 Hz | 761.2 Hz | 764.2 Hz |
| MPC 88.4% | MPC 89.5% | MPC 99.5% | MPC 99.1% | MPC 99.0% |

| 1223.0 Hz | 1224.1 Hz | 1328.0 Hz | 1328.7 Hz | 2019.1 Hz |
| MPC 86.6% | MPC 87.7% | MPC 83.8% | MPC 83.3% | MPC 98.1% |

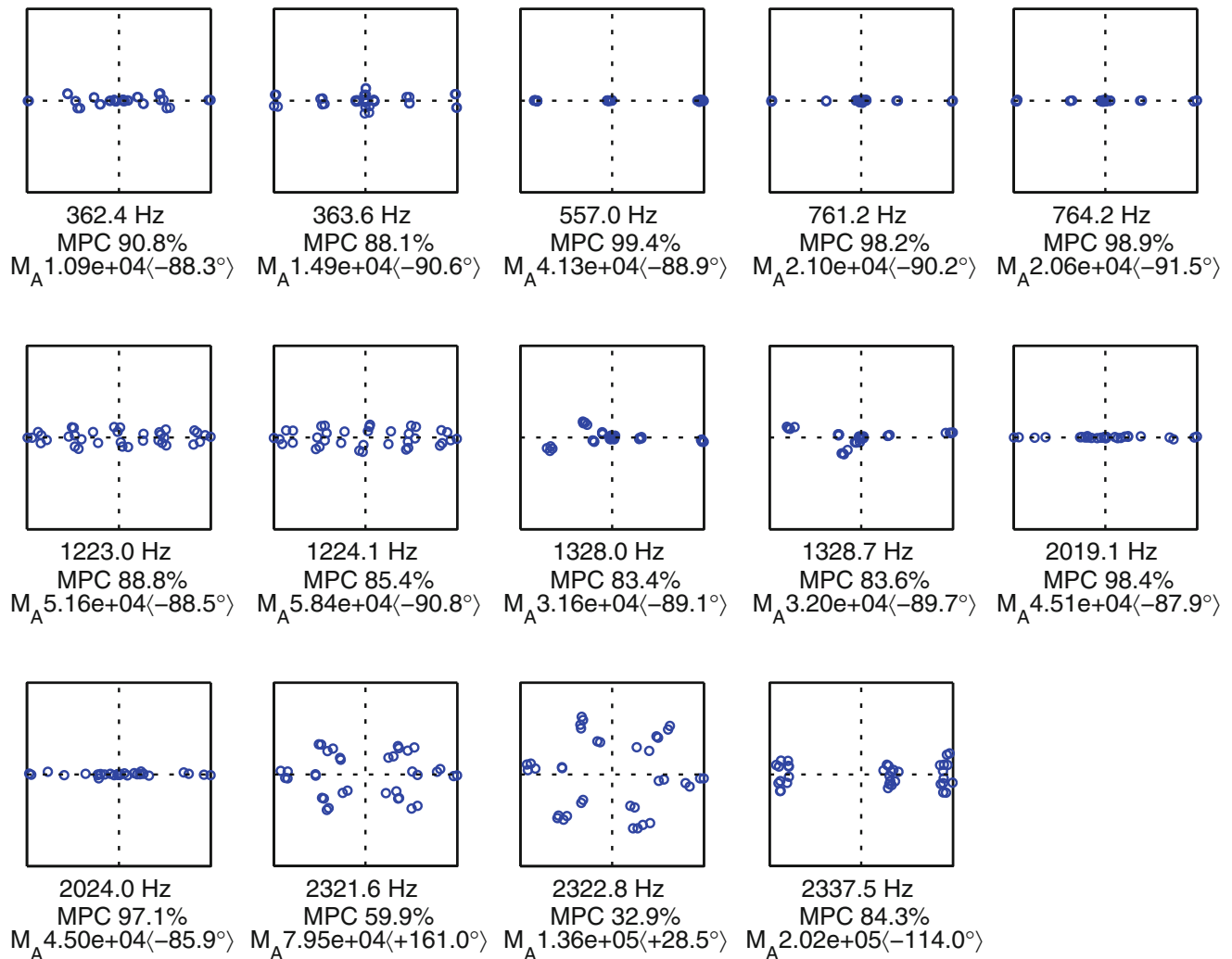| 2024.0 Hz | 2321.6 Hz | 2322.8 Hz | 2337.5 Hz |
| MPC 98.1% | MPC 31.2% | MPC 83.0% | MPC 84.2% |

Fig. 1.9 Case 5: Modal vector complexity plot, multiple references, all DOFs

Case 7:

Modal Vector Complexity Plots

362.4 Hz	363.6 Hz	557.0 Hz	761.2 Hz	764.2 Hz
MPC 99.0%	MPC 98.8%	MPC 99.4%	MPC 98.9%	MPC 99.3%
M_A1.07e+04⟨−88.8°⟩	M_A1.43e+04⟨−89.6°⟩	M_A4.06e+04⟨−88.7°⟩	M_A2.02e+04⟨−90.3°⟩	M_A1.99e+04⟨−91.9°⟩

1223.0 Hz	1224.1 Hz	1328.0 Hz	1328.7 Hz	2019.1 Hz
MPC 97.7%	MPC 96.6%	MPC 95.9%	MPC 97.7%	MPC 98.3%
M_A5.28e+04⟨−89.0°⟩	M_A6.08e+04⟨−89.8°⟩	M_A2.93e+04⟨−91.9°⟩	M_A3.12e+04⟨−91.3°⟩	M_A4.31e+04⟨−88.0°⟩

2024.0 Hz	2322.2 Hz	2322.3 Hz	2337.5 Hz
MPC 95.0%	MPC 95.3%	MPC 97.3%	MPC 96.2%
M_A4.18e+04⟨−84.7°⟩	M_A9.41e+04⟨−89.4°⟩	M_A1.72e+05⟨−86.1°⟩	M_A2.29e+05⟨−92.8°⟩

Fig. 1.10 Case 7: Modal vector complexity plot, multiple references, all DOFs

Case 9:

Modal Vector Complexity Plots

| 362.6 Hz | 363.9 Hz | 557.1 Hz | 761.2 Hz | 764.2 Hz |
| MPC 94.6% | MPC 92.5% | MPC 99.3% | MPC 98.5% | MPC 98.8% |

| 1223.0 Hz | 1224.1 Hz | 1328.0 Hz | 1328.8 Hz | 2019.4 Hz |
| MPC 92.7% | MPC 84.3% | MPC 84.4% | MPC 85.2% | MPC 96.1% |

| 2023.9 Hz | 2322.0 Hz | 2322.5 Hz | 2338.2 Hz |
| MPC 96.6% | MPC 70.1% | MPC 74.9% | MPC 96.0% |
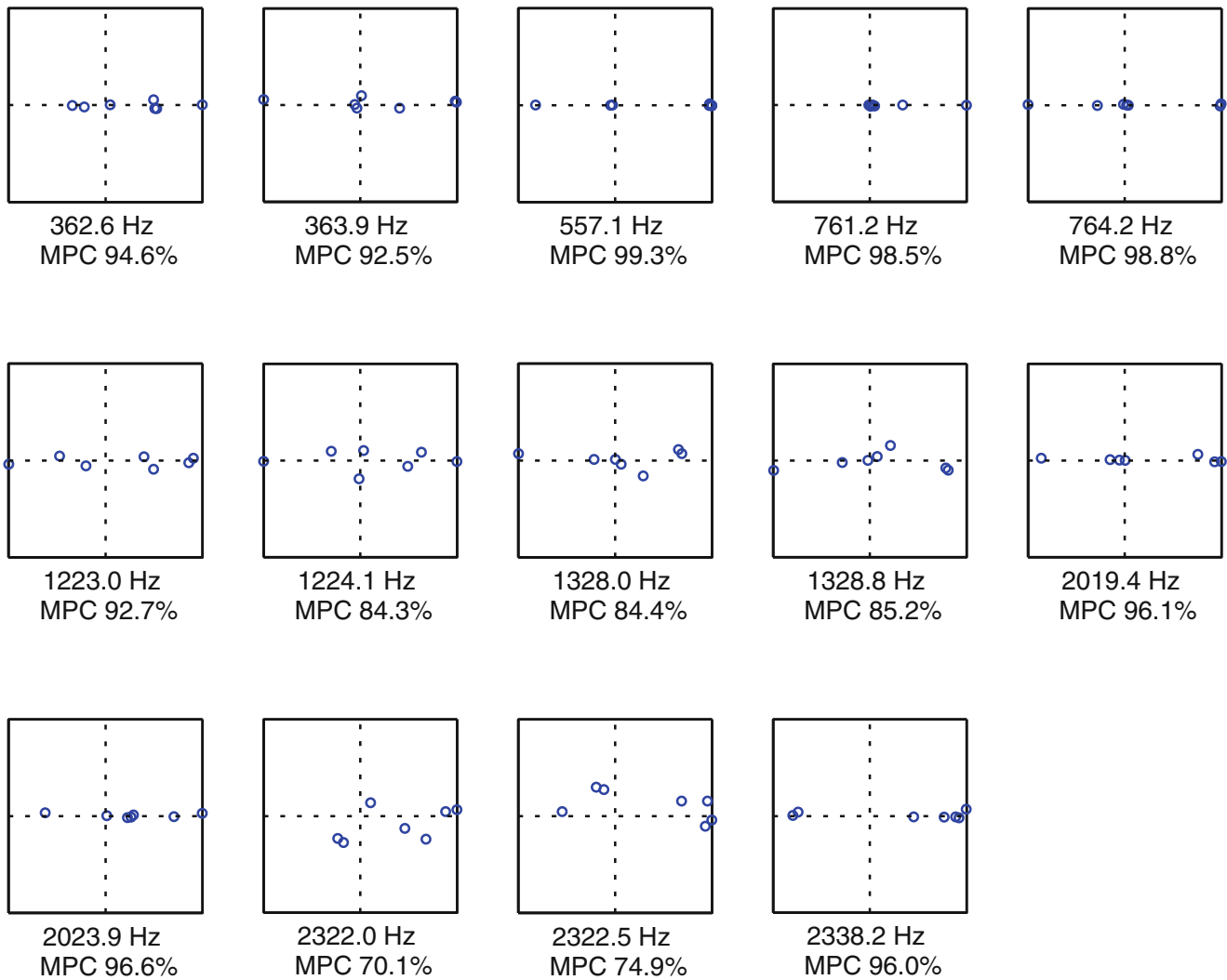
Fig. 1.11 Case 9: Modal vector complexity plot, multiple references, all DOFs

Case 11:

Modal Vector Complexity Plots

362.4 Hz	363.6 Hz	557.0 Hz	761.2 Hz	764.2 Hz
MPC 90.8%	MPC 88.1%	MPC 99.4%	MPC 98.2%	MPC 98.9%
M_A1.09e+04⟨−88.3°⟩	M_A1.49e+04⟨−90.6°⟩	M_A4.13e+04⟨−88.9°⟩	M_A2.10e+04⟨−90.2°⟩	M_A2.06e+04⟨−91.5°⟩
1223.0 Hz	1224.1 Hz	1328.0 Hz	1328.7 Hz	2019.1 Hz
MPC 88.8%	MPC 85.4%	MPC 83.4%	MPC 83.6%	MPC 98.4%
M_A5.16e+04⟨−88.5°⟩	M_A5.84e+04⟨−90.8°⟩	M_A3.16e+04⟨−89.1°⟩	M_A3.20e+04⟨−89.7°⟩	M_A4.51e+04⟨−87.9°⟩
2024.0 Hz	2321.6 Hz	2322.8 Hz	2337.5 Hz	
MPC 97.1%	MPC 59.9%	MPC 32.9%	MPC 84.3%	
M_A4.50e+04⟨−85.9°⟩	M_A7.95e+04⟨+161.0°⟩	M_A1.36e+05⟨+28.5°⟩	M_A2.02e+05⟨−114.0°⟩	

Fig. 1.12 Case 11: Modal vector complexity plot, multiple references, all DOFs

References

1. Wilkinson, J.H.: The Algebraic Eigenvalue Problem. Oxford University Press, Oxford (1965)
2. Phillips, A.W., Allemang, R.J.: Normalization of experimental modal vectors to remove modal vector contamination. In: Proceedings, International Modal Analysis Conference (IMAC), p. 12 (2014)
3. Allemang, R.J., Phillips, A.W.: Un-weighted and weighted versions of the modal assurance criterion (MAC) for evaluation of modal vector contamination. In: Proceedings, International Modal Analysis Conference (IMAC), p. 12 (2014)
4. Allemang, R.J., Phillips, A.W.: The unified matrix polynomial approach to understanding modal parameter estimation: an update. In: Proceedings, International Seminar on Modal Analysis (ISMA), p. 34 (2004)
5. Allemang, R.J., Phillips, A.W.: Spatial information in autonomous modal parameter estimation. Shock. Vib. J. Special ICEDYN Issue, (2014)
6. Allemang, R.: The modal assurance criterion (MAC): twenty years of use and abuse. Sound Vib. Mag. **37**(8), 14–23 (2003)

7. Phillips, A.W., Allemang, R.J., Brown, D.: Autonomous modal parameter estimation: methodology. In: Proceedings, International Modal Analysis Conference (IMAC), p. 22 (2011)
8. Allemang, R.J., Phillips, A.W., Brown, D.: Autonomous modal parameter estimation: statistical considerations. In: Proceedings, International Modal Analysis Conference (IMAC), p. 17 (2011)
9. Brown, D.L., Allemang, R.J., Phillips, A.W.: Autonomous modal parameter estimation: application examples. In: Proceedings, International Modal Analysis Conference (IMAC), p. 17 (2011)
10. Juang, J.N., Pappa, R.S.: An eigensystem realization algorithm for modal parameter identification and model reduction. AIAA J. Guid. Control. Dyn. **8**(4), 620–627 (1985)
11. Juang, J.N.: Mathematical correlation of modal parameter identification methods via system realization theory. J. Anal. Exp. Modal Anal. **2**(1), 1–18 (1987)
12. Van der Auweraer, H., Guillaume, P., Verboven, P., Vanlanduit, S.: Application of a fast-stabilizing frequency domain parameter estimation method. ASME J. Dyn. Syst. Meas. Control **123**(4), 651–658 (2001)
13. Verboven, P., Guillaume, P., Cauberghe, B., Parloo, E., Vanlanduit, S.: *Stabilization charts and uncertainty bounds for frequency domain linear least squares estimators*. Proceedings, International Modal Analysis Conference (IMAC), p. 10 (2003)
14. Verboven, P., Cauberghe, B., Vanlanduit, S., Parloo, E., Guillaume, P.: The secret behind clear stabilization diagrams: the influence of the parameter constraint on the stability of the poles. Proceedings, Society of Experimental Mechanics (SEM) Annual Conference, p. 17 (2004)

Chapter 2
Using Singular Value Decomposition to Estimate Frequency Response Functions

Kevin L. Napolitano

Abstract This paper uses singular value decomposition as an estimator to calculate frequency response functions (FRFs). Both reference and response spectral data are used to estimate a set of orthogonal basis vectors. The basis vectors are used to calculate estimates of the reference and response spectra, which are then used to calculate FRF matrices. It is shown that a singular value decomposition based FRF technique is equivalent to the H_V method for a single response and that a subset of both reference and response vectors can be used to generate the basis vectors. A generalized version of the H_2 method can be derived if only response data is used to generate the basis vectors. The calculation of multiple coherence with respect to different FRF estimators is discussed. A comparison between the different FRF estimators is presented using test data.

Keywords Frequency response function • Singular value decomposition • Eigenvalue analysis • Multiple coherence • Total least squares

2.1 Introduction

A typical modal test involves measuring frequency response functions (FRFs) from inputs that are typically excitation forces and outputs that are typically accelerometers. Inputs are defined here as the controlled inputs into a structure, and output as uncontrolled response due to the inputs. Responses and references are respectively defined as the numerator and denominator terms in the FRF. The references are usually the input measurements, and the responses are usually the output measurements. In some cases, such as transmissibility measurements, outputs are used as references.

The use of linear algebra to estimate FRFs is well established [1, 2]. Least-squares techniques are used to derive the FRF estimators H_1 and H_2, and eigenvalue analysis is used to derive the H_V FRF estimator. The original goal of this internal research project was to determine whether singular value decomposition (SVD), a linear algebra technique that has gained wide acceptance in structural dynamics [3, 4], can also be used to estimate FRFs.

This paper uses singular value decomposition to calculate FRFs. Both reference and response spectral data are used to estimate a set of orthogonal basis vectors equal to the number of independent inputs. The basis vectors are used to calculate estimates of the reference and response spectra, which are then used to calculate FRF matrices.

First, a review of H_1 and H_2 is presented, followed by a review of singular value decomposition. Then an SVD-based FRF estimator, H_{SVD}, is derived and is shown to be equivalent to a generalized version of the H_V estimator. The SVD methodology is derived for the most generalized case where a partial set of inputs and outputs is used to calculate the basis vectors. An equation for multiple coherence that is valid for all FRF estimators is presented. A comparison between H_1, H_{SVD}, H_V, and a generalized version of H_2 is presented showing that obtaining high-quality FRFs depends upon the selection of a set of channels that can adequately represent the proper basis vectors.

K.L. Napolitano (✉)

ATA Engineering, Inc., 13290 Evening Creek Drive South, Suite 250, San Diego, CA 92128, USA

e-mail: kevin.napolitano@ata-e.com

2.2   Review of FRF Estimators

An FRF matrix is a linear estimate of several responses at a given frequency due to several inputs at that same frequency. The equation for an FRF at a single frequency is

$$
\begin{bmatrix} H(\omega) \\ {\scriptstyle N_{RES} \times N_{REF}} \end{bmatrix} \begin{bmatrix} X(\omega) \\ {\scriptstyle N_{REF} \times N_S} \end{bmatrix} = \begin{bmatrix} Y(\omega) \\ {\scriptstyle N_{RES} \times N_S} \end{bmatrix}
\tag{2.1}
$$

The matrix $[H]$ is the FRF matrix at a given frequency ω. Hereafter, the frequency notation is removed and it should be assumed that all matrices presented in this paper correspond to a single frequency. The matrices $[X]$ and $[Y]$ contain the spectral data, usually from a Fourier transform of time-history data, for all the reference and response channels, respectively. The number of rows and columns in $[H]$ are equal to the number of response (N_{RES}) and reference (N_{REF}) channels, respectively, and the number of rows in $[X]$ and $[Y]$ are equal to N_{REF} and N_{RES}, respectively. The number of columns in $[X]$ and $[Y]$ are equal to the number of samples (N_s) used to estimate the FRF matrix. Note that N_s is defined here as the number of events used to estimate the FRF. If the Welch method [5] is used, then N_s is the number of frames of time-history data converted to the frequency domain. If the Daniell method [6] is used, then N_s is the number of spectral lines near the frequency of interest that are used to estimate the FRF.

Equation (2.1) can be reordered by taking the conjugate transpose (i.e., Hermitian), which leads to the standard format for a least-squares solution [7].

$$
[X]^H [H]^H = [Y]^H
\tag{2.2}
$$

Every FRF estimator based on linear algebra follows the same procedure:

1. Define a set of basis vectors that can adequately represent the columns of $[X]^H$ and $[Y]^H$.
2. Use the basis vectors to estimate references and responses. These estimates are defined here as $\left[\tilde{X}\right]^H$ and $[\tilde{Y}]^H$, respectively.
3. Solve for the FRF matrix using estimated reference and response channels as inputs such that

$$
\left[\tilde{X}\right]^H [H]^H = \left[\tilde{Y}\right]^H
\tag{2.3}
$$

2.2.1   Review of H_1

The traditional description of the H_1 method assumes that there is no error on the references and derives an expression to minimize the error on the responses in a least-squares sense. Another way to consider H_1 is that the columns of $[X]^H$ are the basis vectors that are used to describe both the reference and response spectral matrices. Thus the estimated values are a linear combination of the basis vectors such that

$$
\left[\tilde{X}\right]^H = [X]^H [C_X] \quad \text{and} \quad [\tilde{Y}]^H = [X]^H [C_Y]
\tag{2.4}
$$

The constant matrices $[C_X]$ and $[C_Y]$ are solved for by substituting the measured values for the estimated values. The matrix $[C_Y]$ is solved for in a least-squares sense such that $[C_Y] = \left([X][X]^H\right)^{-1} [X][Y]^H$. The matrix $[C_X]$ is the identity matrix since the estimated references are equal to the measured references. Therefore
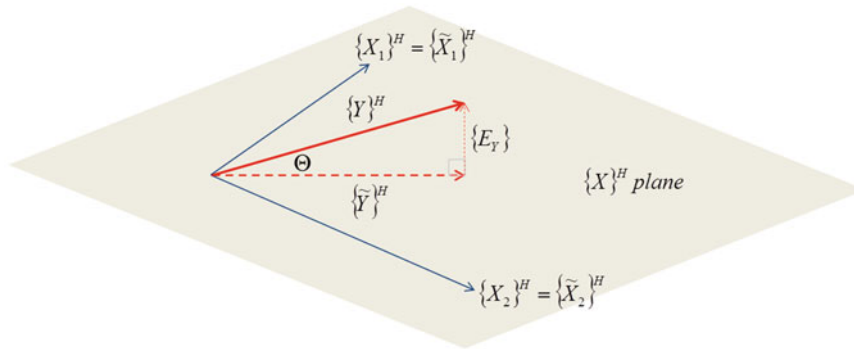
$$
\left[\tilde{X}\right]^H = [X]^H \quad \text{and} \quad [\tilde{Y}]^H = [X]^H \left([X][X]^H\right)^{-1} [X][Y]^H
\tag{2.5}
$$

Substituting Eq. (2.5) into Eq. (2.3) leads to

$$
[X]^H [H_1]^H = [X]^H \left([X][X]^H\right)^{-1} [X][Y]^H
\tag{2.6}
$$
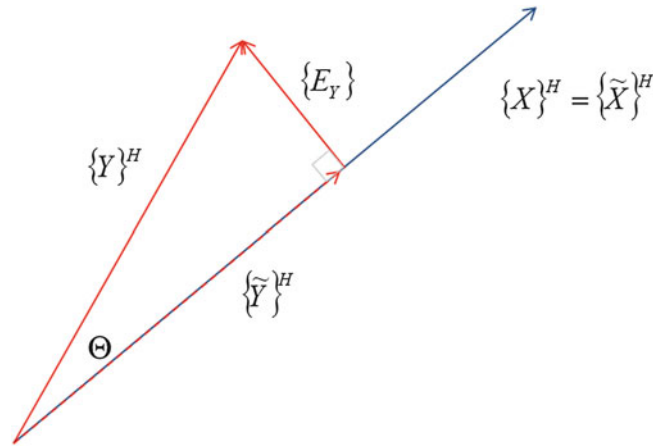
Fig. 2.1 Geometric representation of H_1: single input. The column vector $\{Y\}^H$ is projected onto the basis vector $\{X\}^H$

Fig. 2.2 Geometric representation of H_1: multiple input. Each column vector in $[Y]^H$ is projected onto the plane formed by the basis vectors in $[X]^H$

After pre-multiplying by the pseudo-inverse of $[X]^H$, the conjugate transpose can be taken to obtain the familiar equation for $[H_1]$ as
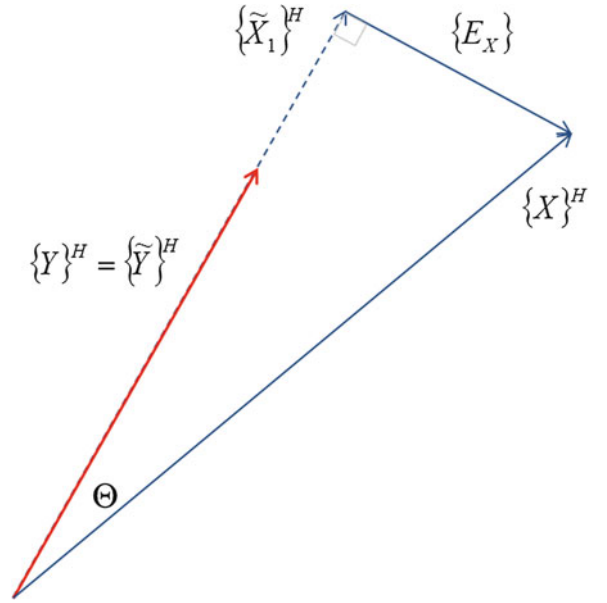
$$[H_1] = [Y][X]^H \big([X][X]^H\big)^{-1} = [S_{YX}][S_{XX}]^{-1}. \tag{2.7}$$

This derivation emphasizes that the main assumption in calculating $[H_1]$ is that both the reference and response channels are estimated from a set of basis vectors, which in this case are the columns of the matrix $[X]^H$. This can be represented geometrically for a single reference as in Fig. 2.1 and for multiple references as in Fig. 2.2. For H_1, the estimate value $\big[\tilde{X}\big]^H$ is taken to be the same as the true value $[X]^H$, and the columns of $[\tilde{Y}]^H$ are a projection of the columns of $[Y]^H$ onto the columns of the basis vectors in $[X]^H$. The resulting error E_y is orthogonal to the estimate.

2.2.2 Review of H_2

The traditional description of the H_2 method assumes that there is no error on the responses and derives an expression to minimize the error on the references in a least-squares sense. Another way to consider H_2 is that the columns of $[Y]^H$ are the basis vectors that are used to describe both the reference and response spectral matrices. Thus, the reference channels $[X]^H$ are a linear combination of the responses. In practice, FRFs are calculated using H_2 when there is a single reference or in the rare case where the number of responses is equal to the number of references. However, the derivation of a generalized version of H_2 given later in this paper allows an unlimited number of responses to be used to estimate the basis vectors.

First, the estimate $\left[\tilde{X}\right]^H$ must be calculated as a linear combination of the columns of $[Y]^H$, or $\left[\tilde{X}\right]^H = [Y]^H [C_X]$. The matrix $[C_X]$ can be solved for in a least-squares sense such that $[C] = \left([Y][Y]^H\right)^{-1} [Y][X]^H$. Therefore

$$\left[\tilde{X}\right]^H = [Y]^H \left([Y][Y]^H\right)^{-1} [Y][X]^H. \tag{2.8}$$

Since the columns of $[Y]^H$ are used as basis vectors, the matrix $[C_Y]$ is the identity matrix, and therefore

$$\left[\tilde{Y}\right]^H = [Y]^H. \tag{2.9}$$

The estimates can then be substituted into the equation for the FRF, $\left[\tilde{X}\right]^H [H_2]^H = \left[\tilde{Y}\right]^H$. Thus,

$$[Y]^H \left([Y][Y]^H\right)^{-1} [Y][X]^H [H_2]^H = [Y]^H. \tag{2.10}$$

Using the same procedure as for H$_1$, the final version of H$_2$ is

$$[H_2] = [S_{YY}][S_{XY}]^{-1}. \tag{2.11}$$

Since an inverse is taken, the number of linearly independent columns in $[Y]^H$ must be equal to the number of linearly independent columns in $[X]^H$. Otherwise the $[S_{XY}]$ matrix is not invertible.

This can be represented graphically for a single reference as in Fig. 2.3. In this case, the vector $\{\tilde{X}\}^H$ is a projection of the columns of $\{X\}^H$ onto the vector $\{Y\}^H$.

2.3   Review of Singular Value Decomposition

Any complex rectangular matrix $[Z]$ can be decomposed such that

$$[U][\Sigma][V]^H = [Z] \tag{2.12}$$

where the left singular matrix $[U]$ and the right singular matrix $[V]$ are unitary; i.e., $[U]^H[U] = [I]$, and $[V]^H[V] = [I]$. The matrix $[\Sigma]$ is a diagonal matrix of real-valued singular values. The singular values represent the contribution of the columns

in $[U]$ and $[V]$ to the matrix $[Z]$. A useful application of SVD is that $[\Sigma]$ and a subset of columns of $[U]$ and $[V]$ can be used to estimate $[Z]$.

$$\left[\tilde{Z}\right] = [U_N]\,[\Sigma_N]\,[V_N]^H \tag{2.13}$$

where $[U_N]$ and $[V_N]$ are the columns of $[U]$ and $[V]$ associated with the N largest singular values and $[\Sigma_N]$ is a diagonal matrix with the N largest singular values.

2.3.1   SVD Relationship to an Eigenvalue Solution

The matrix $[Z]$ can be pre-multiplied by its Hermitian to obtain

$$[V]\,[\Sigma]\,[U]^H\,[U]\,[\Sigma]\,[V]^H = [Z]^H\,[Z]\,. \tag{2.14}$$

Note that $[U]^H\,[U] = [I]$, and therefore

$$[V]\,[\Sigma]^2[V]^H = [Z]^H\,[Z]\,. \tag{2.15}$$

If the result is pre-multiplied by $[V]^H$ and then post-multiplied by $[V]$, the equation becomes

$$[V]^H[Z]^H\,[Z]\,[V] = [\Sigma]^2\,. \tag{2.16}$$

Note that the eigenvalues, $[\Lambda]$, and eigenvectors, $[\Phi]$, of $[Z]^H[Z]$ can be calculated such that

$$[\Phi]^H[Z]^H\,[Z]\,[\Phi] = [\Lambda] \tag{2.17}$$

where the eigenvectors can be scaled such that $[\Phi]^H\,[\Phi] = [I]$, and $[\Lambda]$ is a diagonal matrix.

Therefore, the eigenvectors, $[\Phi]$, and eigenvalues, $[\Lambda]$, of the matrix product $[Z]^H[Z]$ are equivalent to the matrix $[V]$ and the square of the singular value matrix $[\Sigma]$ of the original matrix $[Z]$, respectively. Thus,

$$[\Phi] = [V]\,, \quad \text{and} \quad [\Lambda] = [\Sigma]^2\,. \tag{2.18}$$

One can calculate the singular values or eigenvalues of $[Z]^H[Z]$ to obtain $[V]$ and $[\Sigma]^2$ and then use the relationship

$$[U] = [Z]\,[V]\,[\Sigma]^{-1} \tag{2.19}$$

to obtain the basis vectors $[U]$.

2.4   Derivation of H$_{\text{SVD}}$

The use of singular value decomposition to estimate FRF matrices is equivalent to using a total least-squares approach [8]. Since the response vectors in $[Y]^H$ should be a linear combination of the reference vectors in $[X]^H$, the total number of independent vectors of the combined set of $[X]^H$ and $[Y]^H$ should be equal to the total number of independent inputs. To find the dominant vectors associated with both the response and reference, one can assemble both reference and response vectors into a full matrix,

$$[W]^H = \left[\,[X]^H\ [Y]^H\,\right] = [U_W]\,[\Sigma_W]\,[V_W]^H, \tag{2.20}$$

and then solve for its singular values. Assume the matrices are sorted by decreasing singular value such that the largest singular value is first; these matrices can be partitioned into the first N_{ref} columns, represented by the subscript R, and the remaining columns that are represented by the subscript O. The matrices can then be partitioned as follows:

$$[U_W] = \left[[U_{WR}] \, [U_{WO}] \right], \quad [V_W] = \left[[V_{WR}] \, [V_{WO}] \right], \quad \text{and} \quad [\Sigma_W] = \begin{bmatrix} [\Sigma_{WR}] & [0] \\ [0] & [\Sigma_{WO}] \end{bmatrix} \tag{2.21}$$

Furthermore, $[V_W]$ can be partitioned into rows corresponding to the references and responses such that

$$[V_W] = \left[[V_{WR}] \, [V_{WO}] \right] = \begin{bmatrix} [V_{WXR}] & [V_{WXO}] \\ [V_{WYR}] & [V_{WYO}] \end{bmatrix}. \tag{2.22}$$

Since there are N_{REF} references, $[W]^H$ can be represented by the first N_{REF} singular value vectors. Thus,

$$\left[\tilde{W} \right]^H = [U_{WR}] [\Sigma_{WR}] [V_{WR}]^H. \tag{2.23}$$

Expanding this equation yields

$$\left[[\tilde{X}]^H \, [\tilde{Y}]^H \right] = [U_{WR}] [\Sigma_{WR}] \left[[V_{WXR}]^H \, [V_{WXR}]^H \right]. \tag{2.24}$$

Therefore,

$$[\tilde{X}]^H = [U_{WR}] [\Sigma_{WR}] [V_{WXR}]^H, \quad \text{and} \quad [\tilde{Y}]^H = [U_{WR}] [\Sigma_{WR}] [V_{WYR}]^H. \tag{2.25}$$

The estimated vectors can be geometrically viewed as shown in Fig. 2.4. In this case, the estimates of the reference and response vectors are projections to the basis vectors calculated from the singular value decomposition.

Note that $[\tilde{X}]^H [H_{SVD}]^H = [\tilde{Y}]^H$. Substituting in the estimates of $[X]^H$ and $[Y]^H$ leads to an estimate of $[H_{SVD}]$ such that

$$[U_{WR}] [\Sigma_{WR}] [V_{WXR}]^H [H_{SVD}]^H = [U_{WR}] [\Sigma_{WR}] [V_{WXR}]^H. \tag{2.26}$$

Pre-multiplying by $[\Sigma_{WR}]^{-1} [U_{WR}]^H$ and taking the Hermitian leads to

$$[H_{SVD}] = [V_{WYR}] [V_{WXR}]^{-1}. \tag{2.27}$$
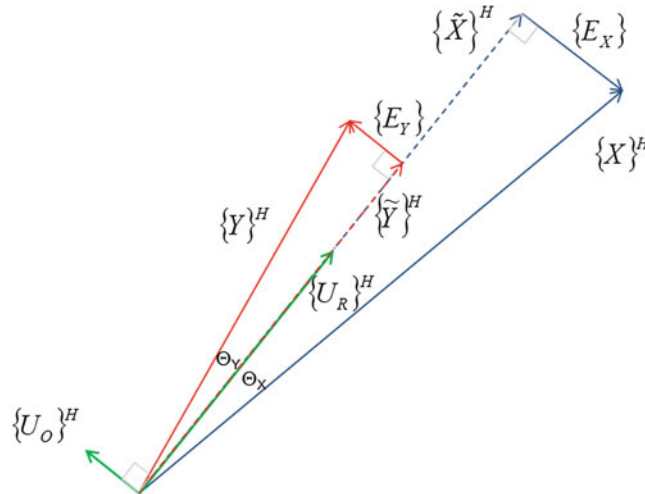
Fig. 2.4 Geometric representation of H_{SVD}. The column vectors of $[X]^H$ and $[Y]^H$ are projected onto the singular value basis vectors $[U]$

Since the left singular vectors $[U_W]$ are not used explicitly, it is more efficient to calculate the singular values (or eigenvalues) of $[W][W]^H$ to obtain the right singular vectors $[V_W]$. Thus,

$$[S_{WW}] = [W][W]^H = \begin{bmatrix} [X][X]^H & [X][Y]^H \\ [Y][X]^H & [Y][Y]^H \end{bmatrix} = \begin{bmatrix} [S_{XX}] & [S_{XY}] \\ [S_{YX}] & [S_{YY}] \end{bmatrix} = [V_W][\Sigma_W]^2[V_W]^H \tag{2.28}$$

The procedure for calculating $[H_{SVD}]$ is as follows:

1. Calculate $[S_{XX}]$, $[S_{YY}]$, and $[S_{YX}]$ and assemble them into $[S_{WW}]$ from Eq. (2.28).
2. Calculate the left singular vectors $[V_{WR}]$ from $[S_{WW}]$.
3. Partition $[V_W]$ into $[V_{WR}]$ and $[V_{WO}]$.
4. Calculate $[H_{SVD}]$ from Eq. (2.27).

2.4.1 SVD Using Partial Set of Reference and Response Channels as Basis Vectors

The previous cases show that FRFs can be calculated using different sets of vectors as basis vectors: H_1 uses the references as basis vectors, H_{SVD} uses all reference and response vectors to calculate the basis vectors, and the generalized form of H_2 uses all of the response vectors to calculate the basis vectors. The most general case is where a partial set of reference and response vectors is used to estimate the basis vectors.

The first step is to partition both the references and responses into those that are part of the singular value decomposition, identified by the subscript "P" and hereafter called the partitioned set or P-set, and those that are not part of the singular value decomposition, which are identified by the subscript "Q" and hereafter called the Q-set.

The results of the singular value decomposition on the partitioned set are used to calculate the estimated values for the responses and references that are part of the singular value decomposition. The references and responses not part of the singular value decomposition are calculated as a least-squares fit of the basis vectors, and then the contribution of the basis vector is removed by inverting the results of the singular value decomposition.

First, the reference and response channels are partitioned into P-set and Q-set such that

$$[X]^H = \left[[X_P]^H \ [X_Q]^H \right], \quad \text{and} \quad [Y]^H = \left[[Y_P]^H \ [Y_Q]^H \right]. \tag{2.29}$$

The vectors that are part of the singular value decomposition can be assembled as

$$[W_P]^H = \left[[X_P]^H \ [Y_P]^H \right]. \tag{2.30}$$

Also, the vectors that are not part of the singular value decomposition can be assembled as

$$[W_Q]^H = \left[[X_Q]^H \ [Y_Q]^H \right]. \tag{2.31}$$

Singular value decomposition of $[W_P]^H$ leads to

$$[U_{W_P}][\Sigma_{W_P}][V_{W_P}]^H = [W_P]^H = \left[[X_P]^H \ [Y_P]^H \right]. \tag{2.32}$$

The matrices can be partitioned into the first N_{REF} columns, represented by the subscript "R," and the remaining columns, represented by the subscript "O."

$$[U_{W_P}] = \left[[U_{W_P R}] \ [U_{W_P O}] \right], \quad \text{and} \quad [V_{W_P}] = \left[[V_{W_P R}] \ [V_{W_P O}] \right] \tag{2.33}$$

Furthermore, the matrix $[V_{W_P R}]$ can be partitioned into rows corresponding to the reference and response signals such that

$$[V_{W_P R}] = \begin{bmatrix} [V_{W_P XR}] \\ [V_{W_P YR}] \end{bmatrix}. \tag{2.34}$$

The estimate of the partitioned channels used for singular values can be written as

$$
\begin{aligned}
\left[\tilde{W}_P\right]^H &= [U_{W_PR}] [\Sigma_{W_PR}] [V_{W_PR}]^H \\
&= [U_{W_PR}] [\Sigma_{W_PR}] \left[[V_{W_PXR}]^H \ [V_{W_PYR}]^H \right] \\
&= \left[[\tilde{X}_P]^H \ [\tilde{Y}_P]^H \right].
\end{aligned}
\tag{2.35}
$$

From this, the following relationships can be extracted:

$$
[U_{W_PR}] = \left[\tilde{W}_P\right]^H [V_{W_PR}] [\Sigma_{W_PR}]^{-1}, \quad \left[\tilde{X}_P\right]^H = [U_{W_PR}] [\Sigma_{W_PR}] [V_{W_PXR}]^H, \quad \text{and} \quad \left[\tilde{Y}_P\right]^H = [U_{W_PR}] [\Sigma_{W_PR}] [V_{W_PYR}]^H. \tag{2.36}
$$

Estimates for the references and responses that were not part of the singular value decomposition can be determined by performing a least-squares fit of the vectors and then substituting the basis vectors with measured channels in the partitioned sets.

$$
\begin{aligned}
\left[\tilde{X}_Q\right]^H &= [U_{W_PR}] [U_{W_PR}]^H [X_Q]^H \\
&= [U_{W_PR}] [S_{W_PR}]^{-1} [V_{W_PR}]^H [W_P] [X_Q]^H \\
&= [U_{W_PR}] [\Sigma_{W_PR}]^{-1} [V_{W_PR}]^H [S_{W_PX_Q}].
\end{aligned}
\tag{2.37}
$$

Likewise,

$$
\left[\tilde{Y}_Q\right]^H = [U_{W_PR}] [\Sigma_{W_PR}]^{-1} [V_{W_PR}]^H [S_{W_PY_Q}]. \tag{2.38}
$$

With the estimates for all references and all responses complete, the next step is to assemble them into the estimate for the FRF matrix from the following equation:

$$
[\tilde{X}]^H [H_{SVD_P}]^H = [\tilde{Y}]^H. \tag{2.39}
$$

Direct substitution of the partitioned matrices leads to

$$
\left[[\tilde{X}_P]^H \ [\tilde{X}_Q]^H \right] [H_{SVD_P}]^H = \left[[\tilde{Y}_P]^H \ [\tilde{Y}_Q]^H \right]. \tag{2.40}
$$

Direct substitution of the estimates leads to

$$
\begin{aligned}
&\left[[U_{W_PR}] [\Sigma_{W_PR}] [V_{W_PRX}]^H \ [U_{W_PR}] [\Sigma_{W_PR}]^{-1} [V_{W_PR}]^H [S_{W_PX_Q}] \right] [H_{SVD_P}]^H \\
&= \left[[U_{W_PR}] [\Sigma_{W_PR}] [V_{W_PRY}]^H \ [U_{W_PR}] [\Sigma_{W_PR}]^{-1} [V_{W_PR}]^H [S_{W_PY_Q}] \right].
\end{aligned}
\tag{2.41}
$$

After pre-multiplying both sides by $[U_{W_PR}]^H$, the Hermitian can be taken to obtain

$$
[H_{SVD_P}] = \begin{bmatrix} [V_{W_PRY}] [\Sigma_{W_PR}] \\ [S_{Y_QW_P}] [V_{W_PR}] [\Sigma_{W_PR}]^{-1} \end{bmatrix} \begin{bmatrix} [V_{W_PRX}] [\Sigma_{W_PR}] \\ [S_{X_QW_P}] [V_{W_PR}] [\Sigma_{W_PR}]^{-1} \end{bmatrix}^{-1}. \tag{2.42}
$$

The required cross-spectral matrices for this calculation are $\left[S_{W_PW_Q}\right]$ and $\left[S_{W_PW_P}\right]$.

The procedure for calculating the FRF matrix H_{SVDp} using a subset of channels to form the basis vectors is as follows:

1. Calculate the matrices $[S_{W_PW_P}]$ and $\left[S_{W_QW_P}\right]$.
2. Calculate the singular value matrices $[V_{W_PR}]$ and $[\Sigma_{W_PR}]$ from $[S_{W_PW_P}]$.
3. Calculate the estimates for the reference and response channels from Eqs. (2.36), (2.37), and (2.38).
4. Perform the calculation for $[H_{SVD_p}]$ from Eq. (2.42).

2.4.2   Generalized H_2

The H_2 estimator can be generalized using singular value decomposition by performing a singular value decomposition on all of the output channels and no input channels such that

$$[W_{H2}]^H = [Y]^H. \tag{2.43}$$

The singular value decomposition of the matrix $[Y]^H$ leads to

$$[U_{H2}] [\Sigma_{H2}] [V_{H2}]^H = [Y]^H \tag{2.44}$$

and the partition of the N_{REF} highest singular values as

$$[U_{H2R}] [\Sigma_{H2R}] [V_{H2R}]^H = [\tilde{Y}]^H. \tag{2.45}$$

In this case, the reference channels are not used in the formation of the basis vectors; therefore $[X]^H = [X_Q]^H$. Also, all response channels are used to calculate the basis vectors, so $[Y]^H = [Y_P]^H$. Making the proper substitutions into Eq. (2.42) leads to the equation for a generalized version of the H_2 estimator as

$$[H_2] = [V_{H2R}] [\Sigma_{H2R}] \left[[S_{XY}] [V_{H2R}] [\Sigma_{H2R}]^{-1} \right]^{-1}. \tag{2.46}$$

The procedure for calculating the generalized version of H_2 is as follows:

1. Calculate the matrices $[S_{XY}]$ and $[S_{YY}]$.
2. Calculate the singular value matrices $[V_{H2}]$ and $[\Sigma_{H2}]$ from $[S_{YY}]$.
3. Perform the calculation for $[H_2]$ from Eq. (2.46).

Note that the same two matrices $[S_{XY}]$ and $[S_{YY}]$ are used in the generalized version of H_2 as are used in the original version of H_2.

2.4.3   Review of H_V

The H_V estimator assumes noise in both the input and the output channels [2]. The row of the FRF matrix associated with a given channel "I" is found by solving the following eigenvalue problem:

$$\begin{bmatrix} [S_{XX}] & \{S_{XY_i}\} \\ \{S_{Y_iX}\} & S_{Y_iY_{iI}} \end{bmatrix} = [V] [\Lambda] [V]^H \begin{bmatrix} [V_{XR}] & \{V_{XO}\} \\ \{V_{Y_iR}\} & V_{Y_iO} \end{bmatrix} \begin{bmatrix} [\Lambda_R] & \{0\} \\ \{0\}^T & \Lambda_O \end{bmatrix} \begin{bmatrix} [V_{XR}] & \{V_{XO}\} \\ \{V_{Y_iR}\} & V_{Y_iO} \end{bmatrix}^H \tag{2.47}$$

where the eigenvectors and eigenvalues are the matrices $[V]$ and $[\Lambda]$, respectively. These matrices can be further partitioned as well. The subscript "R" represents the eigenvectors associated with the largest NREF eigenvalues, the subscript "O" corresponds to the lowest eigenvalue, and the subscripts "X" and "Y_1" correspond to the references and the response of a single channel "i," respectively. The ith row of the FRF matrix is then solved for as follows:

$$\{H_{Vi}\} = -V_{Y_iO}^{-H} [V_{XO}]^H. \tag{2.48}$$

2.4.4   Equivalence of H_{SVD} and H_V

The difference in the solution between the H_{SVD} and H_V estimators is that one uses the eigenvectors associated with the largest eigenvalues and the other uses the eigenvectors associated with the lowest eigenvalues. Their equivalence can be shown by investigating the matrix formed by the identity $[V_W]^H [V_W] = [I]$. This matrix can be partitioned as

$$\begin{bmatrix} [V_{WXR}] & [V_{WXO}] \\ [V_{WYR}] & [V_{WYO}] \end{bmatrix}^H \begin{bmatrix} [V_{WXR}] & [V_{WXO}] \\ [V_{WYR}] & [V_{WYO}] \end{bmatrix} = \begin{bmatrix} [I_{RR}] & [0] \\ [0] & [I_{OO}] \end{bmatrix}. \tag{2.49}$$

The left-hand side can be expanded to

$$\begin{bmatrix} [V_{WXR}]^H [V_{WXR}] + [V_{WYR}]^H [V_{WYR}] & [V_{WXR}]^H [V_{WXO}] + [V_{WYR}]^H [V_{WYO}] \\ [V_{WXO}]^H [V_{WXR}] + [V_{WYO}]^H [V_{WYR}] & [V_{WXO}]^H [V_{WXO}] + [V_{WYO}]^H [V_{WYO}] \end{bmatrix} = \begin{bmatrix} [I_{RR}] & [0] \\ [0] & [I_{OO}] \end{bmatrix} \tag{2.50}$$

The lower-left side can be broken out to obtain

$$[V_{WXO}]^H [V_{WXR}] + [V_{WYO}]^H [V_{WYR}] = [0]. \tag{2.51}$$

After post-multiplying by $[V_{WXR}]^{-1}$ and pre-multiplying by $[V_{WYO}]^{-H}$, the equation becomes

$$[V_{WYR}] [V_{WXR}]^{-1} + [V_{WYO}]^{-H} [V_{WXO}]^H = [0]. \tag{2.52}$$

Moving the second term to the right-hand side yields the following relationship:

$$[H_{SVD}] = [V_{WYR}] [V_{WXR}]^{-1} = -[V_{WYO}]^{-H} [V_{WXO}]^H. \tag{2.53}$$

If the singular value decomposition is applied to a single output channel, then the equation above is equivalent to the solution for H_V.

There are two important items to note. The FRF matrix is more efficiently calculated using the smallest eigenvalues if the number of responses is less than the number of references, which is the case with the H_V estimator where the FRF is calculated one response degree of freedom at a time. However, if all response channels are calculated at once, then the FRF matrix is more efficiently calculated using the H_{SVD} method.

Second, since the two solutions are equivalent, the basis vectors used in H_V are determined from the singular value decomposition of $\left[[X]^H \; [Y_i]^H \right]$. Note that the basis vectors change for each row of $[H_V]$ since the eigenvalue solution is calculated for each response.

2.5   Multiple Coherence

Multiple coherence is defined as the correlation coefficient describing the linear relationship between an output and all known inputs [9, 10]. The references used to calculate FRFs are not necessarily the inputs, and the responses are not necessarily the outputs. However, multiple coherence is used to assess the linear relationship between a single response and all measured references as well. The definition of multiple coherence is

$$MCOH_{Yi} = \frac{\{H_{YiX}\} [S_{XX}] \{H_{YiX}\}^H}{S_{YiYi}}, \tag{2.54}$$

where $\{H_{YiX}\}$ is the ith row of the FRF matrix. This definition works well for the H_1 estimator because the basis vectors are the reference channels. However, if we use this definition for other FRF estimators, then multiple coherence values can be greater than one. The matrix $[S_{XX}]$ can be replaced with $[X][X]^H$, and if we note that the basis vectors for H_1 are equal to the references such that $\left[\tilde{X} \right]^H = [X]^H$, and note that $\left[\tilde{X} \right]^H [H]^H = \left[\tilde{Y} \right]^H$, then multiple coherence can be expanded to

$$MCOH_{Yi} = \frac{\{H_{YiX}\} [\tilde{X}] [\tilde{X}]^H \{H_{YiX}\}^H}{S_{YiYi}} = \frac{[\tilde{Y}_i] [\tilde{Y}_i]^H}{S_{YiYi}} = \frac{S_{\tilde{Y}i\tilde{Y}i}}{S_{YiYi}}. \tag{2.55}$$

If this definition is used, then no matter which FRF estimator is used, multiple coherence will range from 0 to 1. Figs. 2.2, 2.3, and 2.4 show that multiple coherence is the square of the cosine of the angle between the estimated and measured response [11]. This definition is valid for reference channels as well, since both reference and response estimates are used to calculate the FRF matrix. If we group the references and responses into a single matrix, $[W]^H$, we can define multiple coherence as

$$MCOH_{Wi} = \frac{\{\tilde{W}_i\}\{\tilde{W}_i\}^H}{\{W_i\}\{W_i\}^H} = \frac{S_{\tilde{W}_i\tilde{W}_i}}{S_{W_iW_i}}. \tag{2.56}$$

Since the calculation of any FRF matrix involves calculating the estimated reference and response vectors, the calculation of multiple coherence is straightforward and can be performed at the same time as the calculation of the FRF matrix.

2.6 Example

The FRF estimation methodology was investigated on a set of test data where traditional FRF estimators were known to produce non-optimal results. The test data was collected during a previous investigation on estimating fixed base modes by using boundary degrees of freedom as references when calculating FRFs [12]. In that investigation it was shown that the H_V method was superior to the H_1 method. However, in some cases neither method adequately estimated the FRF of low-responding channels at resonant frequencies.

The test article, shown in Fig. 2.5, was an aluminum beam vertically cantilevered from a base platform. The aluminum beam was 30.5 cm tall, 2.54 cm thick, and 7.562 cm wide. The beam was bolted to a plate 1.9 cm thick using two bolts and adhered to the plate using superglue in an attempt to mitigate any nonlinearities at the connection between the plate and the beam. The Y-axis in this example is defined as the vertical direction along the length of the beam, the X-axis is in line with the strong axis of the beam, and the Z-axis is in line with the weak axis of the beam. This plate was then bolted to a larger box beam in an attempt to simulate a seismic mass or a shake table. The test article was excited with an impact hammer at several locations, shown by arrows in Fig. 2.5, to generate time-history data. Six rigid body deformations, designated as node 9999 with directions "X+," "Y+," "Z+," "RX+," "RY+," and "RZ+," were estimated from accelerometers mounted on
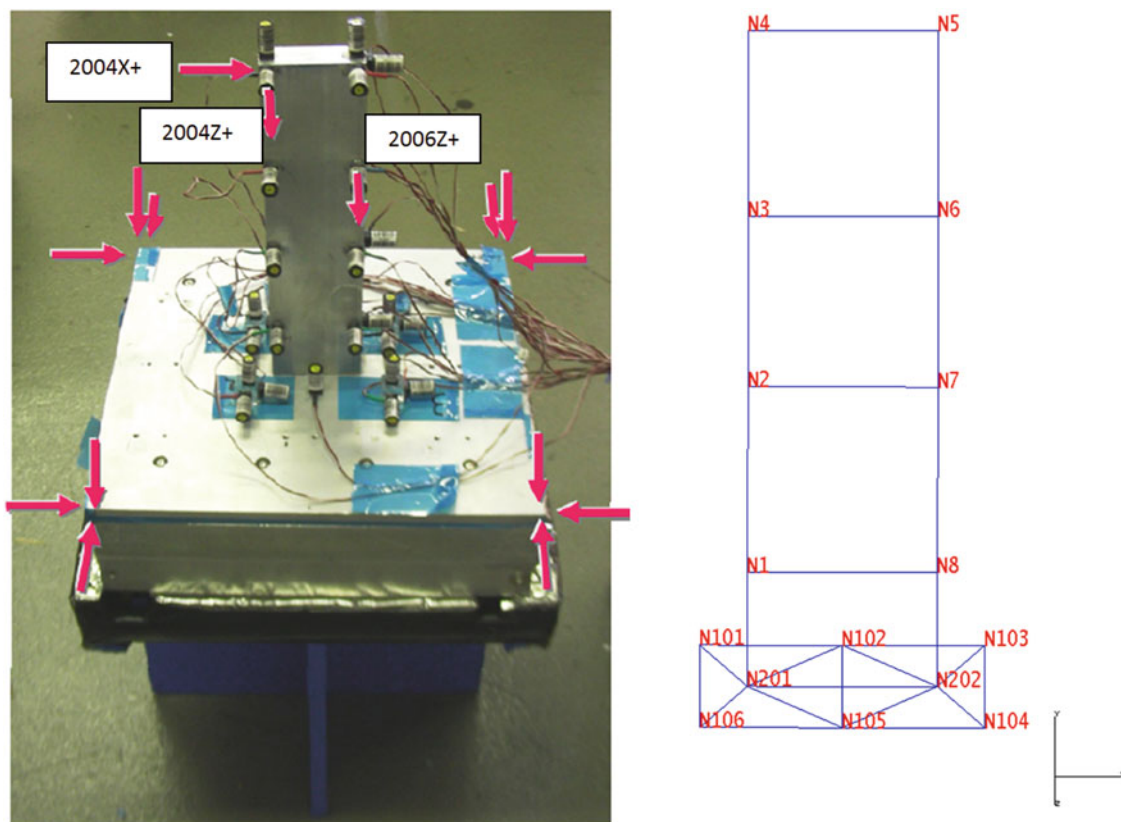
Fig. 2.5 Cantilevered beam mounted to rigid base on soft foam supports, with picture on *left* and test display model identifying test nodes on *right*. Rigid body motion of base plus three impact locations on beam were used as references to calculate FRF

Mode Indicator Function
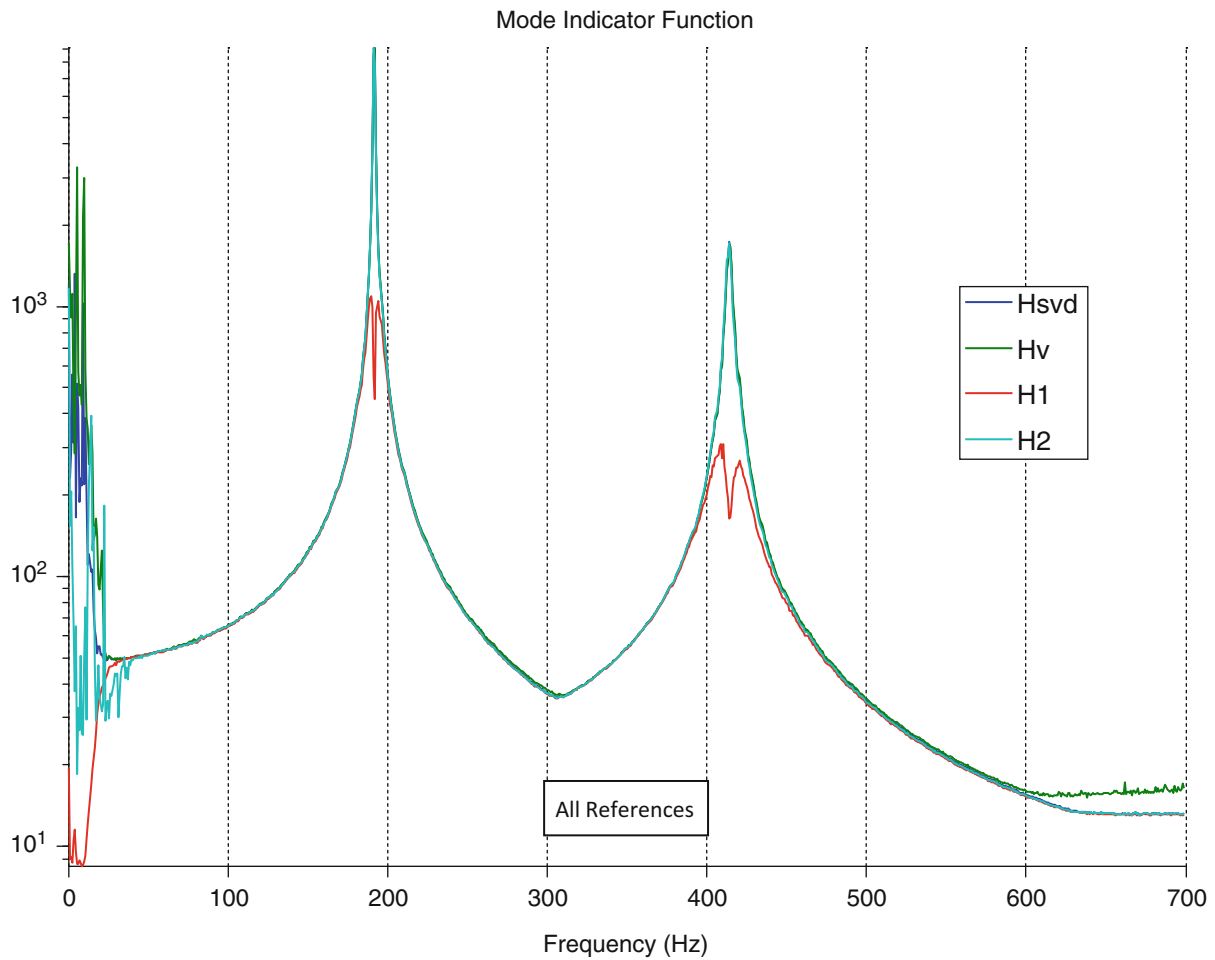
Fig. 2.6 Primary complex mode indicator function using H_{SVD} (*blue*), H_V (*green*), H_1 (*red*), and generalized H_2 (*cyan*)

the base. These six rigid body deformations plus the three forces applied to the beam were used as references when calculating FRFs, for a total of nine reference degrees of freedom. The three forces applied to the beam were near test nodes 4 and 6.

FRF matrices from the H_1, generalized H_2, H_V, and H_{SVD} methods were calculated and compared. The primary curve from the complex mode indicator function (CMIF) from the four estimators is presented in Fig. 2.6. Overall, the H_1 estimator provides a poor estimate of the FRF at resonance. At low frequencies, none of the estimators is able to adequately estimate the FRF. The estimators that are based on singular value decomposition overestimate the FRF. The H_1 estimator underestimates response, which should level out to a constant value of approximately 20 as the frequency approaches zero. The CMIFs were then recalculated using the FRF associated with the three force references and then using the FRF associated with the rigid body base accelerations as references. These CMIFs are shown in Fig. 2.7. The generalized H_2 method poorly estimates the response of the FRF associated with forces at low frequencies. This is likely due to the fact that there are only six independent motions of the structure at low frequencies—the six rigid body modes. To increase that number to the full set of nine independent references, the load cells would need to be part of the basis vector calculation.

The full CMIFs for the H_{SVD} and H_V methods are presented in Fig. 2.8. The CMIF associated with the H_{SVD} estimator is smooth for all singular values. However, the CMIF associated with H_V is not as well behaved near the second resonance at 410 Hz from the fourth-to-last singular value. This summary plot shows that the calculation of the basis vectors from all response coordinates is superior to calculating basis vectors one channel at a time.

Typical estimated FRFs are presented for all methods in Fig. 2.9. Overall, the generalized H_2 method fails at low frequencies, and the H_V method does a poor job of estimating low-responding channels at resonant frequencies. All SVD-based methods perform well when channel response is high. It is believed that the H_{SVD} method performs well near resonance for all channels because having all the channels available allows it to estimate a more accurate set of basis vectors.

A final case was run where one or two accelerometers were added to the references to calculate the basis vectors. The accelerometers added were located at test node 5 in the strong (X) and weak (Z) axes of the beam. Figure 2.10 presents
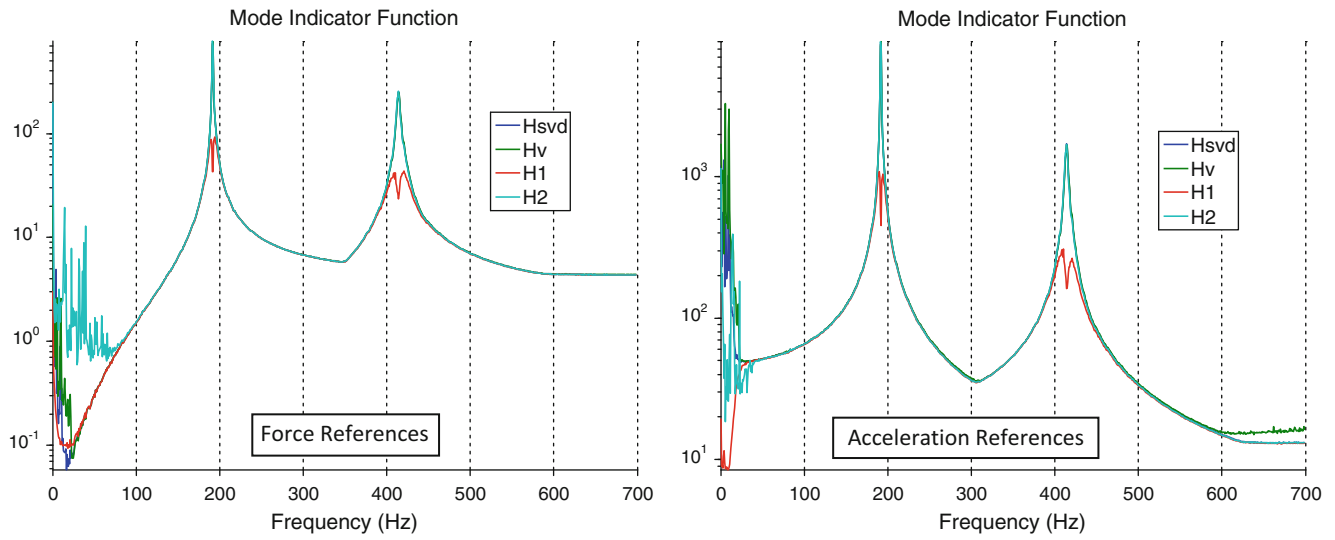
Fig. 2.7 Complex mode indicator function using H_{SVD} (*black*), H_V (*red*), H_1 (*green*), and generalized H_2 (*blue*), using FRFs associated with impact force references (*left*) and with rigid body accelerations (*right*)
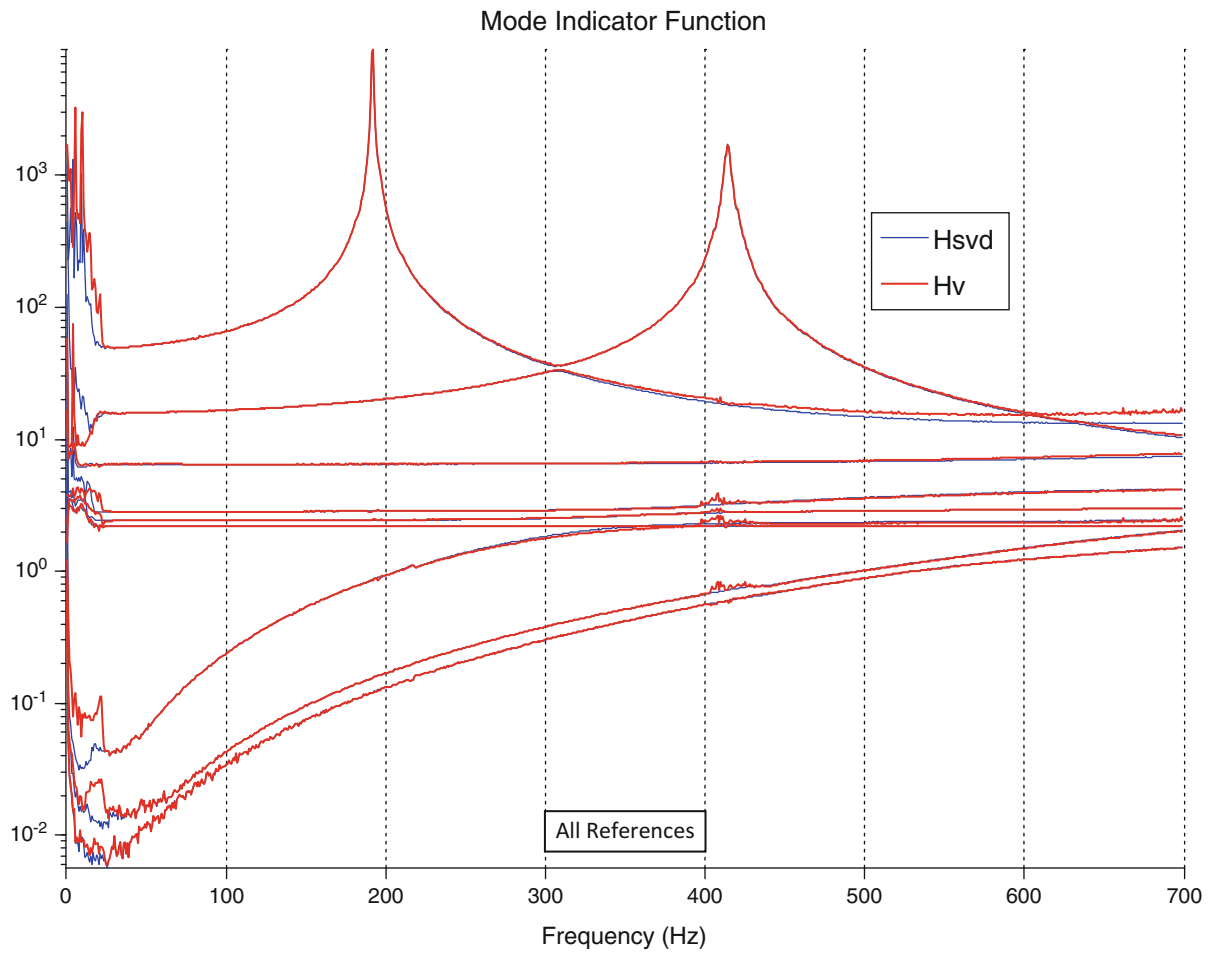
Fig. 2.8 Complex mode indicator function using H_{SVD} (*blue*) and H_V (*red*)
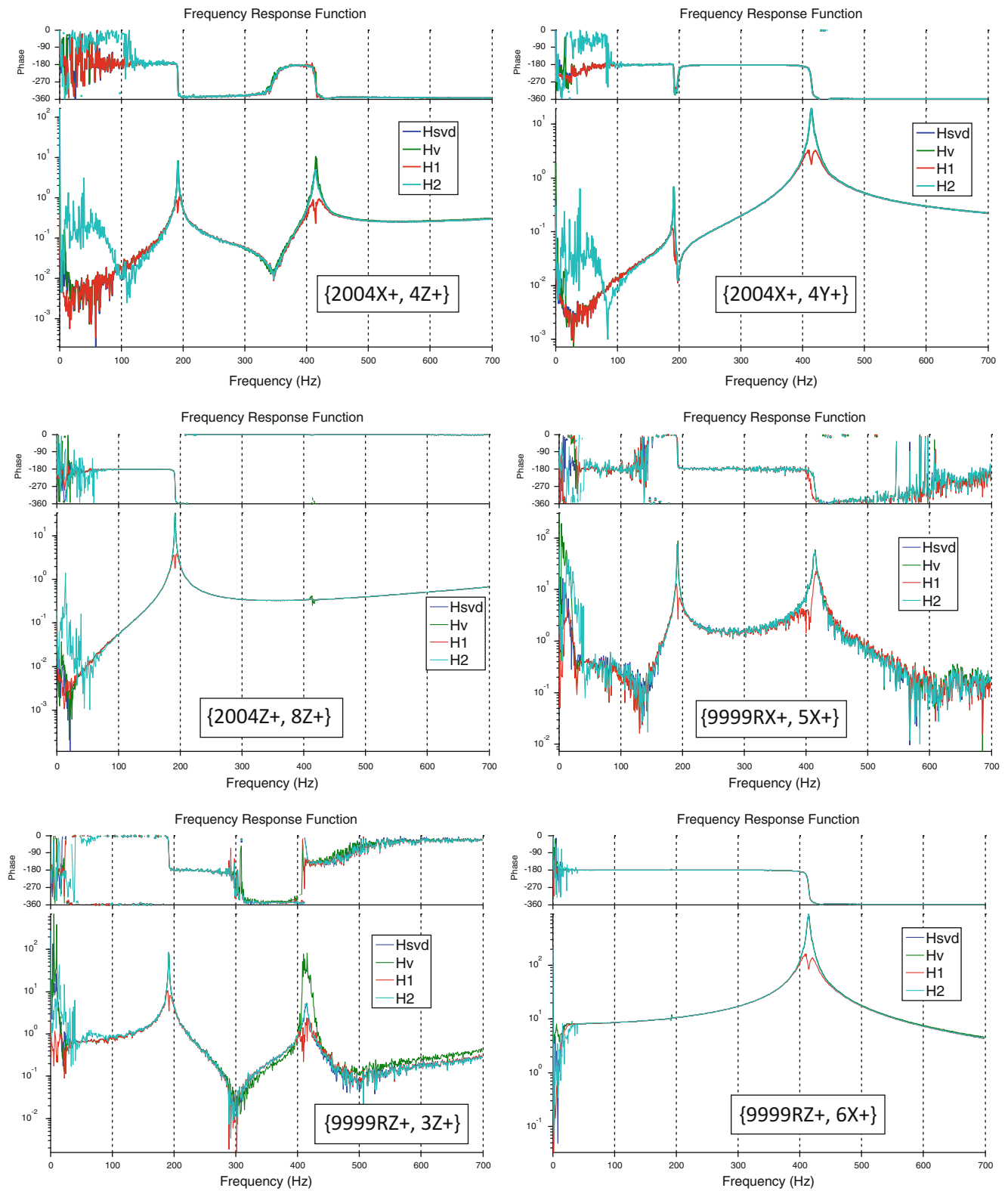
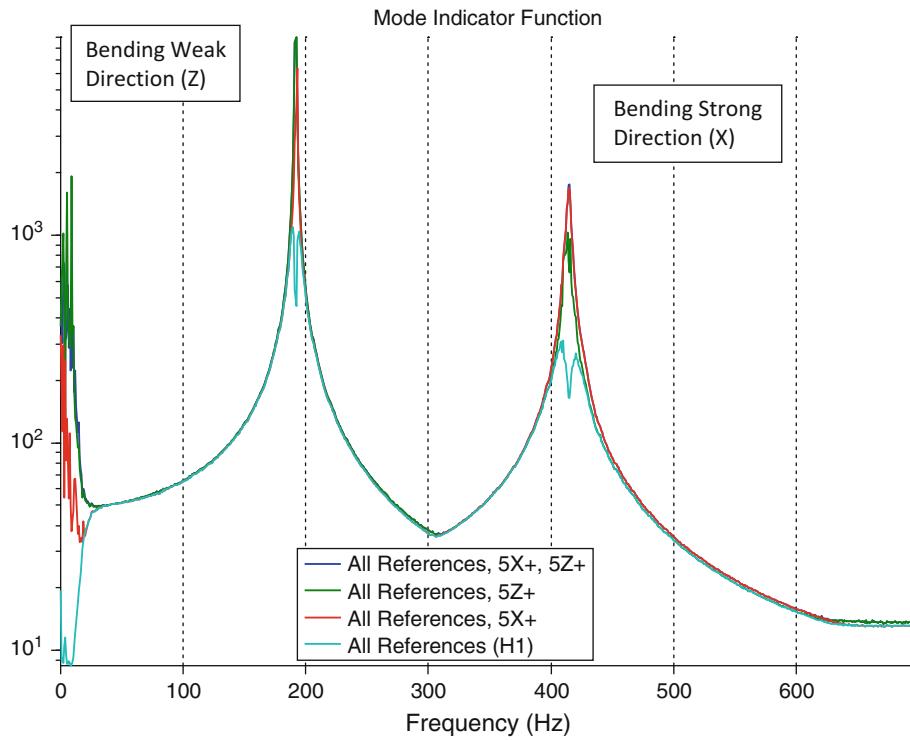**Fig. 2.9** Examples of calculated FRFs using H_{SVD} (*blue*), H_V (*green*), H_1 (*red*), and generalized H_2 (*cyan*)

Fig. 2.10 Primary CMIF using all references and different response channels in singular value decomposition
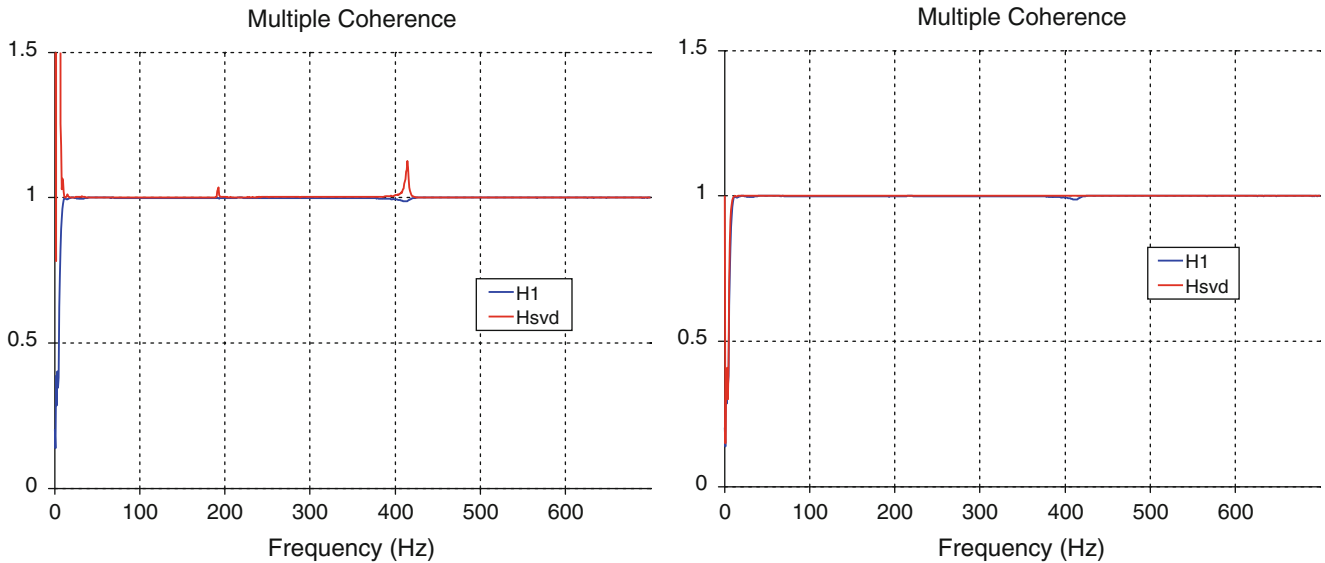
Fig. 2.11 Multiple coherence for response 6X+ using published definition (*left*) and proposed definition (*right*)

the primary CMIF for four cases: 5X+ and 5Z+, 5Z+, 5X+, and no accelerometers. Adding both accelerometers to the singular value decomposition allowed the singular value decomposition to calculate a valid set of basis vectors at resonance, and the resulting FRFs are nearly identical to adding all response channels to the singular value decomposition. There are clear deficiencies in the CMIF in the perpendicular direction when a single accelerometer is added, however. Finally, the results are equivalent to the H_1 estimator when no response channels are used to estimate the basis vectors.

Multiple coherence using the published definition (Eq. (2.54)), and the proposed definition (Eq. (2.56)) for H_1 and H_{SVD} is presented in Fig. 2.11. The published definition of multiple coherence holds for H_1 since the basis vectors in H_1 are the references. However, the published definition leads to a value greater than 1 when H_{SVD} is used because H_{SVD} uses a different set of basis vectors when calculating FRFs.
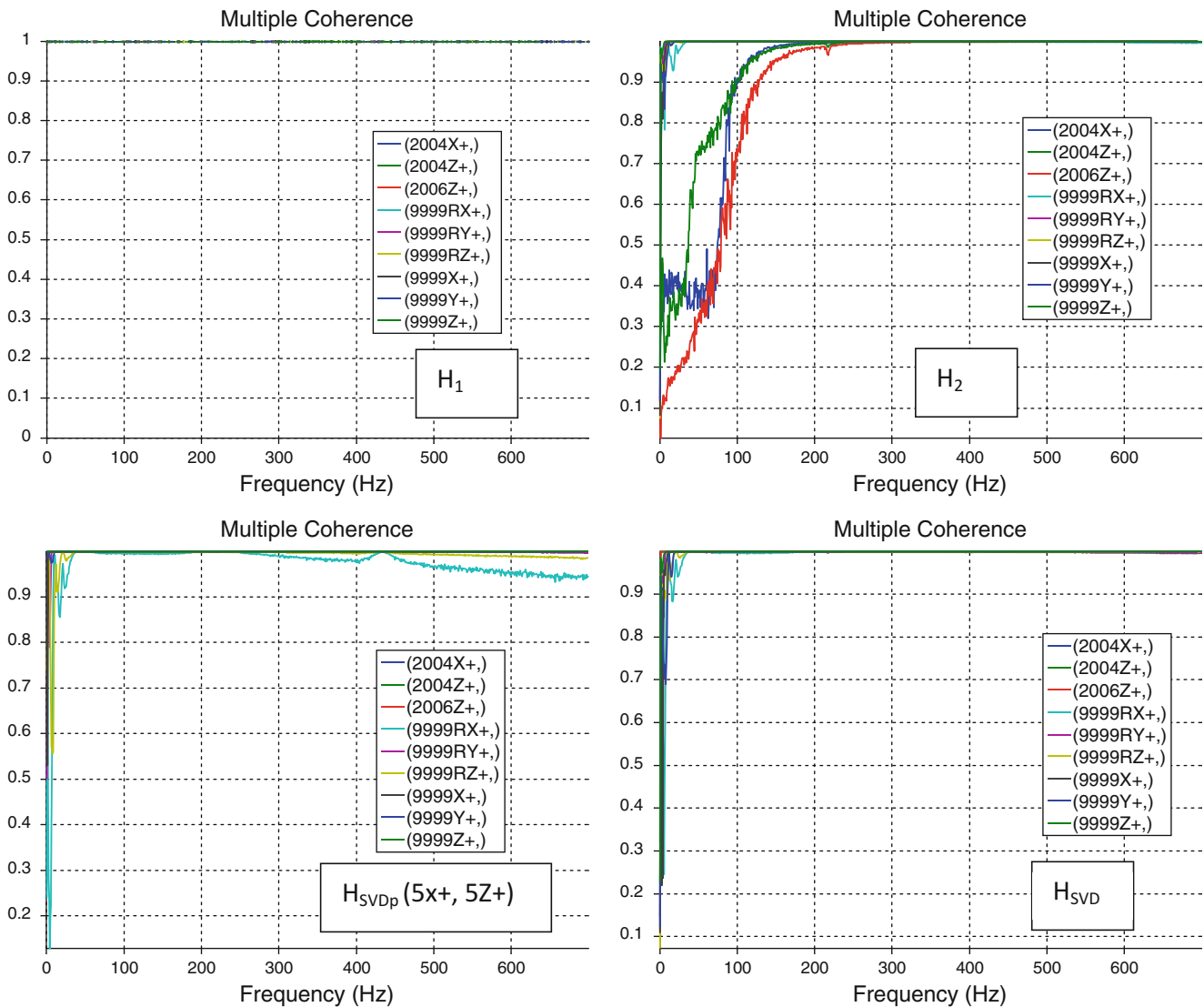
Fig. 2.12 Multiple coherence for all reference channels: H_1 (*upper left*), generalized H_2 (*upper right*), H_{SVDp} (*lower left*), and H_{SVD} (*lower right*).

Finally, multiple coherence for the reference channels is plotted in Fig. 2.12 for four cases: H_1, generalized H_2, H_{SVDp} using all references and 5X+ and 5Z+ to calculate the basis vectors, and H_{SVD}. Note that since the basis vectors of H_1 are identical to the references, the multiple coherence is exactly 1 and provides no insight. This uninteresting result is probably the reason multiple coherence is not calculated for reference channels. The multiple coherence results for the generalized H_2 function verify that the basis vectors do not adequately represent the load cell references (2004X+, 2004Y+, and 2006Z+) at low frequencies. The multiple coherence results using all references and a subset of responses are adequate, especially at the resonant frequencies, and adding all response channels to the calculation of the basis vectors improves the multiple coherence results at higher frequencies.

2.7 Summary

This paper has shown that all FRF estimation techniques based on linear algebra are derived using the same procedure:

1. Define a set of basis vectors.
2. Estimate the reference and response spectra from the set of basis vectors.
3. Use the estimated reference and response spectra to solve for the FRF matrix.

For the cases of H_1 and H_2, the basis vectors are explicitly defined as columns of the reference or the response spectra, respectively. Singular value decomposition of a set of channels can also be used to define the basis vectors. The H_{SVD} method uses all the channels to compute a consistent set of basis vectors for all channels. Other methods such as the generalized H_2 or the H_{SVD_p} method can also be defined that use singular value decomposition on a subset of channels to calculate the basis vectors. The H_V method stands apart from the other methods since it computes a different set of basis vectors for each output channel. As a consequence of developing this method, the definition of multiple coherence has been generalized to include all FRF estimators.

References

1. Allemang, R.J., Rost, R.W., Brown, D.L.: Dual input estimation of frequency response functions for experimental modal analysis of aircraft structures. In: Proceedings, International Modal Analysis Conference, 333–340, 1982
2. Vold, H., Crowley, J., Rocklin, G.: A comparison of $H1$, $H2$, Hv, frequency response functions. In: Proceedings, International Modal Analysis Conference, 272–278, 1985
3. Phillips, A.W., Allemang, R.J., Fladung, W.A.: The complex modal indicator function (CMIF) as a parameter estimation method. Presented at International Modal Analysis Conference, 1998
4. Juang, J., Wright, J.: A multi-point force appropriation method based upon a singular value decomposition approach. Presented at International Modal Analysis Conference, 317–323, 1989
5. Welch, P.D.: The use of fast fourier transform for the estimation of power spectra: A method based on time averaging over short, modified periodograms. IEEE Trans. Audio Electroacoust. **AU-15**, 70–73 (1967)
6. Daniell, P.: Discussion of 'on the theoretical specification and sampling properties of autocorrelated time-series'. J. Royal Stat. Soc. **8**, 88–90
7. Strang, G.: Linear Algebra and Its Applications, 3rd edn. Harcourt Brace Jovanovich Publishers, San Diego (1988)
8. Markovsky, I., VanHuffel, S.: Overview of total least squares methods. Sig. Process. **87**(10), 2283–2302 (2007)
9. Harris, C., Piersol, A.: Harris' Shock and Vibration Handbook, 5th edn. McGraw-Hill, and New York, pp. 21–29
10. Bendat, J., Piersol, A.: Random Data: Analysis and Measurement Procedures. Wiley, New York, p. 160
11. Schmid, J. Jr.: The relationship between the coefficient of correlation and the angle included between regression lines. J. Edu. Res. **41**(4), pp. 311–313 (1947)
12. Napolitano, K., Yoder, N.: Fixed base FRF using boundary measurements as references—analytical derivation. In: Proceedings, 30th International Modal Analysis Conference, February 2012

Chapter 3
Curve Fitting Analytical Mode Shapes to Experimental Data

Brian Schwarz, Shawn Richardson, and Mark Richardson

Abstract In this paper, we employ the fact that all experimental vibration data, whether in the form of a set of FRFs or a set of output-only spectra, is a ***summation of resonance curves***, each curve due to a mode of vibration. We also use this superposition property of modes to calculate a ***modal participation matrix***, a measure of the participation of each mode in the experimental vibration data. First we show how this ***superposition*** property can be used to curve fit a set of FEA mode shapes to EMA mode shapes or ODS's. The modal participation matrix is calculated as a ***least-squared-error solution***, so any number of FEA mode shapes can be curve fit to any number of EMA mode shapes or ODS's. Next we show how an expanded and enhanced set of FRFs, Cross spectra or ODS FRFs is obtained by curve fitting FEA mode shapes to experimental data. This approach in an alternative to FEA Model Updating, where an FEA model is modified so that its modes more closely correlate with experimental data. By curve fitting FEA shapes to experimental data, an extending and enhanced dynamic model is obtained which is more suitable for machinery & structural health monitoring, and for troubleshooting noise & vibration problems using SDM and MIMO methods.

Keywords Frequency response function (FRF) • Auto power spectrum • Cross power spectrum • ODS FRF • Operating deflection shape (ODS) • Finite element analysis (FEA) • Experimental modal analysis (EMA) • FEA mode shapes • EMA mode shapes • Modal assurance criterion (MAC) • Shape difference indicator (SDI) • Structural dynamics modification (SDM) • Multi-input multi-output (MIMO) modeling & simulation

3.1 Introduction

When resonances are excited by dynamic forces in a machine, or in a mechanical or civil structure, response levels can ***far exceed*** deformation levels due to static loads. Moreover, high levels of ***resonance-assisted dynamic response*** can cause rapid and unexpected failures, or over long periods of time, structural fatigue and material failure can often occur.

A mode of vibration is a mathematical representation of a structural resonance. Each mode is defined by three distinct numerical parts; a natural frequency, a damping or decay value, and a mode shape. A mode shape represents the ***"standing wave deformation"*** of the structure at the natural frequency of a resonance. This standing wave behavior is caused when energy becomes trapped within the material boundaries of the structure and cannot readily escape.

3.1.1 Modal Participation

When the dynamic response of a structure is expressed in terms of modal parameters, every solution is a ***summation of contributions*** from all of the modes. Another way of expressing this superposition property is that ***all modes participate*** in or ***contribute*** to the dynamic response when a structure is excited by applied forces. Ideally, all structures have an ***infinite number*** of modes, but in a practical sense only a ***few low frequency modes participate significantly*** in their response.

If a structure's overall dynamic response is represented by time waveforms, these waveforms can also be decomposed into a ***summation of modal contributions***. Likewise, if the dynamic response is represented by a set of frequency functions or spectra, the overall response can also be decomposed into a ***summation of resonance curves*** [4].

B. Schwarz • S. Richardson • M. Richardson (✉)
Vibrant Technology, Inc., Scotts Valley, CA, USA
e-mail: mark.richardson@vibetech.com

3.1.2 FEA Modes

FEA modes are solutions to a set of time domain equations of motion. The equations are a statement of Newton's second law [1–3]. and are written as a set of differential equations,

$$[M]\{\ddot{x}(t)\} + [C]\{\dot{x}(t)\} + [K]\{x(t)\} = \{f(t)\} \tag{3.1}$$

where,

[M] = **(n by n)** mass matrix
[C] = **(n by n)** damping matrix
[K] = **(n by n)** stiffness matrix
$\{\ddot{x}(t)\}$ = Accelerations (**n**-vector)
$\{\dot{x}(t)\}$ = Velocities (**n**-vector)
$\{x(t)\}$ = Displacements (**n**-vector)
$\{f(t)\}$ = Externally applied forces (**n**-vector)

This set of differential equations describes the dynamics between ***n-discrete degrees-of-freedom (DOFs)*** of the structure. Equations can be created for as many DOFs of a structure as necessary to adequately describe its dynamic behavior.

Finite element analysis (FEA) is used to create the coefficient matrices of the differential Eq. (3.1). The mass & stiffness matrices can be generated in a straightforward manner but the damping matrix cannot, hence it is usually left out of the FEA model. The equations are then solved for the analytical FEA mode shapes and their corresponding natural frequencies.

FEA modes are a mathematical ***eigen-solution*** to the homogeneous form of these equations, where the right-hand side is zero. Each natural frequency is an ***eigenvalue***, and each mode shape is an ***eigenvector***.

3.1.3 EMA Modes

EMA mode shapes are obtained by ***curve fitting*** a set of experimentally derived FRFs [1–3]. FRF-based curve fitting is a numerical process by which an analytical parametric model with unknown modal parameters in it is matched to experimental FRF data over a band of frequencies. Equation (3.3) is an expression of the analytical FRF model.

In the frequency domain, the equations of motion are written as algebraic equations, in a form called a ***MIMO model*** or ***transfer function matrix model***. Like Eq. (3.1), this model also describes the ***dynamics between n-DOFs*** of the structure. It contains transfer functions between all combinations of DOF pairs,

$$\{X(s)\} = [H(s)]\{F(s)\} \tag{3.2}$$

where,

s = Laplace variable (complex frequency)
[H(s)] = (**n by n**) matrix of transfer functions
$\{X(s)\}$ = Laplace transform of displacements (**n**-vector)
$\{F(s)\}$ = Laplace transform of external forces (**n**-vector)

These equations can be created between as many DOF pairs on a structure as necessary to adequately describe its dynamic behavior.

When a transfer function is represented analytically as the partial fraction expansion shown in Eqs. (3.3) & (3.4) below, it is clear that its value at any frequency is a ***summation of resonance curves***, one for each mode of vibration.

$$[H(s)] = \sum_{k=1}^{m} \frac{[r_k]}{2j\ (s-p_k)} - \frac{\left[r_k^*\right]}{2j\ \left(s-p_k^*\right)} \tag{3.3}$$

or,

$$[H(s)] = \sum_{k=1}^{m} \frac{A_k\{u_k\}\{u_k\}^t}{2j\ (s-p_k)} - \frac{A_k^*\{u_k^*\}\{u_k^*\}^t}{2j\ \left(s-p_k^*\right)} \tag{3.4}$$

where,

m = Number of modes of vibration
$[\mathbf{r}_k]$ = (**n by n**) residue matrix for the kth mode
$p_k = -\sigma_k + j\omega_k$ = Pole location for the kth mode
σ_k = Damping decay of the kth mode
ω_k = Natural frequency of the kth mode
$\{u_k\}$ = Mode shape for the kth mode (n-vector)
A_k = Scaling constant for the kth mode

Figure 3.1 shows a transfer function for a single mode of vibration, plotted over **half of the s-plane**.

3.1.4 Experimental FRFs

An FRF is defined as the values of a transfer function along the $j\omega$ -**axis** in the s-plane, as shown in Fig. 3.1. FRFs can be calculated from experimental data when **all** of the excitation forces and responses caused by them are **simultaneously acquired**. Equation (3.3) is the analytical form of an FRF that is **used for FRF-based curve fitting** experimental data. The outcome is a EMA pole & mode shape for each modal term that is used during curve fitting of the experimental FRFs.

3.1.5 Mode Shape Curve Fitting

Equation (3.4) also tells us that each FRF can be represented as a **summation of resonance curves**, hence a set of FRFs can be **decomposed** into their resonance curves by **curve fitting them one frequency at a time** with a set of FEA mode shapes.
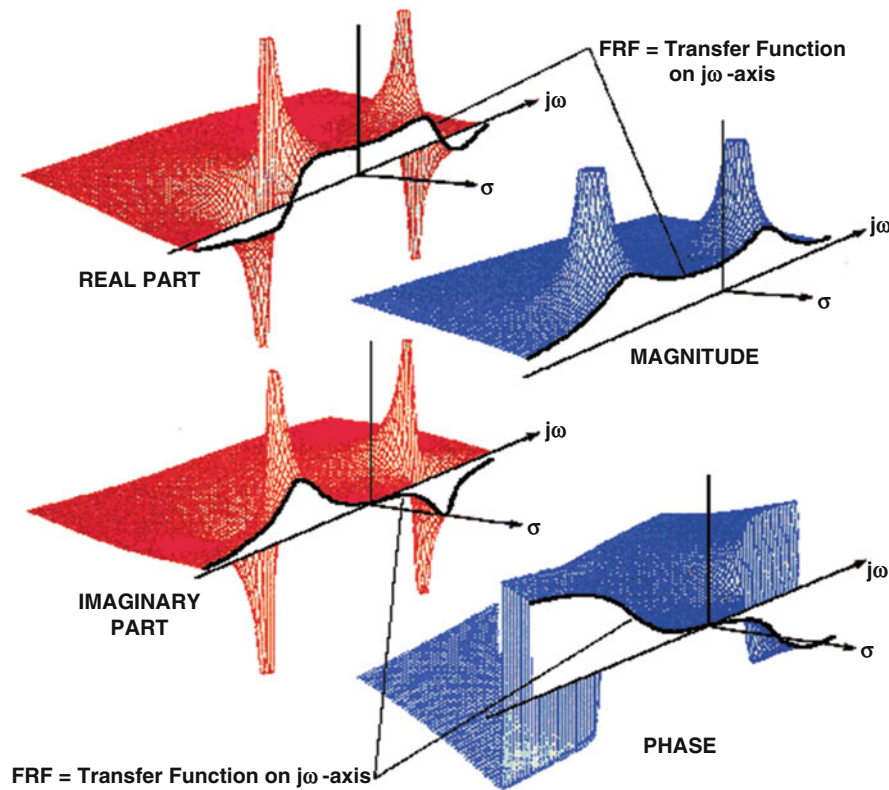
Fig. 3.1 Transfer function & FRF for a single mode in the s-plane

3.1.6 Output-Only Frequency Spectra

In cases where the excitation forces are not measured and therefore FRFs cannot be calculated, three other types of *output-only* frequency spectra can be calculated from acquired response time waveforms; Fourier spectra, Cross spectra, and ODS FRFs.

A **Fourier spectrum** is simply the Digital Fourier Spectrum (DFT) of a digital response time waveform. It is calculated with the FFT algorithm. A **Cross spectrum** is calculated between *two simultaneously acquired responses*. It is the DFT on one signal multiplied by the complex conjugate of the other. An **ODS FRF** is the Auto spectrum of a *roving* response combined with the phase of the Cross spectrum between the *roving* response and a *(fixed) reference* response.

When it can be assumed that these output-only measurements can also be represented as a *summation of resonance curves*, they too can be *decomposed* into a set resonance curves by *curve fitting them one frequency at a time* with a set of FEA mode shapes.

3.1.7 Operating Deflection Shape (ODS)

When a vibration response is analytically modeled or experimentally measured at *two or more points & directions* on a machine or structure, this data is called an **Operating Deflection Shape** (or **ODS)** [2]. Three different types of ODS's are possible; *time-based ODS's*, *frequency-based ODS's*, and *order-based ODS's*.

3.1.8 Time-Based ODS

A time-based ODS is simply the values of two or more simultaneously acquired or calculated time waveforms for the same time value. A time-based ODS is the *true overall response* of the structure at any moment of time.

3.1.9 Frequency-Based ODS

A frequency-based ODS is the values of two or more frequency domain functions (FRFs or spectra) at the same frequency. A frequency-based ODS is the *true overall response* of the structure for any frequency for which the measurement functions were calculated

All frequency domain functions, (except an Auto spectrum) are complex valued (with magnitude & phase), so all frequency-based ODS's are also complex valued.

3.1.10 Order-Based ODS

In a rotating machine, the dominant forces are applied at multiples of the machine running speed, called orders. An *order-based ODS* is assembled from the *peak values* at one of the order frequencies in a set of output-only frequency spectra. These spectra are calculated from response data that is acquired while the machine is running. When displayed in animation on a 3D model of the machine, an order-based ODS is a convenient way of visualizing distributed vibration levels. These distributed levels can also be used for monitoring the health of the machine.

3.1.11 ODS Expansion

In a previous paper [4], it was shown how *modes participate* in an order-based ODS of a rotating machine, and how they participate differently at different operating speeds. It another previous paper [5], it was also shown how the *modal*

participation can be used to *expand* an order-based ODS so that it is a valid representation of the ODS for all DOFs of the machine, both *measured & un-measured*.

3.1.12 Measurement Expansion

In this paper the same curve fitting and expansion equations that were used for ODS expansion will be used to decompose and expand a set of FRFs and sets of output-only Cross spectra and ODS FRFs.

3.2 Expanding EMA Modes Using FEA Modes

The aluminum plate shown in Fig. 3.2 was tested using a roving impact hammer. During the test, a 5 by 6 grid of points was impacted in the vertical direction. A tri-axil accelerometer located at one corner was used to measure the response due to the impacts.

FRFs were calculated from simultaneously acquired force & response data, and the modal parameters of 14 EMA modes were extracted by curve fitting the FRFs using FRF-based curve fitting. A typical curve fit is shown in Fig. 3.3.

3.2.1 Plate FEA Model

Also, an FEA model of the plate was created by adding 180 FEA brick elements to the same model used to display the EMA mode shapes. The first flexible body FEA mode is shown in Fig. 3.4. The 30 impact points are also labeled.
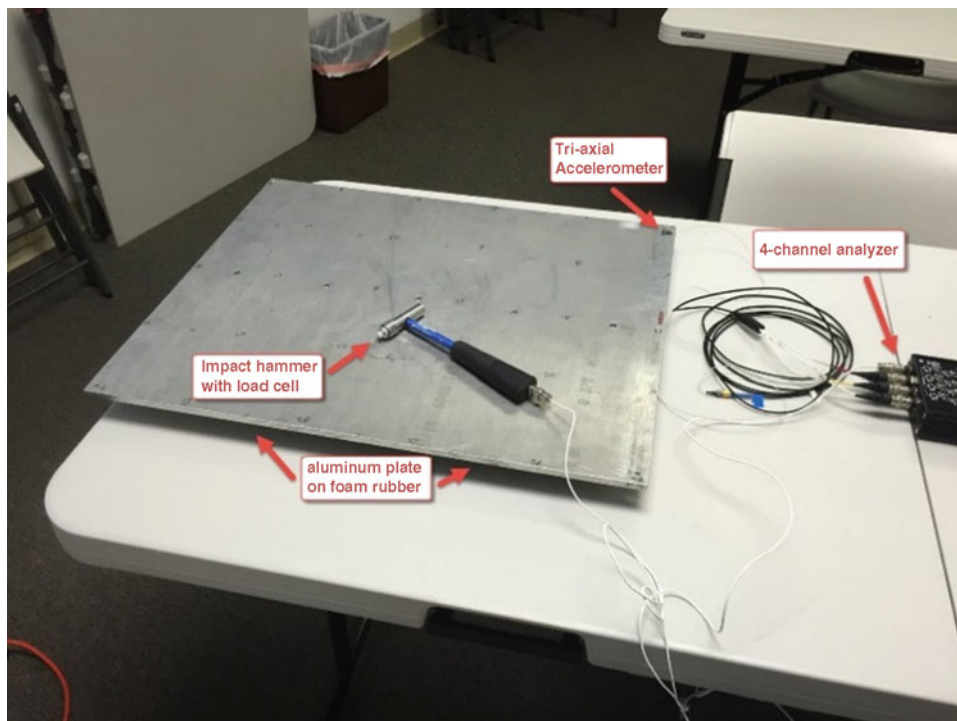
Fig. 3.2 Impact test of aluminum plate
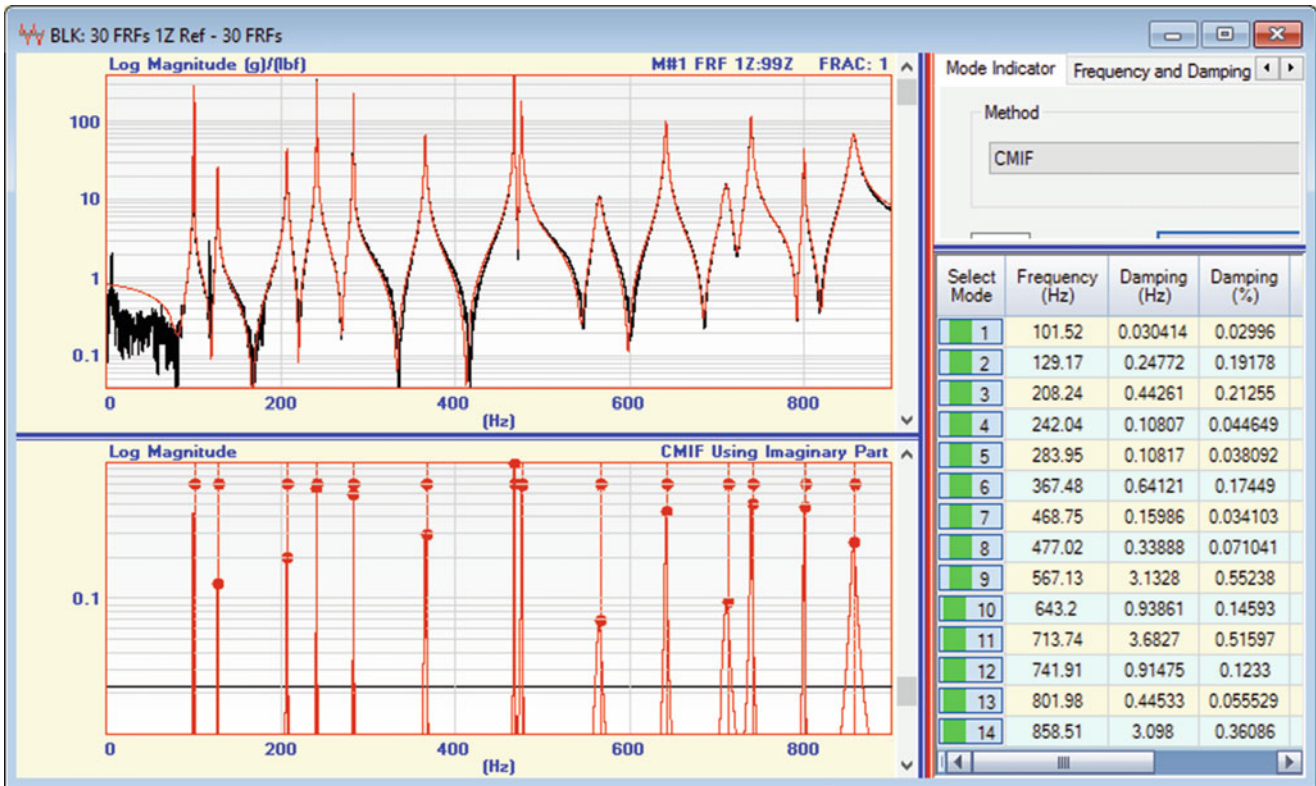
Fig. 3.3 FRF-based curve fit of a measurement
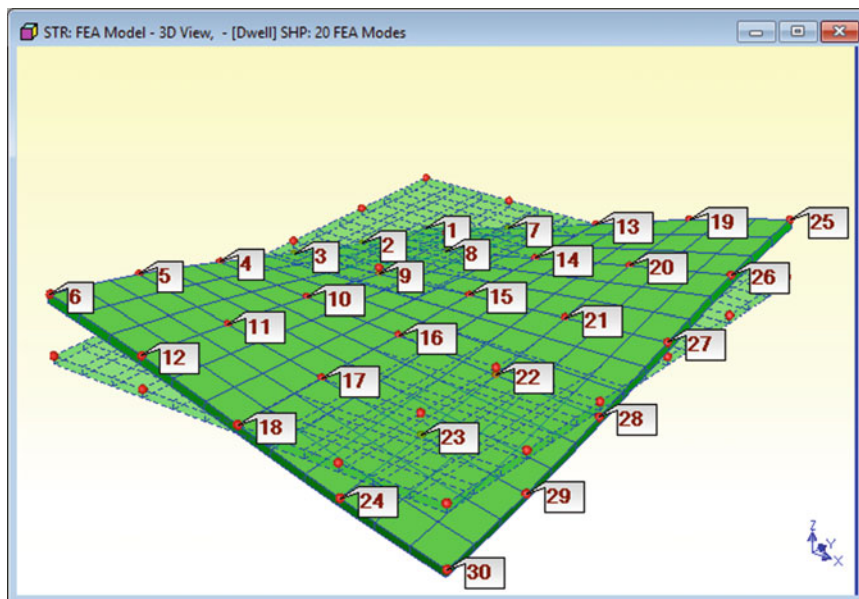
Fig. 3.4 FEA mode shape in animation

3.2.2 Modal Participation

The bar chart of the participations of the first 14 flexible body FEA modes in the 14 EMA modes is shown in Fig. 3.5. The participation values reflect the different scaling of the FEA mode shapes versus the EMA modes. The FEA mode shapes
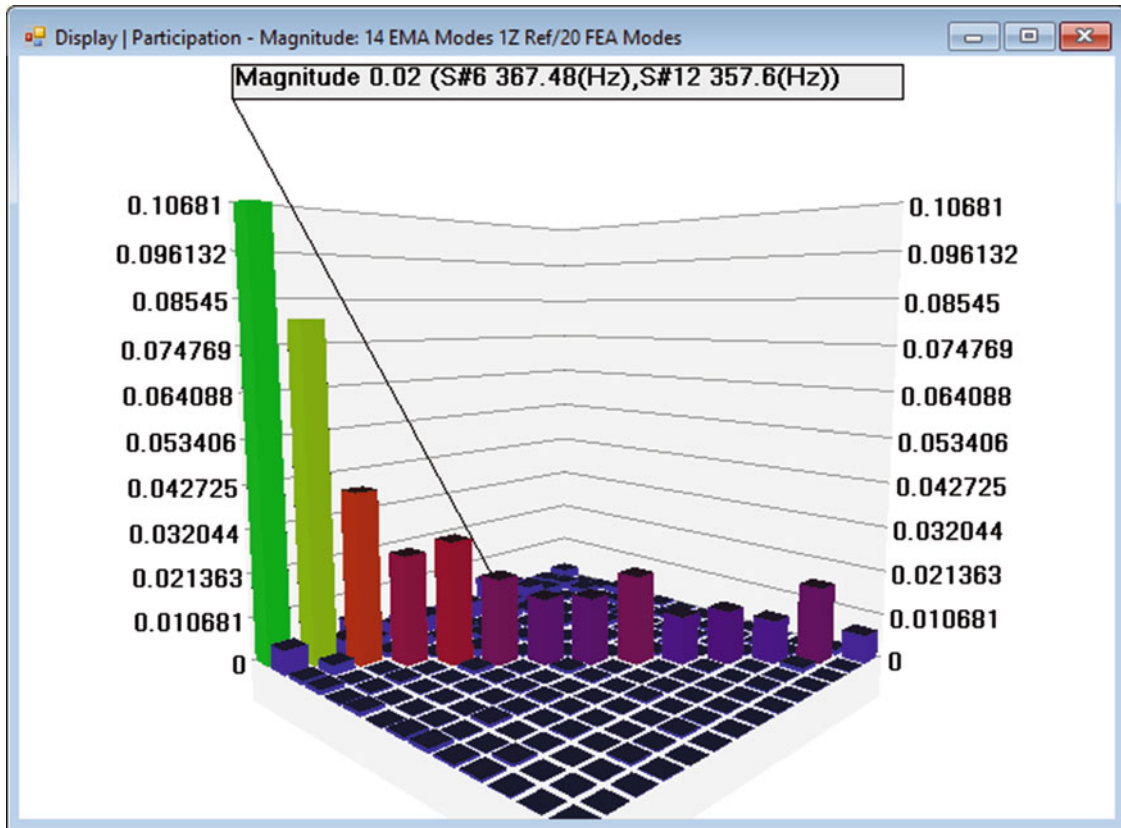
Fig. 3.5 Participation of FEA modes in EMA modes

were scaled to ***Unit Modal Masses***, while the EMA mode shapes contained the ***residues (numerators)*** obtained from using Eq. (3.3) to curve fit the FRFs.

3.2.3 Shape Expansion

The participation factors in Fig. 3.5 were used to expand the EMA modes from 30 DOFs to 1248 DOFs, the number of FEA mode shape DOFs. The MAC values between the expanded & original EMA mode shapes are shown in Fig. 3.6. The SDI values between the expanded EMA and the original EMA mode shapes are shown in Fig. 3.7.

Both Figs. 3.6 & 3.7 indicate that the FEA mode shapes were accurately curve fit to the EMA shapes. MAC indicates the ***co-linearity*** of each shape pair. SDI more strongly indicates that each shape pair has ***nearly the same values*** for the 30 DOFs that are common among the original and expanded shapes.

3.3 FRF Decomposition

The 14 FEA mode shapes were used to decompose the 30 FRF measurements for the aluminum plate at each frequency. The values of the 30 FRFs at each frequency ***make up a frequency-based ODS***. The FEA mode shapes participate differently in the ODS at each frequency, and when the participations are plotted for all frequencies, they create a separate resonance curve for each FEA mode. Figure 3.8 is a plot of the 14 resonance curves obtained from decomposing the 30 FRFs using the FEA modes.

Notice that each resonance curve in Fig. 3.8 has a ***single dominate peak*** in it at the natural frequency of one of the 14 resonances. These resonance curves clearly illustrate the superposition property of modes.
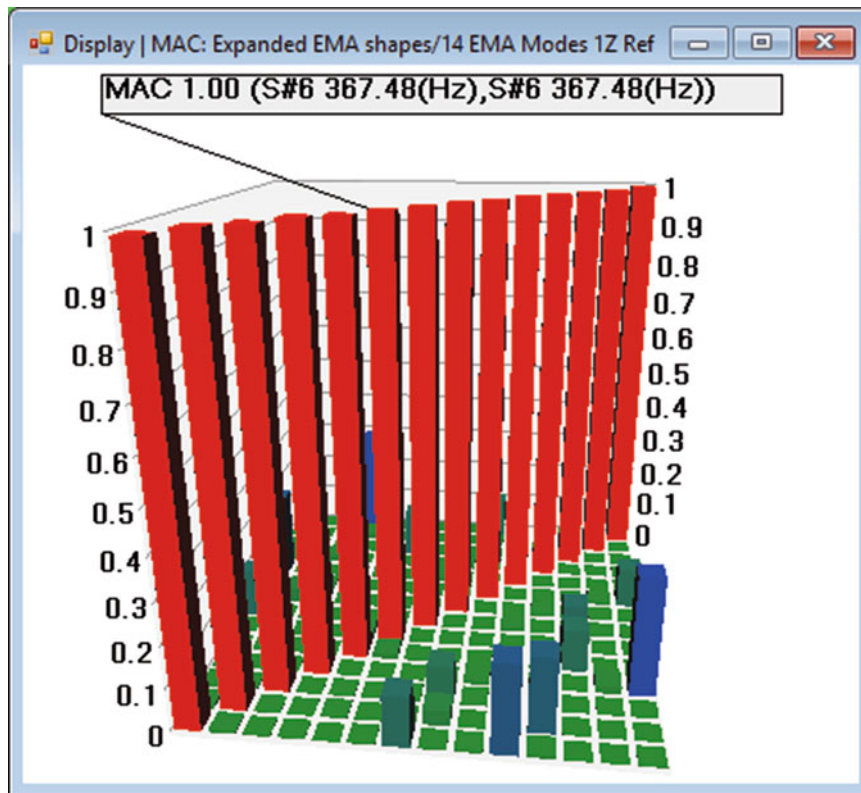
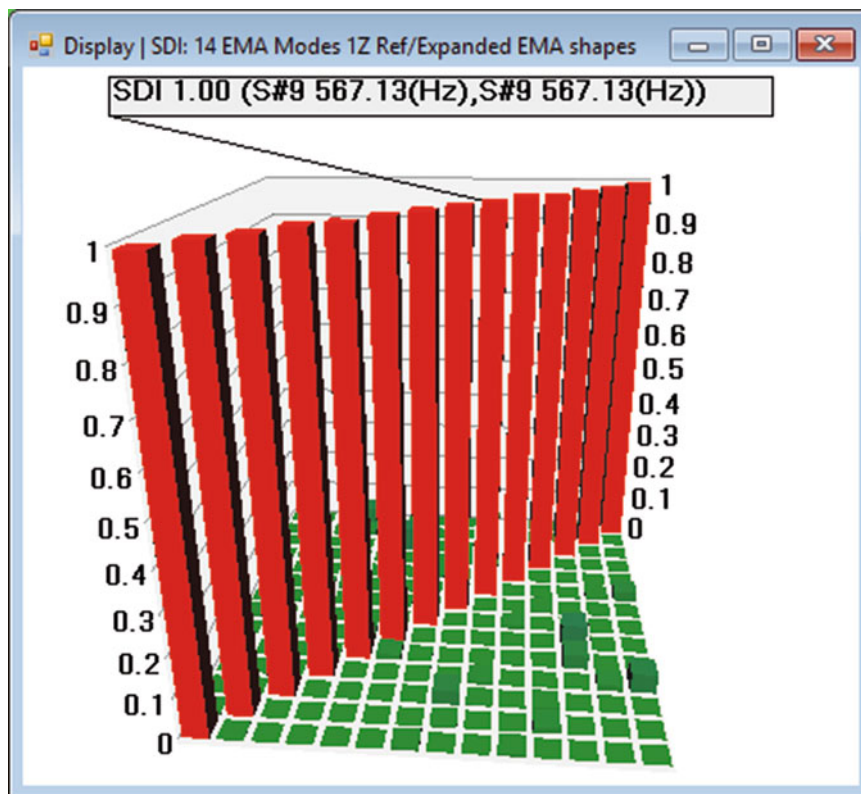**Fig. 3.6** MAC values between expanded & original EMA modes

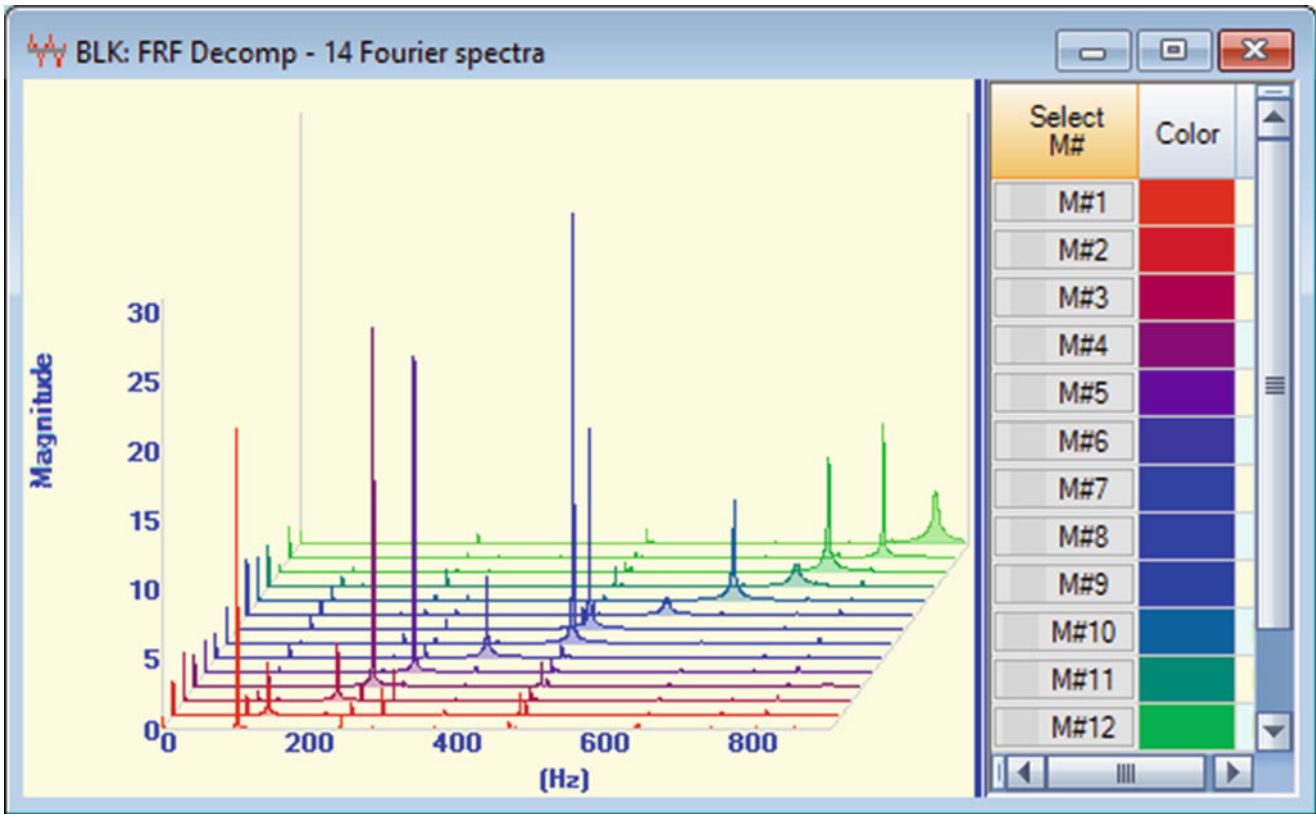**Fig. 3.7** SDI values between expanded & original EMA modes

Fig. 3.8 FRF decomposition using 14 FEA modes

3.4 FRF Reconstruction

A set of ***reconstructed FRFs*** can then be calculated by multiplying the resonance curves in Fig. 3.8 by the FEA mode shapes. Figure 3.9 shows a reconstructed FRF overlaid on its corresponding original experimental FRF.

3.5 FRF Expansion

Not only are the original 30 FRFs reconstructed, but an ***expanded set of 1248 FRFs*** can be calculated using all the DOFs of the FEA mode shapes. This expanded set of FRFs can then be curve fit using FRF-based curve fitting to obtain a set of EMA modes with ***frequency, damping***, and ***mode shapes with 1248 DOFs*** in them.

NOTE: ***Only FEA mode shapes*** are required to perform decomposition, reconstruction, and expansion of experimental vibration data.

Decomposition, reconstruction and expansion can be applied to either time or frequency domain vibration data.

3.6 Cross Spectrum Decomposition

The 14 FEA mode shapes were also used to decompose 30 Cross spectrum measurements for the aluminum plate at each frequency. Figure 3.10 is a plot of the participations of the 14 FEA modes in the Cross spectra measurements.
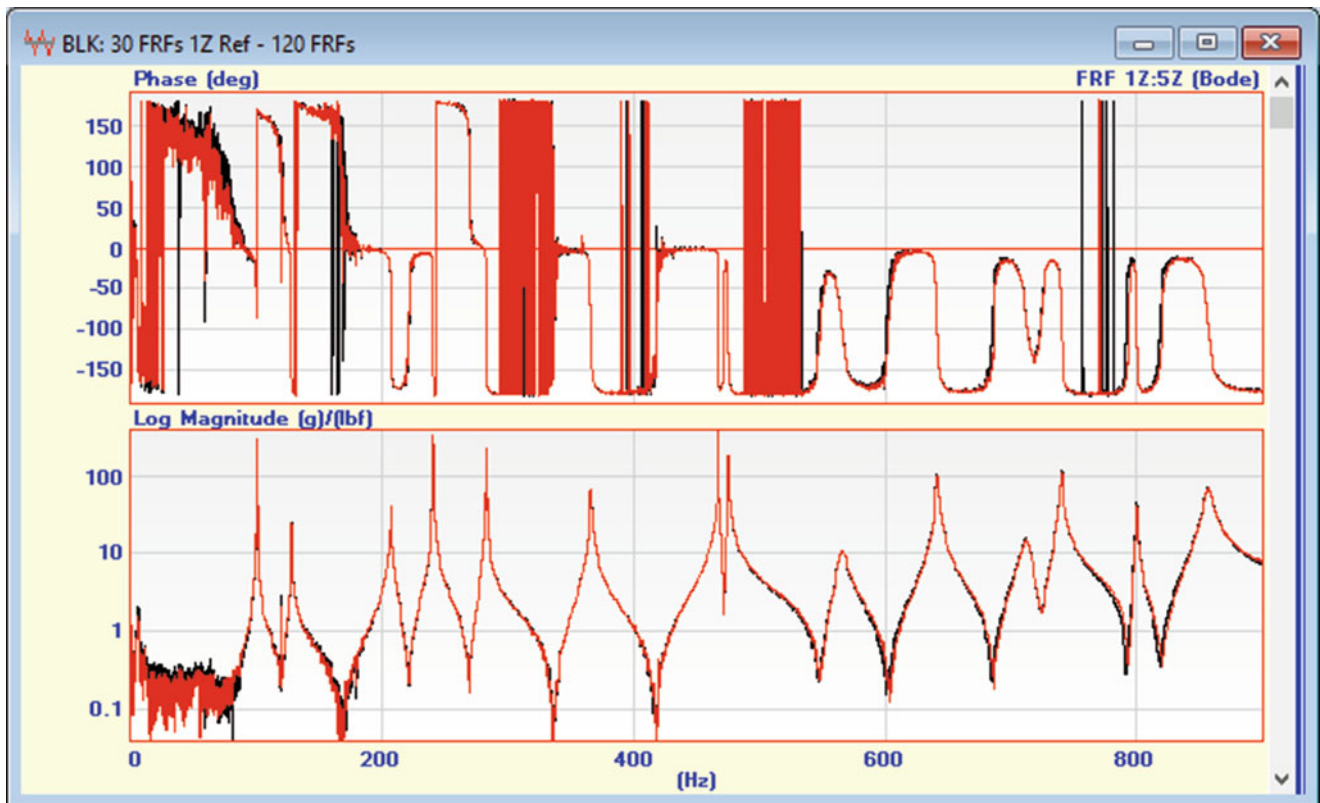
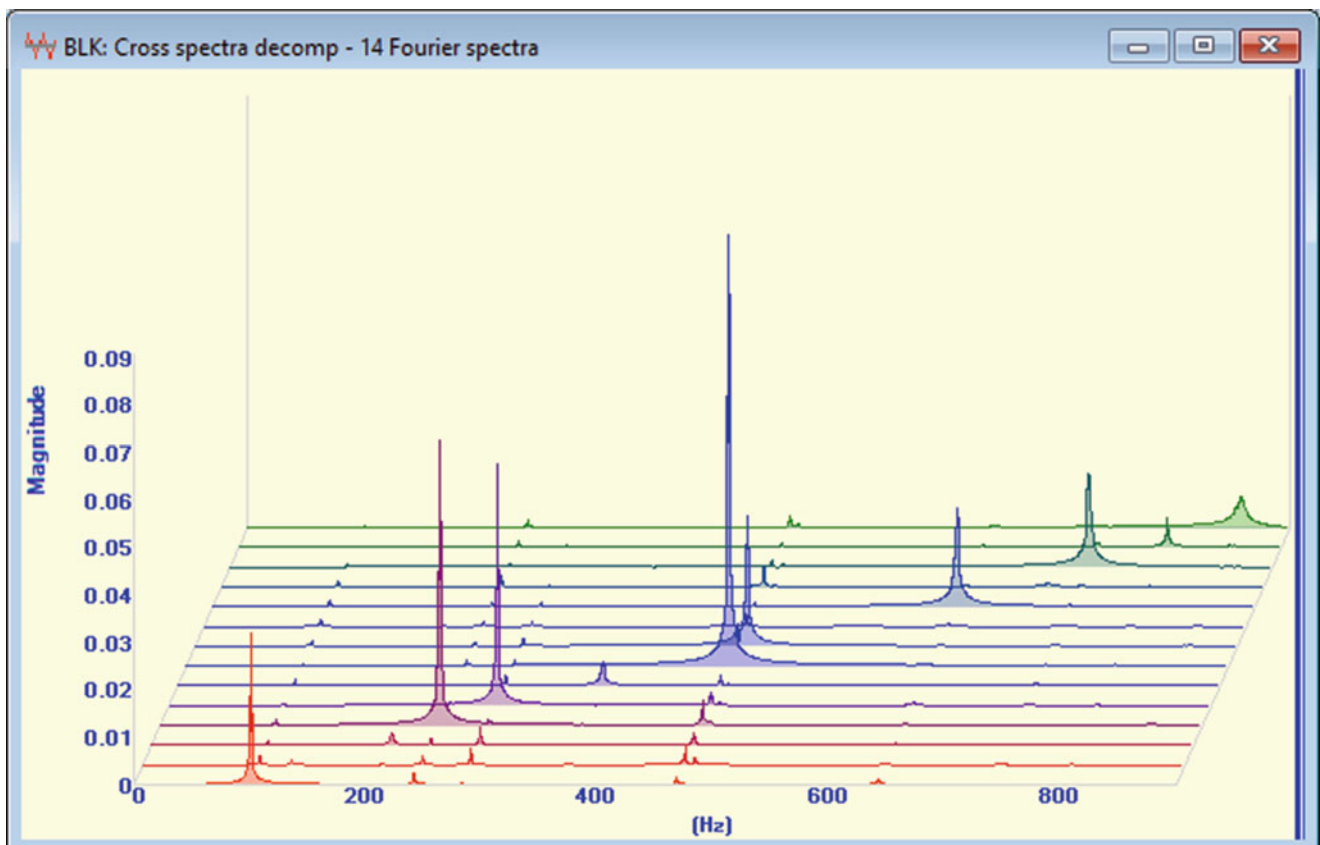**Fig. 3.9** Reconstructed & experimental FRFS overlaid

Fig. 3.10 Cross spectra decomposition using 14 FEA modes

3.7   Cross Spectrum Expansion

Figure 3.11 shows a reconstructed Cross spectrum overlaid on an original experimental Cross spectrum. The reconstructed Cross spectra were calculated by multiplying the resonance curves in Fig. 3.10 by the FEA mode shapes. Again, not only can the original 30 Cross spectra be reconstructed, but an *expanded set of 1248 Cross spectra* can be calculated using all the DOFs of the FEA mode shapes.

3.8   ODS FRF Decomposition

The 14 FEA mode shapes were also used to decompose 30 ODS FRF measurements for the aluminum plate at each frequency. Figure 3.12 is a plot of the participations (or resonance curves) of the 14 FEA modes in the ODS FRF measurements.

3.9   ODS FRF Expansion

Figure 3.12 shows a reconstructed ODS FRF overlaid on an original experimental ODS FRF. The reconstructed ODS FRFs were calculated by multiplying the resonance curves in Fig. 3.12 by the FEA mode shapes. Again, not only can the original ODS FRFs be reconstructed, but an *expanded set of 1248 ODS FRFs* can be calculated using all the DOFs of the FEA mode shapes.

3.10   Measurement Errors

One of the most useful applications of measurement curve fitting and expansion using mode shapes is that experimental errors are quickly identified. Bad measurements are found by overlaying each reconstructed measurement on its corresponding experimental data. One pair of each of the measurement types is overlaid in Figs. 3.8, 3.11, & 3.13.
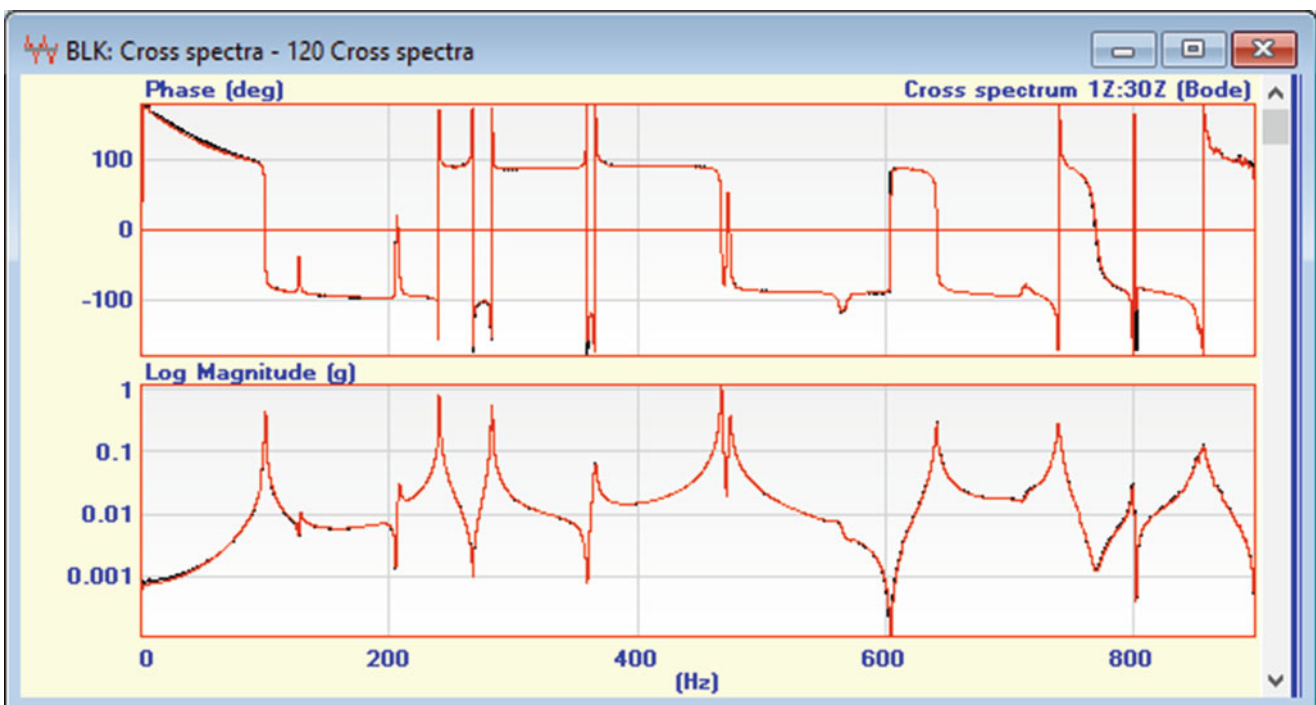

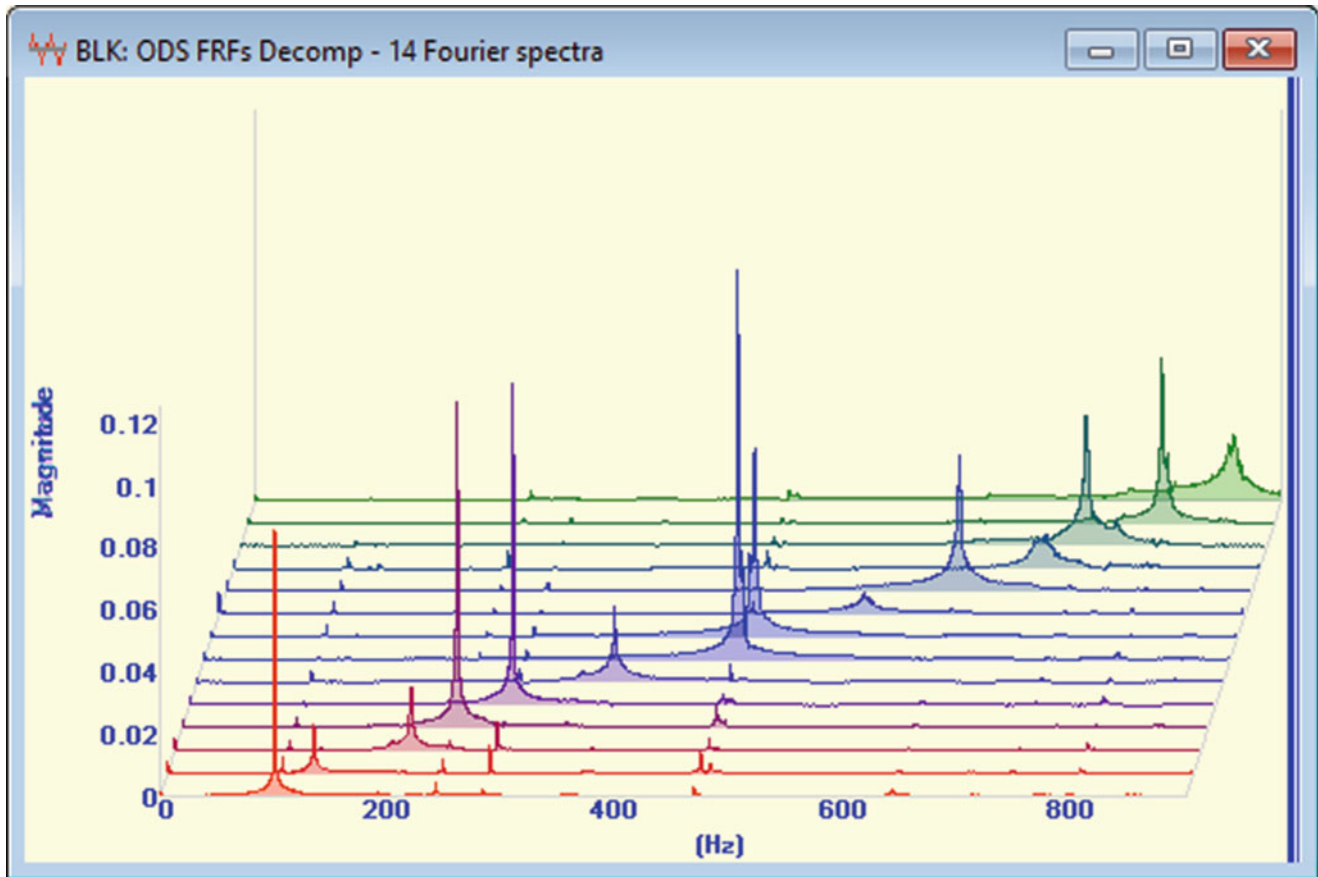**Fig. 3.11**   Reconstructed & experimental cross spectra overlaid

Fig. 3.12 ODS FRF decomposition using 14 FEA modes

3.10.1   Measurement Comparison Using MAC & SDI

Another method for comparing reconstructed & experimental FRFs or frequency spectra pairs is to use MAC & SDI values. Both MAC & SDI have values between 0 & 1. When MAC is applied to pairs of FRFs, it is also called the ***Frequency Response Assurance Criterion*** (or ***FRAC***).

Figure 3.14 is a magnitude plot of the MAC values between the 30 reconstructed & experimental FRFs, ordered from the highest to lowest MAC value. Figure 3.15 is an ordered magnitude plot of SDI values.

Both MAC & SDI have their lowest values for the reconstructed & experimental FRF pair at DOF 14Z. These low values indicate a mismatch between the reconstructed & experimental FRFs. The overlaid reconstructed & experimental FRF pair is shown in Fig. 3.16.

Since all of the other FRF pairs have high MAC & SDI values (close to 1), this is strong evidence that curve fitting the FEA modes shapes to the experimental data provided very accurate reconstructing FRFs, except in a few cases like the pair shown in Fig. 3.16. Since the reconstructed FRFs were the result of a ***least-squared-error curve fit*** to all 30 experimental FRFs, the strongest conclusion from the mismatch in Fig. 3.16 is that ***the experimental FRF data is in error.***

Since the aluminum plate was tested using as roving impact test, it can be concluded that Point 14 on the plate was ***impacted at a different point*** than Point 14 on the FEA model.
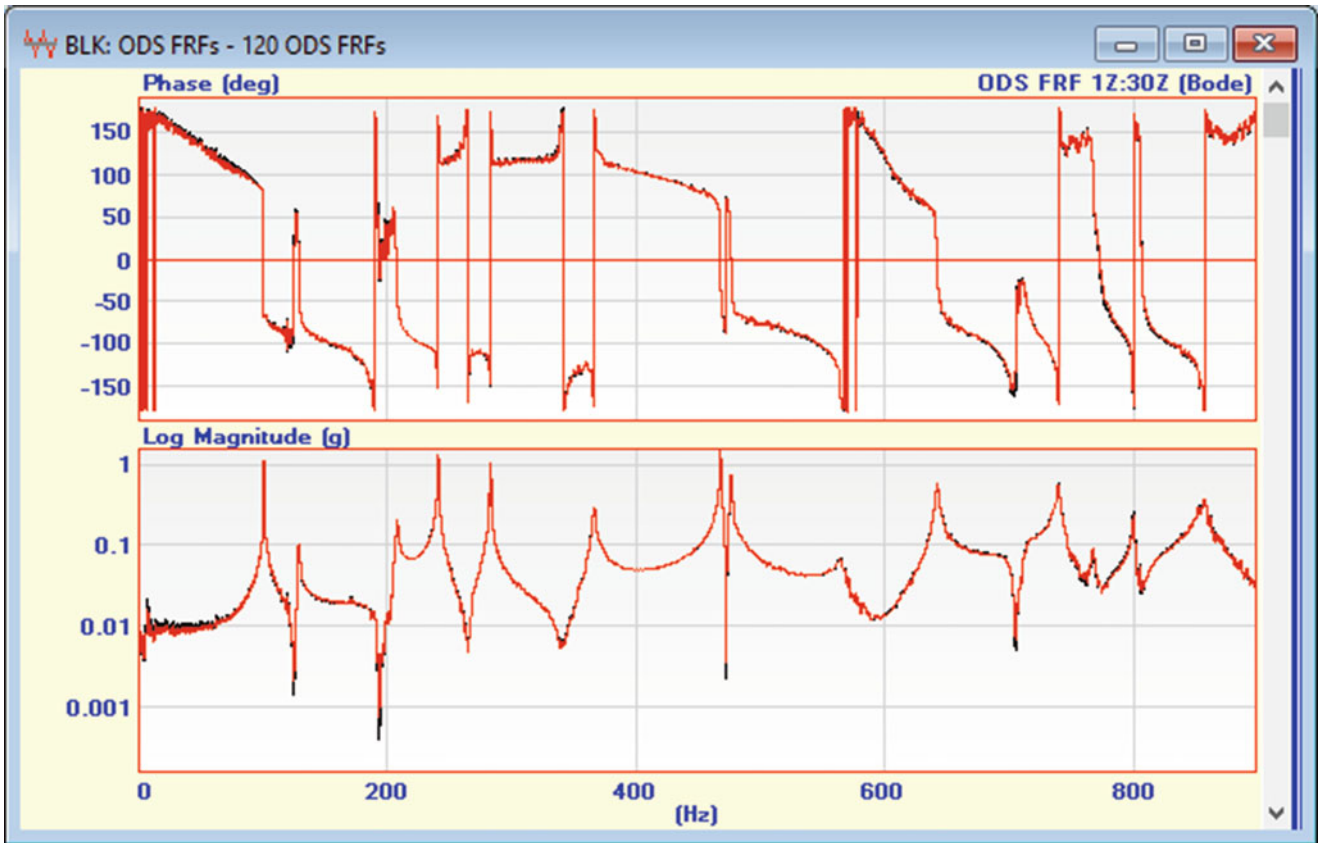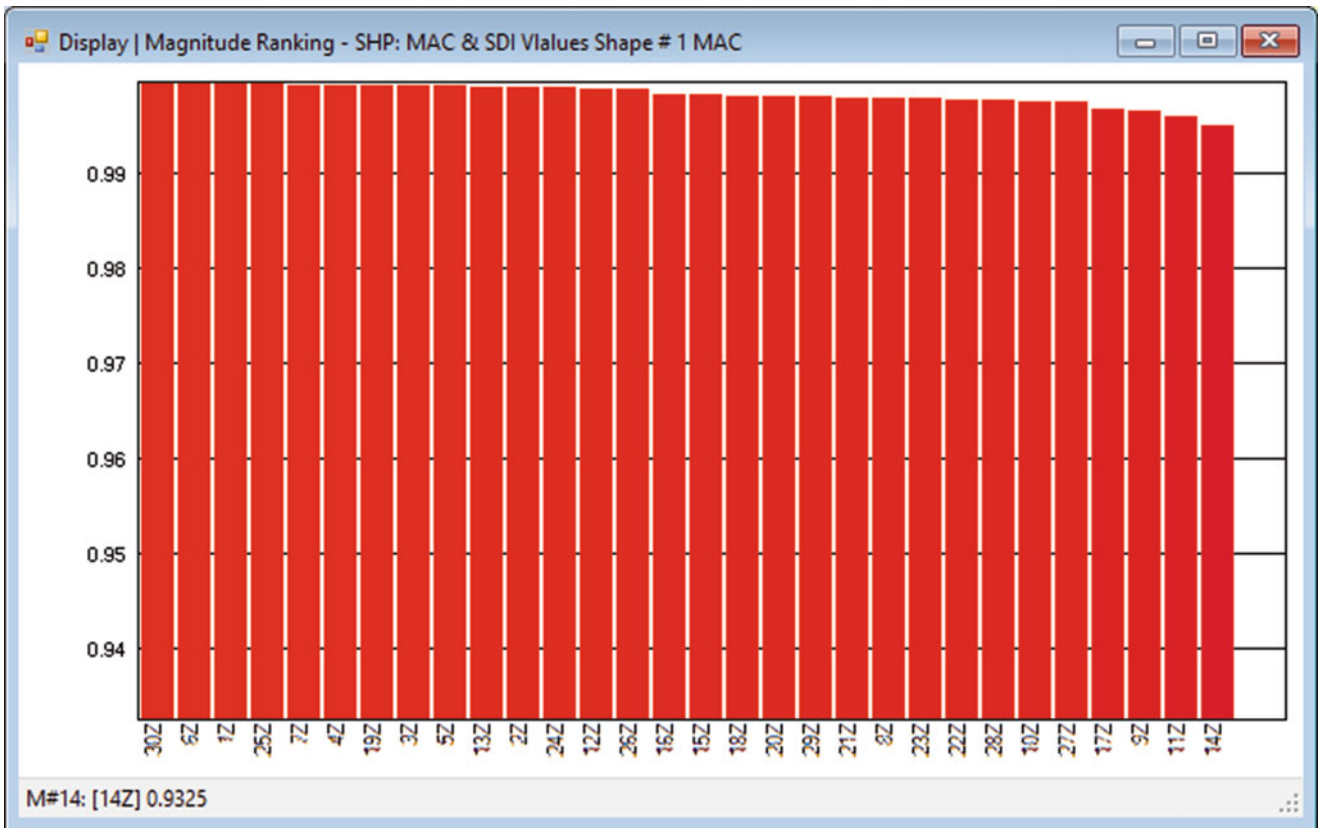
Fig. 3.13 Reconstructed & experimental ODS FRFs overlaid

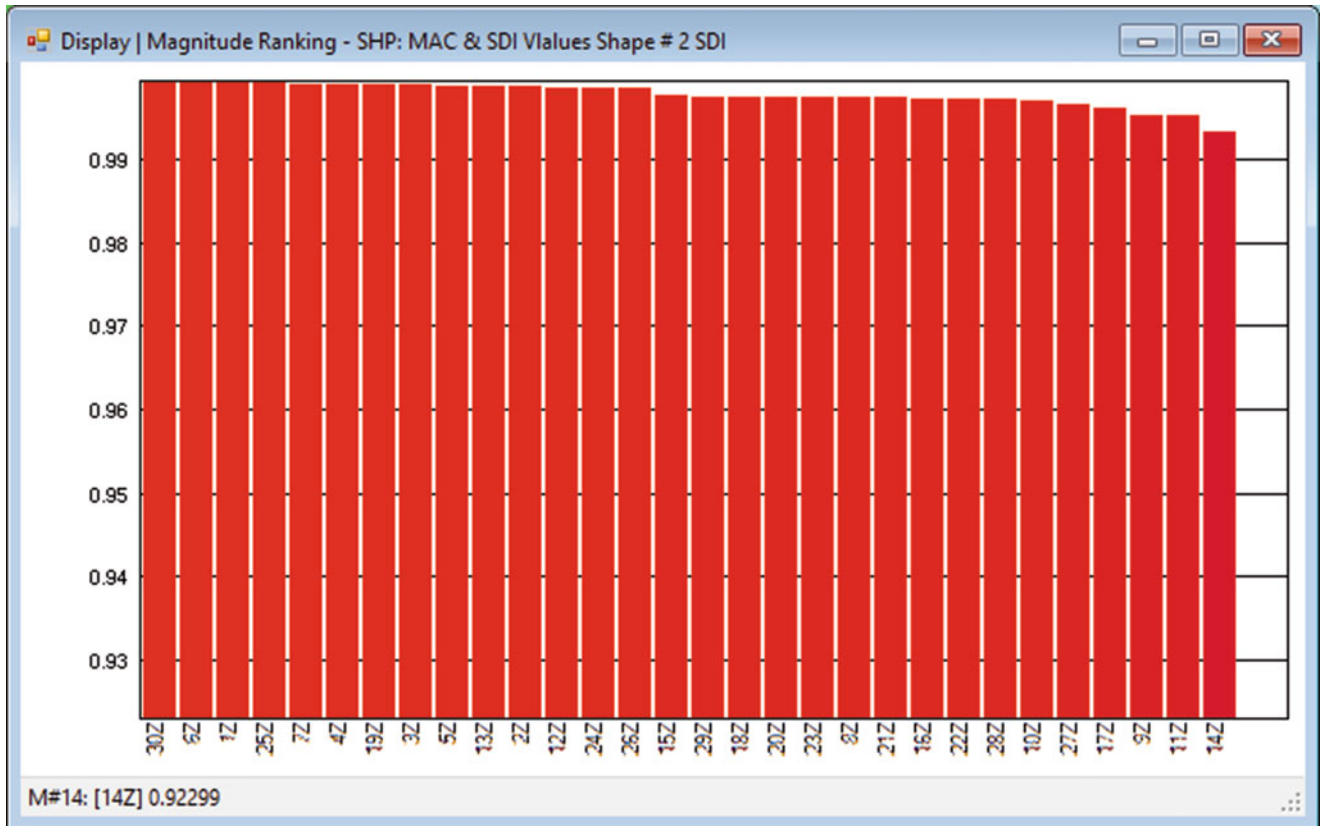**Fig. 3.14** Ordered MAC for reconstructed & Experimental FRF Pairs

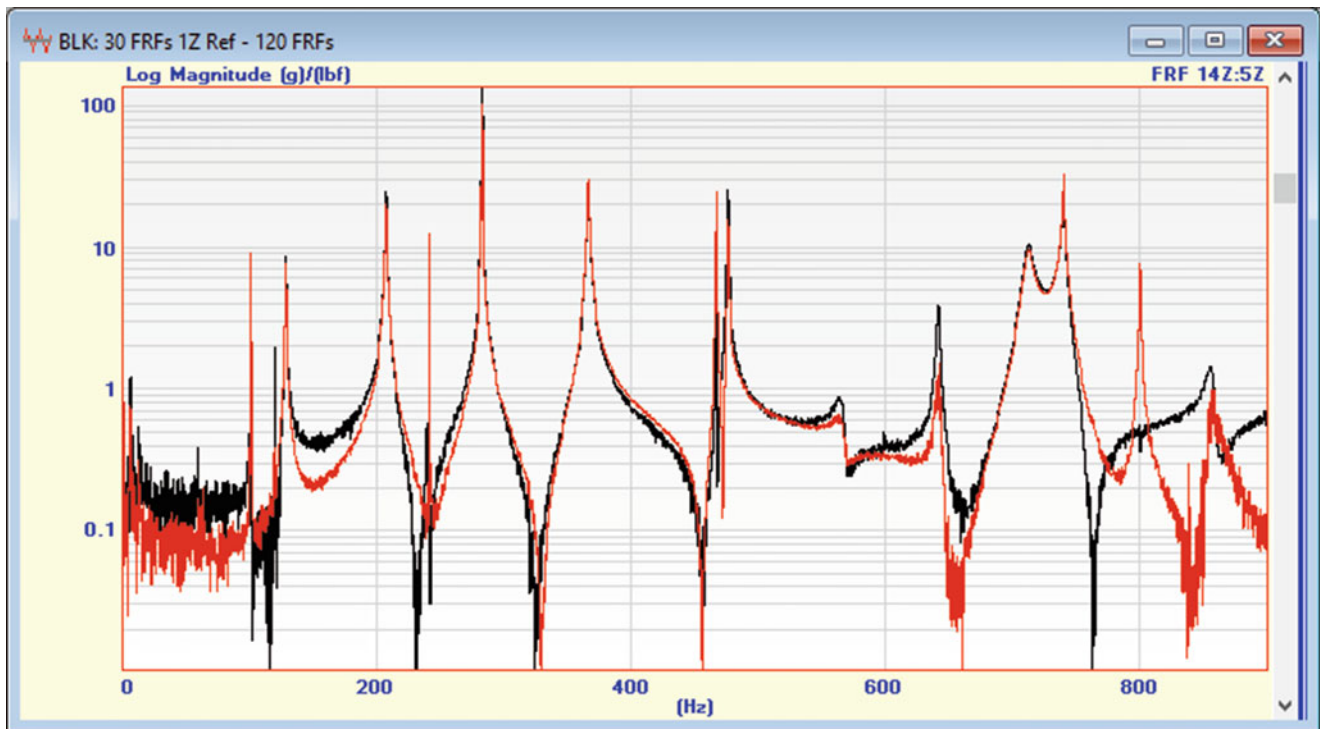**Fig. 3.15** Ordered SDI for reconstructed & experimental FRF pairs

Fig. 3.16 Reconstructed & experimental 14Z:5Z FRFs overlaid

3.11 Conclusions

It was shown how the FEA mode shapes of a machine or structure can be used to decompose, reconstruct, and expand a set of FRFs, Cross spectra, or ODS FRFs. FRFs are normally calculated when all of the excitation forces causing a structure to vibrate are measured. Cross spectra & ODS FRFs are calculated from ***output-only data*** when the excitation forces are not measured.

It was demonstrated in each case that these three types of experimental data can be decomposed into a ***summation of resonance curves*** by curve fitting a set of FEA mode shapes to them, one frequency at a time. Then it was shown that the participations of the modes in the experimental data can be used to construct an ***expanded set of measurements*** using all of the DOFs of the FEA mode shapes, including the DOFs that were common with the experimental data.

A key advantage of this approach is that ***only the FEA mode shapes*** are required in the calculations. Accurate mode shapes can be easily obtained from a simple FEA model. FEA frequencies that match the EMA frequencies usually require a more accurate FEA model, but only the mode shapes are required for this calculation.

Another advantage of this approach is that complex data can be decomposed using ***normal modes***. Modes are called ***normal*** when the FEA model they are derived from has ***no damping terms***, and hence the mode shapes are real valued or normal. Normal modes can be used to expand ***complex mode shape or ODS data*** because the ***modal participation factors are complex*** valued.

This decomposition and expansion capability is primarily useful for creating measurements for all of the ***un-measured DOFs*** on a machine or structure. An expanded set of FRFs can then be curve fit using FRF-based curve fitting to obtain EMA modes with ***frequency, damping***, and ***expanded mode shapes*** in them. This EMA modal model can then be used for SDM and MIMO Modeling & Simulation studies involving ***un-measured DOFs*** of the structure.

This combined use of an analytical model with experimental data provides a more complete characterization of the dynamic behavior of a structure from a ***relatively small number of measurements***. This means that less time & expense are required to obtain meaningful data for use in machinery & structural health monitoring, or for troubleshooting noise & vibration problems.

References

1. Richardson, S.C., Richardson, M.H.: Using photo modeling to obtain the modes of a structure. In: Proceedings of the International Modal Analysis Conference, 2008
2. Richardson, M.: Is it a mode shape or an operating deflection shape? Sound Vib. Mag. (1997)
3. Richardson, M.: Modal analysis versus finite element analysis. Sound Vib. Mag. (2005)
4. Schwarz, B, Richardson, M.: Linear Superposition and modal participation. In: IMAC XXXII, February 3–6, 2014
5. Schwarz, S.R., Richardson, M.: Using mode shapes for real time ODS animation. IMAC XXXIII, February 3–5, 2015

Chapter 4
Acceleration Measurement Optimization: Mounting Considerations and Sensor Mass Effect

Marine Dumont, Andy Cook, and Norton Kinsley

Abstract In the world of acceleration, a common topic is that of modal analysis. Within this topic, applications can range from the study of bridges as vehicles roll across them, to the qualification of very delicate space and aviation equipment. One can see that modal analysis contains a very large spectrum of applications. However, there is a small detail that is commonly overlooked, and that is the proper mounting of very sensitive accelerometers. Mounting options include direct stud mounting, wax mounting, magnetic mounting and a variety of options in-between. Although these options are diverse, they come with varying stiffness and sometimes with the cost of addition mass, termed the mass loading effect. The first part of this paper will take an in-depth look into some of the more common mistakes made during mounting, as well as a look into what can be done to optimize the mounting to avoid unwanted results. In the second part of this paper, there will be an exploration into the results of poorly mounted accelerometers; then a look in more detail at what the mass loading effect and stiffness are and how these can drastically change the measurement results.

Keywords Accelerometers • Resonance • Mounting • Sensor • Frequency

4.1 Sensor Mounting Considerations: Introduction

To obtain useful measurement information, an accelerometer must be coupled so that complete event information is transferred. Mounting methods may vary, with some transferring event information more effectively than others. A high performance accelerometer will behave like a low performance accelerometer if the mounting method is inadequate. The transfer function behavior between the mechanical input properties and electrical output properties can be characterized by a "Single Degree of Freedom" (SDOF) system with a mounted resonance frequency, which will decrease if the mounting method becomes less stiff. This is illustrated in Fig. 4.1.

If we simplify the sensor and its mounting method to be a similar oscillating system with a period T_n in seconds and a natural frequency $f_n = 1/T_n$ in Hz, where Hz = 1/s, the natural frequency of the system will be dependent on the mass m of the system and the stiffness of the system through the spring constant k according to the Eq. (4.1) below:

$$f_n = \frac{1}{2\pi}\sqrt{\frac{k}{m}} \tag{4.1}$$

As a rule, the most rigid and lightest available mounting method option should be used at all times. The easiest mountings, such as magnetic mounting and wax mounting, affect the high frequency event information reaching the accelerometer. The reason for this is that it adds mass m to the system, as in the case of the magnet mounting base, and also reduces the spring constant k as well. The application and the type of data desired should ultimately drive the mounting approach. If low frequency events are being measured, a secure, easy mounting method is suitable.

Figure 4.2 lists numerous accelerometer mounting options. To achieve the most accurate frequency response with the highest stiffness k, the stud mounting method should be used. Unfortunately, this often leads to a more demanding preparation, such as drilling and tapping a mounting hole, creating a high surface quality and incorporating the use of a torque wrench. Although stud mounting an accelerometer produces the most accurate results, drilling and tapping a hole can cause changes detrimental to the structure under study. Adhesive mounting using glue or wax is easier to handle but will restrict the measurement temperature range and may also require solvent or heat to remove the sensor. Magnetic mounting

M. Dumont (✉) • A. Cook • N. Kinsley
Kistler Instrument Corp., 75 John Glenn Drive, Amherst, NY 14228-2171, USA
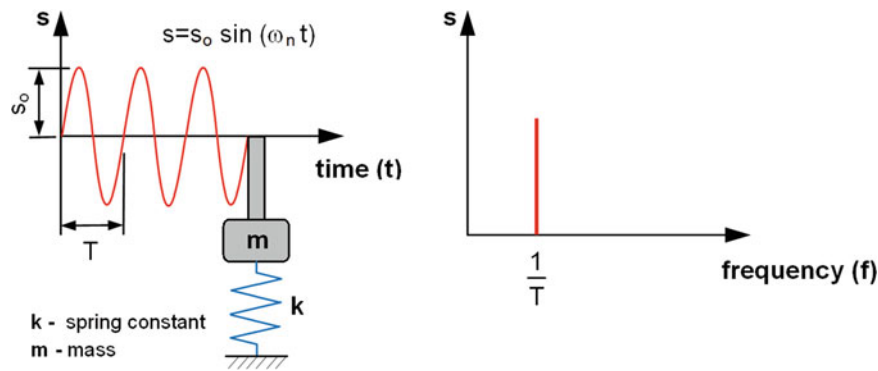e-mail: marine.dumont@kistler.com

Fig. 4.1 Oscillating single degree of freedom system and its corresponding frequency spectrum
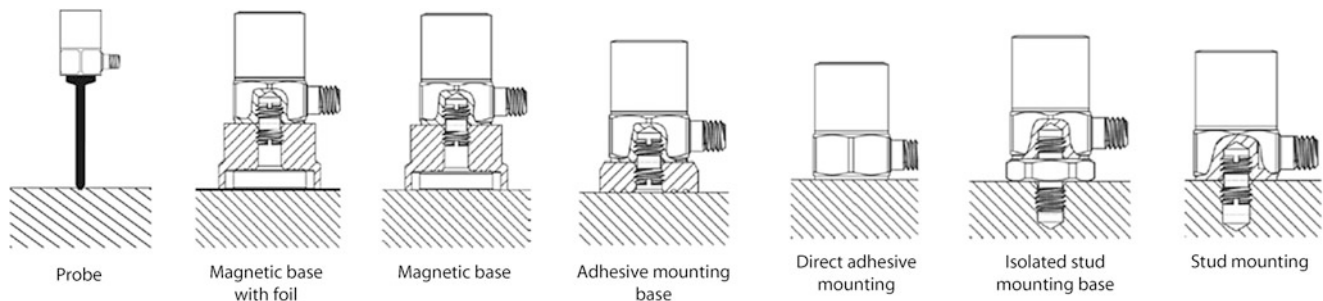

Fig. 4.2 Sensor mounting configurations from lowest mounted resonance to highest mounted resonance

bases allow for a wider range of mounting positions, but with this flexibility, however, the magnetic mounting bases will restrict the acceleration amplitude due to the higher mass m of the sensor and mounting base with respect to the magnetic force holding the sensor to the structure. Magnetic mounting also requires a ferromagnetic surface as well as the additional weight of the magnetic mounting base itself.

4.2   Sensor Mounting and Handling Rules

Once a mounting method is chosen, there are basic rules to follow in order to ensure the best measurement accuracy. First of all, we are going to be looking into the stud mount method, which is the most commonly used mounting method. We can start be looking at an application such as calibration.

Many accelerometers are specifically designed for stud mounting. Most mounting studs are machined from beryllium copper which is known for high strength, low modulus of elasticity and high elastic limits. The studs on many types are removable allowing for both stud and adhesive mounting. The following guidelines should be followed when stud mounting accelerometers. Drill and tap an adequate hole to allow flush mounting of the accelerometer. Make sure the stud does not bottom out and firmly secures the accelerometer. A chamfer should be machined at the top of the mounting hole to ensure that the base of the accelerometer makes full contact with the mounting surface, as seen in Fig. 4.3. Completely clean the surface prior to mounting and apply a thin coat of silicon grease to both the accelerometer and mounting surface. The influence of this will be discussed later in this paper. Always use the proper sockets and a torque wrench when installing accelerometers. Tighten the accelerometer to the torque specified on the individually supplied calibration certificate. Do not overtighten.

Some accelerometers are specifically designed for adhesive mounting and require no special mounting adapters. Units furnished with stud holes can also be used with adhesives. The mounting surface should be smooth and flat. A cyanoacrylate type adhesive such as Eastman 910, Loctite 496, or super glue is recommended. See Table 4.1 for recommendations contingent upon temperature and 'Temporary/Removable' or 'Permanent' configurations. While epoxies can also be used, cyanoacrylate adhesives provide an extremely thin, stiff bond providing optimal frequency response.

When adhesive mounting an accelerometer with a tapped hole, make sure that no adhesive is allowed to enter the hole. This could make stud mounting difficult or impossible at a future time. Remove the sensor with a manufacturer's recommended
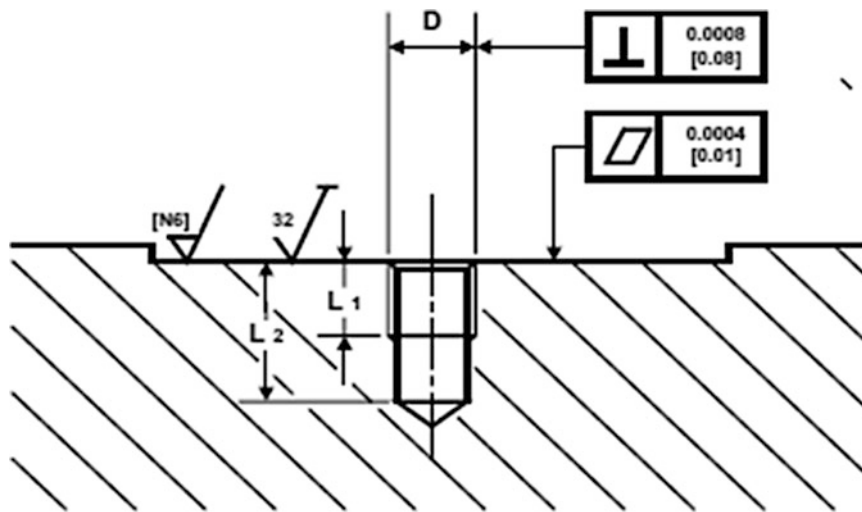
Fig. 4.3 Surface and mounting hole preparation recommendations—L1 and L2 would depend on the stud being used

adhesive solvent. Acetone is effective for the removal of cyanoacrylate adhesives. Once the adhesive is sufficiently softened, you may use the proper size wrench to carefully twist the sensor loose from the mounting surface. Do not impact the sensor with hard objects, such as a hammer, as this can damage the sensor physically and electrically. Do not attempt to remove triaxial accelerometers solely by twisting with pliers, a wrench or impacting. Applying torque with a wrench or other tools will damage the housing or the connector. Remove these accelerometers using a recommended cyanoacrylate solvent (e.g., Loctite 768), then twist with fingers.

If conditions permit, petro-wax is an ideal mounting material for these sensors. Bee's wax has also been used as a mounting agent for many years but the recommended petro-wax (Kistler Type 8432 or P/N P102 from Katt and Associates) is a good replacement for bee's wax since it has been formulated to provide improved frequency response. Wax is a good mounting agent for lightweight sensors in temporary installations where near room temperatures are encountered. It is very often used for calibration of sensors where stud mount is not possible, i.e. adhesive mount sensors only or a triaxial sensor with only one mounting thread.

For all adhesives including wax, there is an optimal thickness to keep the mounting stiffness as high as possible. It is recommended to apply 3 small amounts of wax onto the base of the sensor as illustrated in Fig. 4.4. Press and turn the sensor onto the mounting surface to spread the wax onto the entire surface. The influence of wax layer thickness will be shown later on this paper.

Magnetic mounting is a convenient way to take measurements on ferromagnetic surfaces. A magnetic mounting accessory can add considerable mass m to the sensor and reduces high frequency response as mentioned previously. Care must be taken to make sure the mounting surface is flat and clean. An oil or grease film greatly enhances the coupling characteristics, hence improving the working frequency range. This mounting method is convenient, but it also can be very dangerous to the sensor when mounting to a structure. When attaching to a structure where the magnetic mounting base is already threaded onto the sensor, a sharp metal to metal impact can occur that can lead to sensor overload and damage. In order to prevent it, always try to first mount the magnet onto the surface then thread the sensor onto the magnet mounting base or approach the mounting surface with an angle such as illustrated in Fig. 4.5.

In the next section, we are going to show the results of testing investigations and provide an easy methodology to determine if a sensor and its mounting accessory mass have an influence on the measurement performed. This will also determine if the proper mounting method has been selected to insure the needed frequency response.

4.3   Hsu-Nielsen Source Test: Simple Method for Resonance Frequency Analysis

For a given accelerometer, the working frequency range with a sensitivity deviation of ± 5 % is typically around 20 % of the mounted resonance frequency as illustrated in Fig. 4.6. A higher input frequency spectrum excites the mechanical resonance of the accelerometer and creates 'amplified' output signals. Linearity between the mechanical input and the electrical output signal in this frequency range can be expected.

Table 4.1 Adhesive recommendations according to temperature and Permanent/non-Permanent mounting

Adhesives	Mounting area		Ambient temperature		Availability		Solvent
	Smooth, polished	Rough	Room, Temp.	Temperature range	Manufacture	Kistler	
Tempoary/Removeable							
Synthetic wax/Petro wax	■	■	■			■	Not required
Double-sided glue tape	■	■	■		3M (Type 465,924)		–
One-sided aluminum glue tape	■	■	■		3M (Type 433, 431)		–
Theremosetting plastic glue tape (www.nittousa.com)				Up to 150 °C	Nitto Denki (USA), P-224AMB		
High tensile silicone flash masking tape (www.nittousa.com)				Up to 180 °C	Nitto Denko (USA), PS-1		
Fixed/Removeable/Permanent							
Super glue, liquid	■			Refer to manufacturer instructions	Adhesive, Henkel Teroson, UHC Gmbh		MEK (1)
Super glue, gel	■	■		Refer to manufacturer instructions	Adhesive, Henkel Teroson, UHU GmbH		MEK (1)
Hot glue (w/hot glue gun)	■	■		Up to 65 °C approx	Adhesive, Henkel Teroson, UHU GmbH		
Permanent							
Epoxy resin, 2 components	■	■		Up to 120 °C approx	Adhesive Henkel Teroson, UHU GmbH		
325 Speed bonder	■	■		−55 °C … 180 °C	Adhesive, Hen-kel Teroson		

**Fig. 4.4** Apply three small amounts of wax on the sensor base

**Fig. 4.5** Correct way of approaching mounting surface to installed sensor with magnetic base
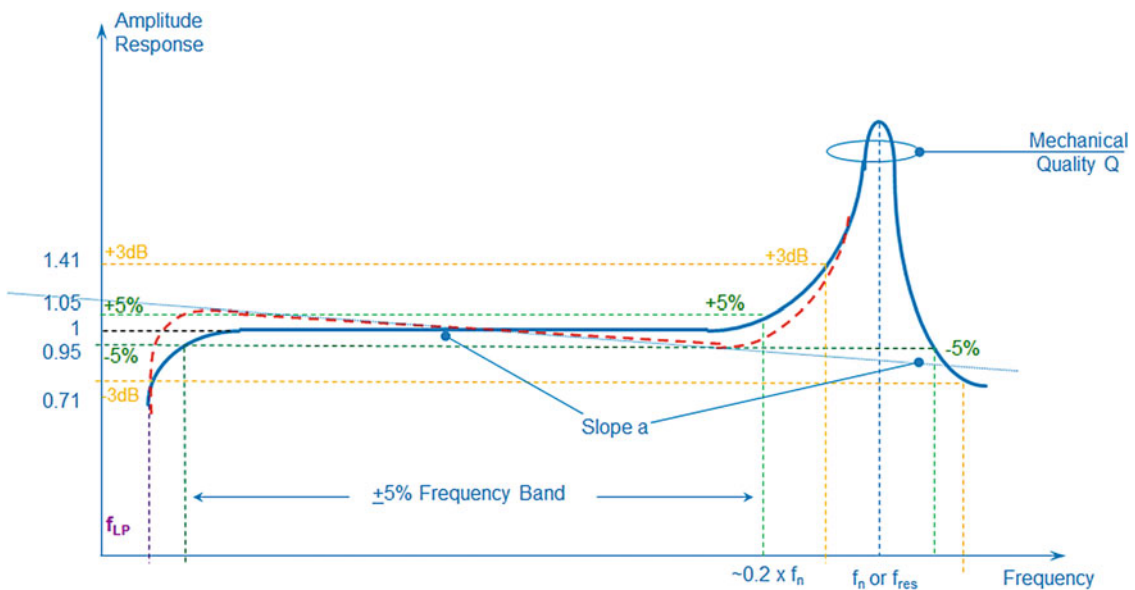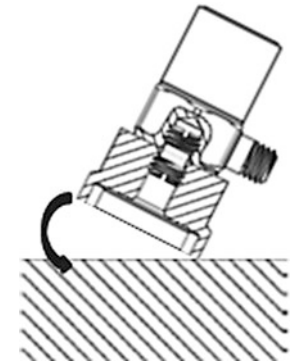
Fig. 4.6 Typical frequency response of an IEPE sensor when stud mounted

The Hsu-Nielson Source test method per EN ASTM Std. E976-1984 is an easy method using the breaking of a mechanical pencil lead to produce wide frequency range excitation signal. Originally used for testing acoustic emission sensors, the test is also excellent for testing the mounted resonance frequency of an accelerometer. The method is shown in Fig. 4.7 in which an accelerometer is connected to an appropriate amplifier and the signal captured on a transient recorder or fast sampling rate scope with trigger mode. Once the pencil lead breaks, it generates a wide frequency content pulse that makes the accelerometer start 'ringing'. This frequency is the resonance frequency in the mounted state for the accelerometer.
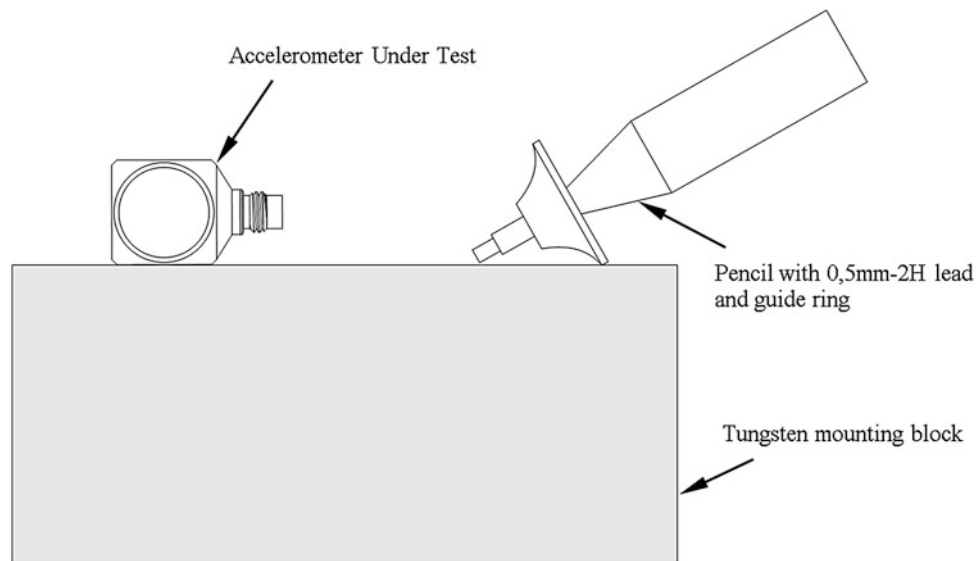
Fig. 4.7 Sample setup of the Hsu-Nielson test to find the resonance frequency of an accelerometer (ASTM E976-10)
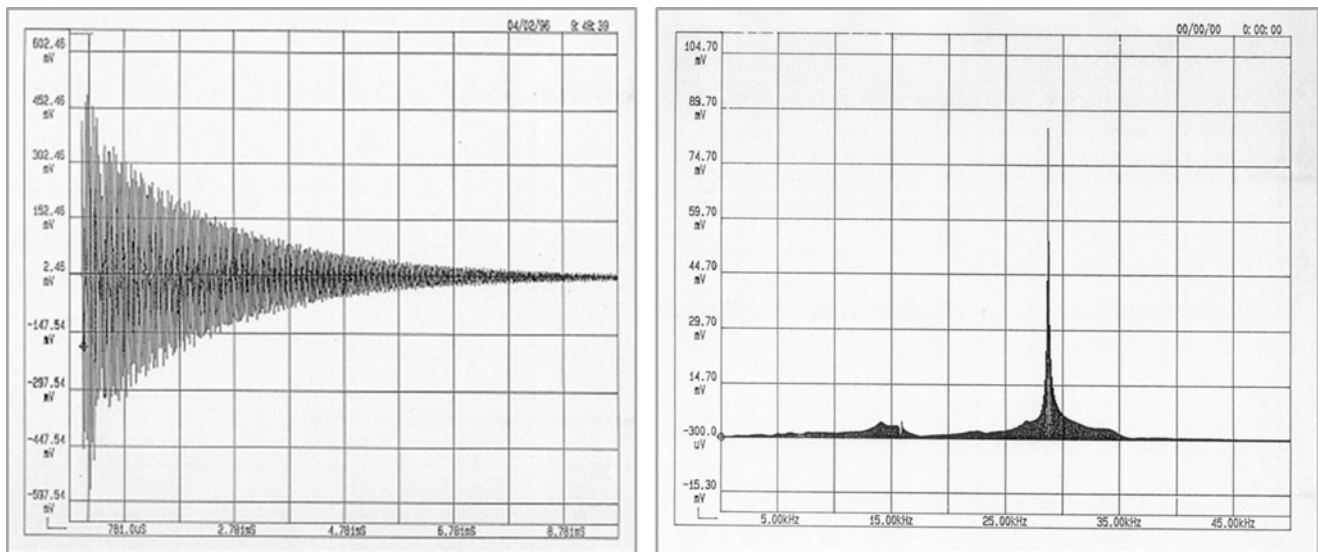
Fig. 4.8 (**a**) & (**b**) Analysis of the transient response with FFT. (**a**) time domain, (**b**) frequency domain)

Typically, a 0.5 mm diameter, 2H pencil lead is used at an approximate length of 3 mm. If a smaller intensity signal is needed, a thinner diameter pencil lead can be used, e.g. 0.3 mm or 0.35 mm diameter. Conversely, if larger signal intensity is needed then a thicker diameter lead, such as a 0.7 mm diameter pencil lead, should be used. A softer pencil lead may also be used to decrease the signal intensity as well. Pencil leads with a hardness of H, HB and B series will produce a lower frequency, lower intensity input signal while harder leads such as the H series will produce a higher frequency, higher intensity input signal. A plastic guide ring such as in Fig. 4.7 is used to provide the right break angle to the surface of the test body. It also prevents contact impact at the same time. Figure 4.8a, b show example of test results.
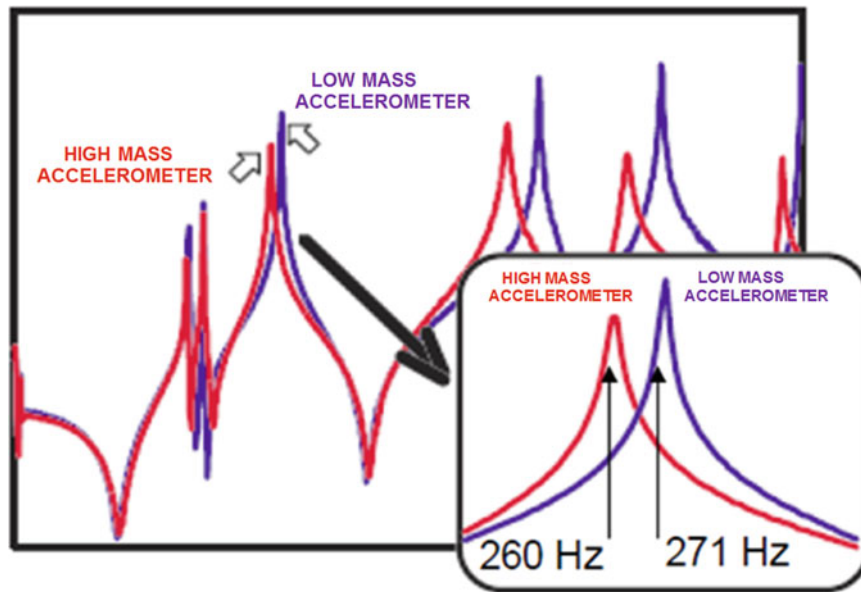
Fig. 4.9 Structural Analysis of the same structure with a high mass accelerometer (*red*) and a low mass accelerometer (*purple*). *Source*: Experimental Techniques, Jan/Feb 2002

4.4 Sensor and Mounting Accessory Mass Effect

The dynamic properties of a structure are dependent on its mass, rigidity and damping. If the mounting of an accelerometer applies an additional mass to the structure, these dynamic properties change. The resonance frequency f_n of the structure reduces by approximately Δf where m is the mass of the structure and m_a is the mass of the accelerometer (4.2). Vibration amplitude a_0 reduces approximately as shown by Eq. (4.3).

$$\Delta f = f_n \left(1 - \sqrt{\frac{m}{m_a + m}} \right) \tag{4.2}$$

$$\frac{a}{a_0} = \frac{m}{m_a + m} \tag{4.3}$$

If the effect of adding an accelerometer to a test structure is found to be negligible, then the mass of the accelerometer must be negligible compared to the mass of the structure being measured. An example can be found in Fig. 4.9, which shows the same measurement being made using a low mass or a high mass accelerometer. One can see very quickly the influence of the sensor mass on the resonance peak frequency and amplitude.

As a part of one's daily work, this can be checked very easily using the Hsu-Nielsen test method from part C. A first Hsu-Nielsen test should be performed with the sensor mounted on the structure and then a second test with double the accelerometer mass using a second sensor used for mass only. If a second sensor is not available, then an equivalent mass can be used. If there is no significant change to the results, this suggests that the sensor mass has little effect on the structure.

4.5 Experimental Analysis of Mounting Method Influence on Frequency Response

A study has been conducted using the Hsu-Nielsen test method to illustrate some of the points mentioned in Sects. 4.1 and 4.2. This will help provide an understanding as to why selecting the right accessory is of high importance and why following the recommendation for usage of this accessory is important for measurement accuracy. The first portion of the study uses a single axis PiezoStar sensor type 8703A50M5. This sensor is specified frequency response up to 10 kHz at ±5 % with a nominal resonance frequency of 40 kHz when stud mounted. The test data will show how the different mounting types can

influence the mounted resonance frequency for the very same sensor when the rules for each recommended mounting option are carefully followed.

The first measurement was conducted with the sensor being stud mounted using mounting grease and the appropriate mounting torque. A resonance frequency of 39.1 kHz is measured as shown in Fig. 4.10. This resonance frequency value will be used as a baseline for other measurement techniques as this method provides the best result. A second measurement was performed with the same test conditions except the accelerometer was mounted using an isolated mounting stud. This should reduce stiffness of the system so should reduce the resonance frequency. As seen in Fig. 4.11, the resonance frequency is slightly lower at 37.9 kHz (−3 % from baseline). The isolated mounting stud had very little influence on the resonance frequency.

The sensor was then wax mounted using the proper amount of wax and proper mounting technique. Figure 4.12 shows the resonance frequency measured at 35.5 kHz (−9 % from baseline). This provides an acceptable result allowing an accurate method for sensor calibration. Of course, this does not allow for as high a frequency measurement as the stud mount.

Last but not least, let's have a look at the same test using a magnetic mounting base. The magnetic mounting base adds mass to the accelerometer/mounting base system. The stiffness of the mounting system relies on the strength of the interaction between the magnet mounting base and mounting surface. The test results show the resonance frequency is lowered down to 17.5 kHz (−55 % from baseline) as shown in Fig. 4.13. This confirms the statement from Sect. 4.1: the most rigid and lightest available mounting method option should be used at all times.

We advised in Sect. 4.2 to use grease and the recommended mounting torque when stud mounting an accelerometer. Figure 4.14 shows measurement results using the 8703A50M5 sensor with different mounting configurations. It can be seen that the worst case scenario would be low mounting torque and no grease. In this case, a reduction of the resonance frequency by 25 % from baseline is observed. In the next case, where grease is used but the mounting torque is still too low, the resonance frequency is reduced by 6 % from baseline. Once the recommended mounting torque is applied along with the usage of grease, the frequency response is optimized. In this test environment, the grease has very little influence on the
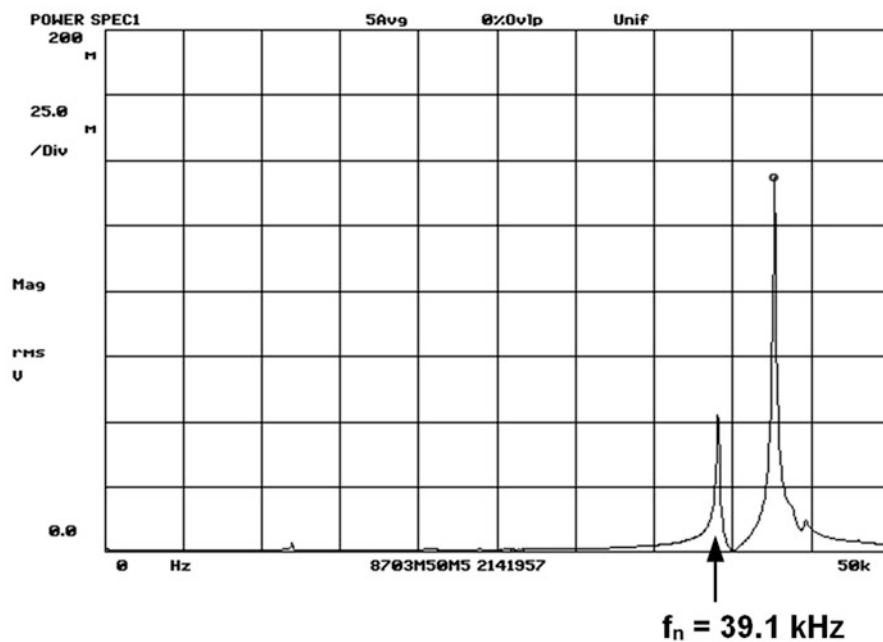

Fig. 4.10 8703A50M5 mounted using stud, recommended mounting *torque* and *grease*, $f_n = 39.1$ kHz
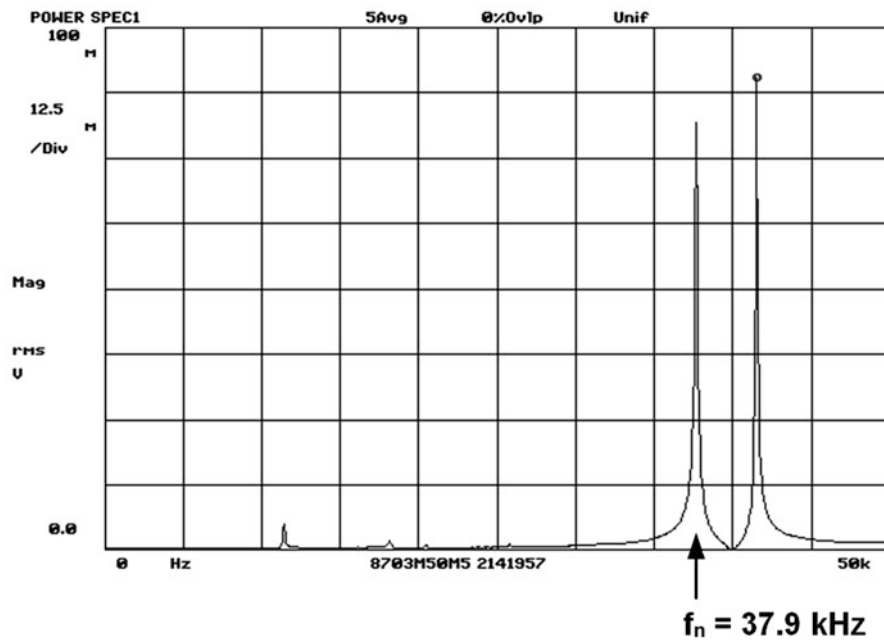
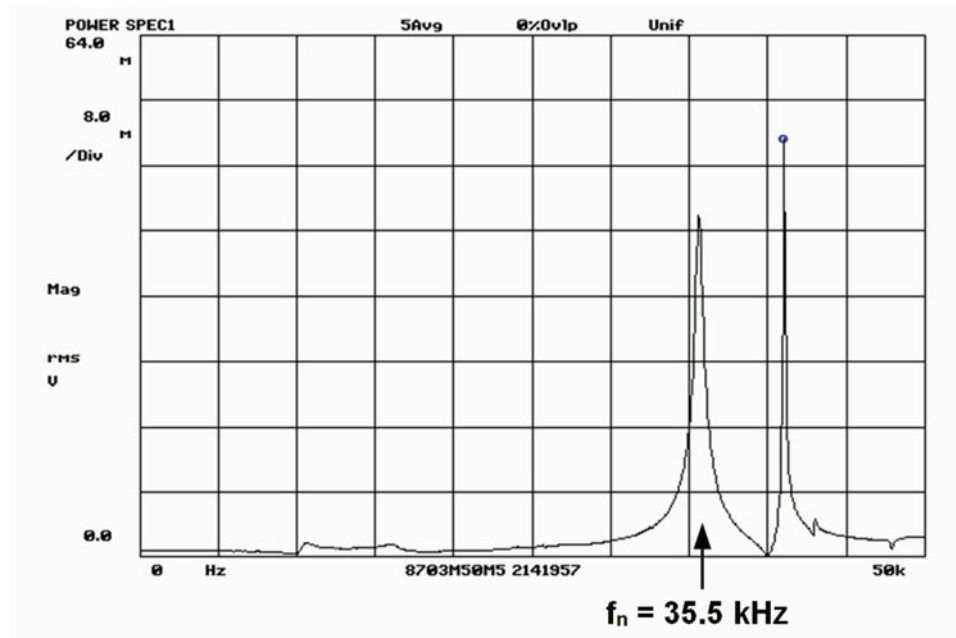**Fig. 4.11** 8703A50M5 mounted using isolated mounting stud, $f_n = 37.9$ kHz

Fig. 4.12 8703A50M5 mounted with ideal amount of wax, $f_n = 35.5$ kHz

resonance frequency due the good quality of the mounting surface. In cases where mounting surfaces are poor and there are gaps between the accelerometer and the mounting surface, the use of grease improves performance due to better adherence between the mounting surfaces and the filling of gaps.

The next part of the study conducted looked into frequency responses using wax mounting methods. Figure 4.15 shows three resonance plots of the same 8703A50M5 used in the other tests. The mounting conditions were defined by using a less than ideal amount of wax, the recommended amount of wax and more than the ideal amount of wax. Figure 4.15b shows little difference in resonance when using a less than ideal amount of wax, only a drop of 5.6 %. But what cannot be seen on the plot is that the strength of the wax mounting bond is much less which in turn leads to a lower useable acceleration level.
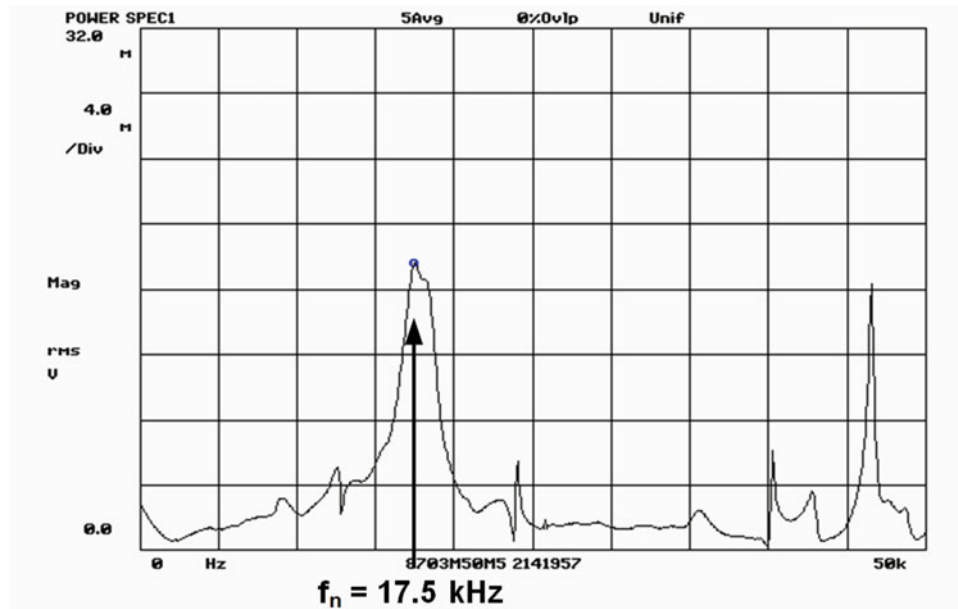
Fig. 4.13 8703A50M5 mounted with magnetic mounting base, $f_n = 17.5$ kHz
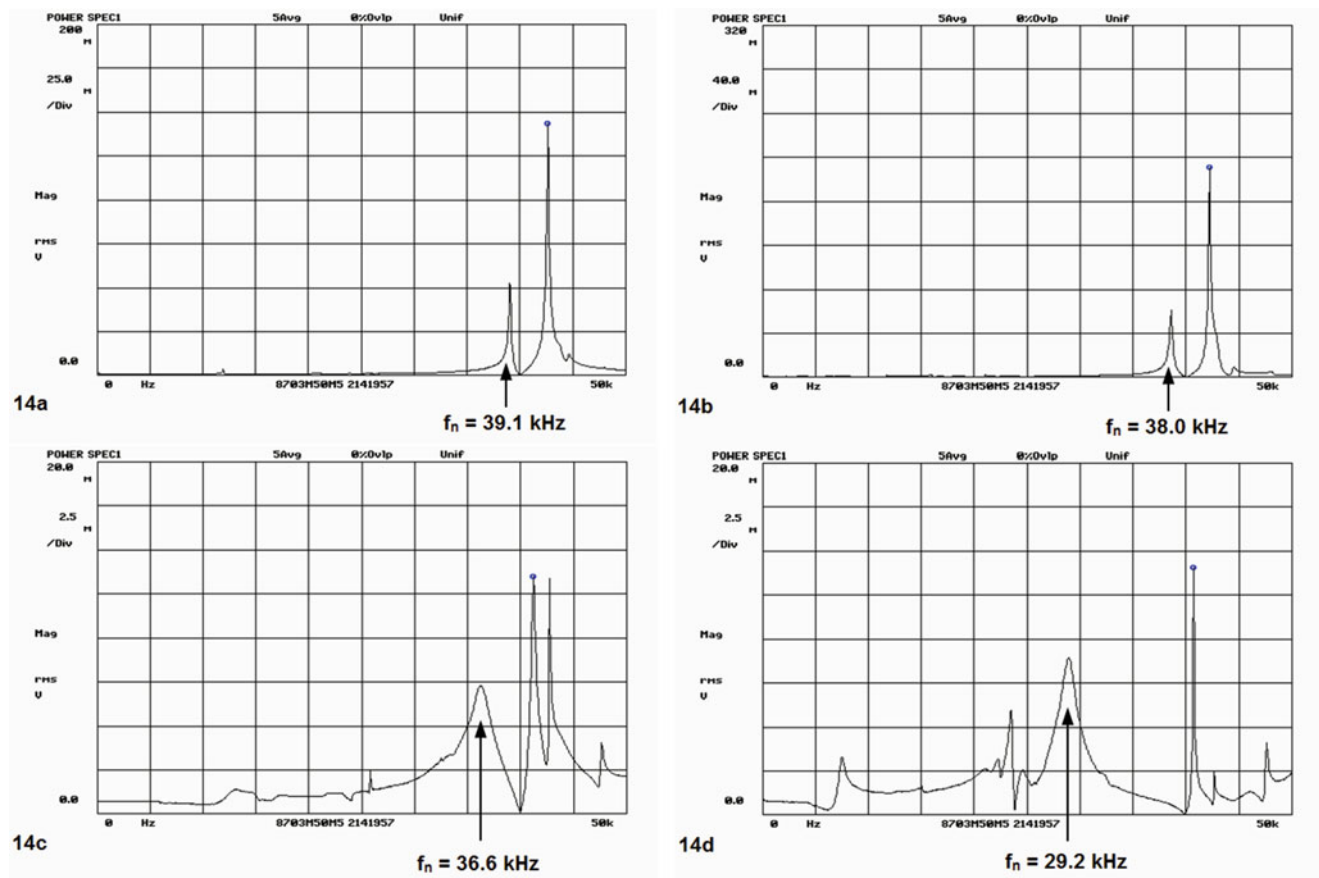
Fig. 4.14 (**a**), (**b**), (**c**) & (**d**) 8703A50M5 stud mounted with vs. without grease and with vs. without recommended mounting *torque*, (**a**) stud mounted using grease and recommended *torque*: $f_n = 39.1$ kHz, (**b**) stud mounted using no grease and recommended *torque*: $f_n = 38.0$ kHz, (**c**) stud mounted using grease and low *torque*: $f_n = 36.6$ kHz, (**d**) stud mounted using no grease and low *torque*: $f_n = 29.2$ kHz

Fig. 4.15 (**a**), (**b**) & (**c**) 8703A50M5 wax mounted, (**a**) ideal amount of wax: $f_n = 35.5$ kHz, (**b**) less than ideal amount of wax: $f_n = 33.5$ kHz, (**c**) more than ideal amount of wax: $f_n = 14.2$ kHz
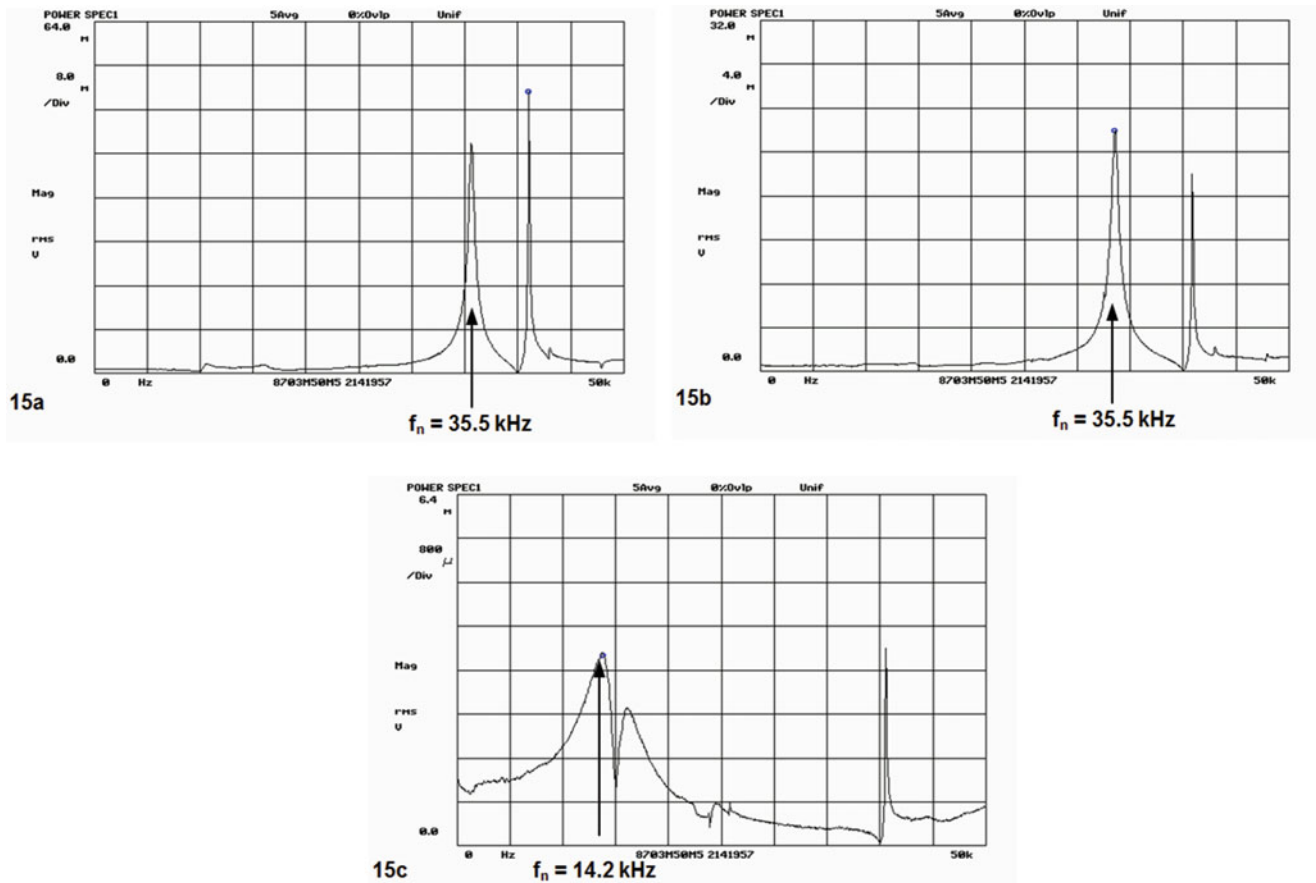
It is much more likely that the accelerometer will detach from the mounting surface when a less than ideal amount of wax was applied. On the other hand, too much wax will lead to a more compliant mount leading to a decrease in resonance frequency of about 60 % from ideal.

4.6 Conclusion

The mounting method of an accelerometer should not only be considered by the ease of mounting criteria, but also by the corresponding upper frequency response for the chosen mounting method. Each mounting solution acts as a spring; the more flexible the coupling, the lower the frequencies that have to be produced in order to induce resonance phenomena. The most rigid connection is possible with a stud mount, while the least rigid can be obtained with magnetic mounting. The wax mounting and adhesive mounting methods fall somewhere in between, with layers as thin and hard as possible while still attaining optimal performance. In this paper, a study of mounted resonance frequencies was performed using the most popular mounting configurations in order to highlight how much sensor mass, mounting accessory mass and rigidity can influence the mounted resonance frequency of the system and hence the frequency response of an accelerometer.

As an easy assessment, the Hsu-Nielsen test can be used to determine the resonance frequency of a mounted accelerometer. From this result, the rule of thumb that the +5 % frequency response deviation is somewhere around 0.2 times the resonance frequency can be applied.

Chapter 5
Experimental Study on the Impact of the Number of Laminas on the Dynamics Behavior of an Electric Machine Stator

F. Chauvicourt, S. Orlando, W. Desmet, J.J.C. Gyselinck, and C.T. Faria

Abstract Electromagnetic forces applied on the stator of an electric machine highly contribute to its overall acoustic noise. Made of steel, the stator core is also considered as the main transfer path contributor to the electrical machine mass and stiffness. Moreover it is composed of axially stacked steel laminations to reduce eddy current losses during the electric motor operation. Those hundreds of laminas do not behave like solid steel which makes the modelling process non-trivial. A systematic approach is then followed in this paper, which starts from modal testing of a single sheet and progressively increasing the number of laminas in a stack until the corresponding length of a full stator is reached. Therefore the effects of the inter-laminar interference on the structural behavior are investigated for the different number of laminas in a stack. Specific nonlinearities checks are also carried out to characterize the different structures. The preliminary results show promising linear behavior for radial-type excitations whilst axial components present some possibly high nonlinearities.

Keywords SRM • Laminated core • Vibration • Experimental modal analysis • Stator

5.1 Introduction

Nowadays electric powertrains are extensively considered as one of the alternatives to the internal combustion engine (ICE) technology. Pure electric vehicles and plug-in hybrid electric vehicles, known for short as P(H)EV, have a higher efficiency when compared to their ICE counterparts, and therefore have attracted much of the researchers' attention and interests in the last few years. Several electric propulsion technologies are already available on the market and involve different electric motor types. In order to lower the cost of these machines, researchers focus on permanent-magnet-less electric motor types, e.g. Switched Reluctance Machines (SRM) [1]. However, these types of machines are commonly associated with high levels of acoustic noise and vibrations issues. Noise, Vibration and Harshness (NVH) analyses need to be performed in order to predict accurately the critical frequencies of interest and allow these issues to be addressed early in the design stage.

Over the past decades the stator vibration due to electromagnetic excitation have been often assumed to be the most important source contributors to acoustic noise [2–4]; other secondary sources such as unbalance or bearing noise have also been studied by other authors [3]. The stator core is not the only structure that vibrates while excited but there are also the windings, the housing and the cooling jacket. Those components might have non-negligible effects on the dynamic behavior of the machine. In particular the distribution of mass and stiffness between each component of the full assembly has to be addressed. For instance, in the case of aluminium housing the core steel allows it to stand upon the largest portion of mass and stiffness of the full assembly. As such most of the e-machine vibration characteristics depend on the stator core ones [5]. This assumption is made in this study. Yet the stator core structural vibrations' prediction is not trivial due to its composition and

---

F. Chauvicourt (✉)
Siemens Industry Software NV, Researchpark 1237, Interleuvenlaan 68, 3001 Leuven, Belgium

Katholieke Universiteit Leuven, Leuven, Belgium

Université Libre de Bruxelles, Leuven, Belgium
e-mail: fabien.chauvicourt@siemens.com

S. Orlando • C.T. Faria
Siemens Industry Software NV, Researchpark 1237, Interleuvenlaan 68, 3001 Leuven, Belgium

W. Desmet
Katholieke Universiteit Leuven, Leuven, Belgium

J.J.C. Gyselinck
Université Libre de Bruxelles, Leuven, Belgium

construction. Nowadays it is always made of thin laminations axially pressed together to considerably reduce eddy current losses [6]. Additionally for some cases, over-heating risks are minimized by impregnating a thin insulation resin between each lamination. The mechanical pressure to hold them is applied through various technologies e.g. clamping with bolts and interlocks. All of these design technologies show different structural behaviors. Nonetheless two distinct mode orientations can be extracted to characterize such structure: axial and radial modes respectively called bending and radial modes [7]. Previous work showed promising comparison between experimental and numerical results for single and five-lamina stacks in bending scenario [8]. Hence it should be mentioned that the work presented in this study describes a work in progress in which the initial observations are documented.

In this paper a few different lamina stacks, with lengths starting from a single sheet to the corresponding length of 185 mm (i.e. 528 laminas) are studied. Section 5.2 details the experimental setups for bending and radial excitation. In Sect. 5.3 the results are displayed for the different stacks under investigation. The last section discusses and presents conclusions on the influence of the number of laminations upon the modal parameters, i.e. natural frequencies, damping ratios and mode shapes.

5.2 Experimental Setup

5.2.1 Test Specimens

For the purpose of modal parameter estimation, Experimental Modal Analyses (EMAs) have been carried out on test specimens of increasing stack length from 1 lamina to 528 laminas corresponding to a full stator designed for automotive application. Figure 5.1 shows four representations of the test specimens under study with their corresponding cartesian and cylindrical coordinates. Their measured thickness, mass and the number of samples available are shown in Table 5.1. Free vibrations were of interest in order to obtain the modal parameters only dependent on the structure itself and not the environment. Flexible ropes have been used to hang each specimen to a static frame. They indeed reproduce free vibrations by avoiding the rigid body modes to interfere with the flexible modes of the specimen. Then the ropes' flexibility is of the utmost importance and entirely depends on each specimen's mass. It is also self-evident that the specimen's length and mass
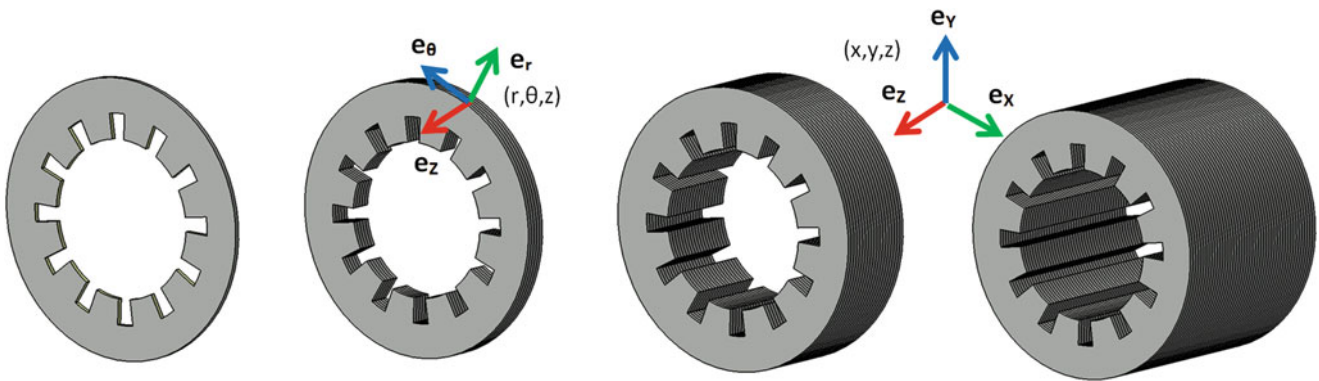

Fig. 5.1 Representation of some samples (from left to right): 1, 10, 178 and 528 laminas

Table 5.1 Lamination stacks under investigation

Number of laminas	Number of samples	Thickness (mm)	Mass (kg)	Number of measurement points & direction	Excitation device
1	3	0.35	0.0268	16 Axial	Hammer
5	2	1.75	0.1327	16 Axial & 16 × 1 Radial	Hammer
10	1	3.50	0.2682	16 Axial & 16 × 1 Radial	Hammer
20	1	7.00	0.5366	16 Axial & 16 × 1 Radial	Hammer
178: 1/3 stator	1	62.3	4.750	16 × 3 Radial	Shaker
528: full stator	1	185	14.250	16 Axial & 16 × 4 Radial	Shaker
528: full stator + windings	1	185	19.200	16 × 4 Radial	Shaker

bring constraints to the possible excitation device; for example, radial excitation was practically not feasible for a single lamina specimen because of its very low thickness. Bearing those limitations in mind, two different experimental setups, referred to as setups A and B, have been built involving two different rope types.

The setup A concerned the specimens lighter than 1 kg i.e. from 1 to 20 lamina-stacks and the setup B was used for the heavier specimens i.e. from 128 to 528 lamina-stacks. For setup A, a lightweight impact hammer (PCB Piezotronics SN14893) was used in combination with a unidirectional accelerometer (PCB Piezotronics 352A24 of 0.8 g). For setup B, an integral shaker (LMS Qsource SN045) was used together with 8 tri-axial accelerometers (PCB Piezotronics SN 356A22) spread around the stator circumference. The data acquisition system was a SCADAS III. It should be noted that the additional mass load brought by the sensors has been minimized by using lightweight sensors. Performing multiple runs allowed for the reduction of mass load as well since the amount of sensors used could be lowered for each run. The measurement point resolution to run the EMA is specimen-dependent and detailed in Table 5.1.

As mentioned in [8], challenging measurements have been encountered especially for lightweight specimens such as 1, 5, 10 and 20 lamina stacks. Therefore the measurements need to be validated by examining several structural testing criteria, e.g. linearity, repeatability and coherence.

5.2.2 Validity of the Measurements

EMA theory holds on linearity principle which can be verified by running two tests that can be called linearity and reciprocity checks. The linearity test verifies if the ratio output/input corresponding to any Frequency Response Function (FRF) is constant. This consequently presupposes the independency of the FRFs on the input magnitude given to the structure, which can be evaluated by performing several tests with different forces input levels. The reciprocity condition implies that the waves follow the same transfer path independently from the input location. One can verify that by measuring the FRF from an input force at a point M and output acceleration at a point N and then reversing the experiment by applying a force in point N and measuring the response at point M. The resemblance between the two FRFs corroborates the reciprocity. Figure 5.2 presents two reciprocity checks for the full stator, both with and without windings. Repeatability principle states that two identical samples tested within the same operational configuration should demonstrate an equal structural behavior. Thus for example temperature, errors of the operators, inaccuracies in the excitation and imperfect manufacturing process must not affect the final measured data. Another consistent estimator of a reliable measurement is the coherence [9]. It has been constantly checked during the experimental campaign.

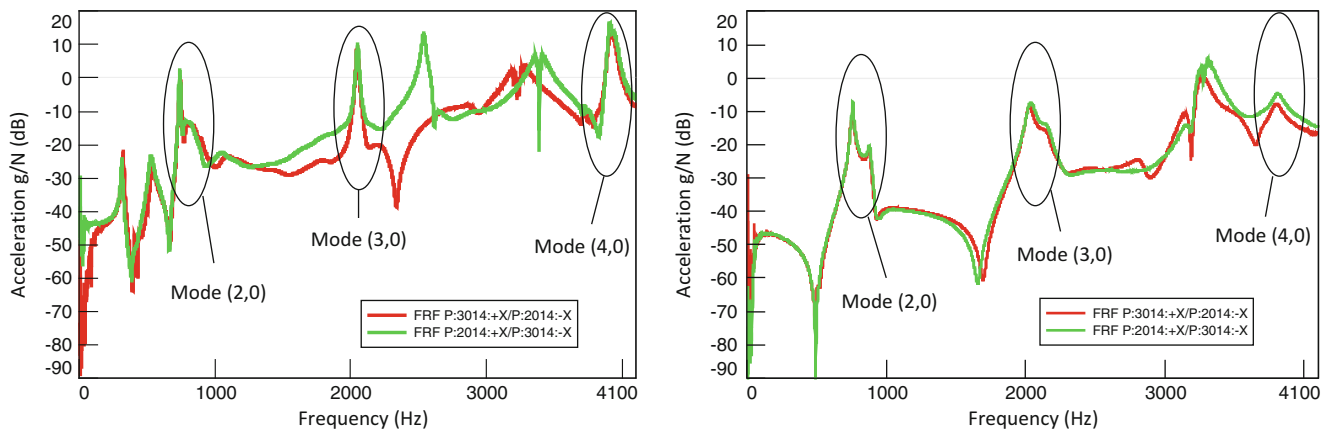All the validity tests have been performed and allowed to assume the linearity of each sample under study.

Fig. 5.2 Reciprocity check of the full stator without (*left*) and with (*right*) windings

5.3 Results

As soon as the linearity is assumed, one can estimate the modal parameters for each test specimen. The theoretical principle to obtain these parameters is widely known nowadays and uses the curve-fitting method as described in [10]. A linear mathematical parametric model provides the theoretical FRF $H(\omega)$ of the structure while our measurements give the real FRFs. Equation (5.1) shows the Multiple Degree of Freedom (MDOF) model where the unknowns are the residuals A_k, damping ratios ξ_k and eigenfrequencies ω_k for each mode k.

$$
H(\omega) = \sum_{k=1}^{n} \frac{A_k}{j\omega - \lambda_k} + \frac{A_k^*}{j\omega - \lambda_k^*}
$$
$$
\text{where } \lambda_k, \lambda_k^* = -\xi_k \omega_k \pm j \sqrt{1 - \xi_k^2} \omega_k
$$

(5.1)

These unknowns are the typical modal parameters to extract. Other algorithms shall be used such as Least Squares Complex Exponential (LSCE) [11], Single Degree of Freedom (SDOF) and PolyMAX [12]. In this study, PolyMAX implemented into LMS Test.lab software is used since it allows easy and fast parameter estimation together with giving high identification capabilities for highly damped structures.

It should also be reminded that two main mode orientations characterize the overall stator core vibrations. The bending modes correspond to its deformation in the z-axis direction while the radial modes represent the one in (r,θ) plane. Since they are uncoupled, the influence of the number of laminas on the dynamic behavior of each stack has been studied separately for the two different mode orientations.

5.3.1 Bending Modes Study

Figures 5.3 and 5.4 show a few mode shapes and the summations of the FRFs obtained for each sample in the case of axial excitation respectively. Figure 5.5 compiles the modal parameters for each bending mode and every sample that allowed such experiment.

The bending mode shapes are reconstructed and easily recognizable. It is important to notice that the higher the thickness, the higher the natural frequency of all the modes. The magnitude of the FRFs also decreases considerably with the number of laminas. In addition, several high modes disappear with the increase of the stack length. The single lamina clearly shows undamped behavior while the full stator displays quite low amplitudes. Yet no trivial relations for the natural frequencies and the damping ratios can be derived.

5.3.2 Radial Modes Study

The radial mode shapes of the full stator with windings in Fig. 5.6 look similar to what can be expected [13]. Besides Figs. 5.7 and 5.8 demonstrate the negligible effect of the number of laminations on the modal parameters; except for the stator with windings. In this last case, the coils act like an extra stiffness and mass in the radial direction. Thus, the natural frequencies slightly rise whilst the damping ratio almost doubles. Additionally the windings have the effect of generating antisymmetric modes of the form (n,1). It indicates that they harden the structure so it behaves such as a solid cylinder [14].
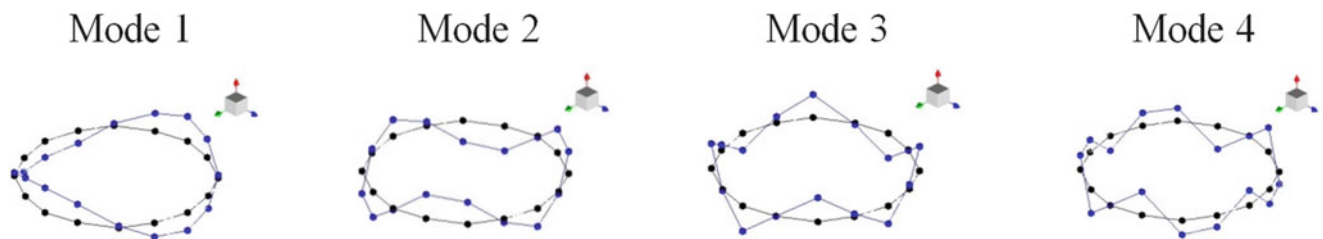

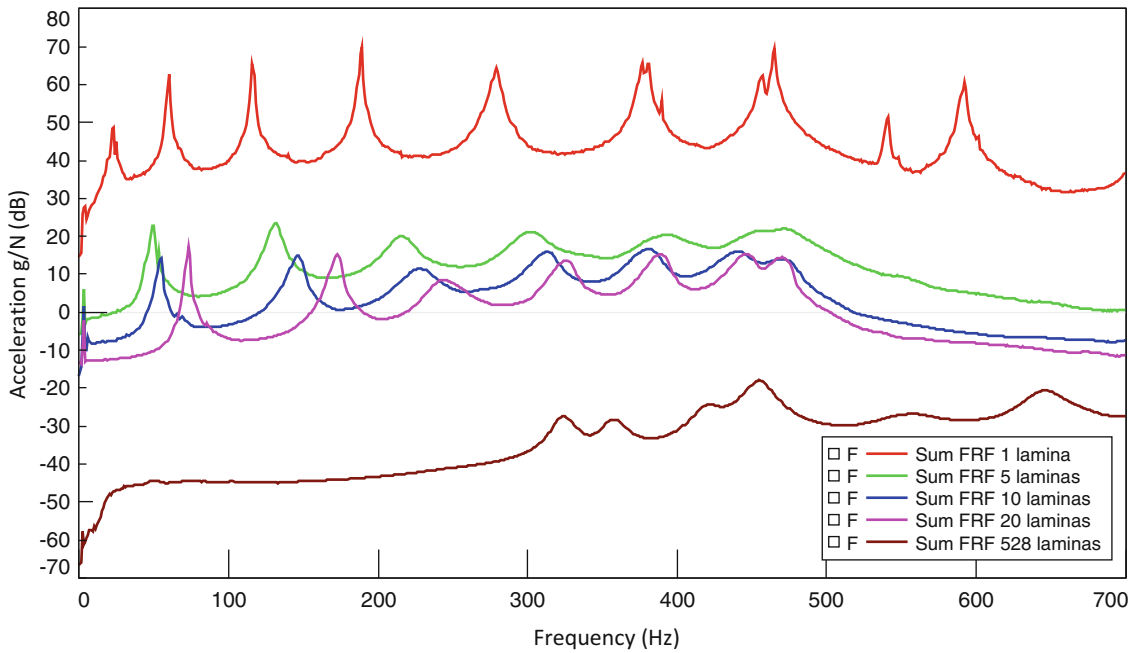**Fig. 5.3** Axial/Bending mode shapes of 10 lamina stack

Fig. 5.4 Summations of the FRFs in axial excitation case for different lamina stacks
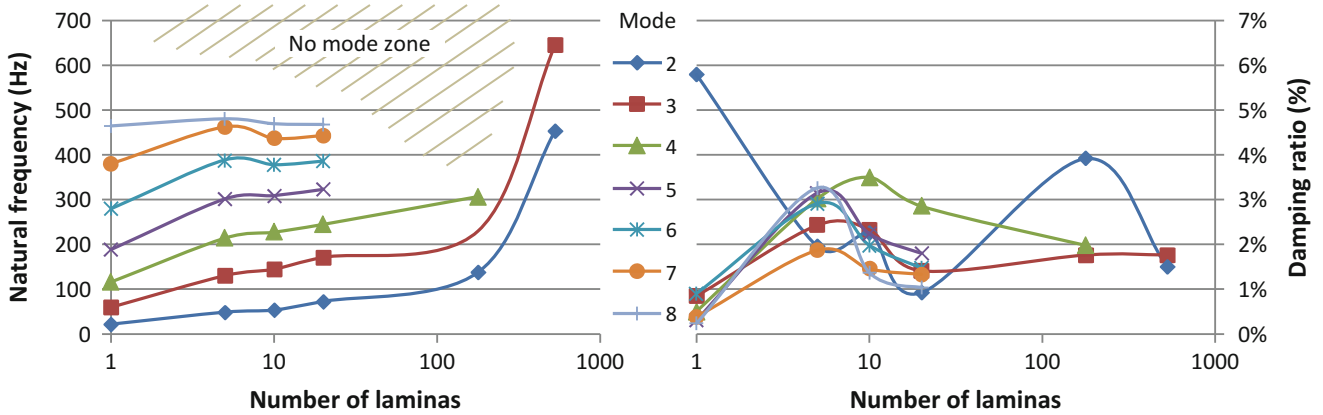

Fig. 5.5 Modal parameters for axial modes

5.4 Conclusions

In this paper, the influence of the laminations on the structural behavior of an SRM stator core has been studied. Several lamination stacks of increasing thickness have been tested starting from single lamina to the corresponding stack of a full stator core. The effects of the windings have also been investigated. The FRF measurements have been validated through standard checks, especially for the linearity assumption on which EMAs rely. One had to treat non-linearity behaviors with caution and could define reliable frequency ranges in which the linearity principle can be assumed. The natural frequencies of the radial modes show non dependency on the number of laminas. Meanwhile, the thicker the stack, the higher the damping ratios and the lower the FRFs magnitudes; although no trivial relation could be derived from the data. In the axial modes frame, all the modal parameters vary with the number of laminas. The laminations give additional stiffness and damping to the core, which leads to a total disappearance of some modes for the thickest samples. Finally, antisymmetric modes occur with the incorporation of the windings in between the poles. The stiffening effect of these windings is not significant since copper is much more flexible than steel. Their fixation to the core is also of importance to characterize their overall influence on the stiffness. On the other hand, the damping ratio is almost doubled compared to the sample without windings.

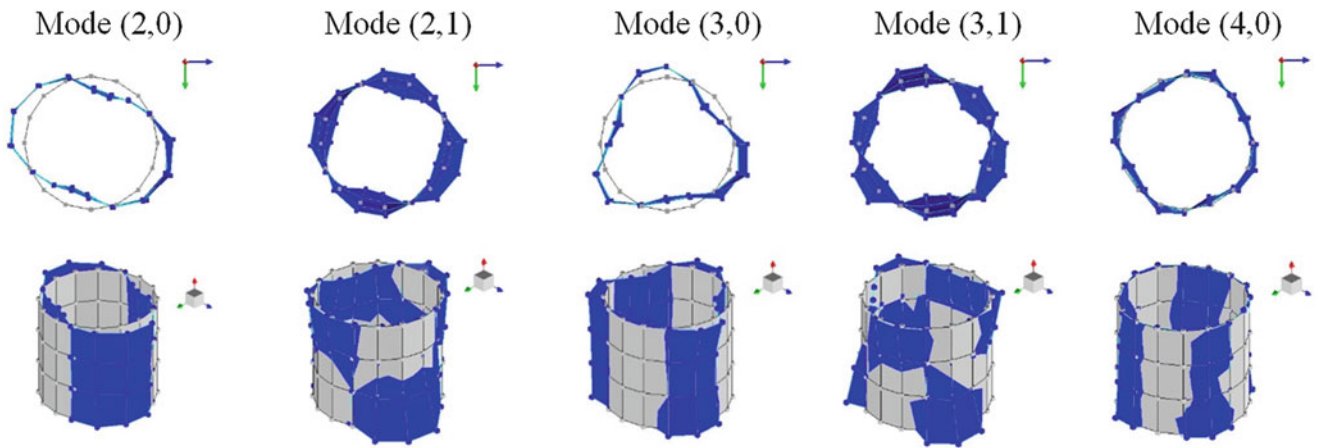**Fig. 5.6** Radial mode shapes of the full stator with windings; undeformed (*grey*) and deformed (*blue*)
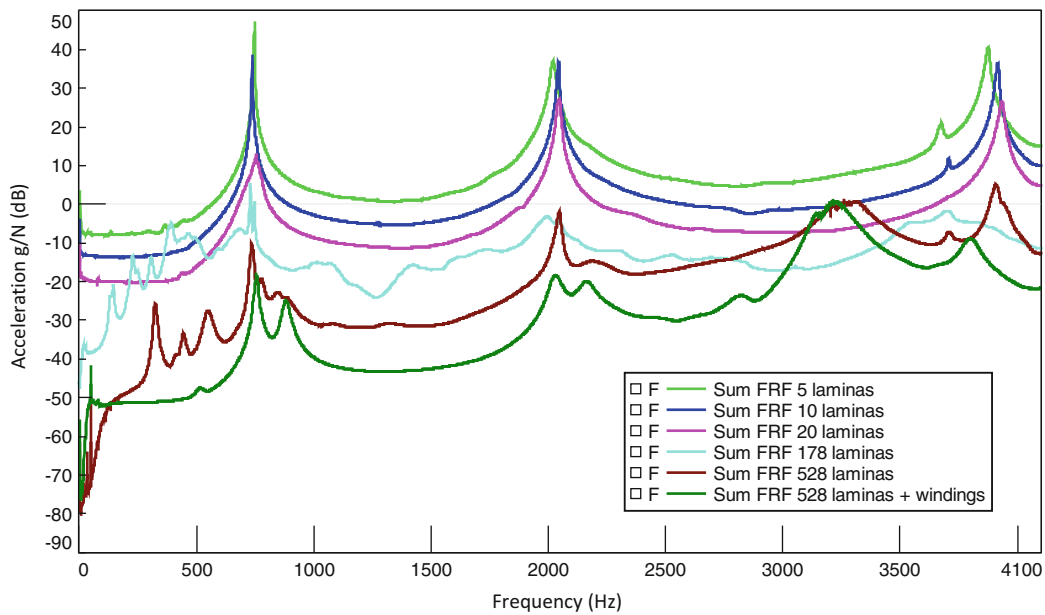

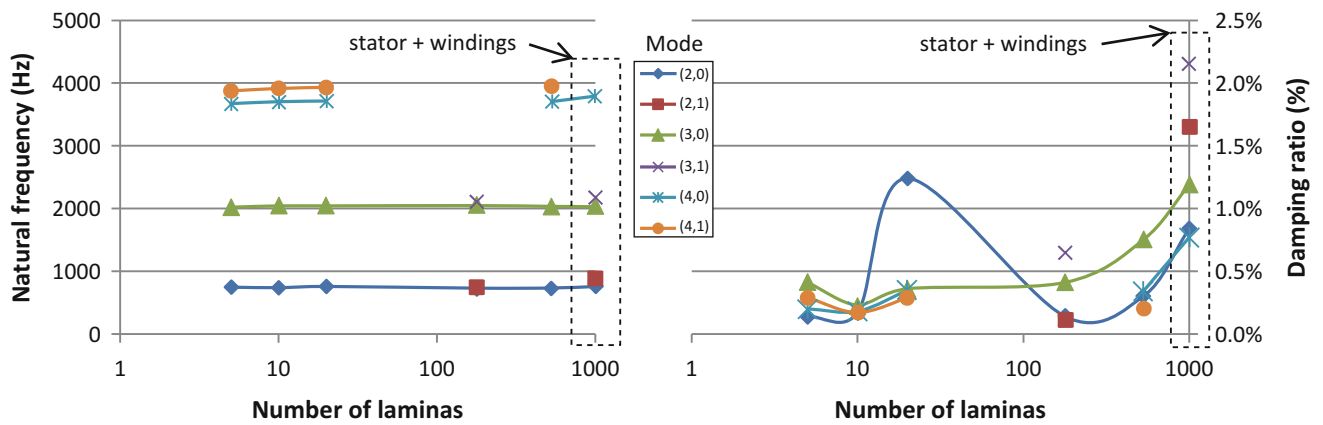**Fig. 5.7** Summations of the FRFs in radial excitation case for different lamina stacks

Fig. 5.8 Modal parameters for radial modes

References

1. Stefanskyi, A., Dziechciarz, A., Chauvicourt, F., Sfakianakis, G.E., Ramakrishnan, K., Niyomsatian, K., Curti, M., Djukic, N., Romanazzi, P., Ayat, S., Wiedemann, S., Peng, W., Stipetic, S.: Researchers within the EU funded Marie Curie ITN project ADEPT, grant number 607361. 2013–2017
2. dos Santos, F.L.M., et al.: Multiphysics NVH modeling: simulation of a switched reluctance motor for an electric vehicle. IEEE Trans. Ind. Electron. **61**(1), (2014)
3. Hendershot, J.R.: Causes and sources of audible noise in electric motors
4. Shiohata, K. et al.: The study on electromagnetic force induced vibration and noise from a normal and an eccentric universal motors. PIERS Proceedings, Marrakesh, 1654–1660 2011
5. Penniman, A.L., et al.: Suppression of magnetic vibration and noise of two-pole turbine generators. AIEE Trans. **60**, 283–288 (1941)
6. Crow, A.: Stator and Rotor Laminations From Prototype to Volume Production. UKMAG Seminar Advances in Machine Manufacture, Newcastle, UK (2013)
7. Garvey, S.: The vibrational behaviour of laminated components in electrical machines. In: Proceedings of 4th International Conference on Electrical Machines, London, 226–231 September 1989
8. Chauvicourt, F. et al.: Experimental and numerical validation of laminated structure dynamics from a SRM stator. ICEDyn Lagos (PT), June 2015
9. Boot, J.: Frequency response measurement in closed loop: brushing up our knowledge. TUe Eindhoven, April 2003
10. Døssing, O.: Structural Testing. Brüel & Kjaer, Denmark (1988). http://www.bksv.com/doc/br0507.pdf
11. Guillaume, P., et al.: Frequency-domain maximum likelihood identification of modal parameters with confidence intervals. In: Proceedings of ISMA 23, the International Conference on Noise and Vibration Engineering, Leuven, Belgium, 16–18 September 1998
12. Peeters, B., et al.: The PolyMAX frequency-domain method: a new standard for modal parameter estimation? Shock Vib. **11**(3–4), 395–409 (2004)
13. Cai, W., et al.: Resonant frequencies and mode shapes of switched reluctance motors. IEEE Trans. Energy Convers. **16**(1), 43–48 (2001)
14. Singal, R.K., et al.: Vibration behaviour of stators of electrical machines, Part II: experimental study. J. Sound Vib. **115**(1), 13–23 (1987)

Chapter 6
Normalization of Complex Mode Shapes by Truncation of Alpha-Polynomial

A.C. Niranjan, R.J. Allemang, and A.W. Phillips

Abstract Finite Element (F.E.) models need validating in order to reliably predict the dynamic properties of the system. One parameter that is necessary for updating the analytical models is the mode shape. The mode shapes obtained from analytical models are real-valued (normal modes), whereas the experimental mode shapes are more often than not complex-valued (complex modes). In order to be able to compare the experimental and analytical mode shapes, the former needs to be normalized. Two techniques to normalize the complex mode shapes will be discussed in this paper. The first technique is a pre-processing technique based on truncation of the α polynomial obtained from the Unified Matrix Polynomial Approach (UMPA) model of modal parameter estimation (MPE). The proposed technique eliminated the damping and normalized the complex modal vectors, however, the undamped natural frequencies deviated from that of the actual system. The disagreement in natural frequencies is explained with the help of 2 and 4 degree of freedom (DOF) analytical models. The second normalization method proposed is a post-processing technique based on the partial fraction method of residue synthesis. The technique successfully normalized the complex modal vectors with a very good correlation with the actual (complex) mode shapes resulting in a very high modal assurance criterion (MAC) value.

Keywords Normalization • Complex modes • Truncation • Damping distribution

6.1 Introduction

Modal Parameters of a system are often required to define its dynamic properties. These modal parameters can be estimated by experimental measurements or through analytical techniques like Finite Element (F.E.) models. The F.E. models, however, might need updating so that the results from the models are comparable to the experimentally obtained results. This process is called model calibration. Model calibration can be defined as the process of adjusting the physical modeling parameters of the system in the computational model to improve agreement with the experimental data [1, 2].

One such modal parameter that needs to be compared to validate the F.E. model is the mode shape. The nature of a mode shape, real or complex, usually depends on the damping characteristic of the system. Proportional or no damping in general yields real mode shapes and non-proportional damping typically yields complex mode shapes. There is no way currently to accurately determine the physical damping distribution of any system [3]. F.E. models, therefore, are comprised of the mass and stiffness properties and the damping is assumed to be proportional to mass and/or stiffness. Therefore, the mode shapes obtained from F.E. models are real in nature, whereas the mode shapes obtained from experimental measurements are complex. It is important to obtain the real-normal mode shapes from the experimental measurements in order to be able to compare it with the mode shapes from analytical model and thereby calibrate or validate it. In this paper, two methods to normalize the complex experimental mode shapes are evaluated.

6.2 Background

The characteristic equation of a MDOF system in the laplace domain can be given as,

$$[[M]s^2 + [C]s + [K]]\{X(s)\} = \{F(s)\} \tag{6.1}$$

A.C. Niranjan (✉) • R.J. Allemang • A.W. Phillips
Structural Dynamics Research Laboratory, College of Engineering and Applied Sciences, University of Cincinnati, Cincinnati, OH 45221-0072, USA
e-mail: niranjaa@mail.uc.edu; addy614@gmail.com

And, the transfer function of the system is given as,

$$[H_{pq}(s)] = \frac{\{X_p(s)\}}{\{F_q(s)\}} = \frac{1}{[M]s^2 + [C]s + [K]} \tag{6.2}$$

where,

$[M]$, $[C]$ and $[K]$ are the mass, damping and stiffness matrices respectively
$\{X_p(s)\}$ is the response at point 'p'
$\{F_q(s)\}$ is the input force at point 'q'

6.2.1 Polynomial Model

The transfer function can also be represented in a polynomial form. The numerator and denominator both are represented by two polynomials with independent variable 's'. The coefficients of these polynomials are different numerical combinations of the discrete values of mass, damping and stiffness of the system. The roots of the denominator are the modal frequencies of the system. The polynomial form for a single input single output (SISO) is given as,

$$H_{pq} = \frac{X_p(s)}{F_q(s)} = \frac{\beta_n(s)^n + \beta_{n-1}(s)^{n-1} + \cdots + \beta_1(s)^1 + \beta_0(s)^0}{\alpha_m(s)^m + \alpha_{m-1}(s)^{m-1} + \cdots + \alpha_1(s)^1 + \alpha_0(s)^0} \tag{6.3}$$

For a MDOF system, the transfer function for this model in concise form can be given as follows,

$$\sum_{k=0}^{m}[[\alpha_k](s)^k][H_{pq}(s)] = \sum_{k=0}^{n}[[\beta_k](s)^k][I] \tag{6.4}$$

The modal frequencies and modal vectors of the system can be estimated from the denominator of Eq. (6.2) as stated in Sect. 6.2.1. For a MIMO system, the modal parameters can be found by solving, using companion matrices, for the roots of the following polynomial with matrix coefficients,

$$\left| [\alpha_m](s)^m + [\alpha_{m-1}](s)^{m-1} + \cdots + [\alpha_1(s)]^1 + [\alpha_0](s)^0 \right| = 0 \tag{6.5}$$

The roots of the polynomial, λ_r, can be given as,

$$\lambda_r = \sigma_r \pm j\omega_r \tag{6.6}$$

where,

σ_r is the modal damping corresponding to the mode r
ω_r is the damped natural frequency corresponding to mode r

6.2.2 Companion Matrix

To find the roots of a polynomial, companion matrices are often used. The eigenvalue decomposition of a companion matrix gives the modal frequencies and vectors of the system. There are different ways in which a companion matrix can be formulated. For instance, the companion matrix of the following equation,

$$[I](s)^m + [\alpha_{m-1}](s)^{m-1} + [\alpha_{m-2}](s)^{m-2} + \cdots + [\alpha_1](s)^1 + [\alpha_0](s)^0 = 0 \tag{6.7}$$

can be given as follows,

$$[C] = \begin{bmatrix} -[\alpha_{m-1}] & -[\alpha_{m-2}] & \cdots & -[\alpha_1] & -[\alpha_0] \\ [I] & [0] & \cdots & [0] & [0] \\ [0] & [I] & \cdots & [0] & [0] \\ \vdots & \vdots & \vdots & \vdots & \vdots \\ [0] & [0] & \cdots & [I] & [0] \end{bmatrix}$$

The developed companion matrix can be used in the following eigenvalue decomposition formulation to obtain the modal frequencies and vectors,

$$[C][\phi] = [\lambda][\phi] \tag{6.8}$$

where,

$[\phi]$ is the eigenvector matrix
$[\lambda]$ is a diagonal matrix of modal frequencies

If the α matrices are of size $n \times n$, and the order of the polynomial is m, then there will be $n \times m$ modal frequencies, λ. And, the eigenvector, $[\phi]$, will have the size $(n \times m) \times (n \times m)$. The eigenvectors will not be the actual modal vectors of the system. The meaningful modal vectors will be the last n rows of the $[\phi]$ matrix. The remaining rows are the meaningful modal vectors multiplied by the modal frequencies raised to an increasing power from 1 to $(m - 1)$.

6.3 Normalization by Truncation of the α Polynomial

6.3.1 Background

For a multiple degree of freedom system, the characteristic equation is given as shown in Eq. (6.1). In the characteristic equation, the damping associated with the system is given by the $[C]$ matrix. Therefore, on eliminating this matrix, the damping can be eliminated from the system which will give the undamped natural frequencies and real mode shapes, as can be seen the damping matrix is the coefficient of the odd powered variable, s^1. Therefore, it can be said that by eliminating the odd powered term in the polynomial, the undamped solution for the system can be obtained. This understanding will be tested further in next few sections on polynomials with an order larger than two.

6.3.2 Elimination of Odd Powered Terms

Using the UMPA model, the second order characteristic system equation is expanded to an α polynomial during the modal parameter estimation. The order of this α polynomial varies with every iteration. For the Rational Fraction Polynomial (RFP) algorithm, the lowest order of the polynomial will be two (i.e. iteration 1). Therefore at iteration 3, the order of the polynomial will be four. The α polynomial with order four can given as,

$$\left| [\alpha_4](s)^4 + [\alpha_3](s)^3 + [\alpha_2](s)^2 + [\alpha_1(s)]^1 + [\alpha_0](s)^0 \right| = 0 \tag{6.9}$$

After eliminating the odd powered terms in the polynomial equation (6.9), it reduces to,

$$\left| [\alpha_4](s)^4 + [\alpha_2](s)^2 + [\alpha_0](s)^0 \right| = 0 \tag{6.10}$$

The companion matrix for this polynomial will be,

$$[C] = \begin{bmatrix} [0] & -[\alpha_2] & [0] & -[\alpha_0] \\ [I] & [0] & [0] & [0] \\ [0] & [I] & [0] & [0] \\ [0] & [0] & [I] & [0] \end{bmatrix} \tag{6.11}$$

Eigenvalue decomposition of Eq. (6.11) will give the eigenvalues and eigenvectors through which the modal frequencies and mode shapes can be obtained.

6.3.3 Application on a Circular Plate

The normalization technique discussed in Sect. 6.3.2 was used on the data obtained from a circular plate. The modal frequencies after truncation are compared with the absolute values of the modal frequencies before truncation i.e. the undamped natural frequencies of the original system. The modal vectors before and after truncation are also compared using the modal assurance criterion (MAC).

6.3.4 Experimental Setup and Material Properties

A steel circular plate with diameter of 0.91 m (3 ft) and 0.20 m (8 in.) diameter hub, thrice the thickness of the circular plate fixed at the center, with seven references was excited with an impact hammer at 36 points on the plate. The data was acquired from 0 to 2555 Hz with Δf of 5 Hz. The FRF data for the circular plate was obtained using this setup. Since the setup had 36 inputs and seven outputs and 512 frequency points, the dimension of the FRF matrix was $7 \times 36 \times 512$.

6.3.5 Pole Setup and Modal Parameter Estimation

For ease of processing and to obtain stable poles the entire frequency range was not processed at once. If too big a frequency range is selected, the number of frequency points will be very high causing the over determination factor to be larger than desirable which may lead to unstable poles [4]. Therefore, two separate bandwidths were selected and processed. Of the two, the normalization technique was executed on the poles obtained from one of the two selected bandwidths and will be compared with the default poles obtained from X-Modal, a modal parameter estimation software package used at the University of Cincinnati, Structural Dynamics Research Laboratory (UC-SDRL). The parameters of the selected bandwidth are shown in Table 6.1. This data was processed using the RFP algorithm discussed.

6.3.6 Even Powered Polynomials

For iteration 3, the order of the polynomial is 4. Therefore, for this iteration, there are five α matrices as can be seen in Eq. (6.9). These matrices were extracted directly from X-Modal. Since the FRF matrix was 7×36 and a high order short basis frequency domain algorithm was used, the α matrices obtained were of dimension 7×7. The α matrices were then

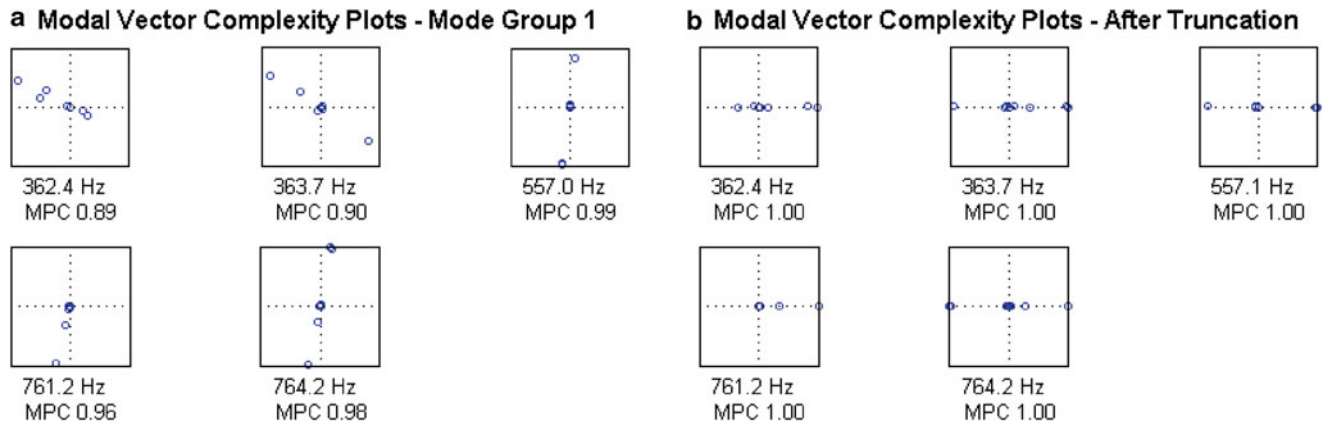**Table 6.1** Parameters for the selected bandwidth

Minimum frequency	145 Hz
Maximum frequency	825 Hz
Minimum time	0.0047 s
Maximum time	0.0998 s
Number of frequency lines	137
Number of time points	131

Table 6.2 Comparison of modal frequencies

Original modal frequencies	Absolute	Modal frequencies after truncation	% Difference
$-3.1498 + 362.3564i$	362.3701	$0.0000 + 362.7741i$	-0.1115
$-3.1498 - 362.3564i$	362.3701	$0.0000 - 362.7741i$	-0.1115
$-3.5025 + 363.6586i$	363.6755	$0.0000 + 363.7470i$	-0.0197
$-3.5025 - 363.6586i$	363.6755	$0.0000 - 363.7470i$	-0.0197
$-2.9191 + 557.0450i$	557.0526	$0.0000 + 556.7307i$	0.0578
$-2.9191 - 557.0450i$	557.0526	$0.0000 - 556.7307i$	0.0578
$-5.1902 + 761.2215i$	761.2392	$0.0000 + 761.4137i$	-0.0229
$-5.1902 - 761.2215i$	761.2392	$0.0000 - 761.4137i$	-0.0229
$-2.5540 + 764.1789i$	764.1831	$0.0000 + 764.1483i$	0.0046
$-2.5540 - 764.1789i$	764.1831	$0.0000 - 764.1483i$	0.0046

a Modal Vector Complexity Plots - Mode Group 1

362.4 Hz MPC 0.89
363.7 Hz MPC 0.90
557.0 Hz MPC 0.99
761.2 Hz MPC 0.96
764.2 Hz MPC 0.98

b Modal Vector Complexity Plots - After Truncation

362.4 Hz MPC 1.00
363.7 Hz MPC 1.00
557.1 Hz MPC 1.00
761.2 Hz MPC 1.00
764.2 Hz MPC 1.00

Fig. 6.1 Modal vector complexity comparison. (**a**) Default. (**b**) After truncation

used to find the modal frequencies and mode shapes using the procedure explained in Sect. 6.3.2. The modal frequencies determined from this technique and the ones obtained from X-Modal, i.e. by considering the complete polynomial are compared in Table 6.2.

In Table 6.2, the modal frequencies in the first column are the original system poles obtained from X-Modal, i.e. the roots obtained by solving the complete polynomial of the system. In the second column are the absolute values of the corresponding modal frequencies in the first column. These absolute values are the undamped natural frequencies of the system. In the third column are the modal frequencies obtained after truncating the polynomial.

As can be seen, the truncation technique eliminates the damping [real part of the modal frequency, Eq. (6.6)] but the obtained frequencies are not the undamped natural frequencies of the system. The percent deviation can be seen in the fourth column of Table 6.2. This deviation in the natural frequency is explained in Sect. 6.5 with the help of 2 and 4 degree of freedom analytical models.

Modal vector complexity plots show the complexity in a particular mode shape or modal vector. The comparison of the complexity of modal vectors before and after truncation is shown in Fig. 6.1. Figure 6.1a shows the default modal vector where some of the estimated modal vectors are real but rotated by an angle. Figure 6.1b shows the modal vectors after truncation. It can be seen that all the modal vectors are real valued and, therefore, it can be concluded that the modal vectors after truncation have been normalized.

The mode shape comparisons are shown in Figs. 6.2, 6.3, 6.4, 6.5, and 6.6.

The modal assurance criterion (MAC) for the modal vectors before and after truncation can be seen in Table 6.3. From the MAC, it can be seen that the modal vectors pre and post truncation are very similar with a MAC coefficient as high as 0.9994. Therefore, it can be concluded that the truncation technique works as far as normalization of complex mode shapes is concerned. However, as stated earlier, the undamped natural frequencies vary from that of the system's.
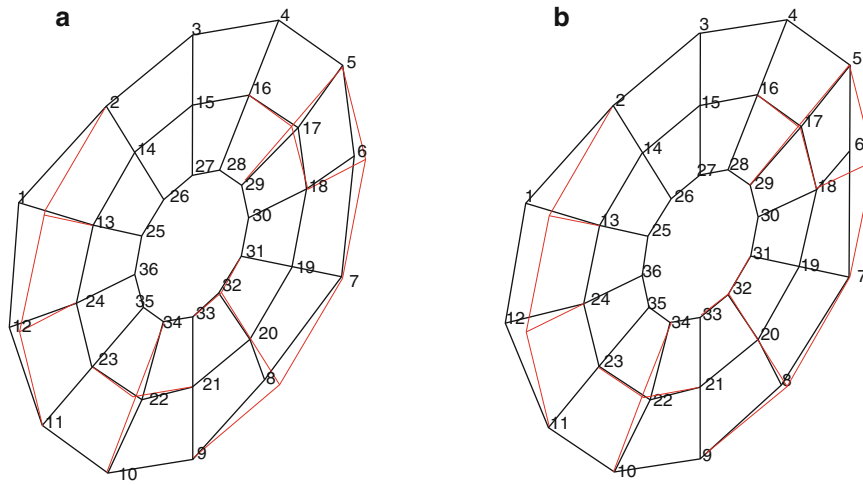
Fig. 6.2 Mode shape at 362 Hz. (**a**) Default. (**b**) After truncation
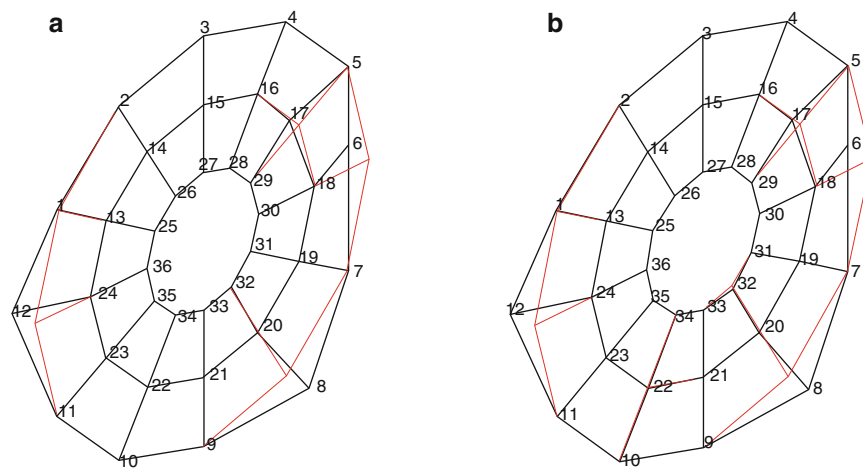
Fig. 6.3 Mode shape at 364 Hz. (**a**) Default. (**b**) After truncation
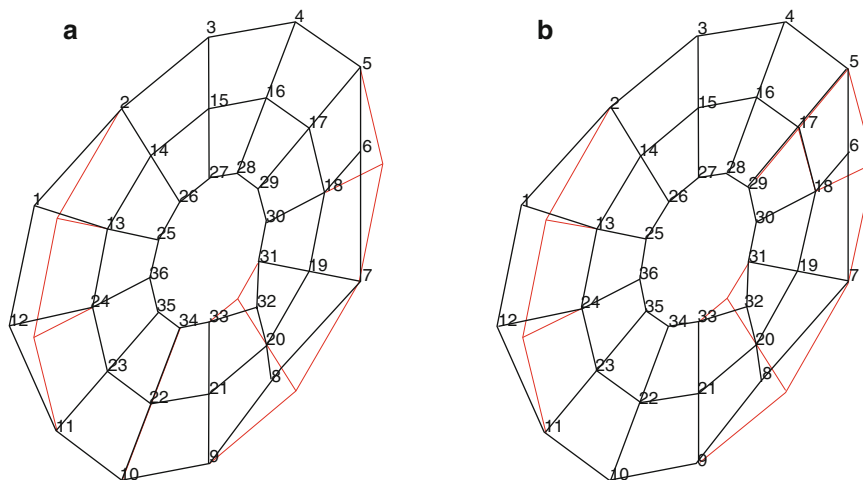
Fig. 6.4 Mode shape at 557 Hz. (**a**) Default. (**b**) After truncation
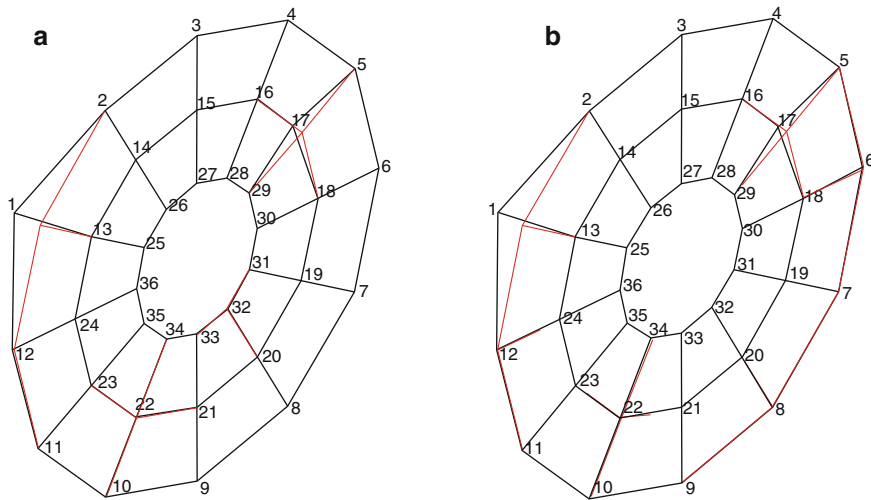
Fig. 6.5 Mode shape at 761 Hz. (**a**) Default. (**b**) After truncation
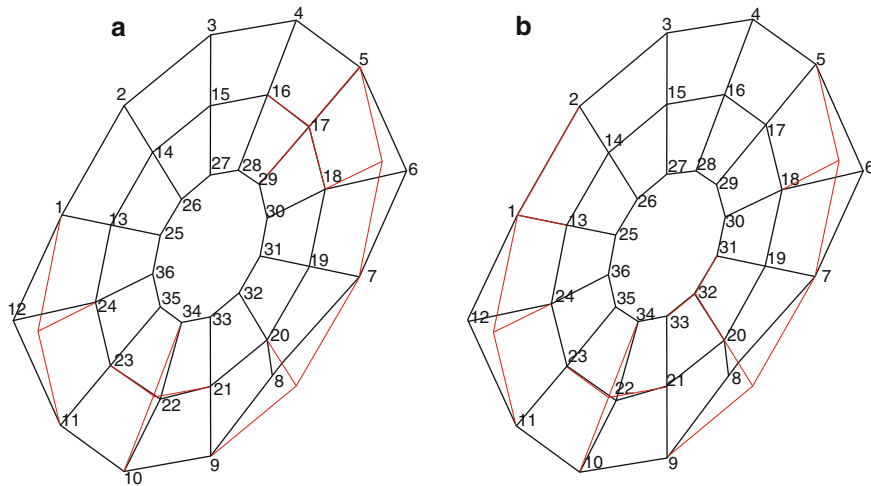
Fig. 6.6 Mode shape at 764 Hz. (**a**) Default. (**b**) After truncation

Table 6.3 MAC for circular plate

Frequency (Hz)	MAC
362	0.8455
364	0.9931
557	0.9998
761	0.9986
764	0.9994

6.3.7 Odd Powered Polynomials

Iteration 2 in the modal parameter estimation using the RFP algorithm, as explained in Sect. 6.3.2, corresponds to the poles obtained by solving the polynomial with an order of 3 which can be given as follows,

$$\left| [\alpha_3](s)^3 + [\alpha_2(s)]^2 + [\alpha_1(s)]^1 + [\alpha_0](s)^0 \right| = 0 \tag{6.12}$$

The companion matrix for this polynomial can be given as,

$$[C] = \begin{bmatrix} -[\alpha_2] & [\alpha_1] & -[\alpha_0] \\ [I] & [0] & [0] \\ [0] & [I] & [0] \end{bmatrix} \qquad (6.13)$$

On using the elimination technique, the companion matrix will change to,

$$[C] = \begin{bmatrix} -[\alpha_2] & [0] & -[\alpha_0] \\ [I] & [0] & [0] \\ [0] & [I] & [0] \end{bmatrix} \qquad (6.14)$$

But, in case of a companion matrix, as shown in Eq. (6.7), the coefficient of the term with the highest order (or lowest, depending on the type of normalization chosen) is normalized to an identity matrix. Therefore, if the odd terms of any odd powered polynomial are eliminated from the companion matrix as shown in Eq. (6.14), not all the odd powered terms will be eliminated. The term with the highest odd power which is not in the companion matrix is still present in the calculations. And if all the odd powered terms are removed from the polynomial before forming the companion matrix, the polynomial will no longer be a third order one, it will be reduced to a second order polynomial. Therefore, in case of odd powered polynomials, this technique does not work.

6.4 Normalization by Manipulation of the Partial Fraction Method of Residue Synthesis

6.4.1 Background

Another method of representing a transfer function is through partial fractions. This is one of the methods of determining residues [4]. Equation (6.2) can be represented, for a single DOF system, as product of roots as follows,

$$H(s) = \frac{1}{Ms^2 + Cs + K} = \frac{1/M}{s^2 + \frac{C}{M}s + \frac{K}{M}} = \frac{1/M}{(s - \lambda)(s - \lambda^*)} \qquad (6.15)$$

This equation can be represented in a partial fraction format as follows,

$$H(s) = \frac{A_1}{(s - \lambda_1)} + \frac{A_1^*}{(s - \lambda_1^*)} \qquad (6.16)$$

Similarly, the frequency response function for a MDOF system can be represented by substituting $s = j\omega$ as,

$$H_{pq}(\omega) = \sum_{r=1}^{n} \frac{A_{pqr}}{(j\omega - \lambda_r)} + \frac{A_{pqr}^*}{(j\omega - \lambda_r^*)} \qquad (6.17)$$

For a system with single reference, N modes and s spectral lines, Eq. (6.17) can be expressed as,

$$\{H_{pq}(\omega)\}_{N_s \times 1} = \left[\frac{1}{j\omega_{N_s} - \lambda_{2N}} \right]_{N_s \times 2N} \{A_{pqr}\}_{2N \times 1} \qquad (6.18)$$

By pre-multiplying both sides of Eq. (6.18) with pseudo-inverse of $\left[\frac{1}{j\omega_{N_s} - \lambda_{2N}} \right]$ and solving FRF by FRF, residues can be obtained.

6.4.2 Normalizing the Residues Using Partial Fraction Method

Normalized residues were obtained by manipulating the residue synthesis procedure explained in Sect. 6.4.1. The imaginary part of $\left[\dfrac{1}{j\omega_{N_s} - \lambda_{2N}}\right]$ and the real part of the FRF matrix, $\{H_{pq}(\omega)\}$, were used for the synthesis of residues as shown below,

$$Re\left(\{H_{pq}(\omega)\}_{N_s \times 1}\right) = Im\left(\left[\frac{1}{j\omega_{N_s} - \lambda_{2N}}\right]_{N_s \times 2N}\right)\{A_{pqr}\}_{2N \times 1} \tag{6.19}$$

Equation (6.19) was pre-multiplied with the pseudo-inverse of $Im\left(\left[\dfrac{1}{j\omega_{N_s} - \lambda_{2N}}\right]_{N_s \times 2N}\right)$ and then solved FRF by FRF to obtain the residues.

6.4.3 Application on a Rectangular Plate

A rectangular steel plate of dimensions of $0.86\,\text{m} \times 0.57\,\text{m}$ ($34.00" \times 22.50"$) and a thickness of $0.0063\,\text{m}$ ($0.25"$) with 21 references was excited over 160 points with an impact hammer. The plate was excited over a range 0–250 Hz with a Δf of $0.1563\,\text{Hz}$. The FRF for 160 inputs, 21 references and 1601 frequency lines will therefore be $21 \times 160 \times 1601$ in size. For the application of this technique on the data, however, only one of the references was selected. Therefore, the FRF matrix will have the dimensions $1 \times 160 \times 1601$ (Table 6.4).

6.4.4 Pole Setup and Modal Parameter Estimation

Similar to first technique, a smaller bandwidth was selected, mainly, to avoid contamination of modal vectors due to repeated roots (refer [5] for details). The parameters of the selected bandwidth are shown in Table 6.5.

The data was processed using RFP algorithm with the highest order term normalized to identity. The residues were then processed for the selected frequency range.

6.4.5 Results

On application of the normalization technique explained in Sect. 6.4.2 on the rectangular plate, purely imaginary residues were obtained. The complexity of the residues before and after normalization can be seen in Fig. 6.7 and the mode shapes

Table 6.4 MAC for rectangular plate

Frequency (Hz)	MAC
95.5664	0.9833
104.5978	0.9999
119.0410	0.9918
137.9729	0.9973
176.2990	0.9975
203.7292	0.9945

Table 6.5 Parameters for the selected bandwidth

Minimum frequency	59.8438 Hz
Maximum frequency	237.1875 Hz
Minimum time	0.0480 s
Maximum time	3.1980 s
Number of frequency lines	1136
Number of time points	1119
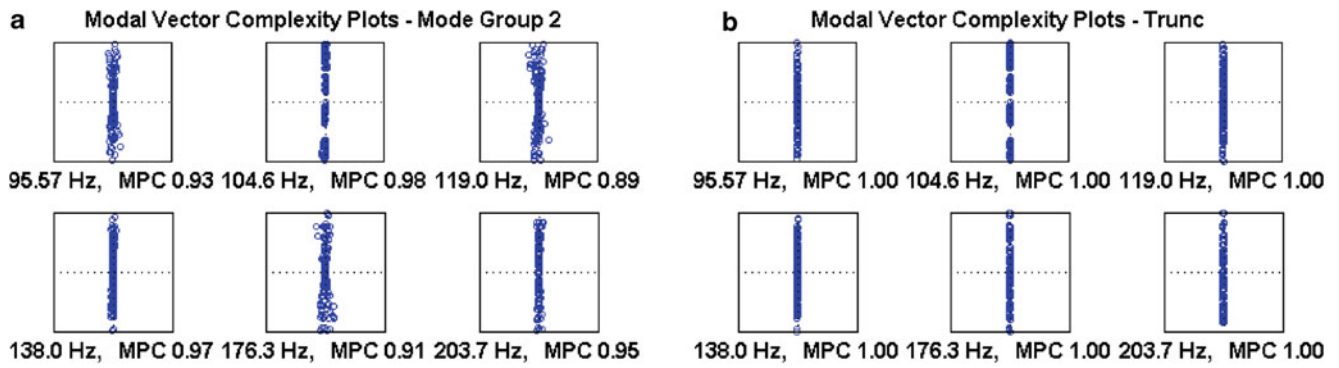
Fig. 6.7 Modal vector complexity residue comparison for rectangular plate. (**a**) Default. (**b**) After truncation
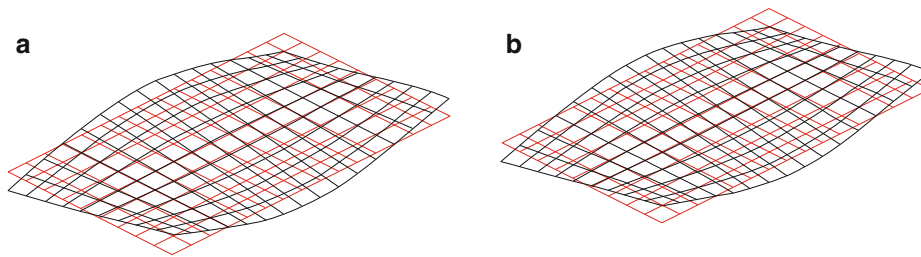
Fig. 6.8 Mode shape at 95 Hz. (**a**) Default. (**b**) After truncation
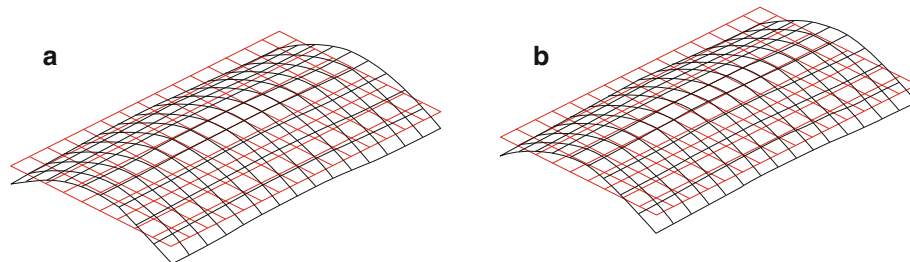
Fig. 6.9 Mode shape at 104 Hz. (**a**) Default. (**b**) After truncation
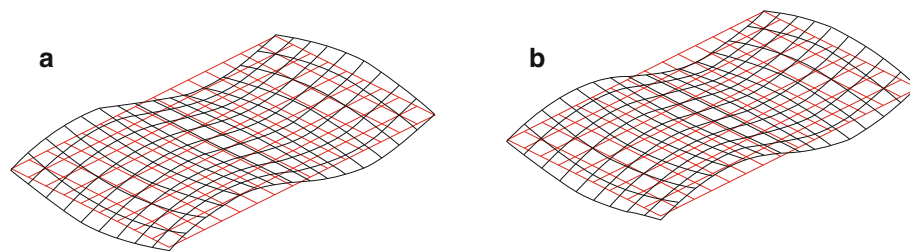
Fig. 6.10 Mode shape at 119 Hz. (**a**) Default. (**b**) After truncation

from Figs. 6.8, 6.9, 6.10, 6.11, 6.12, and 6.13. The residues in both the cases were also compared using the modal assurance criterion (MAC), shown in Table 6.4.

From the complexity plots, it can be concluded that this normalization technique normalizes the complex mode shapes and the normalized mode shapes compare well with the original with a very high MAC value as can be seen in Fig. 6.7, for this case.
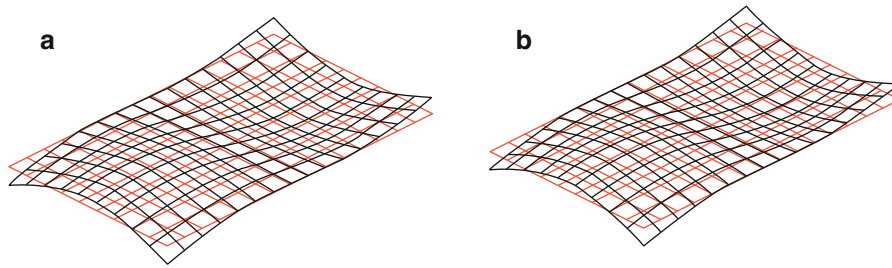
Fig. 6.11 Mode shape at 137 Hz. (**a**) Default. (**b**) After truncation
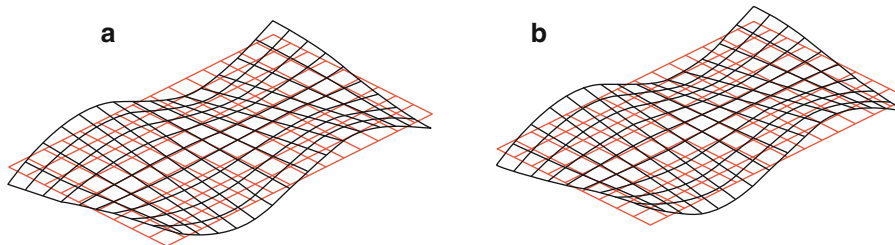
Fig. 6.12 Mode shape at 176 Hz. (**a**) Default. (**b**) After truncation
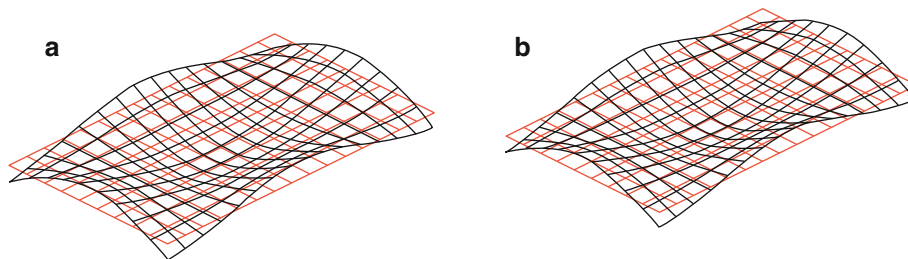
Fig. 6.13 Mode shape at 203 Hz. (**a**) Default. (**b**) After truncation
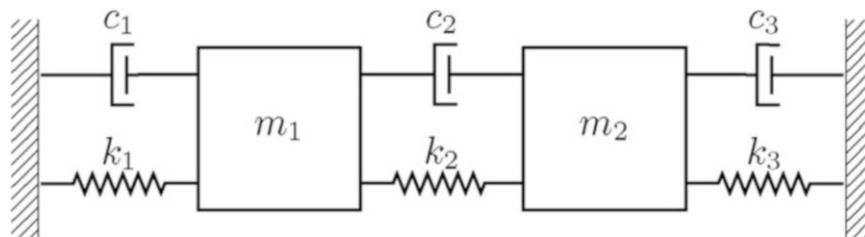
Fig. 6.14 2DOF system

6.5 Explanation for Deviation in Undamped Natural Frequencies

It was shown in Sect. 6.3.6 that the frequencies obtained after truncating the α polynomial deviate by a maximum of 0.1115 % from the undamped natural frequencies of the system as can be seen in Table 6.2. In this section, an explanation for this deviation will be discussed.

6.5.1 Background

Consider a 2 DOF grounded system shown in Fig. 6.14. Where M_1 and M_2 are the two masses, C_1, C_2 and C_3 are the three dampers and K_1, K_2 and K_3 are the three springs in the system. The respective mass, damping and stiffness matrices for this system can be given as,

$$[M] = \begin{bmatrix} M_1 & 0 \\ 0 & M_2 \end{bmatrix}; \quad [C] = \begin{bmatrix} C_1 + C_2 & -C_2 \\ -C_2 & C_2 + C_3 \end{bmatrix}; \quad [K] = \begin{bmatrix} K_1 + K_2 & -K_2 \\ -K_2 & K_2 + K_3 \end{bmatrix} \tag{6.20}$$

The homogeneous form of Laplace domain model,

$$\left[\begin{bmatrix} M_1 & 0 \\ 0 & M_2 \end{bmatrix} s^2 + \begin{bmatrix} C_1 + C_2 & -C_2 \\ -C_2 & C_2 + C_3 \end{bmatrix} s + \begin{bmatrix} K_1 + K_2 & -K_2 \\ -K_2 & K_2 + K_3 \end{bmatrix} \right] \{X(s)\} = \{0\} \tag{6.21}$$

For non-trivial solutions of $\{X(s)\}$, the characteristic equation can be given as,

$$\left\| \begin{bmatrix} M_1 & 0 \\ 0 & M_2 \end{bmatrix} s^2 + \begin{bmatrix} C_1 + C_2 & -C_2 \\ -C_2 & C_2 + C_3 \end{bmatrix} s + \begin{bmatrix} K_1 + K_2 & -K_2 \\ -K_2 & K_2 + K_3 \end{bmatrix} \right\| = 0 \tag{6.22}$$

Adding the matrices and solving the determinant, Eq. (6.22) expands to,

$$(M_1 M_2)s^4 + \underline{(C_1 M_2 + C_2 M_1 + C_2 M_2 + C_3 M_1)s^3} + \boxed{(C_1 C_2 + C_1 C_3 + C_2 C_3)s^2}$$
$$+ (K_1 M_2 + K_2 M_1 + K_2 M_2 + K_3 M_1)s^2 + \underline{(C_1 K_2 + C_2 K_1 + C_1 K_3 + C_3 K_1 + C_2 K_3 + C_3 K_2)s}$$
$$+ K_1 K_2 + K_1 K_3 + K_2 K_3 = 0 \tag{6.23}$$

In Eq. (6.23), the terms in <u>red</u> are all the odd powered damping terms in the system and the terms in $\boxed{green}$ are the damping terms with an even power. As discussed in Sect. 6.2.1, any transfer function can be represented in a polynomial model. From Eq. (6.2), a MDOF system represented by the second order characteristic equation in polynomial form with an order of 2 can be represented as follows,

$$[H_{pq}(s)] = \frac{\{X_p(s)\}}{\{F_q(s)\}} = [[M]s^2 + [C]s + [K]]^{-1} = [\beta_0] \left([\alpha_2]s^2 + [\alpha_1]s + [\alpha_0]\right)^{-1} \tag{6.24}$$

From Eq. (6.24), for a second order system, it can be concluded that the M, C and K matrices correspond to α_2, α_1 and α_0 respectively. Therefore, the expansion in Eq. (6.23) can be said to equate with the α polynomial of the analytical 2 DOF system with an order of 4 which can be compared to the iteration 3 of the RFP algorithm in X-Modal for comparison.

In Eq. (6.23), it can be seen that not all damping terms are odd powered. The damping terms are spread throughout the polynomial from $(n - 1)$ to 1 powered terms, where n is the highest order. Therefore, the variation in the undamped natural frequency of the system as shown in Table 6.2 can be said to be due to the presence of damping in the even powered terms. This hypothesis will be proved in the following sections.

6.5.2   2 DOF Analytical Example

For the 2 DOF system shown in Fig. 6.14, the following mass and stiffness values were assumed,

$$M_1 = 100 \text{ kg}; M_2 = 50 \text{ kg}; \quad K_1 = K_2 = K_3 = 1 \times 10^6 \ \frac{\text{N}}{\text{m}}$$

The damping was assumed proportional to both mass and stiffness with the mass proportionality constant, α, as 0.1 s^{-1} and the damping proportionality, β, as $0.001 \, s$,

$$[C] = \alpha[M] + \beta[K] \tag{6.25}$$

Table 6.6 Comparison of modal frequencies

Original	Absolute	Truncated	No damping
$-6.3897 - 112.4218i$	112.6033	$0.0000 - 111.6370i$	$0.0000 - 112.6033i$
$-6.3897 + 112.4218i$	112.6033	$0.0000 + 111.6370i$	$0.0000 + 112.6033i$
$-23.7102 - 216.2367i$	217.5328	$0.0000 - 219.4156i$	$0.0000 - 217.5328i$
$-23.7102 + 216.2367i$	217.5328	$0.0000 + 219.4156i$	$0.0000 + 217.5328i$
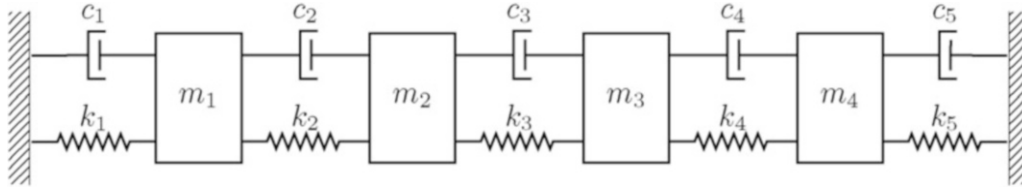
Fig. 6.15 4 DOF system

The above assumed values for M, C and K were then substituted in Eq. (6.23) to determine the poles of the system, s. On obtaining the poles after solving the complete polynomial, the polynomial was truncated using the technique discussed in Sect. 6.3 and by manually eliminating all the damping terms in the equation. On solving the polynomial in those three ways, the results shown in Table 6.6 were obtained.

In the first column of Table 6.6, the original modal frequencies of the system, i.e. the frequencies obtained by solving the complete polynomial, are listed. In the second column are the absolute values of the modal frequencies in the first column, these are the undamped natural frequencies of the system. The third column represents the modal frequencies obtained after truncating the polynomial i.e. eliminating the odd powered terms, the terms highlighted by red in Eq. (6.23), in the polynomial. And, in the fourth column are the modal frequencies obtained on solving the polynomial without any damping terms, i.e. all the terms highlighted by green and red in Eq. (6.23) have been eliminated.

From Table 6.6, it can be seen that the damping terms distributed across the polynomial between $(n-1)$ and 1 powered terms cause the undamped natural frequency to deviate. On eliminating all the damping terms in the polynomial, the red and green terms, the undamped natural frequency of the system can be obtained.

6.5.3 4 DOF Analytical Example

Figure 6.15 is a 4 DOF analytical system where M_1, M_2, M_3 and M_4 are the masses, C_1, C_2, C_3, C_4 and C_5 are the dampers and K_1, K_2, K_3, K_4 and K_5 are the springs.

6.5.3.1 Case I: Second Order Polynomial with 4 × 4 Matrix Coefficients

The following mass and stiffness values were assumed for the 4 DOF system,

$$M_1 = 200 \text{ kg}; \ M_2 = 150 \text{ kg}; \ M_3 = 100 \text{ kg}; \ M_4 = 50 \text{ kg}$$

$$K_1 = K_2 = K_3 = K_4 = K_5 = 1 \times 10^6 \ \frac{\text{N}}{\text{m}}$$

The damping was again assumed proportional to both mass and stiffness with the proportionality constants, α and β, were assumed to be 0.1 s^{-1} and 0.001 s respectively. On using these assumed values, the modal frequencies and vectors shown below were obtained. Since, proportional damping was assumed, the modal vectors are already real.

$$\begin{Bmatrix} -1.4601 + 54.0195i \\ -1.4601 - 54.0195i \\ -5.5386 + 105.1022i \\ -5.5386 - 105.1022i \\ -10.7879 + 146.4903i \\ -10.7879 - 146.4903i \\ -23.8801 + 217.2323i \\ -23.8801 - 217.2323i \end{Bmatrix} \quad \begin{bmatrix} 0.9417 & 0.9417 & 1.0000 & 1.0000 & -0.5759 & -0.5759 & -0.0408 & -0.0408 \\ 1.0000 & 1.0000 & -0.1616 & -0.1616 & 1.0000 & 1.0000 & 0.2313 & 0.2313 \\ 0.5705 & 0.5705 & -0.5365 & -0.5365 & -0.5363 & -0.5363 & -0.7760 & -0.7760 \\ 0.1539 & 0.1539 & -0.1855 & -0.1855 & -0.2911 & -0.2911 & 1.0000 & 1.0000 \end{bmatrix}$$

6.5.3.2 Case II: Fourth Order Polynomial with 2 × 2 Matrix Coefficients

To show that the damping terms are not just present in the odd powers of a polynomial, the above assumed 4 DOF analytical model with a second order characteristic equation was sub-spaced into a 4$^{\text{th}}$ order polynomial with 2×2 sized matrix coefficients such that it gives the same modal frequencies as the second order polynomial did.

A second order polynomial with 4×4 matrix coefficients will give eight modal frequencies. Similarly, a fourth order polynomial with matrix coefficients of 2×2 will give eight modal frequencies as well. So there is no change in the system as far as modal frequencies are concerned, however, instead of 4 DOF, the system will be assumed to have just 2 DOF and hence the modal vectors in this will be 2×8 and not 4×8 as in the first case.

To expand the second order polynomial to a fourth order polynomial, the usual eigenvalue decomposition process was performed in the reverse order. Since the modal frequencies and modal vectors that were supposed to be obtained after the eigenvalue decomposition are known, the companion matrix can be deduced using Eq. (6.8).

Modal vectors corresponding to the first and third DOF of the four output DOF calculated in the first case, Sect. 6.5.3.1, were selected as the new modal vector, $\bar{\psi}$. Using these selected modal vectors, the eigenvector was created (for details, refer [6]). The modal frequencies, λ, however, will remain the same. To obtain the new companion matrix, $\bar{C}$, Eq. (6.8) was post-multiplied with $\{\bar{\phi}\}^{-1}$,

$$[C][\phi][\bar{\phi}]^{-1} = [\phi][\lambda][\bar{\phi}]^{-1}$$
$$[C] = [\phi][\lambda][\bar{\phi}]^{-1} \tag{6.26}$$

Using this technique, the following companion matrix was obtained,

$$\begin{bmatrix} -23.3333 & 0 & -23433.3333 & 66.6667 & -200000 & 133333.3333 & -100000000 & 66666666.6667 \\ 26.6667 & -60 & 26966.6667 & -60533.3333 & 600000 & -1066666.6667 & 300000000 & -533333333.3333 \\ 1.0000 & 0 & 0 & 0 & 0 & 0 & 0 & 0 \\ 0 & 1.0000 & 0 & 0 & 0 & 0 & 0 & 0 \\ 0 & 0 & 0.9999 & 0 & 0 & 0 & 0 & 0 \\ 0 & 0 & 0 & 1.0000 & 0 & 0 & 0 & 0 \\ 0 & 0 & 0 & 0 & 0.9999 & 0 & 0 & 0 \\ 0 & 0 & 0 & 0 & 0 & 0.9999 & 0 & 0 \end{bmatrix} \tag{6.27}$$

The polynomial represented by this companion matrix can be given as,

$$\begin{bmatrix} 1 & 0 \\ 0 & 1 \end{bmatrix} s^4 + \begin{bmatrix} 23.3333 & 0 \\ -26.6667 & 60 \end{bmatrix} s^3 + \begin{bmatrix} -23433.3333 & 66.6667 \\ -26966.6667 & 60533.3333 \end{bmatrix} s^2 +$$

$$\begin{bmatrix} 200000 & -133333.3333 \\ -600000 & 1066666.6667 \end{bmatrix} s + \begin{bmatrix} 100000000 & -66666666.6667 \\ -300000000 & 533333333.3333 \end{bmatrix} = 0 \tag{6.28}$$

This polynomial on solving will give the modal frequencies obtained in Case I. To check the effect of no damping in the modal frequencies on the companion matrix, the absolute values of the modal frequencies calculated in Sect. 6.5.3.1 were used in Eq. (6.26) along with the same eigenvector, $\bar{\phi}$. On solving, the following companion matrix was obtained,

$$\begin{bmatrix} 0 & 0 & -23333.3206 & -0.0001 & 0 & 0 & -99999882.3648 & 66666608.4228 \\ 0 & 0 & 26666.65557 & -59999.97178 & 0 & 0 & 299999702.4389 & -533332787 \\ 0.9999 & 0 & 0 & 0 & 0 & 0 & 0 & 0 \\ 0 & 1.0000 & 0 & 0 & 0 & 0 & 0 & 0 \\ 0 & 0 & 0.9999 & 0 & 0 & 0 & 0 & 0 \\ 0 & 0 & 0 & 0.9999 & 0 & 0 & 0 & 0 \\ 0 & 0 & 0 & 0 & 1.0000 & 0 & 0 & 0 \\ 0 & 0 & 0 & 0 & 0 & 0.9999 & 0 & 0 \end{bmatrix} \quad (6.29)$$

The polynomial represented by this companion matrix can be given as,

$$\begin{bmatrix} 1 & 0 \\ 0 & 1 \end{bmatrix} s^4 + \begin{bmatrix} 0 & 0 \\ 0 & 0 \end{bmatrix} s^3 + \begin{bmatrix} 23333.3206 & 0.0001 \\ -26666.65557 & 59999.97178 \end{bmatrix} s^2 + \begin{bmatrix} 0 & 0 \\ 0 & 0 \end{bmatrix} + \begin{bmatrix} -99999882.3648 & 66666608.4228 \\ 299999702.4389 & -533332787 \end{bmatrix} = 0 \quad (6.30)$$

On comparing the matrices obtained from the two methods, it can be seen that eliminating the odd powered terms in the polynomial might remove the damping (real part) from the modal frequencies, but it will not yield the undamped natural frequencies of the system. From the matrix coefficients in Eq. (6.30), it can be seen that the coefficients of the odd powered terms have been reduced to a null matrix but the other matrices have also been changed. The change in the values of the elements in Eq. (6.30) suggests that the damping in any system is not restricted to the odd powered terms and is spread across all the terms in the polynomial.

6.5.4 Coefficient Condensation

Another possible explanation for the distribution of damping across the polynomial is Coefficient Condensation. It is used to reduce the number of physical output DOFs, N_o to much more reasonable DOFs, N_e, to limit the time consumption for calculations. Using the techniques such as Eigenvalue Decomposition (ED) or Singular Value Decomposition (SVD), the physical coordinates are reduced to virtual coordinates. During this reduction, the information of the physical system is sub-spaced into a smaller virtual subspace which is then used to determine the modal parameters of the system. Due to the transformation, the mass, damping and the stiffness matrices are no longer restricted to the second, first and zero order terms respectively and they get distributed throughout the polynomial similar to distribution of the terms in the analytical examples shown in this section.

Even in the case of high order algorithms like RFP, the coefficient condensation techniques are not used per se, however, the number of physical output DOFs, N_o, are still reduced from infinite to N_o. Thereby, causing the distribution of damping terms throughout the polynomial.

6.6 Conclusion

Two new normalization techniques for complex mode shapes were proposed and tested on experimental data. The first technique, normalization by truncation of the α polynomial, does normalize the complex modal vectors, however, the undamped natural frequencies obtained after truncation, in general, deviates from that of the system's. This deviation is due to the fact that the damping in the system is not restricted to the odd powered terms in the α polynomial but are spread throughout the polynomial as shown in Sect. 6.5. There are two possible reasons for this,

- When high order algorithm such as RFP is used: The second order model is sub-spaced into higher order models which causes the damping terms to distribute across the polynomial as was shown in Sect. 6.5.3.2.
- When coefficient condensation is used for second or first order algorithms such as PFD and ERA: For the lower order algorithms like PFD, coefficient condensation is used to minimize the computation time which causes the damping to distribute throughout the polynomial. Even in the case of high order algorithms like RFP, the number of references selected are reduced from infinite to N_o which could possibly cause the damping terms to spread across the polynomial.

This method of normalization should work fine on second order time and frequency domain algorithms such as Eigensystem Realization Algorithm (ERA) and Polyreference Frequency Domain-2 (PFD-2) as long as coefficient condensation is not used, as that would ensure that the damping is restricted to the odd powered term in the second ordered polynomial and will be eliminated on using the truncation technique.

The second technique proposed was based on the partial fraction method of residue estimation. This technique was tested on data obtained from a rectangular plate. The technique successfully normalized the complex mode shapes as expected. The MAC values between the normalized and original complex modal vectors was very high. The lowest MAC value being 0.9833.

References

1. Avitable, P.: Modal space back to basics. http://sem.org/ArtDownLoad/msmj02.pdf (2002)
2. Kohli, K.: Structural dynamics model calibration and validation of a rectangular steel plate structure. Master's thesis, University of Cincinnati, Cincinnati, OH (2014)
3. Niedbal, N.: Analytical determination of real normal modes from measured complex responses. In: Proceedings of the 25th Structures, Structural Dynamics and Materials Conference, Palm Springs, CA, pp. 292–295 (1984)
4. Allemang, R.J.: Vibrations: analytical and experimental modal analysis. UC-SDRL-CN-20-263-662/663/664 (2008)
5. Hiremaglur, R.: Real-normalization of experimental complex modal vectors with modal vector contamination. Master's thesis, University of Cincinnati, Cincinnati, OH (2014)
6. Niranjan, A.C.: Normalization of complex mode shapes by truncation of alpha-polynomial. Master's thesis, University of Cincinnati, Cincinnati, OH (2015)

Chapter 7
What Is Normal About Normal Modes?

Thomas J.S. Abrahamsson and Randall J. Allemang

Abstract A normal mode of a vibrating system is a mode that is orthogonal to all other normal modes of that system. The orthogonality is in a weighted sense. For an undamped discretized linear mechanical system, the orthogonality is defined with respect to stiffness and mass such that normal modes are mutually stiffness and mass orthogonal. Another commonly used definition of an oscillating normal mode is that it is a pattern of motion in which all parts of the system vibrate harmonically with the same frequency and therefore with fixed relative phase relations between parts. The normality of a mode is thus not in a statistical sense. For lightly damped linear systems, a normal observation, i.e. one very common observation in the statistical sense, is that the phase relation between the motion of different parts of the system deviates very little from zero or pi. However, this normally occurring behavior should not lead us to think that that always has to be the case. Here it is shown by example that the normal modes of an undamped system may have arbitrary phase relations. One such mode of vibration may then possess the property of moving nodal lines, which is often attributed to non-proportionally damped or non-selfadjoint systems. The proper normalization of such modes is discussed and their relation to the well-known modal mass and MAC concepts and also to state-space based normalizations that are usually being used for complex-valued eigenmodes.

Keywords Normal mode • Vibrational mode • Undamped eigenmode • Repeated eigenvalues • Eigenmode orthogonality

7.1 Introduction

Already in the nineteenth century inspired by the work of Jacques Charles François Sturm and Joseph Liouville, the use of eigenfunctions has played a central role for the solution of partial and ordinary differential equations. The remarkable property of the eigenfunctions to decouple the equations to more easily solvable sets of equations was the key that they explored. The eigenfunctions, also known as eigenmodes, were shown by Sturm and Liouville to form a complete set for the solution. The decoupled solutions for each individual eigenmode can be superimposed to form the complete solution of the (Sturm-Liouville) problem. The orthogonality property of the eigenmodes is what makes them agents for decoupling. The non-uniqueness of the eigenmodes is well known and it is common knowledge that an eigenmode scaled by any number (except for zero) is again an eigenmode. This has led to the fixing of eigenmodes with the concept of eigenmode normalization. In structural dynamics it is common to normalize the eigenfunctions such that the mass distribution weighted by the square of the eigenfunction produces the unit mass. Such normalized eigenmodes are called (mass) orthonormalized modes. That fixes the size of the mode which is then unique to within a multiplication factor of −1. The use of the name normal mode stems from that normalization and is somewhat misleading. The orthogonality property of the modes is more important than the possibility to normalize these modes. This is even more misleading since the term "normal mode" is also used for modes that are not normalized. Again in structural dynamics, and similar in other fields with system dynamics, the meaning of a normal mode has been the idea of a free vibration pattern in which all structural particles move in an harmonic motion around their neutral positions with a single frequency that is common for all particles.

In vibration testing of structural systems it is often found that the system damping is very low. In such systems, it is often found that the system displacements or acceleration responses are either in-phase or completely anti-phase with a harmonic excitation force. Since the system response is the superposition of responses from each normal mode this has led

---

T.J. Abrahamsson (✉)

Department of Applied Mechanics, Chalmers University of Technology, Gothenburg, Sweden
e-mail: thomas.abrahamsson@chalmers.se

R.J. Allemang
Structural Dynamics Lab, University of Cincinnati, Cincinnati, OH, USA

to the impression that the eigenmodes are associated with (close to) in-phase and anti-phase motion only. Such modes can be approximated by real-valued functions. Since low damped systems are very common it is easy to believe that the (almost pure) realness of the modes is the most normal physical behavior in a statistical sense. The authors of this paper have heard this meaning of normality in conjunction to eigenmodes. With this paper we hope to share some light of the properties of eigenmodes of lightly damped systems and by that discourage the understanding of "normal" as the attribute of an eigenmode to be associated to an often observed (= normal) behavior.

7.1.1 Limitations

In this paper, only eigenmodes or modal vectors of the undamped system are considered. This is done to limit the discussion and to eliminate the confusion that might exist when damped systems are considered. Once damped systems are considered, the possibility of non-proportional damping will yield the possibility of complex-valued eigenmodes that can occur whether repeated roots are present or not.

However, this paper is not limiting the discussion to common constraints that may be imposed in numerical solutions or common use. For example, it is possible to define an eigenmode that is the product of a complex-valued scalar and a real-valued vector thus yielding a complex-valued eigenmode that is rotated compared to the real-valued vector. It is also possible, for the repeated root case, to define an eigenmode that is a linear combination of two real vectors, each multiplied by different complex scalars. In both of these cases, the resulting eigenmode will mathematically satisfy the necessary orthogonality constraints but will yield complex-valued modal vectors that could be defined alternatively as real valued modal vectors. These complex-valued eigenmodes will yield generalized (modal) mass that will be negative or complex valued if evaluated by current practices. While this is acceptable from the viewpoint that modal mass is just a scaling factor between somewhat arbitrary scaled eigenmodes and the physical properties of the system being studied, most users would probably not find this result acceptable. We are not advocating that this representation be used, simply pointing out the possibility of alternate mathematical forms that fully satisfy all relationships of physical system and of the mathematical solution.

7.2 Theory

A linear mechanical system with viscous damping is often represented by partial differential equations subsequently discretized into a system of ordinary differential equations as

$$M\ddot{q} + V\dot{q} + Kq = Q(t) = P_u u(t) \tag{7.1}$$

Here M, V and K are the system's positive semi-definite mass, viscous-damping and stiffness matrices, q and Q are the generalized displacements and forces and a dot represents time differentiation. This paper focusses on systems with negligible damping, *i.e.* $V = 0$. In many situations, a vast amount of elements of Q are zero and the remaining non-zero elements are collected in the stimulus vector u that relate to Q by the distribution matrix P_u. Many systems are self-adjoint and follows Maxwell-Betti's reciprocity rule which leads to symmetric K and M. For such systems it is well known that they can be transformed into a decoupled system of equations using the real-valued eigenmodes, collected as columns of the modal matrix Φ of the eigenvalue equation

$$K\Phi = M\Phi\Omega^2 \tag{7.2}$$

in which Ω^2 is a diagonal matrix in which the positive roots $\omega_1^2, \omega_2^2, \ldots$ of the characteristic equation $|K - \omega^2 M| = 0$ appear along its diagonal. It is assumed that $\omega_1, \omega_2, \ldots$ is an ordered sequence such that $\omega_1 \leq \omega_2 \leq \ldots$. Using the transformation $q = \Phi z$ and after a pre-multiplication of the transpose of the modal matrix on Eq. (7.1) one obtains the decoupled differential equation of the undamped system as

$$\Phi^T M \Phi \ddot{z} + \Phi^T K \Phi z = \Phi^T Q = \Phi^T P_u u \tag{7.3}$$

with the mass and stiffness matrices being diagonalized into $\Phi^T M \Phi = \text{diag}(m_n)$ and $\Phi^T K \Phi = \text{diag}(k_n)$. Using mass-normalized modes to fill Φ, all modal masses m_n become unity and thus $\Phi^T M \Phi = I$ and the diagonal matrix of modal

stiffnesses $k_n = m_n \omega_n^2$ then becomes $\mathbf{\Phi}^T \mathbf{K} \mathbf{\Phi} = \mathbf{\Omega}^2 = \text{diag}\left(\omega_n^2\right)$. Note that this is simply one form of normalization that can be chosen. Another common form when performing finite element analysis is to normalize the eigenmode so that the largest element in the eigenmode is unity. Another normalization that uses coefficient matrices of an equivalent state-space system is given later.

For the following it is noted that the symmetric and positive semi-definite mass matrix can be decomposed into

$$M = M^{1/2} M^{1/2} \tag{7.4}$$

where the symmetric square root of the mass matrix is

$$M^{\frac{1}{2}} = V D V^T \tag{7.5}$$

in which the eigenmode matrix V and the diagonal matrix of positive eigenvalues D are given by the solution of the eigenproblem for mass matrix formulated as

$$MV = VD^2 \tag{7.6}$$

It can be observed that $M = VD^2V^T$ and the relation for the mass matrix (7.4) and its square root (7.5) holds since; $M = M^{\frac{1}{2}}M^{\frac{1}{2}} = \left(VDV^T\right)\left(VDV^T\right) = VD\left(V^TV\right)DV^T = VDIDV^T = VD^2V^T$ with self-orthonormal V, *i.e* with $V^TV = I$.

For the computation of the eigensolution $\{\mathbf{\Phi}, \mathbf{\Omega}^2\}$, computational methods like the block-Lanczos or the subspace iteration methods can be used to the advantage. In the presence of repeated roots some eigenproblem solution techniques just provide a linearly independent set of normal modes that belongs to these roots. That linearly independent set needs to be made mass and stiffness orthogonal before the eigenvector set can be used for decoupling. An illustration of this is given in Sect. 7.8.1.

Let now v be a matrix holding a linearly independent set of eigenvectors that belong to a set of repeated roots as columns. Then the Gram-Schmidt orthogonalization procedure produces a mass orthonormal set of modes in V as

$$V^H = C^{-1} v^H \tag{7.7}$$

with C being the lower triangular Schur factor of a matrix S. These both matrices are defined by the relations

$$S = CC^H = v^H M v = \left(M^{\frac{1}{2}} v\right)^H \left(M^{\frac{1}{2}} v\right) \tag{7.8}$$

By its construction it can be noted that S is Hermitian, a condition for the Schur decomposition to exist. To see that V forms a mass-orthonormal basis one notes that

$$V^H M V = C^{-1} v^H M v C^{-H} = C^{-1} CC^H C^{-H} = I \tag{7.9}$$

In fact, the normal modes does not have to be real-valued. Let $v = \overline{v}$ be the set of linearly independent complex-valued normal modes associated to the repeated roots of the undamped eigenvalue problem. The Gram-Schmidt orthogonalization procedure as formulated above is not affected by the complexity of the modes.

It is considered a well-known fact that for repeated roots, any linear combination of the associated eigenvectors is also an eigenvector. The commonly used procedure for establishing such linear combinations is by introducing real-valued combination factors. It is considered to be less well-known that also complex-valued combinations of modes of repeated roots are fully valid. Let again v be a matrix holding a linearly independent set of real-valued eigenvectors that belong to a set of repeated roots. Then let

$$\overline{v} = v \alpha \tag{7.10}$$

with α being a square matrix of proper size with combination factors as elements and note that $\overline{v}$ is a matrix of eigenvectors associated to the same roots. If any of the factors are complex-valued, a complex-valued eigenvector will result. After such an operation, however, the modes of $\overline{v}$ are not necessarily orthogonal but may be orthogonalized by use of the Gram-Schmidt procedure explained above. The physical interpretation of such complex-valued eigenvectors is illustrated in Sect. 7.8.

7.3 System Decoupling

The Gram-Schmidt orthogonalization procedure that involves a Schur decomposition as used above suggest that the proper force transformation to decouple the system equations is by the Hermitian (conjugate transpose) of the modal matrix, i.e. $\boldsymbol{\Phi}^H = \mathrm{conj}\left(\boldsymbol{\Phi}^T\right)$. The decoupled second order equation associated with undamped version of Eq. (7.1) is then (c.f. Eq. (7.3))

$$\boldsymbol{\Phi}^H M \boldsymbol{\Phi} \ddot{\mathbf{z}} + \boldsymbol{\Phi}^H K \boldsymbol{\Phi} \mathbf{z} = \boldsymbol{\Phi}^H \mathbf{Q} \tag{7.11}$$

Note that the use of the Hermitian in this case is justified by the orthogonalization procedure and the fact that any complex-valued modal vectors are related to a set of real-valued modal vectors. This would not be the case for a set of complex-valued modal vectors arising from a non-proportionally damped system for which no real-valued modal vectors that decouple the system equations exist.

With mass-normalized real-valued eigenmodes related to unique eigenvalues and possibly complex-valued eigenmodes related to repeated eigenvalues in $\boldsymbol{\Phi}$, the mass matrix is diagonalized into the real-valued identity matrix, i.e. $\boldsymbol{\Phi}^T M \boldsymbol{\Phi} = \boldsymbol{I}$. In order to see that complex-valued mass-orthonormal modes associated to repeated roots also transform the stiffness matrix into a real-valued diagonalized matrix it can be noted that the eigenvalue problem of the associated repeated roots of value $\overline{\Omega}^2$ is

$$K\boldsymbol{v} = M\boldsymbol{v}\boldsymbol{\Omega}^2 = \overline{\Omega}^2 M\boldsymbol{v}\boldsymbol{I} \tag{7.12}$$

By pre-multiplying this by $\overline{\boldsymbol{v}}^H = \boldsymbol{\alpha}^H \boldsymbol{v}^T$ and post-multiplying by $\boldsymbol{\alpha}$ one obtains

$$\boldsymbol{\alpha}^H \boldsymbol{v}^T K \boldsymbol{v} \boldsymbol{\alpha} = \overline{\Omega}^2 \boldsymbol{\alpha}^H \boldsymbol{v}^T M \boldsymbol{v} \boldsymbol{I} \boldsymbol{\alpha} = \overline{\Omega}^2 \boldsymbol{\alpha}^H \boldsymbol{v}^T M \boldsymbol{v} \boldsymbol{\alpha} \tag{7.13}$$

The mass-orthonormal $\overline{\boldsymbol{v}} = \boldsymbol{v}\boldsymbol{\alpha}$ leads to that $\boldsymbol{\alpha}^H \boldsymbol{v}^T M \boldsymbol{v} \boldsymbol{\alpha} = \boldsymbol{I}$ and thus

$$\boldsymbol{\alpha}^H \boldsymbol{v}^T K \boldsymbol{v} \boldsymbol{\alpha} = \overline{\Omega}^2 \boldsymbol{I} \tag{7.14}$$

The complex transformation of the stiffness matrix thus provides a real-valued diagonal matrix with the repeated roots along the diagonal just as the transformation with real-valued eigenmodes.

7.4 Perturbation of Repeated Eigenvalues

It is well known, see e.g. [1, 2] that systems with close or coalescent eigenvalues are very sensitive to parametric perturbations. To investigate the effect of such perturbations an introduction of a suitable system descriptor with damping possibility is useful. One such model that can accommodate the constant damping behavior of structures, as can be observed in testing, is the frequency domain hysteretic model

$$\left(K + i\mathrm{sign}\left(\omega\right)H - \omega^2 M\right)\widehat{\boldsymbol{q}} = \widehat{\boldsymbol{Q}} \tag{7.15}$$

Here H is the hysteresis matrix and $\left(\widehat{\boldsymbol{q}}, \widehat{\boldsymbol{Q}}\right)$ are time-invariant complex-valued amplitudes of the harmonic displacements and loads defined by

$$\boldsymbol{q}(t) = \widehat{\boldsymbol{q}} \exp\left(i\omega t\right) \quad \boldsymbol{Q}(t) = \widehat{\boldsymbol{Q}} \exp\left(i\omega t\right) \tag{7.16a, b}$$

For this perturbation study one eigenvector complexity parameter ξ and one eigenvalue separation parameter ϱ are introduced. A subset of the full eigenvector solution $\boldsymbol{\Phi}$ is introduced as the perturbed set of eigenvectors $\acute{\boldsymbol{v}}$ related to set of real-valued multiple eigenvalues $\boldsymbol{v}$ of the undamped eigenvalue problem as

$$\acute{\boldsymbol{v}} = \acute{\boldsymbol{v}}\left(\boldsymbol{v}, \xi\right) \tag{7.17}$$

with $\acute{v}\,(v,0)\,=\,v$. The perturbed full set of eigenmodes is denoted $\acute{\Phi}$. For illustration purpose the following perturbation study is limited to systems with maximum multiplicity of their repeated roots being two. For the eigenvalue separation perturbation of such systems the perturbed eigenvalues are defined as

$$\acute{\omega}_i = (1 - \varrho)\,\omega_i \quad \acute{\omega}_{i+1} = (1 + \varrho)\,\omega_{i+1} \tag{7.18a, b}$$

for all the undamped system's pairs of multiple eigenvalues (ω_i, ω_{i+1}).

It can be noted from above that complex-valued eigenmodes of undamped reciprocal systems can only exist for repeated roots. The eigenvalue separation perturbation with associated complex-valued modes will thus lead to non-reciprocity. Here mass-orthonormalized modes are used throughout, i.e. $\acute{\Phi}^H M \acute{\Phi} = I$, and the perturbed model is established from the decoupled equations as

$$I\ddot{z} + \text{diag}\left(\omega_n^2\right) z = \acute{\Phi}^H Q \tag{7.19}$$

The full set of eigenmodes is used with $\acute{\Phi}$ being square and invertible and thus $z = \acute{\Phi}^{-1} q$. After pre-multiplication of (7.19) by $\acute{\Phi}^{-H}$ one has

$$\acute{\Phi}^{-H} \acute{\Phi} \ddot{q} + \acute{\Phi}^{-H} \text{diag}\left(\omega_n^2\right) \acute{\Phi}^{-1} q = M\ddot{q} + \acute{\Phi}^{-H} \text{diag}\left(\omega_n^2\right) \acute{\Phi}^{-1} q = Q \tag{7.20}$$

Let the perturbation stiffness matrix $\acute{K}$ and hysteretic damping matrix $\acute{H}$ be defined as

$$\acute{K} = \left\{ \Re e \acute{\Phi}^{-H} \text{diag}\left(\omega_n^2\right) \acute{\Phi}^{-1} \right\} \quad \acute{H} = \left\{ \Im m \acute{\Phi}^{-H} \text{diag}\left(\omega_n^2\right) \acute{\Phi}^{-1} \right\} \tag{7.21a, b}$$

One observes that these two matrices are symmetric $(\acute{K})$ and anti-symmetric $(\acute{H})$ by construction. The perturbed system is thus

$$\left(\acute{K} + i\,\text{sign}\,(\omega)\,\acute{H} - \omega^2 M\right)\widehat{q} = \widehat{Q} \tag{7.22}$$

and the eigenvalue problem for positive frequencies ω associated with the perturbed system is

$$\left(\acute{K} + i\acute{H}\right)\Phi = M\acute{\Phi}\,\text{diag}\left(\hat{\lambda}_n\right) \tag{7.23}$$

By construction, the solution vectors to this eigenvalue problem consists of the perturbed eigenvectors.

7.5   Mode Normalization and Modal Correlation

It was noted above, shown by use of the Schur factorization, that the proper transformation of loading is by the Hermitian transpose of the eigenvectors. It was shown that this transformation leads to the undamped system's decoupled equations in (7.11). Let Ψ be the modal matrix of mass and stiffness orthogonal but not necessarily mass-orthonormal modes. The associated modal normalization factors, the modal masses m_n and the modal stiffnesses k_n, then become the real-valued diagonal elements of

$$\Psi^H M \Psi = \text{diag}\,(m_n) \quad \Psi^H K \Psi = \text{diag}\,(k_n) \tag{7.24a, b}$$

Modes from testing needs another procedure to be normalized. In the test situation, the mass and stiffness distributions of the structure is most often not known or not reliable and thus no K and M matrices are available. In vibration testing, following

from signal processing of the real-world time signals from our sensors, one gets the system's frequency response functions G at discrete frequencies Ω_k. For a receptance frequency response function relating the response at i to the loading at j of the undamped systems this has the form [3]

$$G_{ij}(\Omega_k) = \Sigma_n \frac{\overline{\psi}_i^{(n)} \psi_j^{(n)}}{m_n (\Omega_k^2 - \omega_n^2)} \tag{7.25}$$

With mass-orthonormal modes $\boldsymbol{\phi}^{(n)}$ related to the orthogonal modes by $\boldsymbol{\psi}^{(n)} = \alpha_n \boldsymbol{\phi}^{(n)}$ the modal masses m_n are unity and thus for the direct receptance in which $i = j$ one has

$$G_{jj}(\Omega_k) = \Sigma_n \frac{\left(\mathcal{R}e^2\{\alpha_n\} + \mathfrak{I}m^2\{\alpha_n\}\right)\left(\mathcal{R}e^2\left\{\psi_j^{(n)}\right\} + \mathfrak{I}m^2\left\{\psi_j^{(n)}\right\}\right)}{\Omega_k^2 - \omega_n^2} \tag{7.26}$$

Let Ω_k be the discrete frequencies in a close surrounding of ω_n. Let further m be the multiplicity of the root ω_n and let $n = 1, \ldots, m$ be the given numbers of these roots. For the undamped system, the receptance in a frequency range around these roots are totally dominated by the contribution of the associated eigenmodes.

This leads to the approximation

$$G_{jj}(\Omega_k) \approx \sum_{n=1}^{m} \frac{\left(\mathcal{R}e^2\{\alpha_n\} + \mathfrak{I}m^2\{\alpha_n\}\right)\left(\mathcal{R}e^2\left\{\psi_j^{(n)}\right\} + \mathfrak{I}m^2\left\{\psi_j^{(n)}\right\}\right)}{\Omega_k^2 - \omega_n^2} \tag{7.27}$$

and the complex-valued factors α_n can be determined, e.g. by non-linear least squares fitting, provided the repeated modes are identifiable from the measured direct receptances. One necessary requirement for such identifiability is that the number of receptance functions ($G_{jj}, j = 1, 2, \ldots$) used is at least equal to the root multiplicity. Note that this normalization procedure also works for modes with unique roots.

After mass-orthonormalization of the modes and provided that the set of modes is as large as the set of sensors in the test, the modal matrix is square and invertible. A dynamically equivalent second-order $\{K,M,H\}$ model can thus be constructed using

$$M = \left\{\acute{\boldsymbol{\Phi}}\acute{\boldsymbol{\Phi}}^H\right\}^{-1} \quad K = \Re e\left\{\acute{\boldsymbol{\Phi}}^{-H}\mathrm{diag}\left(\omega_n^2\right)\acute{\boldsymbol{\Phi}}^{-1}\right\} \quad H = \Im m\left\{\acute{\boldsymbol{\Phi}}^{-H}\mathrm{diag}\left(\omega_n^2\right)\acute{\boldsymbol{\Phi}}^{-1}\right\} \tag{7.28a--c}$$

These relations will be used in the numerical example below to show the effect of the skew-symmetric H on the reconstruction of test data, mimicked from a perturbed modal model with complex-valued eigenvectors and non-repeated roots.

For the purpose of correlation analysis of eigenvectors from different sources, the Weighted Modal Assurance Criterion (WMAC) is often employed as a correlation metric. The sources may be from repeated testing, from finite element analysis, from repeated use of various modal parameter extraction methods on same test data, etc. The correlation analysis is most often realized by the use of a condensed mass matrix as a positive definite weighting matrix. This metric requires that eigenvectors from different sources have the same length (same number of elements) and that the system's inertia is condensed to the degrees-of-freedom that correspond to the eigenvector elements. One such mass condensation techniques is the Guyan reduction technique, see e.g. [4]. With the mass factorization given above, the mass weighted eigenvectors associated with the ith eigenvector ψ_i from one source and the jth eigenvector ψ_j from another source are

$$\boldsymbol{\varphi}_i = M^{\frac{1}{2}}\boldsymbol{\psi}_i \quad \boldsymbol{\varphi}_j = M^{\frac{1}{2}}\boldsymbol{\psi}_j \tag{7.29a, b}$$

The associated WMAC correlation index $WMAC_{ij}$ is then [5]

$$WMAC_{ij} = \boldsymbol{\varphi}_i^H \boldsymbol{\varphi}_j \, \boldsymbol{\varphi}_j^H \boldsymbol{\varphi}_i \, / \left(\|\boldsymbol{\varphi}_i\|_2^2 \|\boldsymbol{\varphi}_j\|_2^2\right) \tag{7.30}$$

The auto and cross WMAC are given in the numerical example below for modal models with real-valued and complex-valued modes.

7.6   First Order Modeling

The second order differential Eq. (7.1) can be brought to first order form into

$$\dot{x} = Ax + Bu \tag{7.31}$$

Together with the response (output) equation

$$y = Cx \tag{7.32}$$

it forms what is often called a state-space model with the state vector $x = \left\{ q^T \; \dot{q}^T \right\}^T$. It can be verified that it relates to the coefficient matrices of the second order model by

$$A = \begin{bmatrix} 0 & I \\ -M^{-1}K & -M^{-1}V \end{bmatrix} \quad B = \begin{bmatrix} 0 \\ M^{-1}P_u \end{bmatrix} \tag{7.33a, b}$$

Note that this form of the A and B matrices is one form that can be used to convert from an $N \times N$ second order model into a $2N \times 2N$ first order model. This approach, however, is inconsistent with the definition of Modal A and Modal B that is commonly used for vector scaling of the generally viscously damped problem. The different formulations are discussed in Sect. 7.7.

The output equation gives the output y which can be any quantities that linearly relate to the state x. One specific example is when $C = I$ and $D = 0$ which gives the output vector y being the collection of (generalized) displacement and velocity vectors of the system. The state-space counterpart of the undamped decoupled (modal) differential equation with displacement and velocity output is given by

$$A = \begin{bmatrix} 0 & I \\ -\Omega^2 & 0 \end{bmatrix} \quad B = \begin{bmatrix} 0 \\ \text{diag}\,(m_n)\,\Phi^T P_u \end{bmatrix} \quad C = \begin{bmatrix} \Phi & 0 \\ 0 & \Phi \end{bmatrix} \tag{7.34a–c}$$

It can easily be verified that the system transfer function H (from stimulus to response) is

$$H = C(i\omega I - A)^{-1}B \tag{7.35}$$

Consider the system with complex eigenvectors stored in ψ. Its transfer function from force stimulus to displacement-velocity output is

$$H_\psi = C_\psi (i\omega I - A)^{-1} B_\psi \tag{7.36}$$

with

$$C_\psi = \begin{bmatrix} \psi & 0 \\ 0 & \psi \end{bmatrix} \tag{7.37}$$

The corresponding system with real modes and same system poles is given by its transfer function

$$H_\Phi = C_\Phi (i\omega I - A)^{-1} B_\Phi \tag{7.38}$$

with

$$C_\Phi = \begin{bmatrix} \Phi & 0 \\ 0 & \Phi \end{bmatrix} \quad B_\Phi = \begin{bmatrix} 0 \\ \text{diag}\,(m_n)\,\Phi^T P_u \end{bmatrix} \tag{7.39a, b}$$

Now assume that there is a sensor system with state-dependent properties that gives the signal output

$$y_s = C_s \tilde{y} = C_s S y \tag{7.40}$$

with S being the square calibration matrix that for an ideal sensor system should be $S_{\text{ideal}} = I$ and C_s is the channel selection matrix. The internal states of the sensor system are the elements of $\tilde{y} = Sy$. As an example consider the displacement sensor system with the system output $y = \left\{ q^T \; \dot{q}^T \right\}^T$ is identical to the state vector and C_s connects that to the output signals y_s of the sensor system as

$$y_s = q_s = \begin{bmatrix} C_{sq} & C_{s\dot{q}} \end{bmatrix} Sy = \begin{bmatrix} C_{sq} & 0 \end{bmatrix} SCx \tag{7.41}$$

One notes that the partition that relates to the sensor system's internal velocity state is zero (i.e. $C_{s\dot{q}} = 0$).

7.7 State-Space Modal Normalization

A state-space model that is mathematical equivalent to the state-space model of Eqs. (7.31) and (7.33a, b) is

$$\widehat{A}\dot{x} + \widehat{B}x = \begin{bmatrix} P_{\text{u}} \\ 0 \end{bmatrix} u \tag{7.42}$$

with

$$\widehat{A} = \begin{bmatrix} V & M \\ M & 0 \end{bmatrix} \quad \widehat{B} = \begin{bmatrix} K & 0 \\ 0 & -M \end{bmatrix} \tag{7.43a, b}$$

That the models are equivalent can easily be verified using that

$$\widehat{A}^{-1} = \begin{bmatrix} 0 & M^{-1} \\ M^{-1} & -M^{-1}VM^{-1} \end{bmatrix} \tag{7.44}$$

The related eigenvalue problem is

$$\widehat{A}\Psi = -\widehat{B}\Psi\Lambda \tag{7.45}$$

One notes that $\widehat{A}$ and $\widehat{B}$ are both symmetric and $\widehat{B}$ is indefinite since K and M are both positive definite or K is just semi-definite. Because of symmetry the eigenvalue problem is self-adjoint, meaning that the left-hand and right-hand eigenvectors are identical. Because of the indefiniteness, the eigenvalue problem (7.45) does not normally render real-valued eigenvalues in Λ. In fact, the eigenvalue problem may be deficient leading to that no orthogonal eigenvector set can be found at all.[1] For the non-deficient case, the eigenvalue matrix Λ is diagonal. In that case one has

$$\Psi^T\widehat{A}\Psi \equiv \text{diag}(a_n) = -\Psi^T\widehat{B}\Psi\Lambda \tag{7.46}$$

In which the modal normalization constants a_n are usually referred to as the Modal A constants. The $\widehat{B}$-orthogonality property of Ψ leads to

$$\Psi^T\widehat{B}\Psi = \text{diag}(b_n) \tag{7.47}$$

---

[1]This is a rare case in practice, however mathematically interesting. The simplest such case is probably the critically damped single-degree-of-freedom mass-stiffness-damper system.

The modal scale factors b_n are usually called Modal B constants[2]. The $\widehat{B}$-orthogonality can be used to find the relation between the Modal A constant, the Modal B constant and the eigenvalues as

$$\Psi^{\mathrm{T}}\widehat{A}\Psi = -\Psi^{\mathrm{T}}\widehat{B}\Psi\Lambda = -\mathrm{diag}\,(b_n)\,\mathrm{diag}\,(\lambda_n) = \mathrm{diag}\,(-b_n\lambda_n) = \mathrm{diag}\,(a_n) \tag{7.48}$$

7.8 Numerical Examples

The following numerical examples demonstrate the character of normal modes that correspond to repeated or almost coalescent roots of undamped systems. Some real-valued and some complex-valued such modes of the infinite set of possible modes of a system with truly repeated roots are illustrated in Sect. 7.8.1. In Sect. 7.8.2 this system is perturbed such that its modes are complex-valued and its roots do not longer coalesce. Further, in Sect. 7.8.3, the impact response of a non-reciprocal system and the response of a corresponding reciprocal system with test inaccuracies are compared and show similar behavior. This illustrates that a system with complex-valued modes and a system with real-valued modes can look identical from the viewpoint of test data.

7.8.1 Free Vibration Motion of a System with Repeated Roots

The simplest possible system with repeated roots is shown embedded in Fig. 7.1. It consists of an undamped two-dof sprung particle mass system (mass m) with two perpendicular springs of same stiffness k. The repeated roots are $\omega_1^2 = \omega_2^2 = k/m$. Two proper sets of linearly independent eigenvectors are the columns of v or $\overline{v}$ with
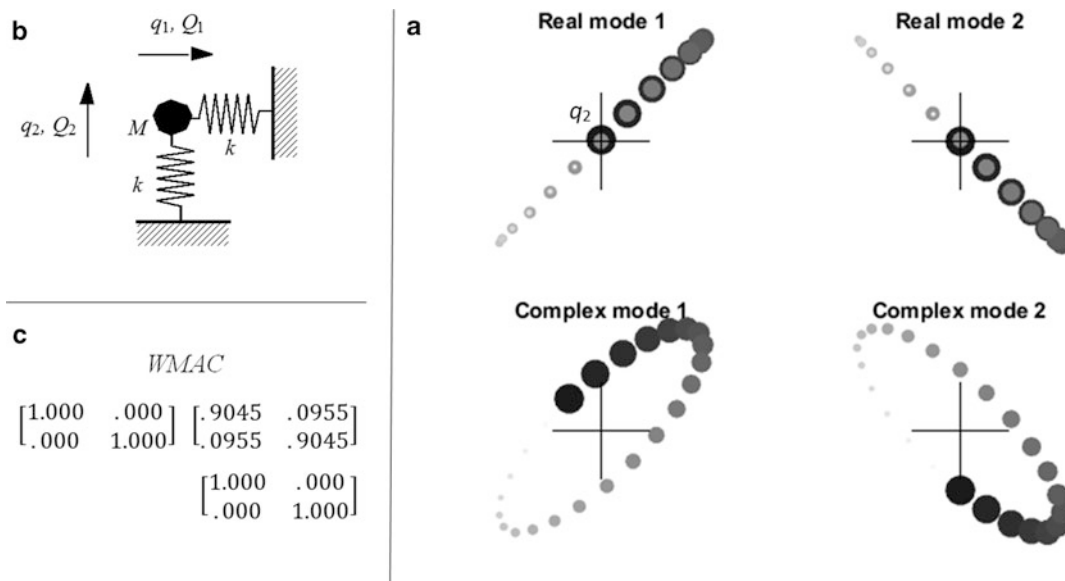
Fig. 7.1 (a) Four examples of free single-eigenmode vibration during an almost full eigenperiod. *Upper two graphs* illustrate motion in each of two mass-orthonormal real-valued modes. *Lower graphs* illustrate motion in each of two mass-orthonormal complex-valued modes. For increasing time the mass particle is made larger and darker. **NB!** Since the eigenmodes of repeated roots are not unique, these are just samples from an infinite set of possible eigenmodes of the system. (b) The two-degree-of-freedom system with particle mass m in planar motion (q_1, q_2) supported by two similar massless linear springs of stiffness k. (c) Auto-*WMAC* 2×2 matrix of Φ (*upper left*), cross-*WMAC* matrix between Φ and $\overline{\Phi}$ (*upper right*), and auto-*WMAC* matrix of $\overline{\Phi}$ (*lower right*)

---

[2]Ref. [6] advocates the use of *modal Foss damping* and *modal Foss stiffness* for the a_n and b_n respectively and gives an abstraction of systems with decoupled complex-valued states. One reason for this naming is that they carry the units of damping and stiffness and the other reason for it is a tribute to K.A. Foss who was one of the first, if not the first, that used the form given by Eq. (7), see [7].

$$v = \begin{bmatrix} 1 & 1 \\ 1 & -1 \end{bmatrix} \quad \overline{v} = \begin{bmatrix} 1 + .325i & 1 \\ 1 - .325i & 0 \end{bmatrix} \tag{7.49a, b}$$

Following the Gram-Schmidt orthogonalization procedure (see Eqs. (7.7) and (7.8)) one obtains the associated mass-orthonormal (i.e. $m_1 = m_2 = 1$) bases

$$\mathbf{\Phi} = \begin{bmatrix} \sqrt{2} & \sqrt{2} \\ \sqrt{2} & -\sqrt{2} \end{bmatrix} \quad \acute{\mathbf{\Phi}} = \begin{bmatrix} .549 + .178i & .408 \\ .549 - .178i & .661 + .480i \end{bmatrix} \tag{7.50a, b}$$

The associated auto-*WMAC* and cross-*WMAC* indices are embedded in Fig. 7.1.

In free vibration from arbitrary initial conditions, the system is set into motion that is fully characterized by its eigenmodes. By initial conditions that are orthogonal to one of the two eigenmodes, the system motion can be fully characterized by the other eigenmode. As an example, let us consider initial conditions that are orthogonal to the second eigenmode (second column of $\mathbf{\Phi}$, i.e. $\mathbf{\Phi}_{.2}$). Let the first column of $\mathbf{\Phi}$, i.e. $\mathbf{\Phi}_{.1}$, be the first displacement eigenmode. The free vibration displacements are then given by, see e.g. [6],

$$\begin{pmatrix} q_1(t) \\ q_2(t) \end{pmatrix} = \beta \, \mathbf{\Phi}_{.1} e^{i\omega t} + \beta \mathrm{conj} \left(\mathbf{\Phi}_{.1} e^{i\omega t} \right) = 2\beta \, \Re e \left(\mathbf{\Phi}_{.1} e^{i\omega t} \right) \tag{7.51}$$

with $\omega = \omega_1 = \omega_2$ and the real-valued β given by the magnitude of the initial displacement and velocity state. A couple of the infinitely many possible eigenmode patterns are illustrated in Fig. 7.1. The free vibration motion of the system subjected to initial conditions that are orthogonal to either the real-valued modes $\mathbf{\Phi}_{.1}$ or $\mathbf{\Phi}_{.2}$ are illustrated in Fig. 7.1 (upper part). The lower part of the figure shows the free vibration of the system vibrating purely in its complex-valued modes $\overline{\mathbf{\Phi}}_{.1}$ or $\overline{\mathbf{\Phi}}_{.2}$ given above.

7.8.2 Frequency Responses of Systems with Closely Spaced Roots

This example demonstrate the close correspondence of the responses of a non-selfadjoint system with complex-valued eigenmodes and a reciprocal system with real-valued eigenmodes. Both systems have closely spaced roots with identical eigenfrequency separation. The systems are created as perturbations of the two-dof system illustrated in Sect. 7.8.1. For the reciprocal system an eigenfrequency perturbation $\varrho = 0.01$ is made and the real-valued eigenvectors are kept, i.e. $\xi = 0$. This leads to mass-orthonormalized eigenvectors as in Eq. (7.50a, b). The non-selfadjoint system is based on the same eigenfrequency perturbation, i.e. $\varrho = 0.01$, with an added eigenvector perturbation $\xi = 0.10$ such that

$$\acute{v} = \begin{bmatrix} 1 + i\xi & 1 \\ 1 - i\xi & -1 \end{bmatrix} \tag{7.52}$$

The corresponding mass-orthonormalized eigenmodes are

$$\acute{\mathbf{\Phi}} = \begin{bmatrix} .7036 + .0704i & .7036 + .0704i \\ .7036 - .0704i & -.7036 + .0704i \end{bmatrix} \tag{7.53}$$

Equations (7.21a, b) give coefficient matrices of the perturbed system. For the selfadjoint system these evaluates to

$$M = \begin{bmatrix} 1 & 0 \\ 0 & 1 \end{bmatrix} \quad K = \begin{bmatrix} 1.0001 & -.0200 \\ -.0200 & 1.0001 \end{bmatrix} \quad H = \begin{bmatrix} 0 & 0 \\ 0 & 0 \end{bmatrix} \tag{7.54a–c}$$

and for the non-selfadjoint system they are

$$M = \begin{bmatrix} 1 & 0 \\ 0 & 1 \end{bmatrix} \quad K = \begin{bmatrix} 1.0001 & -.0196 \\ -.0196 & 1.0001 \end{bmatrix} \quad H = \begin{bmatrix} 0 & -.0040 \\ .0040 & 0 \end{bmatrix} \tag{7.55a–c}$$
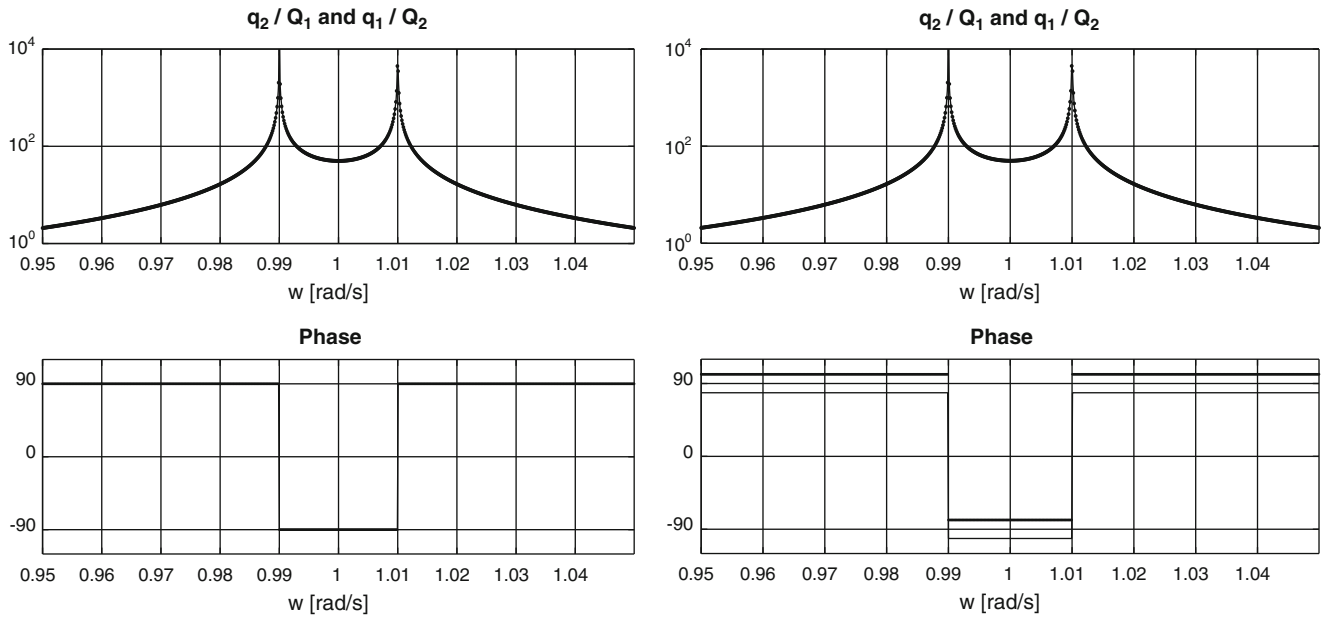
Fig. 7.2 Bode-like plots of the two cross-transfer functions of the selfadjoint (*left*) and non-selfadjoint (*right*) systems. *Dotted curves* are for $\dot{q}_1/Q_2$ and *solid curves* are for $\dot{q}_2/Q_1$

The cross mobility frequency response functions $Q_1 \to \dot{q}_2$ and $Q_2 \to \dot{q}_1$ of the non-selfadjoint system can be seen in Fig. 7.2. It can be observed that the magnitude of the two functions coalesce but that their phase functions differ. This different phase relation is not present for the selfadjoint system based on real-valued modes.

7.8.3 Imperfectly Measured Impact Response of Selfadjoint System with Closely Spaced Roots

A condition in which the real signals from a selfadjoint system with imperfect instrumentation may misleadingly result in the conclusion that the system is non-selfadjoint, and thus possesses complex-valued normal modes, is investigated next. Note that the transfer function to the sensor system's internal states $\tilde{y}$ from a stimulus of a selfadjoint system with real-valued modes $\mathbf{\Phi}$ are given by Eqs. (7.38) and (7.40) as

$$H_s = SC_{\mathbf{\Phi}}(i\omega I - A)^{-1}B_{\mathbf{\Phi}} \tag{7.56}$$

On the other hand, a spurious non-selfadjoint system with complex-valued modes $\mathbf{\psi}$ and same A would have the transfer function

$$H_{\mathbf{\psi}} = C_{\mathbf{\psi}}(i\omega I - A)^{-1}B_{\mathbf{\psi}} \tag{7.57}$$

By setting the transfer function to the observed internal state of the sensor system equal to the transfer functions of a false non-selfadjoint system with results in

$$SC_{\mathbf{\Phi}}(i\omega I - A)^{-1}B_{\mathbf{\Phi}} = C_{\mathbf{\psi}}(i\omega I - A)^{-1}B_{\mathbf{\psi}} \tag{7.58}$$

This leads to

$$B_{\mathbf{\psi}} = (i\omega I - A)\,C_{\mathbf{\psi}}^{-1}SC_{\mathbf{\Phi}}(i\omega I - A)^{-1}B_{\mathbf{\Phi}} \tag{7.59}$$

One notes that the only condition that do not lead to frequency dependence of $B_{\mathbf{\psi}}$ is that

$$C_{\mathbf{\psi}}^{-1}SC_{\mathbf{\Phi}} = I \tag{7.60}$$
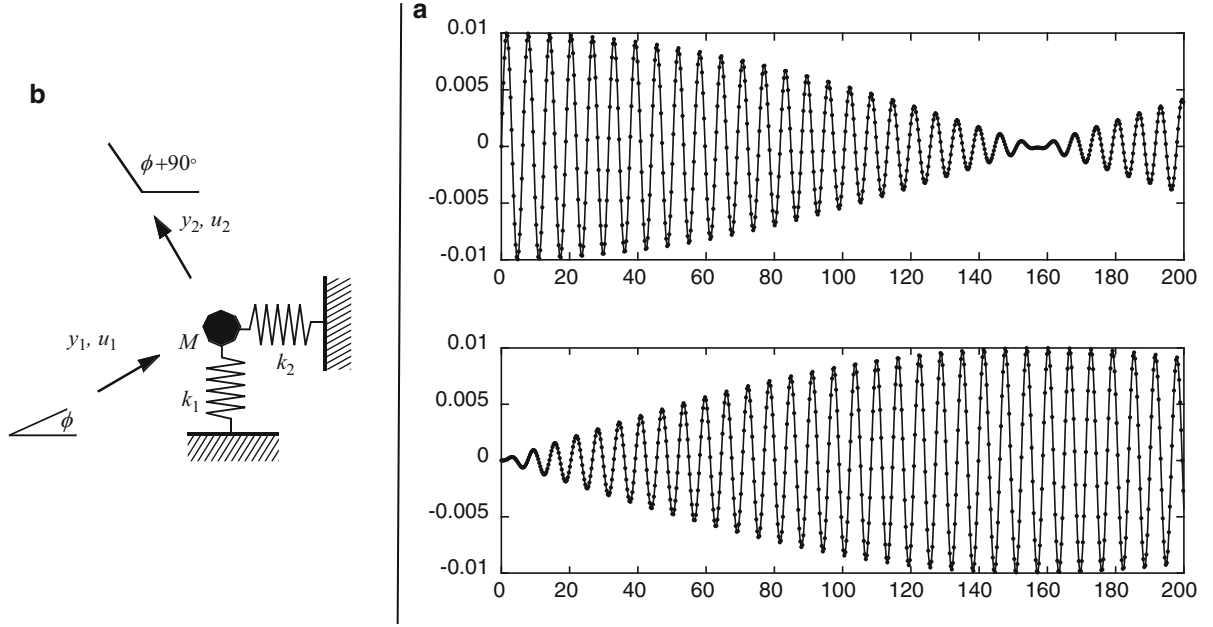
Fig. 7.3 (**a**) Impulse responses of selfadjoint (*solid*) with imperfect sensing and non-selfadjoint (*dots*) two-dof systems with closely spaced eigenfrequencies. Figures show beating velocity responses y_1 (*top*) and y_2 (*bottom*). (**b**) A two-dof system with small eigenvalue separation ($k_1 \approx k_2$). Orientation angle φ of inputs $\boldsymbol{u}$ and responses $\boldsymbol{y}$ are shown

and thus $\boldsymbol{B}_\psi = \boldsymbol{B}_\Phi$ and

$$S = C_\psi C_\Phi^{-1} \tag{7.61}$$

For the selfadjoint system shown in Fig. 7.3, the system matrices related to the local coordinate system ($\varphi = 45°$, $k_1 = 0.9801$ N/m, $k_2 = 1.0201$ N/m, m $= 1$ kg) are

$$M = \begin{bmatrix} 1 & 0 \\ 0 & 1 \end{bmatrix} \quad K = \begin{bmatrix} 1.0001 & -.0200 \\ -.0200 & 1.0001 \end{bmatrix} \tag{7.62a, b}$$

Let the system be excited by u_1 only and thus $\boldsymbol{P}_u = [1\ 0]^T$. This leads to state-space system matrices with displacement and velocity output as

$$A = \begin{bmatrix} 0 & 0 & 1 & 0 \\ 0 & 0 & 0 & 1 \\ -1.0001 & .0200 & 0 & 0 \\ .0200 & -1.0001 & 0 & 0 \end{bmatrix} \quad B = \begin{bmatrix} 0 \\ 0 \\ 1 \\ 0 \end{bmatrix} \quad C = \boldsymbol{I}_{4\times4} \tag{7.63a–c}$$

which can be brought to block-diagonal real form by a similarity transformation as

$$A_\Phi = \begin{bmatrix} 0 & 1.01 & 0 & 0 \\ -1.01 & 0 & 0 & 0 \\ 0 & 0 & 0 & .99 \\ 0 & 0 & -.99 & 0 \end{bmatrix} \quad B_\Phi = \begin{bmatrix} .9951 \\ 0 \\ 0 \\ -1.0051 \end{bmatrix} \quad C_\Phi = \begin{bmatrix} 0 & +.4975 & -.5025 & 0 \\ 0 & -.4975 & -.5025 & 0 \\ -.5025 & 0 & 0 & -.4975 \\ +.5025 & 0 & 0 & -.4975 \end{bmatrix}$$

$$\tag{7.64a–c}$$

The corresponding eigenvectors for displacements and velocities as observed by the output are the columns of $\mathbf{\Phi}$ with

$$\mathbf{\Phi} = \begin{bmatrix} +.4975i & -.4975i & -.5025 & -.5025 \\ -.4975i & +.4975i & -.5025 & -.5025 \\ -.5025 & -.5025 & -.4975i & +.4975i \\ +.5025 & +.5025 & -.4975i & +.4975i \end{bmatrix} \tag{7.65}$$

The real-valued modes that are related to displacements are thus $[+.4975 \; -.4975]^{\mathrm{T}}$ and $[.5025 \; .5025]^{\mathrm{T}}$.

One arbitrarily chosen complex-valued perturbation of $\mathbf{\Phi}$ leads to the complex valued modes of

$$\mathbf{\psi} = \begin{bmatrix} -.0495+.4950i & -.0495-.4950i & -.5025 & -.5025 \\ -.0495-.4975i & -.0495+.4950i & -.5025 & -.5025 \\ -.5000-.0500i & -.5000+.0500i & -.4975i & +.4975i \\ +.5000-.0500i & +.5000+.0050i & -.4975i & +.4975i \end{bmatrix} \tag{7.66}$$

which in turn leads to a non-selfadjoint state-space model that can be brought to block-diagonal real form with the same dynamic matrix $\mathbf{A}$ as given in Eq. (7.64a) and output matrix $\mathbf{C_\psi}$ given by

$$\mathbf{C_\psi} = \begin{bmatrix} -.0495 & +.4950 & -.5025 & 0 \\ -.0495 & -.4950 & -.5025 & 0 \\ -.5000 & -.0500 & 0 & -.4975 \\ +.5000 & -.0500 & 0 & -.4975 \end{bmatrix} \tag{7.67}$$

A non-perfect sensor system that would give the same output from the selfadjoint system as the perfectly measured output from the non-selfadjoint perturbed system would have the sensitivity matrix

$$\mathbf{S} = \begin{bmatrix} 1.0025 & -.0025 & -.0495 & +.0495 \\ -.0025 & 1.0025 & -.0495 & +.0495 \\ +.0505 & -.0505 & 1.0025 & -.025 \\ +.0505 & -.0505 & -.0025 & 1.0025 \end{bmatrix} \tag{7.68}$$

with elements that are off the ideal sensor's by less than 5.1 %. It is seen that the sensitivity matrix has a full structure with off-diagonal elements that give coupling between displacement and velocity states.

The response of the non-selfadjoint model, see Eq. (7.64a, b) and (7.67), is simulated at the action of a 10 ms 1 N impact impulse $u_1(t)$. The velocity responses along the loading direction y_1 and in a perpendicular orientation y_2 are shown in Fig. 7.3. It is compared with the output of an imperfect sensor system with sensitivity matrix given by Eq. (7.68) sitting on a selfadjoint system given by Eq. (7.64a–c). It comes without surprise that the curves are indistinguishable.

7.9 Concluding Remarks

It has been shown that, under a certain condition, an undamped self-adjoint system may vibrate in a normal mode pattern that can best be described by a complex-valued eigenmode. Since the condition is that the system possesses repeated eigenvalues, and these occur with a probability that is almost zero in practice, this is a vibration pattern that is not normally observed. If such non-normally observed modes should occur they are still normal modes. Systems with high degree of symmetry, such as church bells or turbine rotors, are good candidates for studies of such modes. This condition does sometimes occur in experimental data when the modal parameter estimation problem is poorly conditioned (when insufficient references are included in the FRF data set). An example of this is when two modal vectors are very close in frequency (pseudo-repeated roots) but only one mode can be well estimated from data in the frequency region of the pseudo-repeated roots.

Although the conditions for repeated roots (exactly repeated eigenvalues) are seldom met in practice, the spurious output of a non-perfect sensor system may lead to that a system without repeated eigenvalues is mistakenly seen as a system with complex eigenmodes. An example showed a situation with a sensor system that had spurious mixing of displacement and velocity states. In vibration testing the sensors are most often accelerometers. While these are known to have spurious mixing

of acceleration states, known as cross-sensitivity, it is not known by the authors if they can also possess cross-sensitivity to other states. However since an angular velocity of a system results in absolute acceleration away from its rotational center, it might not be impossible to find such velocity-acceleration couplings in accelerometers that are based on the acceleration state of a small seismic mass should those sensors sit on a test-piece with local angular motion.

References

1. Wilkinson, J.H.: The Algebraic Eigenvalue Problem. Oxford University Press, Oxford (1965)
2. Golub, G.H., Van Loan, C.F.: Matrix Computation, 4th edn. John Hopkins University Press, Baltimore (2013)
3. Ewins, D.J.: Modal Testing: Theory, Practice and Application. Research Studies Press, Baldock (2000)
4. Craig Jr., R.R., Kurdila, A.J.: Fundamentals of Structural Dynamics. Wiley, Hoboken, NJ (2006)
5. Allemang, R.J.: The modal assurance criterion—twenty years of use and abuse. J. Sound Vib. **37**(8), 14–23 (2003)
6. Abrahamsson, T.J.S.: Modal-parameter extraction for nonproportionally damped linear structures. Int. J. Anal. Exp. Modal Anal. **3**(2) (1988)
7. Foss, K.A.: Co-ordinates which uncouple the equations of motion of damped linear systems. Technical Report 25–20, Aeroelastic and Structures Research Laboratory, Massachusetts Institute of Technology (1956)

Chapter 8
Generalized Craig-Bampton Method Using Robin Boundary Conditions

Fabian M. Gruber, Johannes B. Rutzmoser, and Daniel J. Rixen

Abstract Dynamic substructuring is an efficient way to reduce the size and to analyse the dynamical behaviour of large models. The most popular approach is a fixed-interface method, the Craig-Bampton method (CBM, 1968), which is based on fixed-interface vibration modes and interface constraint modes. On the other hand, free-interface methods employing free-interface vibration modes together with attachment modes are also used, e.g. MacNeal's method (1971) and Rubin's method (1975). The dual Craig-Bampton method (DCBM, 2004 proposed by Rixen) uses the same ingredients as the methods of MacNeal and Rubin, but assembles the substructures using interface forces (dual assembly). The mixed Craig-Bampton (2011, proposed by Voormeeren et al.) method can deal with a mix of CBM and DCBM reduced substructures but each substructure has to be reduced either with the CBM or with the DCBM. The CBM and DCBM are using interface conditions which are extremal cases of the real connecting conditions. We want to generalize the CBM and the DCBM interface conditions to substructures connected via Robin boundary conditions. The CBM and the DCBM are then the two extreme cases of this generalized formulation, either having infinite stiffness or zero stiffness on the interface. Although reduction bases using interface loading were proposed in the past by Chandler and Tinker (1997), we want to combine in a coherent manner the way the bases are computed at substructure level and the way the assembly is formulated, hoping to construct a quasi-diagonal form for the reduced system.

Keywords Dynamic substructuring • Component mode synthesis • Model order reduction • Craig-Bampton method • Robin boundary condition

8.1 Governing Equations

8.1.1 Substructure Equations

Consider now a finite element model of a global domain Ω. This domain Ω is divided into N non-overlapping substructures called $\Omega^{(s)}$ such that every node belongs to exactly one substructure except for the nodes on the interface boundaries. The linear/linearized equation of motion of one substructure s is written as

$$\boldsymbol{M}^{(s)}\ddot{\boldsymbol{u}}^{(s)} + \boldsymbol{K}^{(s)}\boldsymbol{u}^{(s)} = \boldsymbol{f}^{(s)} + \boldsymbol{g}^{(s)}, \quad s = 1, \dots, N \tag{8.1}$$

where the superscript (s) is the label of the particular substructure. $\boldsymbol{M}^{(s)}$, $\boldsymbol{K}^{(s)}$ and $\boldsymbol{u}^{(s)}$ are the mass matrix, the stiffness matrix and the displacement vector of the substructure, respectively. $\boldsymbol{f}^{(s)}$ is the external force vector and $\boldsymbol{g}^{(s)}$ is the vector of reaction forces on the substructure due to its connection to adjacent substructures at its boundary degrees of freedom (DOF). The local displacements $\boldsymbol{u}^{(s)}$ of each substructure are divided in local internal DOF $\boldsymbol{u}_i^{(s)}$ and boundary DOF $\boldsymbol{u}_b^{(s)}$. The boundary DOF $\boldsymbol{u}_b^{(s)} = \boldsymbol{L}_b^{(s)}\boldsymbol{u}_b$ of the substructure are a subset of the assembled boundary DOF $\boldsymbol{u}_b$ of the global domain Ω.

F.M. Gruber (✉) • J.B. Rutzmoser • D.J. Rixen
Institute of Applied Mechanics, Faculty of Mechanical Engineering, Technische Universität München,
Boltzmannstr. 15, 85748 Garching, Germany
e-mail: fabian.gruber@tum.de; johannes.rutzmoser@tum.de; rixen@tum.de

$L_b^{(s)}$ is a Boolean localization matrix relating the assembled boundary DOF u_b of the global domain to the substructure boundary DOF $u_b^{(s)}$. The equation of motion (8.1) of one substructure s partitioned in that manner writes

$$\begin{bmatrix} M_{bb}^{(s)} & M_{bi}^{(s)} \\ M_{ib}^{(s)} & M_{ii}^{(s)} \end{bmatrix} \begin{bmatrix} \ddot{u}_b^{(s)} \\ \ddot{u}_i^{(s)} \end{bmatrix} + \begin{bmatrix} K_{bb}^{(s)} & K_{bi}^{(s)} \\ K_{ib}^{(s)} & K_{ii}^{(s)} \end{bmatrix} \begin{bmatrix} u_b^{(s)} \\ u_i^{(s)} \end{bmatrix} = \begin{bmatrix} f_b^{(s)} \\ f_i^{(s)} \end{bmatrix} + \begin{bmatrix} g_b^{(s)} \\ 0 \end{bmatrix}. \tag{8.2}$$

8.1.2 Assembly of Substructures

For the sake of simplicity the assembly of only two substructures is considered in the following ($s = 1, 2$). The mass matrix is also omitted for simplicity but can be derived in a similar way. Note that this concept can be easily generalized for the assembly of an arbitrary number of substructures N. The three-field formulation for the assembly of two substructures writes (see for instance [7])

$$\begin{bmatrix} K_{ii}^{(1)} & K_{ib}^{(1)} & 0 & 0 & 0 & 0 & 0 \\ K_{bi}^{(1)} & K_{bb}^{(1)} & 0 & 0 & 0 & -I & 0 \\ 0 & 0 & K_{ii}^{(2)} & K_{ib}^{(2)} & 0 & 0 & 0 \\ 0 & 0 & K_{bi}^{(2)} & K_{bb}^{(2)} & 0 & 0 & -I \\ 0 & 0 & 0 & 0 & 0 & L_b^{(1)^T} & L_b^{(2)^T} \\ 0 & -I & 0 & 0 & L_b^{(1)} & 0 & 0 \\ 0 & 0 & 0 & -I & L_b^{(2)} & 0 & 0 \end{bmatrix} \begin{bmatrix} u_i^{(1)} \\ u_b^{(1)} \\ u_i^{(2)} \\ u_b^{(2)} \\ u_\Gamma \\ g_b^{(1)} \\ g_b^{(2)} \end{bmatrix} = \begin{bmatrix} f_i^{(1)} \\ f_b^{(1)} \\ f_i^{(2)} \\ f_b^{(2)} \\ 0 \\ 0 \\ 0 \end{bmatrix} \tag{8.3}$$

with $L_b^{(s)}$ being a Boolean matrix localizing the DOF from the global interface displacement field corresponding to the boundary DOF $u_b^{(s)}$ of substructure s. u_Γ is an intermediate displacement field between the substructures which is used to govern the interface compatibility between the substructures. The fifths set of Eq. (8.3) expresses the equilibrium of the interface forces over the interface (action equals reaction). The last two equations (row six and seven of Eq. (8.3)) express the compatibility between the interface DOF of each substructure with the intermediate interface u_Γ.

8.2 Craig-Bampton Method (CBM)

Considering the partitioned equation of motion (8.2), the internal DOF $u_i^{(s)}$ of substructure s can be seen as being excited by its boundary DOF $u_b^{(s)}$. This indicates that $u_i^{(s)}$ of each substructure can be approximated by a superposition of a static response and of eigenmodes associated to $M_{ii}^{(s)}$ and $K_{ii}^{(s)}$. The static response is given by

$$u_{i,stat}^{(s)} = -K_{ii}^{(s)^{-1}} K_{ib}^{(s)} u_b^{(s)} = \Psi_{ib}^{(s)} u_b^{(s)}, \tag{8.4}$$

where the columns of matrix $\Psi_{ib}^{(s)}$ are the static response modes (constraint modes). The so-called fixed interface normal modes $\phi_k^{(s)}$ are obtained as eigensolutions of the generalized eigenproblem $K_{ii}^{(s)} \phi_k^{(s)} = \omega_k^{(s)2} M_{ii}^{(s)} \phi_k^{(s)}$. The columns of the $n_i^{(s)} \times n_\phi^{(s)}$ matrix $\Phi_{i\phi}^{(s)}$ contain the first $n_\phi^{(s)}$ fixed interface normal modes $\phi_k^{(s)}$ which can also be considered as the free vibration modes of the substructure s clamped on its boundary DOF $u_b^{(s)}$. The approximation of the internal DOF $u_i^{(s)}$ therefore writes

$$u_i^{(s)} \approx u_{i,stat}^{(s)} + \Phi_{i\phi}^{(s)} \eta^{(s)} = \Psi_{ib}^{(s)} u_b^{(s)} + \Phi_{i\phi}^{(s)} \eta^{(s)} \tag{8.5}$$

and the displacements $\boldsymbol{u}^{(s)}$ of the substructure are approximated by

$$
\boldsymbol{u}^{(s)} = \begin{bmatrix} \boldsymbol{u}_b^{(s)} \\ \boldsymbol{u}_i^{(s)} \end{bmatrix} \approx \begin{bmatrix} \boldsymbol{I}_{bb}^{(s)} & \boldsymbol{0}_{b\phi}^{(s)} \\ \boldsymbol{\Psi}_{ib}^{(s)} & \boldsymbol{\Phi}_{i\phi}^{(s)} \end{bmatrix} \begin{bmatrix} \boldsymbol{u}_b^{(s)} \\ \boldsymbol{\eta}^{(s)} \end{bmatrix} \tag{8.6}
$$

with the vector of modal parameters $\boldsymbol{\eta}^{(s)}$ corresponding to the amplitudes of the fixed-interface normal modes $\boldsymbol{\Phi}_{i\phi}^{(s)}$. Using Eq. (8.3) with $\boldsymbol{u}_b^{(s)} = \boldsymbol{L}_b^{(s)} \boldsymbol{u}_\Gamma$, the primal assembled system of equations is resulting [3].

To sum up, the CBM is using fixed-interface normal modes and constraint modes for the approximation of one substructure. The fixed-interface condition used for the computation of these modes corresponds to an infinite stiff interface. The constraint mode is the static deformation shape when a unit displacement (Dirichlet boundary condition) is applied to one of the $\boldsymbol{u}_b^{(s)}$ coordinates while the remaining DOF of $\boldsymbol{u}_b^{(s)}$ have a zero displacement [2].

8.3   Dual Craig-Bampton Method (DCBM)

Considering the equation of motion (8.2) of substructure s with the vector of reactions forces $\boldsymbol{g}^{(s)} = -\boldsymbol{B}^{(s)^T} \boldsymbol{\lambda}$, each substructure can be seen as being excited by the interface connection forces $\boldsymbol{\lambda}$ and the external forces. $\boldsymbol{B}^{(s)}$ is a signed Boolean matrix acting on the interface DOF. $\boldsymbol{B}^{(s)^T} \boldsymbol{\lambda}$ is representing the interconnecting forces between substructures. This indicates that an approximation of the displacements of each substructure $\boldsymbol{u}^{(s)}$ can be expressed in terms of local static solutions $\boldsymbol{u}_{stat}^{(s)}$ and in terms of eigenmodes associated to the substructure with free interfaces:

$$
\boldsymbol{u}^{(s)} \approx \boldsymbol{u}_{stat}^{(s)} + \boldsymbol{\Theta}^{(s)} \boldsymbol{\eta}^{(s)} = -\boldsymbol{K}^{(s)^+} \boldsymbol{B}^{(s)^T} \boldsymbol{\lambda} + \boldsymbol{R}^{(s)} \boldsymbol{\alpha}^{(s)} + \boldsymbol{\Theta}^{(s)} \boldsymbol{\eta}^{(s)} \tag{8.7}
$$

The matrix $\boldsymbol{K}^{(s)^+}$ is a generalized inverse of $\boldsymbol{K}^{(s)}$ and the matrix $\boldsymbol{R}^{(s)}$ is containing the rigid body modes if the substructure is floating. When there are enough boundary condition to prevent the substructure from floating $\boldsymbol{K}^{(s)^+}$ is equal to the inverse of $\boldsymbol{K}^{(s)}$. The vector $\boldsymbol{\alpha}^{(s)}$ contains the amplitudes of the rigid body modes (if there are any) and the vector $\boldsymbol{\eta}^{(s)}$ contains the amplitudes $\eta_j^{(s)}$ of the local eigenmodes $\boldsymbol{\theta}_j^{(s)}$ being eigensolutions of the generalized eigenproblem $\boldsymbol{K}^{(s)} \boldsymbol{\theta}_j^{(s)} = \omega_j^{(s)^2} \boldsymbol{M}^{(s)} \boldsymbol{\theta}_j^{(s)}$. The matrix $\boldsymbol{K}^{(s)^+} \boldsymbol{B}^{(s)^T}$ corresponds to attachment modes. The matrix $\boldsymbol{\Theta}^{(s)}$ contains only the first retaining $n_\theta^{(s)}$ eigenmodes $\boldsymbol{\theta}_j^{(s)}$ (free-interface normal modes) of this eigenproblem. Since a part of the subspace spanned by $\boldsymbol{\Theta}^{(s)}$ is already included in $\boldsymbol{K}^{(s)^+}$ the residual flexibility matrix $\boldsymbol{G}_{res}^{(s)}$ can be used instead of $\boldsymbol{K}^{(s)^+}$ [5]. This means that residual attachment modes are used instead of attachment modes. As a result the approximation of the displacements $\boldsymbol{u}^{(s)}$ of one substructure writes

$$
\boldsymbol{u}^{(s)} \approx \begin{bmatrix} \boldsymbol{R}^{(s)} & \boldsymbol{\Theta}^{(s)} & -\boldsymbol{G}_{res}^{(s)} \boldsymbol{B}^{(s)^T} \end{bmatrix} \begin{bmatrix} \boldsymbol{\alpha}^{(s)} \\ \boldsymbol{\eta}^{(s)} \\ \boldsymbol{\lambda} \end{bmatrix}. \tag{8.8}
$$

Using Eq. (8.3) with $\boldsymbol{g}_b^{(s)} = -\boldsymbol{B}_b^{(s)^T} \boldsymbol{\lambda}$ the dual assembled system is resulting [5]. In contrast to the methods of MacNeal [4] and Rubin [6], the interface, connection forces remain as unknowns.

To sum up, the DCBM is using free-interface normal modes, rigid body modes and residual attachment modes for the approximation of one substructure. The free-interface condition used for the computation of these modes corresponds to zero stiffness on the interface. The attachment mode is the static deformation shape when a unit force (Neumann boundary condition) is applied at one of the coordinates corresponding to $\boldsymbol{u}_b^{(s)}$ [2].

8.4   Formulation Using Robin Boundary Conditions

In mathematics Robin boundary conditions are a linear (weighted) combination of Dirichlet boundary conditions and Neumann boundary conditions. This effect can be achieved by introducing additional stiffnesses (springs) connected to the boundary DOF $\boldsymbol{u}_b^{(s)}$. Reduction bases using interface loading were proposed in the past [1]. In this contribution we suggest to use now such Robin boundary conditions to construct the reduction basis for the substructures.

On the one hand, applying the CBM Dirichlet boundary conditions are used to approximate the dynamical behaviour of each substructure. The fixed-interface condition results in a too stiff behaviour compared to the real connecting conditions. On the other hand, applying the DCBM Neumann boundary conditions are used to approximate the dynamical behaviour of each substructure. That free-interface condition gives a too flexible behaviour (zero stiffness on the interface) compared to the real connecting conditions. As a consequence the real interface conditions are lying somewhere in between.

Therefore using a fictive stiffness on the interface should give a much better approximation of the dynamical behaviour of the substructures than one of the two extreme cases of zero or infinite stiffness on the interface. Hence the local substructure generalized eigenproblem

$$\tilde{K}^{(s)} \tilde{\theta}_j^{(s)} = \tilde{\omega}_j^{(s)^2} M^{(s)} \tilde{\theta}_j^{(s)} \tag{8.9}$$

with the new stiffness matrix

$$\tilde{K}^{(s)} = \begin{bmatrix} K_{ii}^{(s)} & K_{ib}^{(s)} \\ K_{bi}^{(s)} & K_{bb}^{(s)} + A_{bb}^{(s)} \end{bmatrix} \tag{8.10}$$

has to be solved to get the eigenmodes to approximate the dynamical behaviour of substructure s. The modes obtained that way are better suited to approximate the real behaviour of the substructures.

The assembly of stiffness matrices of this type is obtained from the three-field formulation of Eq. (8.3) by performing the change of variable

$$g_b^{(1)} = \lambda^{(1)} - A_{bb}^{(1)} u_b^{(1)} \tag{8.11}$$

$$g_b^{(2)} = \lambda^{(2)} - A_{bb}^{(2)} u_b^{(2)} \tag{8.12}$$

with the Lagrange-multipliers $\lambda^{(s)}$ which can be interpreted as the resulting forces on each substructure. Then the assembled equation writes

$$\begin{bmatrix} K_{ii}^{(1)} & K_{ib}^{(1)} & 0 & 0 & 0 & 0 & 0 \\ K_{bi}^{(1)} & K_{bb}^{(1)} + A_{bb}^{(1)} & 0 & 0 & 0 & -I & 0 \\ 0 & 0 & K_{ii}^{(2)} & K_{ib}^{(2)} & 0 & 0 & 0 \\ 0 & 0 & K_{bi}^{(2)} & K_{bb}^{(2)} + A_{bb}^{(2)} & 0 & 0 & -I \\ 0 & -L_b^{(1)^T} A_{bb}^{(1)} & 0 & -L_b^{(2)^T} A_{bb}^{(2)} & 0 & L_b^{(1)^T} & L_b^{(2)^T} \\ 0 & -I & 0 & 0 & L_b^{(1)} & 0 & 0 \\ 0 & 0 & 0 & -I & L_b^{(2)} & 0 & 0 \end{bmatrix} \begin{bmatrix} u_i^{(1)} \\ u_b^{(1)} \\ u_i^{(2)} \\ u_b^{(2)} \\ u_\Gamma \\ \lambda^{(1)} \\ \lambda^{(2)} \end{bmatrix} = \begin{bmatrix} f_i^{(1)} \\ f_b^{(1)} \\ f_i^{(2)} \\ f_b^{(2)} \\ 0 \\ 0 \\ 0 \end{bmatrix} \tag{8.13}$$

This system of equations can be interpreted as adding springs on the interface of the substructure and connecting them to a fixed reference. Equation (8.13) can be reformulated to get a symmetric matrix by rearranging the fifths row of the system.

8.5 Future Work

This contribution gives a first suggestion of the application of Robin-like boundary conditions to component mode synthesis. The effect of different kinds of static modes on the reduction of the substructure will be investigated. Moreover, the suggested formulation will be applied to examples to judge on the performance of the proposed formulation. Furthermore other formulations of Robin-like boundary conditions are possible which have to be considered in the future.

References

1. Chandler, K.O., Tinker, M.L.: A general mass-additive method for component mode synthesis. In: Proceedings of the AIAA Structures, Structural Dynamics and Materials Conference, Kissimmee, FL, pp. 93–103 (1997)
2. Craig, R.R.: Coupling of substructures for dynamic analyses: an overview. In: Proceedings of AIAA/ASME/ASCE/AHS/ASC Structures, Structural Dynamics, and Materials Conference and Exhibit, Atlanta, GA, pp. 1573–1584 (2000)
3. Craig, R.R., Bampton, M.C.: Coupling of substructures for dynamic analyses. AIAA J. **6**, 1313–1319 (1968)
4. MacNeal, R.H.: A hybrid method of component mode synthesis. Comput. Struct. **1**, 581–601 (1971)
5. Rixen, D.J., A dual Craig–Bampton method for dynamic substructuring. J. Comput. Appl. Math. **168**, 383–391 (2004)
6. Rubin, S.: Improved component-mode representation for structural dynamic analysis. AIAA J. **13**, 995–1006 (1975)
7. Voormeeren, S.N., Van Der Valk, P.L.C., Rixen, D.J.: Generalized methodology for assembly and reduction of component models for dynamic substructuring. AIAA J. **49**, 1010–1020 (2011)

Chapter 9
Force Reconstruction Using Force Gauges and Accelerometers

Wesley Axtell and Tyler Dare

Abstract Methods of inferring excitation forces from measured accelerometer data have received significant attention in recent years. This paper attempts to combine these techniques with the addition of force gauges to determine excitation forces on a vibrating structure. A mathematical algorithm was derived and applied to experimental data where a known impact force was applied to a plate mounted through force gauges. This experiment was used both to validate the mathematical algorithm and to investigate its limitations. The results show that the applied force for a fixed structure can be reconstructed better than force gauges alone using a combination of force gauge data and free boundary condition modal analysis.

Keywords Force reconstruction • Force gauges • Accelerometers • Rigid body modes • Inverse methods

9.1 Introduction

Force reconstruction involves using the output response of a system in order to infer the dynamic forces and moments that are acting on that system. Various different methods of force reconstruction have been developed over the years. These methods typically use accelerometers and/or strain gauges as the output responses of the system. In this study, force gauges are used in tandem with accelerometers in order to find the forces acting on a test substructure.

The goal for this study is to reconstruct forces on a test structure that is attached to a main structure. Using force gauges allows the test structure to be essentially isolated from the main structure by canceling out any forces exerted on the test structure by the main structure. This is possible by having accelerometers on the test structure since any dynamic excitation on the test structure from the main structure will also be measured by the accelerometers.

The force gauges by themselves could directly measure the forces acting on the structure. However, these force are passing through the structure and creating dynamic vibrations of the structure's resonances. The force gauges also measure the effect of these resonances. Using the accelerometers, along with the measured free mode shapes of the test structure, allows for these resonating features of the structure to also be canceled out.

To find the resonant forces using the accelerometers, the free mode shapes of the test structure (separated from the main structure) are used. Free boundary conditions are used in these calculations so that the test structure is able to be tested separately from the main structure.

9.2 Literature Review

Force identification is an inverse problem that has been investigated for many years and still lacks a universal solution. Stevens gives a good overview of force reconstruction [1]. He expresses the system as an input force (F) being acted on through a transfer function (H) to resolve into the received response:

$$H(\omega)\, F(\omega) = Y(\omega). \tag{9.1}$$

The idea of force identification is that H and Y are known, in some capacity, and that the problem becomes solving for F. The problem with this is that the H matrix is often ill-conditioned. Stevens goes on to say that the advantages that are used for

───────────────

W. Axtell (✉) • T. Dare
The Pennsylvania State University, University Park, PA 16802, USA
e-mail: wxa128@psu.edu

forward problems tend to be disadvantages in the corresponding inverse problem. This leads inverse problems to be ill-posed and that small variations in the response data can cause large variations in the solution. The ill-conditioned matrices and the ill-posed problem makes these inverse problems very difficult to solve for.

This problem may be easier to solve if H is a square matrix, then the solution to Eq. (9.1) would be

$$F(\omega) = H^{-1}(\omega) Y(\omega).$$
(9.2)

However, often times, it is desirable for H to be over determined in order to account for averaging and eliminating random errors in the data. In these cases, a pseudo-inverse, as described by Penrose, can be applied to solve Eq. (9.1) [2].

$$F(\omega) = H^{+}(\omega) Y(\omega).$$
(9.3)

A pseudo inverse is described as H^{+} and is defined as

$$H^{+} = \left[H^{*}H\right]^{-1} H^{*},$$
(9.4)

where H^* is the Hermitian transpose. It should also be noted that this process can help over-conditioned problems, but under conditioned problems with more unknowns then data still gives poor results since there is insufficient data to resolve a unique solution for the problem.

Several other authors have since looked into the force reconstruction problem. Jacquelin et al. attempts to use a procedure that avoids using the pseudo-inverse by using a penalized model that uses Tikhonov Regularization to globally stabilize the solution to avoid the ill-posedness of the problem [3]. Rezayat et al. try to take this a step further by suggesting the use of a more adaptive penalty function to be applied to specific problems [4].

Two solutions have been developed at Sandia Laboratories. The first algorithm, used by Bateman et al. is referred to as the Sum of Weighted Acceleration Technique (SWAT) [5]. This technique utilizes the mode shapes of the structure to create a set of weighting factors, w, for each component of the force and moment vectors. A second technique, described and used in Schoenherr, builds off of SWAT and improves the modal by using a linear combination of the elastic mode shapes through an inverse of the time domain response so that only the rigid body modes need to be defined explicitly [6]. The technique used in this following experiment has similar qualities to these two models.

9.3 Theory

Starting with a standard distributed system,

$$[M]\{\ddot{x}(t)\} + [K]\{x(t)\} = \{f_E(t)\} + \{f_G(t)\},$$
(9.5)

where $[M]$ is a mass matrix, $[K]$ is the complex stiffness matrix, $\{x\}$ is the displacement vector, $\{f_E\}$ is the vector of the external forces, and $\{f_G\}$ is the combined force measured from the force gauges. Both the mass matrix and stiffness matrix are unknown, so this equation cannot be used directly. Measuring the unforced response of the system ($f = 0$) can be done through finite element modeling or modal testing. This can be used to calculate the mass-normalized free mode shapes $[\Phi]$ of the structure. The mode shapes can be related to the displacement vector using the modal displacement vector $\{\psi(t)\}$.

$$\{x(t)\} = [\Phi]\{\psi(t)\},$$
(9.6)

substituting back into Eq. (9.5), along with pre-multiplying everything by Φ^*:

$$[\Phi]^{*}[M][\Phi]\{\ddot{\psi}(t)\} + [\Phi]^{*}[K][\Phi]\{\psi(t)\} = [\Phi]^{*}\{f_E(t)\} + [\Phi]^{*}\{f_G(t)\}.$$
(9.7)

This enables both the mass matrix and the stiffness matrix to be eliminated from the problem since $[\Phi]^{*}[M][\Phi] = [I]$ and $[\Phi]^{*}[K][\Phi] = \left[\omega_m^2\right]$:

$$\{\ddot{\psi}(t)\} + \left[\omega_m^2\right]\{\psi(t)\} = [\Phi]^{*}\{f_E(t)\} + [\Phi]^{*}\{f_G(t)\},$$
(9.8)

where $[\omega_m^2]$ is diagonal matrix of the natural frequencies of the structure. Recall that the original $[K]$ matrix is complex. This allows for internal damping to be taken into consideration for this modal. Likewise, $[\omega_m^2]$ is also complex, utilizing the loss factor ξ to describe the internal damping of the structure. Both the natural frequencies and the loss factors of the system are calculated using modal analysis,

$$[\omega_m^2] = \begin{bmatrix} (2\pi f_1)^2 (1 + j\xi_1) & 0 & \cdots & 0 \\ 0 & (2\pi f_2)^2 (1 + j\xi_2) & \cdots & 0 \\ \vdots & \vdots & \ddots & 0 \\ 0 & 0 & \cdots & (2\pi f_m)^2 (1 + j\xi_m) \end{bmatrix}, \tag{9.9}$$

where for testing purposes, we generalized modal acceleration vector can be replaced by the response of the accelerometers by utilizing the pseudo-inverse of the mode shape matrix for the location of the accelerometers, $[\Phi_R]^+$.

$$\{\psi(t)\} = [\Phi_R]^+ \{x_R(t)\}, \tag{9.10}$$

where $\{x_R\}$ is the instrumented points on the test structure. Substituting this into Eq. (9.8) and solving for the modal external force

$$\{F_{E,modal}(f)\} = [\Phi]^* \{f_E(t)\} = \left([\Phi_R]^+ \{\ddot{x}_R(t)\} + [\omega_m^2] [\Phi_R]^+ \{x_R(t)\}\right) - [\Phi]^* \{f_G(t)\}, \tag{9.11}$$

or in the frequency domain:

$$\{F_{E,modal}(f)\} = [\Phi]^* \{f_E(f)\} = \left([\Phi_R]^+ - \frac{1}{\omega^2} [\omega_m^2] [\Phi_R]^+\right) \{a_R(f)\} - [\Phi]^* \{f_G(f)\}. \tag{9.12}$$

The external modal force, $\{F_{E,modal}(f)\}$, represents a decomposition of the distributed load into the mode shapes. Since the few modes in Φ are rigid body modes, the corresponding entries of the external modal force correspond to the resultant forces and moments on the test structure. For example, if the first free mode is rigid body translation in the x-direction, the first external modal force corresponds to the summation of the external forces in the x-direction.

The mass normalized mode shapes, $[\Phi]$ described above, have two components to them. Modal analysis calculates the elastic modes, $[\phi_1 \ \phi_2 \ \dots]$, of the structure. For this procedure to work properly however, the rigid body modes, $\left[\phi_z \ \phi_{\theta_x} \ \phi_{\theta_y}\right]$ also need to be taken into consideration. This creates the full mode shape matrix

$$[\Phi] = \left[\phi_z \ \phi_{\theta_x} \ \phi_{\theta_y} \ \phi_1 \ \phi_2 \ \dots\right]. \tag{9.13}$$

Since modal analysis doesn't easily calculate the rigid body mode shapes, these need to be calculated separately. For rigid body translation:

$$\{\phi_z\} = \frac{1}{\sqrt{m}} \begin{Bmatrix} (1) \\ (1) \\ \vdots \\ (1) \end{Bmatrix}, \tag{9.14}$$

and for rigid body rotation:

$$\{\phi_{\theta_x}\} = \frac{1}{\sqrt{I_{xx}}} \begin{Bmatrix} d_1 \sin\left(\theta_1 + \frac{\pi}{2}\right) \\ d_2 \sin\left(\theta_2 + \frac{\pi}{2}\right) \\ \vdots \\ d_n \sin\left(\theta_n + \frac{\pi}{2}\right) \end{Bmatrix}, \tag{9.15}$$

where

$$d_n = \sqrt{y_n^2 + z_n^2} \quad \text{and} \quad \tan \theta_n = \frac{z_n}{y_n}. \tag{9.16}$$

These rigid body modes can be easily calculated and applied to the force reconstruction technique. Since these are rigid body modes, the frequency of these modes would be zero and there would be zero internal damping.

9.4 Experiment

To demonstrate this new process of force reconstruction, a test experiment was setup. The test structure was a rectangular plate made of a composite material with dimensions of $9'' \times 12'' \times 0.5''$. A $1''$ grid was made across one of the faces of this plate so that there were a total of 130 points. Three single axis accelerometers were used to find the free mode shapes and resonance frequencies of the plate using a standard roaming hammer. After these mode shapes were calculated, the plate was mounted to a table with four PCB ring force gauges separating the plate from the table. This optics table now represents the main structure, while the plate is the test structure. Ten accelerometers were placed in various locations on the plate. These were placed in relatively random locations with the intention of avoiding placing them on node lines or in equivalent locations as other accelerometers. The test itself was performed using the impact of a modal hammer so that the reconstruction results could be compared to the actual force measured by the hammer. Testing was done in multiple locations with several measurements taken at each (Fig. 9.1).

9.5 Results/Discussion

The above experiment was performed and post-processing was done in the time domain. After post processing and taking the spectral density of the result, we find that the reconstructed force seems to follow the same trend as the original force up to the first mode. As seen in Fig. 9.2, the reconstructed force follows the input hammer force more closely and to a higher frequency band then if the force gauges where used independently.
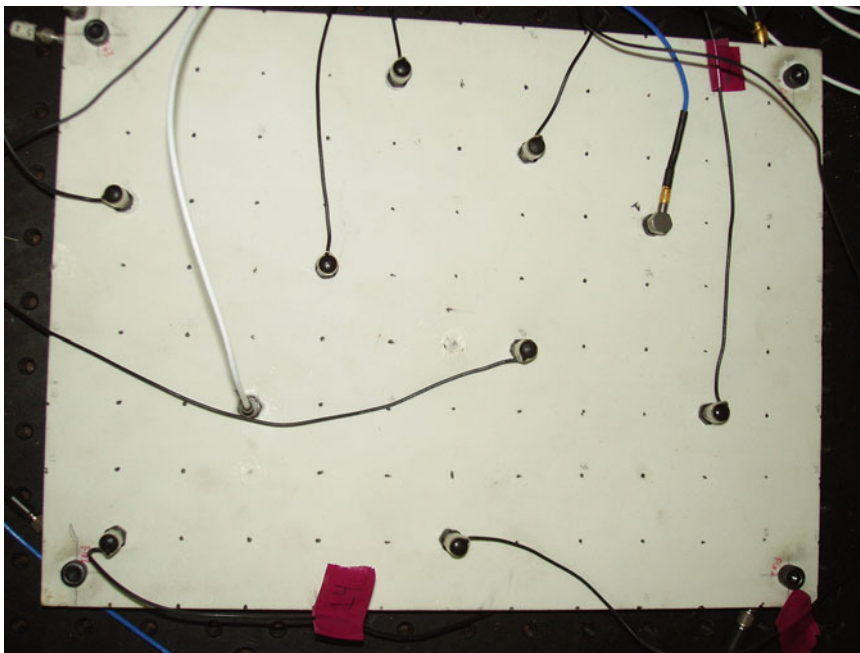
Fig. 9.1 Layout of accelerometers, force gauges are underneath, located at the four corners
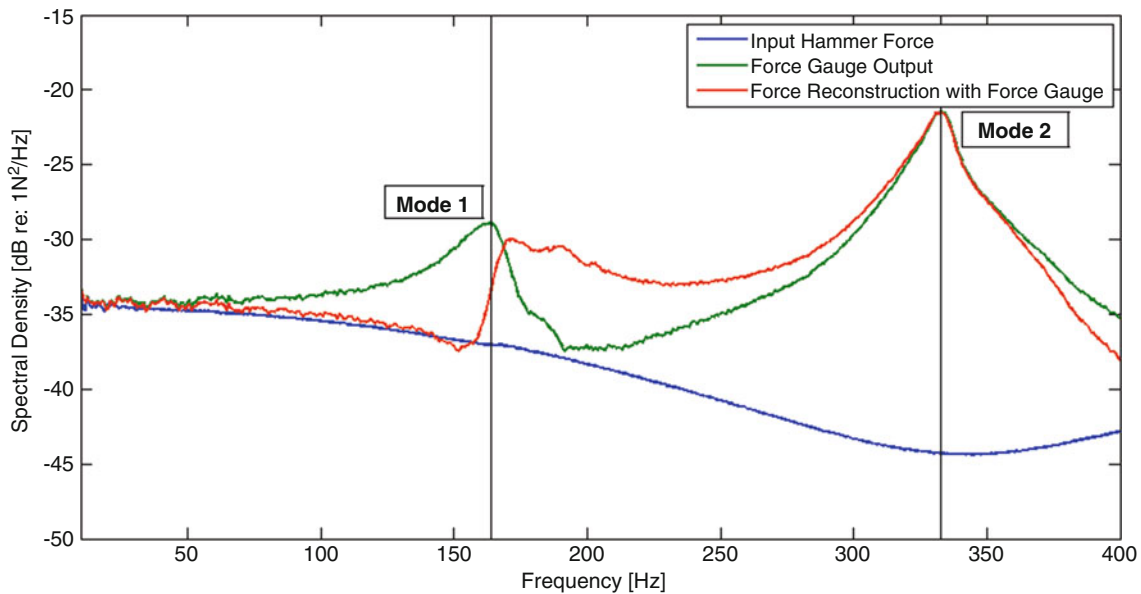
Fig. 9.2 Comparing frequency responses of the input hammer force to the force gauge output and the force reconstruction with the force gauges
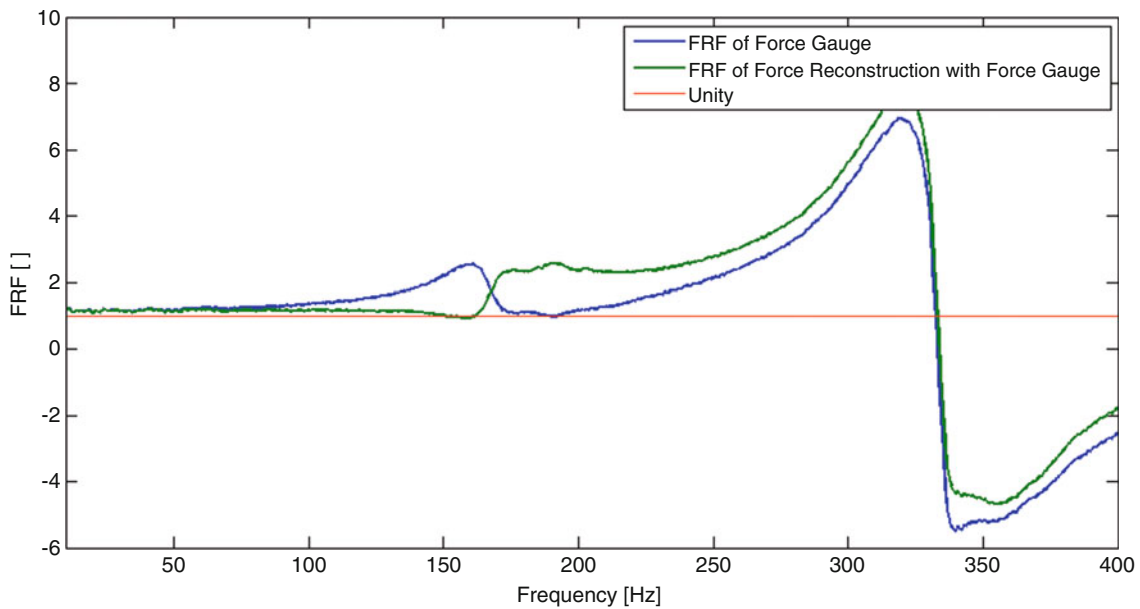
Fig. 9.3 Frequency response functions of the force gauges and the force reconstruction when compared to the original hammer force input

Comparing the frequency responses of the force gauges and the reconstructed force with the original hammer force is best seen looking at the FRF magnitude (Fig. 9.3). The FRF shows how the response of the force reconstruction is able to accurately reconstruct the input force to a higher frequency. Here, it is easier to see that the force reconstruction seems to be suitable up to about 160 Hz whereas the response of the force gauges is only able to represent the input force up to about 80 Hz. This shows that the reconstruction technique is able to increase the usable bandwidth of an indirectly measured signal then if just force gauges were being used.

Demonstrating the usefulness of the reconstruction technique does well to show the useful frequency bands, but being able to see good agreement between the reconstructed force and the original hammer hit can also be seen in the time domain. This is able to show that not only the magnitude, but also phase response of the reconstructed force aligns with the phase of the original hammer hit. Figure 9.4 demonstrates this well by showing the original hammer force compared to the time domain of the force gauges and the reconstructed. All three signals have been low passed filtered at 150 Hz so that only the
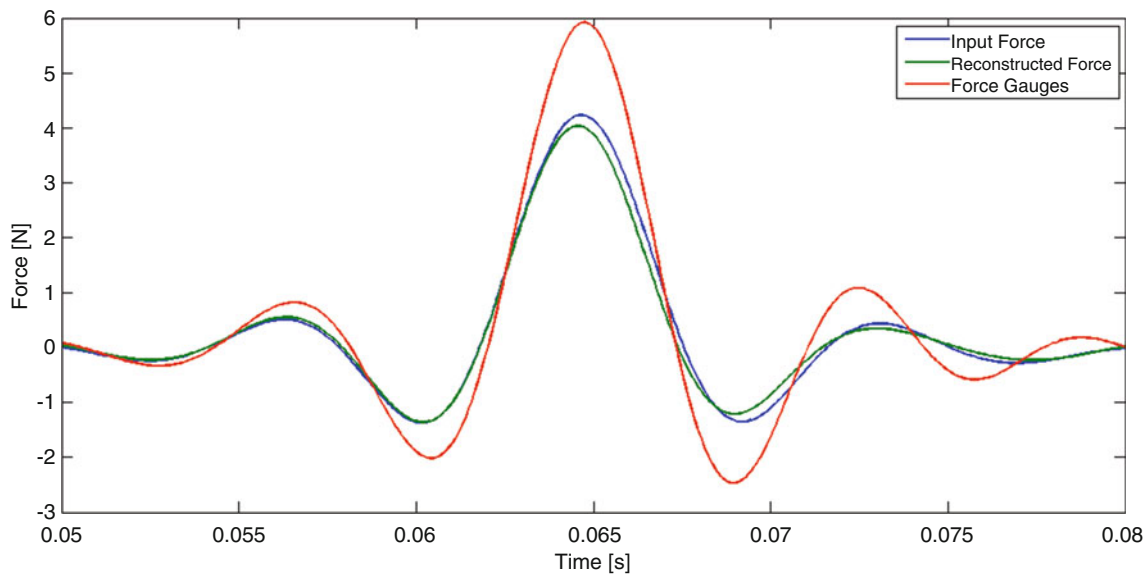
Fig. 9.4 Time domains of the input hammer force, the output of the force gauges, and the reconstructed force, all have been low passed filtered at 150 Hz

usable frequency bandwidth, as found when looking at frequency domain plots, is represented. In Fig. 9.4, the response of the force gauges is seen as being off in both magnitude and phase from the input force while the reconstructed force seems to correlate well with the input force with only some minor error.

All the results seen above are based on an experiment with minimal noise forces coming from the main structure. For this reason, the force gauges seem to fare well all by themselves to reconstruct the input force up to a point. In future experiments, noise will be added to the main structure. Theoretically, that noise will be noticeable in the frequency response of the force gauges. However, the noise should be canceled out using the force reconstruction technique and it should be possible to calculate an accurate frequency response with about the same bandwidth as is shown in this experiment.

The usable bandwidth of this experiment seems to be small. This is likely due to the fact that the experiment was conducted on a composite material with high damping and low frequency resonances. Different test structures will react differently and have different usable bandwidths depending upon the material and the geometry.

This modal analysis of this structure was conducted using free boundary conditions. This enabled the modal analysis of the test structure to be performed independently from the main structure. These results show that this procedure of using the free modes, as opposed to the fixed modes, still work eliminate some of the modal peaks seen in the frequency response.

9.6   Conclusion

Force reconstruction is problem that has no global solution and has to be adapted depending upon the structure and the situation of the measurement. When reconstructing the forces of a test structure independently of the main structure, a solution is using force gauges in combination with accelerometers and the free mode shapes of the test structure. This experiment shows the viability of this setup and procedure and further testing will show its use in added noise situation and with more complicated geometry.

References

1. Stevens, K.: Force identification problems-an overview Proceedings of the 1987 SEM Spring Conference on Experimental Mechanics: Houston, Texas, June 14-19, 1987 Pages 838–844
2. Penrose, R.: A generalized inverse for matrices. Math. Proc. Cambridge Philos. Soc. **51**(3), 406–413 (1955)
3. Jacquelin, E., Bennani, A., Hamelin, P.: Force reconstruction: analysis and regularization of a deconvolution problem. J. Sound Vib. **265**, 81–107 (2002)

4. Rezayat, A., Nassiri, V., Vanlanduit, S., Guillaume, P.: Force identification using mixed penalty functions. In: Proceedings of the 9th International Conference on Structural Dynamics, Porto, Portugal, (2014)
5. Bateman, V., Carne, T., Gregory, D., Attaway, S., Yoshimura, H.: Force reconstruction for impact tests. J. Vib. Acoust. **113**, 192–200 (1991)
6. Schoenherr, T.: Calculating the impact force of supersonic hail stones using SWAT-TEEM. Shock Vibration, Aircraft/Aerospace, and Energy Havesting **9**, 67–79 (2015)

Chapter 10
Experimental and Numerical Elastodynamic Analysis of Compressed Open Thin-Walled Beams

G. Piana, A. Carpinteri, E. Lofrano, R. Malvano, A. Manuello, and G. Ruta

Abstract Compressed thin-walled beams with open section are prone to torsional, or flexural-torsional, buckling. Here we present the results of several studies where, by piezoelectric pickups and a universal testing machine, we experimentally detected the natural frequencies and buckling loads of centrally compressed aluminum thin-walled beams with open cruciform section, exhibiting remarkable warping stiffness. We detected the free vibration frequencies for different values of the compressive force and for both free and (at least partially) restrained warping of the end sections. We compared the behavior of integer elements to that of analogous beams, where we introduced a localized damage, i.e., a sharp variation of a cross-section. For the integer elements, we compared the experimental results with those provided by an *in-house* numerical code, which investigates the elastic stability of possible non-trivial paths of thin-walled beams in a dynamic setting. The results show that, on the one hand, piezoelectric pickups can be efficiently used to extract modal parameters of structural elements; on the other hand, the numerical code proves to be robust and accurate in the determination of the buckling loads of the integer elements, in all the analyzed configurations.

Keywords Natural frequencies • Piezoelectric sensors • Thin-walled beams • Warping constraints • Buckling

10.1 Introduction

It is well known that the mechanical characteristics of thin-walled beams with open profile are their appreciable bending stiffness about at least one principal axis of inertia, and, by contrast, their negligible torsion stiffness. Moreover, since in general the placement of their centroid is different from that of their center of shear, bending and torsion are coupled both in the linear and nonlinear range. As a consequence, their elastic buckling modes are coupled, and the post-buckling behavior is unstable [1]. In addition, also due to their geometry, it is known that Saint-Venant's principle does not hold, and boundary effects propagate throughout the beam length [2]: this makes the effect of warping and warping constraints appreciable, if not dominant [2, 3]. Due to the widespread applications of such profiles, the investigation of their critical load has always been an interesting subject in engineering; some of the authors have published on the matter [4–6].

In the current literature on the critical loads for thin-walled beams, it is usually assumed that the pre-buckling equilibrium path is trivial, i.e., it is taken as reasonable that the applied load does not sensibly deform the considered element [1–3]. This may be a physically reasonable assumption for beams with solid cross-sections, the axial stiffness of which is remarkable; the coupling between bending and torsion is not so important, and warping effects are negligible, too. However, when dealing with thin-walled beams, the pre-buckling path can have much effect on the critical load, and investigations on non-trivial equilibrium paths leading to buckling can be of interest. Some of the authors have performed numerical investigations on the subject [7–9], by elaborating an *in-house* finite differences code based on the model dealt with in [4–6]. Further refinements of the model have been proposed in [10], and additional refinements of the numerical code are in progress, to take into account fully non-conservative loads.

G. Piana (✉) • E. Lofrano • G. Ruta
Department of Structural and Geotechnical Engineering, Sapienza University, Via Eudossiana 18, 00184 Roma, Italy
e-mail: gianfranco.piana@polito.it

A. Carpinteri • A. Manuello
Department of Structural, Geotechnical and Building Engineering, Politecnico di Torino, Corso Duca degli Abruzzi 24, 10129 Torino, Italy

R. Malvano
Private Researcher, Strada Comunale Val Pattonera 99, 10133 Torino, Italy

In the meanwhile, some others among the authors have investigated, numerically and experimentally, the variation of the natural frequencies of compressed beams [11, 12], taking advantage of a vast experience on experimental settings. Indeed, it is important, from the point of view of applications, to detect how natural frequencies change as a function of the state of stress of the considered structural element: such knowledge may result to be useful for design, monitoring, and damage detection.

Now, it is known that the buckling critical load is attained when the relevant natural frequency vanishes (ideal, perfect systems), or reaches a minimum (real, imperfect systems), following a load path in which the same natural frequency diminishes as the load increases, i.e., as the apparent stiffness of the beam goes down. It has been straightforward, then, to design an experimental campaign of validation of the results obtained numerically for thin-walled beams with open profile, with the aim of: (a) generalizing the experimental investigations already performed, in order to keep into account warping and warping constraints, so typical of thin-walled profiles; (b) designing and realizing suitable end constraint devices to match the analytical conditions introduced in the numerical investigation; (c) finding experimental validation of the numerical results obtained so far; and (d) highlighting, by experimental evidence, the role of pre-buckling equilibrium paths, usually neglected in the literature.

Since this is a long-term project, the research group has begun investigating the effect of compressive loads operated by a universal MTS testing machine on simple specimens, suitably constrained at the ends by devices designed and made on purpose, to take into account the warping properties of thin-walled profiles. The first campaign [13] was conducted on an aluminum beam with a doubly symmetric cruciform section, having negligible warping stiffness [1–3]. In that contribution we fully described the obtained experimental results, and the comparisons with the corresponding numerical ones. In particular, we tested the efficacy of the whole experimental set-up, with special reference to the realized end constraints and to the technique adopted to identify the natural frequencies. Moreover, the numerical *in-house* code was validated as well. In [11] some of the authors have adopted laser techniques to detect the natural frequencies of the tested beams, suitably curved to simulate a known imperfection, or a pre-buckling path. On the other hand, in [13] we successfully adopted piezoelectric pickups typical of musical technologies and found that they are effective, precise, robust, and reliable in the experimental campaign. The efficacy of using these sensors in extracting modal parameters of structural element was investigated by some of the authors also in another study [14].

In the present contribution, we extend the preceding analysis on thin-walled profiles by investigating again a doubly symmetric cross-section, but now with a non-negligible warping stiffness. In this way we can put into evidence the effects of warping and warping constraints on the natural frequencies and on the buckling loads of a larger class of thin-walled profiles. In particular, we investigated experimentally two different warping boundary conditions, and compared the behavior of integer elements to that of analogous profiles, where a localized reduction of the warping rigidity was artificially introduced. The detection of the natural frequencies was done by means of piezoelectric pickups in the present study as well.

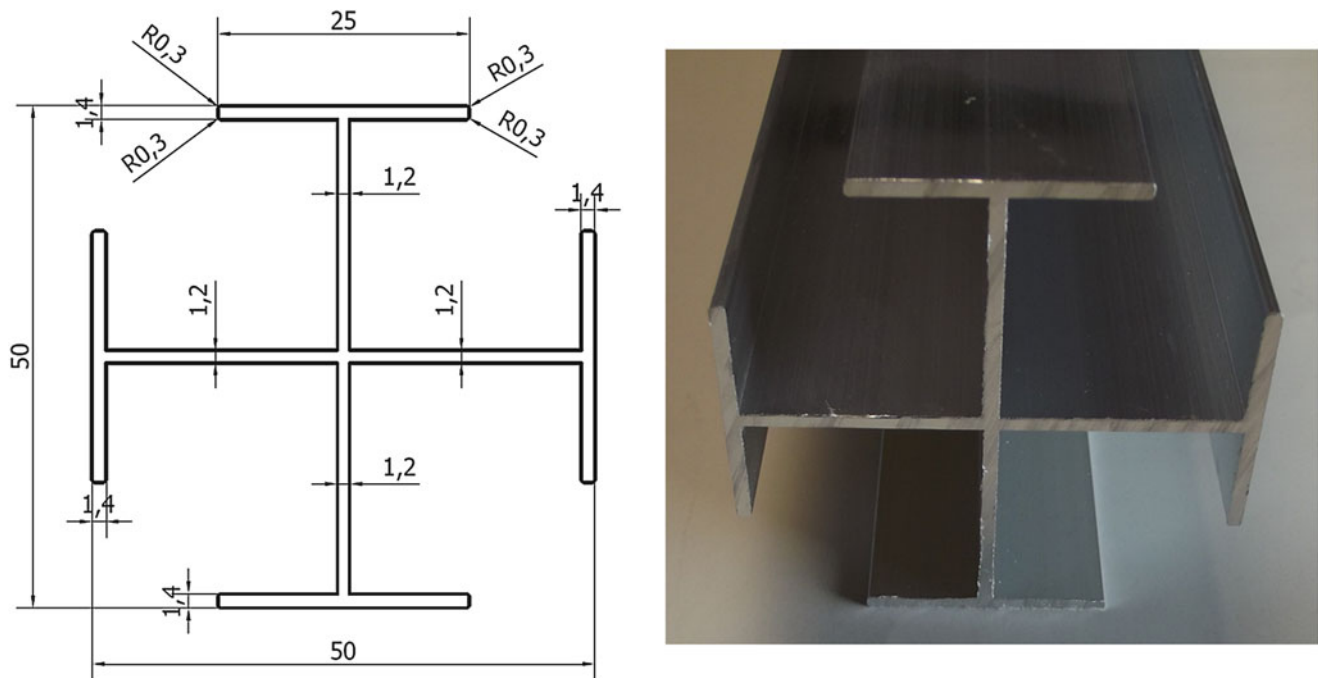## 10.2 Specimens and Experimental Setup

The specimens were constituted by thin-walled open profiles, made of aluminum (6060 T5 alloy), designed and realized on purpose for the experimental campaign. Their geometrical and mechanical properties are reported in Table 10.1. The cross-section of the specimens, shown in Fig. 10.1, is represented by a cruciform, double I section. We know that similar profiles are used as compressed members in civil engineering; we cite, for example, some columns of the New National Gallery of Berlin (Germany), designed by L. Mies van der Rohe and realized between 1962 and 1968; and some columns of the New De Cecco Headquarters in Pescara (Italy), designed by M. Fuksas and realized between 2001 and 2008. This kind of profile has high bending stiffness and relatively low torsion stiffness. Therefore, if they are not excessively long, when compressed, they are more prone to torsional buckling than to flexural buckling [1–3].

In order to investigate directly the effect of warping rigidity on both natural frequencies and buckling loads, a localized variation of the cross-section was introduced in some specimens. This variation was realized by cutting out the four flanges for a length of 1 cm, as shown in Fig. 10.2, in order to strongly reduce the warping rigidity of the section. This localized variation of cross section was introduced at one fourth of the element length, in order to maximize the reduction of the warping stiffness of the element with respect to buckling.
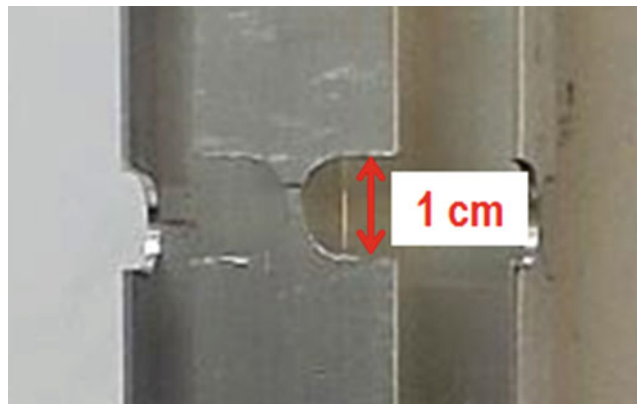
Table 10.1 Geometrical and mechanical properties of the specimens

| Unconstrained length (mm)	Section width (mm)	Section thickness (mm)	Young's modulus (N m^{-2})	Poisson's ratio, -	Mass density (kg m^{-3})
950	50	1.2 (web), 1.4 (flanges)	69×10^9	0.3	2600

Fig. 10.1   Drawing and picture of the specimens' cross-section (dimensions in mm)


Fig. 10.2   Sharp variation of cross-section, introducing a localized reduction of torsion rigidity (damaged elements)

Figure 10.3 shows the experimental setup adopted for the tests. A servo-hydraulic MTS testing machine, with a closed-loop electronic control and a maximum loading capacity of 250 kN, was used to provide the loading. The specimens were positioned vertically, and constrained to the testing machine by means of connections capable of preventing displacements, rotations and twist of the end sections. Figure 10.3a shows an integer element, with the indication of the location of the sensors adopted to detect the natural frequencies. Figure 10.3b shows a damaged specimen, reporting the indication of the localized reduction of the cross-section. As for the end connections, four brass elements were designed and manufactured in order to allow the insertion of the beam ends, with the possibility of permitting or preventing (at least partially) the warping deformation of the terminal sections, as shown in Fig. 10.4. In the case of Fig. 10.4a (free warping condition), only the web is constrained, while the flanges are leaved free. Conversely, in the case of Fig. 10.4b (restrained warping), all the section is inserted into the brass joint, and therefore both web and flanges are constrained. In this case, actually, penetration is prevented, but detachment is allowed; consequently, this condition is close to that of semi-restrained warping. Moreover, the position of the lower joint could be adjusted in the horizontal plane in order to ensure the required vertical alignment with the upper joint (Fig. 10.4). During the tests, the control of the vertical displacement transmitted to the lower beam end by the hydraulic jack operated the loading.
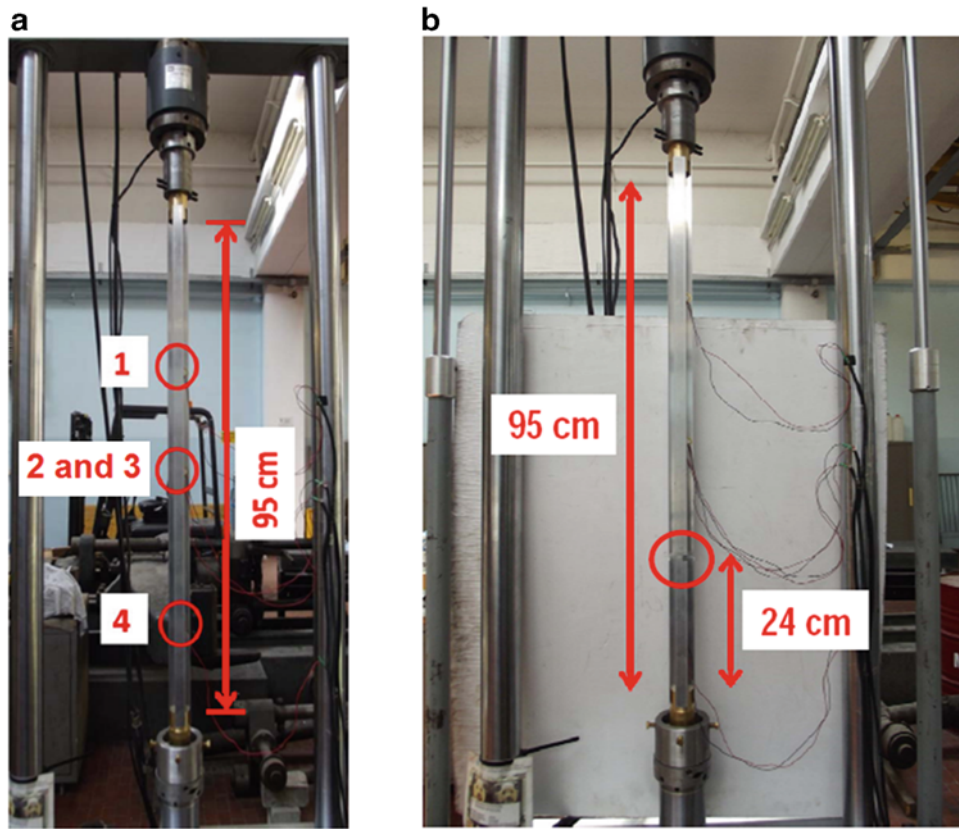
Fig. 10.3 Experimental setup: (**a**) integer specimen with indication of the position of sensors, (**b**) damaged specimen with indication of localized section reduction
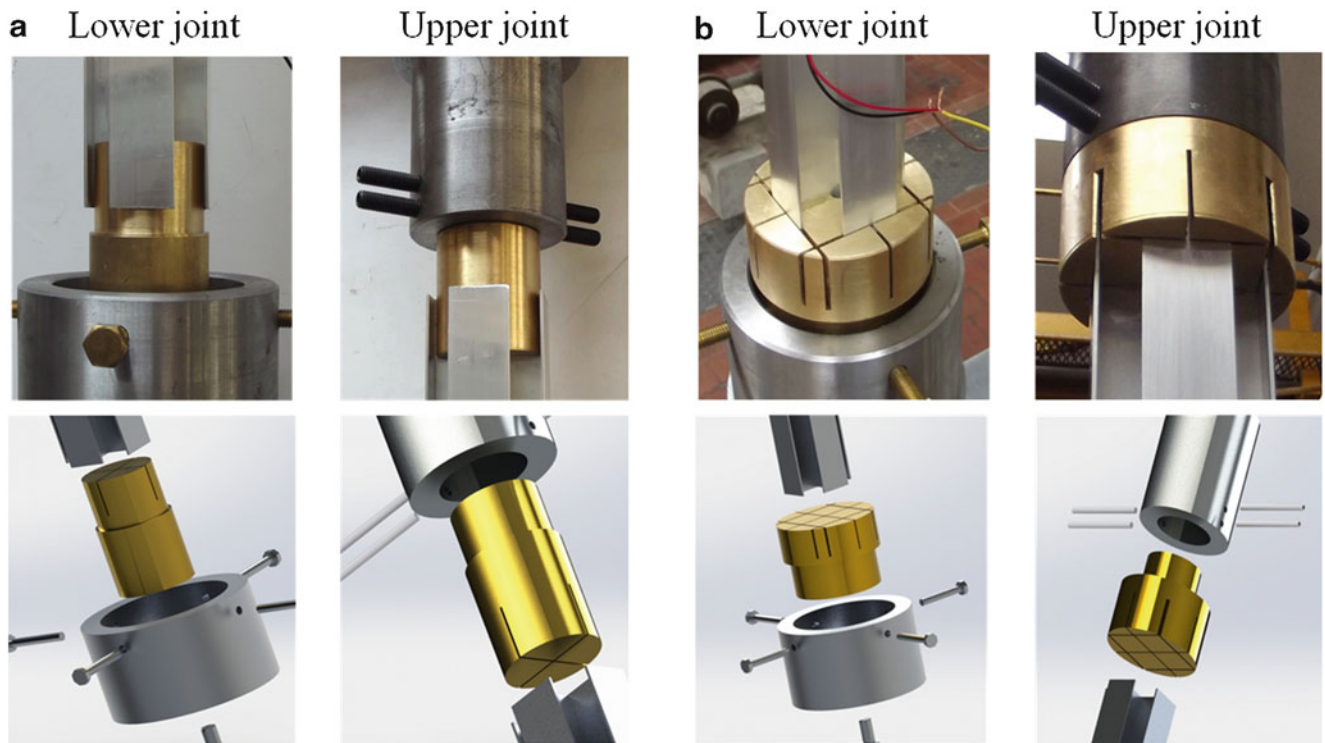
Fig. 10.4 Picture (*top*) and rendering (*bottom*) of end constraints: (**a**) lower (*left*) and upper (*right*) joint for the case of free warping, (**b**) the same in the case of (partially) restrained warping

Table 10.2 Main characteristics of the PZT sensor

External diameter (mm)	Frequency range (kHz)	Resonant frequency (kHz)	Operating temperature (°C)	Weight (g)
20	$\sim$ 0–20	6.0 ± 0.5	-20 to $+50$	$\sim$ 1
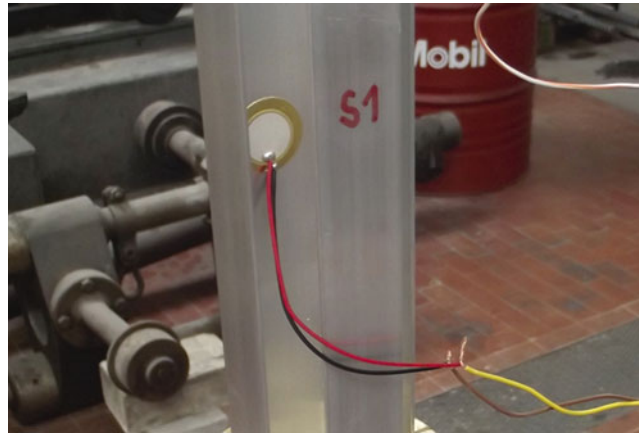
Fig. 10.5 PZT pickup attached to the beam web for the detection of the natural frequencies

As for the measuring devices, piezoelectric disk buzzers (PZT sensors or pickups) were adopted. These sensors possess characteristics such that dynamic identification tests can be conducted with high accuracy, without perturbing the mass of the specimen. The adopted PZT sensor is a transducer that produces an electric voltage signal when subjected to dynamic deformation (direct piezoelectric effect), thus it does not need any supply. The generated signal can be amplified if necessary, acquired by audio acquisition devices as well as classical data acquisition devices, and therefore recorded and post-processed. This sensor can be connected to the surface of the specimen simply by using glue or a thin film of gel, and their usage do not require specific calibration. A preliminary assessment of the capabilities of PZT disks for the experimental modal analysis, conducted by some of the authors, can be found in [14]. The results contained in that communication are being updated and widened, and a new paper is now under preparation. The main features of the adopted laser and PZT sensors are reported in Table 10.2. As can be easily seen, the operating frequency range of the PZT sensor is very large, and its weight is extremely low; this makes such kind of sensor particularly suitable for our experimental campaign.

During the dynamic tests, four PZT sensors were mounted on each specimen (their locations are marked in Fig. 10.3a). Even though one only sensor is, in line of principle, sufficient to detect the natural frequencies, we choose a number of sensors greater than the strict minimum, to increase the measure redundancy. The PZT pickups were attached to the surface of the beam web by a thin film of gel, as shown in Fig. 10.5.

10.3 Outline of Experimental Tests and Numerical Simulations

10.3.1 Experimental Tests

Apart from some specimens used in the preliminary stages, a total of eight beams were tested in the experimental campaign (four integer and four damaged elements). Two kinds of tests were performed using the MTS:

(a) static monotonic compression tests, conducted to determine the axial load-axial displacements curves in order detect the buckling load; and
(b) free vibration tests, in order to identify the natural frequencies for different compression levels, up to buckling and little beyond.

The investigated test configurations were the following:

(1) integer beam, free warping condition;
(2) integer beam, (partially) restrained warping condition;
(3) damaged beam, free warping condition;
(4) damaged beam, (partially) restrained warping condition;
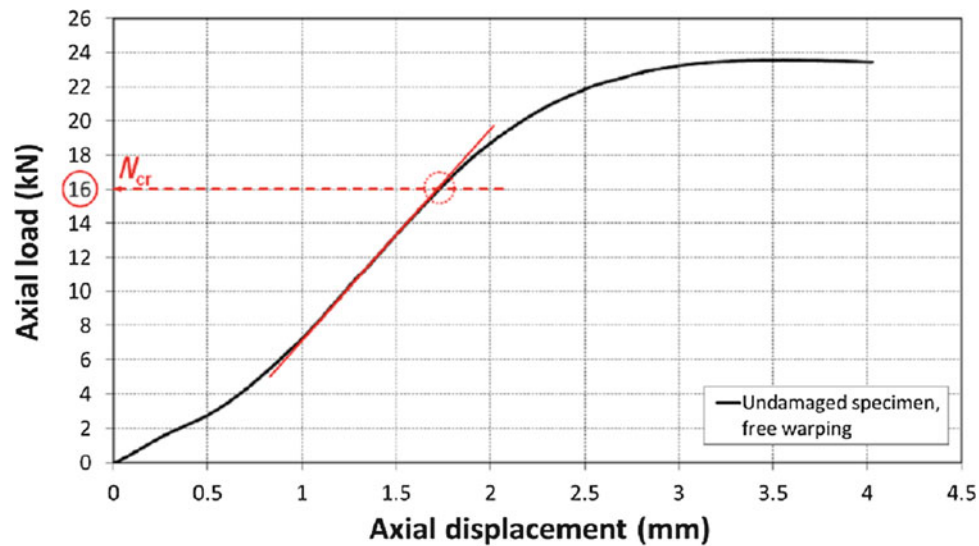
Fig. 10.6 Axial load (output) versus axial displacement (input) curve for the integer beam in the free warping condition, with explanation of the criterion adopted to identify the critical load

Both test types (a) and (b) were conducted, changing the specimen, for each one of the previous test configuration, for a total of eight tests conducted on as many elements. Therefore, for each test configuration, once the buckling load of a specimen was found by a compression test, the free vibration test was conducted on an analogous, virgin specimen, to detect the natural frequencies for different values of the compressive axial force.

The compression tests were conducted operating the loading, in automatic control mode, by imposing a displacement ramp to the hydraulic jack, with a velocity of 4×10^{-6} m s^{-1}. In this way it was possible to measure the axial load carried by the specimen as a function of the imposed axial end displacement. The tests were stopped automatically, by means of specific controls activated for the post-critical branch, or, alternatively, simply by acting manually on the main software. The result of a displacement-controlled monotonic compression test appears as in Fig. 10.6. This is related to the undamaged beam, tested in the free warping condition. The curve shows, after an initial settling, a linear branch, followed by a non-linear one, reflecting the progressive degradation of the apparent beam stiffness. The axial load corresponding to the end of the linear range, i.e., the point corresponding to the first evident stiffness reduction, identifies (according to our criterion) the critical load.

The dynamic tests were conducted by measuring, for different steps of the axial load imposed by the MTS, the free vibration response through the PZT sensors. In this case, the loading levels were obtained by acting on the main software in manual control mode. The specimen was instrumented with four pickups, connected to the PreSonus 1818VSL audio acquisition device. The software Studio One 2 by PreSonus was used to process and record the signals. The signal acquisition was done at a sampling frequency of 44.1 kHz, with a resolution of 24 bits. Data post-processing operations were done using *in-house* programs developed in MatLab. The procedure adopted to extract the natural frequencies is the following. For each loading step, the beam was excited five times by impulsive forces, transmitted to five different points (usually in proximity of the sensors), and the corresponding signals were recorded. A total of 20 signals (five for each of the four sensors) were therefore obtained for each loading step. We eventually identified the resonant frequencies by performing the Fast Fourier Transform of acquired signals, and adopting the Peak-Picking technique. Only the output signals were recorded during this procedure.

10.3.2 Finite Element Models

Finite element models of both integer and damaged beams were implemented in the commercial code Axis VM 12. The following models were built:

(1) integer beam, free warping condition (web restrained, flanges free);
(2) integer beam, free warping condition (centroid restrained, rest of web and flanges free);
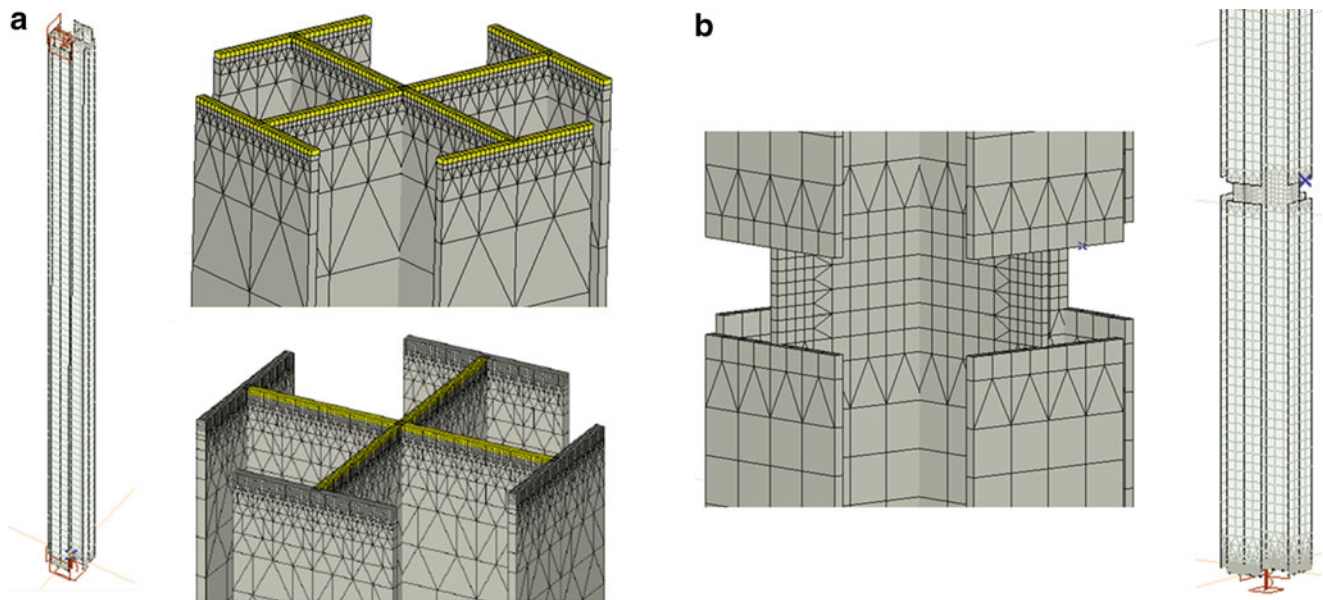
Fig. 10.7 Finite element models: (**a**) integer beam with detail of the mesh near an end in the restrained (*top*) and free (*bottom*) warping condition, (**b**) damaged beam with detail of the mesh around the cross-section variation

(3) integer beam, fully restrained warping;
(4) damaged beam, free warping condition (web restrained, flanges free);
(5) damaged beam, fully restrained warping.

The beams were modeled using shell elements resulting from the coupling of the eight-node Serendipity element and the eight-node Heterosis element (Fig. 10.7). Figure 10.7a shows the model of the integer beam, while that of the damaged beam is shown in Fig. 10.7b. In the latter case, the four flanges underwent a cut 1 cm long, at a section located at one fourth of the beam length from one of the ends. The general end constraints were imposed to the centroidal nodes; in particular, all displacements and rotations were prevented at one end, whereas at the other end the displacement in the longitudinal direction was allowed, preventing all the remaining degrees of freedom at the same time. In addition, further constraints were inserted, when necessary, to prevent the warping of the end sections. The warping constraints were inserted as follows. For the case of fully restrained warping, a thin, almost infinitely rigid layer (1 mm thick, Young's modulus $E = 10^{15}$ N mm^{-2}) was inserted over the whole section at both ends (Fig. 10.7a, top right). For the case of free warping, two different models were adopted. In one case, in order to be closer to the actual experimental conditions (web in contact, flanges free), the infinitely rigid layers were inserted only over the internal cruciform web, leaving the flanges free to warp (Fig. 10.7a, bottom right). In the second case, to be closer to the constraint condition inserted in the one-dimensional model adopted in our numerical finite difference code, the warping of the entire end sections was left free. All constraints inserted in the numerical models are to be intended as bilateral. Lastly, as for the number of elements used in the discretization, 3,680 and 14,720 elements were used to model the integer beam in the restrained and free warping conditions, respectively, while 15,168 elements were used in the case of the damaged beam for both restrained and free warping conditions.

Linear buckling and linear dynamic analyses were therefore run on each model to obtain, respectively, the buckling load and the natural frequencies of the unloaded beam.

10.3.3 In-house *Finite Difference Code*

The beam model used in [4–10] is direct and one-dimensional, and is based on the standard theory of beams with shearing deformation (a.k.a. Timoshenko beam model), enriched with a coarse descriptor of warping and the possibility to describe kinematics with respect to the two parallel axes of the centroids and of the shear centers. In this way, it is possible to describe kinematics exactly, and to obtain linearized measures of strain pulled back to the reference configuration, which is fundamental in the investigations of elastic buckling. The addition of a coarse scalar descriptor of warping has the same

Table 10.3 Sectional properties of the specimens

A (mm²)	$A_2 = A_3$ (mm²)	$A_{23} = A_{32}$ (mm²)	J (mm⁴)	I_c (mm⁴)	$I_2 = I_3$ (mm⁴)	$x_{c2} = x_{c3}$ (mm)	$I_{f2} = I_{f3}$ (mm⁵)	Γ (mm⁶)
251.84	110.38	0	148.36	111,028	55,514	0	0	4,305,656

meaning as the introduction of a new state parameter, that is, the warping descriptor is not, in principle, a displacement at a point, but rather a measure of how the cross-section has come out of its original plane. This makes it possible to introduce standard constraints of literature [1–3] between the warping descriptor and the torsion curvature, and to find the usual balance equations of force and couple, plus the auxiliary equation for the bi-shear and the bi-moment, in a straightforward way from a standard procedure based on the balance of power (or, otherwise, virtual work), plus localization and regularity arguments.

In order to take into account a general behavior, non-linear hyper-elastic constitutive relations complete kinematics and balance, and reflect known results of the literature on thin-walled models. This makes it possible to investigate perturbations of non-trivial equilibrium paths, and examine their stability by means of standard Ljapounov criteria; for the details on the model and on the derivation of the governing equations, we refer to [4–10].

Since closed-form solutions are not possible in these cases, we search them numerically by an *in-house* code based on a proposal of literature [15]. Intrinsic balance, compatibility and constitutive equations are written in terms of finite differences and their numerical solution is searched for, taking into account the boundary conditions. Then, stability is analyzed as a complex eigenvalue problem, in which the imaginary parts of the eigenvalues represent the free vibration frequencies of the considered beam around the equilibrium configuration. The stability of the system relies on the real part of the eigenvalues: when all eigenvalues have negative real part, equilibrium is stable; when an eigenvalue is real and positive, or has a real positive part, buckling or flutter occurs.

For the implementation of the procedure, besides the values of length L, Young's modulus E, Poisson's ratio ν (whence the tangential elastic modulus $G = E/[2(1 + \nu)] = 26.54 \times 10^9$ Nm^{-2}) and density ρ, sectional properties are needed. From the dimensions in Table 10.1, and letting $\{O, x_1, x_2, x_3\}$ a central principal Cartesian system, Table 10.3 lists the values of the section properties, where: A, A_j are the area and the shear shape modified areas; A_{ij} are the mixed shear shape modified areas; J is the Saint-Venant torsion inertia factor; I_c is the polar moment of inertia with respect to the shear centre; I_j are the central principal moments of inertia; x_{cj} are the coordinates of the shear centre in the chosen Cartesian system; I_{fj} are the flexural-torsion constants, and Γ is the cross-section warping constant ($i,j = 2,3$). Since the cross-section is doubly symmetric, the mixed shear shape modified areas, the coordinates of the shear centre and the flexural-torsion constants vanish, i.e., $A_{ij} = x_{cj} = I_{fj} = 0$.

10.4 Results and Comparisons

Figure 10.8 shows the result of the buckling test performed on the integer beam in the free warping condition, compared to corresponding numerical one obtained using finite elements. Figure 10.8a shows that the beam buckled in a torsional mode, i.e., the cross-sections rotate around the beam-axis, which remains straight; the maximum rotation is attained at mid-length. During the test, the beam was pushed, in the post-critical range, until large rotations took place; consequently, plastic deformations were induced. Figure 10.8b shows the detail of the warping deformation of the end sections corresponding to large post-critical rotations. The experimental critical load is about 16–18 kN, while the values given by the finite element analysis are equal to 16.5 kN for completely free warping, and to 17.7 kN when only the flanges were free to warp.

Figure 10.9 shows the result of the buckling test conducted on the integer beam in the restrained warping condition. Figure 10.8a shows a global deformation similar to that of the previous case. However, the difference lies in the deformation of the end sections, as shown in Fig. 10.9b, where it can be seen that there is no warping. The bottom left picture of Fig. 10.9b shows the (plastic) local buckling of the flanges due to the restriction of warping, after large post-buckling rotations. The top left picture of the same figure (which applies to both free and restrained warping conditions) shows a top view of the plastic post-buckling twisted configuration. In this case, the experimental and numerical critical loads are equal to about 22–24 and 38.4 kN, respectively. However, while warping was totally restrained in the finite element model, the experimental constraint condition was closer to that of a semi-restrained warping, as pointed-out before. Respect to the free warping condition, the critical load is increased by about 13 % in the experimental case, and by about 22 % in the numerical case.

The experimental and simulated buckled configurations of the damaged beams, tested in the free and in the restrained warping conditions, are shown in Fig. 10.10. Also in these cases, the beams buckled in a torsional mode; small bending deformations appeared in the post-critical branch only after large plastic rotations, due to some asymmetries that arose
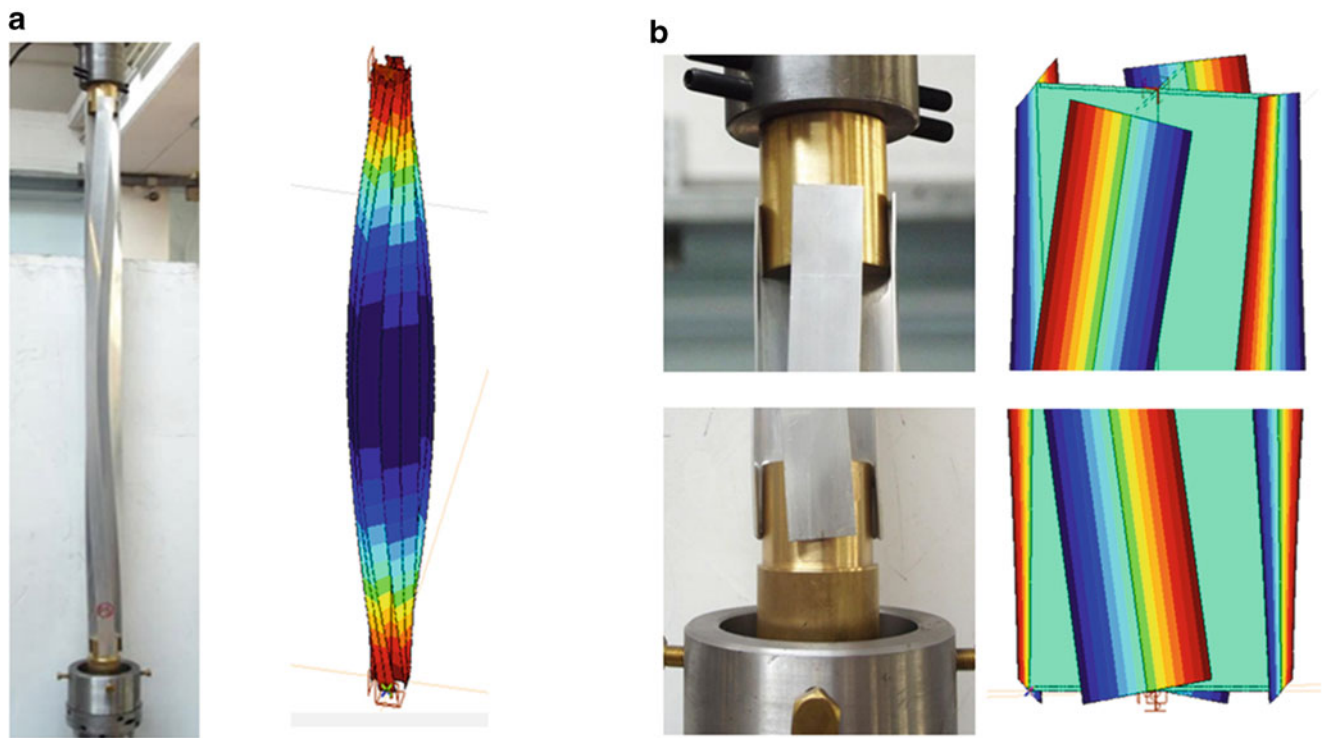
Fig. 10.8 Instability of the integer beam in the free warping condition: (**a**) torsion buckling mode, (**b**) detail of warping of the end sections
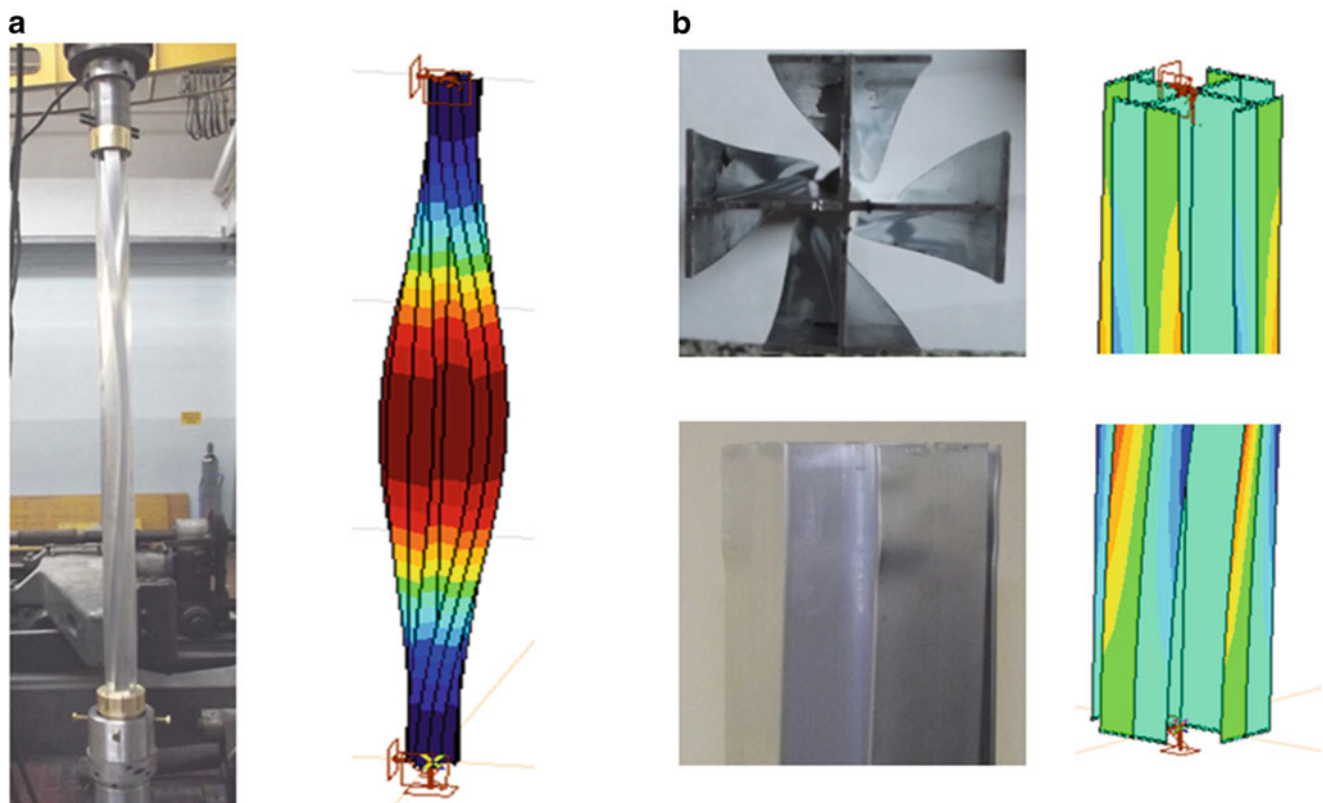
Fig. 10.9 Instability of the integer beam in the partially (experiments) and fully (FE models) restrained warping condition: (**a**) torsion buckling mode, (**b**) detail of the end sections and top view of the plastic post-buckling twisted configuration; notice (*bottom left*) the (plastic) local buckling of the flanges due to the restriction of warping, after large post-buckling rotations
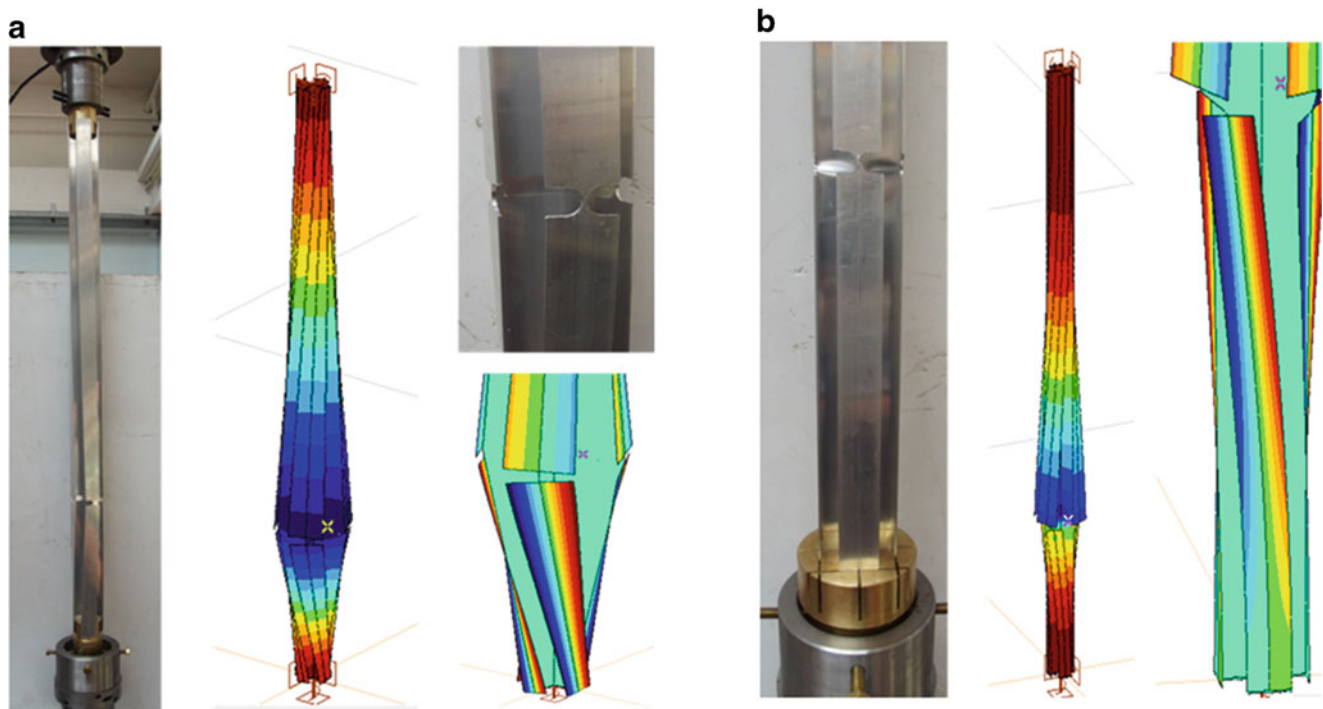
Fig. 10.10 Instability of the damaged beams: (**a**) free warping condition, (**b**) partially (experiments) and fully (FE models) restrained warping condition; notice that maximum rotations localized near the weaker section

near the weaker section. In these cases, differently from those of the integer beam, maximum torsion rotations occurred in correspondence of the weaker section (Fig. 10.10); in general, for the rest the behavior was analogous to that of the integer beam. The values of the experimental and numerical critical loads are respectively equal to 8–10 and 9.8 kN for the free warping condition. These values are about the 50 % (experimental) and the 40 % (numerical) lower than the corresponding values obtained for the integer beam. The experimental buckling load of the damaged beam in the (partially) restrained warping condition is equal to 16.5–18 kN, while the numerical value for the fully restrained warping condition is 29.6 kN. These values are about the 30 % lower than the corresponding values obtained for the integer beam.

Figure 10.11 collects all the experimental frequency-load paths obtained for the integer and damaged beams, in both the tested constraint conditions (the first three natural frequencies are reported). For the integer beam (in both constraint conditions) and for the damaged beam in the free warping condition, the first frequency is of a torsional mode, the second one is of a flexural mode (repeated twice because of the symmetry), and the third one is again of a torsional mode (with a central node). For the damaged beam in the restrained warping configuration, instead, the first vibration mode is a torsional one, the second is a torsional mode with a central node, and the third one is a flexural mode (repeated twice because of the symmetry).

In all cases, the variation of the natural frequencies with increasing loads is not a trivial one. In general, they decrease as the load increases, but this is not always the case, as shown in Fig. 10.11. In particular, especially for the damaged beams, possible mode interaction, as well as crossing of modes, may appear, mostly for loads larger than the critical one. These variations are not easy to predict, especially because of the presence of initial imperfections that generally have a large influence.

Among all natural frequencies, the most important in relation to elastic stability are the fundamental ones, since they govern the critical buckling mode (and load). As can be easily seen in Fig. 10.11, the fundamental frequencies of all the analyzed cases decrease with the axial load, but never go down to zero, either near or after the critical load. This particular behavior is typical of imperfect beams subjected to impressed axial end displacements [11, 12, 16–19]. In the case of the undamaged beam, the fundamental frequencies fall by 50 %, those of the damaged beam fall by 40 % in case of free warping, and by the 25 % when warping is partially restrained.
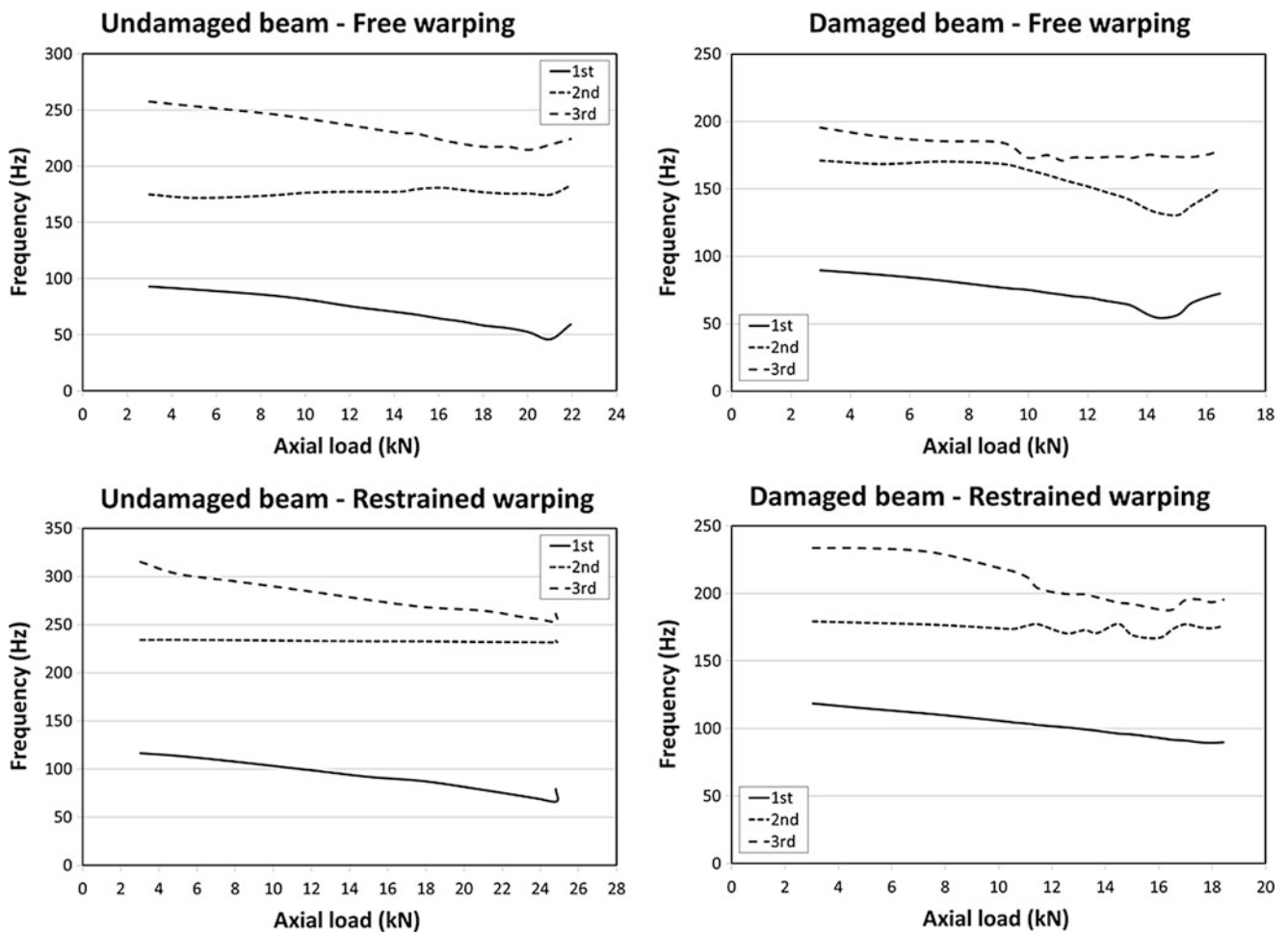
Fig. 10.11 Experimental frequency-load paths for integer and damaged beams in both tested constraint configurations

A comparison among the fundamental frequencies corresponding to each of the analyzed configurations is reported in Fig. 10.12. As it can be easily seen, the introduction of end warping constraints increases both the frequency and the critical load. On the other hand, the localized reduction of the beam warping rigidity considered in the present study strongly reduces the buckling load, leaving the frequency-load path almost unchanged at the same time.

The results obtained for the integer beam through the *in-house* code, using a discretization of 40 elements, are shown in Fig. 10.13. The figure compares fundamental frequency versus axial load curves for three different constraint conditions: free, semi-restrained, and restrained warping. In order to numerically detect the buckling load, the compression force is increased from zero to the critical condition, i.e., the vanishing of the fundamental frequency. The results of Fig. 10.13 clearly highlight the critical compressive axial load for the three cases. Since, in this case, the fundamental frequency is associated to a torsional motion, when it becomes zero the beam has lost its stiffness with respect to that motion, and, if perturbed, twists in a torsional buckling mode, as shown before.

All experimental and numerical values of the buckling load obtained for the integer beams, in all the analyzed configurations, are collected in Table 10.4. This comparison shows that the numerical values obtained through the *in-house* finite difference code are in good agreement both with the experimental results and the results obtained by the finite element commercial code.
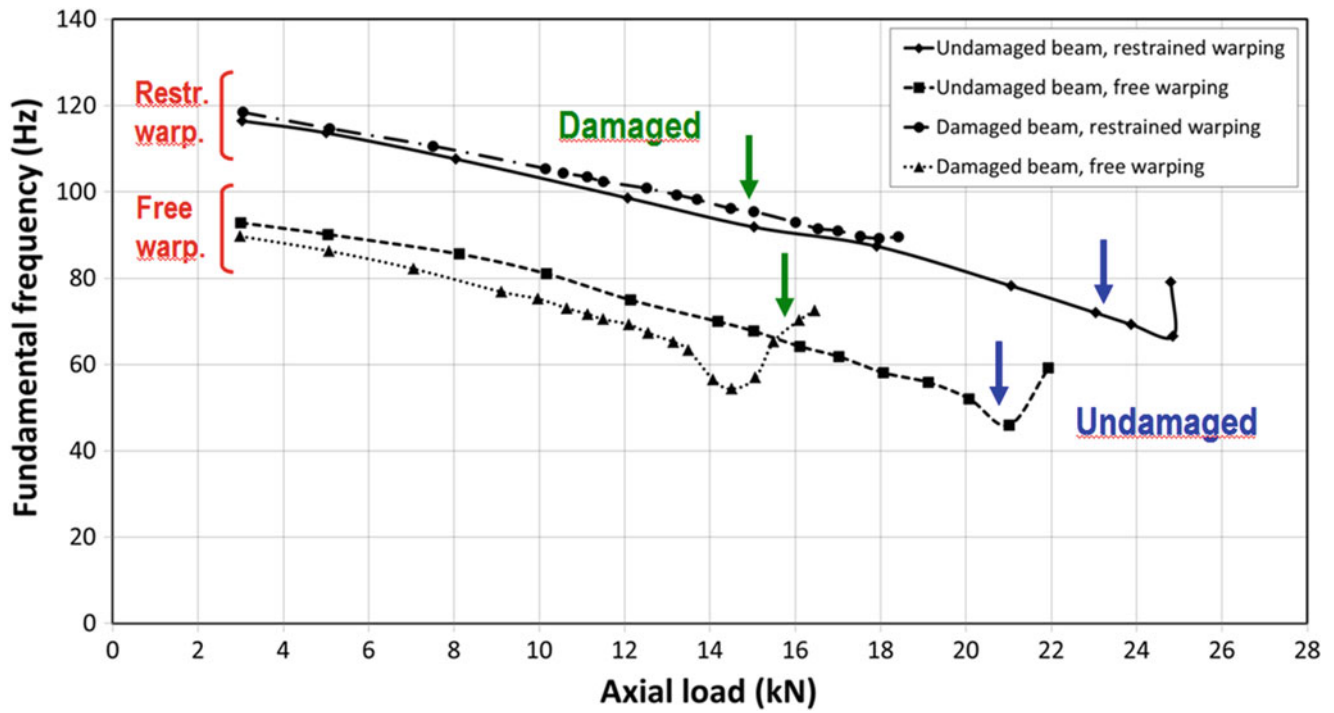
Fig. 10.12 Experimental fundamental frequency versus axial load curves: comparison among all tested configurations
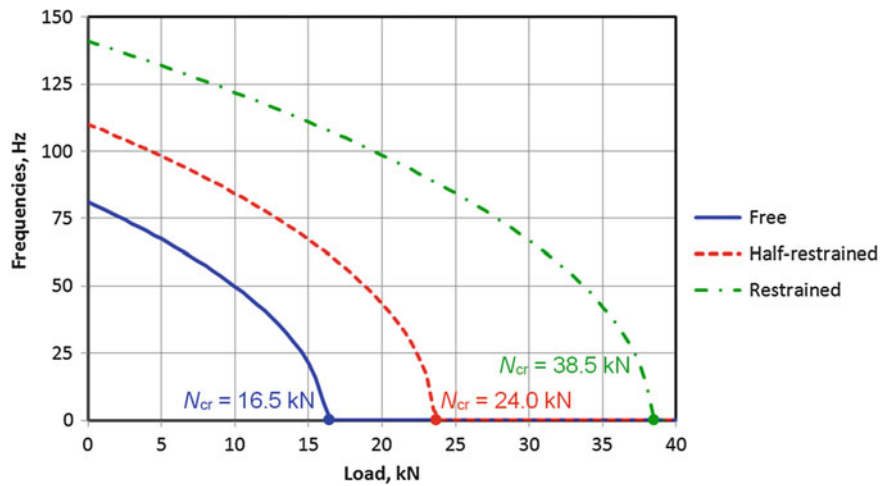
Fig. 10.13 Numerical fundamental frequency versus axial load curves for the integer beam: comparison among free, half-restrained, and restrained warping conditions

Table 10.4 Comparison among experimental and numerical critical loads for the integer beam

Case	N_{cr} Exp. (kN)	N_{cr} FEM (kN)	N_{cr} FDM (kN)
Free warping	16–18	16.5[a], 17.7[b]	16.5
Semi-restrained warping	22–24	–	24.0
Fully restrained warping	–	38.4	38.5

[a]Centroid restrained
[b]Web restrained

10.5   Final Remarks

By means of a universal testing machine (MTS) and piezoelectric pickups, we investigated the frequency-load paths in compressed thin-walled beams with a double I cruciform section. More precisely, we compared the responses of integer beams to those of analogous elements where a localized reduction of the cross-section, which greatly diminished the torsional rigidity, was introduced. Thus, after developing a suitable experimental setup, we were able to test the specimens under two different axial constraint conditions, i.e., free and partially restrained warping of the end sections. The specimens, clamped at both ends in flexure and torsion, were therefore subjected to increasing compressive axial displacements up to the post-buckling condition. Thus, the effects of warping rigidity on both natural frequencies and buckling loads were investigated.

The tested profiles were such that elastic instability occurred by torsion buckling, as well as the fundamental vibration mode was a torsional one. Moreover, for such profiles, the great contribution to the torsional stiffness was due to the warping rigidity, the primary (Saint-Venant's) torsional rigidity being quite small. The experimental results reveal a large influence of warping and warping constraints on natural frequencies and buckling loads for the analyzed thin walled profiles. In particular, the restriction of warping deformation of the end sections increases both natural frequencies and buckling loads. On the other hand, the localized reduction of the warping rigidity of the section consistently reduces the buckling load, leaving the variation of the fundamental frequency almost unchanged. This indicates that the influence of the section warping rigidity is larger on the buckling load than on the natural frequency.

For the case of the integer elements, the experimental results were compared, in terms of critical loads, with those obtained from numerical simulations. In particular, we implemented finite element models in a commercial code, and we performed numerical computations using an *in-house* code based on a finite difference procedure. The latter adopts a Timoshenko-like beam model enriched with a new scalar parameter describing the average warping of the cross-sections. All the numerical results are in agreement to each other, as well as to the experimental findings. This represents a validation of our *in-house* code for the prediction of the buckling load. The main advantages with respect to finite element shell models are: (a) the high accuracy compared to the small computational cost (relatively small number of subdivisions versus the large number of nodes/elements typical of finite element shell models); (b) the easy and fast introduction of input data required to create/modify a full model; (c) the possibility to investigate, in an easy and rapid way, even non-conventional boundary conditions, like that of a semi-restrained warping, which is not of immediate implementation in a finite element model; and (d), most importantly, the possibility to take into account, by default, the influence of non-trivial pre-critical equilibrium paths in elastic stability analysis.

A final comment must be reserved to the obtained frequency-load curves. The experimental results clearly show that static instability (buckling) may occur at a fundamental frequency other than zero. Actually, the zero-frequency condition in correspondence of the critical load is attained only in perfect systems, where a bifurcation of the equilibrium path occurs. Conversely, in real systems, where several initial imperfections are present, the pre-critical equilibrium path shows a progressive reduction of the stiffness with respect to a deformation mode, eventually followed by a stiffness recovery in the case of systems that exhibit a stable post-critical branch. This variation of structural stiffness with the axial load is reflected in the frequency-load paths, where the fundamental frequency decreases down to a minimum (near the critical load) as the compression load is increased; after, it may start increasing again with the load in case when the post-critical is stable. This behavior has been observed and investigated for slender beams with compact cross-sections by several researchers, included some of the authors of the present paper [11, 12, 16–19].

This last fundamental aspect must be well taken into account, for example, when monitoring the stability of in-service structural elements and components by measuring their fundamental frequency. In this case, refer to the zero-frequency condition as an indicator of instability may induce a dangerous overestimate of the stability limit. In any case, it must be observed that the presence of an initial geometrical imperfection, although it affects the equilibrium path, have no influence on the critical load furnished by second-order analyses [1, 2]. This implies that the zero-frequency condition can still be used to predict the critical load by means of analytical or numerical computations, like in the case of our *in-house* code. On the other hand, a different problem is that of the correct prediction of the variation of the natural frequencies (not only the fundamental one) of axially loaded beams in presence of initial imperfections or other particular conditions: the solution of this last problem is other that trivial, as shown by the experimental results of our study.

References

1. Pignataro, M., Rizzi, N., Luongo, A.: Stability, Bifurcation, and Postcritical Behaviour of Elastic Structures. Elsevier, Amsterdam (1991)
2. Timoshenko, S., Gere, J.M.: Theory of Elastic Stability. McGraw-Hill, New York (1961)
3. Vlasov, V.Z.: Thin-Walled Elastic Beams. Monson, Jerusalem (1961)
4. Ruta, G., Pignataro, M., Rizzi, N.: A direct one-dimensional beam model for the flexural-torsional buckling of thin-walled beams. J. Mech. Mater. Struct. **1**, 1479–1496 (2006)
5. Ruta, G., Pignataro, M., Rizzi, N.: A beam model for the flexural-torsional buckling of thin-walled members. Thin-Walled Struct. **46**, 816–822 (2008)
6. Pignataro, M., Rizzi, N., Ruta, G., Varano, V.: The effects of warping constraints on the buckling of thin-walled structures. J. Mech. Mater. Struct. **4**, 1711–1727 (2010)
7. Lofrano, E., Paolone, A., Ruta, G.: Stability of non-trivial equilibrium paths of beams on partial visco-elastic foundation. Acta Mech. **223**, 2183–2195 (2012)
8. Lofrano, E., Paolone, A., Ruta, G.: A numerical approach for the stability analysis of open thin-walled beams. Mech. Res. Commun. **48**, 76–86 (2013)
9. Brunetti, M., Lofrano, E., Paolone, A., Ruta, G.: Warping and Ljapounov stability of non-trivial equilibria of non-symmetric open thin-walled beams. Thin-Walled Struct. **86**, 76–86 (2015)
10. Brunetti, M., Paolone, A., Ruta, G.: On inner shearing constraints for a direct beam model coarsely describing warping. Meccanica **48**, 2439–2451 (2013)
11. Carpinteri, A., Malvano, R., Manuello, A., Piana, G.: Fundamental frequency evolution in slender beams subjected to imposed axial displacements. J. Sound Vib. **333**, 2390–2403 (2014)
12. Piana G., Manuello A., Malvano R., Carpinteri A., Fundamental frequencies of slender beams subject to imposed axial end displacements, N. Sottos, R. Rowland, K. Dannemann (eds.), *Experimental and Applied Mechanics, Volume 6: Proceedings of the 2014 Annual Conference on Experimental and Applied Mechanics*, Conference Proceedings of the Society for Experimental Mechanics Series, 2014.
13. Lofrano, E., Carpinteri, A., Malvano, R., Manuello, A., Piana, G., Ruta, G.: PZT experimental detection of natural frequencies for compressed thin-walled beams. In: SEM 2015 Annual Conference and Exposition on Experimental and Applied Mechanics, Costa Mesa, CA, June 8–11, 2015
14. Piana, G., Brunetti, M., Carpinteri, A., Malvano, R., Manuello, A., Paolone, A.: On the use of piezoelectric sensors for experimental modal analysis. In: SEM 2015 Annual Conference and Exposition on Experimental and Applied Mechanics, Costa Mesa, CA, June 8–11, 2015
15. Hodges, D.H.: Geometrically exact, intrinsic theory for dynamics of curved and twisted anisotropic beams. AIAA J. **41**, 1131–1137 (2003)
16. Dickinson, S.M.: The lateral vibration of slightly bent slender beams subject to prescribed axial end displacement. J. Sound Vib. **68**(4), 507–514 (1980)
17. Kim, C.S., Dickinson, S.M.: The flexural vibration of slightly curved slender beams subject to axial end displacement. J. Sound Vib. **104**(1), 170–175 (1986)
18. Yamaki, N., Mori, A.: Non-linear vibrations of a clamped beam with initial deflection and initial axial displacement, Part I: theory. J. Sound Vib. **71**(3), 333–346 (1980)
19. Ilanko, S.: The vibration behaviour of initially imperfect simply supported beams subject to axial loading. J. Sound Vib. **142**(2), 355–359 (1990)

Chapter 11
Experimental Validation of Nonlinear Model Tracking with Varying Conditions

Timothy A. Doughty, Andrew W. Belle-Isle, and Nicholas Pendowski

Abstract Mechanical systems can be described with models involving mass, damping, stiffness and nonlinear parameters, albeit with varying complexity. With known healthy model values, investigation of beam failure by crack initiation and propagation can be approached through monitoring model values while the system is excited. This approach uses harmonic excitation and focusses on the nonlinear model value. This experimental testing is performed near the system's second natural frequency in a thin cantilever beam. Holding continuous sinusoidal forcing, significant shifts in the beam's nonlinear parameter serve as an early warning of the system's failure. This study is a continuation of iterative research [Song et al.: Mech. Syst. Sig. Process. **49**(1–2), 13–23 (2014)] to verify the integrity and robustness of this particular type of health monitoring in cantilevered beams. This study explores how varying beam geometry, material, excitation frequency, and introducing an additional mass to the system will affect the expected change in the nonlinear parameter as well as how standard beams excited by discretely changing frequencies will give rise to these changes. Results indicate these variables alter the nature of the model, yet still provide significant warning of system failure. In practice, the scope of applicability becomes apparent in both the type of systems and excitations to prevent catastrophic failure.

Keywords Nonlinear • Health monitoring • Vibrations • Cantilever • Premonition

11.1 Introduction

Many mechanical systems are engineered so that the operating range is far from its natural frequencies to avoid failures within the system. In some cases, engineered systems are subject to unpredictable excitations and cannot avoid these conditions. When harmonic excitation is continuously applied to these systems catastrophic failure can occur. This failure is most commonly manifested through fatigue and crack propagation. The ability to detect changes that parallel imminent failure in a system is paramount to establishing warning signs before failure ensues. While most systems are often constructed with a range of materials and geometries, it is preferable to begin monitoring the health of a simpler system such as a cantilevered beam. In commonly practiced techniques, many rely on a determination of the onset and location of cracks through the changes in a system's natural frequency as well as the system mode shapes. Other techniques measure the growth of pre-existing cracks by using an estimation of a system's energy absorption. Research in the field of Nondestructive Evaluation (NDE) has received a considerable amount of attention in recent decades; see Doebling et al. [1] for a comprehensive review.

The notion that all physical systems have the potential to exhibit nonlinear behavior is foundational to this study. Many NDE procedures use linear approximations despite the sometimes prominent nonlinearities [2–6] and the well-established notion of nonlinearity in crack dynamics within vibrating structures [7]. Using health monitoring, detecting shifts in the approximations of nonlinear parameter can serve as indication of failure. These shifts correspond to crack initiation and propagation. As methods for crack detection in vibrating systems develop, the area of NDE continues to advance [8–11]. Recent novel methods include using marked beams monitored by slow motion cameras analyzed with computer vision algorithms to extract the modal shapes for wavelet transform damage detection [12]. Additionally, recent exploration of crack presence and location detection through pitch-catch method, involving transmission and reception of ultrasonic vibrations via embedded piezoelectric transducers has proven a successful tool in health monitoring for various structures [13].

Here the Nonlinear Model Tracking (NMT), which has been proven successful [14–16], is subjected to a variety of conditions to challenge its robustness. The robustness of this method of Nondestructive Evaluation is intended to be accurate in lieu of varying linear parameters of the physical system. Moreover, varying these linear parameters such as stiffness is

T.A. Doughty (✉) • A.W. Belle-Isle • N. Pendowski
University of Portland, 5000 N Willamette Blvd, Portland, OR 97203, USA
e-mail: doughty@up.edu

tedious and time consuming as this method often involves stress-strain analysis and tension testing. For mechanical systems, the reduction in stiffness results in a decrease of the system's natural frequency. This has been explored through a simple mathematical relation [7, 17] and presents a solid case for the implementation of NDE-type analyses. For NDE analysis, previous studies have implemented system identification on a regular cantilever beam continuously excited at its second natural frequency. In this study system identification parameters will remain integral, however each linear parameter will be fixed at the onset of Continuous Time Based testing. A nonlinear term, alpha, will express any changes in the system and therefore will represent the aggregate of linear and nonlinear parameter shifts. With variations in mass, material, geometry, and excitation frequency, robustness of the NDE analysis is assessed. With varying geometries beams may experience a torsional mode of excitation, which is not accounted for in the nonlinear model for the system. This theoretical model accounts only for one degree of freedom. Further system identification requires a collection of acceleration data of harmonic excitation of the beam through a continuous time identification method to demonstrate the model's variation. Prior to experimentation, acceleration data is collected from the healthy beam at near resonant frequencies to use as relative data as the natural frequency changes in order to exhibit this variation in the nonlinear model. A significant drift in the nonlinear parameter has been shown to indicate eminent failure well before the end of the system's life [18].

The work of this research is a progressive and ongoing effort. In previous iterations, the method has achieved success even in the absence of accurate system parameters or without a sufficient understanding of the model form. A sensitivity study was carried out to address the benefits of using complete nonlinear models with accurate linear parameters. This study presented the notion that as long as system parameters remain constant for the model, premonition of failure can still be seen in changes of the nonlinear parameter.

11.2 Theoretical Model

For this investigation, a cantilevered beam is excited in the vertical direction by a 45 N shaker (Model: Model 50) at the beam resonance frequency as determined by an increasing and decreasing frequency sweep. This configuration is presented in Fig. 11.1.

In this assumed model as well as the mathematical interpretation of said model, v represents the vertical displacement of the beam. Furthermore, m is mass per unit length, c is damping, D_ξ is the bending stiffness, A is the amplitude of the base displacement, Ω is the frequency of excitation, t is time, s is a reference variable, and L is the beam length. This assumed model has proven successful in studies involving more complicated systems, such as pipes [19]. The mathematical model for the transverse displacement of a cantilevered beam with nonlinear bending stiffness as seen in [20] is provided below:

$$m\ddot{v} + c\dot{v} + D_\xi \left\{ v^{iv} + \left[v'\left(v'v''\right)'\right]' \right\} = -mA\Omega^2 \cos\left(\Omega t\right), \tag{11.1}$$

$$v\left(0, t\right) = v'\left(0, t\right) = v''\left(L, t\right) = v'''\left(L, t\right) = 0. \tag{11.2}$$
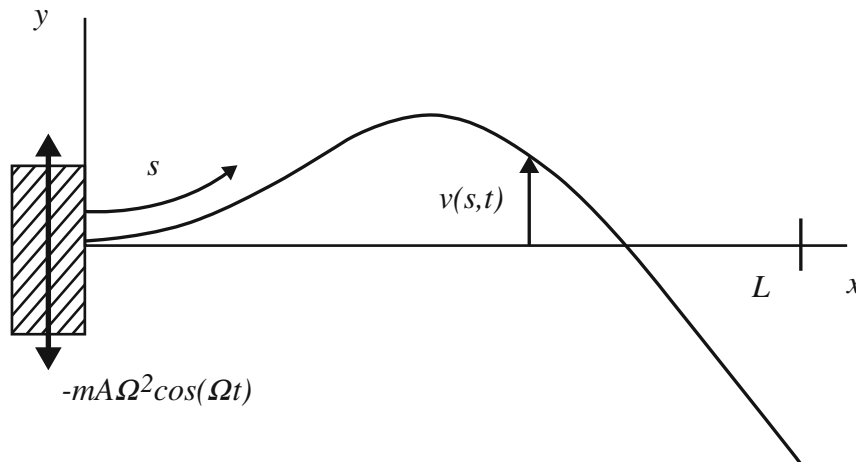

Fig. 11.1 Theoretical configuration for cantilevered beam demonstrating the second mode shape

In the case of modal excitation, spatial dependence is assumed to be known. By setting $\Phi(s)$ as the orthonormalized mode shape which satisfies the states boundary conditions, we find:

$$\Phi(s) = C\left[\sin(\beta s) - \sinh(\beta s) - \Psi(\cos(\beta s) - \cosh(\beta s))\right] \tag{11.3}$$

Where:

$$\Psi = \frac{\sin(L\beta) + \sinh(L\beta)}{\cos(L\beta) + \cosh(L\beta)} \tag{11.4}$$

And:

$$\beta L = 4.694. \tag{11.5}$$

Letting $v(s, t) = a(t) \cdot \phi(s)$, the nonlinear partial differential equation can be reduced to the form:

$$m\ddot{a} + c\dot{a} + ka + \alpha a^3 = F(t), \tag{11.6}$$

In which:

$$k = \left\{ D_\xi \int_0^L \phi\phi^{iv}\,ds \right\}, \tag{11.7}$$

$$\alpha = \left\{ D_\xi \int_0^L \phi\phi''^3 + 4\phi\phi'\phi''\phi''' + \phi\phi'^2\phi^{iv}\,ds \right\}, \tag{11.8}$$

And:

$$F(t) = \int_0^L \phi\,ds\left(-mA\Omega^2\right)\cos(\Omega t). \tag{11.9}$$

With a collection of input, $F(t)$, and the response, $a(t)$, data, our system parameters can be estimated for this nonlinear model. Note that when the nonlinear term, α, is set to zero, the differential equation is simplified to a standard linear model for a forced mass-spring-damper system.

11.3 System Identification

With the nonlinear model, system parameters are estimated using stimulus and response data (F(t) and a(t), respectively). Proven methods inspired by previous studies suggested that physical accuracy of linear parameters is not significant to the success of the NMT method. With a least square method, these values were solved using initial time data. Although these parameters are expected to change due to some of the inaccuracies in the system model, they may lack physical meaning. However, for this method they are important and relevant for the computation of the nonlinear term.

Nonlinear behavior is far more complex than linear behavior. Investigating parameters for a nonlinear system is performed in a manner that pronounces most nonlinear behavior. Although Multiple Time Scales and Harmonic Balance, and the Continuous Time Method are all proven successful for identification of nonlinear model parameters [18], Continuous Time method was selected for its ease of applicability to the transient time data.

Accelerometers are used here to acquire forcing and response data, which is integrated to produce velocity and displacement vectors. These vectors are organized in a matrix relating forcing data to response data in terms of acceleration, velocity, displacement, and displacement cubed. These vectors correlate with mass, dampening, stiffness, and the nonlinear parameter. The method most indicative of premonition of failure for the NMT was deemed to include one the nonlinear

parameter, being cubic stiffness [16]. Other methods, which included nonlinearities due to inertia and drag, resulted in an excess of flexibility in the nonlinear parameter's ability to adapt to the changing behavior, and incapable of anticipating failure.

The nonlinear parameter is solved for by rearranging Eq. (11.3) into matrix form:

$$\left[\ddot{a}(t)\ \dot{a}(t)\ a(t)\ \ a(t)^3 \right] [m\ c\ k\ \alpha]^T = F(t), \tag{11.10}$$

And:

$$\left\{ a(t)^3 \right\} [\alpha] = \left\{ F(t) - \ddot{m}a(t) - c\dot{a}(t) - ka(t) \right\}. \tag{11.11}$$

Equation (11.10) can be used to directly estimate the value for the parameter vector. This equation can be rearranged so that α is the only unknown, as seen in Eq. (11.11). Other vectors are related to the steady state time responses from select excitation frequencies. Eq. (11.11) can then be solved for the nonlinear parameter in a least squares sense.

Prior to testing, six steady state data points are collected across a range of select excitation frequencies in order to more accurately define the system parameters. The range of frequencies was chosen near the resonant frequency on both sides. Previous simulations have proven that a range of frequencies can be used to determine accurate nonlinear models [11, 21, 22].

Earlier studies have shown the reuse of preliminary data to be effective [16]. Similar beams behave the same way as they have in the past. Healthy steady state data can be utilized for beams with similar qualities, defined by geometry, material, boundary conditions, and mode of response. However, this study will not be reusing preliminary data; such qualities are being varied to challenge the nonlinear tracking method.

State entries are updated using streaming data in the system identification code with MATLAB. A large change in the nonlinear term, α, will result when the updated data shows an essential change in the system. Ideally, changes in the system's response due variations to input (i.e. frequency and amplitude) will not yield significant changes in the nonlinear parameter [15].

11.4 Experiment and Analysis

For this study, the beam geometry, mass, material, and stimulus frequency were altered (See Fig. 11.2). The underlying experimental configuration was consistent throughout each variant. 6061 Aluminum bar stock was chosen as the material for the cantilevered beam throughout all experiments. These beams were subsequently excited using a 45 N shaker operating around the second natural frequency of the beam. This frequency was determined by two incremental sweeping functions in

Fig. 11.2 Alterations to beam geometry. From *bottom* to *top* we have: regular beam, asymmetric beam, symmetric beam and weighted beam

LabVIEW. The graphical interface of this "virtual instrument" included a frequency response function (FRF) as well as the phase shift of the system to visually indicate the resonance frequency. The highest recorded magnitude in the FRF data file was chosen and the corresponding resonance frequency was selected. The first sweep function was a frequency sweep from low to high, while the latter sweep started at the higher frequency and decreased. This is done because of the pronounced nonlinear effects near and at the natural frequency, which results in hysteresis. This sweep was used in conjunction with a standard, sinusoidal function generator created in LabVIEW. Then six steady state points were used to back out the damping parameter of the system. This was done in increments of 0.75, 1.25, and 2.00 Hz both above and below the natural frequency point. Readings at sampling rate of 1 kHz were taken over a period of 3 s for each particular frequency. Once, steady state points were recorded, the constant function generator was re-adjusted to the desired resonance frequency and the beam was shaken until failure.

This software was utilized in conjunction with National Instruments data acquisition units to record the data from the accelerometer at the base of the shaker as well as at the selected distance of 4.5 cm out from the clamped end of the beam. This was accomplished using two PCB accelerometers. The acceleration data from the predesignated location on the beam was differenced from the acceleration at the base of the shaker to find the relative acceleration of the beam. This acceleration was then scaled according to the accelerometer's calibration and spatial location along the beam. The signals from each accelerometer were sent through two battery-powered PCB signal conditioners to help filter analog noise from the readings. These conditioned signals then were processed by the DAQ unit and populated through the LabVIEW software. The differenced acceleration was then multiplied by the mass of the beam and scaled with the mode shape in accordance with Eq. (11.6). These voltage readings were the outputs of the system. The data from the accelerometers are stored in an .lvm (LabVIEW) file, which is then post-processed by a combination of MATLAB codes. Beam conditions were altered according to the following:

For the beam geometries, both an asymmetric and symmetric form was used. The standard width of all beams was approximately 1.3 cm. For the asymmetric beam the end width was 0.77 cm and only one side was machined. For the symmetric beam the end width was also 0.77 cm with both sides of the beam machined. The cut for each desired geometry started where the beam exited the clamp, which was 7.5 cm out from the start of the beam. Additional beams of the same geometry types were precipitate heat-treated. The particular ASM heat treatment designation was T6 for 6061 extruded bar [23]. Specifically, the beams were heated in an oven for 8 h at 350 °F and were subsequently quenched in room temperature water for 5 s.

The weighted beams had the same two 5 cm stock beam pieces, glued together, with a total mass of 3.9 g centered 17.5 cm out from the fixed end. They were tightly secured with tape.

For beams ran with varying frequencies, refer to Table 11.3 for specific time and frequency intervals. Two frequencies were chosen at ± 1.5 Hz away from the natural frequency for the purpose of remaining within the steady state bounds and second natural frequency. The presence of nonlinearities was still desired. Resonance and these two frequencies were varied systematically up to the first 220 min of the experiment. Here, the frequencies were set to ± 1.0 Hz from the natural frequency, still changed methodically. After 360 min, the beam was excited at resonance for the remainder of its life.

11.5 Results

Experimental results indicate success in nonlinear model tracking using continuous time method. In each case the beam's health was monitored and premonition of failure was observed. By holding the linear model parameters constant the nonlinear parameter absorbed all the changes in the system as the beam experiences plastic deformation, crack initiation, and propagation. Additionally, it was observed in many beams that significant changes in the nonlinear term corresponded to the change in appearance of the beam's response (Figs. 11.3, 11.4, 11.5, 11.6, 11.7, 11.8, 11.9, 11.10, 11.11, and 11.12).

Some beams of varying geometries displayed unexpected results. However, in all of the beams, regardless of their geometry, mass, material or excitation frequency, dramatic shifts in alpha appeared as they progressed toward failure. In the some cases, the first varying frequency regular beam (Fig. 11.13), the second asymmetric beam (Fig. 11.7) and second heat treated regular beam (Fig. 11.9), the shift in alpha, occurring between 25 and 30 % of their total life. Otherwise, the first heat treated regular beam (Fig. 11.8), the second symmetric beam (Fig. 11.3), and second varying frequency beam (Fig. 11.14), changes in alpha occurred at approximately 75 % of their total lifespan (Table 11.1).

Quantitatively, the shift in alpha occurred at 51, 54, and 47 % for beams with machined geometries, heat treatment, and regular geometry, respectively. Among all of the beams tested in this study, average alpha change occurred at 51 % of the total life. Qualitative, results are not as easily understood. Some beams displayed unexpected results, as seen in Figs. 11.8,
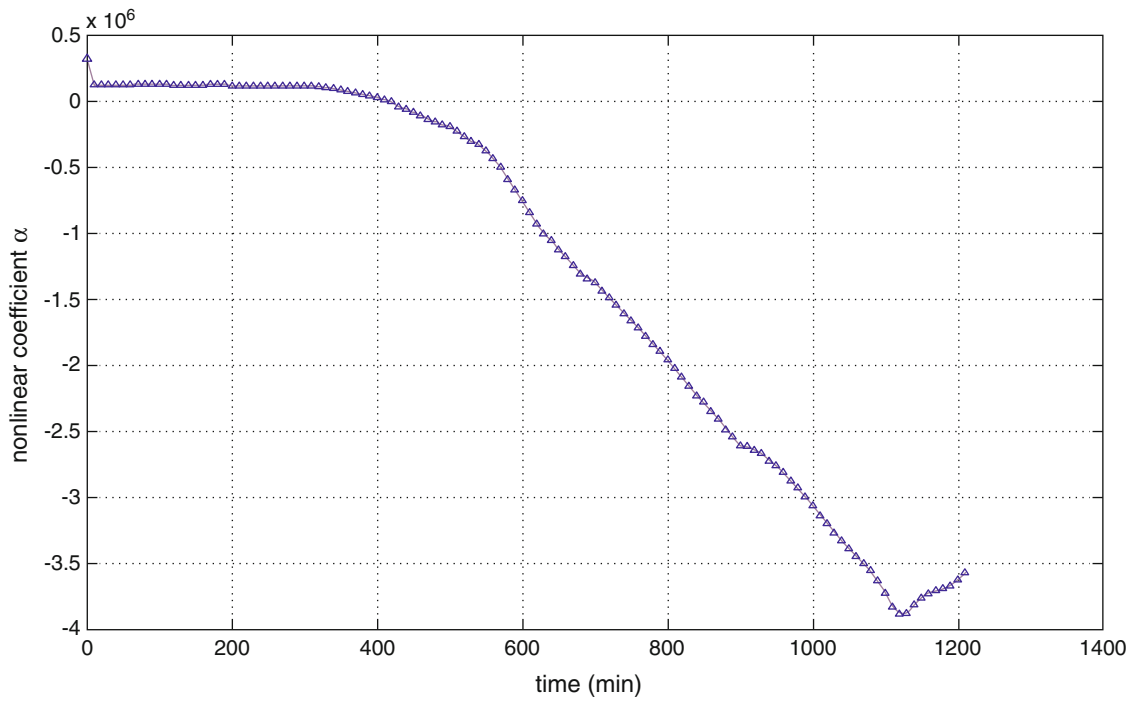
Fig. 11.3 Mapping of nonlinear coefficient over life of Asymmetric Beam 1. Significant change occurred at 625 min
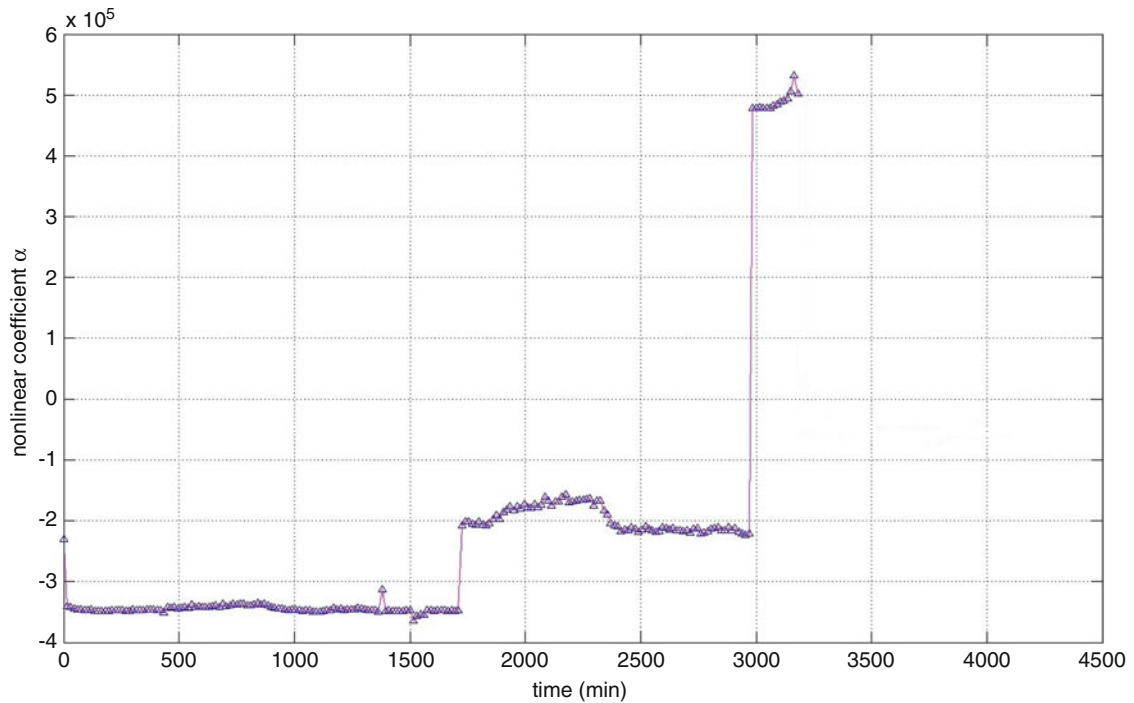
Fig. 11.4 Mapping of nonlinear coefficient over life of Asymmetric Beam 2. Significant change occurred at 2400 min

11.9, 11.11 and 11.15. This is also the case for the beams subjected to varying excitation frequency (Figs. 11.13 and 11.14). All other beams demonstrated relatively constant values of alpha prior to a drastic shift in alpha (Table 11.2).

For the beams with varying frequency, during the first 6 h of experimentation, initial shifts in the nonlinear parameter directly correspond to the time at which excitation frequency was altered (Table 11.3 & Figs. 11.13 and 11.14). Each time the shaker was returned to resonant frequency, alpha returned to its original constant value. Changing excitation above or

Fig. 11.5 Visually enhanced plot of Asymmetric Beam 2. This disregards the shifts due to amplitude change
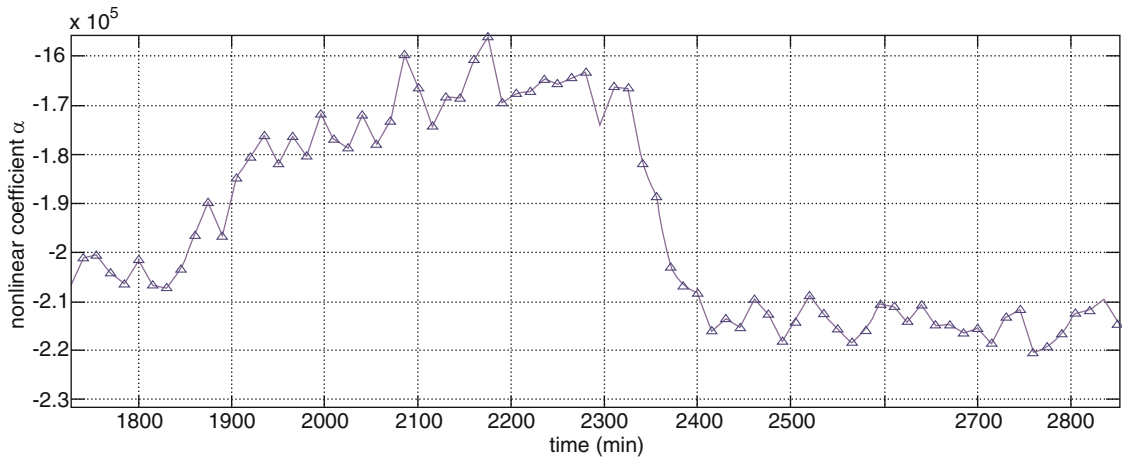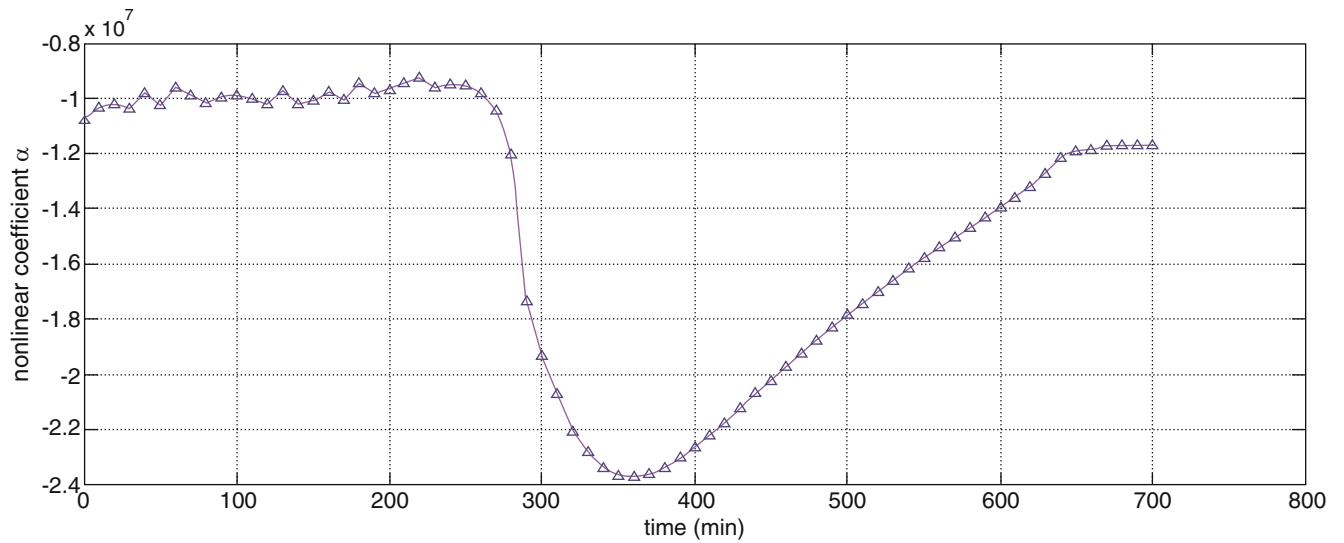

Fig. 11.6 Mapping of nonlinear coefficient over life of Symmetric Beam 1. Significant change occurred at 280 min
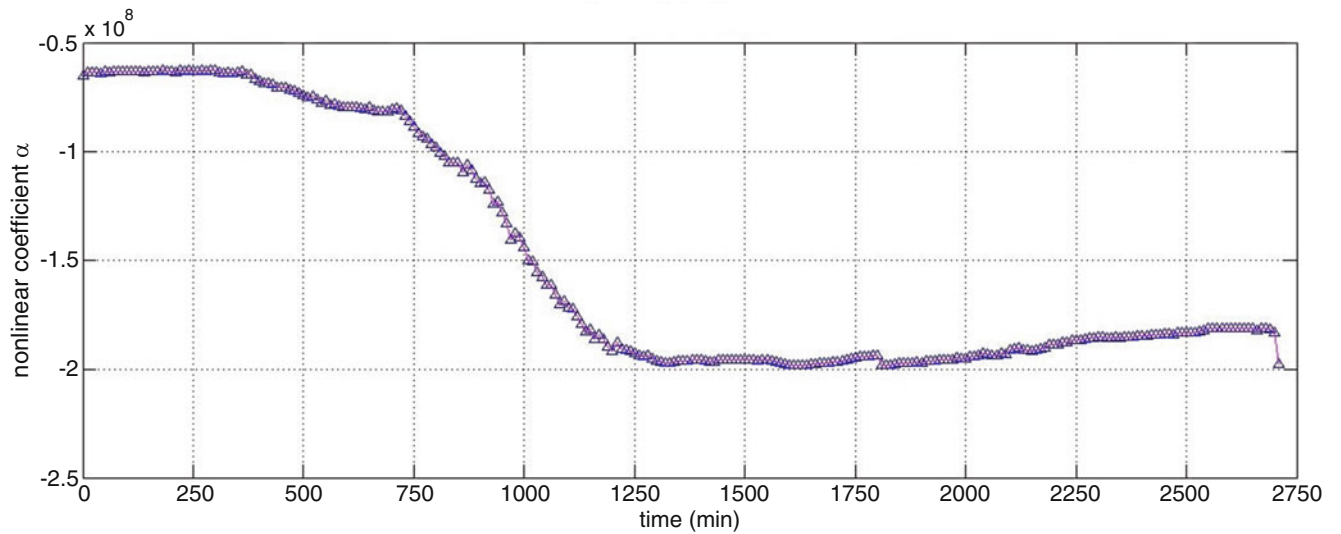
Fig. 11.7 Mapping of nonlinear coefficient over life of Symmetric Beam 2. Significant change occurred at 800 min

Fig. 11.8 Mapping of nonlinear coefficient over life of Heat Treated Regular Beam 1. Significant change occurred at 1600 min

Fig. 11.9 Mapping of nonlinear coefficient over life of Heat Treated Regular Beam 2. Significant change occurred at 360 min

Fig. 11.10 Mapping of nonlinear coefficient over life of Heat Treated Asymmetric Beam 1. Significant change occurred at 850 min
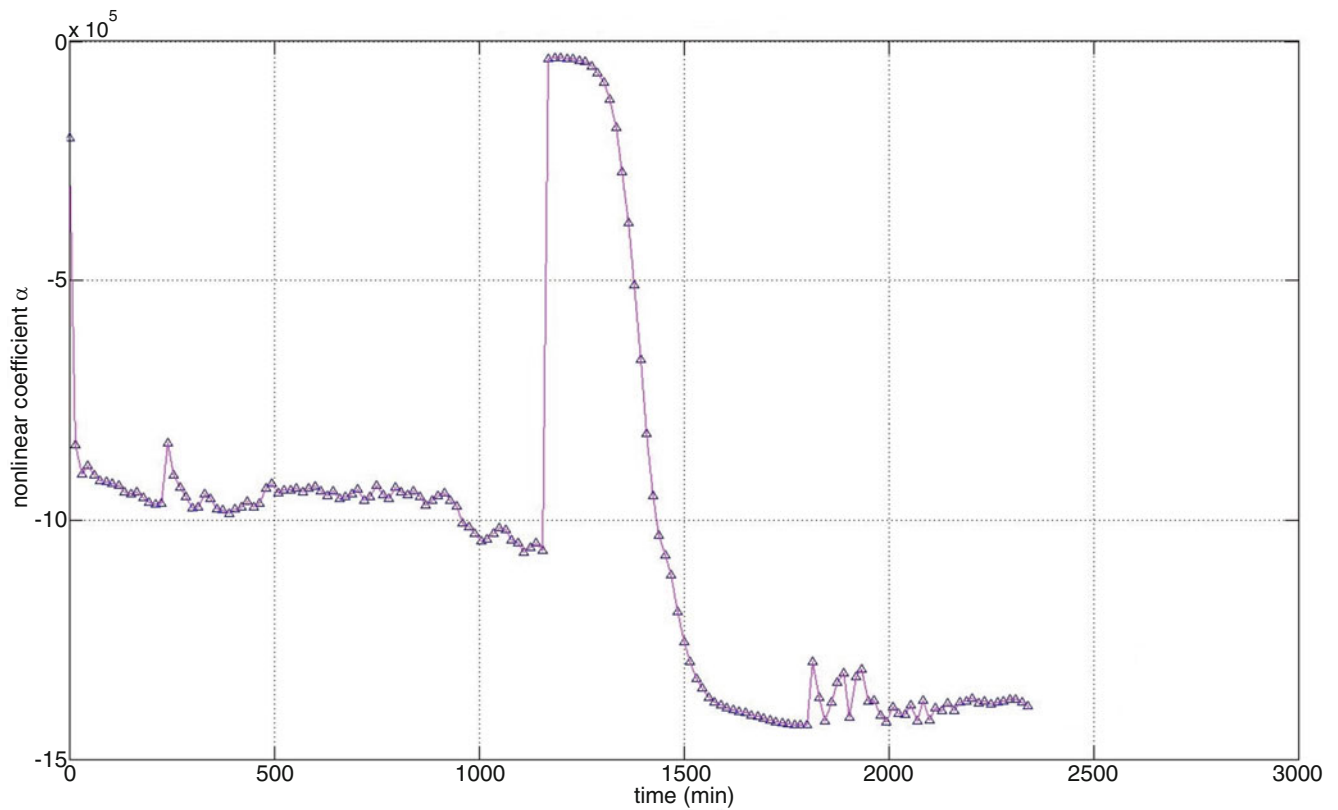
Fig. 11.11 Mapping of nonlinear coefficient over life of Heat Treated Asymmetric Beam 2. Significant change occurred at 1400 min
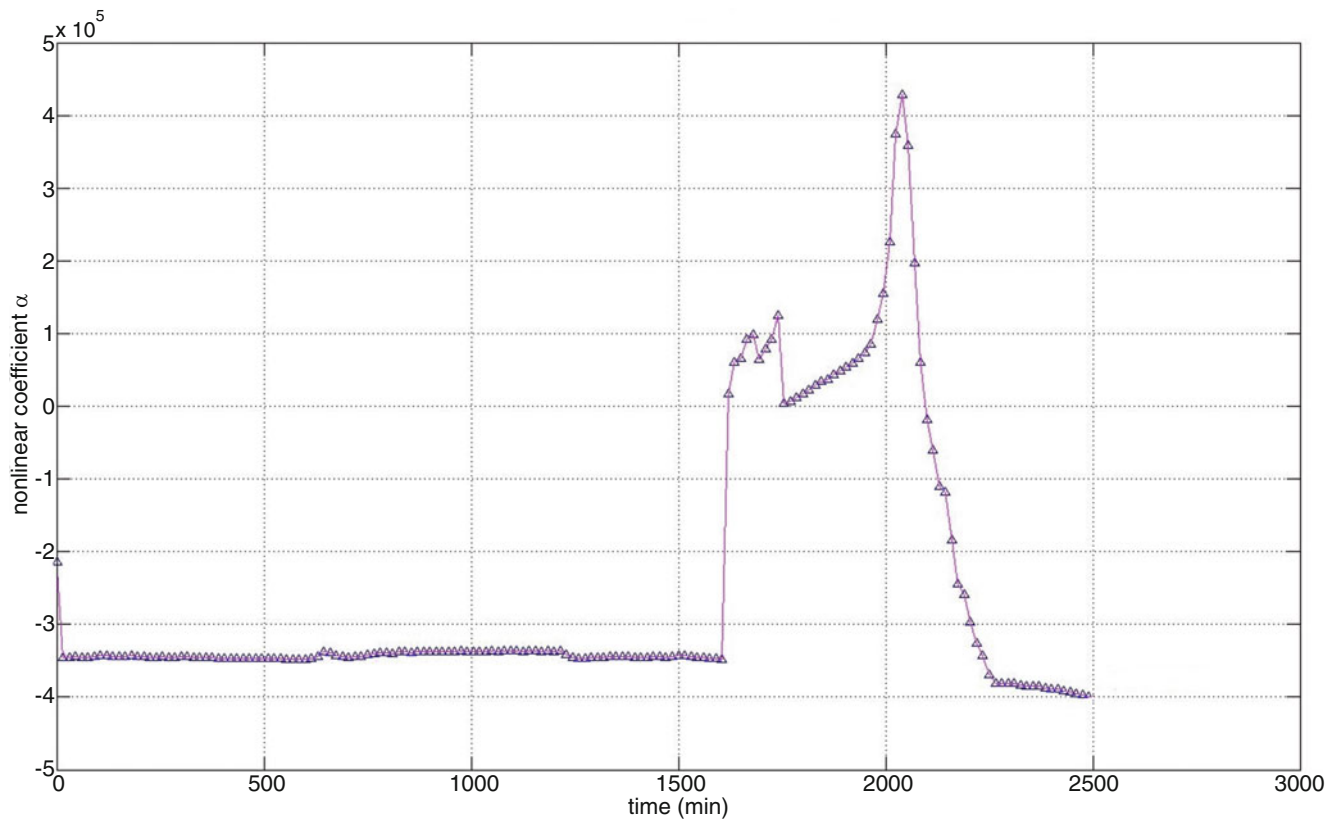
Fig. 11.12 Mapping of nonlinear coefficient over life of Heat Treated Symmetric Beam. Significant change occurred at 1680 min
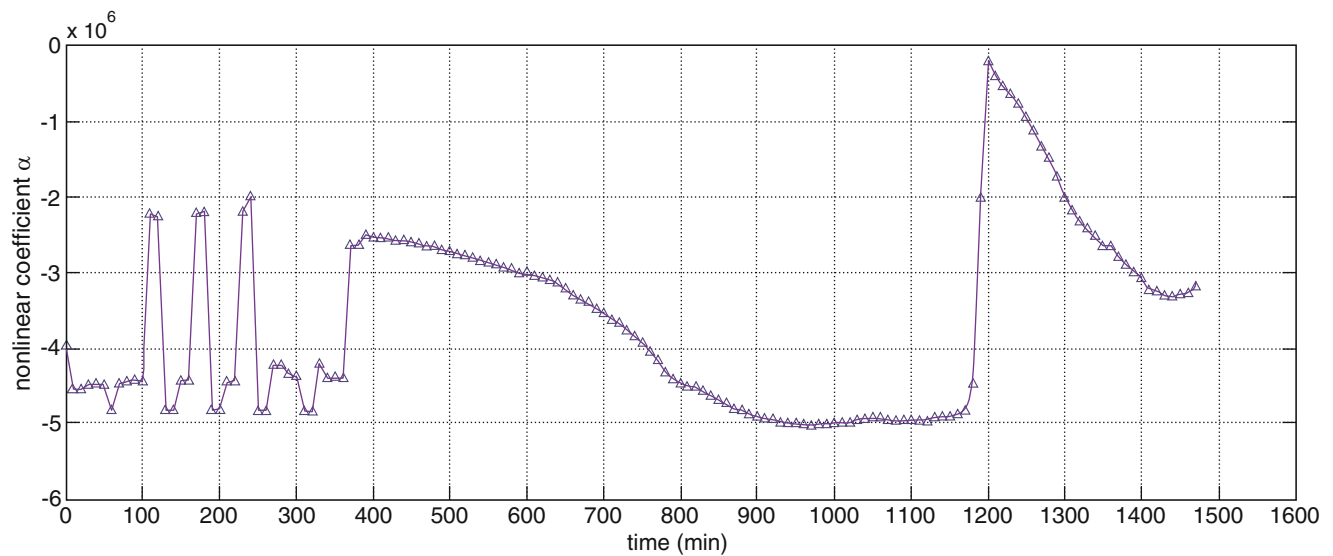
Fig. 11.13 Mapping of nonlinear coefficient over life of Varying Frequency Beam 1. Significant change occurred at 370 min

below resonance frequency did not correspond to the nonlinear coefficient being relatively above or below the value at resonance. Each frequency of excitation produced a relatively constant value for alpha for that respective forcing frequency. Visual responses were noted for each excitation frequency tested.

The figures above correspond to beams of one variable: machined geometries, in which torsional modes were witnessed. These results display the nonlinear coefficient, alpha, changing as the beams' health decays. On average, these beams failed at a longer than average lifespan. In order to hasten failure, forcing amplitude was increased. For the second asymmetric
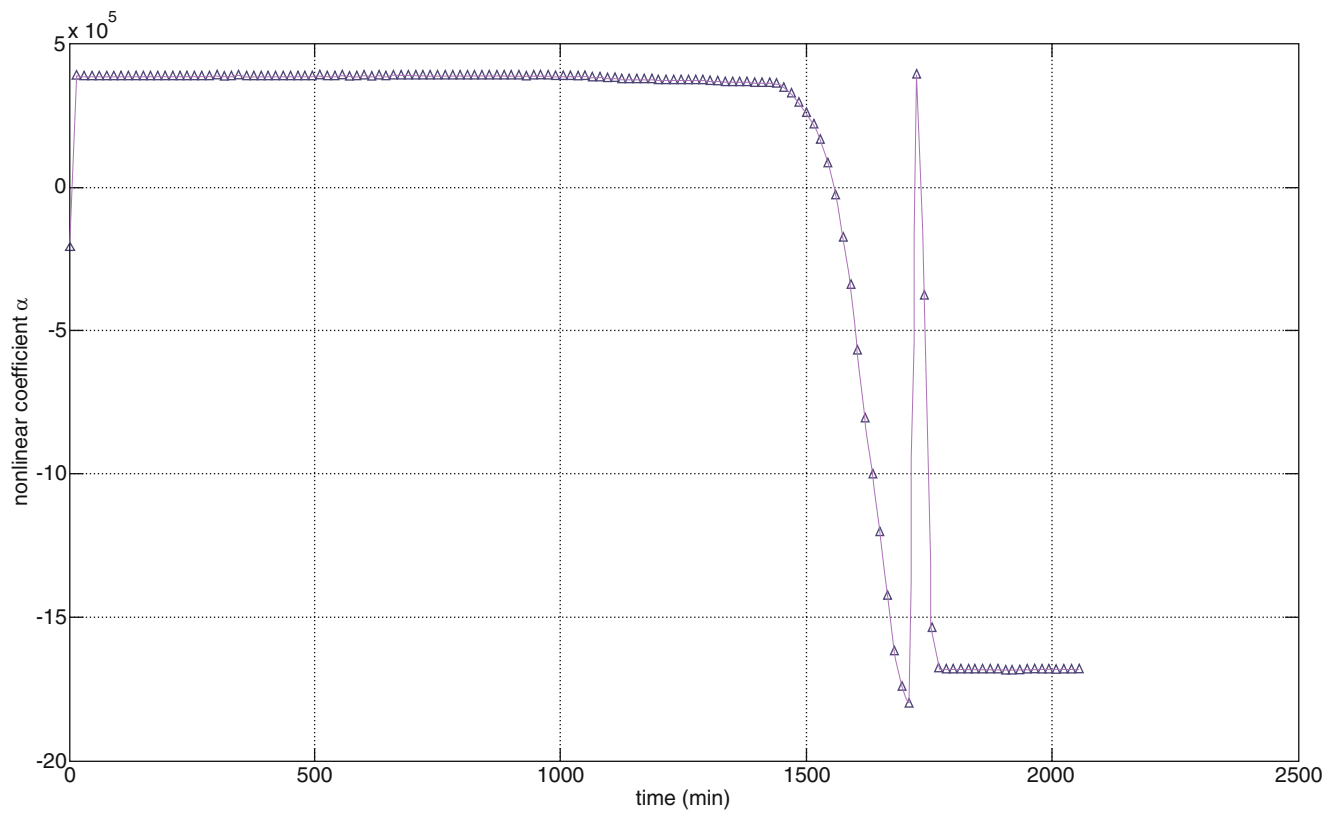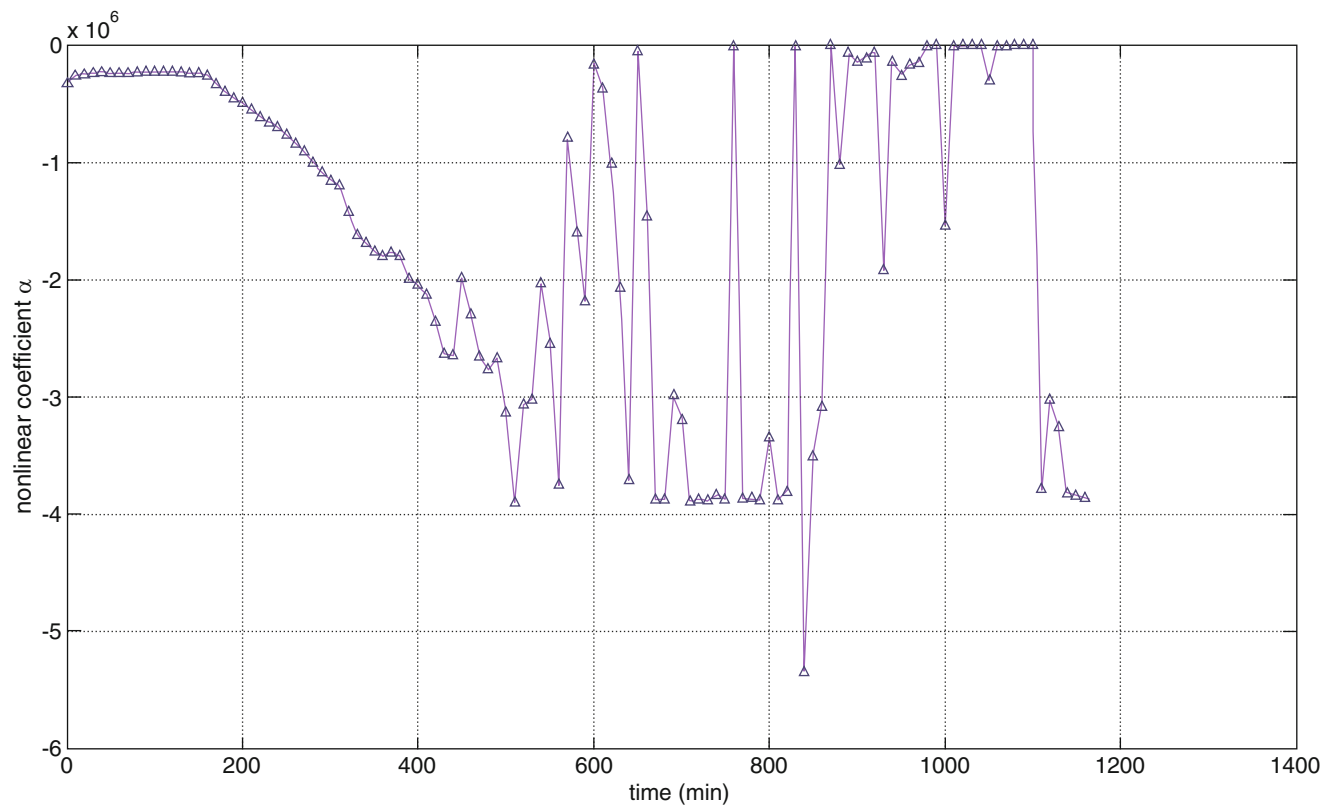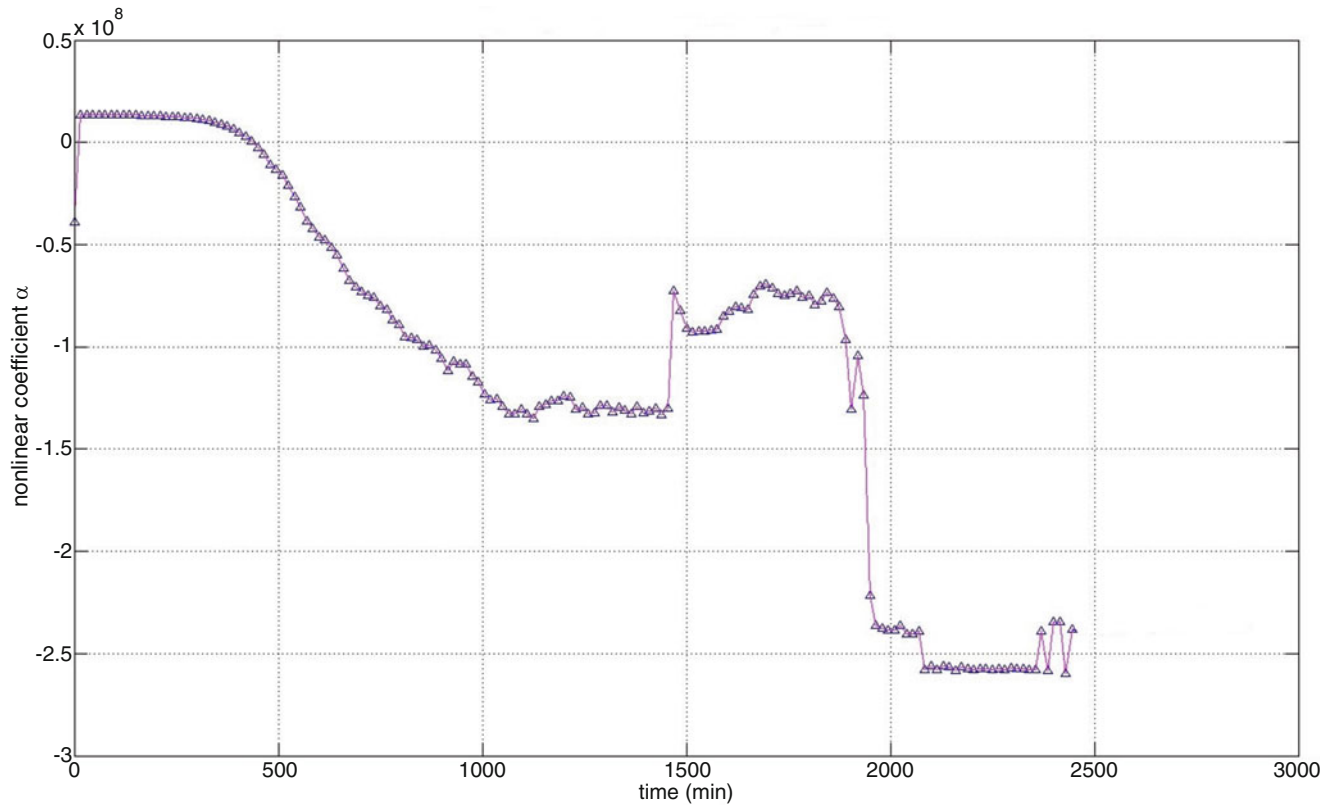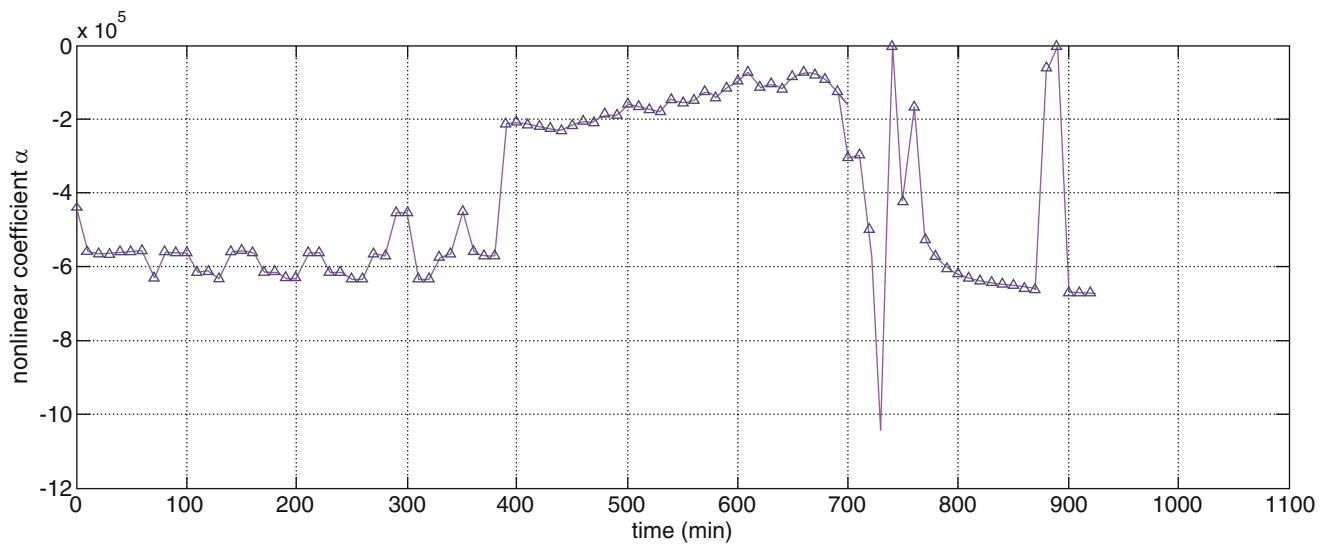
Fig. 11.14 Mapping of nonlinear coefficient over life of Varying Frequency Beam 2. Significant change occurred at 700 min

Table 11.1 Lifespan and failure warning of assortment of beam conditions subjected to NDE. Healthy cantilever beams extended from a 45 N exciter were shaken at their second natural frequency until failure

Type of beam	Failure prediction (% of life)	Total life (min)	Observational torsion
Symmetric (1)	40.0	700	Present
Symmetric (2)	29.6	2700	Present
Asymmetric (1)	52.1	1200	Present
Asymmetric (2)	75.0	3200	Present
Point mass regular (1)	36.5	1300	Minimal
Point mass regular (2)	34.8	575	Minimal
Varying frequency regular (1)	47.5	1475	Minimal
Vary frequency regular (2)	75.7	925	Minimal
Heat treated regular (1)	76.2	2100	Minimal
Heat treated regular (2)	30.4	1150	Minimal
Heat treated symmetric (1)	67.2	2500	Present
Heat treated asymmetric (1)	34.7	2450	Present
Heat treated asymmetric (2)	59.6	2350	Present

Acceleration data was collected and analyzed using continuous time method to produce the nonlinear stiffness parameter as the beam progressed towards failure

beam (Figs. 11.4 and 11.5), amplitude was increased at minutes 1700 and 2950. For the second symmetric beam, amplitude was increased at minute 1770 (Fig. 11.7). These amplitude changes corresponded to shifts in alpha.

Five figures above (Figs. 11.8, 11.9, 11.10, 11.11, and 11.12) correspond to all of the heat treated beams; three of these beams also had machined geometries. These results illustrate the nonlinear parameter, alpha, as the beams' health declines. By observation, the three beams with varied geometry also experience torsional modes. Amplitude was increased for some of these beams in order to hasten failure. For the first heat treated asymmetric beam (Fig. 11.10), amplitude was increased at minute 1460. For the second heat treated asymmetric beam (Fig. 11.11), amplitude was increased at minute 1170. For the only heat treated symmetric beam, amplitude was increased at minutes 1545, 1935, and 2025 (Fig. 11.12). (Note: data from the second heat treated symmetric beam was omitted because of signal noise due to a low battery in the signal conditioner).

The last four figures include the beams of two variables, varying excitation frequency and introducing a point mass (Figs. 11.15 and 11.16). Torsional modes seemed minimal for all these regular beams. The results demonstrate the nonlinear parameter changing as the beams approach failure, except for the cases of initial changes due to varying forcing frequency. Amplitude was increased for both varying frequency beams, in order to decrease time to failure, at minute 380 (Figs. 11.13 and 11.14).
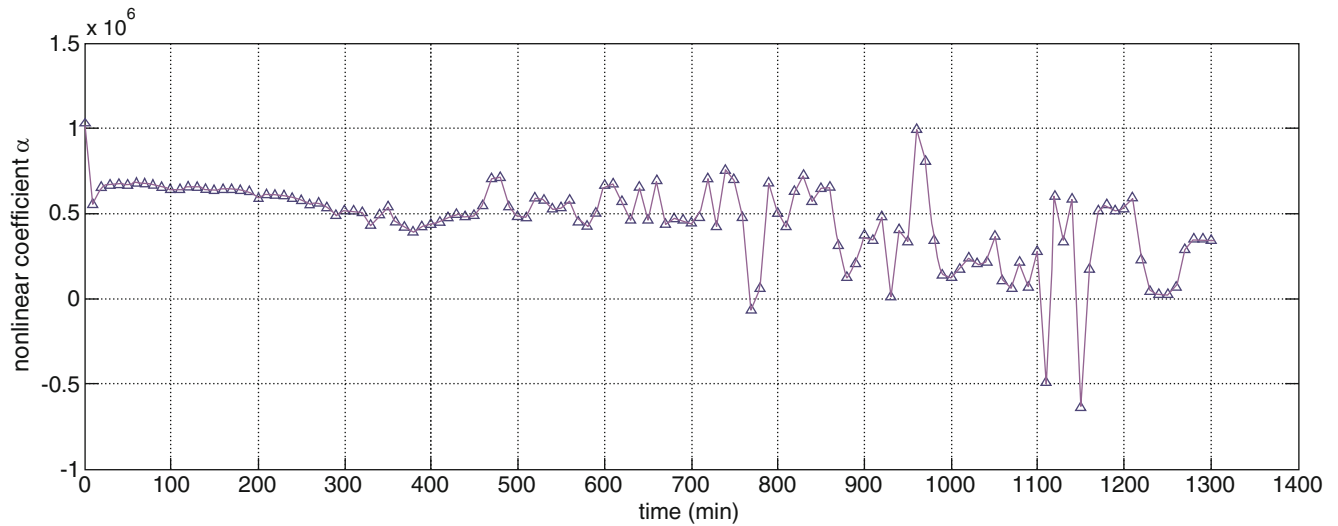
Fig. 11.15 Mapping of nonlinear coefficient over life of Point Mass Beam 1. Significant change occurred at 480 min

Table 11.2 Average lifespan and indication of failure for different beam conditions

Averages		
Type of beam	Failure prediction (% of Life)	Total life (min)
Symmetric	35	1700
Point mass	36	938
Heat treated asymmetric	47	2400
Heat treated symmetric	67	2500
Asymmetric	64	2200
Heat treated regular	53	1625
Varying frequency	50	1200
Varied geometries (ALL)	51	2157
Heat treated (ALL)	54	2110
Regular beams (ALL)	47	1254
All beam conditions	51	1740

11.6   Discussion

In all of the experiments performed on these beams of varied conditions: geometry, mass, material, and excitation frequency, the NMT method successfully monitored the nonlinear stiffness parameter as it altered with the health of the beams. A phenomenon known as early onset drift, or an initial spike in alpha, can be observed in many of these beams tested. This only occurred within the first 10 min of the experiment, which has improved since previous studies [11, 14–16]. This drift does not invalidate the NMT method, as the nonlinear parameter almost always levels to a relatively constant value following this phenomenon. The next significant change in the nonlinear term, alpha, following the reasonably constant value (indicative of a healthy beam), is recognized to correspond to the onset of plasticity and crack initiation, as observed in past experiments with cantilever beams.

Within the current system model, there is only one degree of freedom accounted for, that being the second mode in the direction the acceleration is measured during experimentation. For beams of varying geometries, machining imperfections, deterioration on the exciter clamp edge, and inherent material imperfections significantly amplified torsional modes easily seen by the naked eye. These additional modes are unaccounted for in analysis, and as observed in the results, may have convoluted some of the initial constant nonlinear parameter. Some beams of varied geometries experienced more initial fluctuation of the nonlinear term compared to those of regular beam geometries (point mass, heat treated regular, etc.), despite the oscillation manifested by varying excitation frequency. In which case, it appears that the alpha value for resonance remained constant for the first few hours of experimentation.

Table 11.3 Systematic frequency variation for two beams (see Figs. 11.13 and 11.14). Excitation frequency was altered in order to observe its effects on the NMT method

Varying frequency			
Regular Beam 1		Regular Beam 2	
Time (min)	Frequency (Hz)	Time (min)	Frequency (Hz)
0–60	31.89 (resonance)	0–60	28.3 (resonance)
60–70	30.39 (Low visual response)	60–70	26.8 (Low visual response)
70–100	31.89	70–100	28.3
100–120	33.39 (High visual response)	100–120	29.8 (Med visual response)
120–140	30.89	120–140	26.8
140–160	31.89	140–160	28.3
160–180	33.39	160–180	29.8
180–200	30.39	180–200	26.8
200–220	31.89	200–220	28.3
220–240	33.39	220–240	29.8
240–260	30.89 (Low visual response)	240–260	27.3 (Low visual response)
260–280	31.89	260–280	28.3
280–300	32.89 (High visual response)	280–300	29.3 (Low-med visual response)
300–320	30.89	300–320	27.3
320–340	31.89	320–340	28.3
340–360	32.89	340–360	29.3
360–380	31.89	360–380	28.3
380+	Amplitude increase	380+	Amplitude increase
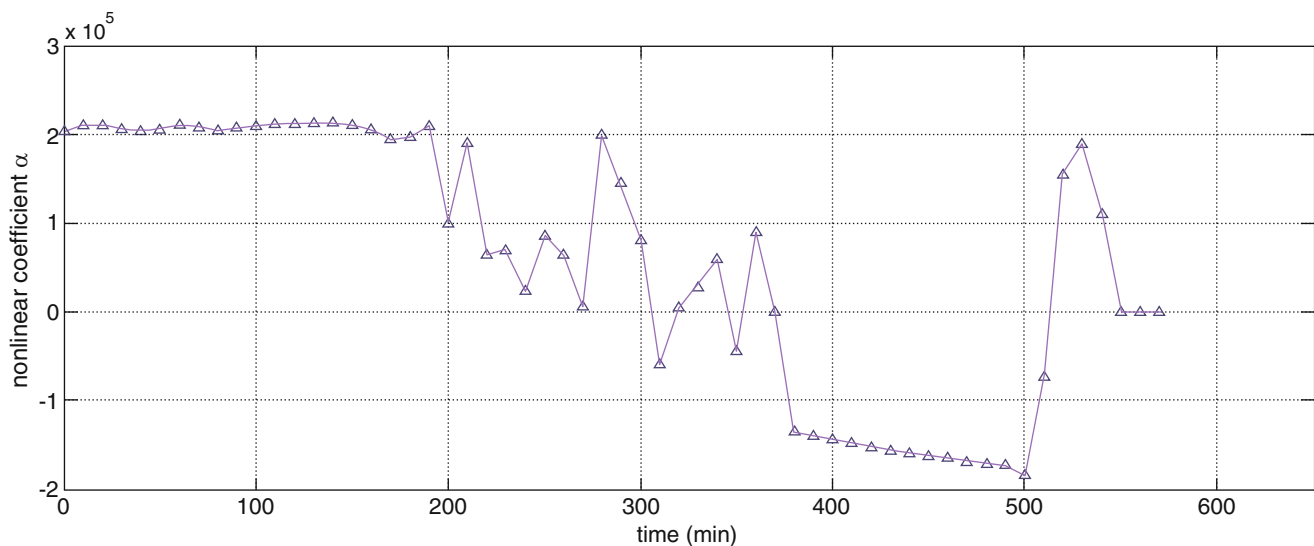
Fig. 11.16 Mapping of nonlinear coefficient over life of Point Mass Beam 2. Significant change occurred at 700 min

For varying excitation frequency, initial shifts in the nonlinear parameter directly corresponded to changing the forcing frequency. When the frequency was returned back to resonance, the alpha value remained constant until it either reached an unhealthy state, or had its amplitude increased. Similarly, these variations in alpha also corresponded to how the beam looked to the naked eye, suggesting a change in visual response correlates to a change in alpha. This is also the case for other beams; when their response was attenuated, alpha was significantly varied. Expectations are confirmed in that the nonlinear behavior changes as the beam experiences different excitations; however in the case of plastic deformation, the nonlinear parameter remains shifted away from the constant initial value or behaves erratically. The initial shifts in the nonlinear coefficient when excitation frequency is changed are not ideal. They may be a product of the type of analysis, in using double integration, which can produce an offset drift. Further research will investigate using data from a strain gage and analysis with double differentiation to solve for the nonlinear coefficient, in addition to choosing different excitation frequency values.

Likewise, when the forcing amplitude was increased, intending to truncate the time until beam failure, the nonlinear parameter usually experienced a shift. This can be seen in results from the second asymmetric beam, both heat treated asymmetric beams and symmetric beam, and the second varying frequency beam. In some cases, when the beam already reached an unhealthy state, an amplitude increase did not correspond to a large shift in the nonlinear parameter, instead it was almost unnoticeable. This was the case for the first varying frequency beam and the second symmetric beam at minutes 390, and 1770, respectively. This is expected due to the behavior of an unhealthy beam compared to its healthy counterpart. After plastic deformation and crack initiation, its overall response remains greatly diminished despite an increase in amplitude. For a healthy beam, increasing excitation amplitude at resonance simultaneously intensifies its response and thus the presence of nonlinearities. Further studies will constantly monitor the visual state of the beam, and increase amplitude before and after visual indications of plasticity.

Nonlinear model tracking predicted impending failure by a shift in the nonlinear parameter on average within 14 h of failure. An unhealthy state was confirmed visually on some beams, as their response was greatly reduced, however many of the beams could not be constantly monitored since they ran for over 24 h. This larger than usual lifespan was anticipated, as for beams with machined geometries, the mass of the beam decreased as a function of the extended length. Thus, relatively less stress presided at the beam's base. The life of the varied frequency was expected to be greater as well, since the first 6 h of excitation were not continuously at resonance, although on average these two beams did not last as long as varied geometry beams. Conversely, the average shorter lifespan of the weighted beams corresponded with expectations as the extended mass is greater, resulting in more stress at the beam's fixed end. Future experiments should avoid removing excessive amounts of material to avoid extensive beam life.

Overall, results were understandable, yet not as smooth as they have been in previous studies, some other factors may have played a role. Such as the varying cross-section and thus stiffness being a function of length, unaccounted for in analysis could be a very probable cause for some deviation from the expected results. However, the accuracy and precision of theses beam's linear parameters was omitted in order to improve the robustness of the model. The theoretical model used assumes the beam responds with only 1 degree of freedom, although in many cases at least 2 degrees of freedom was observed. These inconsistencies were acknowledged and results suggest they did not hinder the success of the particular NMT technique implemented. Among all of the variables, both controlled (geometry, material, mass, and excitation frequency) and uncontrolled (presence of torsion, imperfections in machining, beams defects, and deterioration of shaker clamp edge), the model still produced understandable results that predicted the change in nature of the nonlinearities in the system, such as plastic deformation, crack initiation and crack propagation.

11.7   Conclusion

The NMT method used was able to predict beam failure for all cases, with a varying range of remaining integrity of the beam life. Provided that some of the beam conditions involved additional nonlinearities, such as torsion, cross-sectional area and stiffness varying with length, which were unaccounted for in the model, the results still clearly indicate the nonlinear stiffness parameter changing as the beam's health decays. Thus, the model is considered to be robust among varying conditions.

Conversely, for variations in forcing conditions, such as excitation amplitude and frequency, the nonlinear parameter can shift and in some cases notably. Worth noting, for changes in forcing frequency in a healthy beam, the nonlinear term would change with frequency, yet it still maintained a relatively constant value for each specific frequency. In the case of amplitude variation, a healthy beam will produce a larger shift in the nonlinear parameter than it will in for an unhealthy beam. This is due to the diminished response of the beam that has already undergone plastic deformation, while the untarnished beam only has its nonlinearities pronounced. Further investigation is needed in this area to understand this phenomenon for both amplitude and frequency in healthy and unhealthy, and regular and irregular beams. Analytical differentiation will be used in the future with a strain gage to provide comparison to this approach, which used accelerometers. This may eliminate any offset drifting associated with these shifts. Upon further understanding, this model can be applied to systems of varying frequencies and amplitudes to accurately predict imminent failure.

References

1. Doebling, S.W., Farrar, C.R., Prime, M.B.: A Summary of vibration-based damage identification methods. Shock Vib. Dig. **30**, 91–105 (1998)
2. Khiem, N.T., Lien, T.V.: Multi-crack detection for beam by the natural frequencies. J. Sound Vib. **273**, 175–185 (2004)
3. Loutridis, S., Douka, E., Hadjileontiadis, L.J.: Forced vibration behavior and crack detection of cracked beams using instantaneous frequency. NDT E Int. **38**, 411–419 (2005)
4. Lee, Y.Y., Liew, K.M.: Detection of damage locations in a beam using the wavelet analysis. Int. J. Struct. Stab. Dyn. **1**, 455–465 (2001)
5. Gudmundson, P.: Changes in modal parameters resulting from small cracks. Proc. Int. Model Anal. Conf. Exhib. **2**, 690–697 (1984)
6. Kim, J-T., Ryu, Y.-S., Cho, H.-M., Stubbs, N.: Damage identification in beam-type structures: frequency-based method vs. mode-shape based method. Eng. Struct. **25**, 57–67 (2003)
7. Ding, J.L., Pazhouh, J., Lin, S.B., Burton, T.D.: Damage characterization by vibration test. Scripta Met. Mater. **30**, 839–834 (1994)
8. Sih, G.C., Tzou, D.Y.: Mechanics of Nonlinear Crack Growth: Effects of Specimen Size and Loading Step. Martinus Nijhoff Publications, Boston, MA, pp. 155–169 (1984)
9. Bovsunovsky, A., Bovsunovsky, O.: Crack detection in beams by means of the driving force parameters variation at non-linear resonance vibrations. Key Eng. Mater. **347**, (Damage Assessment of Structures VII), 413–420 (2007)
10. Andreaus, U., Casini, P., Vestroni, F.: Nonlinear features in the dynamic response of a cracked beam under harmonic forcing. In: Proceedings of the ASME International Design Engineering Technical Conferences and Computers and Information in Engineering Conference—DETC2005, vol. 6 C, 5th International Conference on Multibody Systems, Nonlinear Dynamics, and Control, Long Beach, CA, 2083–2089, 2005
11. Doughty, T.A., Leineweber, M.J.: Investigating nonlinear models for health monitoring in vibrating structures. In: ASME International Mechanical Engineering Congress and Exposition, Lake Buena Vista, FL, November 2009
12. Song, Y.Z., Bowen, C.R., Kim, H.A., Nassehi, A., Padget, J., Gathercole, N., Dent, A.: Non-invasive damage detection in beams using marker extraction and wavelets. Mech. Syst. Sig. Process. **49**(1–2), 13–23 (2014)
13. Giurgiutiu, V.: Embedded non-destructive evaluation for structural health monitoring, damage detection, and failure prevention. Shock Vib. Dig. **37**(2), 83–105 (2005)
14. Doughty, T.A., Dally, M.R., Bacon, M.R.: Nonlinear model tracking for varying system geometries. In: International Model Analysis Conference, Garden Grove, CA 2013
15. Doughty, T.A., Higgins, N.S., Etzel, N.: Nonlinear model tracking in application to non destructive evaluations. In: ASME International Mechanical Engineering Congress and Exposition, Denver, November 2011
16. Doughty, T.A., Higgins, N.S.: Effect of nonlinear parametric model accuracy in crack prediction and detection. In: SEM Annual Conference & Exposition on Experimental and Applied Mechanics, Indianapolis, 2010
17. Liang, R.Y.: Quantitative NDE technique for assessing damages in beam structures. J. Eng. Mech. **118**:7(1468), 1468–1487 (1992)
18. Wowk, V.: Machinery Vibration Measurement and Analysis. McGraw Hill, New York (1991)
19. Lee, S.-H.: Steady-state vibration analysis of modal beam model under parametric excitation. Int. J. Precis. Eng. Manuf. **13**(6), 927–933 (2012)
20. Crespo da Silva, M.R.M., Glynn, C.C.: Nonlinear flexural-flexural-torsional dynamics of inextensional beams, II. Forced motions. Int. J. Solids Struct. **6**, 449–461 (1978)
21. Doughty, T.A., Davies, P., Bajaj, A.K.: A comparison of three techniques using steady-state data to identify nonlinear modal behavior of an externally excited cantilever beam. J. Sound Vib. **249**(4), 785–813 (2002)
22. Doughty, T.A.: System identification of modes in nonlinear structures. Ph.D. Thesis, Ray W. Herrick Laboratories, School of Mechanical Engineering, Purdue University (2002)
23. Strengthening by Heat Treatment. Heat treating of aluminum alloys, heat treating, Vol. 4, ASM Handbook, ASM International, 841–879 (1991)

Chapter 12
Spatial Distribution of Acoustic Radiation Force for Non-Contact Modal Excitation

Thomas M. Huber, Mikaela Algren, and Cole Raisbeck

Abstract In modal testing, a common excitation method is a transducer in mechanical contact with the object under test. However, for some structures it is desirable to excite vibrations without physical contact. One promising excitation technique is the acoustic radiation force. However, a challenge in using this technique is that the acoustic radiation force is spread out over a finite-diameter focal region. We describe a method to directly measure the spatial distribution of this force. An ultrasound transducer emitted sine waves with frequencies of, for example $f_1 = 600.610$ kHz and $f_2 = 600$ kHz; the resulting radiation force had a component at the difference frequency f_1-$f_2 = 610$ Hz. A MicroAcoustic Instruments BAT6 ultrasound transducer was focused to an approximately 2 mm diameter spot on a 19.6 by 8.1 by 0.37 mm clamped-free brass cantilever with a 610 Hz fundamental frequency. A vibrometer measured the response as this focus spot traversed the edge of the cantilever. This enabled determination of the distribution of the acoustic radiation force being delivered by the transducer. This may be helpful in future studies that involve modeling the force applied to a structure using the acoustic radiation force.

Keywords Ultrasound • Radiation force • Line-spread function • Vibrometer • Cantilever

12.1 Introduction

In modal testing of small objects, one challenge can be to excite the vibrational modes without distortions due to mass loading. Using a laser Doppler vibrometer, it is relatively straightforward to measure the vibration in a non-contact manner; however, it is not always possible to excite these vibrations without contact. The ultrasound radiation force is a non-contact method of excitation resulting from insonifying a structure with a pair of ultrasound frequencies. The frequency difference is adjusted to the resonance frequency of the structure. Previous studies have demonstrated that this technique can be used in modal testing in air for structures as small as microcantilevers [1] to as large as the face of a classical guitar [2]. These previous studies demonstrated the feasibility of determining resonance frequencies of structures and also operating deflection shapes using a laser Doppler vibrometer. They, did not, however, quantify the magnitude or distribution of the applied radiation force.

The current study focused on using the ultrasound radiation force applied to a cantilever to directly measure the edge-spread function for an ultrasound transducer. Similar to its definition in optics, the edge-spread function is a measure of the integrated force distribution for a sharp-edged section of the circular ultrasound focus point. This was determined by translating the ultrasound focus point across the edge of a cantilever and monitoring the resulting radiation force using a single-point vibrometer. The line-spread function was the determined by numerical differentiation. The technique described is unique in that it enables measurement of the distribution of acoustic radiation force without the requirement of calibrated ultrasonic pressure measurement transducers.

T.M. Huber (✉) • M. Algren • C. Raisbeck

Department of Physics, Gustavus Adolphus College, 800 College Avenue, Saint Peter, MN 56082, USA

e-mail: huber@gac.edu

12.2 Theory

12.2.1 Acoustic Radiation Force

Previous papers have described in detail the mechanism for ultrasound stimulated audio-range excitation, both in air [3] and in water [4, 5]. If an object is insonified with a pair of ultrasound frequencies, f_1 and f_2, interference between the two frequencies produces a radiation force that results in a vibration of the object at the difference frequency $\Delta f = f_2 - f_1$. Both frequency components were emitted from a single transducer using a double-sideband suppressed-carrier amplitude modulated (AM) waveform [6]. The fundamental mode of a cantilever was excited using a difference frequency Δf by a transducer emitting two different ultrasound frequencies, $f_1 = f_c - \Delta f/2$ and $f_2 = f_c + \Delta f/2$, symmetric about a central frequency f_c. Previous studies have shown that this radiation force can be used for modal excitation of a variety of systems [7–9].

As shown in Ref. [10], the acoustic radiation force on the object, in this case a cantilever, is proportional to the square of the acoustic pressure $p(\boldsymbol{r}, t)$ on the object. In particular, for a section of an object of area dS with drag coefficient $d_r(\boldsymbol{r})$, the acoustic radiation force would be given by [5]

$$F(\boldsymbol{r}, t)\, dS = p(\boldsymbol{r}, t)^2 / \rho c^2 d_r(\boldsymbol{r})\, dS. \tag{12.1}$$

As described above, for the current experiment, the total pressure field is a double-sideband suppressed-carrier waveform with frequencies of f_1 and f_2. This results in a total acoustic pressure

$$p(\boldsymbol{r}, t) = P(f_1, \boldsymbol{r})\ \cos\left[2\pi f_1 t + \varphi_1(\boldsymbol{r})\right] + P(f_2, \boldsymbol{r})\ \cos\left[2\pi f_2 t + \varphi_2(\boldsymbol{r})\right] \tag{12.2}$$

where $P(f, \boldsymbol{r})$ is spatial distribution of the incident pressure field at frequency f. The phase differences $\varphi_1(\boldsymbol{r})$ and $\varphi_2(\boldsymbol{r})$ result from the waves of different frequencies traversing the distance between the transducer and the arrival point $\boldsymbol{r}$.

The acoustic radiation force, with its dependence on the square of the acoustic pressure, will have a time-independent component, a component at the difference frequency $\Delta f = f_2 - f_1$, and high-frequency components at $2f_1$, $2f_2$, and $f_1 + f_2$. In the current experiment, the pair of frequencies were adjusted so that the difference frequency corresponded to the cantilever's 610 Hz resonance frequency when the central frequency of the transducer was about 600 kHz. This means that the high-frequency components were far beyond the resonance frequency of the cantilever, and thus did not produce a measurable excitation. Also, because the two frequencies f_1 and f_2 differ by less than 0.1 %, the phase of both frequency components can be considered equal $\varphi_1(\boldsymbol{r}) = \varphi_2(\boldsymbol{r})$. This results in an acoustic radiation force at frequency Δf that can be written as $F_{\Delta f}(\boldsymbol{r}) \cos(2\pi t \Delta f)$ where the magnitude of the radiation force is

$$F_{\Delta f}(\boldsymbol{r}) = P(f_1, \boldsymbol{r})\, P(f_2, \boldsymbol{r}) / \rho c^2. \tag{12.3}$$

The total magnitude of the acoustic radiation force on a surface S can thus be written as the surface integral

$$F_S = \iint_S F_{\Delta f}(\boldsymbol{r})\, d_r(\boldsymbol{r})\, dS = \frac{1}{\rho c^2} \iint_S P(f_1, \boldsymbol{r})\, P(f_2, \boldsymbol{r})\, d_r(\boldsymbol{r})\, dS. \tag{12.4}$$

In the case where the drag coefficient $d_r(\boldsymbol{r})$ is essentially constant over the ultrasound focus region, such as the current case where the target is a cantilever [11], and the focus region is much smaller than the size of the cantilever, the drag term can be taken outside of the integral, resulting in an acoustic radiation force

$$F_S = k \iint_S P(f_1, \boldsymbol{r})\, P(f_2, \boldsymbol{r})\, dS. \tag{12.5}$$

where k is a constant that depends on the target geometry, drag force, and other constants.

To eliminate standing waves between the transducer and surface, the frequencies f_1 and f_2 were rapidly varied using a random carrier packet algorithm [12] that maintained the difference frequency Δf.

a Side View
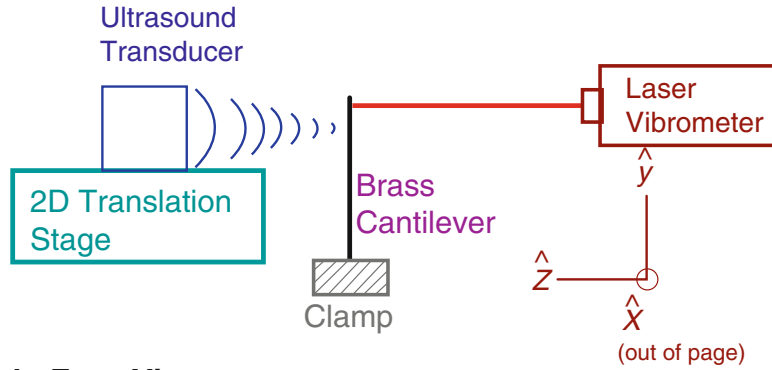
b Face View
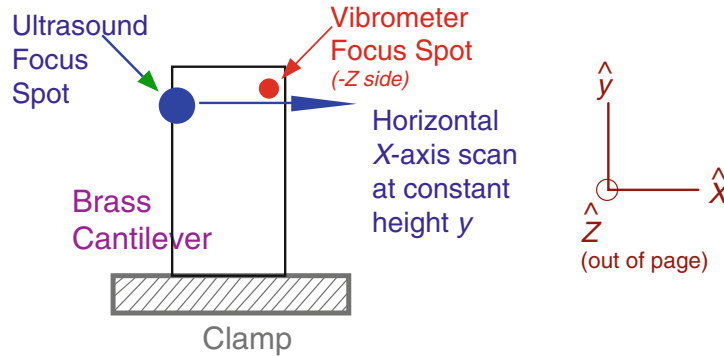
Fig. 12.1 Schematic diagram of apparatus used for measuring edge-spread functions for ultrasound radiation force excitation. The ultrasound focus spot is moved horizontally across the width (*x*-axis) of the cantilever keeping the vertical position (*y*-axis) fixed. The vibrometer focus spot, used to measure the cantilever response, is fixed

12.2.2 Relationship Between Integrated Pressure And Acoustic Force Distributions

The goal of the current experiment was to correlate acoustic pressure distributions with acoustic radiation force measurements. Section 12.3 describes how a focused transducer was directed at the surface of a clamped-free cantilever. As shown in Fig. 12.1, the transducer was translated to multiple locations along the *x*-axis, ranging from positions where the ultrasound focus spot did not insonify the cantilever, to positions where the entire ultrasound focus spot was incident on the cantilever. For each *x*-position of the transducer, the acoustic radiation force was measured. In this case, the surface integral of Eq. (12.5) includes all *x*-values larger than *x*, and is called the edge-spread function $ESF(x)$

$$ESF(x) = k \int_{x'=x}^{+R} \int_{y'=-R}^{+R} dx' dy' P\left(f_1, x', y'\right) \ P\left(f_2, x', y'\right) \ . \tag{12.6}$$

This definition of the edge-spread function is analogous to its usage in optics, where it is defined as the fraction of a circular beam pattern that passes by a sharp knife-edge surface [13]. In the current case, the sharp edge used to obtain the edge-spread function is the side of the cantilever. In the integral of Eq. (12.6), the limits of integration go to a value R. This is the effective maximum radius of the ultrasound focus spot; it is assumed that beyond this radius R, the ultrasound pressure is small enough that it would provide a negligible contribution to the edge-spread function. The integral for the edge-spread function can be rewritten as

$$ESF(x) = \int_{x'=x}^{+R} LSF\left(x'\right) dx' \tag{12.7}$$

where $LSF(x')$ is called the line-spread function, and is given by

$$LSF\left(x'\right)\,dx' = k\left[\int\limits_{y'=-R}^{+R} P\left(f_1,x',y'\right)\,P\left(f_2,x',y'\right)\,dy'\right]dx'.\qquad(12.8)$$

Physically, the line-spread function can be considered as the acoustic radiation force that results from a narrow strip of the ultrasound distribution along the y-axis that is located at position x'. As will be discussed in Sect. 12.4.2, for the current experiment, the pressure distribution at frequencies f_1 and f_2 were nearly identical. This means that the integrand of Eq. (12.8) can be replaced by the square of the pressure at the central frequency f_C, in other words

$$LSF\left(x'\right)\,dx' = k\left[\int\limits_{y'=-R}^{+R} P\left(f_c,x',y'\right)^2\,dy'\right]dx'.\qquad(12.9)$$

From Eq. (12.7), it is clear that another method for determining the line-spread function is to take the numerical derivative of a measured edge-spread function [13]

$$LSF\left(x'\right) = \left.\frac{d}{dx}\right|_{x=x'} ESF(x).\qquad(12.10)$$

12.2.3 Numerical Differentiation Using Low-Noise Lanczos Technique

As described in Sect. 12.4.3, the line-spread function was obtained by taking the numerical derivative of the measured edge-spread function. Because of random noise in the edge-spread function, a simple two-point technique leads to large fluctuations in the numerical derivative. Therefore, it is helpful to employ a multi-point numerical differentiation technique. One such algorithm is the low-noise Lanczos algorithm [14]. One of the advantages of this technique is that it is symmetric around a central point and it is efficient at smoothing random noise [15]. For a data set with y-values f_k discretely sampled with a uniform x-axis spacing of h, the Lanczos N-point numerical estimate of the derivative at x' is determined by

$$\left.\frac{df}{dx}\right|_{x=x'} \approx \frac{3}{h}\sum_{k=1}^{m} k\frac{f_k-f_{-k}}{m\left(m+1\right)\left(2m+1\right)},\quad\text{where}\quad m=\frac{N-1}{2}.\qquad(12.11)$$

12.3 Experimental Setup and Procedure

Figure 12.1 shows schematically the apparatus used in the current experiment. The cantilever was a strip of brass with dimensions of 19.6 by 8.1 by 0.37 mm clamped at one end in a machinist's vise. The vise had a mass of about 2 kg and was bolted to a Newport optical vibration isolation table to make a stable support. The resonance frequency of the lowest operating deflection shape of this cantilever was 610 ± 2 Hz and corresponds to the 1st bending mode.

The BAT6 transducer used was a custom-made ultrasound transducer for operation in air (MicroAcoustic Instruments, Gatineau, Quebec, Canada). This transducer has a focal length of 70 mm and produces a focused ultrasound spot with a beam profile roughly 2.5 mm in diameter. The transducer had a central maximum located near 700 kHz with a bandwidth of over 200 kHz. Measurements by the manufacturer indicated that the pressure field produced by the BAT6 transducer was circularly symmetric at the focal point. Namely, the pressure amplitude at any radius r from the center of the distribution was essentially independent of the angle. The manufacturer provided a data set for the radial pressure distribution function $P(r)$ at a distance of 76 mm from the surface of the transducer; this radial pressure distribution was measured by scanning a 250 μm measurement transducer across the BAT6 transducer's focal spot.

In the current experiment, the BAT6 transducer was attached to an orthogonal pair of Newport 423 translation stages with computer-controlled Zaber Technologies T-NA08A25 micrometers with 0.05 μm resolution and 25.4 mm travel. Thus, the

location of the transducer focus point could be raster scanned over a range of positions, including points that were beyond the edges of the cantilever.

The transducer's waveforms were output from a 4-channel Strategic Test UF2e-6022 60 MSamples/Second Arbitrary Waveform Generator PCI express board (Stockholm, Sweden). This board generated the Double-Sideband, Suppressed Carrier (DSB-SC) waveform of Eq. (12.1) with a carrier frequency in the vicinity of 600 kHz, and a pair of sidebands separated by 610 Hz. This waveform was amplified using an ENI-240L RF amplifier to about 250Vpp. Another DAC output channel continuously cycled a simple 610 Hz sine wave that was used as a reference signal.

To determine the vibration of the cantilever, a Polytec PSV-400 Scanning Laser Doppler Vibrometer (Waldbronn, Germany) was focused near the free end of the cantilever. The vibrometer analog output signal was routed into a Zurich Instruments HF2LI Lock-In Amplifier (Zurich, Switzerland) with the reference signal being the 610 Hz sine wave produced by the Strategic Test card.

12.4 Results

12.4.1 Experimental Measurement of Edge-Spread Function of BAT6 Ultrasound Transducer

For a point source applied to a clamped-free cantilever near its free end, simple Euler-Bernoulli beam theory predicts that fundamental mode response of the cantilever is independent of horizontal position [11]. For the current experiment, this was demonstrated using a reciprocal approach [16]. The ultrasound transducer was driven using a DSB-SC waveform with a carrier frequency near 600 kHz that had a difference frequency equal to the 610 Hz resonance frequency of the fundamental mode of the cantilever. With this fixed excitation transducer, the scanning vibrometer beam measured the vibration along a horizontal slice where the y axis position was fixed. For a y location within about 10 mm of the free end of the cantilever, the amplitude of vibration for any of these horizontal slices varied by less than 3 % across from width of the cantilever. By reciprocity this implies that for a roving point-source force, where a point-source was translated horizontally across the width of the cantilever, a fixed-location vibrometer would measure essentially the same amplitude regardless of where the point-source was applied along the x axis.

The apparatus shown in Fig. 12.1 was used to demonstrate that a roving-transducer technique could be utilized to measure the edge-spread and line-spread functions for the ultrasound transducer. As discussed in Section 12.2, the ultrasound transducer produced a DSB-SC waveform that had a difference frequency of 610 Hz. The vibrometer beam was located at a fixed position on the cantilever, and was used to monitor the vibration of the cantilever at its 610 Hz resonance frequency. The ultrasound transducer was positioned about 5 mm below the free end of the cantilever along the y-axis. Using the computer-controlled translation stage system, the transducer was positioned at multiple locations along the horizontal x-axis. The vibrometer measured the cantilever response at 610 Hz for each transducer location. Figure 12.2 shows the normalized vibration amplitude for each transducer location; these were normalized by dividing each vibration amplitude by the maximum vibration amplitude. In this figure, the $x = 0$ point corresponds to the transducer being centered on one edge of the cantilever. For large negative x values, the transducer was directed to a location where it was not striking the cantilever, and for large positive x values, the entire focal spot was incident on the cantilever.

Theoretically, if the output of a transducer was focused to an infinitesimally small radius, in other words a point-source force, the response function of Fig. 12.2 would be a square edge that would rapidly go from 0 to 1. However, because of the finite size of the ultrasound focus spot, the distribution shown in Fig. 12.2 shows that the cantilever's response varies from 0 to 1 over a range of several mm centered on the edge of the cantilever. The edge-spread function for this transducer was measured by performing horizontal sweeps similar to Fig. 12.2 for both the left and right edges of the cantilever, with similar results. A previous study [17] demonstrated that by performing a vertical transducer scan, and fitting the resulting measured distribution to the deflection shape predicted by Euler-Bernoulli beam theory, the result was an edge-spread function that was nearly identical in shape to Fig. 12.2.

12.4.2 Determination of Line-Spread Function from Manufacturer-Measured Radial Pressure Distribution

A major goal of the current research study was to demonstrate the feasibility of using the measured edge-spread function of Fig. 12.2 to determine the line-spread function of the transducer. To verify this hypothesis, it was necessary to independently
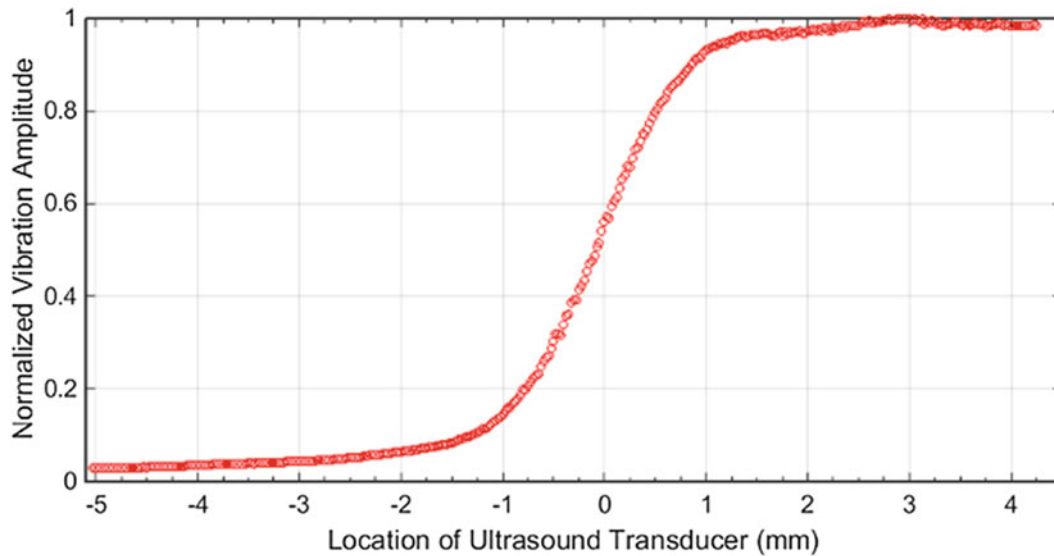
Fig. 12.2 Normalized response, also known as the edge-spread function, obtained when the ultrasound focus point was scanned across horizontal width of cantilever

determine the line-spread function. The line-spread function, defined by Eq. (12.9), was determined by integrating narrow strips of the 2-dimensional pressure distribution. The manufacturer provided a 1-d scan of the pressure distribution as a function of radius. Because the transducer's pressure distribution was circularly symmetric, the radial distribution could be rotated around the origin to obtain the 2-dimensional pressure distribution shown in Fig. 12.3. This pressure distribution was measured for a single frequency at 600 kHz with a focal depth of 76 mm. The central spot size for this pressure distribution was about 2.5 mm across. During the current study, a DSB-SC signal was used, where the carrier frequency was randomly varied within a range of 575 to 625 kHz. There would be pair of sidebands separated by 610 Hz for every carrier frequency. Based on measurements at other frequencies provided by the manufacturer, it was estimated that the width of the focal spot would vary by only about 0.1 mm for the range of frequencies used in the current experiment. Therefore, in the analysis that follows, the pressure distribution of Fig. 12.3 was used as representative for all frequencies used. This is constituent with the assumption that was made in deriving Eq. (12.9) where the acoustic radiation force was proportional to the square of the pressure distribution measured at a single frequency.

Figure 12.3 graphically illustrates the integral used for determining the line-spread function as a narrow black strip. The X's in Fig. 12.4 show the line-spread function obtained by taking integral of the square of the pressure, as in Eq. (12.9), for narrow strips of width $dx' = 0.1$ mm.

12.4.3 Determination of Line-Spread Function Using Numerical Differentiation of Edge-Spread Function

Determining of line-spread function, as described in Sect. 12.4.2, required knowledge of the pressure distribution, in this case furnished by the manufacturer. The goal of the current study was to demonstrate the feasibility of determining the line-spread function of the ultrasound transducer using a vibrometer. From Eq. (12.10), the numerical derivative of the measured edge-spread function (e.g. Fig. 12.2), was used to obtain the line-spread function. When a simple two-point derivative approximation was used, random noise caused rapid fluctuations in the numerical derivative. Therefore, the data set was differentiated using a multipoint method, in this case the low-noise Lanczos method of Eq. (12.11). Applying an $N = 9$ point numerical differentiation technique resulted in the plot shown with open circles in Fig. 12.4. In experimenting with different values for the order parameter N, a tradeoff was observed: a large value of N led to a smoother curve with better noise reduction, but also meant a loss of other structure such as the shoulder expected in the vicinity of +/-2 mm. It was determined that an $N = 9$ point derivative gave an acceptable tradeoff between smoothing noise without eliminating the structure of the distribution.
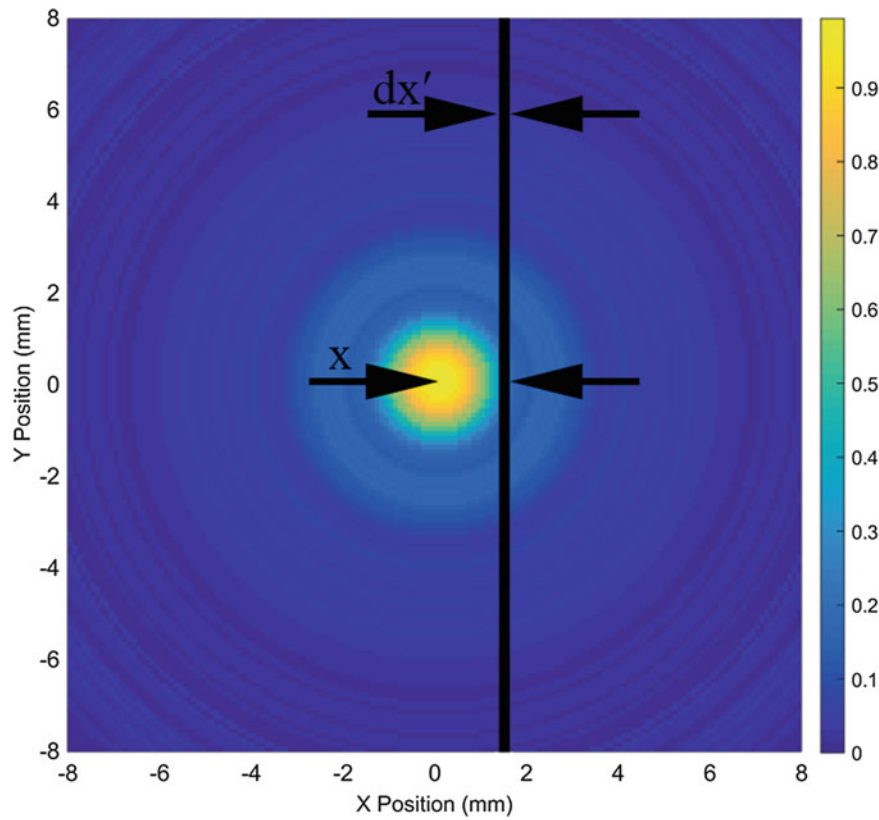
Fig. 12.3 Two-dimensional ultrasound pressure distribution for BAT6 transducer used in the current experiment. This plot was obtained by rotating the radial pressure distribution, measured by the manufacturer, around the central focus point. The narrow *black line* illustrates the integral of Eq. (12.9) used to calculate the line-spread function
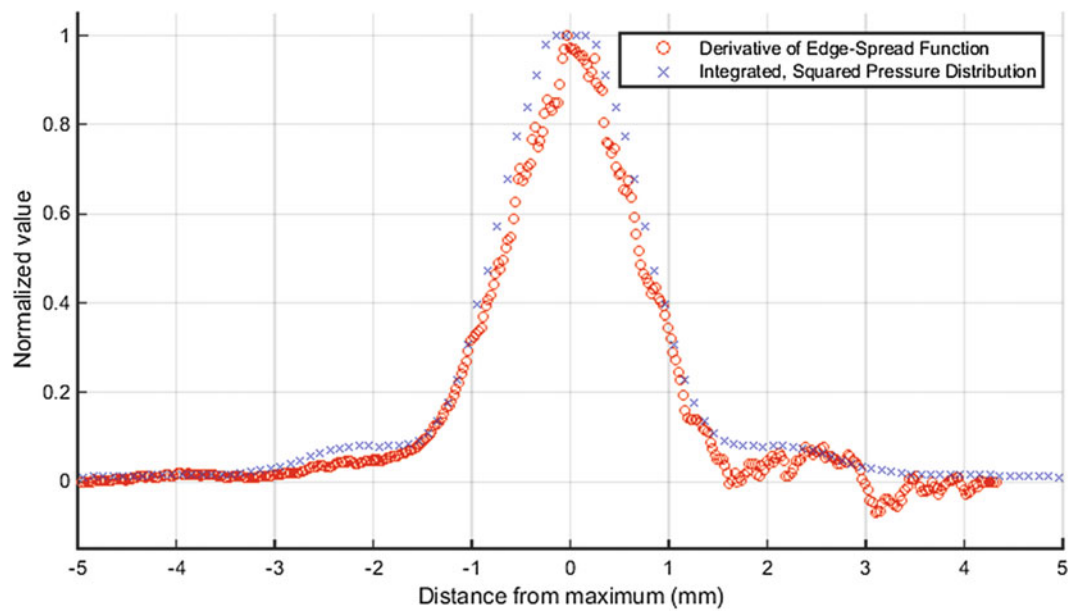
Fig. 12.4 Comparison of line-spread functions for BAT6 ultrasound transducer. The measured edge-spread function of Fig. 12.2 was numerically differentiated to give the plot with *open circles*. The plot with X symbols is the integrated slice of the square of the pressure distribution (provided by the manufacturer). The agreement between these curves demonstrates the capability to extract an estimate of the line-spread function from an easily measurable edge-spread data set

12.5 Conclusions

The current experiment demonstrates that it is possible to use the ultrasound radiation force of a roving transducer moving across a fixed-free cantilever to measure the edge-spread function of an ultrasound transducer. By taking the numerical derivative of this edge-spread function, the transducer's line-spread function could be determined. This is important because it is essential to know the spatial distribution, in particular the line-spread function, when modeling the radiation force applied to a structure.

In comparing the two plots in Fig. 12.4, there are some important conclusions. Most important, the line-spread function determined using a vibrometer and translation stage has a width and overall structure that is in good agreement with a line-spread function obtained by integration of pressure measurements. This vibrometer-measurement technique may be advantageous because many engineering labs have a single-point or scanning vibrometer, but might not have instrumentation needed to measure a radial pressure distribution directly. One major difference was the relatively large dips that occur at about 1.5 and 3.2 mm in the vibrometer measurement of line-spread function. These dips were due to some oscillations that are observed in the edge-spread function of Fig. 12.2, and will be investigated in more detail in future studies with different transducers.

Future studies will also involve utilizing the edge-spread function and line-spread function to determine the radial-distribution and 2-d distribution of the ultrasound radiation force applied by a transducer. One ultimate goal of this research program is determination of frequency response functions (FRF's) using a fully non-contact method for both excitation and measurement.

References

1. Huber, T.M., Abell, B.C., Mellema, D.C., Spletzer, M., Raman, A.: Mode-selective noncontact excitation of microcantilevers and microcantilever arrays in air using the ultrasound radiation force. Appl. Phys. Lett. **97**, 214101 (2010)
2. Huber, T.M., Beaver, N.M., Helps, J.R.: Noncontact modal excitation of a classical guitar using ultrasound radiation force excitation. Exp. Tech. **37**(4), 38–46 (2013)
3. Huber, T.M., Fatemi, M., Kinnick, R., Greenleaf, J.: Noncontact modal analysis of a pipe organ reed using airborne ultrasound stimulated vibrometry. J. Acoust. Soc. Am. **119**, 2476–2482 (2006)
4. Fatemi, M., Greenleaf, J.F.: Ultrasound-stimulated vibro-acoustic spectrography. Science **280**, 82–85 (1998)
5. Silva, G.T., Chen, S.G., Greenleaf, J.F., Fatemi, M.: Dynamic ultrasound radiation force in fluids. Phys. Rev. E **71**, 9 (2005)
6. Fatemi, M., Greenleaf, J.F: Acoustic force generation by amplitude modulating a sonic beam. US Patent 5,921,928, 1999
7. Fatemi, M., Greenleaf, J.F.: Mode excitation and imaging by the radiation force of ultrasound. J. Acoust. Soc. Am. **111**, 2472 (2002)
8. Mitri, F.G., Trompette, P., Chapelon, J.Y.: Detection of object resonances by vibro-acoustography and numerical vibrational mode identification. J. Acoust. Soc. Am. **114**, 2648–2653 (2003)
9. Huber, T.M., Calhoun, D., Fatemi, M., Kinnick, R. R., Greenleaf, J.F.: Noncontact modal testing of hard-drive suspensions using ultrasound radiation force. In: Proceedings of International Modal Analysis Conference XXIV, St Louis MO, February 2006
10. Westervelt, P.J.: The theory of steady forces caused by sound waves. J. Acoust. Soc. Am. **23**, 312–315 (1951)
11. de Silva, C.W.: Euler-Bernoulli beam theory. In: Vibration: Fundamentals and Practice, pp. 346–351. CRC Press, Taylor & Francis Group, Boca Raton, FL (2007)
12. Huber, T.M., Beaver, N.M., Helps, J.R.: Elimination of standing wave effects in ultrasound radiation force excitation in air using random carrier frequency packets. J. Acoust. Soc. Am. **130**(4), 1838–1843 (2011)
13. Optical transfer function. Wikipedia, the free encyclopedia. 02-Sep-2015
14. Lanczos, C.: Applied Analysis. Dover Books, New York, NY (1988)
15. Holoborodko, P. Low-noise Lanczos differentiators. [Online]. Available: http://www.holoborodko.com/pavel/numerical-methods/numerical-derivative/lanczos-low-noise-differentiators/ Accessed 11 October 2015
16. Avitabile, P. Experimental modal analysis: A Simple Non-Mathematical Presentation. Sound Vib. Mag. **35**, 1–15 (2001)
17. Huber, T.M., Batalden, S.M., Doebler, W.J.: Measurement of vibration resulting from non-contact ultrasound radiation force. In: Proceedings of International Modal Analysis Conference (IMAC-XXXIII), Orlando, FL 2015

Chapter 13
Modal Parameter Identification Algorithm Based on Pure Normal Mode Test Technology

J.M. Liu, F. Liu, and W.D. Zhu

Abstract There is common denominator for the FRFs of mode test which determine the modal frequency and damping. For the modal parameter identification of SIMO or MISO, one row or one column of FRF matrix is known, by applying pure normal mode test technology which is often used in the Ground Vibration Test (GVT) of aeroplane, a group of real coefficients can be computed out, each coefficient corresponds to one FRF, the sum of all the FRF multiplying the computed coefficient constructs one new FRF which includes only one mode. By this way, the precise modal frequency and modal damping can be identified. Changing the coefficients, the other mode's frequency and damping can also be identified. For MIMO test, one new group FRFs which include only one mode can be constructed in similar way. The precise modal frequency, modal damping and modal shape can be identified. Changing the coefficients, the other mode's parameter can also be identified. Even if the number of FRF groups for MIMO is not enough, one new group FRFs can be obtained which greatly deleting the nearest mode's influence, improve the preciseness of identified modal parameters, especially the modal shape. In this paper, the method of computing the coefficients are introduced for SIMO, MISO and MIMO test. The real engineering example is given to verify the effective and correct of new algorithm. For mode test with very big damping, the coupling of different modes is very seriously, the new algorithm can realize the decoupling easily and obtain the precise modal parameters.

Keywords Modal parameter identification • FRF • Pure normal mode test • Decoupling • MvMIF

13.1 Introduction

One of the Ground Vibration Test (GVT) of aeroplane is the pure normal mode test [1]. In the test a number of exciters are used at the same harmonic frequency which is one mode's frequency. By adjusting each exciter's amplitude and direction, the pure normal mode will be excited out with precise modal shape. This methodology can be used to modal parameter identification of Experimental Modal Analysis (EMA) and Operational Modal Analysis (OMA).

For the modal parameter identification of EMA and OMA, there is common denominator in the FRF or Half Spectrum [2–4].

In SIMO or MISO test, one row or one column FRF matrix is known. If each FRF multiplying a suitable real coefficient, the sum of them will construct one new FRF which includes only one mode in its denominator, thus the precise modal frequency and damping ratio can be identified in the condition that the nearest mode is not very close.

For MIMO test, there are multi groups of FRF. If the number of groups is enough, the sum of each group FRF multiplying a suitable real coefficient will construct one new group FRF, which includes only one mode in their common denominator, thus the precise modal frequency, damping ratio and especially modal shape can be identified. Even if the number of group is not enough, the obtained new group FRF can greatly delete the influence of nearby modes and improve the preciseness of

J.M. Liu (✉)
China Orient Institute of Noise & Vibration, Beijing 100085, China
e-mail: liujm@coinv.com

F. Liu
Beijing Institute of Technology, Beijing 100081, China

W.D. Zhu
University of Maryland, Baltimore County, Baltimore, MD 20250, USA

identified modal parameters. For each mode, the real coefficients can be solved by the Multivariate Mode Indicator Function (MvMIF) algorithm [5, 6]. When the value of MvMIF is below 0.1, the mode shape can be directly obtained from the imaginary part of FRF.

13.2 Theory Deduction

13.2.1 SIMO or MISO Modal Test

When one row or one column of FRF matrix that correspond to SIMO or MISO test is known, the modal parameter identification can proceed.

The FRF between any two exciting point and responding point can be written as:

$$H_{ij}(\omega) = \sum_{r=1}^{n} \frac{\psi_{ir}\psi_{jr}}{m_r\left(\omega_r^2 - \omega^2 + j2\xi_r\omega_r\omega\right)} \tag{13.1}$$

In which, i is exciting point and j is responding point, r is the mode order, n is the total mode orders in analysis frequency district, m_r is general modal mass.

Equation (13.1) often be written as

$$H_{ij}(\omega) = \sum_{r=1}^{n} \frac{A_r}{j\omega - s_r} + \frac{A_r^*}{j\omega - s_r^*} \tag{13.2}$$

Here $\bullet^*$ is conjugate complex. A_r is complex residue.

$$s_r = -\xi_r\omega_r + j\omega_r\sqrt{1 - \xi_r^2} \tag{13.3}$$

When A_r is pure imaginary, the real part of A_r is 0, $A_r^* = -A_r$. From Eq. (13.1)

$$\psi_{ir}\psi_{jr} = m_r A_r\left(s_r - s_r^*\right) \tag{13.4}$$

$\psi_{ir}\psi_{jr}$ is real. Here after, the vibration shape will be assumed as real.

If the modal shape is unified with unit general modal mass, the Eq. (13.1) can be rewritten as:

$$H_{ij}(\omega) = \sum_{r=1}^{n} \frac{\psi_{ir}\psi_{jr}}{\omega_r^2 - \omega^2 + j2\xi_r\omega_r\omega} \tag{13.5}$$

There is common denominator of all FRFs. For modal parameter identification of one mode, the influence of the other modes needs to be considered.

Assuming m FRFs are chosen to add together with real coefficient weighting, here $m \geq n$ is required, the sum of them is a new FRF:

$$H(\omega) = \sum_{r=1}^{n} \frac{\psi_{ir}\sum_{j=1}^{m}\alpha_j\psi_{jr}}{\omega_r^2 - \omega^2 + j2\xi_r\omega_r\omega} \tag{13.6}$$

That is

$$H(\omega) = \sum_{j=1}^{m}\alpha_j H_{ij}(\omega) \tag{13.7}$$

If suitable real coefficients α_j can be found, enable for the equations:

$$\sum_{j=1}^{m} \alpha_j \psi_{jr} = 0 \tag{13.8}$$

Here r is mode order, $r \neq k$. Only in one order mode $r = k$, $\sum_{j=1}^{m} \alpha_j \psi_{jr}$ is not zero. By unification, let $\sum_{j=1}^{m} \alpha_j \psi_{jr} = 1$. This time, from Eq. (13.7), the FRF which includes only one mode is obtained. Without considering the influence of the other modes, the modal frequency and damping ration of this mode can be identified precisely from the new FRF.

When the frequencies and damping ratios of all modes are obtained, the modal shape can be extracted from the original FRFs point by point.

To obtain the FRF of single mode, the real coefficients α_j ($j = 1, 2, \cdots m$) need to be computed out first.

The FRF of accelerator or displacement with single mode is illustrated as Fig. 13.1:

Here after, the type of FRF means displacement or accelerator. For the FRF of velocity, the real part and imaginary part need to exchange. For the Half Spectrum of OMA, the type can be looked as velocity.

In Fig. 13.1, with the mode frequency as center, one frequency district will be chosen. Outside this frequency district, the ration absolute imaginary part to absolute real part is

$$\mu = \left| 2\xi_r \omega_r \omega / \left(\omega_r^2 - \omega^2 \right) \right| \tag{13.9}$$
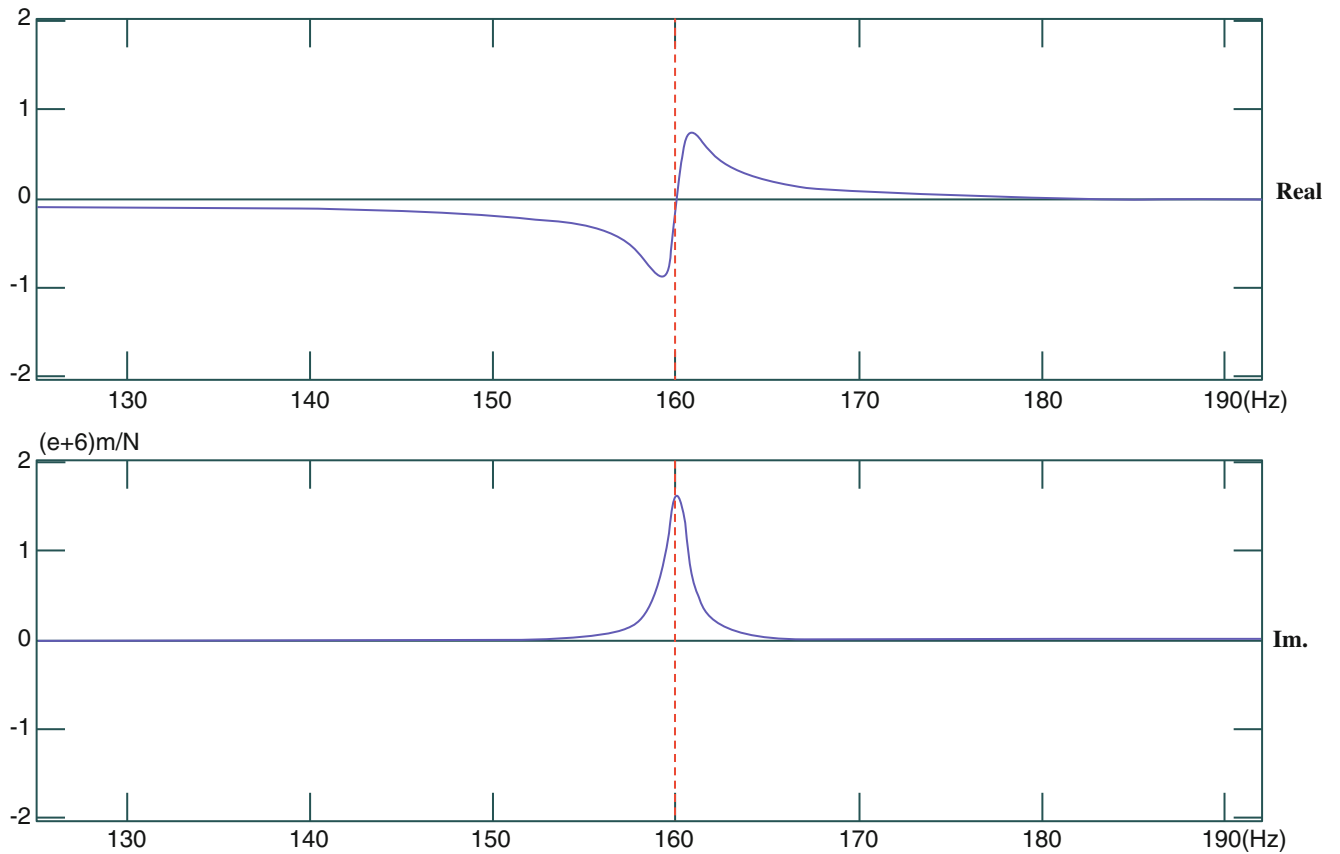

Fig. 13.1 FRF real and imaginary curves of single mode

To ensure $\mu < 0.01$, the frequency range is

$$\omega < \left(\sqrt{1 + (100\xi_r)^2} - 100\xi_r \right) \omega_r \tag{13.10}$$

$$\omega > \left(\sqrt{1 + (100\xi_r)^2} + 100\xi_r \right) \omega_r \tag{13.11}$$

When $\xi_r < 0.005$, the outside frequency district is $\omega < 0.62\omega_r$, $\omega > 1.62\omega_r$.

When $\xi_r < 0.001$, the outside frequency district is $\omega < 0.90\omega_r$, $\omega > 1.11\omega_r$.

In all the FRFs, to chose m FRFs with great absolute value of imaginary part in the frequency district, or all the FRFs.

Outside frequency district, assuming the number of spectrum lines of FRF is N, thus the equation to decide real coefficients α_k is

$$\begin{bmatrix} HI_{01} & HI_{02} & \cdots & HI_{0m} \\ HI_{11} & HI_{12} & \cdots & HI_{0m} \\ \vdots & \vdots & \ddots & \vdots \\ HI_{N1} & HI_{N2} & \cdots & HI_{Nm} \end{bmatrix}_{(N+1)\times m} \begin{bmatrix} a_1 \\ a_2 \\ a_3 \\ \vdots \\ a_m \end{bmatrix}_{m\times 1} = \begin{bmatrix} 1 \\ 0 \\ \vdots \\ 0 \end{bmatrix}_{(N+1)\times 1} \tag{13.12}$$

It can be simplified as

$$A\alpha = \begin{bmatrix} 1 & 0 & 0 & 0 \end{bmatrix}^T_{(N+1)\times 1} \tag{13.13}$$

In Eq. (13.13), $\bullet^T$ is transform matrix, HI is the imaginary part of FRF. In element HI_{ij}, when i is not 0, is the spectrum lines order of outside frequency district, $i = 0$ represents the spectrum is in the peak of FRF inside the frequency district, the small position error is permitted without disturbing the preciseness of parameter identification; j is the point number of FRF. In Eq. (13.12), the element 1 in right side matrix can be assuming to other constant.

From Eq. (13.13), the least square solution is

$$\alpha = \left(A^T A \right)^{-1}_{m\times m} A^T_{m\times(N+1)} \begin{bmatrix} 1 & 0 & 0 & 0 \end{bmatrix}^T_{(N+1)\times 1} \tag{13.14}$$

That is

$$\alpha = \left(A^T A \right)^{-1}_{m\times m} \begin{bmatrix} HI_{01} & HI_{02} & \cdots & HI_{0m} \end{bmatrix}^T_{m\times 1} \tag{13.15}$$

For SIMO or MISO test, the obvious shortage of above algorithm is not suitable for close modes and great damping ratio mode.

If two close modes frequency are separated with more than 2 spectrum lines, that is the error of two mode frequencies is greater than $2\Delta f$, here $\Delta f = SF/N$, SF is sampling frequency, N is FFT number . These parameters of two modes can be identified.

Paying attention to Fig. 13.1, the value of real part is near to 0 when the line position is in the mode frequency. So adding one row to Eq. (13.12), the new equation is

$$\begin{bmatrix} HI_{01} & HI_{02} & \cdots & HI_{0m} \\ HR_{01} & HR_{01} & \cdots & HR_{0m} \\ HI_{11} & HI_{12} & \cdots & HI_{1m} \\ \vdots & \vdots & \ddots & \vdots \\ HI_{N1} & HI_{N2} & \cdots & HI_{Nm} \end{bmatrix}_{(N+2)\times m} \begin{bmatrix} a_1 \\ a_2 \\ a_3 \\ \vdots \\ a_m \end{bmatrix}_{m\times 1} = \begin{bmatrix} 1 \\ 0 \\ \vdots \\ 0 \end{bmatrix}_{(N+2)\times 1} \tag{13.16}$$

The two close modes can be separated. The adding one row is HR, the real part of FRF, in the position FRF peak inside the frequency district, the same position as to first row.

For the FRF including single mode, $H(\omega) = \frac{\varphi_r}{\omega_r^2 - \omega^2 + j2\xi_r\omega_r\omega}$, Three parameters ω_r, ξ_r, φ_r need to be identified inside the frequency district decided by Eqs. (13.10) and (13.11). The equation is

$$
\begin{bmatrix}
HR_1 & -HI_1\omega_1 & -1 \\
HI_1 & HR_1\omega_1 & 0 \\
HR_2 & -HI_2\omega_2 & -1 \\
HI_2 & HR_2\omega_2 & 0 \\
\vdots & \vdots & \vdots \\
HI_N & HR_N\omega_N & 0
\end{bmatrix}_{2N\times3}
\begin{bmatrix}
\omega_r^2 \\
2\xi_r\omega_r \\
\varphi_r
\end{bmatrix}_{3\times1}
=
\begin{bmatrix}
HR_1\omega_1^2 \\
HI_1\omega_1^2 \\
HR_2\omega_2^2 \\
HI_2\omega_2^2 \\
\vdots \\
HI_N\omega_N^2
\end{bmatrix}_{2N\times1}
\tag{13.17}
$$

Here HR_k is the real part of H, HI_k is the imaginary part of H, k is the spectrum order, ω_k is ω of spectrum line k, and N is the total spectrum lines number inside the frequency district.

Simplified as

$$
E_{2N\times3}X_{3\times1} = Y_{2N\times1}
\tag{13.18}
$$

The least square solution is

$$
X = \left(E^T E\right)^{-1} E^T Y
\tag{13.19}
$$

Here $X = \begin{bmatrix} X_1 & X_2 & X_3 \end{bmatrix}^T$, Thus

$$
\begin{aligned}
\omega_r &= \sqrt{X_1} \\
\xi_r &= 0.5X_2/\sqrt{X_1} \\
\varphi_r &= X_3
\end{aligned}
\tag{13.20}
$$

The modal frequency, damping ratio and vibration shape of reference point are obtained. With these parameters, the synthesized theoretical FRF can be constructed. The fitting extent of theoretical FRF and constructed pure FRF can reflect the preciseness of this mode's identified parameters. When the fitting extent is miserable, maybe there are more than one mode inside the frequency district, or the chosen frequency district is not wide enough for the damping ration is great.

13.2.2 MIMO Test

For MIMO Test, The MvMIF can be used directly, to obtain the coefficients, to construct one group pure FRFs.

The known FRF matrix is $H_{q\times p}$, q is the number of total response points, p is number of exciting points.

The Real coefficients are looked as exciting vector force $F_{p\times1}$, $\|F\| = 1$, the one group of new FRF is $(HF)_{q\times1}$. So the problem is the same as pure mode problem, can be defined as

$$
\min \frac{F^T H_{\mathrm{Real}}^T H_{\mathrm{Real}} F}{F^T \left(H_{\mathrm{Real}}^T H_{\mathrm{Real}} + H_{\mathrm{Imag}}^T H_{\mathrm{Imag}}\right) F} = \lambda
\tag{13.21}
$$

In each spectrum line, defined matrix

$$
A = H_{\mathrm{Real}}^T H_{\mathrm{Real}}
\tag{13.22}
$$

$$
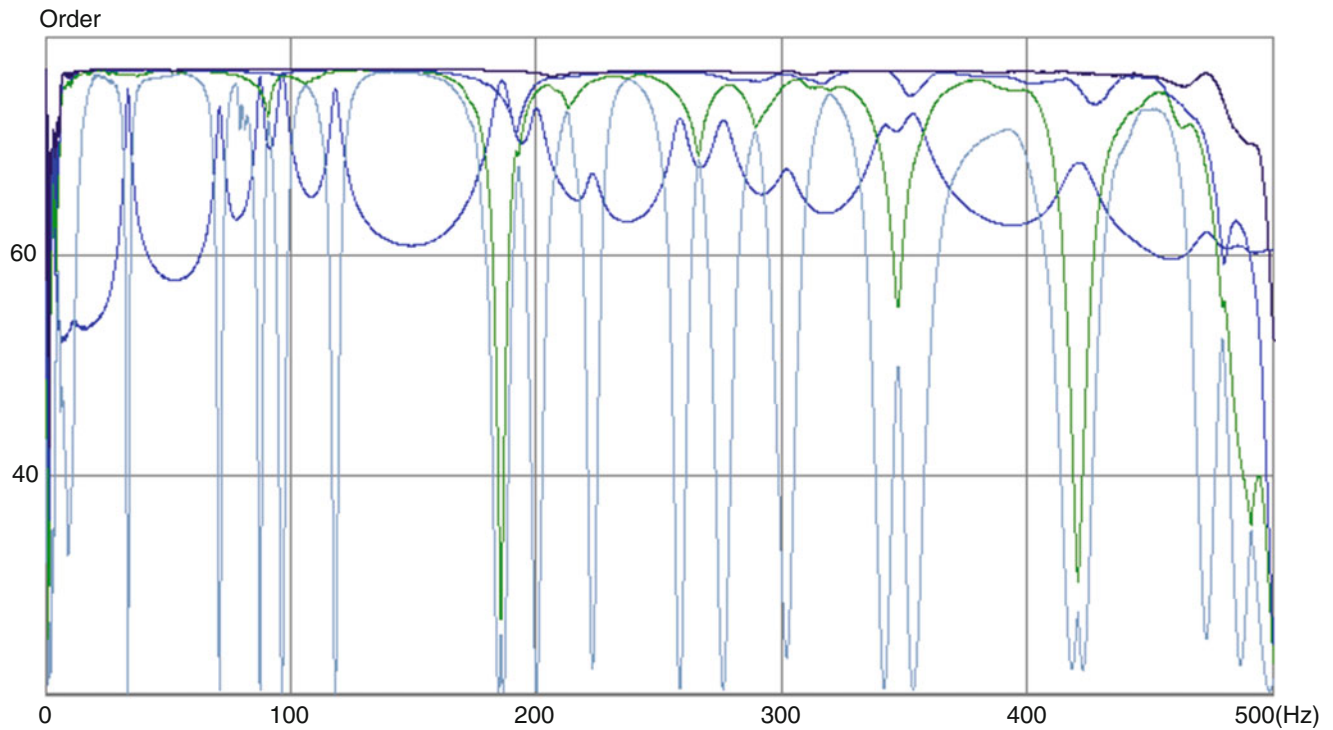B = H_{\mathrm{Imag}}^T H_{\mathrm{Imag}}
\tag{13.23}
$$

Order

Fig. 13.2 MvMIF curves

From Eq. (13.21), obtain

$$AF = (A + B) F\lambda \tag{13.24}$$

Thus

$$F^T (A + B)^{-1} AF = \lambda \tag{13.25}$$

In each spectrum line, decompose the singular value of symmetry real matrix

$$(A + B)^{-1} A = USU^T \tag{13.26}$$

Here S is a real positive diagonal matrix with elements from big to small, U is unified real matrix. $UU^T = I$. I is unify matrix.

The curves of MvMIF can be drawn, as illustrated in Fig. 13.2.

For number of p exciting points, there are number of p MvMIF curves. Each curve is consisted by the element of diagonal matrix S with the same order.

By the minimum points of MvMIF, the mode position can be found. The real coefficients are one column of matrix U corresponding to the singular value in the curve.

When coefficients are known, one group of new FRF $(HF)_{q \times 1}$ with pure mode can be obtained. When the value of MvMIF is less than 0.1, the mode shape can be directly obtained from imaginary part of FRFs in the FRF peak position.

The minimum value of MvMIF depends on the number and position of exciting pints. When there are 4 modes closely, at least 3 exciting points are needed at suitable position. When the number of exciting points is enough and their positions are properly separated, even the repeat modes' parameters can be identified easily.

When one group pure FRFs are obtained, the Eq. (13.17) expends to

$$
\begin{bmatrix}
{}^1HR_1 & -{}^1HI\omega_1 & -1 & 0 & \cdots & 0 \\
{}^1HI_1 & {}^1HR_1\omega_1 & 0 & 0 & \cdots & 0 \\
\vdots & \vdots & \vdots & \vdots & \ddots & 0 \\
{}^1HI_N & {}^1HR_N\omega_N & 0 & 0 & \cdots & 0 \\
{}^2HR_1 & -{}^2HI\omega_1 & 0 & -1 & \cdots & 0 \\
{}^2HI_1 & {}^2HR_1\omega_1 & 0 & 0 & \cdots & 0 \\
\vdots & \vdots & \vdots & \vdots & \ddots & \vdots \\
\vdots & \vdots & \vdots & \vdots & \ddots & \vdots \\
{}^qHR_1 & -{}^2HI\omega_1 & 0 & 0 & \cdots & -1 \\
{}^qHI_1 & {}^qHR_1\omega_1 & 0 & 0 & \cdots & 0 \\
\vdots & \vdots & \vdots & \vdots & \ddots & 0 \\
{}^qHI_N & {}^qHR_N\omega_N & 0 & 0 & \cdots & 0
\end{bmatrix}_{2qN\times(2+q)}
\begin{bmatrix}
\omega_r^2 \\
2\xi_r\omega_r \\
\varphi_1' \\
\vdots \\
\varphi_q'
\end{bmatrix}_{(2+q)\times1}
=
\begin{bmatrix}
{}^1HR_1\omega_1^2 \\
{}^1HI_1\omega_1^2 \\
\vdots \\
{}^1HI_N\omega_N^2 \\
{}^2HR_1\omega_1^2 \\
{}^2HI_1\omega_1^2 \\
\vdots \\
\vdots \\
{}^qHR_1\omega_1^2 \\
{}^qHI_1\omega_1^2 \\
\vdots \\
{}^qHI_N\omega_N^2
\end{bmatrix}_{2qN\times1}
\tag{13.27}
$$

Here in the elements ${}^iHR$ and ${}^iHI$, i represents the *ith* FRF in the group of pure FRFs.

Directly solve Eq. (13.27) is time consuming. From Eqs. (13.27), (13.28) can be obtained.

$$
\begin{bmatrix}
{}^1HI_1 & {}^1HR_1\omega_1 \\
\vdots & \vdots \\
{}^1HI_N & {}^1HR_N\omega_N \\
{}^2HI_1 & {}^2HR_1\omega_1 \\
\vdots & \vdots \\
\vdots & \vdots \\
{}^qHI_1 & {}^1HR_1\omega_1 \\
\vdots & \vdots \\
{}^qHI_N & {}^1HR_1\omega_1
\end{bmatrix}_{qN\times2}
\begin{bmatrix}
\omega_r^2 \\
2\xi_r\omega_r
\end{bmatrix}_{2\times1}
=
\begin{bmatrix}
{}^1HI_1\omega_1^2 \\
\vdots \\
{}^1HI_N\omega_N^2 \\
{}^2HI_1\omega_1^2 \\
\vdots \\
\vdots \\
{}^qHI_1\omega_1^2 \\
\vdots \\
{}^qHI_N\omega_N^2
\end{bmatrix}_{qN\times1}
\tag{13.28}
$$

The modal frequency and damping ration can be solved first.

Then, the vibration shape can be obtained according to Eq. (13.27)

$$
\varphi_i' = \left(\sum_{k=1}^{N} {}^iHR_k \left(\omega_r^2 - \omega_k^2 \right) - 2\xi_r \, {}^iHI_k \omega_r \omega_k \right)/N \qquad (i = 1, 2, \cdots q) \tag{13.29}
$$

For unified general mass, there is equation

$$
\varphi_i' = \varphi_v \varphi_i \qquad (i = 1, 2, \cdots q) \tag{13.30}
$$

Here φ_v can be looked as vibration shape of the virtual exciting point of SIMO system.

$$
\varphi_v = \left(\varphi_1 \; \varphi_2 \; \cdots \; \varphi_p \right) F_{p\times1} \tag{13.31}
$$

φ_1, φ_2, …, φ_p are the vibration shape of exciting points.

From Eq. (13.31), conduct

$$
\varphi_v^2 = \left(\varphi_1' \; \varphi_2' \; \cdots \; \varphi_p' \right) F_{p\times1} \tag{13.32}
$$

By Eq. (13.30), φ_v can be solved. The real vibration shape of *rth* mode is

$$
\varphi_i = \varphi_i'/\varphi_v \qquad (i = 1, 2, \cdots q) \tag{13.33}
$$

13.3 Engineering Example

Example 1. This is a plate mode test with four measured points in the four corners, illustrated as Fig. 13.3. And a hammer with force transducer is being used to knock at all the grid points at Fig. 13.4. Four groups of FRFs are obtained. The MvMIF curve is displayed at Fig. 13.2.

Name the new algorithm as pure mode algorithm. The result of new algorithm is compared to ERA algorithm.

Table 13.1 is the modal frequency and damping ration obtained by two algorithms. Figure 13.5 is the Cross MAC of two algorithms to compare the difference of vibration shape.

From Table 13.1 and Fig. 13.5, it's obvious that the results of two algorithms are very close. Among all the mode orders, order 6 and order 7 are very close.

Fig. 13.3 A plate with hole in the center
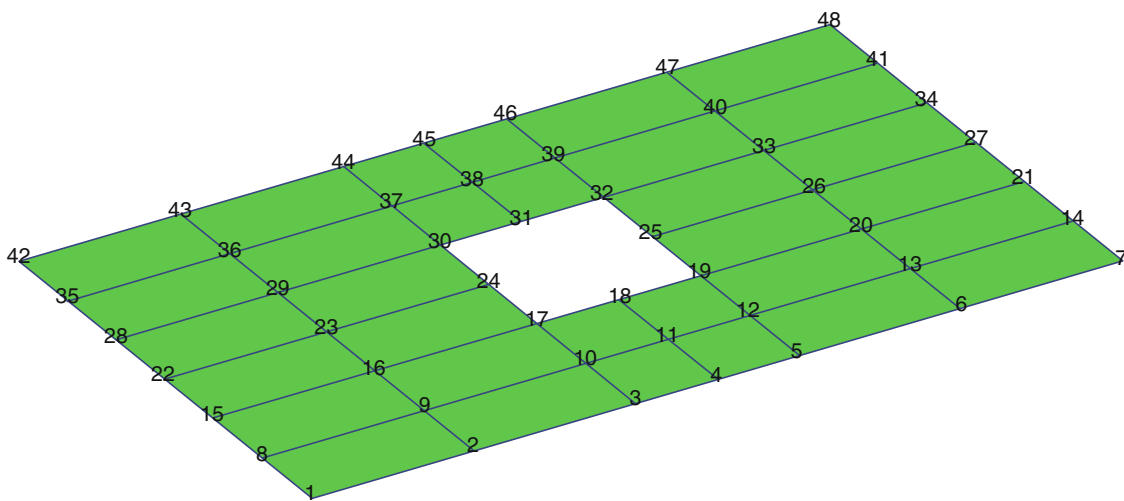
Fig. 13.4 The grid for mode test

Table 13.1 The analysis result comparing of tow algorithms

| Order	Pure mode		ERA	
	Frequency (Hz)	Damping (%)	Frequency (Hz)	Damping (%)
1	33.586	1.603	33.591	1.605
2	70.987	1.205	70.991	1.266
3	87.439	0.997	87.483	1.107
4	96.397	1.465	96.418	1.488
5	118.015	1.270	118.086	1.296
6	184.437	1.476	184.596	1.538
7	186.397	1.326	186.511	1.384
8	199.971	1.365	199.947	1.442
9	222.719	0.910	222.841	1.173
10	258.237	1.094	258.264	1.174
11	275.833	1.372	275.854	1.441
12	301.631	1.078	301.560	1.589
13	341.377	1.272	341.384	1.350
14	353.209	1.394	353.046	1.448
15	417.771	1.164	417.988	1.544
16	422.187	1.025	422.001	1.334
17	472.246	0.669	472.668	1.161
18	485.886	0.858	484.554	1.567
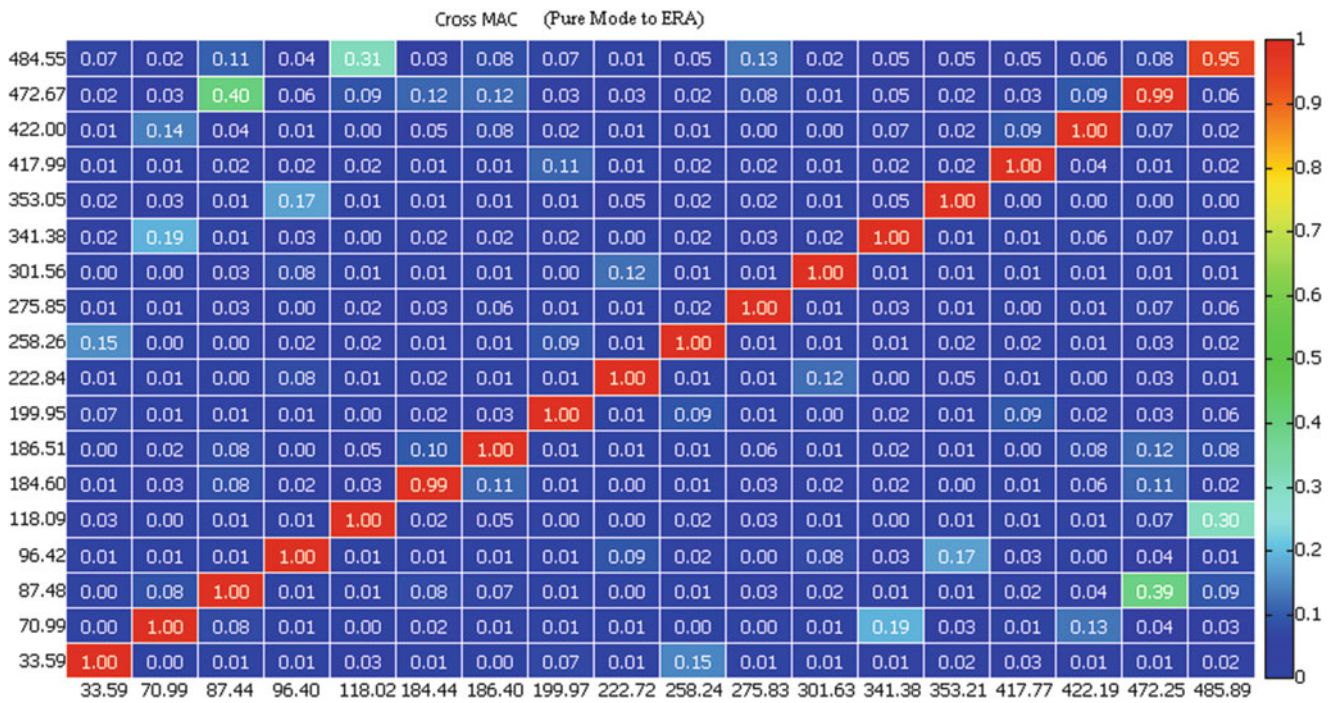
Fig. 13.5 Cross MAC of Pure Mode to ERA

Example 2. This is a mode test of isolating vibration platform with super great damping, which is designed by China Electric Academy 10. The size of platform is length: 40 m, width: 7 m, height 0.7 m. Its mass is 10,000 kg. The foremost 3 rigid modes are with very great damping, damping ration is from 28 to 40 %. The three great damping modes are coupled together, cause difficult to identify the modal parameters with common algorithm, especially to obtain the harmonious modal shape.

Table 13.2 The analysis result

Order	Frequency (Hz)	Damping ratio (%)	Shape illustration
1	1.753	40.939	Bound
2	1.950	37.670	Pitch
3	2.402	28.116	Roll
4	6.228	2.799	1st Bend
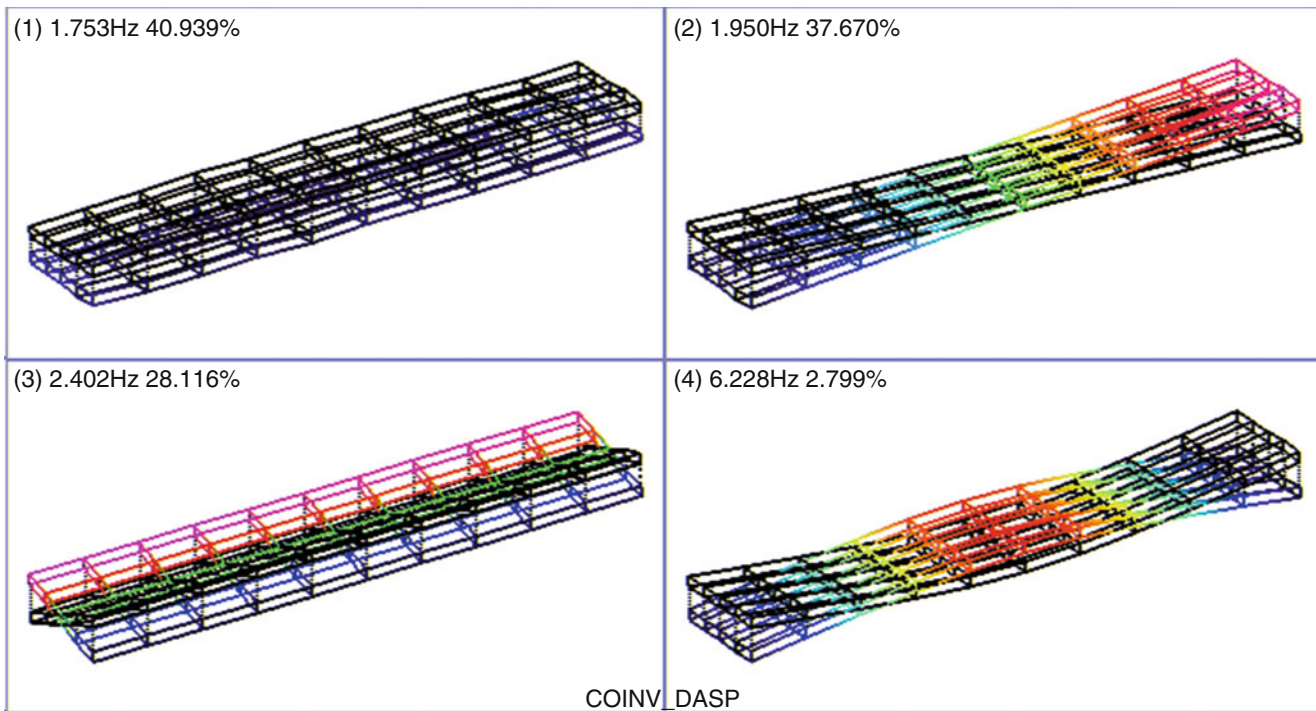
Fig. 13.6 4 orders modal shape

Considering the symmetry of the structure, the exciting points of MIMO test are chosen at the four corners with vertical direction, four groups of FRFs are obtained. The face of platform is divided to 10×4 gridding evenly. There are total 55 measuring points. The above and below platform face are looked with the same vibration, only vertical direction is measured. The transducer is type 941 made by Mechanics Academy of China Earthquake Bureau measuring velocity. The analysis frequency range is from 0 to 8 Hz.

Table 13.2 is the analysis result.

Figure 13.6 is 4 orders modal vibration shape.

The foremost 3 orders are coupled together seriously. The all FRFs are displayed at Fig. 13.7.

Figure 13.8 is the stability graph obtained by ERA algorithm, the curve in the graph is CMIF complex index function.

Figure 13.9 is stability obtained by PolyLSCF [3] algorithm.

Figure 13.10 is stability obtained by PolyIIR [4] algorithm.

Among three algorithms, the clearest stability grapy is obtained by ERA. But even with ERA algorithm, there are one or two points which are not in harmonious modal shape in rigid modes.

To construct the pure mode FRFs, the coefficients of each exciting points is listed as Table 13.3:

The four groups FRF multiplying by different coefficients listed at Table 13.3, construct one new pure group FRF. In Fig. 13.11 all pure FRFs are displayed with order 1 and order 4. The parameters of order 1 and order 4 can be identified separately considering only one mode in FRF, the vibration shape of Bound and 1st Bend are harmonious. In Fig. 13.12 all pure FRFs are displayed with order 2 and in Fig. 13.13 all pure FRFs are displayed with order 3.
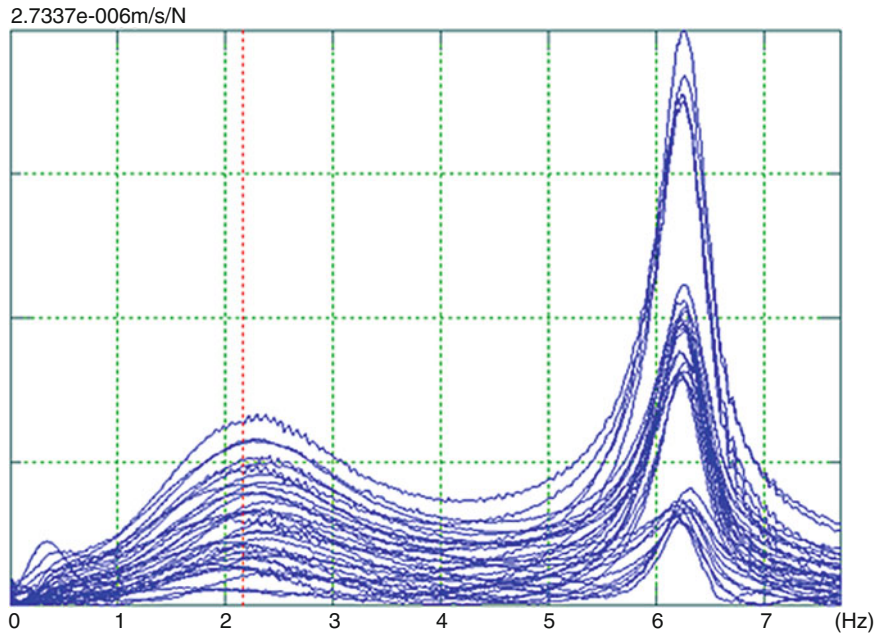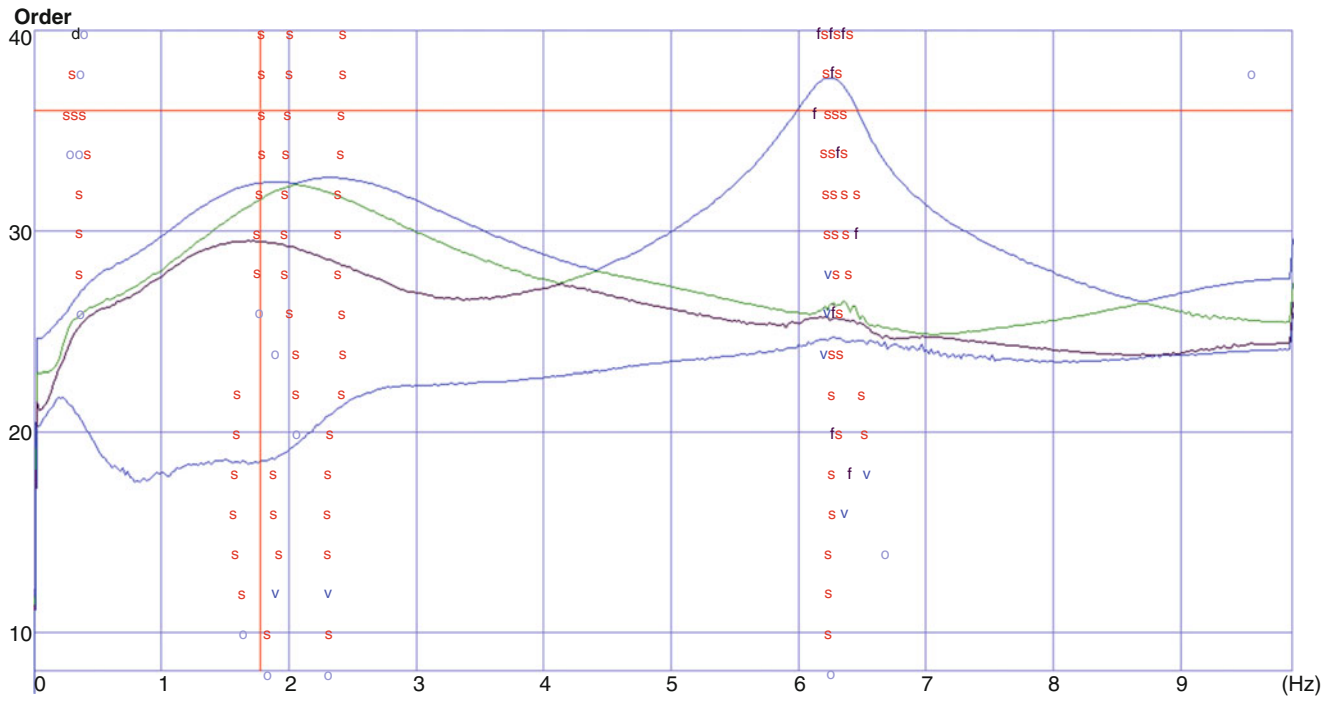
2.7337e-006m/s/N

Fig. 13.7 All FRFs display

Fig. 13.8 The stability graph obtained by ERA algorithm
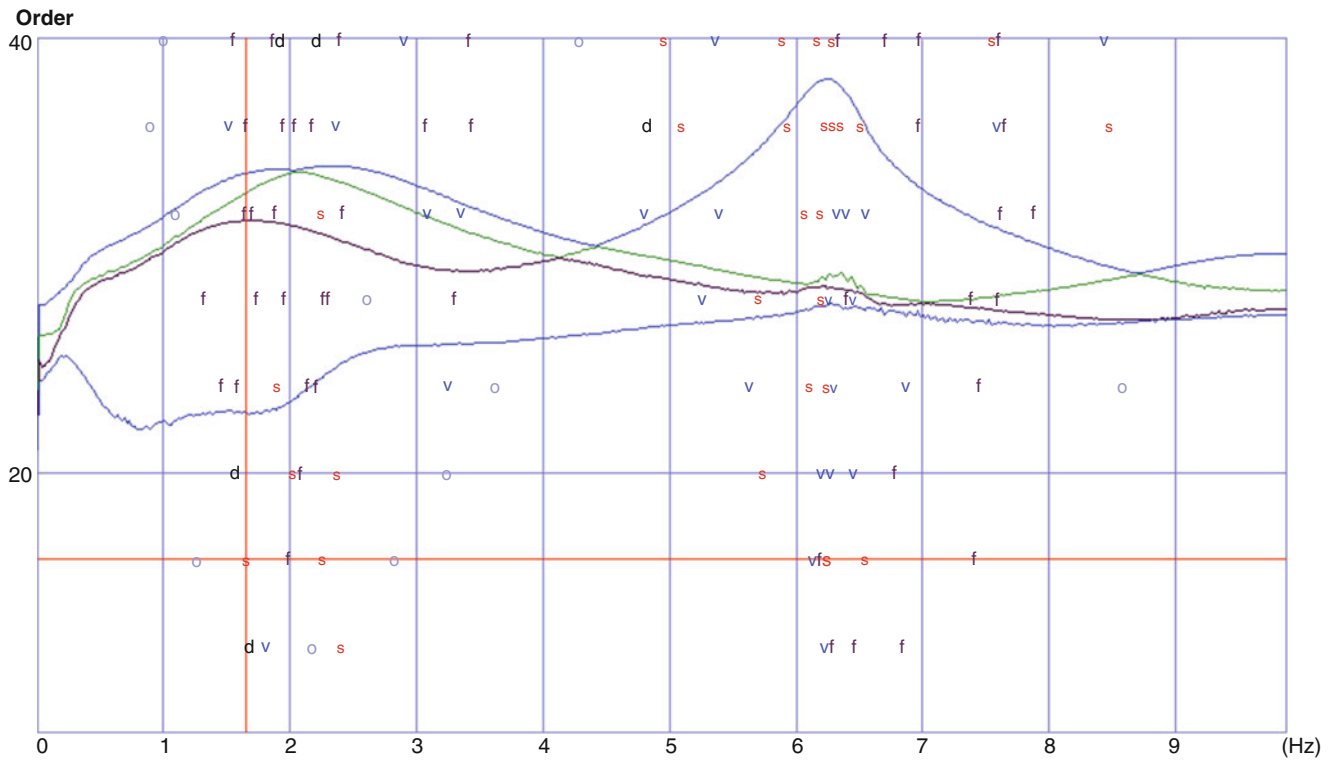
Fig. 13.9 The stability graph obtained by PolyLSCF algorithm
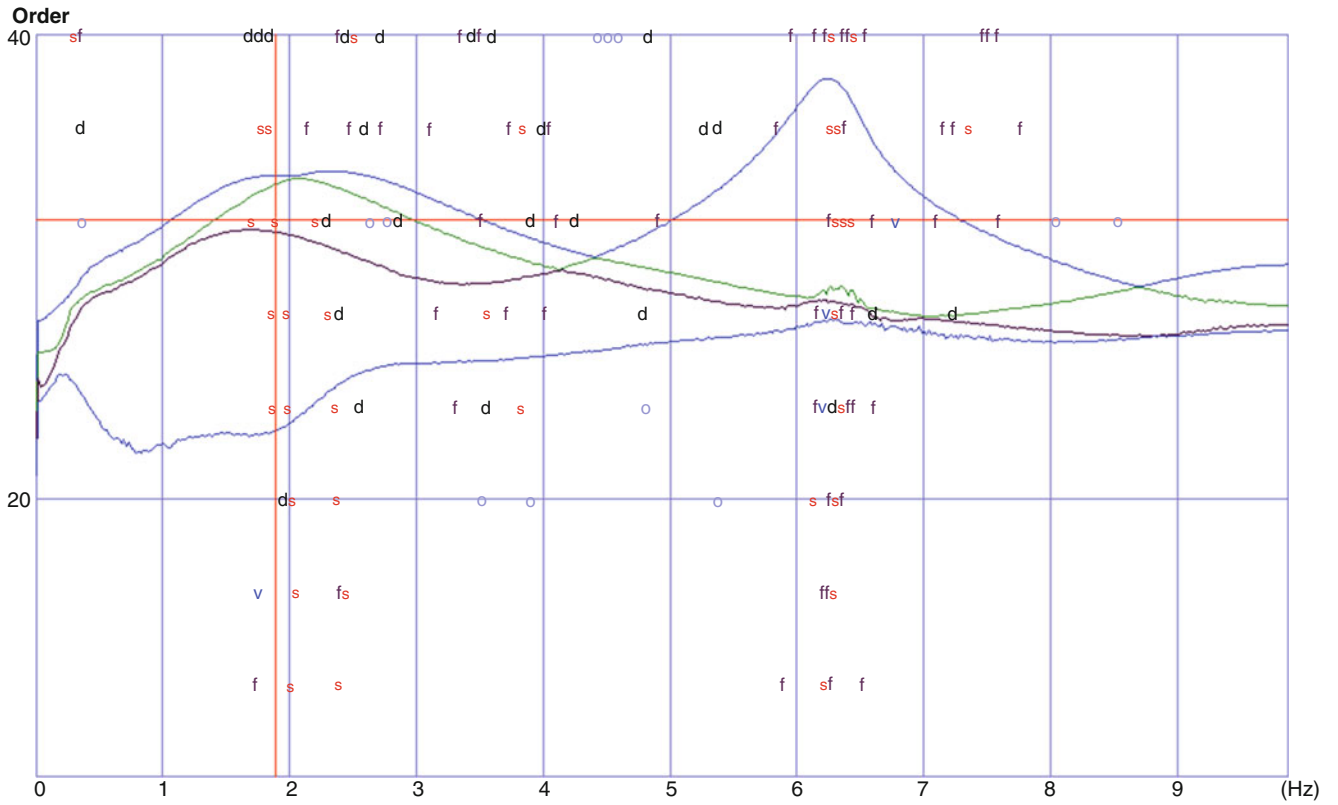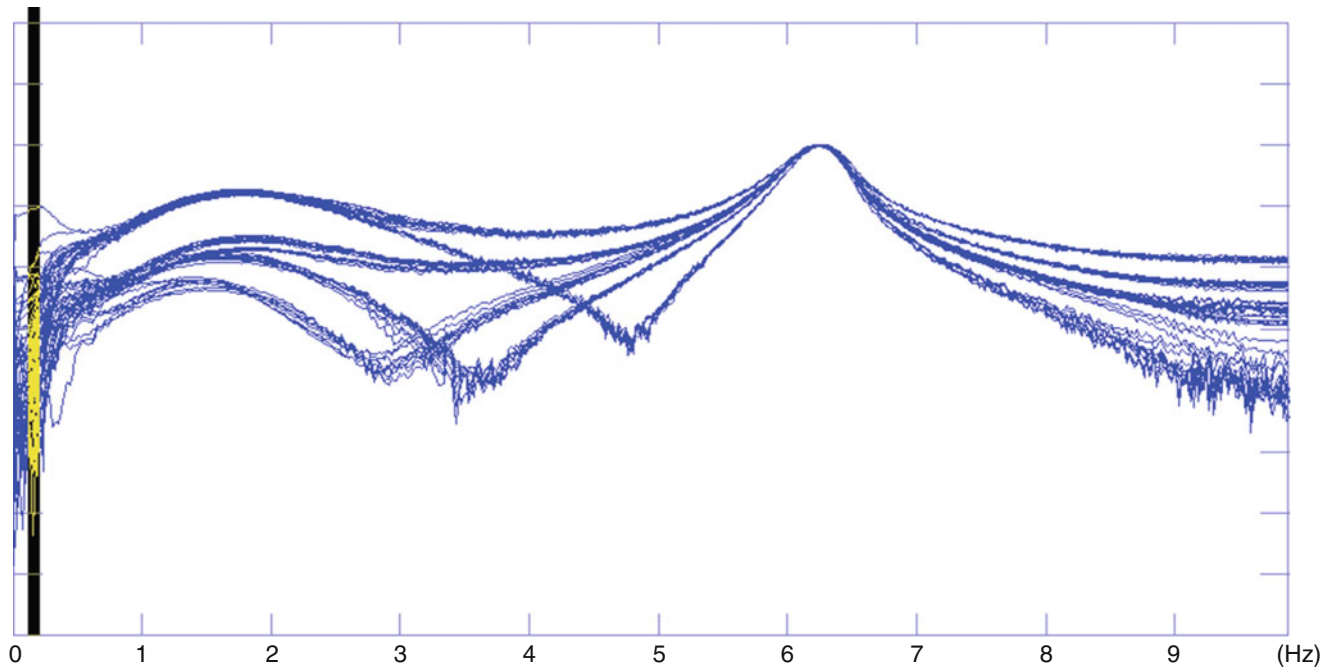

Fig. 13.10 The stability graph obtained by PolyIIR algorithm

Table 13.3 The coefficients of 4 exciting point

Order	Exc. point 1	Exc. point 2	Exc. point 3	Exc. point 4	Shape illustration
1	0.5	0.5	0.5	0.5	Bound
2	0.5	0.5	−0.5	−0.5	Pitch
3	0.5	−0.5	0.5	−0.5	Roll
4	0.5	0.5	0.5	0.5	1st Bend

Fig. 13.11 All pure FRFs displayed with order 1 and order 4

13.4   Conclusion

1. In SIMO and MISO test, the pure modal FRF algorithm can identify modal parameters at the condition of light damping and the nearest modal frequency being $2\Delta f$ away.

2. For MIMO test, the MvMIF theory is used to obtain one group pure FRFs. The preciseness of identified parameters is depending on the minimum value of MvMIF, which is determined by the number and position of exciting points. If the number of exciting points is enough and their positions are properly separated, even the repeat modes' parameters can be identified easily.

3. For the pure mode algorithm introduced here, if one pure FRF is obtained in SIMO or MISO test, or one group of pure FRFs are obtained in MIMO test, the process of parameter identification is very simple because only one mode is including in the pure FRF. The computation speed is faster than any other algorithms. The modal vibration shape will be more harmonious when other algorithms failed to extract harmonious modal vibration shape.

4. From the engineering example, it is obvious that the modal frequency can be displayed directly in pure FRFs even the original FRFs are seriously coupled with great modal damping ratio.

5. The new algorithm develops the MvMIF theory. The original MvMIF curve can tell the mode's position and closeness. The new algorithm can identified the modal parameters further and by the minimum value of MvMIF, whether the number of exciting points is great enough and their position is chosen properly can also be known.
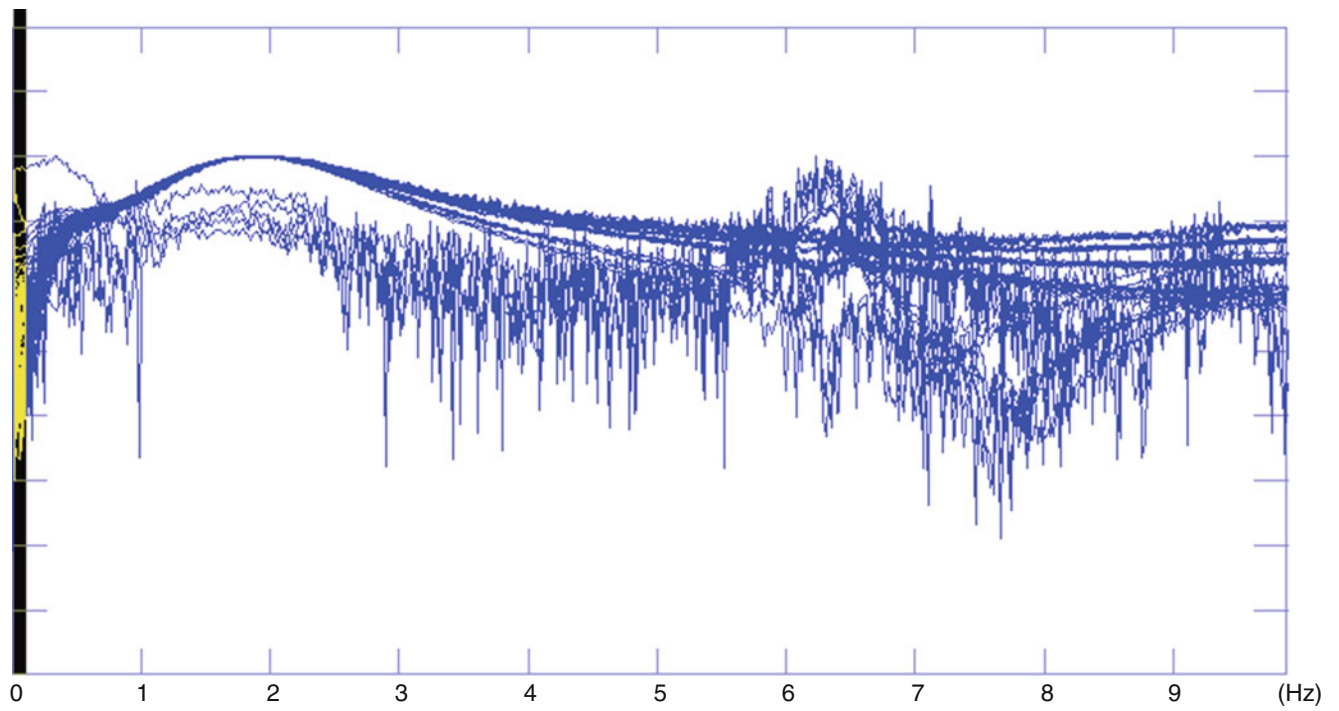
Fig. 13.12 All pure FRFs displayed with order 2
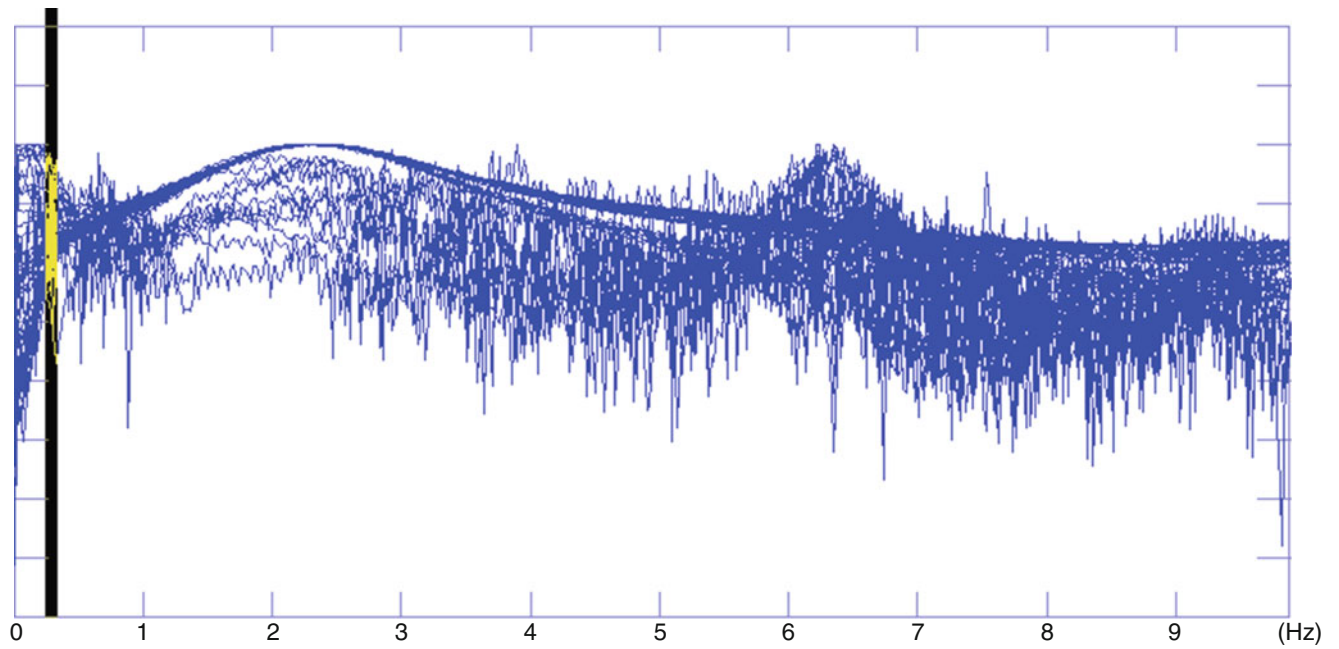
Fig. 13.13 All pure FRFs displayed with order 3

References

1. Liu, J.M., Lu, Q.H., Ying, H.Q.: The best force design of pure modal test based upon a singular value decomposition approach, advanced aerospace applications, volume 1. Conf. Proc. Soc. Exp. Mech. Ser. **4**, 119-129 (2011). doi:10.1007/978-1-4419-9302-1_11
2. Heylen, W., Lammeans, S., Sas, P.: Modal Analysis Theory and Testing. KU Leuven, Belgium (1998)
3. Coleman, R.E., Allemang, R.J.: Experimental Structural Dynamics, 2004, Author House
4. Liu, J.M., Dong, S.W., Ying, M., Shen, S.: Dynamic parameters identification technology in bridge health monitoring. In: Proceeding of the 14th Asia Pacific Vibration Conference, HongKong, December 2011
5. William, R.: The Multivariate Mode Indicator Function in Modal Analysis Proc, 3th IMAC 1985
6. Nash, M.: Use of the multivariate mode indicator function for normal mode determination. In: Proceedings of 6th IMAC, 1988

Chapter 14
The Influence of Parameter Choice in Operational Modal Analysis: A Case Study

Volkmar Zabel, Filipe Magalhães, and Christian Bucher

Abstract Even if the development of several software packages has facilitated the performance of experimental and operational modal analysis in recent years, modal identification is still a complex task which requires experience and a solid theoretical background of the analyst since the results are influenced by several factors. One of these factors that may have a significant influence on the results is the choice of parameters that govern the respective algorithm. Even though it is generally well known by experienced analysts that the parameter choice has an influence on both the performance of an algorithm and the results, this topic has been hardly addressed in literature. The influence of some of these parameters on the identification of modal parameters by means of the covariance-driven SSI and the Poly-reference least-squares complex frequency domain method (p-LSCF) were investigated in a case study. For several modes, clear trends related to respective analysis parameters became obvious. Even though such clear findings could not be identified for all modes, respective influences and resulting uncertainties were observed and quantified.

Keywords Operational modal analysis • Stochastic subspace identification • p-LSCF • Parameter choice • Uncertainty quantification • Railway bridge

14.1 Introduction

Operational modal analysis has become a well established and very popular tool to determine modal parameters of a system without measuring the excitation. Most algorithms were originally developed from classical experimental modal analysis methods assuming respective statistical properties for the unknown input. While in some methods the data is analyzed in time domain, other algorithms refer to frequency domain.

The probably most widely used frequency domain algorithms are the frequency domain decomposition (FDD) [3, 4] and the Poly-reference least-squares complex frequency domain method (p-LSCF) [6] which is also known under the name PolyMAX [14–16]. With respect to time domain, the stochastic subspace identification (SSI) methods are probably most established. The most prominent SSI algorithms are the data-driven SSI (SSI-DATA) [21–23], and the covariance-driven SSI (SSI-COV), [12, 13]. Overviews about these and further operational modal analysis methods are given, for example, in [9, 12, 18, 19].

Many modal analysis algorithms, the so-called parametric methods, are based on the identification of parameters of a mathematical model such as state space or fraction polynomial models. In a second step of analysis, the modal parameters are derived from the respective identified system. One difficulty with respect to these methods is that the order of the

---

V. Zabel (✉)

Institute of Structural Mechanics, Faculty of Civil Engineering, Bauhaus-University Weimar, Marienstraße 15, 99421 Weimar, Germany
e-mail: volkmar.zabel@uni-weimar.de

F. Magalhães

Laboratory of Vibrations and Structural Monitoring (ViBest), Faculty of Engineering, University of Porto, R. Dr. Roberto Frias, s/n, 4200-465 Porto, Portugal
e-mail: filipema@fe.up.pt

C. Bucher

Vienna University of Technology, Faculty of Civil Engineering, Institute for Building Construction and Technology, Karlsplatz 13, A-1040 Vienna, Austria
e-mail: christian.bucher@tuwien.ac.at

corresponding mathematical model is usually unknown. Even though approaches for the identification of the model order have been proposed, as for example in [5, 12, 13], the most common approach to select those solutions that are related to physical modes is based on stabilization diagrams. Each solution indicated in a stabilization diagram refers to one set of modal parameters.

According to experience, the modal parameters of any single mode estimated from the same set of data but for different orders of the mathematical system model usually deviate to a certain extent. The statistical characteristics of such a cluster of modal parameters can be expressed by a mean value and the respective standard deviation, as for example in [24].

These deviations occur due to uncertainties in the analysis of any single point estimate. Approaches to estimate the uncertainties of a point estimate with respect to several modal analysis methods were proposed, for example in [1, 2, 7, 8, 17, 20].

However, one aspect that is not very much considered in literature is the question of how much the result of a modal identification depends on the parameters that were chosen in system identification. Such parameters are, for example, the number of blocks in the block Hankel or Toeplitz matrix used within a covariance-driven SSI or the number of included frequency lines in an analysis applying the p-LSCF algorithm. This gave the motivation of the investigations described in this contribution.

14.2　Description of the Case Study

14.2.1　The Structure

As a case study, a railway bridge with a single span of 32.50 m is considered. It crosses a small river and is part of a highly frequented line in Germany. Both freight and passenger trains of different types are operated on the tracks passing the bridge.

The superstructures were erected in the so-called PREFLEX technology. Each bridge deck consists of several prefabricated, pre-stressed composite beams that were assembled on site and completed with in-situ concrete to form a composite steel-concrete cross-section. A brief description of the construction of a PREFLEX bridge deck as well as further notes about the bridge are given in [25].

As it is typical for many railway bridges, the deck consists of two adjacent superstructures which can be considered as statically independent simply supported beams, each carrying one track laid on ballast. The ballast bed is continuous over the two superstructures. Therefore, the ballast, which cannot be taken into account as a structural member in a static analysis, contributes not only to the inertia but to a certain extent also to the stiffness of the structure. This can also be noticed in effects of a weak coupling of the two superstructures also influencing the dynamic behaviour of the bridge deck. A photograph of the track bed and a sketch of the cross-section are shown in Fig. 14.1.
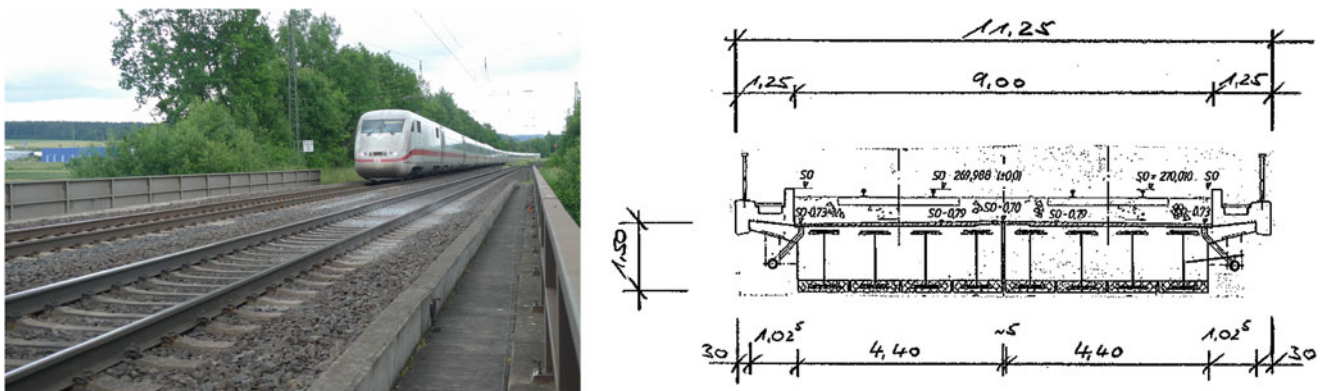

Fig. 14.1 Investigated railway bridge: tracks on ballast (*left*) and cross-section (*right*)
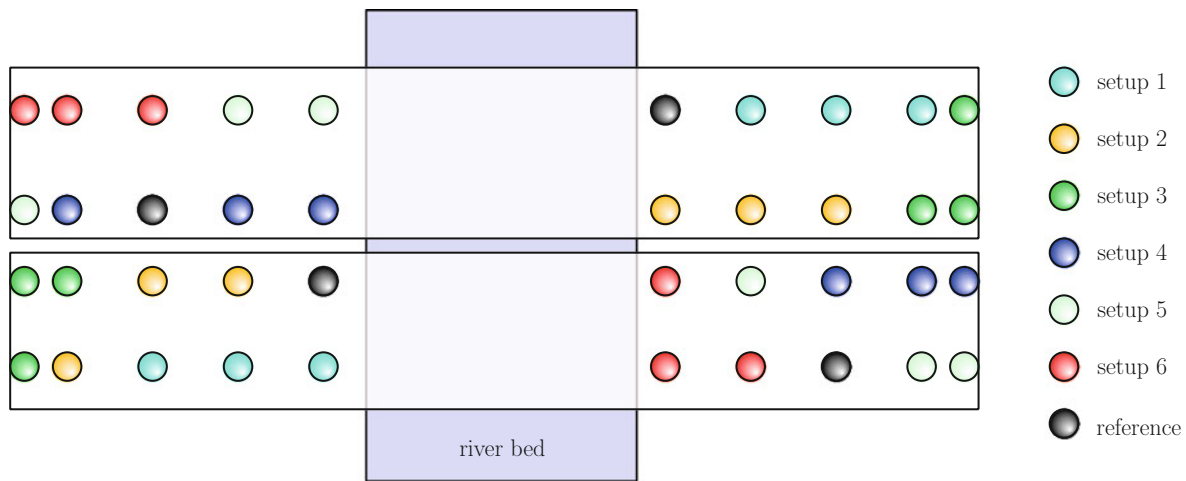
Fig. 14.2 Sketch of measuring points instrumented in six setups in plan

14.2.2   Vibration Measurements

As it is very common for vibration measurements on small and medium size railway bridges, the dynamic tests were carried out as a one-day campaign. All sensors had to be installed on the bottom side of the bridge since the operation of the trains could not be interrupted for the tests. During the measurements only the structural response in vertical direction was measured by means of seismic accelerometers with a nominal sensitivity of $1 \frac{V}{g}$. To increase the excitation of as many modes as possible, multiple impulses were imposed to the bridge deck from underneath during the measurements.

The accessibility of the bridge deck from underneath was limited to the areas to both sides of the river, an installation of accelerometers in the central third of the span was not be possible. Therefore, the resulting spacial resolution did not allow for a complete graphical representation of all identified mode shapes. However, it was well possible to assign the identified modes to typical mode shapes by means of experience and a finite element model.

The measurements were performed using six sensor setups with four reference and six roving sensors. Figure 14.2 gives an overview about the location of the resulting 40 measuring points and their organization in the setups.
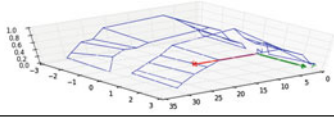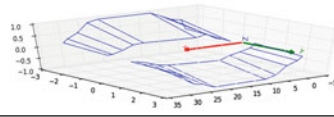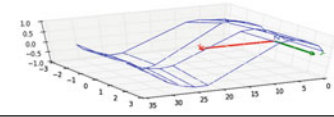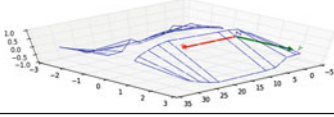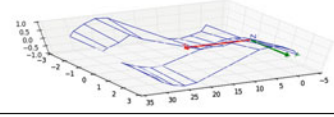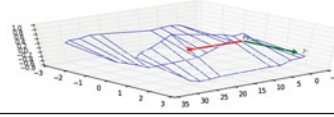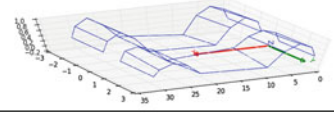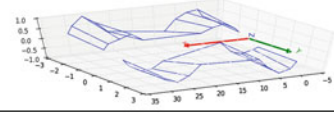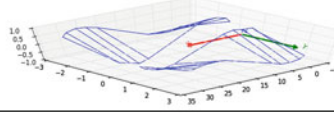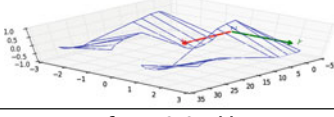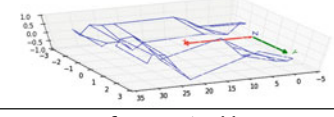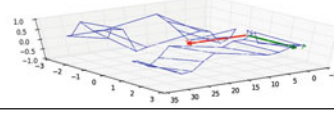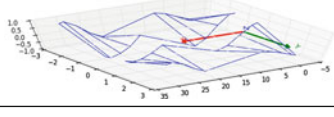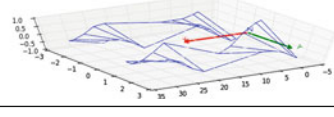
Due to the fact that it is hardly possible to identify modes with a reasonable quality from signals acquired during train passages, the measurements had to be performed during breaks between train passages. As the traffic density over the investigated bridge was relatively high, each of the measurements was only approximately 3 min long. During the tests, the environmental conditions did not change significantly, the measured air temperature underneath the bridge varied between approximately 16 and 19 °C.

14.3   Data Processing and Modal Analyses

To obtain an overview about the modes that can be identified from the measured data, first operational modal analyses by means of both the SSI-COV and the p-LSCF methods were performed. In both cases, the reference-based versions of the algorithms were applied, using the signals acquired at the four reference sensor locations also as references in the modal identification. Prior to the modal analysis, the time series were decimated from an original sampling rate of 2048 Hz by a factor of 16 which resulted in a sampling rate of 128 Hz. To merge the modal parameters estimated from the different setups, both the post separate estimation re-scaling (PoSER) [9] and the post global estimation re-scaling (PoGER) [11] and [9] strategies were used. From theses analyses 14 modes could be identified.

An overview about these identified mode shapes and respective natural frequencies is given in Table 14.1. Both, mode shapes and natural frequencies are the results of point estimates. From the identified mode shapes one can already conclude that the dynamic behaviour of the bridge is clearly influenced by a weak coupling between the two superstructures.

Table 14.1 Summary of identified mode shapes

f = 3.52 Hz 1st order bending, in phase	f = 7.04 Hz 1st order bending, anti-phase with torsion	f = 11.77 Hz 2nd order bending, in phase
f = 11.97 Hz 1st order torsion, anti-phase	f = 14.96 Hz 2nd order bending	f = 21.24 Hz 1st order torsion, in phase
f = 23.89 Hz 3rd order bending, in phase	f = 25.68 Hz 3rd order bending, anti-phase	f = 26.90 Hz 2nd order torsion, anti-phase
f = 31.40 Hz 2nd order torsion, in phase	f = 38.88 Hz 4th order bending, in phase	f = 40.01 Hz 4th order bending, anti-phase
f = 53.37 Hz 3rd order torsion, anti-phase	f = 55.14 Hz 3rd order torsion, in phase	

14.3.1 Analysis by Means of the SSI-COV/Ref Method

Apart from the pre-processing of the measured data, the choice of parameters for the respective modal identification algorithm has an influence on the results of the analysis. In case of the SSI-COV method, such a parameter is the number of blocks considered in the block-Hankel or block-Toeplitz matrix. In the study presented here, the number of block columns and block rows were chosen to be the same and varied from 100 to 440 in steps of 10. Based on each of these matrices, system matrices of model orders up to 200 were identified.

To facilitate the numerical investigations the whole process had to be automated. Therefore, the methodology of post global estimation re-scaling (PoGER) was chosen as merging strategy for the data from the six setups. Furthermore, the selection of the modal parameters of the identified modes had to be selected automatically as well. For this purpose a set of reference solutions for the 14 identified modes was chosen first. Then those solutions of each analysis were assigned to a respective reference mode that satisfied the conditions:

- $0.95 f_{r,ref} \leq f_{r,i} \leq 1.05 f_{r,ref}$,
- $0.00 \leq \zeta_{r,i} \leq 0.10$,
- $MAC(\varphi_{r,ref}, \varphi_{r,i}) > 0.95$.

Here $f_{r,i}$ and $f_{r,ref}$ denote the rth natural frequency of solution i and of the reference solutions while $\zeta_{r,i}$ refers to the modal damping ratio of mode r of solution i. The respective MAC value between the reference shape $\varphi_{r,ref}$ and the one of solution i, $\varphi_{r,i}$ is denoted by $MAC(\varphi_{r,ref}, \varphi_{r,i})$.

Following this approach, for each mode a set of modal parameters corresponding to different model orders was selected from the results referring to a specific number of block columns of the block-Hankel or block-Toeplitz matrix.

14.3.2 Analysis by Means of the p-LSCF Method

The p-LSCF method was applied after decimating the time series by a factor of 32 such that the a sampling frequency of the analyzed data became 64 Hz. This decision was taken since the identification of the first mode with lower decimation orders was less clear. As in the analysis with the SSI, the four reference channels of the test were also chosen as references in the modal analysis.

Furthermore, the merging strategy of post global estimation re-scaling (PoGER) was also applied in the p-LSCF analysis. This means that all setups were processed together without pre-scaling of the spectral matrices associated with each setup, the scaling was performed after identification of the mode shapes using the reference degrees of freedom.

In order to study the sensitivity of the results to the parameters of the method, the number of spectral lines of the halfspectra, estimated from the collected acceleration time series, in the frequency interval under analysis (0–32 Hz), was varied from 128 to 4096. For each number of spectral lines the order of the model fitted to the data was varied from 5 to 50. The results were then organized in stabilization diagrams. Figures 14.3, 14.4, and 14.5 show the stabilization diagrams for the results obtained with 128, 1024 and 2048 spectral lines, respectively.
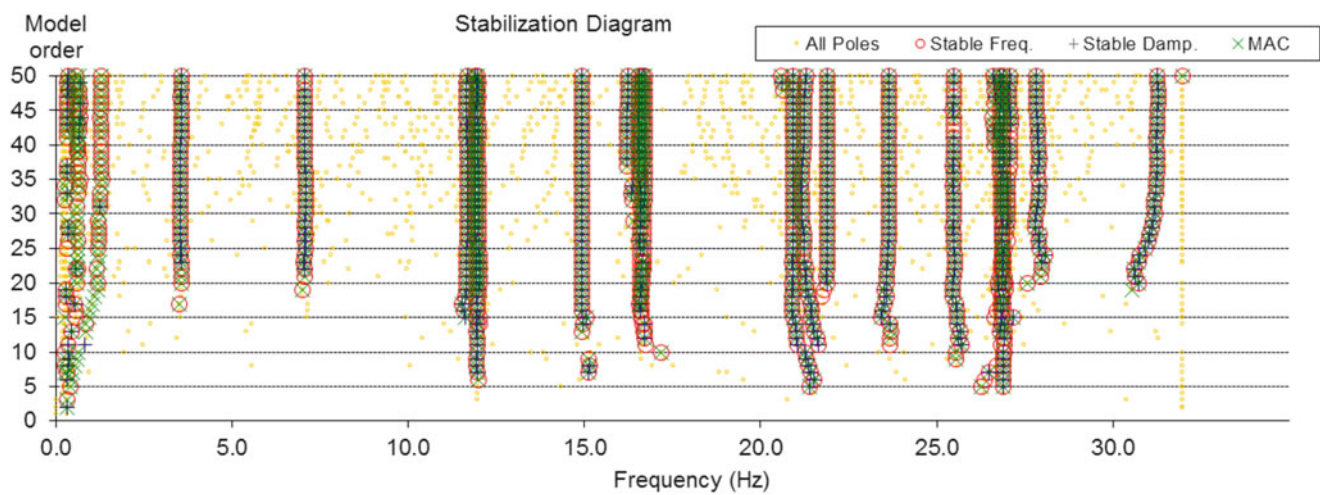
Fig. 14.3 Stabilization diagram of the p-LSCF analysis with 128 frequency lines
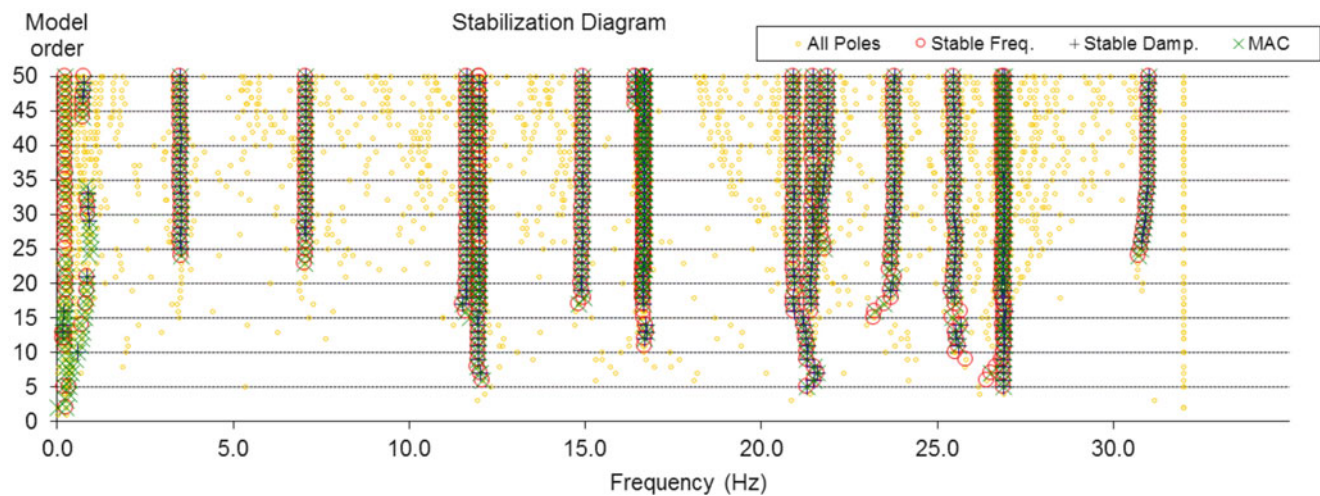
Fig. 14.4 Stabilization diagram of the p-LSCF analysis with 1024 frequency lines
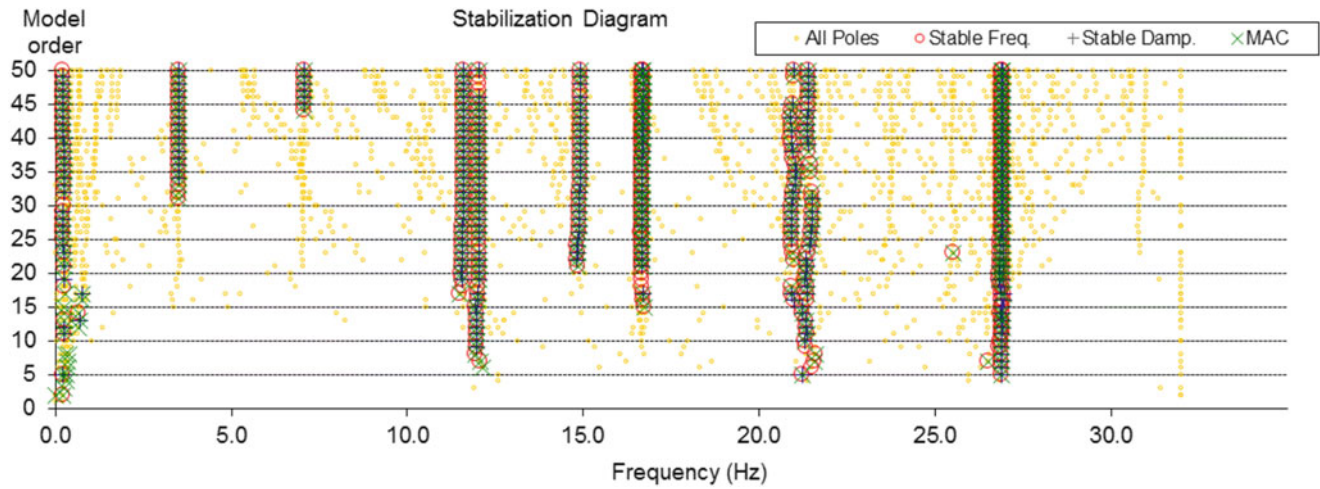
Fig. 14.5 Stabilization diagram of the p-LSCF analysis with 2048 frequency lines

These stabilization diagrams were post-processed by a hierarchical clustering analysis that groups the poles with similar natural frequencies and mode shapes. To assign the appropriate solutions to clusters referring to the same mode, Eq. (14.1) was used as metrics [10].

$$d_{i,j} = \left| \frac{f_i - f_j}{f_j} \right| + \left(1 - MAC_{i,j} \right) \leq 0.05 \tag{14.1}$$

14.4 Statistic Analysis of the Identified Modal Parameters

14.4.1 Results from the Analysis with SSI-COV

From the modal estimates the mean value and the coefficient of variation were computed to obtain information about the uncertainty with respect to the choice of the number of block columns of the block-Hankel or block-Toeplitz matrix and the selected model order. In Table 14.2 all computed mean values and coefficients of variation of the natural frequencies and modal damping ratios identified with the SSI-COV approach are summarized.

While the results collected in Table 14.2 represent the statistic parameters considering all identified results obtained for the respective modes, they do not give sufficient information about the distribution with respect to a specific chosen number of block columns of the block-Toeplitz matrix. To illustrate, that these distributions can be very different, two examples for the identified natural frequencies and modal damping ratios are given in Fig. 14.6. It is interesting that in case of the first mode, relatively clear trends for both the natural frequencies and damping ratios can be observed while the plots suggest for the mode with $\bar{f}_r = 26.86$ Hz a decrease of variance with increasing number of block columns of the block-Toeplitz matrix.

For the sake of enhanced clarity, the mean values and coefficients of variation of both natural frequencies and modal damping ratios were computed for all chosen numbers of block columns. Figures 14.7 and 14.8 show the mean values and coefficients of variation of the two modes that were already considered in Fig. 14.6 for all chosen numbers of block columns. The data presented in these diagrams seems to confirm the observations from Fig. 14.6. It indicates that both the mean values and uncertainties converge with increasing number of block columns of the block-Toeplitz matrix. This observation applies to several other modes as well, but cannot be generalized. It has also to be mentioned that some modes were not well identified in all analyses.

Table 14.2 Mean values and coefficients of variation of the natural frequencies ($\bar{f}_r$, $COV(f_r)$) and modal damping ratios ($\bar{\zeta}_r$, $COV(\zeta_r)$) identified with the SSI-COV method

$\bar{f}_r$ (Hz)	$COV(f_r)$ (%)	$\bar{\zeta}_r$ (%)	$COV(\zeta_r)$ (%)
3.50	0.18	1.12	29.22
7.00	0.46	2.79	17.25
11.78	0.27	3.52	11.37
11.99	0.15	1.14	15.90
14.94	0.41	4.70	11.34
21.24	0.38	3.20	16.64
23.95	0.25	3.50	4.38
25.67	0.10	2.27	4.72
26.89	0.13	1.24	15.69
31.41	0.36	1.46	46.80
39.07	0.58	3.43	11.38
40.00	0.12	2.05	7.62
53.35	0.09	1.56	13.77
55.11	0.18	2.16	30.79
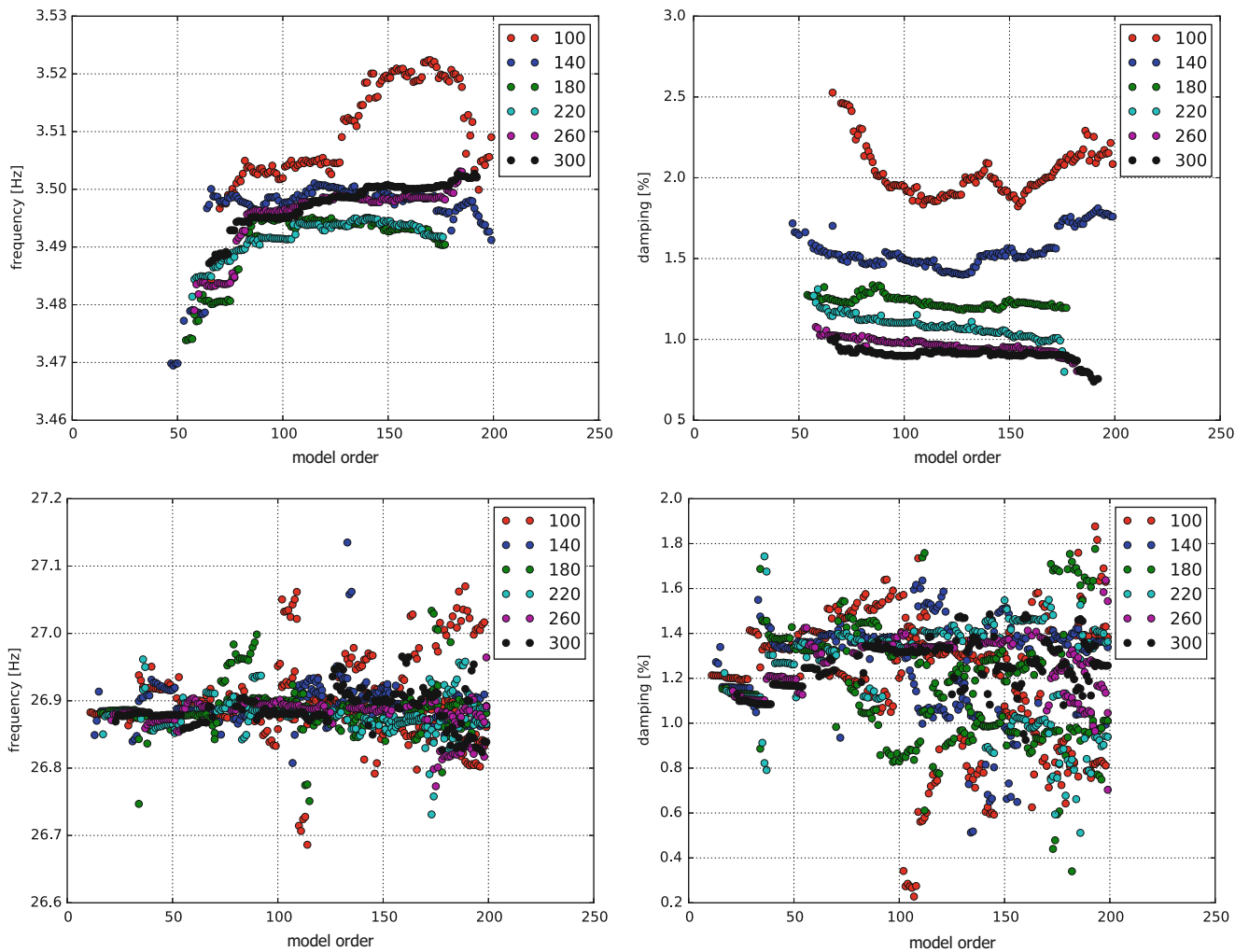
Fig. 14.6 Natural frequencies and modal damping ratios of the modes with $\bar{f}_r = 3.50$ Hz (*top*) and $\bar{f}_r = 26.86$ Hz (*bottom*) identified with the SSI-COV for 100, 140, 180, 220, 260 and 300 block columns
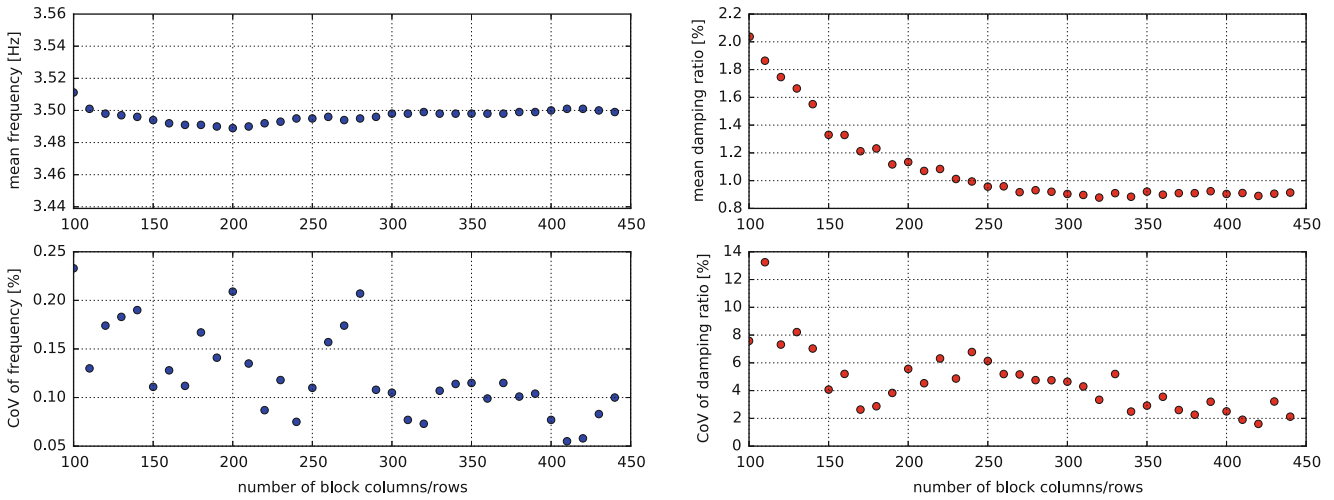
Fig. 14.7 Mean values and corresponding coefficients of variation of the natural frequencies (*left*) and modal damping ratios (*right*) identified with the SSI-COV for the mode with $\bar{f}_r = 3.50$ Hz for all chosen numbers of block columns
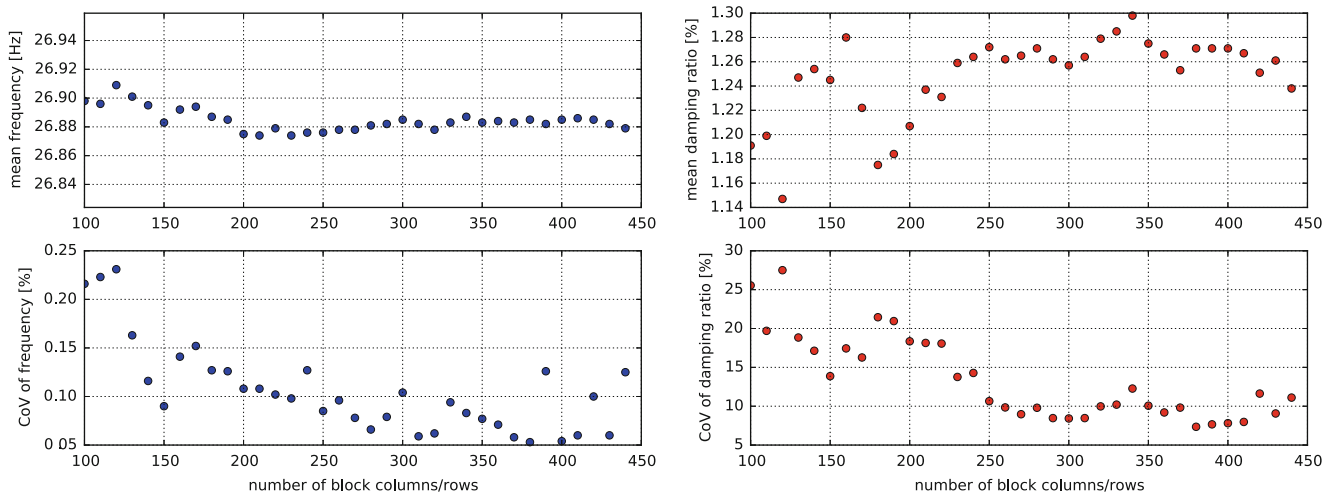
Fig. 14.8 Mean values and corresponding coefficients of variation of the natural frequencies (*left*) and modal damping ratios (*right*) identified with the SSI-COV for the mode with $\bar{f}_r = 26.86$ Hz for all chosen numbers of block columns

Table 14.3 Mean values and coefficients of variation of the natural frequencies ($\bar{f}_r$, $COV(f_r)$) and modal damping ratios ($\bar{\zeta}_r$, $COV(\zeta_r)$) identified with the p-LSCF algorithm

$\bar{f}_r$ (Hz)	$COV(f_r)$ (%)	$\bar{\zeta}_r$ (%)	$COV(\zeta_r)$ (%)
3.53	0.40	0.74	25.12
7.08	0.10	1.19	42.73
11.77	1.28	2.72	39.97
12.01	0.18	1.17	27.49
14.93	0.10	3.88	35.36
20.97	0.69	2.54	41.50
23.70	0.32	1.81	49.19
25.48	0.16	1.42	50.72
26.91	0.23	1.46	84.92

14.4.2　Results from the Analysis with p-LSCF

The results obtained from the identification by means of the p-LSCF algorithm were analyzed in the same way as described in Sect. 14.4.1 for the results obtained by applying the SSI. In Table 14.3 the mean values and coefficients of variation of the identified natural frequencies and corresponding damping ratios are summarized.
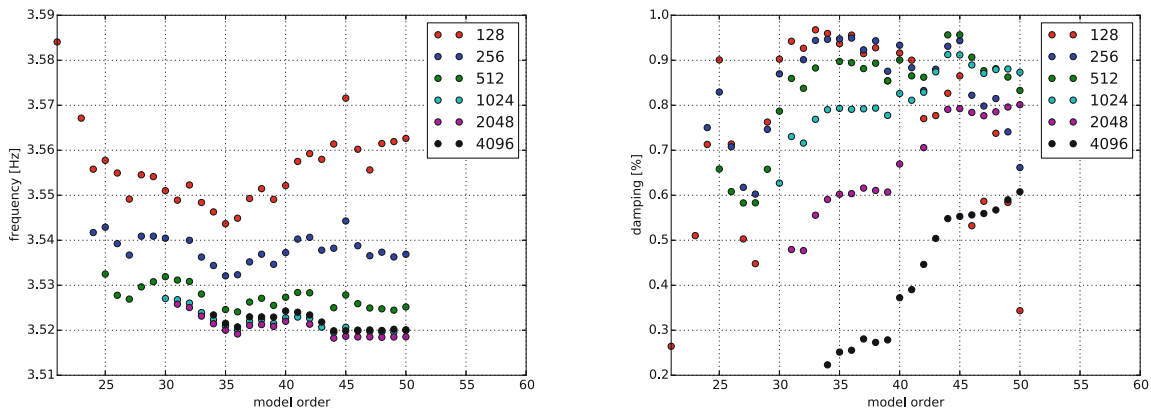
Fig. 14.9 Natural frequencies and modal damping ratios of the mode with $\bar{f}_r = 3.53$ Hz identified with the p-LSCF for 128, 256, 512, 1024, 2048 and 4096 spectral lines
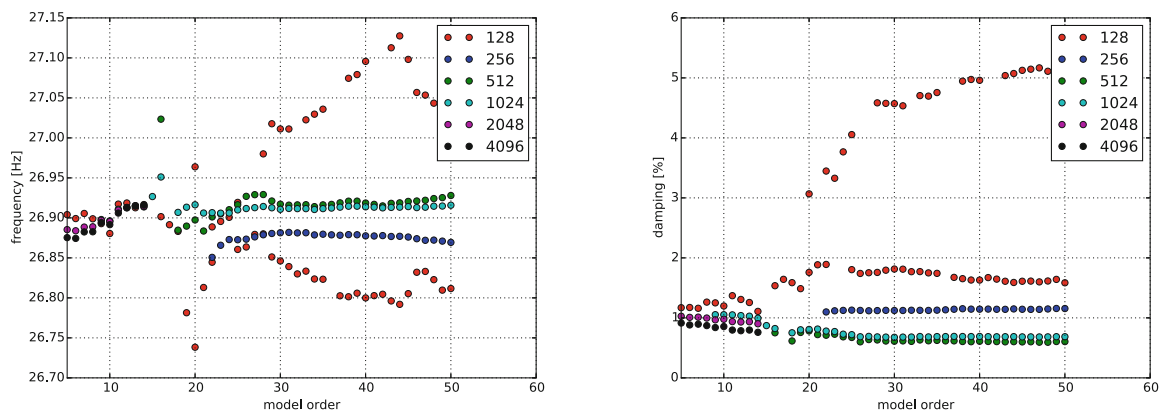
Fig. 14.10 Natural frequencies and modal damping ratios of the mode with $\bar{f}_r = 26.91$ Hz identified with the p-LSCF for 128, 256, 512, 1024, 2048 and 4096 spectral lines

These results are similar to those identified by applying the SSI-COV. Major differences in the values can be noticed in the results for the damping ratios. However, one has to take into account, that the results are related to the complete analysis including the modal identification, merging and the automatic selection. Furthermore, the maximal number of model orders chosen in the two analyses were not the same.

For a better interpretation of the statistical parameters, the respective samples for the two modes identified with mean natural frequencies of 3.53 and 26.91 Hz are illustrated in Figs. 14.9, 14.10, 14.11, and 14.12.

For the first mode, the diagrams suggest that the identified modal parameters converge with increasing number of chosen frequency lines and increasing model order. In case of the mode with $\bar{f}_r = 26.91$ Hz, this observation cannot completely be confirmed. The major reason for the difference comes from the fact that this mode could not be well identified at higher model orders from the analyses with higher numbers of chosen spectral lines.

14.5   Conclusions

The investigations presented here have shown, that the results of an operational modal analysis by means of a parametric method depend on the choice of parameters chosen for the respective identification algorithm. Beside the modal analysis itself, also the used strategy to merge the modal parameters identified from different setups plays a significant role as well as the process of automatic mode assignment.
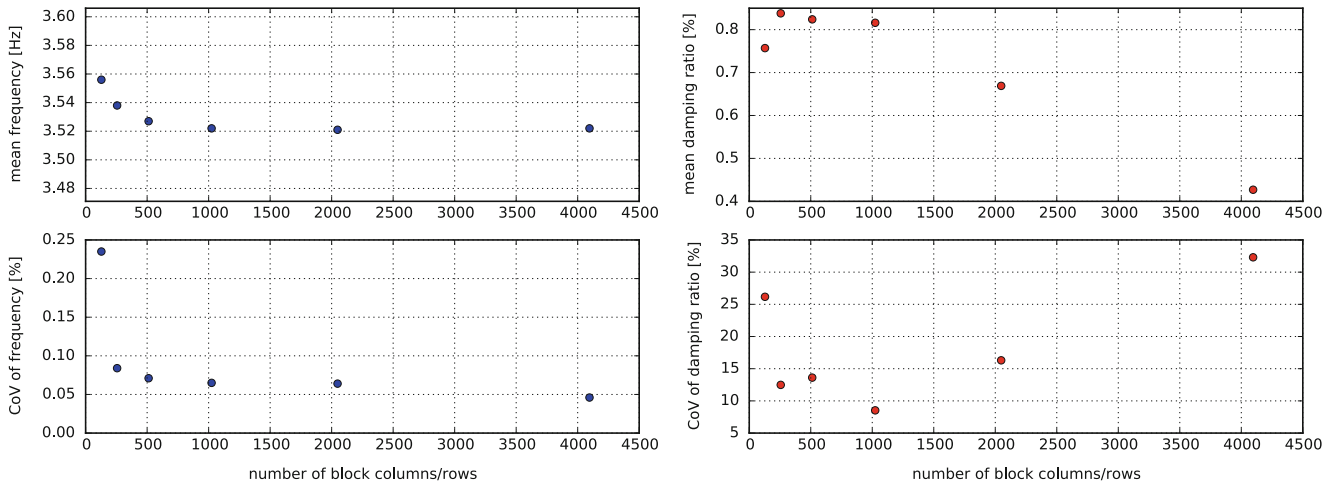
Fig. 14.11 Mean values and corresponding coefficients of variation of the natural frequencies (*left*) and modal damping ratios (*right*) identified with the p-LSCF for the mode with $\bar{f}_r = 3.53$ Hz for all chosen numbers of spectral lines
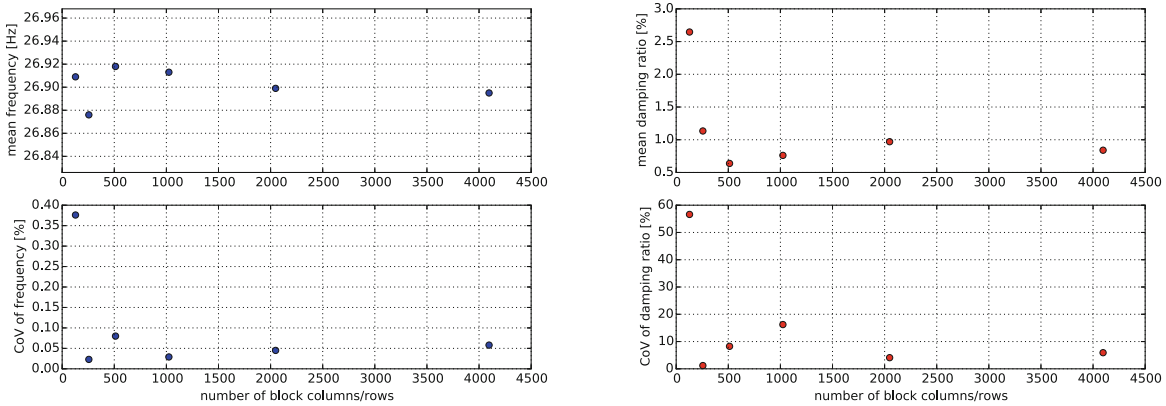
Fig. 14.12 Mean values and corresponding coefficients of variation of the natural frequencies (*left*) and modal damping ratios (*right*) identified with the p-LSCF for the mode with $\bar{f}_r = 26.91$ Hz for all chosen numbers of spectral lines

Fig. 14.13 Singular values of the power spectral density matrices referring to the six measurement setups
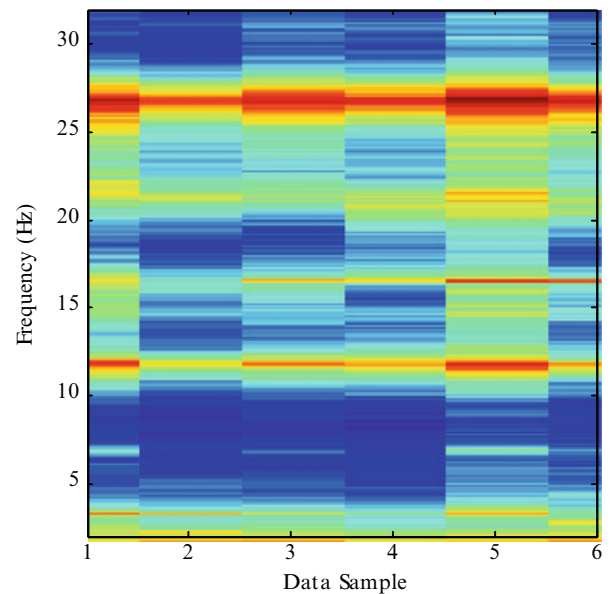
As, for example, can be seen in Figs. 14.6 and 14.10, in some analyses two or more poles were assigned to the same mode. The PoGER merging strategy assumes that the system is linear and time-invariant. In case of the investigated bridge, it is likely that at least the latter assumption was not completely true. As several trains passed the bridge between the measurements in different setups, it is easily possible that in particular the coupling between the two superstructures slightly varied which lead to respective variations of some modal parameters.

Furthermore, as is illustrated in Fig. 14.13 that shows the singular values of the power spectral density matrices computed for the six setups, not all modes were apparently excited with the same intensity in all setups. This leads to further uncertainties in the modal analysis.

Even though the investigations described in this article refer to a single case study, it is concluded that there are several parameters that have an influence on the uncertainty in the identified modal parameters. In some cases trends were well observable while this was not clearly the case for all modes. For generalizations with respect to an appropriate parameter choice, further investigations are necessary.

References

1. Andersen, P.: Identification of civil engineering structures using vector ARMA models. Ph.D. thesis, Aalborg University, Department of Building Technology and Structural Engineering, Aalborg, Denmark (1997)
2. Andersen, P., Brincker, R.: Estimation of modal parameters and their uncertainties. In: Proceedings of the 17th International Modal Analysis Conference (IMAC), Kissimmee, FL, pp. 323–329 (1999)
3. Brincker, R., Andersen, P., Zhang, L.: Modal identification from ambient responses using frequency domain decomposition. In: Proceedings of the 18th International Modal Analysis Conference (IMAC), San Anonio, TX, pp. 625–630 (2000)
4. Brincker, R., Andersen, P., Zhang, L.: Damping estimation by frequency domain decomposition. In: Proceedings of the 19th International Modal Analysis Conference (IMAC), Kissimmee, FL, pp. 324–330 (2001)
5. Cara, F.J., Jesús, J., Alarcón, E., Reynders, E., De Roeck, G.: Modal contribution and state space order selection in operational modal analysis. Mech. Syst. Signal Process. **38**, 276–298 (2013)
6. Cauberghe, B.: Applied frequency-domain system identification in the field of experimental and operational modal analysis. Ph.D. thesis, Vrije Universiteit Brussel, Faculteit Toegepaste Wetenschappen, Brussels (2004)
7. Döhler, M., Mevel, L.: Efficient multi-order uncertainty computation for stochastic subspace identification. Mech. Syst. Signal Process. **38**, 346–366 (2013)
8. Guillaume, P., Schoukens, J., Pintelon, R.: Sensitivity of roots to errors in the coefficient of polynomials obtained by frequency-domain estimation methods. IEEE Trans. Instrum. Meas. **38**(6), 1050–1056 (1989)
9. Magalhães, F.: Operational modal analysis for testing and monitoring of bridges and special structures. Ph.D. thesis, Universidade do Porto, Faculdade de Engenharia, Porto (2011)
10. Magalhães, F., Cunha, A., Caetano, E.: Online automatic identification of the modal parameters of a long span arch bridge. Mech. Syst. Signal Process. **23**, 316–329 (2009)
11. Parloo, E.: Application of frequency-domain system identification techniques in the field of operational modal analysis. Ph.D. thesis, Vrije Universiteit Brussel, Faculteit Toegepaste Wetenschappen, Brussels (2003)
12. Peeters, B.: System identification and damage detection in civil engineering. Ph.D. thesis, Katholieke Universiteit Leuven, Departement Burgerlijke Bouwkunde, Leuven (2000)
13. Peeters, B., De Roeck, G.: Reference-based stochastic subspace identification for output-only modal analysis. Mech. Syst. Signal Process. **13**(6), 855–878 (1999)
14. Peeters, B., Van der Auweraer, H.: PolyMAX: a revolution in operational modal analysis. In: Proceedings of the 1st International Operational Modal Analysis Conference (IOMAC), Copenhagen, April 2005
15. Peeters, B., Van der Auweraer, H., Guillaume, P., Leuridan, J.: The PolyMAX frequency-domain method: a new standard for modal parameter estimation? Shock Vib. **11**, 395–409 (2004)
16. Peeters, B., Vanhollebeke, F., Van der Auweraer, H.: Operational PolyMAX for estimating the dynamic properties of a stadium structure during a football game. In: Proceedings of the 23rd International Modal Analysis Conference (IMAC), Orlando, FL (2005)
17. Pintelon, R., Guillaume, P., Schoukens, J.: Uncertainty calculation in (operational) modal analysis. Mech. Syst. Signal Process. **21**, 2359–2373 (2007)
18. Rainieri, C., Fabbrocino, G.: Operational Modal Analysis of Civil Engineering Structures. Springer, New York, NY (2014)
19. Reynders, E.: System identification and modal analysis in structural mechanics. Ph.D. thesis, Katholieke Universiteit Leuven, Departement Burgerlijke Bouwkunde, Leuven (2009)
20. Reynders, E., Pintelon, R., De Roeck, G.: Uncertainty bounds on modal parameters obtained from stochastic subspace identification. Mech. Syst. Signal Process. **22**, 948–969 (2008)

21. Van Overschee, P., De Moor, B.: Subspace algorithms for the stochastic identification problem. In: Proceedings of the 30th Conference on Decision and Control, Brighton, December 1991
22. Van Overschee, P., De Moor, B.: Subspace algorithms for the stochastic identification problem. Automatica **29**(3), 649–660 (1993)
23. Van Overschee, P., De Moor, B.: Subspace Identification for Linear Systems – Theory, Implementation, Applications. Kluwer Academic Publishers, Dordrecht (1996)
24. Verboven, P., Guillaume, P., Cauberghe, B., Parloo, E., Vanlanduit, S.: Stabilization charts and uncertainty bounds for frequency-domain linear least squares estimators. In: Proceedings of the 21st International Modal Analysis Conference (IMAC), Kissimmee, FL (2003)
25. Zabel, V., Gössinger, J.: Modal analysis and numerical models of a typical railway bridge. In: Proceedings of the International Modal Analysis Conference IMAC-XXXII, Orlando, FL, February 2014

Chapter 15
Dynamic Modulus Properties of Objet Connex 3D Printer Digital Materials

Katherine K. Reichl and Daniel J. Inman

Abstract This paper examines the damping properties of digital materials from the Objet Connex 3D Printer from Stratsys. The Objet Connex printer is a unique 3D printer because in a single print job, ten different materials with different stiffness can be utilized. The printer utilizes two base materials and mixes them in different ratios to obtain varying stiffness levels. The first base material, VeroWhitePlus[TM] is a rigid opaque plastic and the second base material, TangoPlus[TM] is a rubbery translucent material. This 3D printer has a variety of applications including the development of metastructures for vibration suppression. It has been demonstrated that both the VeroWhitePlus[TM] and TangoPlus[TM] materials exhibit viscoelastic behavior but extensive studies have not be carried out to determine the Young's Modulus and loss factor data in terms of frequency. This paper is the first step towards that goal. The paper begins by going into more detail about the properties of the printer and examines some previous work on determining the material properties. Next, the test method used it outlined and lastly the experimental set-up is described. In order to obtain data for a high range of frequencies, the material must be tested at various temperatures.

Keywords Viscoelastic materials • Additive manufacturing • Oberst beam method • Passive damping • Vibration suppression

15.1 Introduction

Additive manufacturing (or 3D printing) has become increasing more popular across almost all engineering fields. The field of interest to the authors is in applications for metastructures to be used for vibration suppression [1, 2]. The specific 3D printer of interest is the Objet Connex printer for multiple reasons. Firstly, this printer is able to print rubber-like materials which exhibit viscoelastic properties which is of particular interest for vibration suppression [3]. This printer uses PolyJet printing technology which allows for the printer to easily mix to different base materials in various ratios to create a gradient of material with various rubbery levels. The PolyJet printing works much like an inkjet printer. The parts are made by depositing small dots of materials; the end result is a 3D part. For the digital materials the dots of material deposited switch from one base material to the other to create an end material that appears homogenous [4]. This also allows parts to be made in a single print with both rigid and rubber-like material. The University of Michigan's Design and Prototyping Lab Objet Connex printer is used to form the materials investigated here. The purpose of this paper is a step towards the determination of the viscoelastic material properties of the digital materials. The Object Connex printer has the capability to create a large number of materials but for this paper the focus will be on the digital materials created using the two base materials, VeroWhitePlus[TM] and TangoPlus[TM]. VeroWhitePlus[TM] is a rigid opaque material and TangoPlus[TM] is a rubber-like transparent material [5] (Fig. 15.1). Using these two base materials, ten different digital materials can be created [6]. These ten materials can be seen in Fig. 15.2 below. The more flexible materials are shown in various deformed state to give the readers a better idea of the flexibility of the materials. In the field of active composites and origami, H. Jerry Qi has done extensive work using the Objet Connex 3D printer and his papers provide many details the actual mechanisms the 3D printer utilizes [7].

Other researcher have begun to look at the dynamic properties of these materials [7, 8] but there has not been any comprehensive testing of the properties hence the experiments presented here. This paper does not provide a complete

K.K. Reichl (✉) • D.J. Inman

Department of Aerospace Engineering, University of Michigan, François-Xavier Bagnoud, 1320 Beal Avenue, Ann Arbor, MI 48109, USA

e-mail: reichl@umich.edu
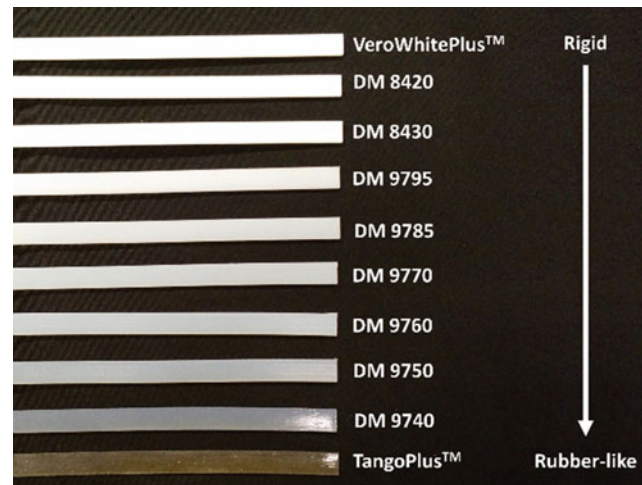
Fig. 15.1 Digital materials from the Objet Connex printer
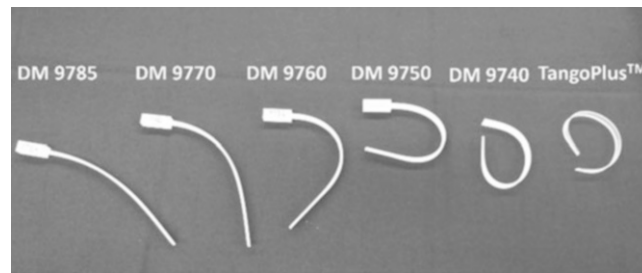
Fig. 15.2 The flexible digital materials from the Objet Connex in various deformed state

set of results but mostly describes the test methods to be utilized to obtain these complete results. The goal of the future work is to obtain data for Young's modulus and loss factor versus frequency for all ten of the digital materials under various conditions.

15.2 Test Method

The damping properties of these materials are determined using ASTM E756 (Standard Test Method of Measuring Vibration-Damping Properties of Materials) this is also known as the vibrating beam method or the Obsert beam method. This test method measures the loss factor, μ and the Young's modulus, E over a range of frequencies [9]. A variety of other authors provide additional information about the execution of this test, namely Jones's book on viscoelastic damping which describes the test method but also describes in detail the post-processing data requirements. He specifically goes into detail about creating the reduced-frequency nomogram and includes examples [10]. Another useful paper by Koruk and Sanliturk provides an overview of experimental considerations that should be taken into account to obtain reliable data [11].

The basis of the test method is to create a long cantilever beam such that the Euler-Bernoulli beam assumptions are satisfied. Modal analysis is performed on the beam and the natural frequencies and the half-power bandwidth are extracted from the resulting frequency response function (FRF). Since an analytical expression for the natural frequencies of an Euler-Bernoulli beam is known. The Young's modulus can be calculated from a measurement of the natural frequencies using the known geometry. Similarly, the loss factor is determined from the half-power bandwidth values. By looking at multiple natural frequencies, the modulus at various frequencies can be determined. To obtain the value at even more frequencies, a change in temperature is utilized. A change in temperature can be correlated to a change in frequency. Thus, testing in an environmental chamber can provide us with modulus and damping data at many different frequencies. This paper only performs testing at room temperature [10].

Fig. 15.3 Testing configurations (**a**) uniform beam, (**b**) modified Oberst beam, (**c**) sandwich beam

Table 15.1 List of materials tested and configuration used

Material	Testing configuration
VeroWhitePlus	Uniform
DM 8420	Uniform
DM 8430	Not tested
DM 9795	Not tested
DM 9785	Not tested
DM 9770	Not tested
DM 9760	Not tested
DM 9750	Not tested
DM 9740	Not tested
TangoPlus™	Not tested

Depending on the stiffness of the beam, different testing configurations should be utilized. These are shown above in Fig. 15.3. If the damping material is self-supporting the uniform beam configuration is used. For materials that are not self-supporting either the modified Oberst beam or the sandwich beam configurations are used. There is an additional configuration, known as the Oberst beam where damping material is applied on only one side on the beam. This is not ideal for testing at high temperatures because curling can occur, therefore the symmetric modified Oberst beam configuration is preferred [10]. For configurations that require a base beam, the bare base beam must be tested first to obtain its natural frequencies. Then the damping material is glued on and the resulting composite beam is tested to determine its natural frequencies. A stiff adhesive must be used to ensure the damping from the adhesive does not contribute to the damping calculations. The specific configurations used for the different digital materials are listed in Table 15.1. The following sections provide the equations needed to solve for the Young's modulus and loss factor data based off of the experimental measurements. It should be noted that multiple configurations may be necessary for some materials which undergo significant material property changes.

15.2.1   Uniform Beam

This testing configuration is to be used for material that are able to support themselves. The ASTM standard provides recommendations for the dimension of the beams. They recommend that they length of the beam should be between 180 and 250 mm and the beams tested in this paper have a length of 203 mm (8 in.). The recommended width is 10 mm which was used and they recommend the thickness to be between 1 and 3 mm. These beams are 3 mm thick.

When testing, a FRF must is obtained and the natural frequencies and half-bandwidth frequency determined from the FRF. The equations utilized to obtain the desired properties are derived from the standard cantilever beam equations for calculating the natural frequency of a beam. These are also list the ASTM standard [9] and are:

$$E = \frac{12\rho l^4 f_n^2}{H^2 C_n^2} \tag{15.1}$$

$$\eta = \frac{\Delta f_n}{f_n} \tag{15.2}$$

Where,

C_n = coefficient for mode n, of clamped-free beam
E = Young's modulus of beam material, Pa
f_n = the resonance frequency for mode n, Hz
Δf_n = the half-power bandwidth of mode n, Hz
H = thickness of beam in vibration direction, m
ℓ = length of beam, m
n = mode number: 1, 2, 3, . . .
η = loss factor of beam material, dimensionless
ρ = density of beam, kg/m^3

15.2.2 Modified Oberst Beam

This configuration is used when the material is not self-supporting but still relatively stiff. The ASTM suggests this configuration should be used for materials with a Young's modulus approximately greater than 100 MPa. If lower, the sandwich beam configuration should be used. A base beam is utilized and care must be taken when determining the geometric dimensions of both the base beam and the thickness of the damping material. The equations take advantage of the changes in properties from the base beam to the composite beam, thus these changes must be significant. The same recommendations are given for the base beam for this configuration as were given for the uniform beam. It is also suggested that the damping material has the same thickness as the base beam to begin. Then varied in order to ensure adequate difference in values from the base beam. Additionally, the term $(f_m/f_n)^2 (1 + DT)$ should be equal to or greater than 1.01. If this condition is not met, the geometric of the testing specimen should be modified such that the condition is met. The used to calculate the material properties at the natural frequency are derived in Jones [10] and the resulting equations are:

$$E_1 = E \frac{(f_m/f_n)^2 (1 + DT) - 1}{8T^3 + 12T^2 + 6T} \tag{15.3}$$

$$\eta_1 = \eta_m + \frac{E\eta_m}{E_1 (8T^3 + 12T^2 + 6T)} \tag{15.4}$$

Where,

$D = \rho_1/\rho$, density ratio, dimensionless
E = Young's modulus of base beam, Pa
E_1 = Young's modulus of damping material, Pa
f_n = resonance frequency for mode n of base beam, Hz
f_m = resonance frequency for mode m of the composite beam, Hz
Δf_m = the half-power bandwidth of mode m of the composite beam, Hz
H = thickness of the base beam, m
H_1 = total thickness of one side of the damping material, m (both sides are the same thickness)
m = index number: 1, 2, 3, . . . $(m = n)$
$T = H_1/H$, thickness ratio, dimensionless
$\eta_m = \Delta f_m/f_m$, loss factor of the composite beam, dimensionless
η_1 = loss factor of damping material, dimensionless
ρ = density of base beam, kg/m^3
ρ_1 = density of the damping material, kg/m^3

15.2.3 Sandwich Beam

This configuration is used when the material for the most flexible materials. The ASTM suggests this configuration should be used for materials with a Young's modulus approximately less than 100 MPa. If higher, the modified Oberst beam configuration should be used. The term $(f_s/f_n)^2 (2 + DT)$ should be equal to or greater than 2.01. If this condition is not met, the geometry of the testing specimen should be modified such that the condition is met. These equations used to determine the material properties from the natural frequency are an approximation that is only acceptable for the second mode and higher thus the first natural frequency cannot be used for this configuration [10]. The equations are:

$$G_1 = \left[A - B - 2(A - B)^2 - 2(A\eta_s)^2\right] * \frac{2\pi C_n EHH_1/l^2}{(1 - 2A + 2B)^2 + 4(A\eta_s)^2} \tag{15.5}$$

$$\eta_1 = \frac{A\eta_s}{A - V - 2(A - B)^2 - 2(A\eta_s)^2} \tag{15.6}$$

Where,

$A = (f_s/f_n)^2 (2 + DT) (B/2)$
$B = 1/\left[6(1 + T)^2\right]$
$C_n =$ coefficient for mode n, of clamped-free beam
$D = \rho_1/\rho$, density ratio, dimensionless
$E =$ Young's modulus of base beam, Pa
$E_1 =$ Young's modulus of damping material, Pa
$f_n =$ resonance frequency for mode n of base beam, Hz
$f_s =$ resonance frequency for mode m of the composite beam, Hz
$\Delta f_m =$ the half-power bandwidth of mode m of the composite beam, Hz
$H =$ thickness of the base beam, m
$H_1 =$ total thickness of one side of the damping material, m (both sides are the same thickness)
$m =$ index number: 1, 2, 3, $\ldots$ $(m = n)$
$T = H_1/H$, thickness ratio, dimensionless
$\eta_m = \Delta f_m/f_m$, loss factor of the composite beam, dimensionless
$\eta_1 =$ loss factor of damping material, dimensionless
$\rho =$ density of base beam, kg/m^3
$\rho_1 =$ density of the damping material, kg/m^3

15.3 Experimental Set-Up

When testing for the damping properties of materials, it is important to not add additional damping to the structure. Thus for this testing only non-contact transducers where utilized. The beams were excited using a magnetic transducer (B&K MM-0002) (Fig. 15.4). A small high permeability disk (mass of 0.17 g) was attached to the tip of the beam using adhesive see Fig. 15.5. The transducer was placed approximately 5 mm from the disk and a sinusoidal voltage was used to excite the beam. A laser vibrometer was used to measure the response. Both the excitation and the response were measured at the tip of the beam. The beam was clamped at the base using large blocks to ensure the boundary condition assumptions are adequately met.

The testing set-up included the beam configuration clamped to a table with an apparatus next to the beam to position the magnetic transducer in the appropriate position. A laser vibrometer is positioned such that the beam detects movement at the tip of the beam. The magnetic transducer is connected to a data acquisition device (DAQ) via a power amplifier and is controlled using LabVIEW. The measurement output from the power amplifier, is also feed into the DAQ to get an accurate reading of the excitation input. The laser vibrometer is connected to its signal conditioner.

The LabVIEW program generates a logarithmic sine sweep which slowly sweeps through the frequencies of interest and produces a FRF. This FRF is then utilized to determine the natural frequency and damping of modes 2 through 5. The first mode of the beam typically not used as standard practice and additionally, the testing area has much ambient noise at the lower frequencies.

Fig. 15.4 Non-contacting
magnetic transducer used for
excitation
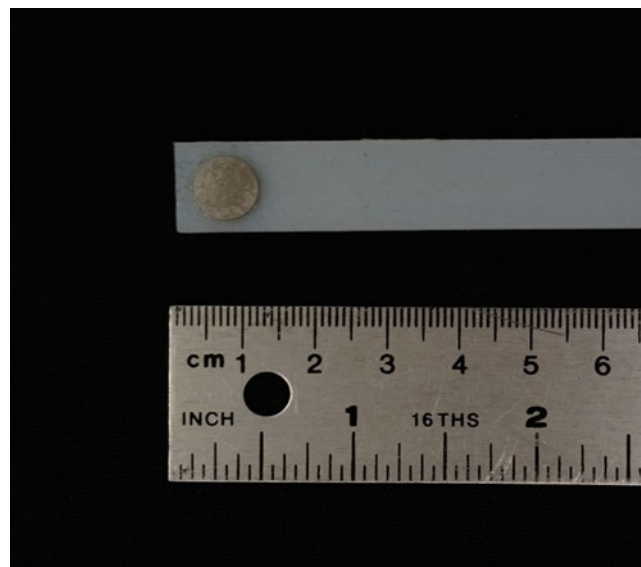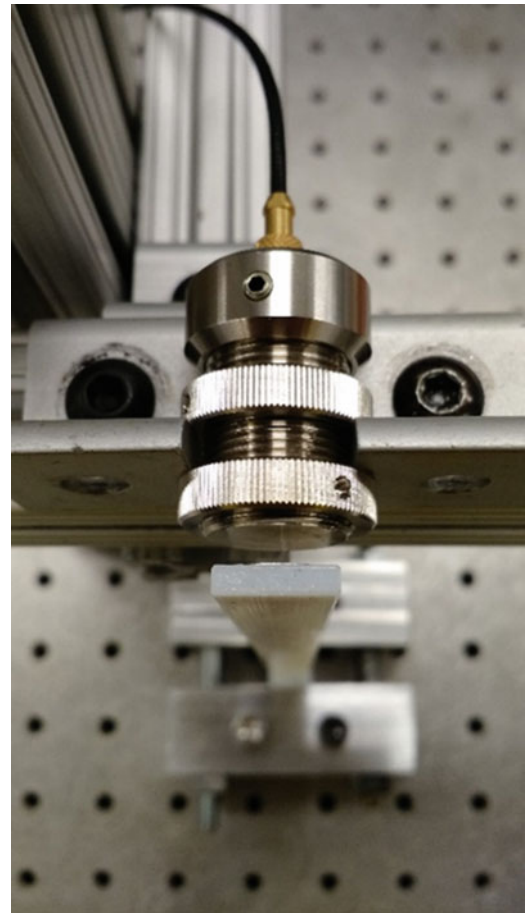
Fig. 15.5 High permeability disk glued to the tip of the beam to allow for non-contact excitation

15.4 Results

This section highlights the results for the materials tested. VeroWhitePlus and DM 8420 were tested at room temperature.

15.4.1 VeroWhitePlus^{TM}

VeroWhitePlus^{TM} is the most rigid of the digital materials. Figure 15.6 shows the frequency response function obtained showing modes 2 through 5. The calculated property values based off of the frequency response function are shown in Table 15.2.

15.4.2 DM 8420

Below are the experimental results for DM 8420. Figure 15.7 shows the FRF and Table 15.3 shows the calculated properties based off of the frequency response function. The FRF shown is an average of ten experiments and shows modes 2 through 5.

15.5 Conclusions

This paper provides modulus and loss factor data for the digital materials VeroWhitePlus^{TM} and DM 8420 and from the Objet Connex 3D printer. All testing was done at room temperature.
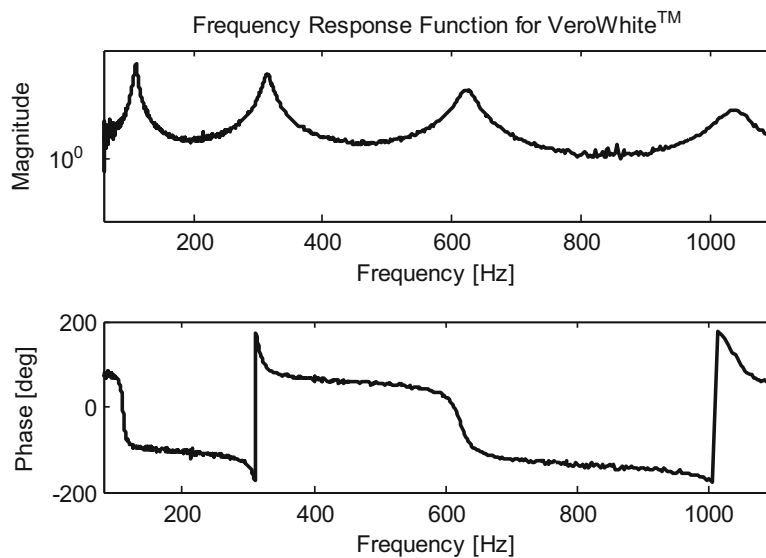
Fig. 15.6 FRF response plot for VeroWhitePlus^{TM}

Table 15.2 Calculated material properties values for VeroWhitePlus^{TM}

Frequency (Hz)	Modulus (GPa)	Loss factor (−)
109.6	2.59	0.0048
314.5	2.3	0.0039
623.6	2.79	0.0036
1038.1	2.83	−
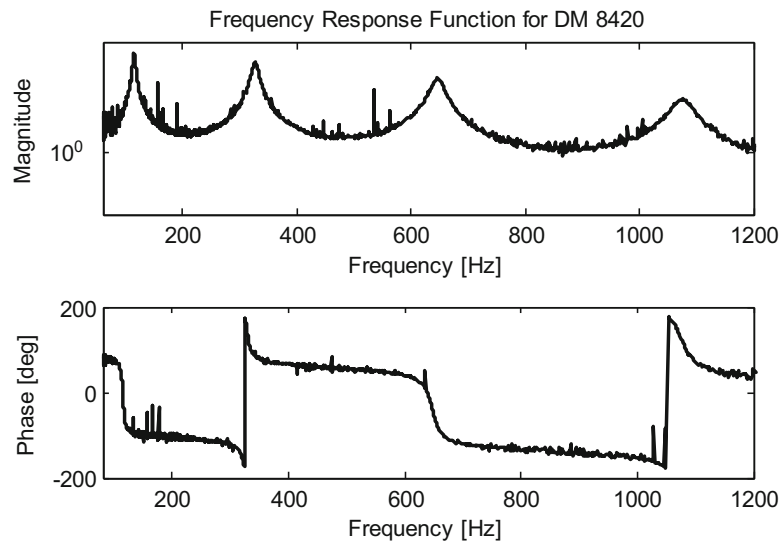
Fig. 15.7 FRF response plot for DM 8420

Table 15.3 Calculated material property values for DM 8420

Frequency (Hz)	Modulus (GPa)	Loss factor (−)
114.5	2.83	0.0036
325.7	2.92	0.0035
644.8	2.98	0.0033
1075.3	3.03	−

References

1. Reichl, K.K., Inman, D.J.: Modelling of low-frequency broadband vibration mitigation for a bar experiencing longitudinal vibrations using distributed vibration absorbers. In: 20th International Conference on Composite Materials, Denmark, Copenhagen, 19–24 July 2015
2. Hobeck, J.D., Laurant, C.M.V., Inman, D.J.: 3D printing of metastructures for passive broadband vibration suppression. In: 20th International Conference on Composite Materials, Denmark, Copenhagen, 19–24 July 2015
3. Ge, Q., Dunn, C.K., Qi, H.J., Dunn, M.L.: Active origami by 4D printing. Smart Mater. Struct. **23**(094007), 1–15 (2014)
4. Objet Connex 3D Printers: http://www.stratasys.com/3d-printers/design-series/connex-systems (Online) (2015). Accessed 17 Oct 2015
5. Stratasys PolyJet Materials Data Sheet: http://usglobalimages.stratasys.com/Main/Secure/Material Specs MS/PolyJet-Material-Specs/Digital_Materials_Datasheet.pdf?v = 635581278098921962 (Online) (2014). Accessed 17 Oct 2015
6. Stratasys Digital Materials Data Sheet: http://usglobalimages.stratasys.com/Main/Secure/Material Specs MS/PolyJet-Material-Specs/Digital_Materials_Datasheet.pdf?v = 635581278098921962 (Online) (2015). Accessed 17 Oct 2015
7. Ge, Q., Mao, Y., Yu, K., Dunn, M.L., Qi, H.J.: Active composites and 4D printing. In: 20th International Conference on Composite Materials, Denmark, Copenhagen, 19–24 July 2015
8. Wang, Y., Inman, D.J.: Experimental and finite element analysis for a multifunctional beam with frequency-dependent viscoelastic behavior. J. Sound Vib. **332**(23), 6177–6191 (2013)
9. ASTM: Standard test method for measuring vibration-damping properties of materials. ASTM **5**(E756), 1–14 (2010)
10. Jones, D.I.G.: Handbook of Viscoelastic Vibration Damping. Wiley, Chichester (2001)
11. Koruk, H., Sanliturk, K.Y.: On measuring dynamic properties of damping materials using Oberst method. In: ASME 10th Biennial Conference on Engineering Systems Design and Analysis, pp. 1–8 (2010)

Chapter 16
Optimized 3D Printed Chiral Lattice for Broadband Vibration Suppression

Brittany C. Essink and Daniel J. Inman

Abstract This paper presents an experimental study of optimized numerical simulations on a metastructure created for the purpose of broadband vibration suppression. The proposed structure uses a stiff outer frame with periodic inserts as internal resonators in a beam like assembly to achieve high damping broadband performance. With the rapid improvement of 3D printing capabilities, chiral lattice inserts can be quickly created from an elastomeric material for use in the structure. The stiff outer frame is used to maintain the integrity of the structure while the flexible chiral lattice and annular masses dissipate the energy. This combined assembly is characterized by high frequency bandgaps and tuned vibration attenuation at low frequencies. These inserts and masses have been previously optimized to find the optimal topology and tuning to reduce global vibration levels of the beam. Experimental results demonstrate the suppression capabilities of this structure for possible use in vibration absorption in load carrying structural members.

Keywords Metastructures • 3D printed materials • Chiral lattice • Vibration suppression • Internal resonators

16.1 Introduction

Vibration absorption is a widely investigated field of research which has more recently been applied to load bearing structural members. One challenge in creating these designs is that, traditionally, a stiffer structure means less vibration absorption capability, and changing to materials with improved absorption properties removes their ability to be load bearing. A new category of acoustic metamaterials has grown out of this need for high damping structures termed metastructures. These metastructures are composed of a primary structure with additional vibration suppression systems designed to reduce vibration in the structure at a specific frequency band. This suppression system operates while still allowing the primary structure to perform its original function.

Some of the first metastructures used were structural bars and beams with internally resonant behavior due to coupling with spring-mass resonator arrays [1, 2]. The resonance frequency of the arrays generates an attenuation band caused by two elastic waves with different speeds and wavelengths. This attenuation bandwidth can also be expanded by tuning the resonators to different frequencies. Internal resonance combined with beam structures and high damping materials has led to the creation of a load bearing structure with vibration attenuation capabilities [3].

In these structures, stiffness requirements are satisfied through a load bearing outer frame, while vibration attenuation is accomplished by an MDOF internal lattice insert. These lattice inserts are based on chiral configurations that were previously created [3] and further updated for this specific use [4, 5]. The idea behind choosing the lattice structure is that it deforms in such a way that leads to increased attenuation and has the capability to be easily tunable to specific frequency bandgaps by altering geometric parameters. Additionally, the circular regions created by the lattice design process lend to the addition of annular masses to introduce resonances and further attenuate vibrations in the structure.

Further optimization of the original chiral beam assembly using genetic algorithm methods has been performed [6] resulting in optimal designs for the structure based on specific varying parameters. Two of these optimized metastructures were fabricated and experimentally tested and the results are presented in this paper.

B.C. Essink (✉) • D.J. Inman

Department of Aerospace Engineering, University of Michigan, François-Xavier Bagnoud Building,
1320 Beal Avenue, Ann Arbor, MI 48109, USA
e-mail: essinkb@umich.edu

16.2 Methodology

16.2.1 Concepts

Lattice structures were originally chosen over other viable geometries due to the large number of alterations possible for frequency tuning. These optimal chiral configurations all have eight ligaments connected to each circular mode and all nodes have annular masses. A closeup of the annular mass and ligaments is shown in Fig. 16.1. Parameters that were considered in the optimization routine included the original four design parameters (number of circular nodes in x direction, number of circular nodes in y direction, angle of asymmetry of the lattice, and the thickness of the ligaments) [3, 5, 7], as well as new parameters that determined the optimal radii of the masses and the optimal spacing distances for the nodes [6].

16.2.2 Experimental Fabrication

The outer frames were cut from a solid plate of 6061 Aluminum using a waterjet cutter. Both lattice structures were fabricated using an Objet Connex 500 3D printer. Due to the large size of the chiral lattice inserts, the lattice components were printed in two parts to fit in the 3D printer. The inserts were glued together using Alteco Ace-D cyanoacrylate adhesive. The lattice inserts were then fixed to the aluminum frame using DP 460 epoxy. Annular masses were milled from 12L14 steel bar stock to the correct sizes to fit into the chiral nodes.

A photograph of the fabricated beams with frame dimensions and labeled parts can be seen in Fig. 16.2. Dimensions of the beams and annular masses were taken from the optimized designs detailed in [6]. Designs chosen from the optimization to experimentally test were of the periodic chiral lattice topology for the Case 1 frame and the optimal chiral lattice topology for the Case 2 frame. For further discussion, the design using the Case 1 and Case 2 frames will be referred to as Case 1 and Case 2 respectively. Case 1 was printed using a lattice made of TangoPlus. The Case 2 lattice was fabricated from DM 8340—a combination of VeroWhite and TangoPlus (the stiffest and least stiff digital materials for the printer respectively). The material properties for each of these materials are listed in Table 16.1.

16.2.3 Experimental Setup

The setup is shown in Fig. 16.3. The base was clamped to an optical table to create fixed-free boundary conditions. Both Case 1 and Case 2 experiments used a PCB 086C01 impact hammer to excite the structures. Velocity data was collected using a Polytec OFV-534 laser vibrometer and a Polytec OFV-5000 laser vibrometer controller. LabVIEW was used as a controller for National Instruments data acquisition hardware to collect and display real time data at a rate of 20 kHz on a PC laptop. The impact hammer and laser vibrometer data were saved to a file for data reduction.

Fig. 16.1 Close up view of annular mass and ligaments
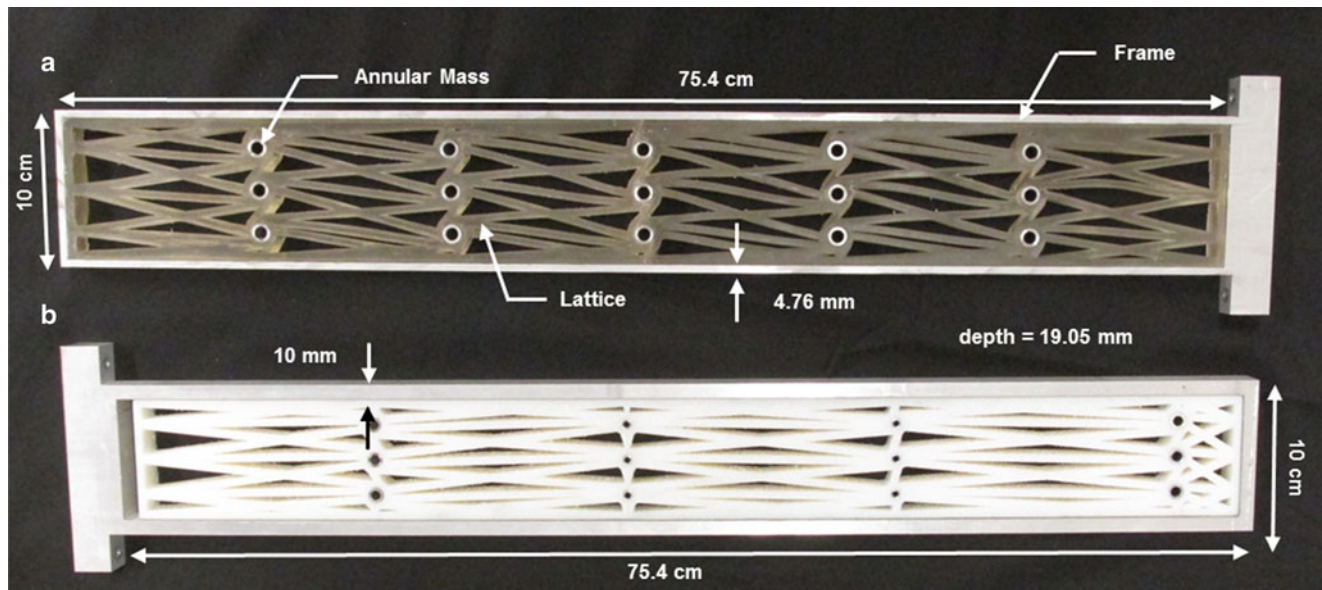
Fig. 16.2 Assembled beams with frame dimensions: (**a**) Case 1 and (**b**) Case 2

Table 16.1 Material properties [8]

Component	Material	Young's modulus [E]	Density [ρ]
Frame	Aluminum	69 GPa	2700 kg/m^3
Annular masses	Steel	193 GPa	7870 kg/m^3
Chiral lattice Case 1	TangoPlus	0.99 MPa	1120 kg/m^3
Chiral lattice Case 2	DM 8430	1750 MPa	1170 kg/m^3

16.3   Results

Both Case 1 and Case 2 frame and assembly data were obtained by impacting the frame 10.5 cm from the base. The velocity data was collected at the free end of the beam opposite the impact side. Velocity data was converted to displacement and the magnitude is reported in mm/N. The main areas of interest for the beams were from 0 to 200 Hz. The transmissibility for Case 1 and Case 2 are shown in Figs. 16.4 and 16.5 respectively.

As can be seen in Fig. 16.4, the internal member in the frame greatly attenuates the vibrations in the structure and shifts the natural frequencies to lower values. These strong attenuation properties are attributed to the high vibration dissipation properties of the chiral material. The lattice material also decreases the influence of the other bending modes on the structure response.

The Case 2 data shown in Fig. 16.5 also demonstrates that the response is damped compared to the frame only, but in this case, the first resonant frequency is shifted higher due to the additional stiffness from the lattice. Additionally, this stiff material in the Case 2 beam does not attenuate the vibrations as quickly as the less stiff Case 1 material; however the structure is still successfully decreasing the effects of the impact.

Comparing both data sets, the thicker frame used in Case 2 stiffens the structure, decreases the impact transmission, prevents torsional and out of plane motion, and makes the entire structure less susceptible to the influence of other modes. If DM 8430 were used in the thinner frame of Case 1, it may be stiff enough to provide this independence to the thinner frame. In both cases, the results depict the expected vibration attenuation due to the addition of the lattice structure and annular masses.
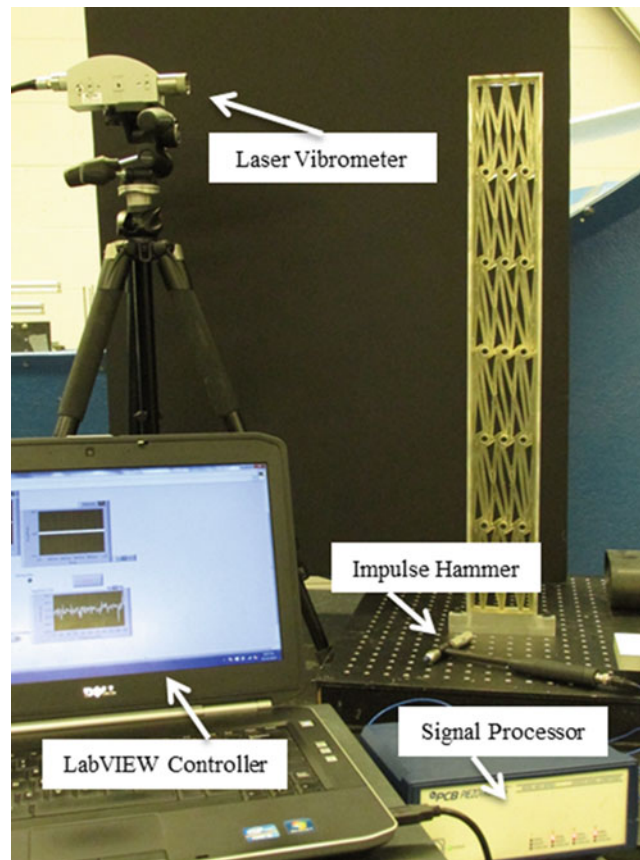
Fig. 16.3 Experimental setup
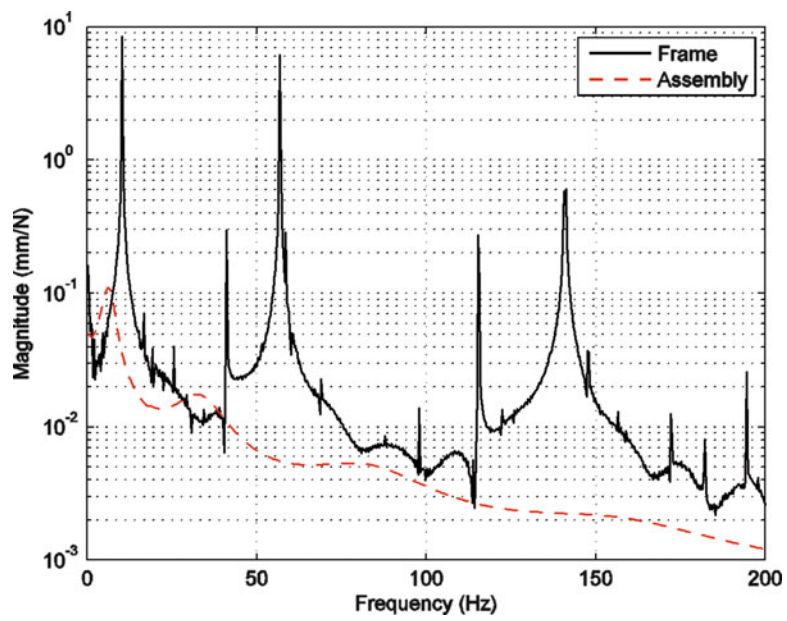
Fig. 16.4 Case 1 response data
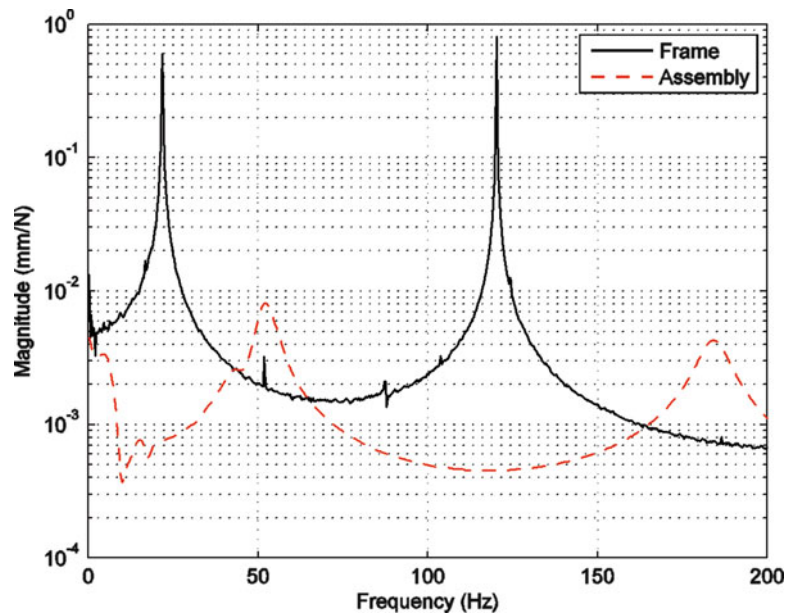
Fig. 16.5 Case 2 response data

References

1. Pai, P.: Metamaterial-based broadband elastic wave absorber. J. Intell. Mater. Syst. Struct. **21**, 517–528 (2010)
2. Sun, H., Du, X., Pai, P.: Theory of metamaterial beams for broadband vibration absorption. J. Intell. Mater. Syst. Struct. **21**, 1085–1101 (2010)
3. Zhu, R., Liu, X., Hu, G., Sun, C., Huang, G.: A chiral elastic metamaterial beam for broadband vibration suppression. J. Sound Vib. **333**, 2759–2773 (2014)
4. Baravelli, E., Carrara, M., Ruzzene, M.: High stiffness, high damping chiral metamaterial assemblies for low-frequency applications. In: Proceedings of the SPIE Smart Structures/NDE 2013, San Diego, CA, 10–14 March 2013.
5. Baravelli, E., Ruzzene, M.: Internally resonating lattices for bandgap generation and low-frequency vibration control. J. Sound Vib. **332**, 6562–6579 (2013)
6. Abdeljaber, O., Avci, O., Inman, D. J.: Genetic algorithm use for internally resonating lattice optimization: case of a beam-like metastructure. In: IMAC XXXIV A Conference and Exposition on Structural Dynamics, Orlando (2016)
7. Liu, X., Hu, G., Sun, C., Huang, G.: Wave propagation characterization and design of two-dimensional elastic chiral metacomposite. J. Sound Vib. **330**(11), 2536–2553 (2011)
8. Stratsys Ltd.: PolyJet Materials Data Sheet. www.stratasys.com (2014). Accessed October 2, 2015

Chapter 17
Embedding Sensors in FDM Plastic Parts During Additive Manufacturing

Lexey R. Sbriglia, Andrew M. Baker, James M. Thompson, Robert V. Morgan, Adam J.Wachtor, and John D. Bernardin

Abstract In additive manufacturing, there is a necessity to qualify both the geometrical and material characteristics of the fabricated part, because both are being created simultaneously as the part is built up layer by layer. Increased availability of open source fused deposition modeling machines has expanded the parameter space for which the user has control during the build process. This work quantifies the effects of operator choices, such as print speed, printer head and build plate temperatures, layering thickness, or building in a thermally controlled or fully open environment, on the quality and reproducibility of the build. Modal analyses were performed on completed builds using an electrodynamic shaker and integrated circuit piezoelectric accelerometers embedded in the parts during the build process. Experimental measurements of the fused deposition modeled parts were benchmarked against eigenvalue analysis results for an idealized part with homogenous material properties to gauge the suitability of such analysis to fused deposition modeling additive manufacturing. Follow on work will use this embedded technique for state-of-health monitoring in deployed systems and real-time diagnostics and control of the build process.

Keywords Additive manufacturing • Fused deposition modeling • FDM • Modal analysis • Embedded sensors

Nomenclature

AM   Additive manufacturing
CAD   Computer-aided design
DAQ   Data acquisition
FDM   Fused deposition modeling
FEA   Finite element analysis
FFT   Fast fourier transform
SoH   State-of-health
STL   Stereolithography file
3D   Three dimensional

17.1 Introduction

Additive manufacturing (AM), more broadly know as three-dimensional (3D) printing, is the process by which an object is created vertically, layer-by-layer, in a Cartesian coordinate system. A variety of AM techniques have been developed for a wide range of printed materials, ranging from titanium and steel alloys [1] to cakes and gummy candies [2, 3]. The AM

L.R. Sbriglia
Department of Mechanical Engineering, University of Nevada, Reno, 1664 N. Virginia Street, Reno, NV 89557, USA

A.M. Baker
Materials Physics and Applications Division, Los Alamos National Laboratory, P.O. Box 1663, Los Alamos, NM 89557, USA

J.M. Thompson • R.V. Morgan • A.J. Wachtor (✉) • J.D. Bernardin
Applied Engineering and Technology Division, Los Alamos National Laboratory, P.O. Box 1663, Los Alamos, NM 87545, USA
e-mail: ajw@lanl.gov
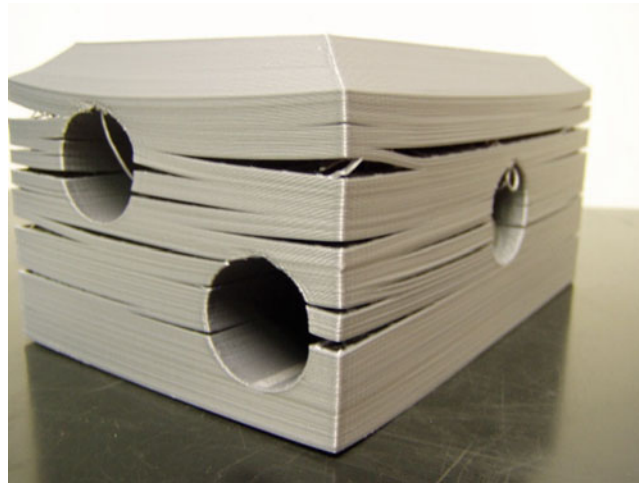
Fig. 17.1 Failed FDM part showing extensive delamination between printed layers

method used in this paper is known as fused deposition modeling (FDM). FDM is an AM technique commonly used for plastic parts which extrudes spooled thermoplastic material through a nozzle that heats the plastic to its melting point. The heated plastic is deposited in sequential two-dimensional layers to create the desired 3D object design [4]. Heat is transferred from the newly added plastic to the previous layer below it, partially re-melting that layer and bonding the layers together.

AM is advantageous because it can lower manufacturing costs of complex geometrical designs and reduce lead times [4], allows for rapid prototyping and design iteration, and can reduce the need for post processing [1]. A recent emergence of low cost, open source FDM printers have opened up the technology to a much larger user base. These open source printers give the user complete control of the wide array of print parameters, e.g. material, print head temperature, bed plate temperature, print speed, layer thickness, shell thickness, infill percentage, etc. However, putting the control into an inexperienced user's hands can result in a steep learning curve of identifying which parameters most greatly contribute to print failures, as in Fig. 17.1. Final geometrical and structural quality of parts is also most often determined by the individual's own success with a trial and error approach.

Material properties for AM parts are formed during the build process. Even with constant printer settings, the material properties can vary throughout the part depending on the part geometry, how much heat is retained in the previous layer when the next layer is printed, and how much heat is conducted from the print bed through the part. In this work, vibration analysis [5–7] was used as a means to quantify the effects operator choices for key parameters have on the structural characteristics of completed parts. Results are compared against a numerical solution of an eigenvalue analysis, for which constant material properties are assumed, to assess the extent to which these tools may be used to help gain insight into FDM produced parts.

There are a wide variety of applications for which embedding sensor technology directly into the part is desired to protect the sensor from harsh environments and prolong the lifetime of the sensor in use. In this work, sensors were embedded into the builds in order to directly measure the frequency response of the part during vibration testing. Although not necessary for this application, embedding the sensors did allow assessment of sensor embedment in FDM parts for future needs.

17.2　Experimental Setup

17.2.1　3D Printer

A Lulzbot Taz 5 with a 0.013 in. diameter extruder nozzle was used for printing all test articles. The print bed of the Taz 5 is 11.81 in. × 11.81 in. consisting of a borosilicate glass plate (0.118 in.) between a polyetherimide film print surface (<0.04 in.) and an adhesive silicone pad heater (0.118 in.). The gantry housing the print head translated in the x- and z-directions, while the print bed translated in the y-direction. Print parameters were set and G-code was generated using Cura Lulzbot Edition software.
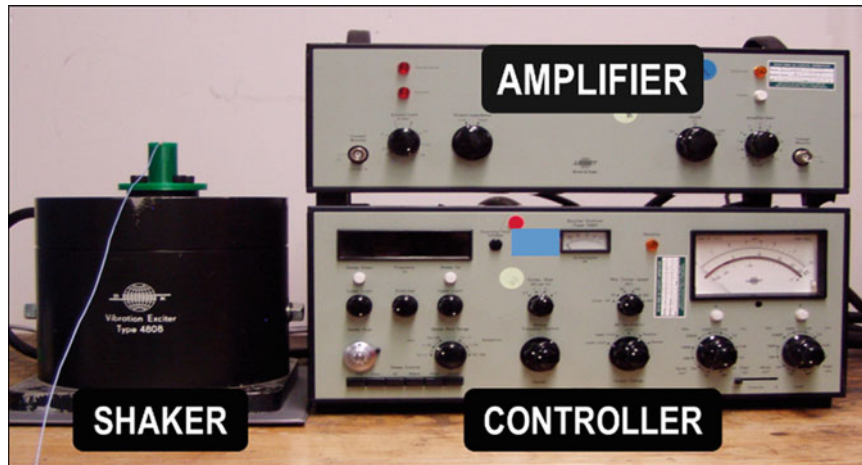
Fig. 17.2 Brüel & Kjær electrodynamic shaker setup

Fig. 17.3 Excitation frequency sweep performed for each printed part using Brüel & Kjær electrodynamic shaker
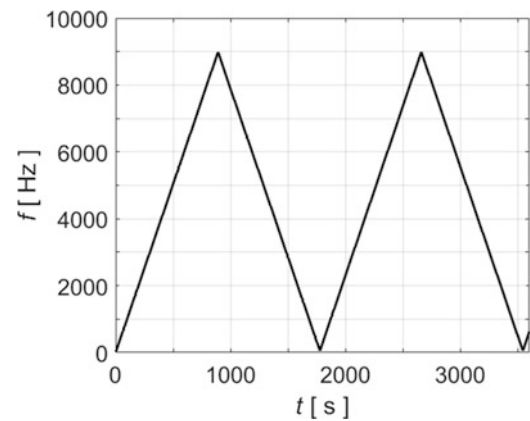
17.2.2 Shaker Table

Modal analysis was performed using a Brüel & Kjær shaker system consisting of the 4808 electrodynamic shaker, 2712 power amplifier, and 1047 exciter controller, pictured in Fig. 17.2. The table had a diameter of 2.45 in. and bare table operable frequency range of 5 to 10 kHz and maximum acceleration of 71 g. The controller was programmed to perform a repeated linear frequency sweep from 50 to 9 kHz and data was collected for each part for just over 4 complete sweeps as shown in Fig. 17.3. The data had very little variance (<0.5 % mean value) between sweeps for a given data collection run, so although all collected data is reported here, that from repeated sweeps for a given part are essentially indistinguishable from one another.

17.2.3 Data Acquisition

Frequency response measurements were collected using PCB Model 352A21 integrated circuit piezoelectric accelerometers powered with a 2.1 mA constant current supply from a National Instruments USB-4431 DAQ system with a sampling range from 1 to 102.4 kS/s with a resolution of 2.1 mS/s that was controlled using Matlab. The single axis accelerometers were specifically chosen for their compact design and measurement accuracy—0.02 oz weight, <0.02 in.^{3} total volume, 10 mV/g sensitivity ($\pm$15 %), and $\pm$500 g peak measurement range. An accelerometer was attached to the flat surface of one of the hex bolts used to anchor the part to the shaker table to measure the frequency at which the shaker was accelerating the part. The frequency response for the accelerometer on this bolt was measured directly against an accelerometer on the bare table and found to have average gain of 1.0804 with a standard deviation of 0.1316, which is orders of magnitude below the response level from the parts and therefore deemed acceptable for use as a measurement of the forced acceleration of

the table. The frequency response of the part was measured using a second accelerometer that was either embedded into the part during the build or place on the top surface of the column. In all cases, adhesion of the accelerometer to the part was performed using petro wax (PCB 080A109).

17.2.4 Part Design

A simple geometry of a single cylindrical column of 1 in. diameter (D) and 2.75 in. height (H) with solid infill was chosen for this study. To make for direct part mounting to the electrodynamic shaker used to perform the modal analysis, a flanged base (D: 3 in., H: 0.25 in.) was added to the cylindrical column that included four 5/16 in. holes corresponding to the bolt pattern on the Brüel & Kjær 4808 shaker described above. In order to embed the accelerometers directly into the build, a cavity based on the specific geometry of the PCB 352A21 was in inserted into the column 1.75 in. above the flange base, Fig. 17.4. To accomplish the sensor embedment, the G-code generated by Cura was modified to include a 2 min pause in the print at the layer height before the cavity was to begin being covered over. During that time, the printer bed was translated to its maximum y-position to provide easy access for manual insertion of the accelerometer. Presumably a smaller pause time could have been used, but the 2 min was found to be sufficient to ensure that enough care could be taken to guarantee that no part of the inserted sensor was sticking out above the current highest printed layer before printing resumed. In doing so, the tool path of the printer head was completely unobstructed for printing subsequent layers.
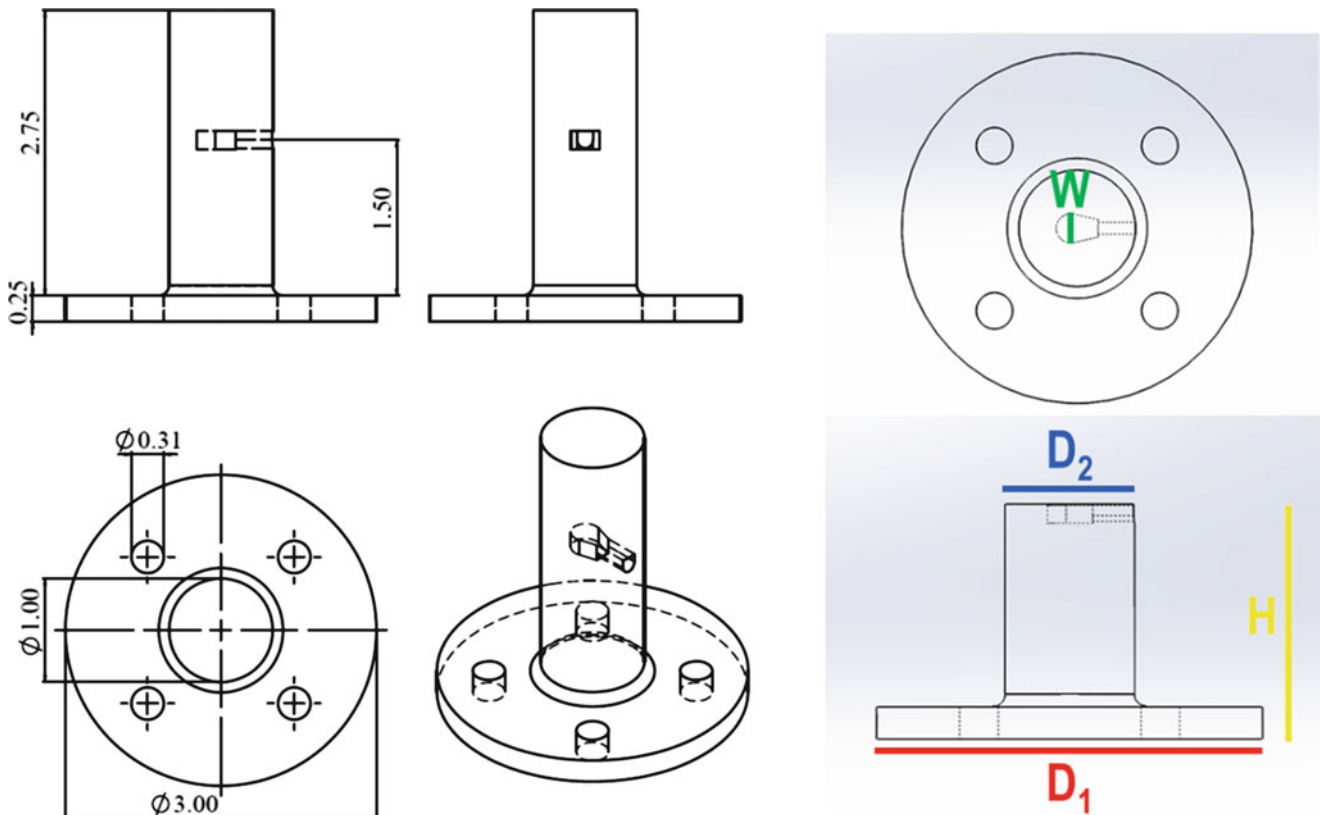
Fig. 17.4 Geometry of test articles with measurements shown in inches (*left*). Measurements used for geometrical quantification of material choice (*right*)

17.3 Results

17.3.1 Material Choice

The Lulzbot is capable of printing with a variety of stock materials; high impact polystyrene (HIPS), acrylonitrile butadiene styrene (ABS), and polylactic acid (PLA) were all assessed to be used in this study. To do so, parts were printed with each material up to the layer before the cavity was to be covered using the manufacturer's recommended settings, Fig. 17.5. The printed parts were then measured to see how closely they compared to the computer-aided design (CAD) geometry, Table 17.1.

As seen in Fig. 17.5, both the ABS and HIPS parts produced very poor surface finishes and each layer within the column had a larger footprint than was prescribed in the CAD design. This resulted in the sensor cavity being too small to fit the accelerometer. Since it was desired to have as short of a pause in the print as possible to embed the sensor, so that chances of delamination were minimized, this aspect of the print was highly undesirable.

Although, the CAD file could have been adjusted to accommodate for the increased footprint with ABS and HIPS, it was found that the PLA was able to provide a much better quality part that had better surface finish and could house the accelerometer without any CAD modification. Therefore, PLA offered the best option for successful prints when changing only a single parameter from the recommended setting and was chosen to be used for all subsequent prints, the parameters of which are listed in Table 17.2.

Fig. 17.5 Parts printed up to the top of the accelerometer cavity with manufacturer's suggested settings for different materials

Table 17.1 Measurements of variation from CAD geometry for key geometrical dimensions of parts printed only up to the top of the sensor cavity, see Fig. 17.4

Material	D_1 (in)	D_2 (in)	W (in)	H (in)
ABS	(−) 9.1e-3	(+) 0.04	(−) 3.9e-3	(+) 0.02
HIPS	(−) 0.01	(+) 0.02	(−) 7.1e-3	(+) 0.02
PLA	(−) 7.1e-3	(−) 7.1e-3	(+) 0.01	(+) 0.02

Table 17.2 Print parameters for each build

Build #	1-3	4	5	6	7	8	9	10
Layer height (in)	9.45e-3	9.45e-3	**0.019**	**4.72e-3**	9.45e-3	9.45e-3	9.45e-3	9.45e-3
Shell thickness (in)	0.059	0.059	0.059	0.059	0.059	0.059	**0.256**	**0.512**
Bottom/Top thickness (in)	0.031	0.031	0.031	0.031	0.031	0.031	0.031	0.031
Fill density (%)	100	100	100	100	100	100	100	100
Print speed (in/s)	1.97	1.97	1.97	1.97	**2.95**	**0.984**	1.97	1.97
Printing temperature (°F)	401	401	401	401	401	401	401	401
Bed temperature (°F)	140	140	140	140	140	140	140	140
Filament diameter (in)	0.114	0.114	0.114	0.114	0.114	0.114	0.114	0.114
Filament flow (%)	100	100	100	100	100	100	100	100
Embedded sensor	Y	N	N	N	N	N	N	N
Estimated print time (h)	4.60	4.60	**2.48**	**8.92**	**3.60**	**7.67**	**5.32**	**5.73**

Differences from prints done with recommended setting highlighted in bold
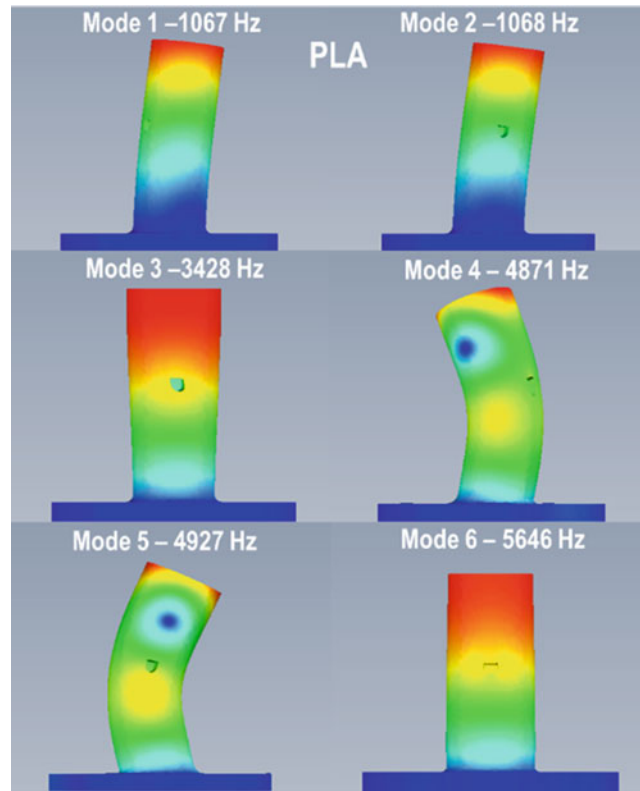
Fig. 17.6 Mode shapes for modes 1-6 determined from Solidworks Simulation frequency analysis of PLA part

Table 17.3 First 8 modes resulting from the Solidworks Simulation frequency analysis for the PLA test article

Mode #	1	2	3	4	5	6	7	8
f (Hz)	1067	1068	3428	4875	4928	5646	9847	9888
MP_x (%)	35.5	–	–	18.3	–	2.3e-2	16.5	–
MP_y (%)	1.1e-3	35.6	1.1e-3	–	18.5	–	–	15.5
MP_z (%)	–	–	–	3.8e-2	–	47.3	5.3e-3	–

Mass participation (MP) for each Cartesian direction is listed, but values that fell below 0.001 % were negligible and therefore omitted from the table

17.3.2 Frequency Analysis Simulation

A Solidworks Simulation frequency analysis was performed using the CAD file for the test article. Restricted movement of the bolt holes and the portion of the bottom of the part that was in contact with the table was accounted for. Figure 17.6 shows the first six natural frequency modes that the eigenvalue analysis determined. Motion in the x- and y-directions was largely identical, with only a small frequency shift due to the presence of the asymmetric cavity introduced into the column to house the accelerometer. The mode pairs of 1-2, 4-5, 7-8 were largely characteristic of fixed-free beam motion, while mode three was a low energy torsional mode. Table 17.3 shows that the mode with the greatest mass participation (MP) was mode 6, which is a compressional mode in the z-direction. The shaker was set up to accelerate the test articles in the z-direction, therefore, large amplifications of this mode were expected to be seen in the experimental measurements.

17.3.3 Reproducibility Between Builds with Identical Settings

A set of four prints was performed with identical settings to assess the amount of variation that can be attributed simply due to the build process. Embedded sensors were placed in three of the four prints. This operation was done manually. After
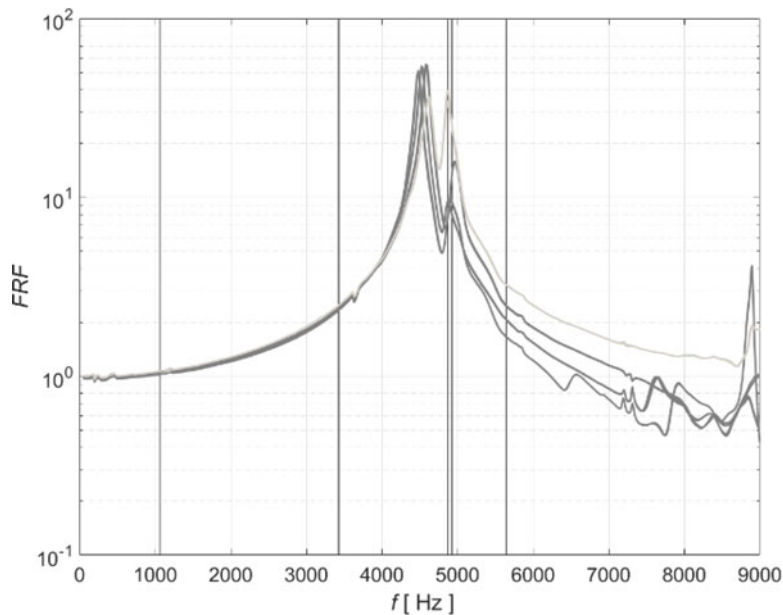
Fig. 17.7 Frequency response function for Build # 1-3 (*dark gray*) and 4 (*light gray*). Vertical lines at resonant frequencies predicted by Solidworks Simulation

completing the task once, it was found that the 2 min pause programmed into the G-code was sufficient to place the sensor and ensure that it would not interfere with the path of the printer head when printing resumed. The pause duration could have been reduced to around 30 s, but desire to keep consistency between these prints was higher than the small time savings that would have provided. In fact, the same 2 min pause was incorporated into the G-code for all prints, regardless of whether an accelerometer was placed in the print, or mounted to the top of the print after completion.

Since the sensors used for measurement were only single axis accelerometers aligned to measure in the z-direction, measured frequency response amplitudes were expected to be greatest around the frequencies associated with either modes with large z-motion or containing some component of motion in the z-direction. In Fig. 17.7, the average peak in the frequency response function (FRF) was found at 4553 Hz with a standard deviation of 63 Hz for these prints. Low frequency response is largely governed by the material stiffness. In this region, excellent agreement was observed between all the FRF curves below the peak value, including a small bump in the FRF around 1200 Hz and a dip at 3630 Hz, which were likely due to contributions from modes 1–3. The maximum peak and secondary peaks are believed to be associated with modes 4–6. Although, there is some rough agreement with the values of the resonant frequencies measured in the experiments and those predicted by the Solidworks Simulation frequency analysis that helped with this interpretation, the actual prediction of the resonant frequencies was well off of that measured. This may be attributed to the fact that the Solidworks Simulation assumed that the part is 100 % solid and has constant material properties. However, that is not the case for these FDM parts.

17.3.4 Effect of Print Layer Height

To assess the effect of print layer height, the layer height was doubled (Build # 5) and halved (Build # 6) from that prescribed for Builds # 1-4. Doubling the layer height resulted in a very poor surface finish and a significant shift in the peak FRF down to 4295 Hz, Fig. 17.8. When the layer height is increased in FDM, the amount of surface contact between the recent layer and the previous layer is reduced, weakening the fusion between those layers. Thus, this downwards shift is most likely due to the stiffness of the part being reduced as the adjoining layers were not fully fused throughout the build.

Halving the layer height did have the opposite effect of doubling it, in that the max FRF peak shifted upwards to 4643 Hz, just outside the range seen in Build # 1-4. The fact that this shift was smaller than that seen for doubling the layer height may be attributed to the fact that the settings for Build # 1-4 likely already had adequate layer fusion, so there was not much more opportunity left to increase the surface contact between the layers. Although, Build # 6 did have the best surface finish and its shift in the peak FRF frequency suggests it has increased strength, the time required to build the part was nearly 9 h. In that time nearly two full parts would have been capable of being printed using the basic printer settings of Build # 1-4.
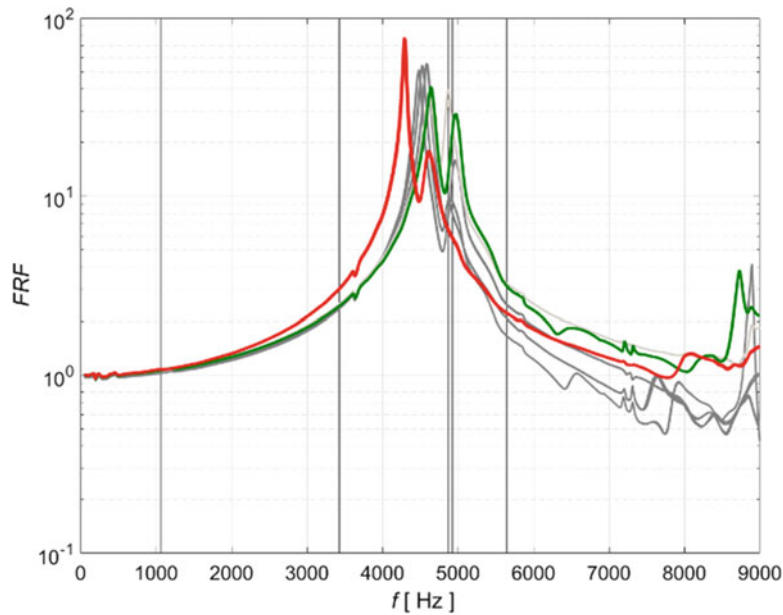
Fig. 17.8 Frequency response function for Build # 1-3 (*dark gray*), 4 (*light gray*), 5 (*red*), and 6 (*green*). Vertical lines at resonant frequencies predicted by Solidworks Simulation
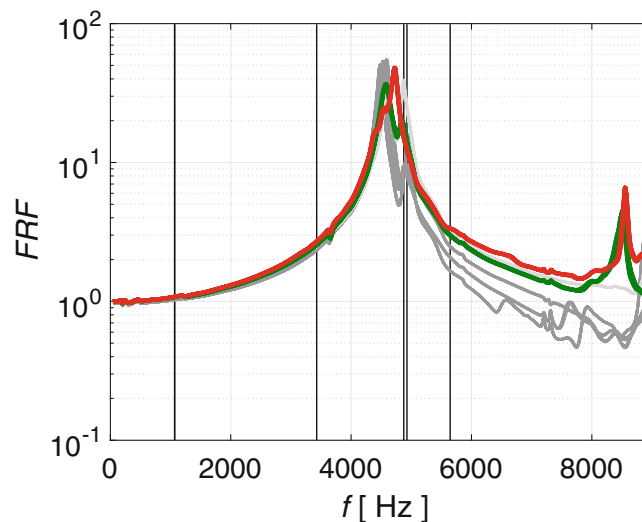
Fig. 17.9 Frequency response function for Build # 1-3 (*dark gray*), 4 (*light gray*), 7 (*red*), and 8 (*green*). Vertical lines at resonant frequencies predicted by Solidworks Simulation

17.3.5   Effect of Print Speed

Often the operator of an FDM machine is faced with a tradeoff between print resolution and the time to print completion. In this work the print speed was tested by increasing the speed 1.5x and decreasing it 0.5x. The increased speed resulted in a build with lower quality surface finish, and moved the primary FRF peak up to 4726 Hz, Fig. 17.9. There was also a small bump in the FRF around 4550 Hz, that may correspond to the same primary mode that was found in Build #1-4. For the build carried out at the slower speed, the FRF peak was 4581 Hz and the build quality was comparable to Build # 1-4. Therefore, this option did not produce any advantages over the basic print settings. And if a longer time is available to complete the print, one should instead consider reducing the layer height instead of the print speed to improve surface finish of the completed part.
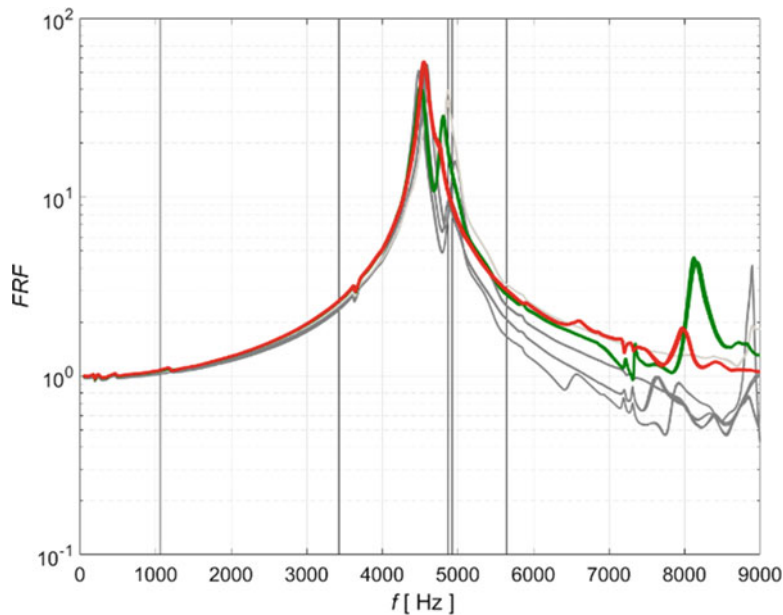
Fig. 17.10 Frequency response function for Build # 1-3 (*dark gray*), 4 (*light gray*), 9 (*red*), and 10 (*green*). Vertical lines at resonant frequencies predicted by Solidworks Simulation

In both Build # 7 and 8, a distinct peak in the FRF was measured around 8600 Hz. A peak of this magnitude was not seen in Build # 1-4 or in the Solidworks predictions. This may be a result of the Young's modulus differing between these FDM builds and the values given in the literature that were used in the Solidworks simulation. The inhomogeneities in the FDM parts appear to reduce the stiffness of the part significantly enough that Modes 7-8 then fell into the measurement range.

17.3.6 Effect of Tool Path

The tool path prescribed by Cura Lulzbot Edition first printed the outside perimeter of the cylinder in circular paths until the shell thickness was met, then performed the solid infill largely using a linear snake pattern. By increasing the shell thickness, more circular print paths were used in the build. The shell thickness was adjusted to half the cylinder radius and to the full radius. Figure 17.10 shows the effects that these changes have on the frequency response. Build # 9 consisted of a column with a radius of half axisymentric and half linear tool paths, and although the peak in the FRF was 4514 Hz and close to that of Build # 1-4, the secondary peak was moved in so close to the primary peak that it almost was nearly indistinguishable from the decay from the primary resonance peak. The build with a fully circular build path also had a primary peak, 4558 Hz, that was close to those of Build # 1-4, and a secondary peak that was shifted down. However, in Build # 10 the secondary is still clearly distinguishable from the primary peak.

In both Build # 9 and 10, a prominent high frequency peak is present around 8000–8200 Hz. Similar to the results from changing printer speed, this suggests that this printing change resulted in fundamentally different structural properties than those built using the manufacturer's recommended settings and is a demonstration that the tool path used to build the part also affects its material properties. On one hand, this results should not be surprising, because the tool path defines the thermal history of the part. However, controlling the tool path is largely outside of the user's hands, as it is an automated process done through software, putting a limit on the extent to which the user's choices can control the build.

17.4 Conclusion

This work largely lays the foundation for a much larger parameterized study of operator choices for FDM builds using open source machines, and also future work for embedding sensors into AM parts. Due to the limited amount of information collected using single axis accelerometers, the orientation of excitement relative to the part was later modified to excite a

greater response of the fixed-free beam modes. This was accomplished by fixing a 6061-T6 aluminum cube to the shaker and mounting the parts to the side of the aluminum fixture. The FRFs for the FDM parts using this orientation produced clear resonance peaks near, but almost always below, the predicted Solidworks Simulation predictions, suggesting that the effective stiffness of the FDM parts is lower than that which would be found in parts made through subtractive manufacturing of the same material. It is the intention of the authors to publish the results using the alternative excitation orientation in a future publication, but any interested reader is encouraged to contact the authors directly.

It was found that operator choices have a direct impact on the structural properties of the part, e.g. stiffness, and can be measured using techniques like the vibration analysis demonstrated here. The limited parameter variation presented suggests that there is a range for each of the values tested which result in a small variance from characteristics of the recommended printer settings. However, once outside that range, printer settings may result in significant deviations from what would have been measured with the recommended settings, e.g. doubling the print speed. A more detailed parameter variation should be performed to find these limits.

Analysis of a complete parameterized study could be used to guide operator choices and avoid user induced failure. As the tool path for the print was found to affect the thermal history of the print, and subsequently the material properties, the extent to which fine control over the material properties can be achieved is still an open question. If one were truly seeking to print an FDM part with homogeneous material properties, they would either need to simulate the thermal history of the build process and create an algorithm that adjusts the printer properties throughout the build, or be able to actively measure temperature in the top build layers and design a closed feedback control to be used during the print process.

Embedding sensors in FDM parts can be useful for state-of-health (SoH) monitoring in deployed systems [8]. The embedment method used in this paper was rather simple, so that parts could later be cut open and sensors removed for use in future studies. However, since this would not be desirable for SoH applications, the method may be improved upon to ensure that the sensor remains in proper contact with the part for its lifetime.

References

1. Wong, K.V., Hernandez, A.: A review of additive manufacturing. Int. Scholarly Res. Netw. Mech. Eng. **2012**, 1–10 (2012)
2. http://3dprintingindustry.com/food/
3. http://3dprinting.com/food/
4. Li, H., Taylor, G., Bheemreddy, V., Iyibilgin, O., Leu, M., Chandrashekhara, K.: Modeling and characterization of fused deposition modeling tooling for vacuum assisted resin transfer molding process. Additi. Manuf. **7**, 64–72 (2015)
5. White, C., Li, H.C.H., Whittingham, B., Herzberg, I., Mouritz, A.P.: Damage detection in repairs using frequency response techniques. Comp. Struct. **87**(2), 175–181 (2009)
6. Martínez, J., Diéquez, J.L., Ares, E., Pereira, A., Hernández, P., Pérez, J.A.: Comparative between FEM models and FDM parts and their approach to a real mechanical behavior. Proc. Eng. **63**, 878–884 (2013)
7. Chaitanya, S.K., Reddy, K.M., Harsha, S.N.S.H.: Vibration properties of 3D printed/rapid prototype parts. Int. J. Innov. Res. Sci. Eng. Technol. **4**(6), 4602–4608 (2015)
8. Stark, B., Stevenson, B., Stow-Parker, K., Chen, Y.Q.: Embedded sensors for health monitoring of 3D printed unmanned aerial systems. In: 2014 International Conference on Unmanned Aircraft Systems, 175–180, 2014

Chapter 18
A Neural Network Approach to 3D Printed Surrogate Systems

Rodrigo Sarlo and Pablo A. Tarazaga

Abstract The geometry of a Stradivarius violin was recently replicated through additive manufacturing, but nevertheless failed to produce a tone of professional quality. Due to the material limits of additive manufacturing, it is clear that purely geometric replicas are unlikely to create violins of comparable sound. We propose a "surrogate" system approach, which tailors some combination of a structure's material and geometric properties to mimic the *performance* of a target system. Finite element (FE) methods can approximate the vibrational performance of a violin or similar structure with high precision, given its specific physical properties and geometry. Surrogate systems, however, require the solution of the inverse problem. This can be achieved through artificial neural networks (ANN), a powerful tool for non-linear function estimation. As a stepping-stone to the violin problem, we first developed a surrogate method for simple beam structures. A neural network was trained on 7500 randomized beams to predict a thickness profile for a set of desired mode shapes and frequencies. Numerical simulation shows surrogates with good performance (<8 % modal error, <18 % frequency error) for target structures with a similar degree of thickness variation to that used in training the neural network. Performance improves dramatically (<2 % modal error, <7 % frequency error) for slightly less complex target structures.

Keywords Surrogate • Additive manufacturing • Neural networks • Finite element • Inverse problem

18.1 Introduction

The Stradivarius violin family is recognized for its distinctive sound, which is held as the gold standard among professional violinists. In 2011, the additive manufacturing company EOS produced a fully functional replica of one of these instruments, with a realistic violin sound [1]. Nevertheless, its tone fell observably short of professional quality. The difference lies in the material choice, a high density polymer, which significantly differs from wood. Stradivarius wood, in fact, is often cited as the source of their distinctive sound. Because of the limits in material choice in additive manufacturing, it is clear that geometric violin replicas are unlikely to close the apparent gap in sound. Additive manufacturing can, however, compensate for material differences through strategic modifications in the geometry, density and even composition of the base material.

To address this challenge, we propose a "surrogate" system approach, which tailors a structure's physical and geometric properties to mimic the performance of a target system which is fundamentally different in some physical characteristic, e.g. material composition. The problem falls into a general class of problems, called inverse problems, which aim to reconstruct the physical features of a structure based on its dynamic response, typically expressed in terms of natural frequencies, modes and damping ratios. Since modes are not necessarily unique to a structure [2], there is a potential to achieve similar responses in structures through variations of complementary physical or geometric properties. A surrogate Stradivarius violin then, would achieve a quality sound without the need for a very particular type of wood.

The direct problem, that is the prediction of a response based on a physical model, can be quickly and accurately solved using finite element (FE) methods. This means that we can execute multiple forward trials in an attempt to solve the inverse problem. Model updating is a popular technique which searches for the optimal parameter set by modifying a baseline model, but requires a new optimization for each case. In addition, it discards the results of unsuccessful trials [2]. This work presents a more holistic approach by using neural networks (NNs), a machine learning algorithm, to "learn" the underlying relationship between the model parameters and the response based on a large number of observations and their solutions. This technique requires solving one large optimization initially, but can then quickly predict solutions for new observations.

R. Sarlo (✉) • P.A. Tarazaga

Department of Mechanical Engineering, Vibrations, Adaptive Structures and Testing (VAST) Laboratory, Virginia Tech,
635 Prices Fork Road, Blacksburg, VA 24060, USA
e-mail: sarlo@vt.edu

Neural networks are a powerful tools for non-linear function estimation. In addition, they do not require a priori knowledge of the functional form of the system behavior. They have been successfully applied to structural engineering problems [3–6]. In particular, neural networks have been tested in structural health monitoring to predict locations of damage based on the behavior of healthy and damaged systems, with promising results. In a majority of these applications, the algorithms were trained on finite element models, where damage was simulated as a local reduction in element stiffness [7–9]. The health state of these structures was correlated with natural frequencies and mode shapes, which have been identified as good predictors of structural changes [10, 11].

As a stepping-stone to the violin problem, this work implements a neural network solution to the surrogate system problem for a simple one-dimensional beam structure. The goal vary the cross-section thickness of the beam to best match the mode shapes and frequencies of a target system. The reasoning behind the choice of thickness as the "free" parameter is twofold: first, thickness has a cubic relationship to local stiffness and thus a significant effect on mechanical response. Second, complex geometries can be easily achieved through current additive manufacturing technology. The latter could be leveraged to create a prototype for the test results. For a beam of fixed geometry and material density, the algorithm will be tasked with accurately mapping a deflection mode shape of the beam to a stiffness distribution along its length. The algorithm will be trained with modal data generated from a finite element model, in an approach inspired by previous structural health monitoring applications [7–9].

18.2   Neural Networks

Neural networks are built from a unit called a perceptron, a mathematical analogue to the biological neuron [12]. A perceptron accepts an arbitrary number of inputs passes the sum through an activation function to create an output signal. The activation can be any function; in this study we will employ the popular sigmoidal function, which gives the perceptron a non-linear response. To form a neural network, layers of perceptrons are linked through weighted connections, whereby the outputs of one layer are distributed to the inputs of the next, creating a complex signal flow that can approximate many non-linear behaviors. The first layer is the input and the last layer is the output. Intermediate layers are known as "hidden layers." Our case is a supervised learning problem, where we would like to find a mapping from a set of inputs to a set of known outputs. From a training dataset with known outputs, a neural network can "learn" which combination of interconnection weights minimizes the output error [13]. In this study, we will use one of the most common neural network training techniques to minimize this error: gradient descent with backpropagation. Gradient descent seeks to minimize the error, defined by some cost function, by following the steepest negative gradient of that function to locate its minimum [14].

There are number of parameters that can be modified to improve training performance, including the number of hidden layers and hidden layer size. The best number of hidden layers is often determined through trial and error, as no systematic methods are available [7]. In this study, we focus on neural networks of only one hidden layer, since this is typically a good starting point. The appropriate hidden layer size was chosen through a grid search methods (see Sect. 18.3).

18.3   Approach

The surrogate design in this paper considered a simple beam as stepping stone problem to more complex systems, in order to evaluate the feasibility of the approach. The goal is to create a beam of variable thickness throughout its span that has an equivalent modal response (for a certain number bending modes and frequencies) as a target beam of unknown physical characteristics. Thickness was chosen as the design parameter due to its cubic relationship to bending stiffness, which strongly affects the beam's response. In addition, variations in thickness are easy to model and 3D print, paving the way for physical prototypes.

Figure 18.1 outlines the surrogate beam approach. Data is generated from multiple iterations of a one-dimensional finite element Euler-Bernoulli beam model. The beam is modeled in a free-free condition and solved for the first four natural frequencies and bending modes. The material properties of the entire beam are kept constant and correspond to experimentally validated properties of 3D printing material (Stratasys Verowhiteplus). The finite element mesh (120 elements) is partitioned into 20 equally sized groups and each group is assigned a random thickness value within about 0.5–5 % of the beam's total length. Table 18.1 shows a summary of the beam model parameters; its geometric and material properties can be changed freely depending on the scale of the application and the available prototyping material. These values should not affect the neural network performance, but will determine the set of possible solutions. The finite element
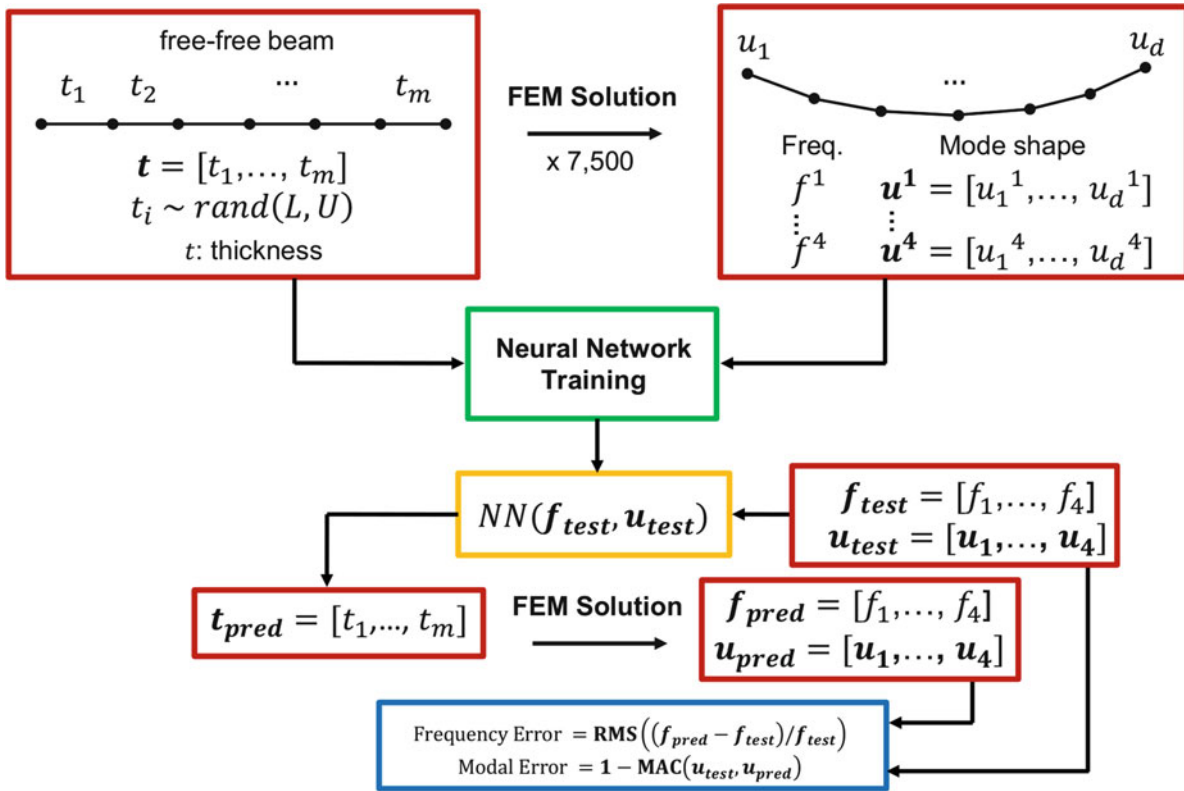
Fig. 18.1 Flow chart of the surrogate approach. $m =$ groupnumber, $d =$ meshsize

Table 18.1 Relevant parameters for beam model sample generation

Physical properties	
Elastic modulus	3.5 GPa
Density	1175 kg/m^2
Beam length	180 mm
Beam width	50 mm
Thickness variation	1–10 mm
Thickness distribution	Uniformly random
Finite element parameters	
FE mesh size	120
Group number (thickness)	20

parameters determine the complexity of the problem. The mesh size controls the resolution of the mode shapes while the number of thickness groups controls the spatial resolution of the surrogate beams thickness profile.

Seven thousand five hundred random thickness beams and corresponding FE solutions are generated to train the neural network solution. Each random thickness value was drawn independently from a uniformly random distribution, which covers the solution set well and tends produce good results [9]. Training sets much larger than 7500 samples did not seem to produce significant improvements in performance. Another 1500 samples are set aside for validating the network and testing its performance. Since we are interested in learning a mapping from a specific response to a thickness profile, we treat the response as the input to the neural network and the thickness distribution as the output. The input vector contains the first four natural frequencies and deflection mode shapes. For mesh of 120 beam elements, in this case, there are 488 input values (4 frequencies + 121 nodes * 4 modes). The output is the vector of thickness values that produced that response and is equal to the number of thickness groups, 20 in this case.

After the finite element program has generated the randomized input-output pairs of these vectors, a backpropagation neural network with one hidden layer is trained to generate a function ($NN(\mathbf{f}, \mathbf{u})$ in Fig. 18.1) that will predict a thickness profile from a response. To determine the optimal hidden layer size, we trained several networks on random subsets of the training set, varying the hidden layer size from 20 to 300 perceptrons. We observe the average prediction mean squared
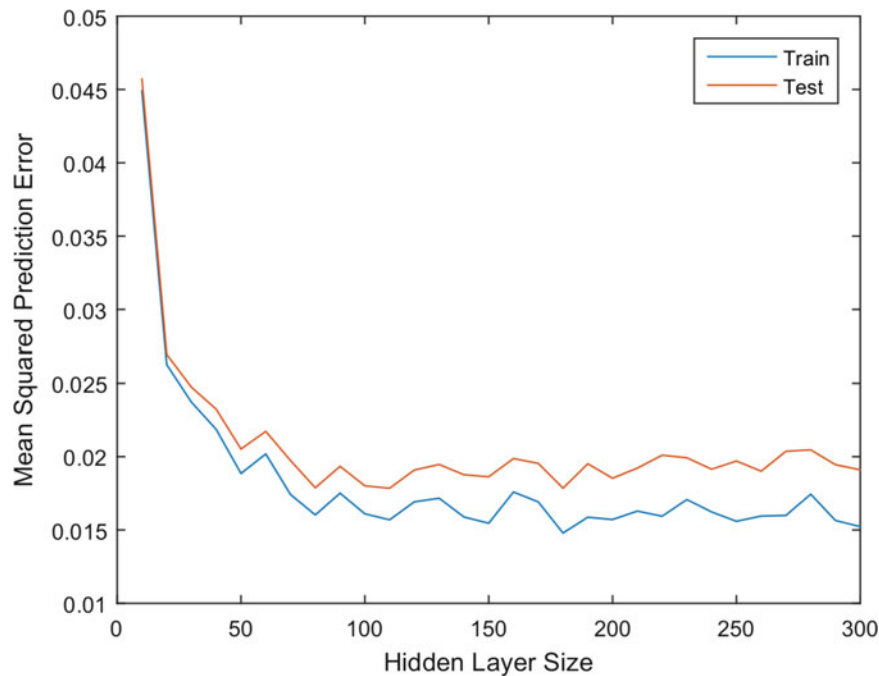
Fig. 18.2 Demonstration of how one hidden layer neural network error decreases with increasing layer size

(of the thickness profile) error both for the 7500 training samples and the 1500 test samples. The results in Fig. 18.2 show how the train and test errors decrease rapidly initially and then plateau around a hidden layer size 150. No further improvement in prediction accuracy seems to occur after this point, so we select this as the optimal size. The small gap between training and test error shows that the network is able to generalize well to cases that it has not yet observed.

The performance criterion of interest is how well the response of the predicted profile ($\mathbf{f_{pred}}, \mathbf{u_{pred}}$) matches the input to the predictor function ($\mathbf{f_{test}}, \mathbf{u_{test}}$). The error in the responses taken as the root mean squared (RMS) error of the normalized frequencies and one minus the modal assurance criterion (MAC). This performance criteria evaluates how well the surrogate system matches systems where the physical properties are unknown or irrelevant. In this study, the majority of the performance evaluation is done with responses from the finite element model, and thus subject to modeling errors when translated to the experimental domain. It is possible, albeit more time-consuming, to follow this approach using only experimental responses.

18.4 Results and Discussion

The surrogate prediction performance was first tested on 1500 variable thickness beams. These were generated in the same way as the training set, but were not seen in training. This evaluates how well the network learned the relationship between the beam thickness and response. In this test, as shown by an example result, we can compare not only frequency and mode shape (Fig. 18.3) but also the predicted geometry (Fig. 18.4). Notice from Fig. 18.4 that the predicted thickness profile (in blue) follows the true geometry (in red) quite closely, even in the presence of large sudden changes in thickness. The corresponding mode shapes to these geometries (Fig. 18.3) also have quite extreme features, yet they match quite closely. Modes 1–4 have MAC values of 99.8 %, 99.5 %, 97.3 %, and 98.3 % respectively.

Table 18.2 shows the frequency and modal average performance for the 1500 trials. The modal error (1-MAC) is below 3 % for the first mode and gradually increases to just under 12 % for the fourth mode. This is intuitive, since the complexity of the modes increases with their order. Nevertheless, these numbers show an acceptable degree of accuracy, since MAC errors below 10 % typically indicate modal consistency [15] The frequency performance is slightly worse, with a total average root mean squared error of around 18 %. This is most likely because there is one frequency value for every 120 modal value in the input vector, therefore the neural network optimization will favor reducing modal prediction errors. To improve this performance in the future, frequency error could be penalized more. Alternatively, two networks could be trained separately on frequency and mode shape inputs and then combine the results (ensemble method).
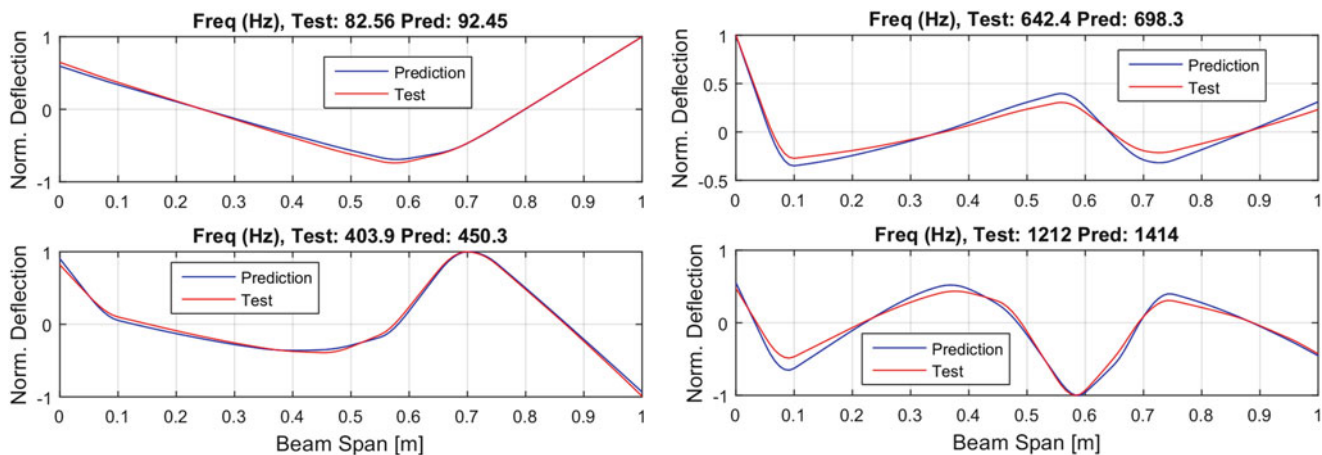
Fig. 18.3 Example mode comparison of a test (the target) and predicted (the surrogate) beam. The test beam was a variable thickness beam, shown in Fig. 18.4
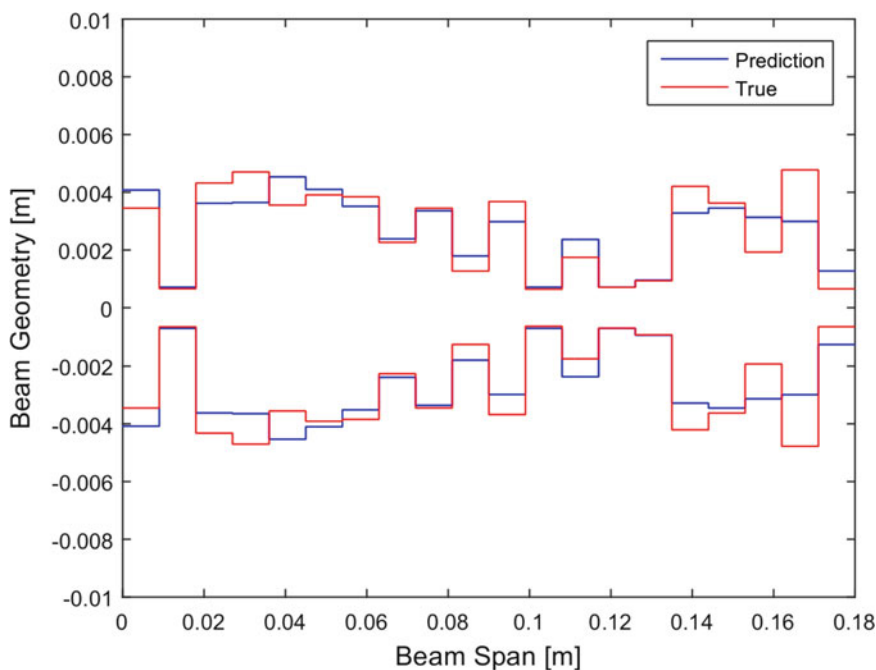
Fig. 18.4 Example thickness cross-section comparison of a test (the target) and predicted (the surrogate) beam. The beams correspond to the responses shown in Fig. 18.3

Table 18.2 Surrogate model performance for 1500 test samples of beams with random thickness distribution

	Freq. RMS error (%)	1-MAC (%)
	Mean (std. dev.)	Mean (std. dev.)
Mode 1	8.82 (3.30)	2.62 (4.24)
Mode 2	20.64 (20.78)	7.04 (9.54)
Mode 3	21.02 (19.55)	10.42 (13.36)
Mode 4	21.28 (19.16)	11.75 (14.13)
Total avg.	17.94 (15.70)	7.96 (10.32)

However, a realistic target beam may vary not just in thickness but additional physical properties (e.g. elastic modulus, density). To analyze how well the variable thickness beam generalizes to these cases, we generated 1000 beam samples where each of the 20 groups, in addition to a random thickness, was assigned a random elastic modulus and density value. The elastic modulus and density were varied randomly with bounds of $\pm 33\%$ and $\pm 10\%$ around the nominal values listed

Table 18.3 Surrogate performance results for 1000 test samples of beams of random thickness, density and elastic modulus

	Freq. RMS error (%)	1-MAC (%)
	Mean (std. dev.)	Mean (std. dev.)
Mode 1	28.52 (32.10)	5.60 (8.76)
Mode 2	30.38 (28.84)	13.29 (16.16)
Mode 3	30.05 (26.74)	20.09 (20.73)
Mode 4	29.47 (26.67)	24.49 (22.80)
Total avg.	29.60 (28.59)	15.87 (17.11)
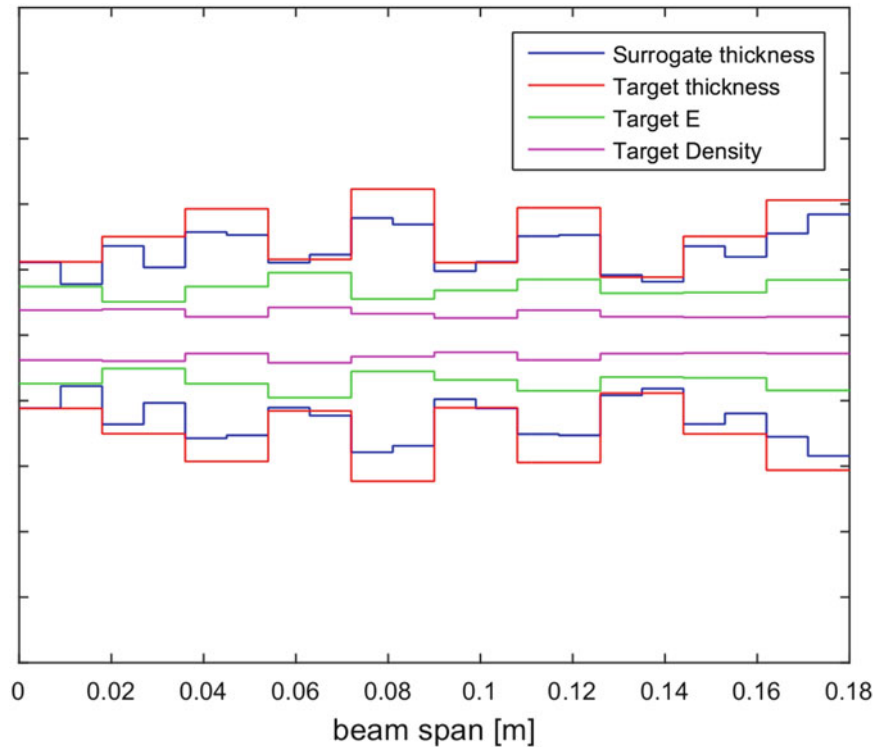
Fig. 18.5 Illustration of feature variation at different spatial resolutions. Features not to scale

in Table 18.1. The average results are shown in Table 18.3. As expected, the error values and standard deviations increase, particularly at higher orders, because the space of responses due to variable thickness cannot cover the much larger solution space encompassed by multiple parameters.

We can overcome this inability to generalize the surrogate beam response in two ways. The first is to retrain the network on combinations of several physical parameters to try to cover the entire solution space. This would require a more complex neural network and an exponentially larger training set, since the effects of the physical parameters are coupled. Another potential solution is to increase the spatial resolution of the beam, i.e the number of groups. Varying the thickness at a finer rate may account for other, more complex, changes in the structure. This has the advantage of still focusing on one parameter, and would require only moderate increase in complexity compared to the first method.

To examine how finer resolution might help general surrogate performance, we created another set where the beams had randomly varying thickness, elastic modulus and density. The spatial resolution, however, was reduced to 10 groups per span (half that of the training set). This gave the variable thickness surrogate a chance to compensate. An illustration of this concept in shown in Fig. 18.5. Notice how the surrogate beam (blue) thickness varies at twice the resolution of the target features. The mode matching example in Fig. 18.6 now reveals less extreme features and thus an easier fit.

The overall results in Table 18.4 show a dramatic improvement in performance over both previous tests. The modal and frequency errors are all well below 5 % and 10 %, respectively, and the reduced standard deviation values show more consistent performance. Clearly, the reduction in resolution of the target reduced the number of possible responses, making the surrogate prediction task much easier. Even though the target resolution was decreased, the result is analogous to increasing the resolution of the surrogate beam.
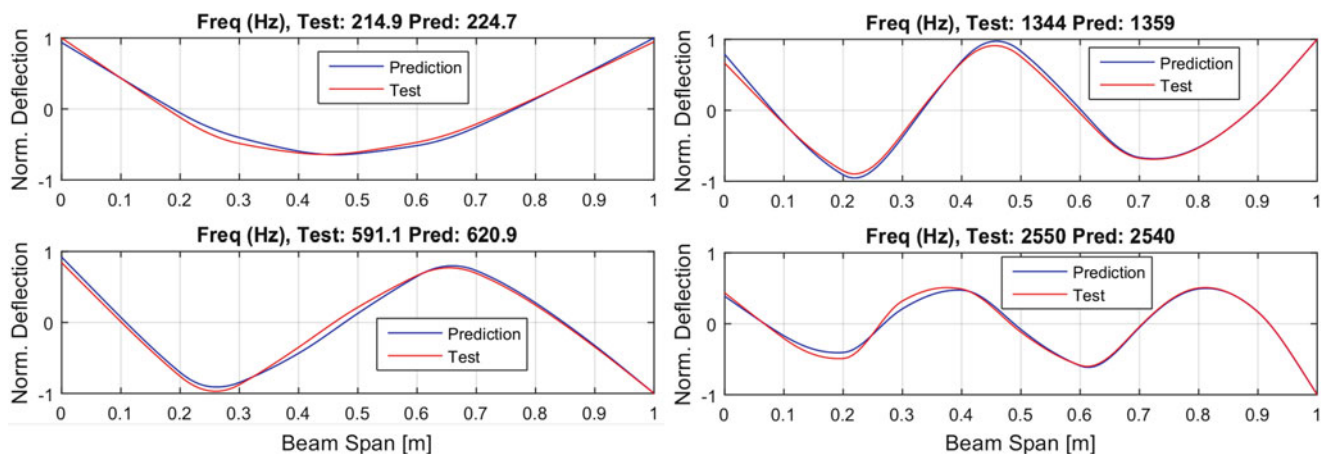
Fig. 18.6 Example mode comparison of a test (the target) and predicted (the surrogate) beam. The test beam was a beam with variable thickness, elastic modulus and density

Table 18.4 Surrogate performance results for 1000 test samples of beams of random thickness, density and elastic modulus at 1/2 spatial resolution

	Freq. RMS error (%)	1-MAC (%)
	Mean (std. dev.)	Mean (std. dev.)
Mode 1	3.84 (0.87)	0.35 (0.69)
Mode 2	7.81 (8.87)	0.98 (1.24)
Mode 3	7.97 (9.48)	2.19 (4.48)
Mode 4	7.32 (7.87)	3.94 (6.68)
Total avg.	6.74 (6.77)	1.86 (3.27)

18.5 Conclusions

We have presented an approach to designing surrogate systems, capable of replicating the dynamic characteristic of a target whose physical characteristics are inaccessible or unknown. The approach is inspired by an attempt to 3D print a Stradivarius violin replica, where significant material differences resulted in a low-quality sound. Possible applications are expandable to many structural design scenarios. This work uses a beam surrogate example to study the feasibility of this approach. The surrogate beam is given one free parameter, thickness, which can be varied spatially in order to modify its frequencies and mode shapes. The optimal thickness profile to achieve a target response is determined by a neural network algorithm, which is trained on a set of 7500 random beam thickness profiles. The algorithm shows an ability to predict surrogates with low modal error (<12 %) and moderate frequency error (<18 %) to targets which did not appear in training. It falls short, however, in more realistic scenario when the target beam varies with several physical parameters at once (thickness, elastic modulus, and density). We were able to show, that this inaccuracy can be dramatically improved by increasing the spatial resolution of the thickness profile.

Despite the specific parameters used in this study, the method can be adapted to any scale and material without loss in neural network performance. The choice of the free parameter(s) is also up to the user. The critical detail is that the training set cover the appropriate solution space. One obvious way is to increase the number of free parameters in the set, but this may have high complexity costs. Our results indicate that the solution space is substantially increased, at a lower cost, by instead increasing the free parameter spatial resolution. Future work in surrogate systems should expand the approach to more complex structures, such as plates and 3D solids, to assess whether these conclusions hold.

References

1. The Economist: Print me a Stradivarius. Economist 7 (2011). http://www.economist.com/node/18114327
2. Atalla, M.J., Inman, D.J.: On model updating using neural networks. Mech. Syst. Signal Process. **12**(1), 135–161 (1998)
3. Hung, S.-L., Adeli, H.: Object-oriented backpropagation and its application to structural design. Neurocomputing **6**(1), 45–55 (1994)
4. Wu, X., Ghaboussi, J., Garrett, J.H.: Use of neural networks in detection of structural damage. Comput. Struct. **42**(4), 649–659 (1992)
5. Adeli, H., Park, H.S.: Counterpropagation neural networks in structural engineering. J. Struct. Eng. **121**(8), 1205–1212 (1995)
6. Kaminski, P.: The approximate location of damage through the analysis of natural frequencies with artificial neural networks. Proc. Inst. Mech. Eng. E J. Process. Mech. Eng. **209**(2), 117–123 (1995)
7. Zhao, J., Ivan, J.N., DeWolf, J.T.: Structural damage detection using artificial neural networks. J. Infrastruct. Syst. **4**(3), 93–101 (1998)
8. Ferregut, C.M., Osegueda, R.A., Ortiz, J.: Artificial neural networks for structural damage detection and classification. In: Smart Structures & Materials' 95, pp. 68–80. International Society for Optics and Photonics, Bellingham, WA (1995)
9. Chang, C., Chang, T., Xu, Y., Wang, M.: Structural damage detection using an iterative neural network. J. Intell. Mater. Syst. Struct. **11**(1), 32–42 (2000)
10. Ni, Y., Wang, B., Ko, J.: Constructing input vectors to neural networks for structural damage identification. Smart Mater. Struct. **11**(6), 825 (2002)
11. Yun, C.-B., Bahng, E.Y.: Substructural identification using neural networks. Comput. Struct. **77**(1), 41–52 (2000)
12. McCulloch, W.S., Pitts, W.: A logical calculus of the ideas immanent in nervous activity. Bull. Math. Biophys. **5**(4), 115–133 (1943)
13. Lippmann, R.P.: An introduction to computing with neural nets. IEEE ASSP Mag. **4**(2), 4–22 (1987)
14. McClelland, J.L., Rumelhart, D.E., PDP Research Group, et al.: Parallel Distributed Processing, vol. 2. MIT Press, Cambridge (1987)
15. Pastor, M., Binda, M., Harčarik, T.: Modal assurance criterion. Proc. Eng. **48**, 543–548 (2012)

Chapter 19
Modal Test and Parameter Updating of Metal Laser Sintered Components

Joseph D. Schoneman and Matthew S. Allen

Abstract Recent advances in additive manufacturing technology have made feasible the use of materials such as titanium and high-temperature nickel alloys in the construction of complex parts intended for production through techniques such as direct laser melting or direct laser sintering. These parts can be manufactured at a level of quality suitable not only for prototyping, but even for use as flight hardware. However, the evaluation of material properties is a challenge; melted metals will not retain the same properties as an equivalent cast metal, and factors such as part geometry, print density, and any post-processing techniques used will all influence the material properties of a given component. This paper uses modal analysis to update the isotropic material properties of metal components which are representative of flight hardware within the subsystems of a liquid rocket motor. Two different materials are examined: Ti 64 titanium alloy and INCONEL 718 nickel alloy.

Keywords 3D printing • Modal test • Model updating

19.1 Introduction

The advent and spread of additive manufacturing (AM) technologies, such as fused deposition modeling (FDM), selective laser sintering (SLS) or direct metal laser sintering/melting (DMLS/DMLM)—commonly referred to as *3D printing*[1]—has been met with rapid adoption in many areas of the aerospace industry. AM techniques are best applied to components which feature complex design features, low production runs, optimization for light weight, and exotic material requirements. Such requirements are prevalent in the aerospace industry in general, and the launch industry in particular. In the subfield of liquid rocket motor design, additively manufactured designs can make use of superalloys that would be either impossible or prohibitively expensive to manufacture using conventional casting or machining techniques.

A major area of interest related to AM technology is the estimation or validation of material properties of the built components. Depending on the manufacturing technique and material in question, the material may be extruded into a wire or powdered prior to the build; during the build process, either a laser or heated extruder head melts or lays down material in a layer-by-layer process which eventually builds up the full component. The various mechanical operations and phase changes which the material is subjected to may lead to significant changes from tabulated mechanical properties. Further, the layer-by-layer build process leads to the potential for orthotropic material properties which depend on build orientation.

Key elastic properties of a material can be evaluated through the use of the static tensile test; most significantly, the elastic modulus E, yield stress σ_y, ultimate stress σ_u, and Poisson's ratio ν. Biaxial testing can be used to identify the elastic constants of an anisotropic material. However, only specifically constructed test billets can be used on a tensile testing machine; tensile testing of operational components is not possible.

AM build processes admit the possibility of property variations between different component designs. First, since AM processes all rely on the heating and cooling of the build material, different components will feature different patterns of residual stresses. Perhaps more significant is the common use of "skin and core" construction [1], as shown in Fig. 19.1.

---

[1] Under some definitions, "3D printing" refers specifically to the manufacture of plastic parts, though it is often used as a catch-all term for any sort of additive manufacturing process. Here, the abbreviation "AM" is used to encompass all possible additive processes, and the more specific "DMLS" abbreviation is used to refer to the specific process in use for this paper.

J.D. Schoneman (✉) • M.S. Allen
Department of Engineering Physics, University of Wisconsin, 1500 Engineering Drive, Madison, WI 53706, USA
e-mail: schoneman@wisc.edu; matt.allen@wisc.edu
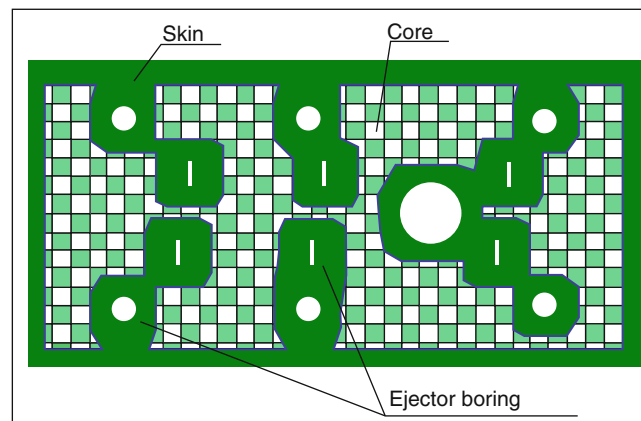
Fig. 19.1 Demonstration of the "skin & core" construction technique commonly used in AM processes[1]. The skin of the structure is built at full density, often to a thickness of 1–3 mm, while the inner core is built at reduced density to save weight and cost

The outer skin of the structure is built at full density, often to a thickness of 1–3 mm, to maintain strength on the outer surface of the part. To save weight and material costs, the interior of the part is built at a reduced density. This is a useful design technique, but complicates the task of identifying accurate mechanical properties for a given material.

As an alternative to static tensile testing, modal testing allows the recovery of natural frequencies and mode shapes of a component. From these, relevant material properties and physical dimensions can be inferred. Compared to static tensile testing, modal testing has several disadvantages when used to determine the material properties of a specific part:

- The material properties are only *estimated*, not observed. Estimation of the actual material properties requires a suitable model—usually a finite element model—which itself may be subject to error.
- The natural frequencies of a structure depend on both the density and elasticity of its material; if the density cannot be estimated, then accurate estimation of both parameters is difficult.
- Dimensional variations in the structure affect the natural frequencies and mode shapes independently of the material properties.
- No estimates of yield strength or ultimate strength can be made from a modal test.

However, several key advantages are apparent as well:

- Modal testing serves as a method to validate a finite element model as a whole—large discrepancies in frequencies or mode shapes can be found and rectified.
- Modal testing recovers the damping characteristics of the component, which heavily influence the design requirements for several types of dynamic loading and are difficult to compute in general.
- Modal testing is non-destructive and can be used on any component. Unlike tensile tests, modal tests do not require specialized geometry.

With these factors in mind, a modal test was conducted in conjunction with Orbital Technologies Corporation (ORBITEC); a propulsion and spacecraft systems company located in Madison, WI. In order to evaluate the accuracy and capabilities of AM techniques for the construction of propulsion components, ORBITEC commissioned a set of test articles from GPI Prototyping, Inc; an AM vendor located in Rockford, IL. The test components are shown in Fig. 19.2; no surface finish was specified beyond the removal of support material. The print direction was from top to bottom as pictured in Fig. 19.2. Two materials were evaluated: Titanium—6 % Aluminum—4 % Vanadium alloy (Ti 64) and an INCONEL 718 (INCO) nickel "superalloy."

Nominal mechanical properties for each material are shown in Table 19.1 [2, 3].

The remainder of this paper describes the construction of a finite element model, test procedures, and the parameter update procedure used to evaluate these components.
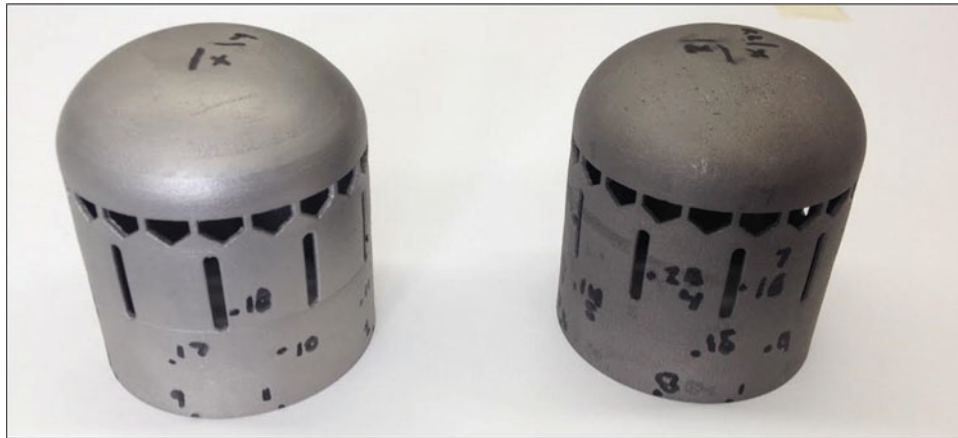
Fig. 19.2 INCO 718 (*left*) and Ti 64 (*right*) test components manufactured using the DMLS (Direct Metal Laser Sintering) process

Table 19.1 Nominal material properties used for initial finite element analysis

Material	Elastic modulus [lb/in^2]	Density [slug/in^3]
INCO 718	29,000	7.62×10^{-4}
Ti 64	16,000	4.12×10^{-4}

19.2   Finite Element Model Development

The use of a modal test to estimate material properties is dependent on the presence of a representative structural model, either analytical or numerical. For all but the most trivial of structures, analytical models are not feasible and instead the finite element method (FEM) is used to obtain the natural frequencies and mode shapes. In this case, Abaqus® finite element (FE) software was used for the analysis. Geometry from SolidWorks® modeling software can be directly imported into Abaqus as a deformable solid. Once this is accomplished, a mesh is applied to the geometry.

Several meshing approaches are available. Tetrahedral elements can be used to mesh a solid of arbitrary shape at the cost of significantly increased element count, since the four-vertex tetrahedron does not fill nearly as much space as a six-vertex hexahedron. Hexahedral meshes, on the other hand, allow for much smaller element counts but almost always require significant geometric simplification of the component. Finally, a shell mesh applied to thin geometries is much more efficient and accurate than a mesh of solid elements over a thin cross section. Each of these approaches was evaluated for this geometry as follows:

- The full geometric complexity of the model was retained and a quadratic tetrahedral mesh (C3D10 elements in Abaqus) was applied.
- All filleted edges were removed in SolidWorks prior to import and a quadratic hexahedral mesh (C3D20) was applied to the entire model.
- Using the non-fillet geometry, a linear hexahedral mesh (C3D8) was applied to the "dome" area of the part, and "solid shell" elements (SC8R) were applied to the remainder of the component. "Solid shell" elements use a shell formulation, but inherit their thickness directly from the thickness of the solid geometry which they are applied to. The linear hexahedral mesh was required for element compatibility.

In the third case, a reduced integration formulation was examined to counteract the expected stiffness resulting from linear quadratic elements, but was found to provide overly soft results relative to the other two methods.

To evaluate the convergence properties of each mesh, three separate modal analyses using different refinement levels for each mesh type were performed. INCO 718 material properties were used for the convergence study. For initial analysis, isotropic elastic behavior was used, on the assumption that any anisotropic material would be evident in the test results. Table 19.2 and Fig. 19.3 show the mesh parameters and results. Due to the near-symmetric configuration of the component, the first six modes appear as pairs of close natural frequencies; the lower of each frequency pair is reported as the first, third, and fifth frequency in Table 19.2. All of these are "flapping" modes of various orders, with the free edges of the cylinder predominant in the response. A three-dimensional view of the first mode pair is shown in Fig. 19.4, while top-down views of the first ten modes of the INCO 718 structure (those of the Ti64 component are comparable) are depicted in the appendix.

Table 19.2 Mesh characteristics and frequency results of FEM convergence study

Type	DOF count	Total time [s]	Memory [MB]	f_1 [Hz]	f_3 [Hz]	f_5 [Hz]
Quad. Tet.—Coarse	542859	101	6111	1453	3689	6637
Quad. Tet.—Medium	832059	261	9838	1452	3686	6631
Quad. Tet.—Fine	1948953	1924	25,575	1450	3680	6617
Quad. Hex.—Coarse	195351	70	2348	1451	3681	6618
Quad. Hex.—Medium	450000	214	5948	1450	3677	6604
Quad. Hex.—Fine	1706199	7305	26,776	1448	3674	6591
Lin. Hex + Shell—Coarse	32940	5	316	1461	3618	3684
Lin. Hex + Shell—Medium	83502	16	781	1455	3684	6618
Lin. Hex + Shell—Fine	246642	52	2366	1451	3676	6600

All listed frequencies correspond to "flapping modes" of different orders
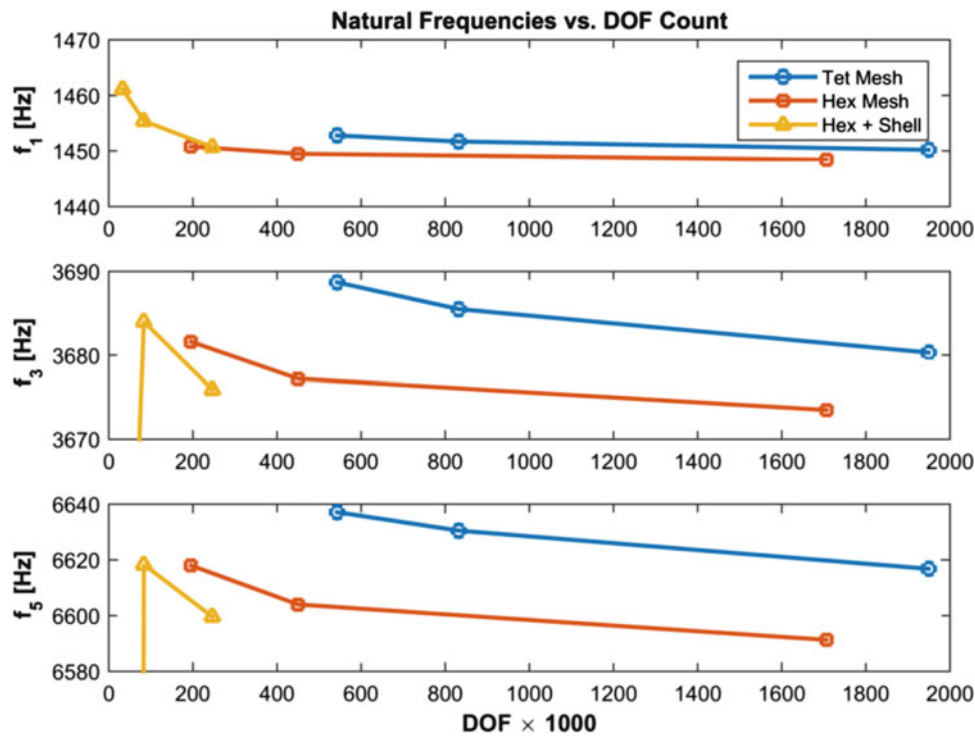
Fig. 19.3 Visual depiction of the convergence study results

Note that the finest refinements of the solid meshes both exceeded the 12 GB installed RAM of the workstation, leading to drastically longer computational time requirements incurred by read/write to the hard disk. Furthermore, the sensor placement procedure used below requires that the Abaqus results be imported into MATLAB, which places further restrictions on the largest model that can be accommodated. Examination of the results reveals that the "medium" refinement level of the solid/shell predicted only a slightly higher first natural frequency than the solid mesh counterparts, and was midway between the tetrahedral and hexahedral results for the third and fifth frequencies. As such, this was the model selected for import into MATLAB for sensor set selection.

A "truth" model for later comparison to experimental results was also selected. In this case, a balance between frequency convergence and model size led to selection of the medium hexahedral mesh; the finest refinement of this mesh showed only a marginal downward shift in frequency relative to the moderate level, at a greatly increased computation time.
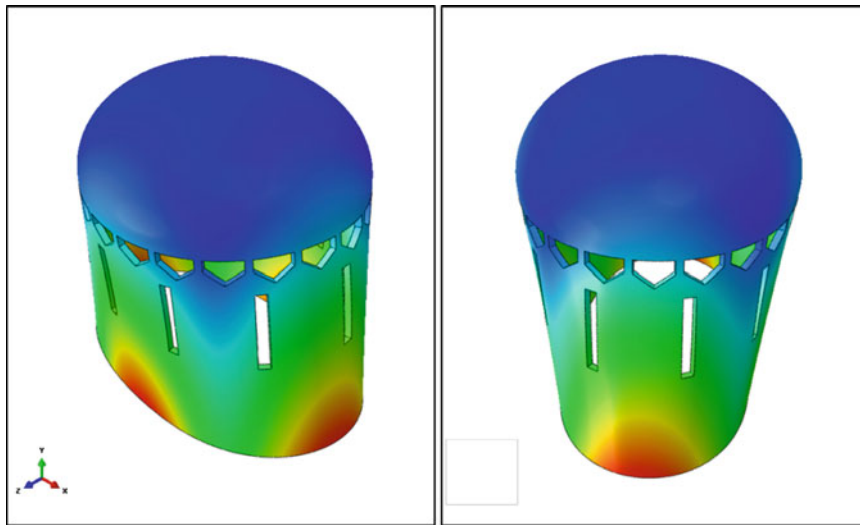
Fig. 19.4 Three dimensional view of the one/two mode pair; contours depict modal deformation levels
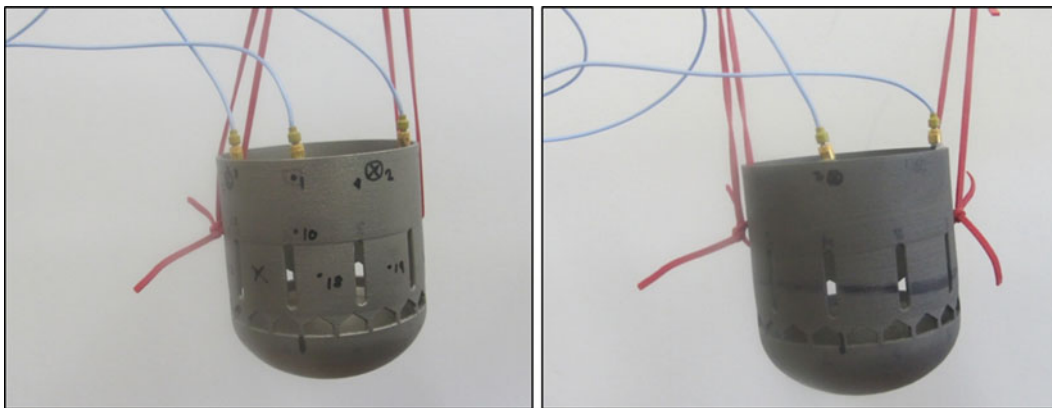
Fig. 19.5 INCO 718 (*left*) and Ti 64 (*right*) articles during the test procedure

Table 19.3 Acquisition properties for each test case

Component	Frequency range [kHz]	Frequency interval [Hz]
Ti 64	20	3.1
INCO 718	10	1.56

19.3 Modal Test Setup

Once the prototype parts were fabricated, the modal test was performed. The test method used was a roving hammer impact test. A four-channel data acquisition unit was available; three accelerometers were used as references. The components were tested in a free-free suspended condition; Fig. 19.5 shows the articles instrumented for testing.

Bruel and Kjaer software was used to monitor the input/output and compute accelerance frequency response functions for each impact point. Different sample frequencies and time windows were used for the Ti 64 and INCO 718 parts; a larger frequency range was used for the titanium version to attempt measurement of higher modes, while a closer frequency spacing was used for the Inconel version to better distinguish the closely spaced modes. Table 19.3 gives the acquisition settings for each test case. At each impact location, three signal averages were used to determine the frequency response function (FRFs) corresponding to that point.

While only three accelerometer channels were available, an arbitrary number of hammer excitation points could be selected. Increasing the number of impact points increases the resolution of the mode shapes, but the set of modes that
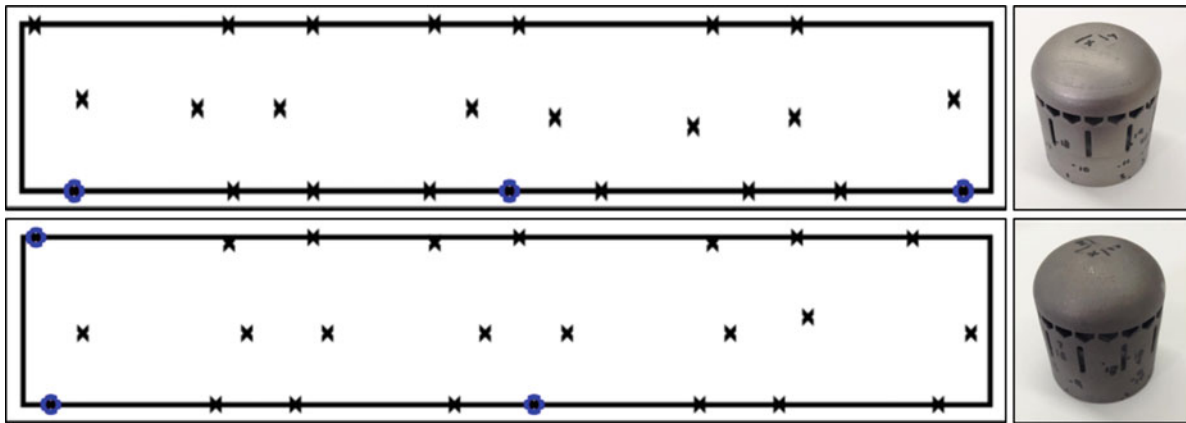
Fig. 19.6 Hammer impact (*black crosses*) and accelerometer (*blue circles*) locations for each part. *Top*: INCO 718 component. *Bottom*: Ti 64 component

Table 19.4 Modal test results for both components

| Mode | INCO 718 | | | | Ti 64 | | | |
	FEm freq [Hz]	Test freq [Hz]	Pct. error	ζ [%]	FEm freq [Hz]	Test freq	Pct error	ζ [%]
1	1448	1361	6.44	0.43	1487	1474	0.93	0.45
2	1451	1367	6.16	0.25	1487	1482	0.32	0.32
3	3673	3420	7.40	0.25	3773	3715	1.57	0.36
4	3678	3431	7.19	0.28	3773	3734	1.03	0.34
5	6590	6111	7.84	0.29	6776	6598	2.69	0.93
6	6595	6131	7.57	0.47	6776	6623	2.31	0.71
7	–	–	–	–	8988	8712	3.17	0.85
8	–	–	–	–	8991	8831	1.81	0.50
9	–	–	–	–	9807	9987	−1.81	0.36
10	–	–	–	–	9957	10014	−0.57	0.56

can be identified is limited by the reference (accelerometer) locations. To select both the accelerometer and impact locations, the method of "Effective Independence" was used [4]. This technique seeks to maximize the Fisher Information Matrix **Q** of a structure, defined as

$$\mathbf{Q} = \mathbf{\Phi}^T \mathbf{\Phi} \tag{19.1}$$

where $\mathbf{\Phi}$ is the target modal matrix of the structure at each reference location. For the INCO component, the target mode set included the first six modes; for the titanium structure, the first ten. There are multiple methods to place sensors and actuators using Effective Independence. In this case, an "additive" technique starting from a single accelerometer location was used [5]. Since the accelerometers and impact locations act in the radial direction on the structure, rather than the Cartesian coordinate system used in the finite element program, the FE mode shapes were transformed to a cylindrical coordinate prior to sensor selection. Only the external radial locations were included in the possible set of locations. Three accelerometer/impact locations and 21 impact-only locations were selected, for a total of 24 impact locations. Figure 19.6 shows the resulting impact and accelerometer locations for each version of the part.

With the test complete and FRFs obtained, an implementation of the algorithm of mode isolation (AMI) [6] was used to obtain each component's modal parameters. The implementation in question is a multi-input multi-output method using a single degree-of-freedom linear least squares fit, with the option to use a multi-degree-of-freedom linear least squares fit in the presence of close or repeated modes. The resulting natural frequencies and critical damping ratios identified for each component are presented in Table 19.4, while the measured FRF envelope and estimated curve fit FRF is shown in Fig. 19.7. The modal assurance criterion (MAC) matrices of the test results are shown in Fig. 19.8.

The INCO 718 test results are clearly superior to those from the Ti 64 component. The titanium was a more difficult material on which to obtain clean hammer impacts due to the lighter weight of the component. Any clear "double-hits" were ignored and re-tested, but the overall quality of the Ti 64 measurements was lower than those from the INCO part.
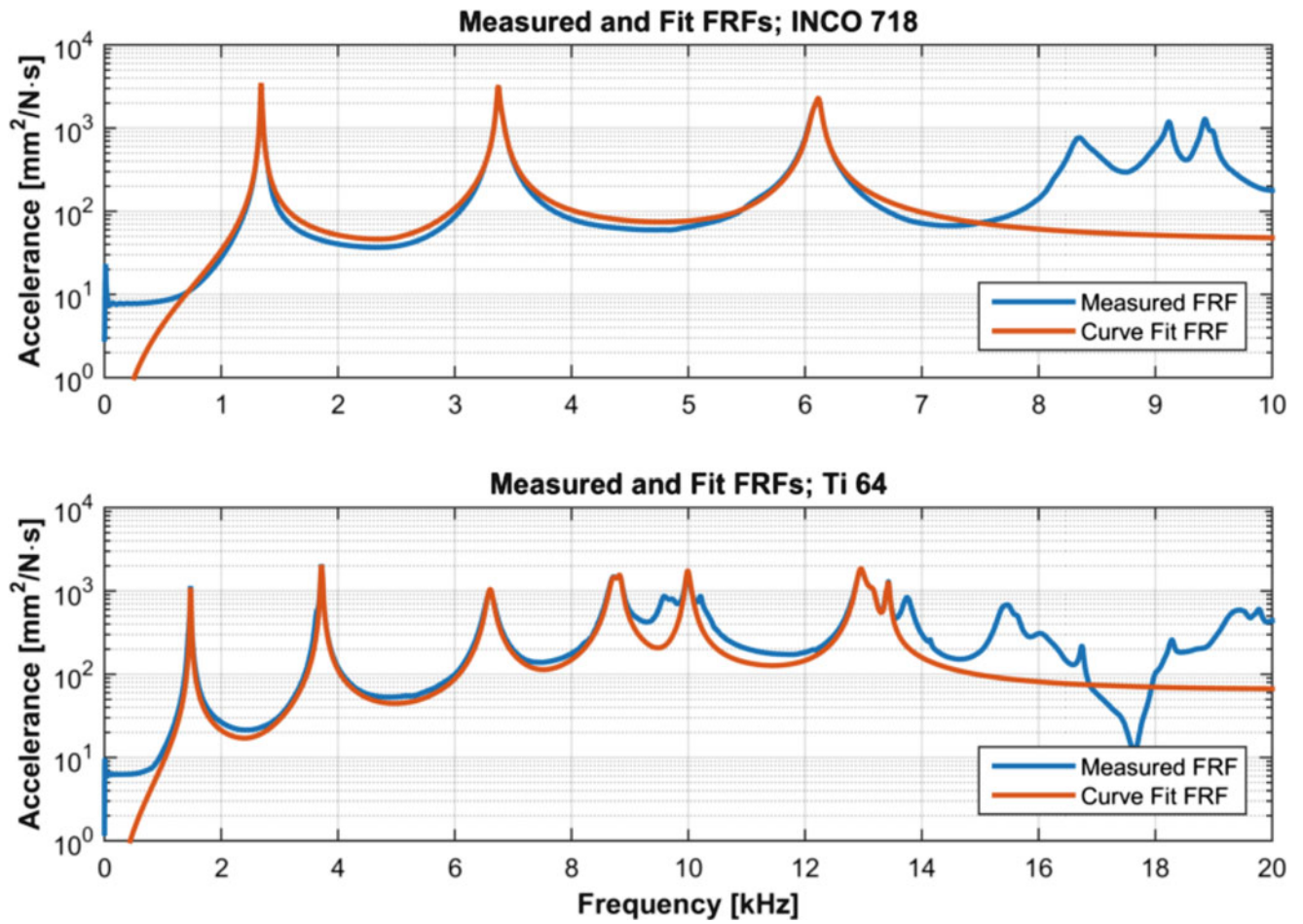
Fig. 19.7 Measured and estimated composite FRFs of each component
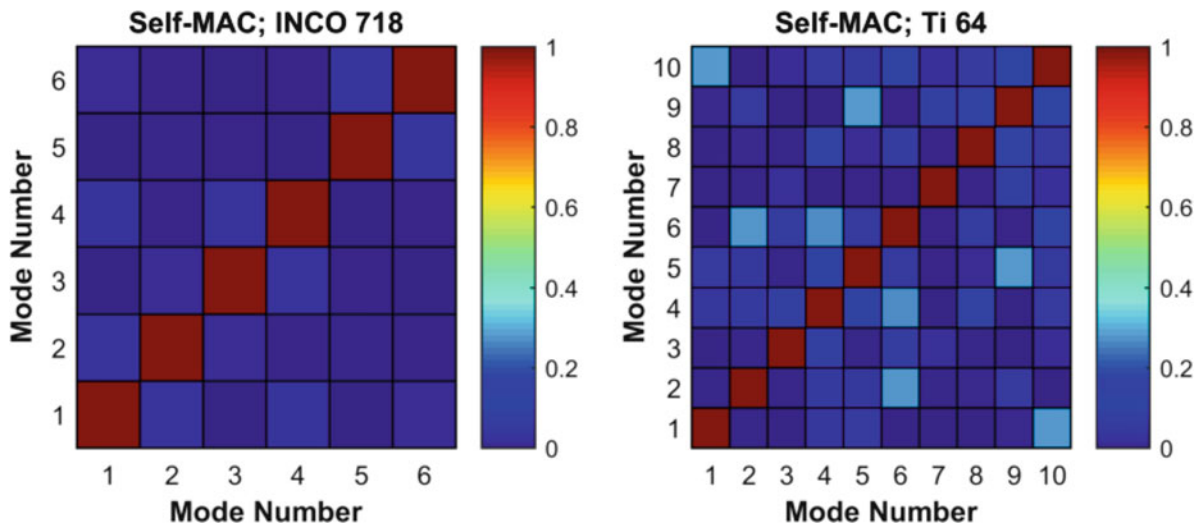
Fig. 19.8 Self-MACs of the test results for each component

19.4 Parameter Update Procedure

With a numerical model and set of test result in hand, the final task is to use these values to estimate each material's density and modulus of elasticity. In general, model updating requires an optimization framework linked to a full finite element code. Commercial software packages, such as ATA Attune™, are also available to perform model correlation procedures.

In this case, frequency errors are already quite low and all modes seem to be in error by similar amounts, suggesting acceptable results can be achieved by assuming isotropic material properties and concentrating on the ratio of density to modulus of elasticity. Given the size of these components, their actual densities can be estimated as well. Based on the minimum and maximum feasible values of measured density, upper and lower bounds on the modulus of elasticity can be formed.

19.4.1 Density Estimation

The weight of each component is easily measured with high accuracy, but a volume estimate was more difficult to obtain. The volume of water displaced by each item was measured in a 2.75 inch diameter test tube, however, the total displacement levels were small and sensitive to measurement errors. Two sets of marks were made for each displacement measurement; the averages of these two distances were used as upper and lower bounds on component volume. Finally, maximum and minimum density values were estimated by dividing the largest possible mass by the smallest possible volume and vice versa. Table 19.5 summarizes the density estimation measurements and results for each material.

19.4.2 Least-Square Parameter Fit

With an available value for material density, the natural frequencies are assumed to be functions of the elastic modulus only. A least-squares approach involving only the natural frequencies can be used to infer the values of this material property. From common analytical expressions for the natural frequencies of other types of structures, the ith natural frequency of this component is assumed to take the form

$$f_i = \sqrt{\frac{E}{\rho}}\alpha_i \tag{19.2}$$

where α_i is a value which depends on the geometry of the structure and the modeshape in question. To estimate the actual elastic modulus, set up a least-squares minimization problem in E:

$$\min_{E} \quad \mathbf{y}(E)^T\mathbf{y}(E) \tag{19.3}$$

where the vector $\mathbf{y} = \dfrac{\mathbf{f}_{FE}^2(E) - \mathbf{f}_t^2}{\mathbf{f}_t^2}$ is an error vector written in terms of the finite element frequencies $\mathbf{f}_{FE}(E)$ and test frequencies $\mathbf{f}_t$; the exponent and division symbols are understood to refer to "elementwise" operations. Re-writing in terms of Eq. (19.2) leads to

$$y_i = \frac{E_{FE}}{E_t}\frac{\rho_t}{\rho_{FE}}\left(\frac{\alpha_{FE}}{\alpha_t}\right)_i^2 - 1 \tag{19.4}$$

Table 19.5 Mass and volume measurements for each component along with the resulting estimated density values

	INCO 718	Ti 64
Mass [g]	110.05 ± 0.01	61.07 ± 0.01
Volume [in^3]	$8.249 \times 10^{-1} \pm 1.262 \times 10^{-2}$	$8.382 \times 10^{-1} \pm 2.227 \times 10^{-3}$
Density [slug/in^3]	$7.621 \times 10^{-4} \pm 1.173 \times 10^{-5}$	$4.161 \times 10^{-4} \pm 1.037 \times 10^{-6}$

for the ith element of $\mathbf{y}$. The "FE" subscript refers to nominal properties used to compute the natural frequencies, while the "t" subscripts refer to actual properties of the test article. The density ρ_t has been estimated for each component, so only E_t remains to be found. Re-write Eq. (19.4) by setting $x = \frac{E_{FE}}{E_t}$ and $\beta_i = \frac{\rho_t}{\rho_{FE}}\left(\frac{\alpha_{FE}}{\alpha_t}\right)^2_i$ so that $y_i = x\beta_i - 1$. The least-squares problem is solved by finding an x such that

$$\nabla \mathbf{y}^T(x)\mathbf{y}(x) = 0 \tag{19.5}$$

Since only a single optimization variable is in use, each element of $\nabla \mathbf{y}(x)$ is simply $\frac{\partial y_i(x)}{\partial x} = \beta_i$ and x can be found from

$$x = \frac{\sum_i \beta_i}{\sum_i \beta_i^2} \tag{19.6}$$

Finally, β_i can be written in terms of the known test frequencies, finite element frequencies, and density ratio as

$$\beta_i = \frac{\rho_t}{\rho_{FE}}\left(\frac{f_t}{f_{FE}}\right)^2_i \tag{19.7}$$

where ρ_{FE} is the "nominal" material value from Table 19.1 and ρ_t, with its associated upper and lower bounds, is the estimated density value from Table 19.5. Once x is found, the modulus of elasticity is estimated using

$$E_t = xE_{FE} \tag{19.8}$$

19.4.3   Estimation Results

In principle, the procedure above can be performed iteratively through the finite element program, but a single pass of the calculation proved sufficient to provide acceptable results. The updated elastic modulus and density value for each component, along with upper and lower bounds, are shown in Table 19.6.

The finite element models were re-analyzed in Abaqus using these values; resulting frequencies for the INCO 718 component are shown in Table 19.7, those for the Ti 64 component are shown in Table 19.8.

Table 19.6 Updated parameter estimation results from the frequency-only least squares minimization technique

| | INCO 718 | | Ti 64 | |
	Value	Percent of nominal	Value	Percent of nominal
Density [slug/in^3]	$7.62 \times 10^{-4} \pm 1.17 \times 10^{-5}$	100.07 ± 1.54	$4.23 \times 10^{-4} \pm 6.54 \times 10^{-6}$	102.68 ± 1.59
Elastic modulus [lb/in^2]	$2.53 \times 10^7 \pm 3.90 \times 10^5$	87.27 ± 1.34	$1.59 \times 10^7 \pm 2.46 \times 10^5$	99.27 ± 1.54

Table 19.7 Updated natural frequency results for the INCO 718 component

| Mode | Frequencies [Hz] | | | Error [%] | |
	FEA—nominal	Test	FEA—updated	Nominal	Updated
1	1448	1361	1358	6.44	−0.18
2	1451	1367	1358	6.16	−0.65
3	3673	3420	3446	7.40	0.75
4	3678	3431	3446	7.19	0.42
5	6590	6111	6188	7.84	1.27
6	6595	6131	6189	7.57	0.94

Table 19.8 Updated natural frequency results for the Ti 64 component

Mode	Frequencies [Hz]			Error [%]	
	FEA—nominal	Test	FEA—updated	Nominal	Updated
1	1487	1474	1454	0.93	−1.36
2	1487	1482	1454	0.32	−1.95
3	3773	3715	3687	1.57	−0.73
4	3773	3734	3688	1.03	−1.26
5	6776	6598	6622	2.69	0.37
6	6776	6623	6623	2.31	−0.00
7	8988	8712	8785	3.17	0.83
8	8991	8831	8787	1.81	−0.50
9	9807	9987	9585	−1.81	−4.03
10	9957	10,014	9732	−0.57	−2.82

19.5   Conclusion

A modal test and frequency-only model update procedure was performed for metal parts manufactured using the DMLS process. Two materials, INCO 718 and Ti 64, were examined.

Test results from the INCO 718 component showed a uniform overestimation of the first six natural frequencies by roughly 6–8 %. Damping ratios between 0.2 and 0.5 % were observed for these modes. Based on the uniformity of the frequency error, an isotropic parameter update procedure was used, together with a measured estimate of the density, to obtain on updated value of the elastic modulus as 87.3 % of the nominal value of 29 KSI. Post-update, the maximum frequency error fell to 1.3 % for mode 5, with all other frequency errors below 1 %.

The Ti 64 component showed much less departure from its nominal elastic modulus, with a maximum error of 3.2 % between test and nominal FEA results. Damping ratios between 0.3 and 1.0 % were measured for the first ten modes of the titanium article. The update procedure yielded a modulus of elasticity at 99.3 % of nominal from a comparison of the first ten natural frequencies. Post-update frequencies were in some cases worse than their nominal counterparts, with modes 9 and 10 increasing and their respective errors of −4.0 and −2.8 % the largest magnitude present. All other errors were below 2 % in absolute value.

Orthotropic effects may have influenced the Ti 64 component to some extent, but were not observable for the first six modes of the INCO component. For this particular configuration, the measured modes all involved motions featuring predominantly axial stretching, making it difficult to observe the effects of anisotropy. Additionally, the thin-walled construction seems to have avoided any significant level of variable-density material in the structure, as seen from the measured values of density for each material.

As additive manufacturing techniques continue to gain prominence, modal testing techniques will continue to be an important part of the model validation toolbox. Additive techniques allow for complex designs featuring variable density, minimum use of material, and complex integral features; the ability to validate material properties on a component basis is critical to designing durable and efficient structures for future aerospace applications. As a non-destructive test method applicable to nearly any structure, modal tests will play a key role in enabling these capabilities.

Appendix

The first ten mode shapes and frequencies of the INCO 718 component obtained from a finite element analysis are shown in Fig. 19.9. A top-down viewpoint is used, and only the lowermost nodes in the structure are included. All of the modes are "flapping modes" of various order, and all but modes nine and ten occur as pairs of "close" natural frequencies.
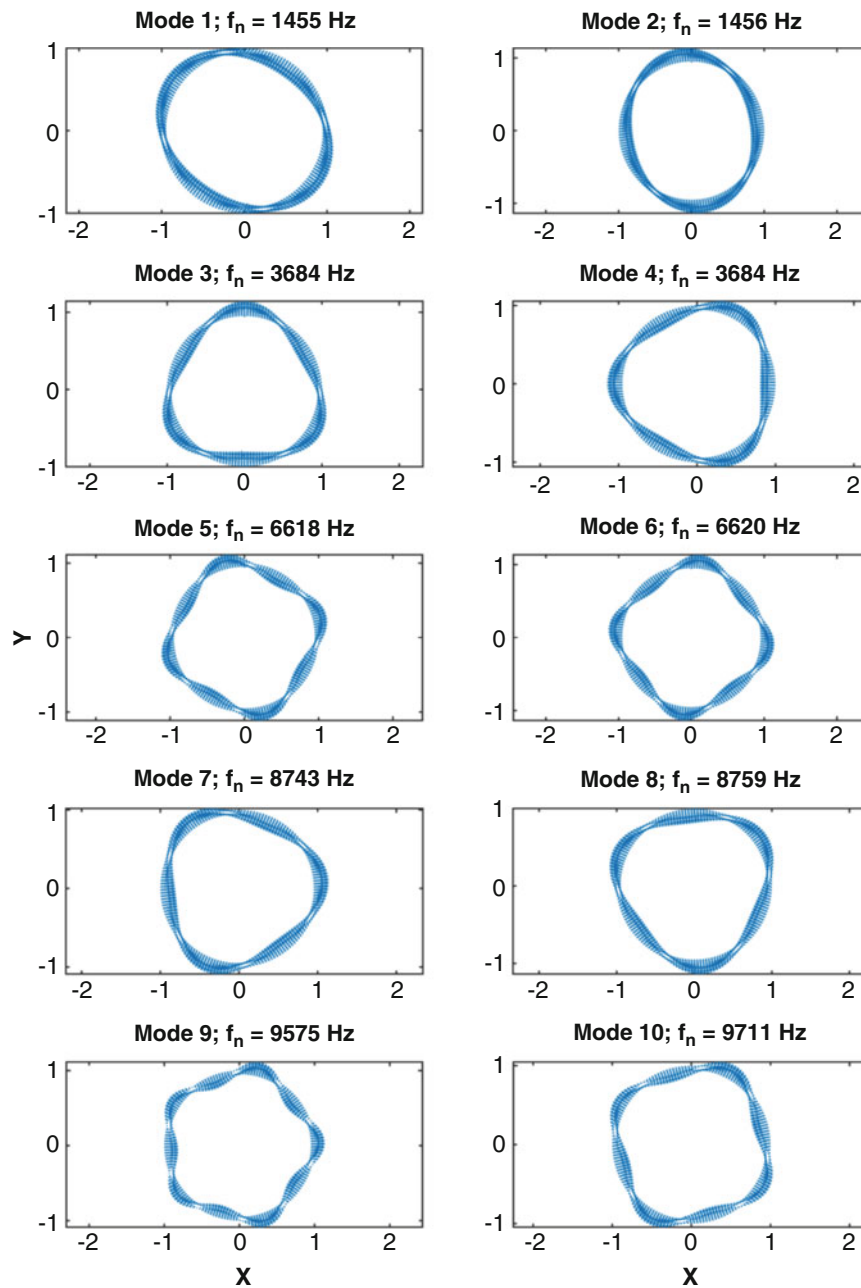
Fig. 19.9 Mode shapes and frequencies of the INCO 718 component, shown from a top-down view. Only the lowermost nodes are included in these images

References

1. Electro optical systems GmbH, Design Rules for DMLS, 2013
2. Special metals, INCONEL alloy 718, 2007
3. Electro optical systems GmbH, Material Data Sheet, EOS Titanium 64, October 2011
4. Kammer, D.C.: Sensor placement for on-orbit modal identification and correlation of large space structures. J. Guid. Control. Dyn. **14**(2), 251–259 (1991)
5. Kammer, D.C.: Sensor set expansion for modal vibration testing. Mech. Syst. Signal Process. **19**(4), 700–713 (2005)
6. Allen, M.S., Ginsberg, J.H.: A global, single-input multi-output (SIMO) implementation of the algorithm of mode isolation and application to analytical and experimental data. Mech. Syst. Signal Process. **20**(5), 1090–1111 (2006)

Chapter 20
In-Process Ultrasonic Inspection of Additive Manufactured Parts

Ian Cummings, Elizabeth Hillstrom, Rielly Newton, Eric Flynn, and AdamWachtor

Abstract This project introduces an in-situ application of ultrasonic inspection techniques to fused deposition modeling (FDM) in order to detect defects as they are produced in a 3D printed plastic part. The growth of additive manufacturing into performance critical applications has revealed the need for precise quantitative evaluation of printed parts. Ultrasonic testing has been extensively demonstrated as a means of detecting small geometric defects in materials, but has not previously been applied in-process to thermoplastic FDM. This experiment used four piezoelectric transducers bonded to the build plate of an FDM machine printing Acrylonitrile Butadiene Styrene (ABS) to ultrasonically inspect parts periodically during the printing process. Every 30 s, the partially formed model is interrogated with an ultrasonic chirp signal and the response recorded. The normalized frequency response is then compared to an experimentally determined ideal response in order to detect faults in the most recently deposited layers. This analysis is based on the hypothesis that the frequency response of the part will be substantially altered if unexpected (defective) geometries are present. Due to the complexity added by low-density internal structures, this work investigates only parts with a solid fill and simple external geometries. However, with sufficient signal processing capabilities, it is feasible to extend this technique to more complicated part shapes and low-density fill patterns, as might be expected in a manufacturing setting.

Keywords Additive manufacturing • Ultrasonic testing • Fused deposition modelling • Delamination • In-process qualification

20.1 Introduction

Fused deposition modeling (FDM) is a common additive manufacturing technique used for plastic parts. Plastic filament is drawn from a reel and extruded through a print head, which melts and deposits the plastic on a heated print bed. The print head is then scanned over a programmed profile to form each layer of a part Lack of proper calibration, poor precision, or unpredictable environmental factors can introduce errors in the part, resulting in incorrect dimensions, failed bonding between layers, thermal warp or curl, or unintentional addition or loss of material. Delamination is a common failure mechanism that particularly affects large prints. This occurs because the time required to deposit one layer is so long that the previous layer has cooled by the time new material is added on top, resulting in a lack of fusion. This causes delamination between layers and part curl due to thermal stresses (Fig. 20.1). There is currently no method to detect, stop, or correct a fault in-situ during an FDM print.

Ultrasonic testing (UT) has been extensively applied to the problem of detecting geometric irregularities in solid materials. Some ultrasonic testing methods involve the transmission of an ultrasonic pulse through a part and analysis of the frequency

I. Cummings
Electrical and Computer Engineering Department, Michigan Technological University, 1400 Townsend Drive, Houghton, MI 49931, USA

E. Hillstrom
Mechanical Engineering Department, Stanford University, 450 Serra Mall, Stanford, CA 94305, USA

R. Newton
Mechanical Engineering Department, Tennessee Technological University, 1 William L. Jones Drive, Cookeville, TN 38505, USA

E. Flynn (✉)
National Security Education Center, Los Alamos National Laboratory, P.O. Box 1663, Los Alamos, NM 87545, USA
e-mail: eflynn@lanl.gov

A. Wachtor
Applied Engineering and Technology Division, Los Alamos National Laboratory, P.O. Box 1663, Los Alamos, NM 87545, USA
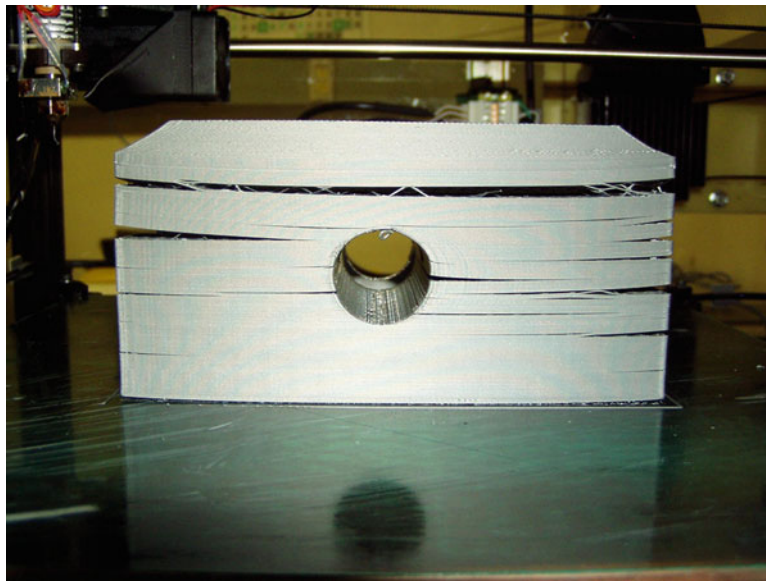
Fig. 20.1 Delamination in large 3D printed ABS parts [1]

Fig. 20.2 Ultrasonic testing
illustration
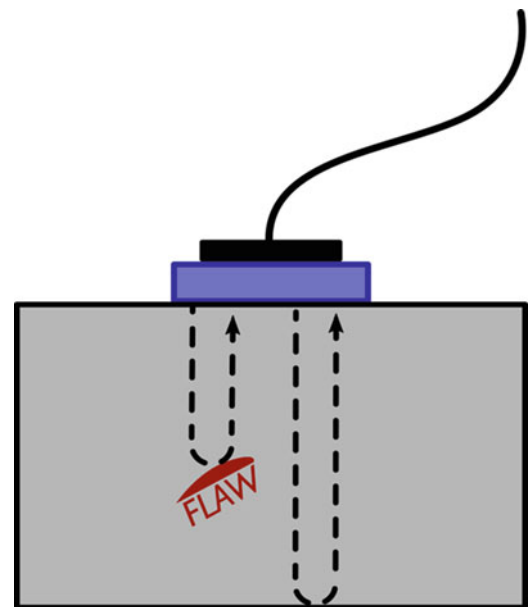
response to determine resonances of the structure, while other methods analyze time of flight or signal attenuation (Fig. 20.2). The resonant frequencies of a structure depend on physical characteristics of the piece, e.g. elasticity, stiffness, geometry, and density. This means that geometric differences in a sample (e.g. defects) should have noticeable effects on the resonant frequencies of the response signal. The sensitivity of this evaluation technique was demonstrated by F. Honarvar and A. N. Sinclair when they found noticeable resonant frequency alterations resulting from just a 5% change in material properties, in their case elasticity [2]. Using this technique, Honarvar and Sinclair were also able to accurately detect delamination in cladding of copper-clad aluminum rods, a problem conceptually similar to debonding events in 3D printed parts.

While methods of acoustic spectroscopy have been thoroughly investigated in the general field of structural monitoring for homogenous materials, 3D printed parts are far from homogenous, with internal boundary structures creating geometric complexity. Little work has been done on the application of acoustic spectroscopy methods to inhomogeneous materials. However, in a study of highly attenuating steel specimens, it was found that ultrasonic material characterization was possible despite inhomogeneity, although the noise level was higher and occasional instances of multiple reflections (reverberation) were observed due to the internal structure of the material. Because of this, defect detection was not possible with a single channel arrangement, except in the special case of through transmission, but acceptable images were obtained from a multi-channel sensor array [3].

In a study of composite materials using ultrasonic inspection, which pose similar problems of noisy signal reflected within the material, the experimenters approached the problem from a signal processing perspective. They found that higher frequencies tended to be more strongly attenuated by the inhomogeneous materials, and so developed an algorithm based on application of a set of low pass filters. The algorithm was an improvement over existing methods, but occasionally did not have enough sensitivity to discern features from noise [4]. Although the FDM parts interrogated in this study are not composites, they are inhomogeneous and share the same macroscopic lattice characteristics as some composite materials, posing similar inspection problems.

Typical ultrasound spectroscopy requires contact with the part, either directly or through a fluid medium. The former is difficult, due to the constantly changing geometry of the building part, and the latter would require unreasonable modification to the printer and print process. Air-coupled ultrasonic spectroscopy is an alternative approach that frees the test setup from a contact or fluid medium requirement, but can introduces substantial variability if sufficiently precise air-coupled piezoelectric transducer devices are not used. High quality sensor devices of this type are typically quite expensive, so an air-coupled test apparatus was not pursued for this experiment. The difficulties inherent to air-coupled ultrasonic testing are outlined by D.E Chimenti (2014) [5] and D.W. Schindel (1996) [6]. The most substantial of these are the challenge of matching the acoustic impedance of air, the much lower speed of compressional waves in air, as opposed to a medium like water, the restrictions on incident angle of waves, and the fundamental issue of effectively transferring energy between two media with very different mass-densities. Because of the additional attenuation of the signal traveling through air and the dynamic configuration of printer components, air-coupled ultrasonic spectroscopy was not ideal for this research.

Due to the nature of ultrasonic testing during the additive manufacturing process, it is expected that significant variance in frequency response will be observed due to temperature variation in parts. Sound attenuation increases with temperature, which is caused by effective damping due to change in the elastic properties of the material. One manufacturer of ultrasonic test equipment lists an increase in attenuation of a 5 MHz signal from approximately 2 to 15 dB per 100 mm one-way sound path in carbon steel with an increase from room temperature to 500 °C. It also states that attenuation in polymers can be expected to be several times higher. In addition, sound velocity varies with material temperature, requiring recalibration for particular environments [7]. For this work, significant thermal effects arise due to the thermal gradient from build plate to extrusion tip.

The most difficult barrier to overcome in applying ultrasonic testing to additive manufacturing is the necessity of having good contact with the part in order to effectively send and receive signals through the test specimen and maintain a detectable output signal.

20.2 Methodology and Simulation

This experiment was conducted on a TAZ 5 LulzBot printer with a 0.35 mm extruder nozzle. The 30×30 cm print bed is a Borosilicate glass plate (3 mm) sandwiched between a PEI print surface (<1 mm) and an adhesive silicone pad heater (∼3 mm). The four corners of the print bed were clamped to stiff springs mounted on the printer gantry.

The test setup shown in Fig. 20.3 was implemented with four piezoelectric transducer modules. In the configuration shown, one transducer served as an excitation source with the other three used as receivers. This arrangement was determined by brief experimentation to be a good compromise between maximum sensor response and the need to keep sensors out of the path of the print head for the duration of the print. The sensor modules were composed of 25.35 mm diameter by 2.05 mm thick piezoelectric transducers (APC International, Ltd., Material 850, Wrap Around contacts), soldered to 30 AWG braided shielded cable using lead-free solder. These connections were then encased in a large mass of clear epoxy to prevent joint failure. The sensors were bonded to the build plate with cyanoacrylate adhesive (Loctite Superglue, Professional Liquid). In order to avoid direct sensor-to-specimen contact it is possible to excite and receive signal from another structure (in this case, the print bed itself) in contact with the specimen of interest. For this experiment, a system of sensor mounting directly on the printer bed was chosen to take advantage of this effect. Because the specimen necessarily must have firm contact with the print bed, this was seen as an acceptable solution for conducting ultrasonic testing on the parts in situ.

Data acquisition was handled by a National Instruments USB X Series DAQ. Three piezoelectric transducers were connected directly to the DAQ and grounded to make measurements. To remove interference, both the signal and ground ports for the sensors were tied separately to ground using one 33 (+/− 5 %) kOhm resistor for each line. The shielding of the cable was grounded to an analog ground port. The overhead fluorescent lights present in the laboratory were turned off in order to eliminate noise produced at approximately 55 and 70 kHz. The transmitted signal was driven by an output on the DAQ fed through an amplifier and out to the transmitting piezo.
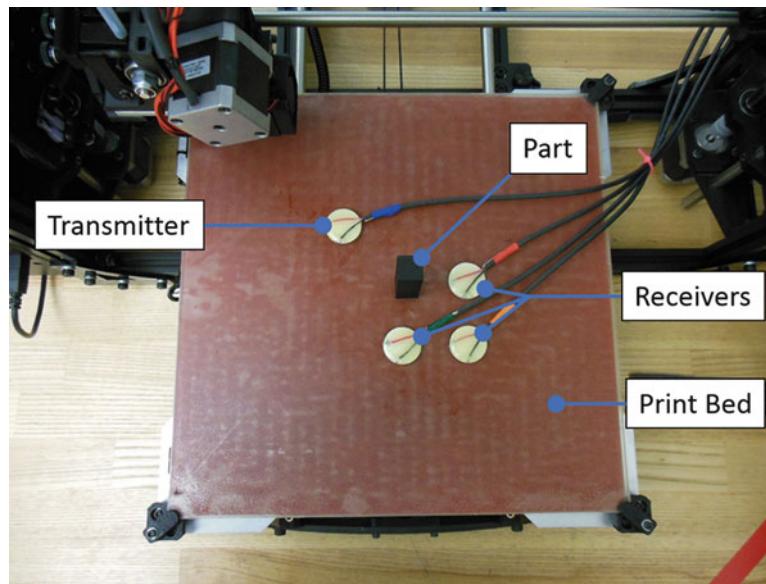
Fig. 20.3 Print bed test setup
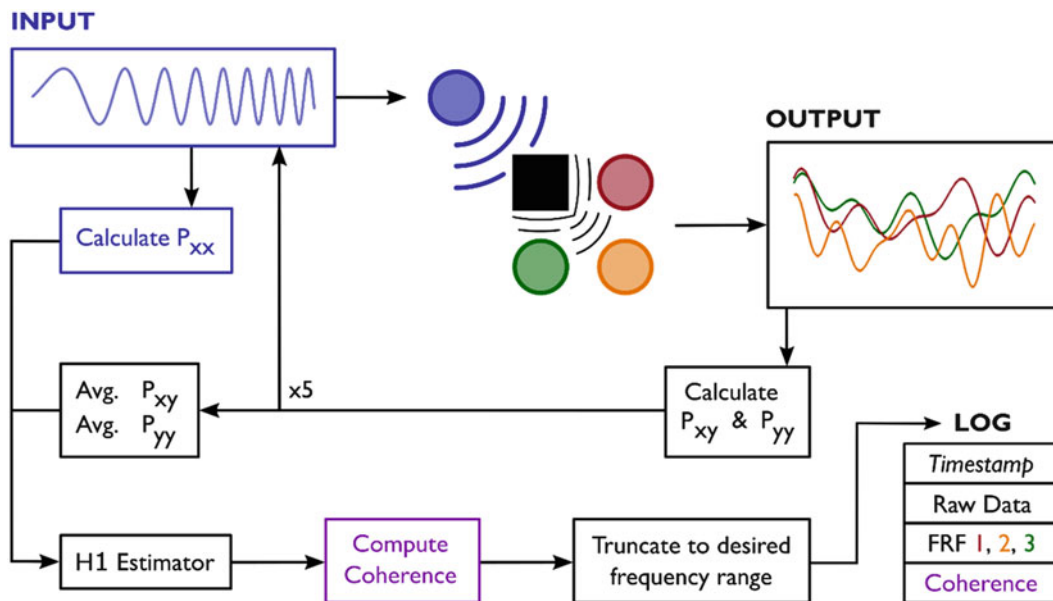
Fig. 20.4 Data collection and logging process

This experiment investigated a frequency range from 50 to 100 kHz. Tukey windowing was applied in order to reduce leakage in the calculation of the frequency response and coherence of the measured signals. In order to ensure that windowing did not attenuate responses for frequencies in the range of interest, this range was padded on either side to allow for the first 5 % and last 5 % of frequencies to be later discarded. The excitation signal, a 0.1 s sine chirp, was created from this padded range, using a sampling rate of 333,333 samples/s, which was the maximum allowed by the DAQ while using three receiving sensor channels.

For each interrogation, five chirps were transmitted and the response waveforms recorded in MATLAB. Autocorrelation and cross-correlation were computed for each pair of excitation and response waveforms and these values were averaged across the five interrogations before finding the transfer function using the H1 estimator. This transfer function was then truncated to the original range of interest from 50 to 100 kHz. Coherence over this range was also calculated. The transfer function and coherence were then logged for each interrogation (Fig. 20.4). Measurements were taken at 30 s increments, for approximately 550 samples of the undamaged part (the exact number of samples varied from test to test due to variations in when data acquisition was stopped after the test had completed).
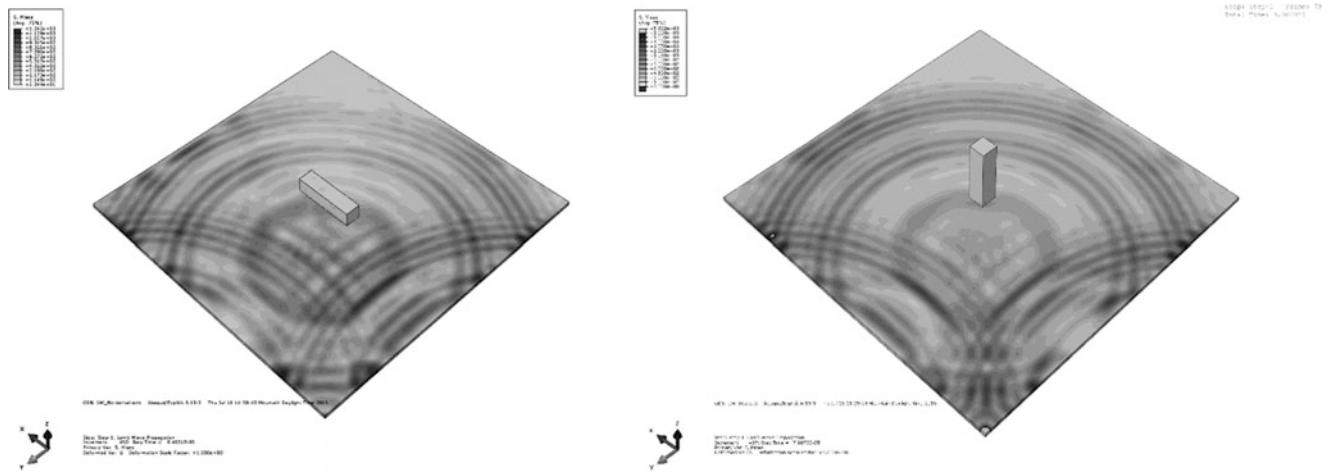
Fig. 20.5 Transient analysis of an excitation signal passing through the part and the build plate in horizontal and vertical orientations
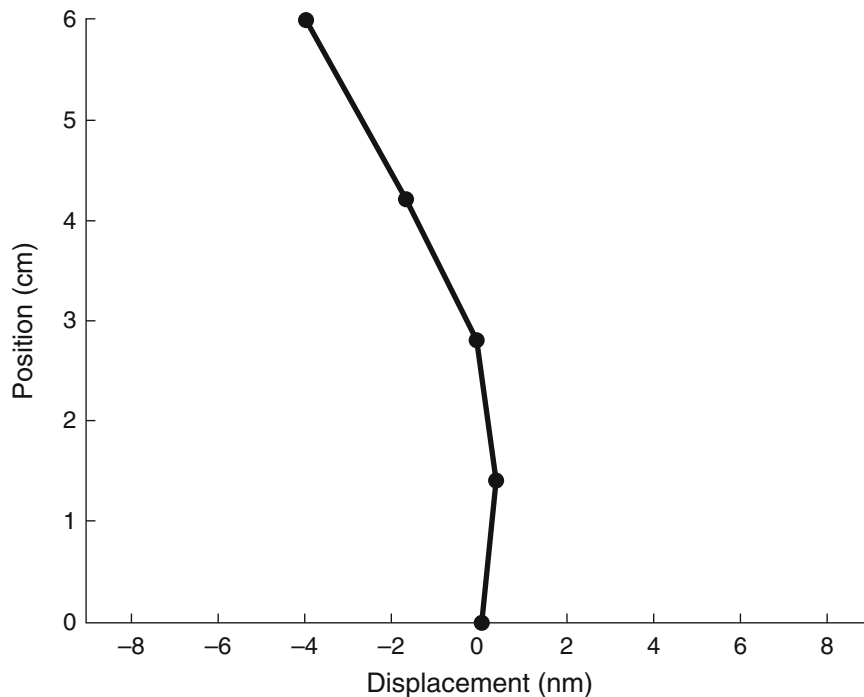
Fig. 20.6 FEA model data of healthy part motion at five points spaced vertically along the part

The test specimens were $1.5 \times 1.5 \times 6.0$ cm square columns. They were printed vertically such that the square cross-section mated with the build plate with the print fill density set at 100 % in the slicing software which produces the gcode for the printer. The part was modeled as a column, rather than a shorter rectangular block, in order to produce the largest amplitude response from the structure. This was verified with Finite Element Analysis of the part printed horizontally and vertically as shown in Fig. 20.5. The horizontally bonded part proved much less responsive to the input signal according to displacement values extracted from both models.

A Finite Element Model (FEM) of the full part and build plate was constructed to confirm that excitation of the part was not simply causing rigid body motion of the whole column. A dynamic explicit analysis was done to efficiently compute the large number of small time increments in the simulation. In order to cut down computation time, simplified boundary conditions were used. The corner edges of the build plate were fixed in the x, y, and z direction. In the FEM simulation, an 80 kHz sine burst was used to excite the build plate in the same location as the excitation transducer in the test setup. The response of the part was measured at five nodes spanning the height of the column as shown in Fig. 20.6. A 0.002 m mesh size was used, designed to exceed the excitation wavelength. In order to minimize computation time, the model of the

Fig. 20.7 Healthy part (*left*) and faulted part (*right*)

print bed was simplified to a sheet of borosilicate glass (as opposed to the true composite of PEI, glass, and silicone) after determining that the glass dominated the response of the plate as a whole. The exact damping properties for the borosilicate glass and ABS plastic part were not known and the model did not account for damping or thermal gradients. However, for the purpose of the simulation, which was only to determine that the part truly exhibited bending motion, these other properties are inconsequential. The displacement data from the FEM transient analysis showed that the part was responding in a mode other than simple rigid body motion caused by the displacement of the plate. The part itself had its own vibrational response to the input excitation shown in Fig. 20.6. Thus the signal measured by the transducers would receive the vibrational response of the part superimposed on the response of the plate.

20.3 Fault Mechanism

To simulate a delamination event, a common issue for FDM parts, a fault was introduced by increasing the layer offset in the z-axis for a single layer of the print. The normal layer offset is 0.1 mm, which creates a well bonded, relatively homogenous layer. Increasing the offset causes the lines of plastic to fail to bond with the layer beneath it well. This offset created a visible weakness in the part, and caused curling around the edges of the layer in some cases (Fig. 20.7). Measurements were taken in the same manner as the undamaged parts.

20.4 Characteristics of the Frequency Response

In order to characterize the frequency response behavior of the printer system in isolation, a set of measurements was taken without plastic deposited on the build plate. The printer was run through the toolpath for a full print, and measurements were taken at the same intervals as the normal procedure, but the plastic filament was not fed into the machine, resulting in an "empty print." The results of one such empty print can be seen in Fig. 20.8. The most notable characteristic is the relative lack of variation across time, which seems to indicate that the action of the printer and changing geometric configuration does not significantly alter the frequency response of the system.
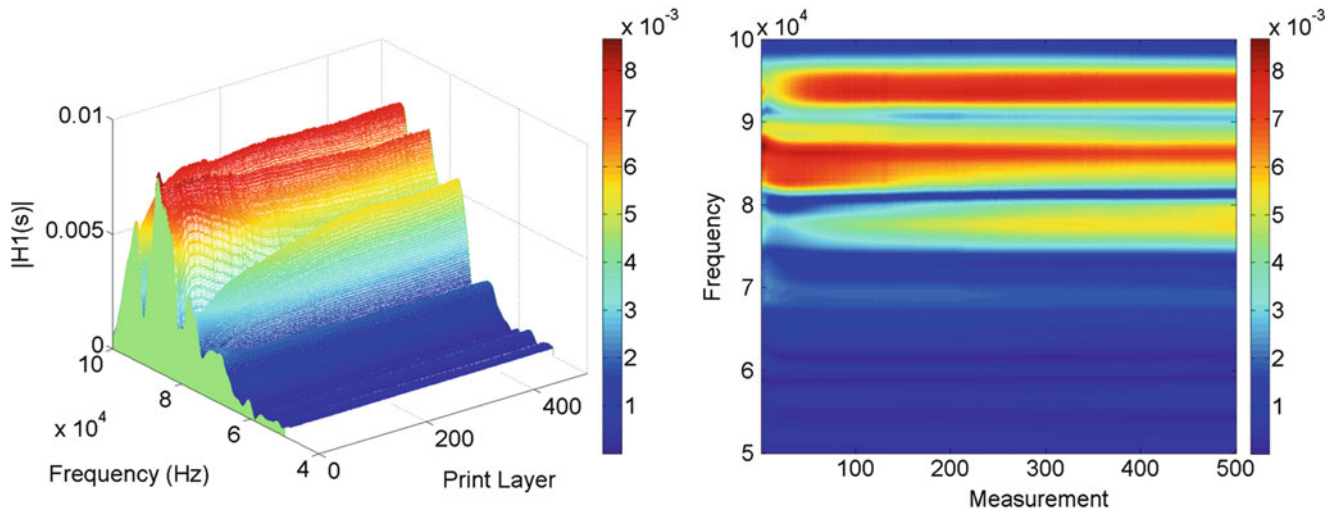
Fig. 20.8 Parts printed without plastic filament demonstrate that the response of the system is relatively constant through time
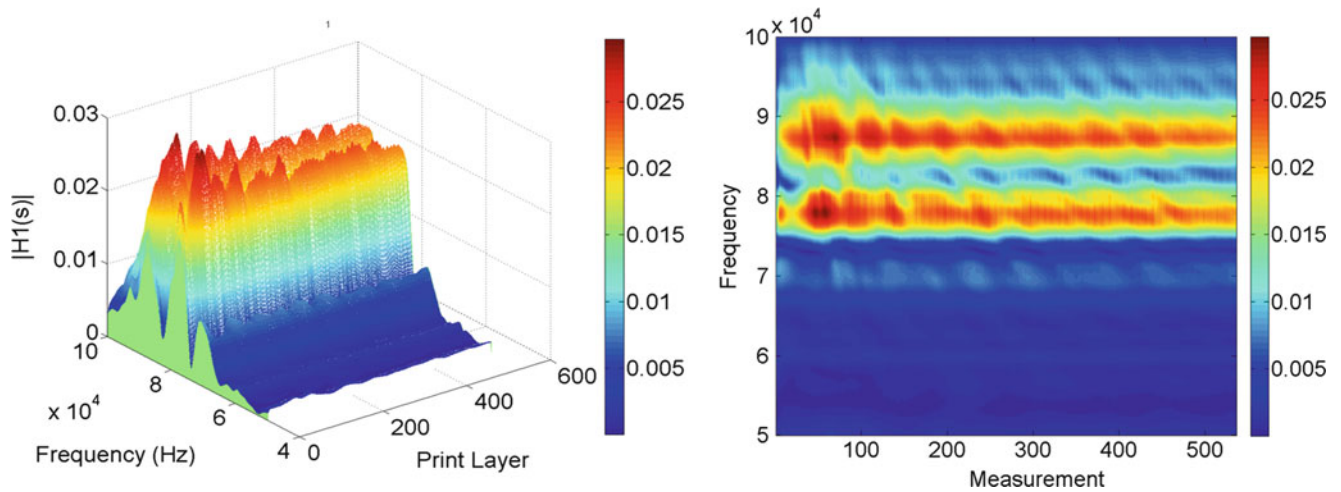
Fig. 20.9 Healthy part measurements show striations that lower in frequency with added length of the part

As a point of comparison, a baseline "healthy" measurement was established by averaging a set of undamaged data sets for separate print runs of the same part geometry. The most visually apparent feature of these measurements is a set of modulations in the response of a given frequency through time. When viewed on a color map (Fig. 20.9) these appear as striations that lower in frequency with time, corresponding to the lengthening of the plastic part as it is built.

One possible explanation for these shifting modulations of frequency response is that they correspond to resonances of the plastic part itself. This makes intuitive sense: each bar drops in frequency as the print progresses, corresponding to a lowering of resonant frequencies as the part becomes an ever longer beam (see Eq. (20.1), the resonant frequencies of a cantilever beam). It is also important to note that the striations could not occur from the effect of only depositing mass on the print plate, as this would shift all of the primary resonant peaks down in frequency with time uniformly, which is not the case here. The FEA model of the print bed and completed part also suggests that the vibrational response of the part cannot simply be rigid body motion. From this, we can say with reasonable confidence that the striations in the frequency response functions result from the resonant responses of the printing part.

$$\omega_n = \alpha_n^2 \sqrt{\frac{EI}{\rho A L^4}}, \ n = 1, \ 2, \ 3 \dots \tag{20.1}$$

To analytically investigate this possibility, the trends were extracted using a peak finding algorithm, and a trend line inversely proportional to the length of the part raised to a variable power was fitted to each trend, corresponding to a generalized form
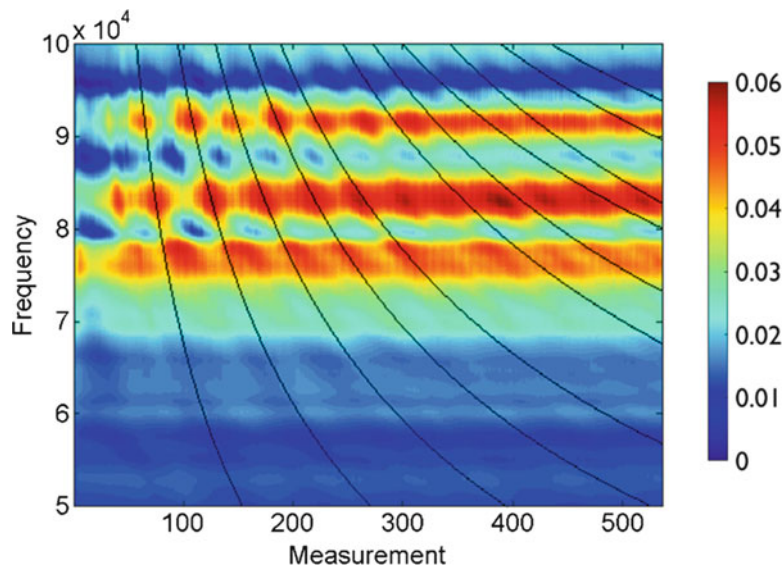
Fig. 20.10 Trend lines with linear variation in order from $L^{-0.4}$ (*left*) to $L^{-0.7}$ (*right*) seem to closely characterize shifts in frequency of striations
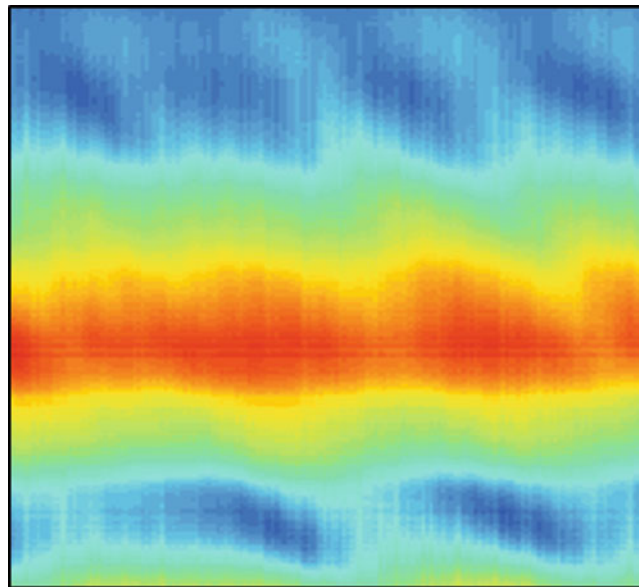
Fig. 20.11 Close-up view of the hairline modulations in the frequency response which occur approximately every 30 measurements

of the equation for resonant frequency as a function of part length. Several possibilities were tested for the value of a in this equation, with the most well matched being a linearly increasing set of a values that ranged from 0.4 to 0.7 across the length of the print (Fig. 20.10). Although this does not explicitly match an established equation for resonant frequencies, it is possible that it reflects the fact that the part builds through various model approximation regimes, i.e. it begins as a plate, then becomes a block, and eventually acts as a cantilevered beam. This might account for the shift in order of the trend lines as the print progresses.

Another interesting artifact of the presence of a plastic part in the frequency response is a fine set of modulations that appear periodically in the time history (Fig. 20.11). Because these seem to occur approximately every 30 layers, we attribute this to a characteristic of the data collection method. The cycle time for measurements is about 30 s, while the time it takes to print one layer for this particular part geometry averages 29 s. This means that there is a 1 s "walk" in the measurement point for each data point, i.e. the print head will contact the part at a different location for adjacent measurements. Because the print head can act as a force to 'pin' the top of the column, it is therefore reasonable to expect that some measurable difference
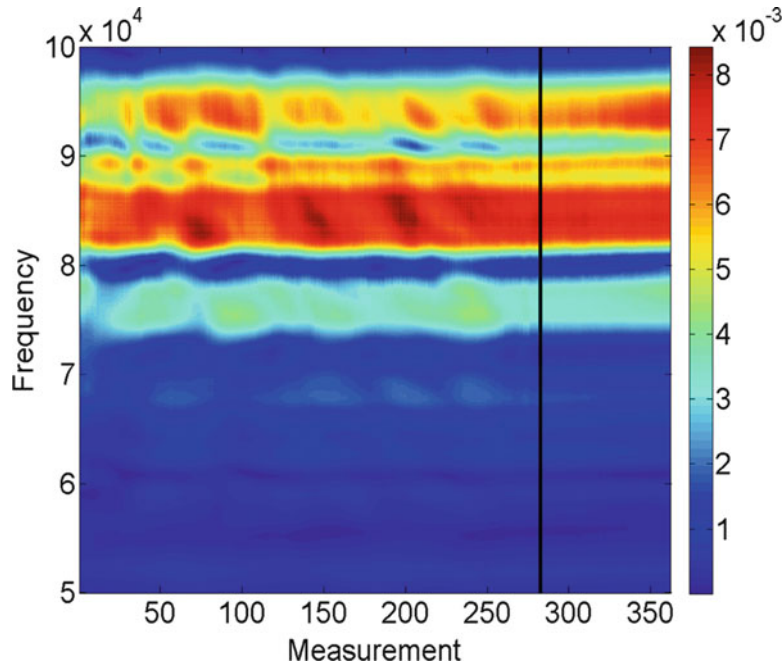
Fig. 20.12 Striations are no longer visible after defect is introduced

in frequency might be observed when the print head happens to fall at a particular point in the layer. This explains the 30 layer periodicity of the phenomenon, but suggests that more work may need to be done to fully standardize the measurement technique if absolute consistency is required.

All of these characteristics seem to clearly suggest that the shifting modulations result from the presence of the plastic part on the plate. Therefore, it is plausible that analysis of the striations may give information about geometric differences (e.g. defects) between parts. This was tested by intentionally introducing a fault in an otherwise identical part by the method described earlier. The impact of this defect on the frequency response of the part can be seen in Fig. 20.12. It can be clearly seen that striations halt after a defect is introduced, and the frequency response of the part remains more or less constant from this point on in time.

It is unclear exactly what causes this immediate stop in resonant response to happen, but one potential explanation is that the defect is severe enough that the bond does not allow vibrational energy to translate upwards into the part, as it normally does when the piece is "solid." This means that mass built on top of the fault simply acts as a damping mass for vibrations, rather than serving to add length to the cantilever. If this form of simulated defect is characteristic of actual faulting mechanisms, this is a fairly dramatic signature of damage. The next section covers a set of statistical detectors that were used to numerically analyze this indicator of damage.

Toward the end of the testing, it was discovered that the overall magnitude of the frequency response between testing was decreasing. This is documented in Fig. 20.13, which plots the median frequency response magnitude for each sensor in each print in chronological order. It is hypothesized that the bond between the transducers and the built plate degraded with the repeated thermal cycling it underwent for each print run.

20.5 Fault Detection Analysis

Our first approach to establish a metric of damage was to compare the undamaged measurements to the damaged cases at each sampling point by calculating the Mahalanobis Distance for each point and each sensor (Eq. (20.2)).

$$\left(\overline{X} - \overline{\mu}\right)^T C^{-1} \left(\overline{X} - \overline{\mu}\right) < t$$
$$t = Threshold, \ \overline{X} = Sample\ Response\ Vector,$$
$$\overline{\mu} = Standard\ Response\ Vector, \quad C = Covariance\ Matrix$$

(20.2)
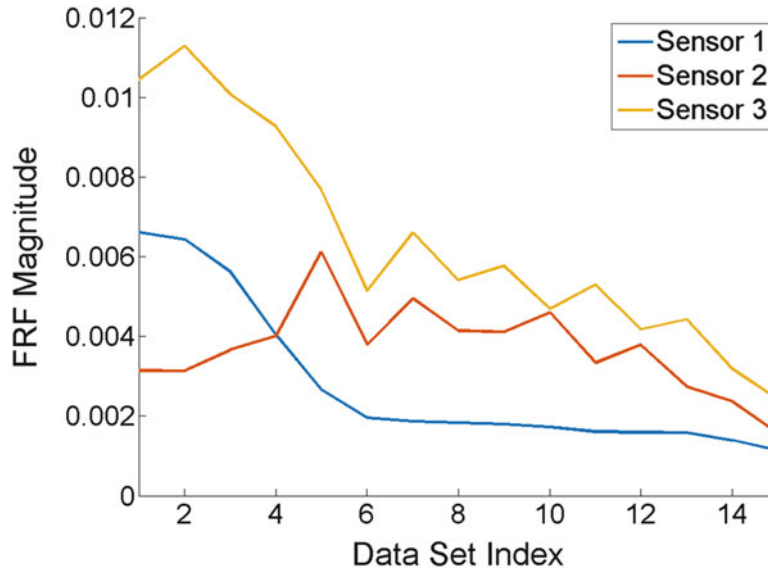
Fig. 20.13 Median frequency response function over the course of the experiment

As there was not enough healthy part data to populate a full covariance matrix, the covariance matrix was assumed to be diagonal, implying that each frequency component of the transfer functions is independent (see Eq. (20.3)). Each element on the diagonal was calculated by finding the average variance in a given frequency bin across the healthy data sets (referred to as σ^2_i in Eq. (20.3)). The inverse covariance matrix was calculated for each sensor.

$$C^{-1} = \begin{bmatrix} \dfrac{1}{\sigma^2_{1,i}} & \cdots & 0 & \vdots & \ddots & \vdots & 0 & \cdots & \dfrac{1}{\sigma^2_{n,i}} \end{bmatrix} \tag{20.3}$$

$$i = Sensor\ Number, \quad n = Number\ of\ Frequency\ Bins$$

The test statistic was calculated for each sensor at each layer and summed across sensors and then plotted in Fig. 20.14. A marked spike in the test statistic would be expected near the location of the fault (Layer 300 for all prints except Debond 1, which was faulted at Layer 50). Although a small increase in the statistic can be seen at the expected location for Debond 1 (Layer 50), it does not differ significantly enough from other measurements to be conclusive and the effect was not clearly seen in other measurements.

The next attempted detector measured the root mean square (RMS) of time series measurements from each sensor and summed the results at each layer (see Eq. (20.4)). Based on observation of frequency response maps from debonded parts, it was hypothesized that a general decrease in amplitude of frequency response would occur at the fault location, so this detector sought to identify particularly steep decreases in signal energy.

$$RMS\ Value, \quad Signal\ Energy\ of\ the\ nth\ sample: \quad RMS_n = \sum_{j=1}^{M} \sum_{k=1}^{L} \sqrt{\frac{1}{N} \sum_{i=1}^{N} x^2_{(i,j,k)}} \tag{20.4}$$

$$x_{(i,j,k)} = ith\ value\ of\ the\ kth\ repetition\ of\ the\ jth\ sensor, \quad N = number\ of\ samples,$$
$$M = number\ of\ sensors$$

While a large undulation is observed in Fig. 20.15 at approximately measurement 50, this does not correspond to an induced fault, and seems to occur as a "startup effect" of the beginning of a print cycle. Because this statistical method shows no difference when the fault was induced (Measurement 300), it is not a conclusive detector.

As a next step, it was hypothesized that the coherence of the returned frequency response could serve as a detector for non-linearity, which could occur as a result of the fault. The physical explanation for this would be that one side of the delaminated section repeatedly struck the other as the part was excited. To investigate this effect, we averaged the coherence values for all frequency bins across all sensors for each time step and plotted the results.
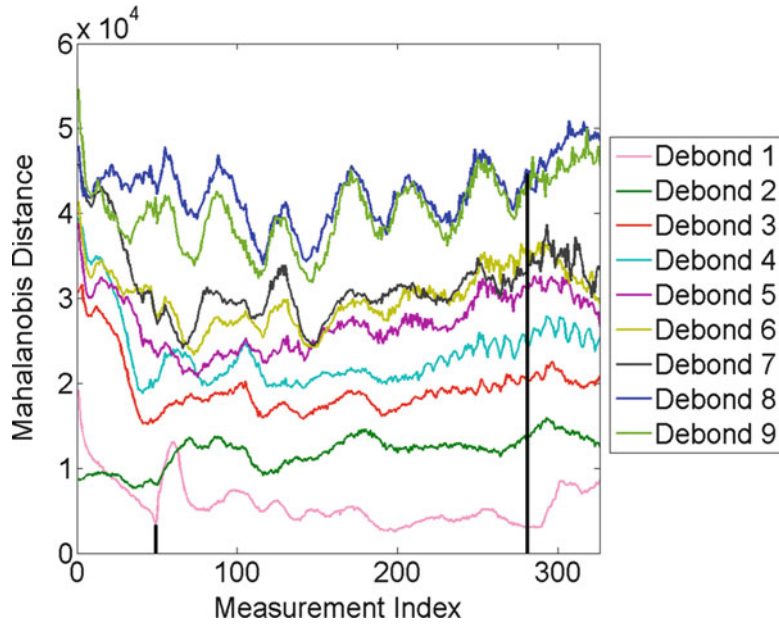
Fig. 20.14 Mahalanobis test statistic results
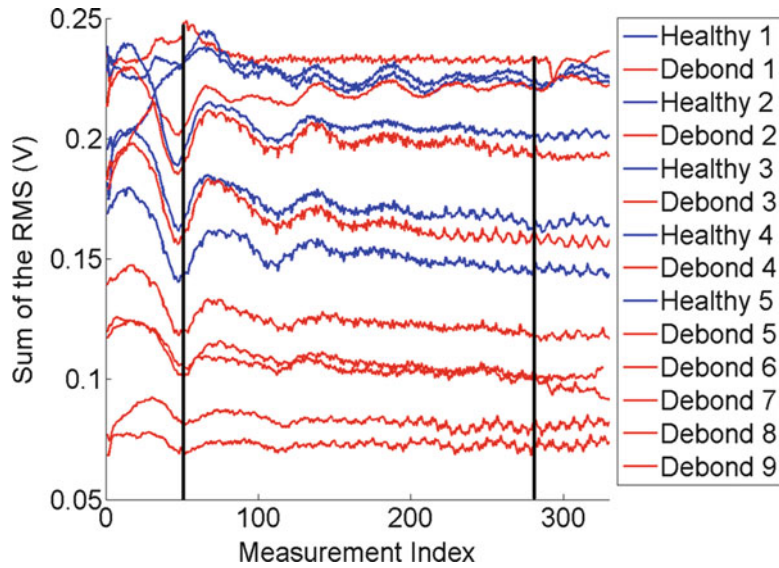
Fig. 20.15 RMS detector results

$$Coherence\ Function\ of\ the\ nth\ Measurement: \quad C(f)_n = \frac{|P_{xy}(f)_n|^2}{P_{xx}(f)_n * P_{yy}(f)_n} \tag{20.5}$$

$$P_{xx} = auto\ power\ spectral\ density, \quad P_{xy} = cross\ power\ spectral\ density$$

Unfortunately, the coherence-based detector, shown in Fig. 20.16, did not provide a reliable means of fault detection as the faulted data should generally mimic the healthy data up until just before Measurement Index 300, where, if a non-linearity were present, we would expect to see a clear drop in the coherence value. This difference was not observed, meaning either that the method of delamination does not create a non-linearity, or that the data contains too much variability to demonstrate clear effects. One likely cause of the drop in coherence from test case to test case was the degradation over time that we saw in the bond between the sensors and the build plate (see Fig. 20.13).

The last attempt made at a statistical detector for damage was based on the observation that the small striations in frequency response that result from the steadily building part die out, at least temporarily, after the fault event (see Fig. 20.12).
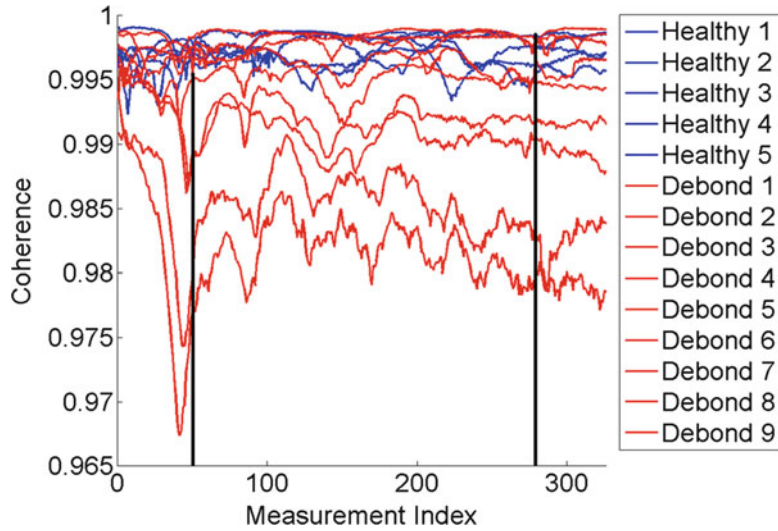
Fig. 20.16 Coherence-based detector results
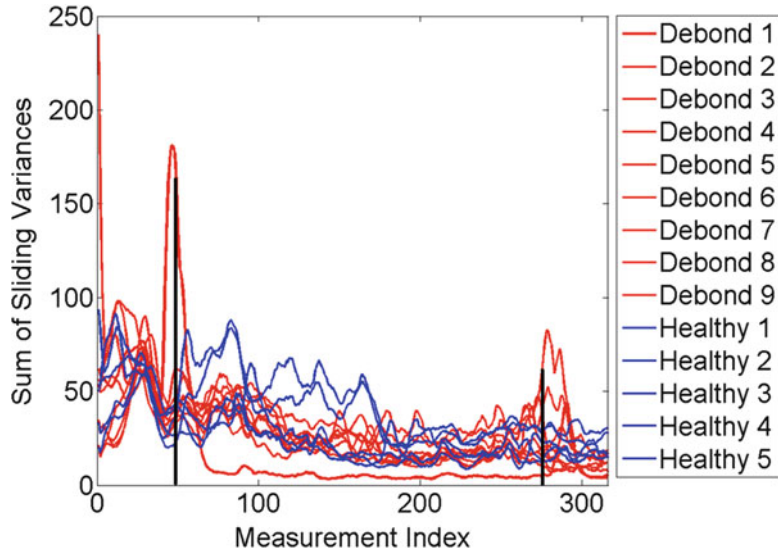
Fig. 20.17 Sliding variance detector results (Bin Width = 15)

This is likely due to poor energy transfer through the fault. To investigate this effect as the basis for a detector, we calculated variance over a sliding window for each of the sensors according to Eq. (20.6) and then summed the results across sensors. We hypothesized that this should show jumps in variance at induced faults, due to the change in modulation pattern at these locations

$$Sliding\ Variance\ Calculations: \ \sigma_n^2 = \frac{1}{B-1}\sum_{i=B+n}^{2B+n}(x_i - \mu_i)^2, \ \mu_i = \frac{1}{B}\sum_{j=i}^{i+B}x_j$$

$$\sigma_n^2 = n^{th}\ sliding\ variance, \ x_i = i^{th}\ measurement, \ \mu_i = i^{th}\ sliding\ mean,$$

$$n = current\ measurement\ (n \geq B), \ N = length\ of\ time\ series\ (samples), \ B = bin\ width$$

(20.6)

The peak seen at Measurement Index 50 in Fig. 20.17 is from the Debond 1 data set, which had a fault at that location in addition to the one near measurement 300 that is shared by all data sets. The variance was expected to peak as it does because the local lack of striations caused a drop in the general magnitude of the frequency response function; this drop causes a great deal of variance in a short amount of time. Furthermore, if the fault is significant enough to cause the striations to cease, then the variance should then to fall below that of a healthy print as the Debond 1 data set does in Fig. 20.16. Several peaks in

faulted data sets near Measurement Index 300 can also be seen, as expected, along with a similar drop in variance below the healthy data set. However, there is not enough separation in the healthy and faulted data sets to make strong conclusions as to the effectiveness of this detection method.

20.6   Conclusions

Although this research did not build a conclusive statistical detector for faults in 3D printed parts, this work does answer several foundational questions about the characteristics of in-situ ultrasonic inspection for 3D printing, laying the groundwork for future research in the field. Primarily, this work has demonstrated that ultrasonic signal energy excites an ABS FDM part and that the effects of physical characteristics of the part on the measured frequency response are visible. However, a decrease in measurement variance or increase in sample size would be needed in order to make conclusive statistical claims as the basis for a detector.

Between healthy data sets, a non-trivial amount of variance appeared in our data. A fundamental concern with the experimental setup was the resolution of the TAZ 5 printer. Due to the higher resolution of commercial plastic and metal printers, it is expected that data from those machines would exhibit lower part to part variance, increasing the feasibility of detector development. This was likely the largest obstacle that prevented the development of a robust detector.

Other sources of variability were identified in the experimental setup. One approach to achieving a higher signal to noise ratio would be to determine a more advantageous placement of the ultrasonic transducers such that the frequency response function is not dominated by the response of the printer and build plate. This might also be achieved by changing the sensors themselves, perhaps using air-coupled ultrasonic receivers in order to isolate the response of the part itself from the response of the moving print bed and extrusion head.

Furthermore, it was observed that, due to the repeated thermal cycling of the printer, the adhesive bond between the transducers and the print bed degrades over time (see Fig. 20.13). This suggests that a more thermally durable adhesive or a mechanical attachment solution for the transducers should be investigated. Additionally, it was observed that the measurement process may need to be more carefully synchronized to the printing process in order to prevent small erroneous periodic trends in the frequency response functions.

To the extent that the variability in the data allows, it seems that the sliding variance detector holds the most promise at this time. The performance of the Mahalanobis Distance detector would improve significantly given the improvements in experimental setup suggested above, and with a larger healthy reference set. Yet, ideally a qualification system would require a minimally sized reference set, if it even required one at all, making the sliding variance an attractive option.

Open-source FDM plastic printers simplify the testing and data acquisition process because they typically allow open access to the print area for sensor placement and cable routing. Additionally, commercial FDM machines and printers implementing other methods of printing (both plastic and metal parts) heat a print chamber, which could cause problems with sensors and cables unless specifically designed for such an environment. However, assuming those issues could be overcome, it is likely that metal prints would produce more consistent data sets in future research, as it is expected that signals would propagate with much less attenuation in metal parts, and thus that the signal to noise ratio of the measured signals would be much higher. We conclude that in-situ ultrasonic inspection of 3D printed parts could be a feasible means of fault detection for delamination events, for higher resolution plastic and metal printers with an improved experimental setup as described above.

References

1. Sbriglia, L.R., Thompson, J.M., Morgan, R.V., Wachtor, A.J., Bernadin, J.D.: Embedding sensors in FDM plastic parts during additive manufacturing. In: Proceedings of the 34th International Modal Analysis Conference, Orlando (2016)
2. Honarvar, F., Sinclair, A.N.: Nondestructive evaluation of cylindrical components by resonance acoustic spectroscopy. Ultrasonics **36**, 845–854 (1998)
3. Ramos, A., et al.: On limitations of the ultrasonic characterization of pieces manufactured with highly attenuating materials. Phys. Proc. **63**, 152–157 (2015)
4. Zellouf, D., et al.: Ultrasonic inspection of composite hydrogen reservoirs using frequency diversity techniques. Ultrasonics **39**, 203–209 (2001)
5. Chimenti, D.E.: Review of air-coupled ultrasonic materials characterization. Ultrasonics **54**, 1804–1816 (2014)
6. Schindel, D.W.: Capacitive and piezoelectric air-coupled transducers for resonant ultrasonic inspection. Ultrasonics **34**, 621–627 (1996)
7. Olympus Corp: High temperature ultrasonic testing [online]. http://www.olympus-ims.com/en/applications/high-temperature-ultrasonic-testing/

Chapter 21
Experimental Modal Analysis of Rolled Multi Layer Cylindrical Shell

Can Nerse and Semyung Wang

Abstract Cylindrical shells are frequently encountered in industry, flight structures, pipeline systems and marine crafts. In these applications cylindrical shells are commonly subjected to harmonic excitations induced by pumps, turbines, compressors etc. Structures exposed to such loads can have structural failure due to sustained effect originated from the vibration by the dynamic load, and structural resonances. For suppression of noise and vibration in the system many design techniques have been employed, and the concept of laminated or multi layer shell has been utilized in several work. In such configuration layers with or without additional damping material stacked on top of each other to achieve the optimum vibration behavior. In rolled multi layer cylindrical shells this phenomenon is realized by rolling a thin plate around a cylindrical shell. Analyzing the coupled system in frequency domain, it is observed that the contact relation between adjacent layers change the system eigenvalues and eigenvectors, as well as resulting in overall reduction in noise and vibration compared to simple shell. In this research experimental modal analysis has been done, and case studies have been presented for different thickness configurations of rolled multi layer shell structure.

Keywords Experimental modal analysis • Impact hammer testing • Cylindrical shell • Multi shell • Vibration reduction

21.1 Introduction

Cylindrical shells are commonly used as structural members and as mechanical components. They are employed in aircrafts, ships, automobiles, pipeline systems, turbines and compressors. In these applications cylindrical shells coupled with other mechanical elements are always subjected to the extreme environment and dynamic loads, which result in fatigue damage and radiated noise, and consequently reduce their mechanical and physical properties. Therefore, it is of great significance to understand thoroughly the vibration behavior of the cylindrical shells. Vibration of cylindrical shells has been studied for decades, and in literature it is possible to find analytical and empirical solutions.

In order to suppress the noise and vibration in the overall structure, a number of passive damping treatments have been applied on the cylindrical shells. One such treatment utilizes the idea of multi layer shell structure, where layers are stacked on top of each other. In recent years, researchers have suggested using additional damping material between the stiffer materials that lack the sufficient damping by themselves. Cheng et al. [1] studied the vibrations of multi layer cylindrical shell where they added viscoelastic damping material between the aluminum layers. Using a layerwise shell model, they investigated the cylindrical shell in frequency domain, and frequency response functions (FRFs), mode shapes and the modal loss factors were compared with a base thick aluminum panel without a viscoelastic layer. Zhang et al. [2] proposed an experimental analysis approach to a cylindrical shell treated with partially passive constrained layer damping (PCLD). They used vibration level difference method to evaluate the damping effect of PCLD structures that has different thicknesses of damping layer and constrained layer.

In this paper, multi layer cylindrical shell concept is achieved via conventional rolling technique that is frequently used in manufacturing rolled sheet metal. Instead of employing a damping layer, a thin metal plate is rolled around a thicker cylindrical shell of same material. In this work, damping and vibration behavior of the obtained rolled multi layer cylindrical shell is studied experimentally with using different shell thicknesses. Experimentally measured FRFs are compared.

C. Nerse (✉) • S. Wang
Intelligent System Design Laboratory, School of Mechatronics, Gwangju Institute of Science and Technology (GIST), 123 Cheomdangwagi-ro, Buk-gu, Gwangju 61005, Republic of Korea
e-mail: can@gist.ac.kr

21.2 Experimental Study

In this experimental study rolling is utilized to achieve the multi layer shell where a thin plate is deformed continuously using rollers, and finely welded at the seam to form a circular cylindrical shell. The obtained thin shell is, then, joined with a thicker cylindrical shell using interference fit, and rolled multi layer cylindrical shell is obtained as shown in Fig. 21.1. Impact hammer test has been done on the rolled multi layer cylindrical shells, and FRFs of the coupled structures are compared with respect to different shell thicknesses that correspond to different number of rolls of metal plate.

21.2.1 Experiment Setup

In order to measure the response of the cylindrical shell, impact hammer test has been applied. For data acquisition as well as analysis, LMS Test.Lab Structures and Siemens LMS SCADAS Mobile system is used for the capabilities it offers in experimental modal analysis. Endevco instrumented impulse hammer is used for impulse excitation. The vibration responses were measured using an accelerometer (B&K type 4393). Sixty-four nodes are specified on the cylindrical shell structure for excitation and measurement, of which 32 nodes were designated at the outer surface of the cylinder evenly sparse in circumferential and axial directions. Similarly 32 nodes were specified on the inner surface of the cylinder. Free–free boundary conditions are simulated using a string net. Schematic representation of experiment setup configuration is shown in Fig. 21.2.
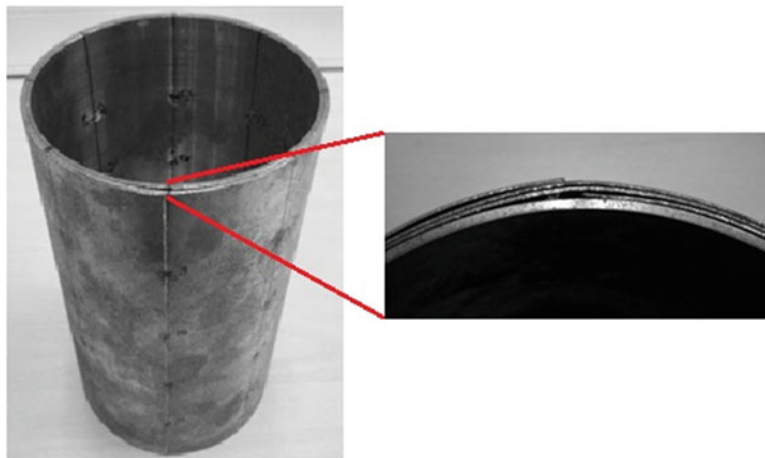
Fig. 21.1 Rolled multi layer cylindrical shell used in the experimental study
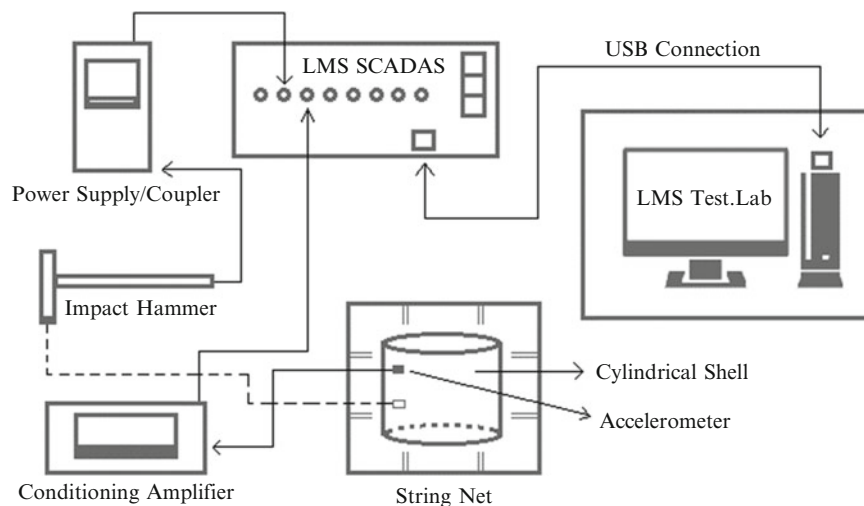
Fig. 21.2 Schematic representation of experiment setup

Table 21.1 Cylindrical shell configurations used in the experiment

	Number of roll of the thin plate	Total thickness of the shell [mm]
Shell 1	0	2.6
Shell 2	1	3.1
Shell 3	2	3.6
Shell 4	3	4.1
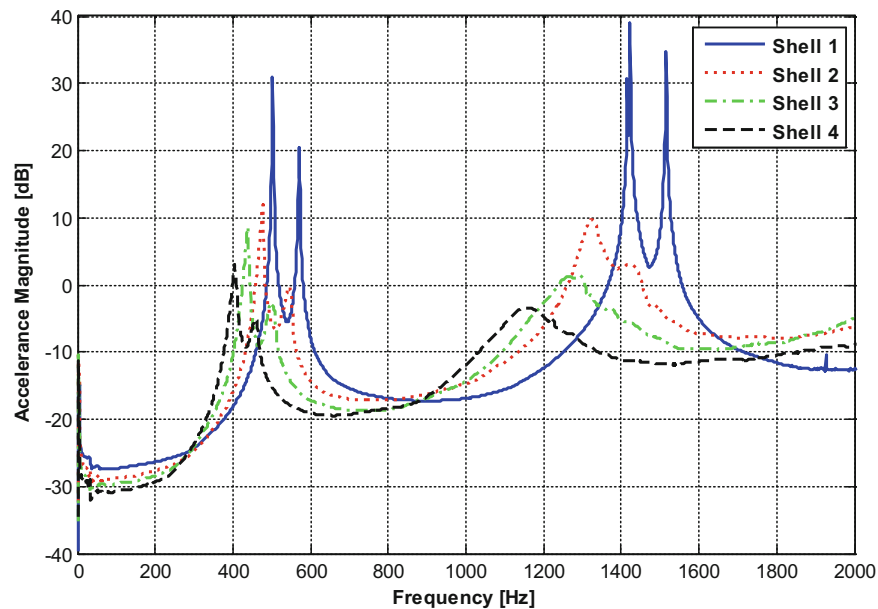
Fig. 21.3 Comparisons of cylindrical shells with different layer configurations

Table 21.2 Modal parameters for cylindrical shell configurations

Mode		Shell 1		Shell 2		Shell 3		Shell 4	
Index	m/n	Freq. [Hz]	Loss factor	Freq. [Hz]	Loss factor	Freq. [Hz]	Loss factor	Freq. [Hz]	Loss factor
1	m = 0 n = 2	501	0.0016	468	0.0182	439	0.0038	400	0.0351
2	m = 1 n = 2	568	0.0015	536	0.0102	495	0.0179	455	0.0199
3	m = 0 n = 3	1423	0.0002	1318	0.0145	1251	0.0350	1154	0.0459
4	m = 1 n = 3	1519	0.0006	1412	0.0151	1297	0.0365	1218	0.0508

The diameter of the thick cylindrical shell is 118 mm, its length is 203 mm and thickness is 2.6 mm. The thickness of the rolled plate is 0.5 mm. Table 21.1 shows the cylindrical shell configurations with total thickness and number of roll of the thin plate.

21.2.2 Comparison of Measured FRFs

The frequency resolution was set to be 1 Hz in entire frequency range of interest. For each node, three hits were performed and their averages were taken in calculation of FRFs. Accelerance FRFs for different cylindrical shell layer configurations are plotted and compared in Fig. 21.3.

As can be seen in Fig. 21.3, the vibration amplitude gradually decreased when the number of roll of the thin plate around the thicker cylindrical shell were increased, and the resonance frequencies shifted to the lower frequencies. The increase in damping can especially be seen for the third and fourth non-rigid body modes where the peak amplitudes are smoothed. The resonance frequencies and loss factors are tabulated in Table 21.2 with the corresponding mode shapes where m and n refer to axial mode parameter and circumferential mode parameter respectively [3], and the individual mode shapes are shown Fig. 21.4. To represent the overall mode shape behavior, only the mode shapes for single layer cylindrical shell (Shell 1) is presented.
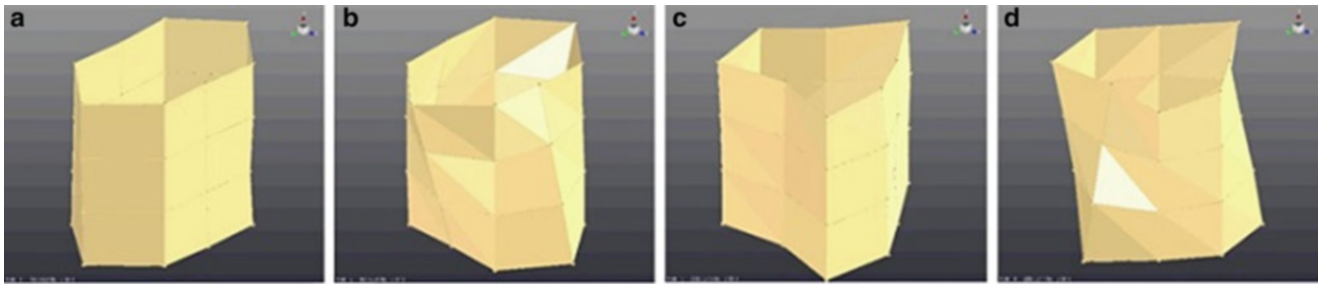
Fig. 21.4 Cylindrical shell mode shapes (**a**) m = 0 n = 2 (**b**) m = 1 n = 2 (**c**) m = 0 n = 3 (**d**) m = 1 n = 3
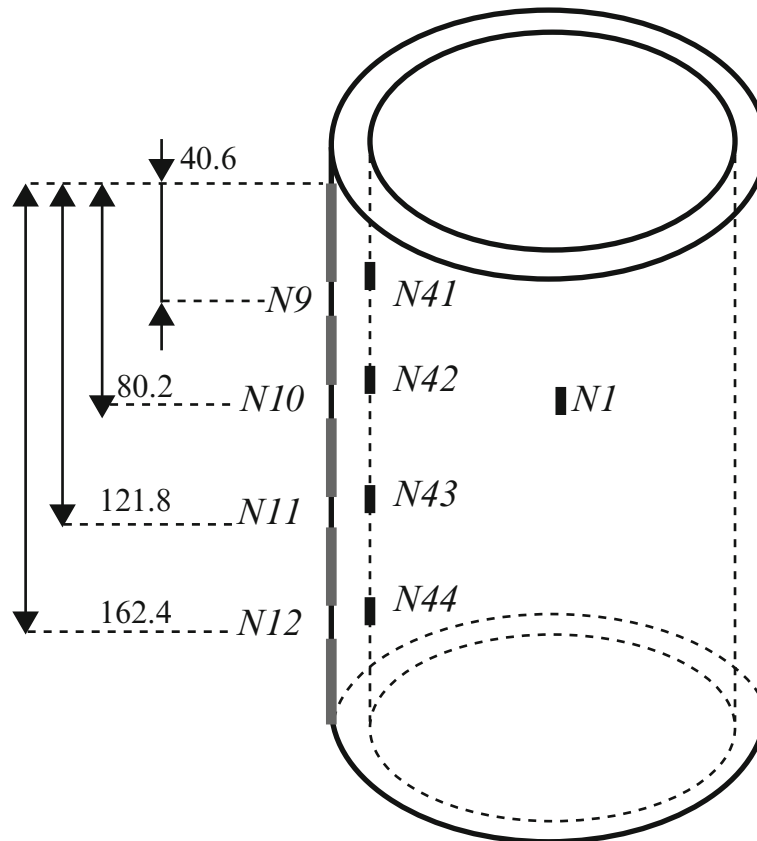
Fig. 21.5 Accelerometer and impact hammer locations on the rolled multi layer cylindrical shell

21.2.3   Further Experiments: Investigation of Welded Joint

In order to further investigate the trend of damping observed in initial experiment, a series of experiments were performed. The cylindrical shells were again excited using an impact hammer. However, the resultant accelerations were measured using an accelerometer mounted sequentially at four nodes specified on the welding line on the outer surface of the coupled shell structure, as well as on the inner surface that lies on same radial direction as shown in Fig. 21.5. The excitation point is denoted as N1, and measurement nodes are N9-N12 and N41-N44, where N9-N12 are the nodes on the welding line. As can be seen from Fig. 21.6a, b, the accelerance transfer FRFs corresponding to node 9 and node 41, on inner and outer surfaces of Shell 2 respectively, followed each other closely for the first two modes while deviating significantly beyond 1 kHz, showing increased energy dissipation due to contact friction between the layers. Similar behavior was observed for Shell 3 and Shell 4 as shown in Figs. 21.7 and 21.8.
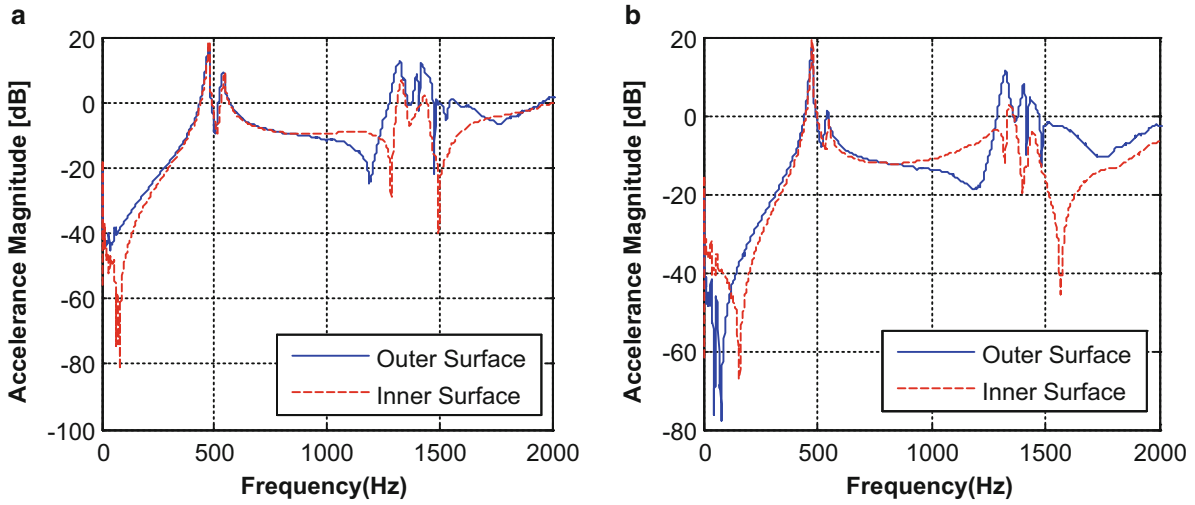
Fig. 21.6 Comparison among transfer FRFs for Shell 2 (**a**) N9 vs N41 (**b**) N10 vs N42
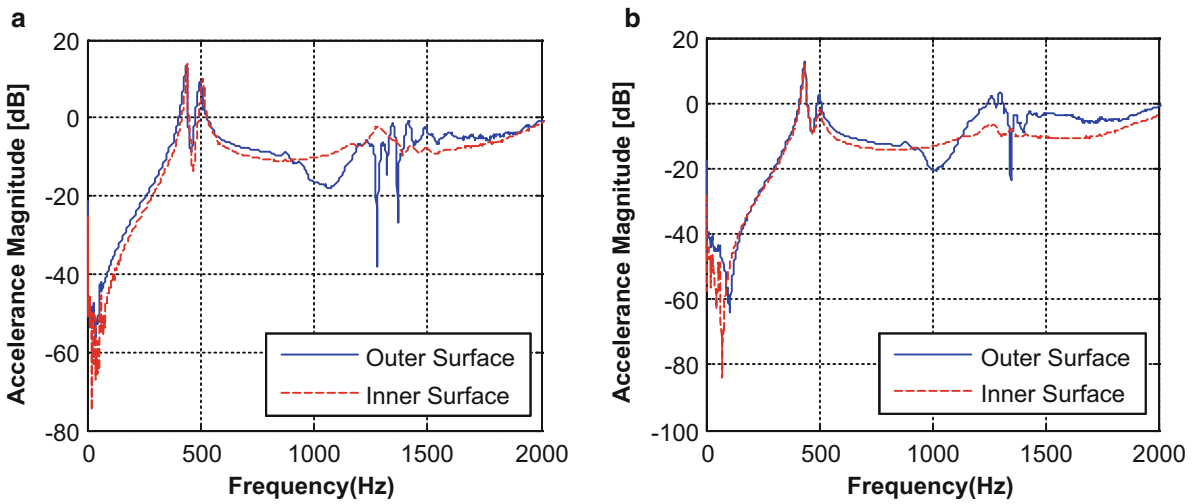
Fig. 21.7 Comparison among transfer FRFs for Shell 3 (**a**) N9 vs N41 (**b**) N10 vs N42
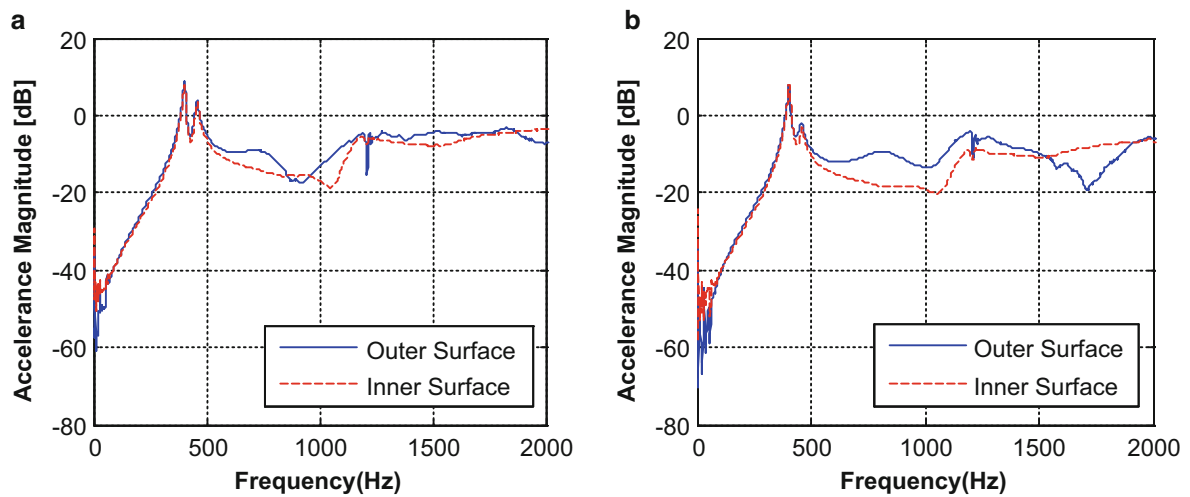
Fig. 21.8 Comparison among transfer FRFs for Shell 4 (**a**) N9 vs N41 (**b**) N10 vs N42

21.3 Discussion and Conclusion

In this study experimental modal analysis for the rolled multi layer cylindrical shell is carried out. Impact hammer test is applied, and response is measured on the inner and outer surfaces of the coupled shell structure. Comparison of the FRFs with respect to different number of rolled thin plate has shown that the resonance frequencies shifted to the lower frequencies while overall damping increased as the number of layers increased.

Additional experiments performed on the welded joint in each multi layer shell shows a nonlinearity in mid frequency region which resulted in large deviation of acceleration magnitude with respect to inner and outer surface measurements. A further investigation is needed to find out the effect of contact mechanism between the adjacent surfaces. Although the welded joint has produced a similar vibration behavior as conventional bolted or riveted joints used in literature [4, 5], the identification of the joint properties is necessary for numerical simulation and verification.

References

1. Cheng, T.H., Li, Z.Z., Shen, Y.D.: Vibration analysis of cylindrical sandwich aluminum shell with viscoelastic damping treatment. Adv. Mater. Sci. Eng. **2013**, 1–7 (2013)
2. Zhang, X., Zhu, S., Liu, G.: An experimental and analytical vibration study of a thin cylindrical shell treated with constrained layer damping. Adv. Mater. Res. **216**, 763–767 (2011)
3. Norton, M., Karczub, D.: Fundamentals of Noise and Vibration Analysis for Engineers. Cambridge University Press, Cambridge (2003)
4. Walker, S.J.I., Aglietti, G.S., Cunningham, P.R.: Experimental analysis of damping across joints in metal plates. Appl. Mech. Mater. **5–6**, 391–398 (2006)
5. Hellar, L., Foltête, E., Piranda, J.: Experimental identification of nonlinear dynamic properties of built-up structures. J. Sound Vib. **327**, 183–196 (2009)

Chapter 22
High-Resolution Mode Shape Identification Using Mobile Sensors

Thomas J. Matarazzo, Matthew Horner, and Shamim N. Pakzad

Abstract Structural health monitoring (SHM) procedures such as system identification (SID) or damage detection were originally developed to process data from fixed sensor networks. Interest in mobile sensors has recently grown with the popularity of mobile devices and smartphones. As documented in the literature, a mobile sensor network is capable of collecting spatially rich data using only a few sensors. Thus, mobile sensor networks can provide comparable or superior information at a lower monitoring cost when compared to a dense fixed sensor network. Until a recent breakthrough, a framework for SID using mobile sensor data sets was unavailable, since the data class is fundamentally different from fixed sensor data sets.

When mobile sensor data is classified as dynamic sensor network (DSN) data, changes in sensors' positions can be properly incorporated into a mathematical model, enabling SID via the structural identification using expectation maximization (STRIDE) algorithm. In this study, a wireless mobile sensor platform, comprised of a motor-drive pulley system, is implemented to record ambient vibrations of a simple beam structure. Using only two mobile sensors, mode shapes with twenty points are computed, further exhibiting the high spatial capacity of mobile senor data.

Keywords Mobile sensors • System identification • Wireless sensors • Dynamic sensor networks • Signal processing

22.1   Introduction

Output-only system identification (SID) methods are a valuable component of structural health monitoring (SHM); they assist engineers with determining a structural system's operational modal properties and its expected response to dynamic loads. As the collected data contain increasing spatial and temporal information, SID modal estimates will become more accurate [1, 2]. However, in fixed sensor networks, the spatial capacity in the data is limited by the number of sensors and their locations thus, additional sensors are required to improve spatial information. Significant efforts are necessary to achieve dense spatial information with fixed sensors. The installation of this type of network demands a large quantity of sensors to be available as well as experienced staff for proper configuration, a process which is further challenged by the physical constraints of a structure [3, 4]. Fixed sensor networks provide restricted spatial information—this is their greatest pitfall. Mobile sensor networks offer improvements where fixed sensor networks fall short [5, 6]. With mobile sensing, few sensors can provide rich spatial information that is comparable or superior to that from a dense fixed sensor network.

Over the past few years, mobile sensor networks have gained attention in SHM, however their immediate advantages over fixed sensors were not fully demonstrated. In [7, 8] flexible mobile sensing nodes were developed to navigate over a structure and collect multiple fixed data sets. The response data was collected while the sensors were stationary, then processed using the Eigensystem Realization Algorithm [25]. Partial SID applications have included frequency identification of single bridge spans [9–11] and theoretical analyses with some experimental results [12, 13]. In 2015, a theoretical framework for the use of mobile sensors for SID [14] was established, enabling comprehensive modal identification, which consists of frequency, damping, and mode shape estimates, from sensors that collect structural response data while in motion. The structural identification using expectation maximization (STRIDE) algorithm [15] is an output-only SID method that accepts

T.J. Matarazzo (✉)
Disaster Prevention Research Institute, Kyoto University, Gokasho, Uji, Kyoto 611-0011, Japan
e-mail: thomasjmatarazzo@gmail.com

M. Horner • S.N. Pakzad
Department of Civil and Environmental Engineering, ATLSS Engineering Research Center, Lehigh University, 117 ATLSS Drive, Imbt Labs, Bethlehem, PA 18015, USA
e-mail: mph214@lehigh.edu; pakzad@lehigh.edu

fixed sensor data, incomplete data (data sets with missing observations) [6], mobile sensor data [14, 16], BIGDATA [17], and more.

In [16], the STRIDE algorithm identified four modes using data from six moving sensors, including mode shapes with twenty points. This paper focuses on estimating mode shapes with a high spatial resolution, using only two mobile sensors. The main objective of this paper is to highlight the high spatial capacity of mobile sensing data to clearly establish its superiority over fixed sensor data in this regard.

This paper is organized as follows: an exact mathematical model for mobile sensing data is presented; SID with STRIDE is explained briefly; the mobile sensing testbed is described; the experimental results are given; and the study's conclusions are provided.

22.2   Truncated Physical Model for Dynamic Sensor Network Data

How are the responses at one point in a structure related to those at another point? This is the fundamental question that must be addressed to properly incorporate mobile sensing data into a mathematical model. In fixed sensor networks, the sensor data play the role of observations in the stochastic state-space model [18, 19]. In this model, system states are defined at points where the sensors were installed; therefore, after identification, the computed modal ordinates correspond to the locations of these states, i.e., for fixed sensor data, the observations and the system states are spatially coincident. However, mobile sensor data is quite different; they belong to the class of dynamic sensor network (DSN) data [20] because the data matrix is mixed with responses from various points on the structure. So, regarding a model for mobile sensing data: at which points on the structure are the observations and system states defined? The truncated physical model (TPM) [20] is a new state-space approach derived to overcome this modeling task.

Since SHM methods were conceived to examine data from fixed sensor networks, special models are often required to efficiently process data from novel collection techniques or with unique sensing formats, e.g., sensor data fusion [21], incomplete data [6], BIGDATA [20], etc. In DSN data, information from a very large number of sensing nodes are available; however, in most cases it is not computationally feasible, nor is it necessary, to select a model with a degree-of-freedom (DOF) at every sensing node, that is, a point where a sensor measured the response. For example, even if a mobile sensor measures acceleration from 5000 different points on a structure, subsequent analyses may not require a structural model with 5000 DOF, i.e., sensing nodes should not necessarily correspond to system states. The TPM integrates rich spatial information into a relatively small-sized model by defining system states at user-selected *virtual probing locations* (VPL) denoted as $\mathbf{s}_x$. At each time-step, the TPM instantaneously maps the observations at the moving sensors to the VPL; in the case of acceleration data, $\ddot{u}_k(\mathbf{s}_o) = \Omega_k \ddot{u}_k(\mathbf{s}_x)$, at time-step k the observations are $\mathbf{y}_k = \ddot{u}_k(\mathbf{s}_o)$, the states are $\mathbf{x}_k^* = \ddot{u}_k(\mathbf{s}_x)$, the locations of the mobile sensors are $\mathbf{s}_o$, and Ω_k is the *mode shape regression* (MSR) term, which supplies the answer to the opening question (details on this term are available in [20]).

The system states are derived by a transformation from modal coordinates to physical coordinates. The following equations are based on the relationship $\mathbf{x}^* = T\mathbf{z}$, where T is the transformation matrix that maps modal states $\mathbf{z}$ (from the modal state-space model) to a special set of physical states $\mathbf{x}^*$. The TPM parameters in Eqs. (22.1), (22.2), and (22.3) are defined in terms of modal state-space model parameters [22], and the state and observation equations are Eqs. (22.4) and (22.5):

$$A^* = TA^{\langle M \rangle}T^{-1} \tag{22.1}$$

$$B^* = TB^{\langle M \rangle} \tag{22.2}$$

$$C^* = C^{\langle M \rangle}T^{-1} \tag{22.3}$$

$$\mathbf{x}_k^* = A^*\mathbf{x}_{k-1}^* + B^*\mathbf{\eta}_{k-1} \tag{22.4}$$

$$\mathbf{y}_k = \Omega_k C^*\mathbf{x}_k^* + \mathbf{\upsilon}_k \tag{22.5}$$

where $A^{\langle M \rangle}$ is the modal state matrix; $B^{\langle M \rangle}$ is the modal state input matrix; $\mathbf{\eta}_{k-1} \sim N(0, Q)$ is the modal input vector; $C^{\langle M \rangle}$ is the modal observation matrix [22]; and $\mathbf{\upsilon}_k \sim N(0, R)$ is random measurement noise. The superscript $\langle M \rangle$ indicates modal

truncation at structural mode M. The TPM model parameters A^*, B^*, and C^* are in physical coordinates. The initial state is assumed to follow $\mathbf{x}_1^* \sim N(0, V)$.

Unlike other physical state-space models, the size of the TPM is not governed by the spatial resolution of the sensor network. The model size is small in consideration of its spatial capacity. The TPM's size is defined by the number of modes included in the analysis and is equivalent the modal state-space model's. Additionally, since the TPM state variable is not restricted, each new analysis permits mode shape estimates at a new set of VPL thus, improving the spatial resolution of the mode shapes without requiring more data. In summary, the TPM offers a versatile technique for extracting rich spatial information from DSN data.

22.3 Modal Identification of the TPM Using STRIDE

The structural identification using expectation maximization (STRIDE) [6, 15] algorithm can be adapted to identify the TPM. An overview of the procedure is provided in this section; details are available in Chap. 6 of [14]. STRIDE is used to determine maximum likelihood estimates (MLE) for the TPM parameters. The algorithm begins with an initial estimate of such parameters, which are updated through iterations of the expectation step (E-step) and equations in the maximization step (M-step) until convergence. The E-step and M-step are designed to optimize the conditional expectation of the log-likelihood function for the TPM. STRIDE converges to its final parameter set, the MLE, when the slope of the likelihood function becomes practically equal to zero. The algorithm initializes with $j = 0$ and continues for each new set of parameters Ψ computed in the M-step:

$$\Psi_j = \left(\overline{\boldsymbol{\mu}}_j, \overline{V}_j, A_j, Q_j, C_j, R_j \right) \tag{22.6}$$

$$\Psi_j \rightarrow \Psi_{j+1} \tag{22.7}$$

Notice the MSR term Ω_k, is a fixed time-variant parameter and is not included in Ψ. The iterations of STRIDE proceed until the convergence criterion for the slope of the conditional likelihood function is reached. When the estimated slope is below the slope threshold (typically $\theta = 5 \times 10^{-4}$), the likelihood function is practically at its maximum and the MLE for the TPM are available:

$$\Psi_{ML} = \left(\overline{\boldsymbol{\mu}}_{ML}, \overline{V}_{ML}, A_{ML}, Q_{ML}, C_{ML}, R_{ML} \right) \tag{22.8}$$

Equations (22.9), (22.10), and (22.11) specify the computation of natural frequencies, damping ratios, and mode shapes from the MLE of the state matrix A_{ML} and the observation matrix C_{ML} (Λ_{ML} and Γ_{ML} are the eigenvalue and eigenvector matrices of A_{ML} respectively) with Δt as the sampling period and $\measuredangle$ as the phase angle:

$$\mathbf{f}_{ML} = \frac{2\pi \, |\ln (diag(\Lambda_{ML}))|}{\Delta t} \tag{22.9}$$

$$\boldsymbol{\zeta}_{ML}(\%) = -\cos(\measuredangle \ln (diag(\Lambda_{ML}))) \cdot 100\% \tag{22.10}$$

$$\Phi_{ML} = C_{ML} \cdot \Gamma_{ML} \tag{22.11}$$

22.4 Mobile Sensor Network Experiment

A mobile sensing platform and test bed were developed in ATLSS at Lehigh University to validate the theory presented. A previous study [16] on this specimen successfully identified four modes of the beam structure using six moving sensors—more specifically, twenty points were determined for each mode shape. In this experiment, two mobile sensing cars scan the 12-foot (3.66 m) long steel beam structure in ambient vibration conditions. Figure 22.1 displays the mobile sensor car and an overview of the flexible beam structure. The wireless sensor was partly produced by MEMSIC and consisted of an IPR2420 Imote2 preconfigured with the TinyOS bootloader, which used Java to allow more reliable data collection [1]. Then, the code
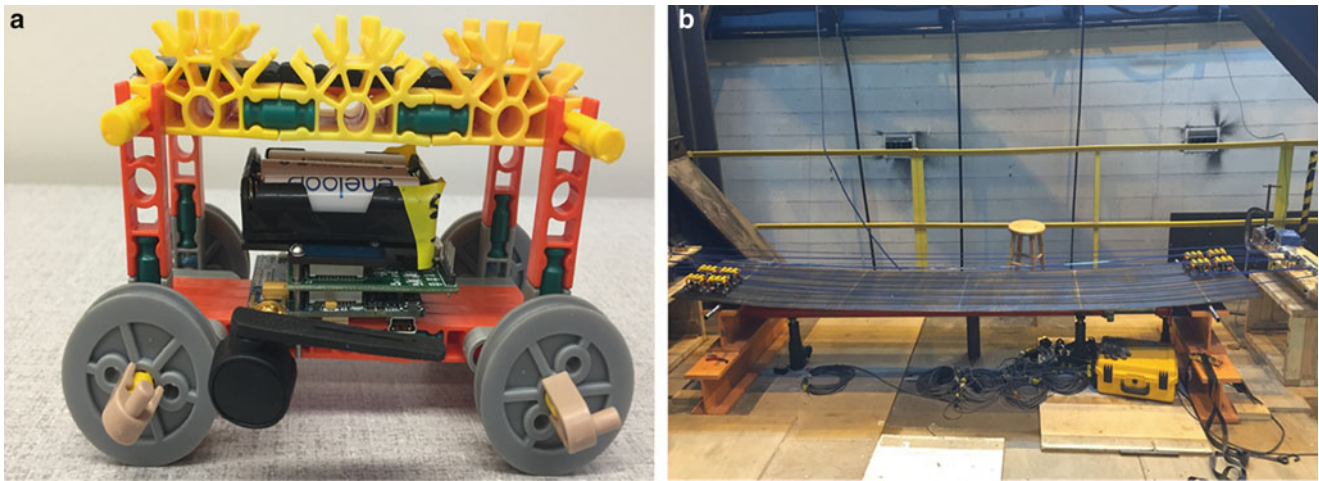
Fig. 22.1 (**a**) Close-up of mobile sensor car carrying the IBB2400CA battery board, ISM400 sensor board, and IPR2420 Imote2 (**b**) Steel beam sits on two rods for simple support, while a motor (*right end*) allows *blue belts* to pull sensor cars across the beam

was sent to an IIB2400 interface board for debugging by JTAG (Imote2). The IBB2400CA battery board was powered by three 1.2 V batteries, and an ISM400 sensor board recorded acceleration data [23].

Belts extend over the span of the beam and carry the sensor cars across. The belts are one component of a pulley assemblage that is driven by a computer-controlled motor. In particular, the motor is a STAC6-Si from Applied Motion and is controlled by the Si Programmer software [24]. With a pulley system that permits two-way traffic, the 25-in. (63.50 cm) wide simply supported beam serves as a roadway for an array of mobile sensor cars.

The mobile sensing setup in this study is simple to better illustrate this technique's ability to produce high-resolution mode shapes using a minimum number of sensors. Two mobile sensors began at opposing supports and each sampled points in space as they traversed to the other support and then returned in reverse to end at their respective starting positions. The mobile sensor data consisted of 7675 points, sampled at 280 Hz, and represented 3837 points on the structure.

22.5 Results and Discussion

The mobile sensing data was filtered and downsampled to 20 Hz (1525 samples) to focus on the first two vertical modes. The STRIDE algorithm was implemented at model order four with the default slope threshold, using initial state and observation estimates from ERA-OKID-OO [18]. In total, STRIDE was repeated ten times, once for each VPL choice—note the same data set was used in each run. Table 22.1 documents the identified modal properties for the first two vertical modes of the beam structure. In each STRIDE run, the number of VPL was two (equal to the number of mobile sensors), thus ten STRIDE runs produced mode shapes with twenty ordinates. The normalized VPL selected for each STRIDE run are given in the first column of Table 22.1 and densely cover the inner 60 % of the beam. Theoretically, the VPL may be chosen at any point on the structure. Table 22.2 provides the statistics for the modal properties computed over the STRIDE runs; the mean values can be considered as point estimates for frequency and damping. As indicated by the standard deviations, the modal frequency estimates did not vary significantly among the various STRIDE runs, however it would be beneficial to verify these estimates with additional data sets. The damping estimates showed a larger variation, which is expected for SID [18], but were rather consistent over the runs nonetheless.

Figure 22.2 provides the main findings of this study: estimates of the first and second vertical mode with twenty points each. Similar markers in the plots indicate the same STRIDE run (note there are only five unique symbols, so these repeat beginning with the sixth set of VPL; refer to Table 22.1 for details). Twenty modal ordinates from only two sensors defines an unprecedented ratio of spatial information per sensor. With fixed sensor networks, it is only possible to obtain one modal ordinate for each sensor. The estimated mode shapes have a high resolution given they are estimated using only two sensors. These results demonstrate the high spatial capacity available exclusively with mobile sensors.

Table 22.1 Identified frequencies, damping ratios, and mode shapes for each VPL selection

Normalized VPL $s_o = (s_1, s_2)$	Marker in Fig. 22.2	1st Frequency (Hz)	2nd Frequency (Hz)	1st Damping ratio (%)	2nd Damping ratio (%)
(0.20, 0.53)	x	6.568	13.022	0.742	0.826
(0.23, 0.57)	+	6.536	12.970	0.755	0.976
(0.27, 0.60)	*	6.524	12.969	0.811	1.209
(0.30, 0.63)	.	6.519	12.957	0.859	1.542
(0.33, 0.67)	o	6.517	13.008	0.714	1.649
(0.35, 0.68)	x	6.516	13.009	0.733	1.627
(0.38, 0.72)	+	6.510	12.994	0.876	1.998
(0.42, 0.75)	*	6.508	13.004	0.975	1.924
(0.45, 0.78)	.	6.496	13.109	1.289	0.569
(0.48, 0.82)	o	6.457	13.147	0.965	0.472

Table 22.2 Statistics for identified modal properties

	1st Frequency (Hz)	2nd Frequency (Hz)	1st Damping ratio (%)	2nd Damping ratio (%)
Mean value	6.515	13.019	0.872	1.279
Standard deviation	0.028	0.062	0.174	0.550
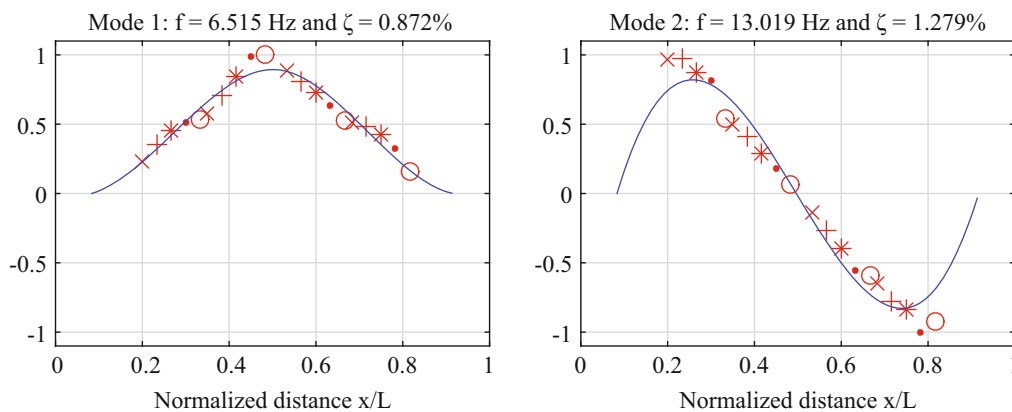
Fig. 22.2 Mode shapes with 20 points and spline fit, identified using only two moving sensors

22.6 Conclusions

In this paper, a mathematical model and identification method were presented for mobile sensor network data. The goal of this study was to utilize the high spatial capacity of mobile sensor networks to estimate mode shapes with a high-resolution, using only two sensors. The truncated physical model (TPM), required to process mobile sensor data, was presented and the structural identification using expectation maximization (STRIDE) algorithm was outlined. The mobile sensing test bed at Lehigh University was described, in which two cars, each equipped with a wireless sensor, were towed over the span of a simple steel beam by belts of a motor-driven pulley system. The versatile mobile sensing platform permits sensors to travel over the beam in opposite directions simultaneously, similar to traffic on a highway.

Two mode shapes, each with twenty modal ordinates were identified using only two mobile sensors and the theory discussed in this paper, defining an unprecedented ratio of spatial information per accelerometer. Fixed sensor networks are limited to one modal ordinate per sensor. The novelty within the TPM and STRIDE is the ability to extract the rich spatial information hidden within the mobile sensor data and shows promise for large-scale applications. This paper further quantified the superior spatial information that is provided exclusively by mobile sensors and verified the underlying theory of the TPM and STRIDE algorithm.

References

1. Pakzad, S.N., Fenves, G.L., Kim, S., Culler, D.E.: Design and implementation of scalable wireless sensor network for structural monitoring. J. Infrastruct. Syst. **14**(1), 89–101 (2008)
2. Pakzad, S.N., Dryden, M., Fenves, G.L.: Parametric bootstrap for system identification of a scaled reinforced concrete bridge. In: Griffis, L., Helwig, T., Waggoner, M., Hoit, M. (eds.) Structures Congress, pp. 397–405. American Society of Civil Engineers, Austin (2009)
3. Matarazzo, T.J., Pakzad, S.N.: Mobile sensors in bridge health monitoring. In: Structural Health Monitoring 2013: A Roadmap to Intelligent Structures: Proceedings of the Ninth International Workshop on Structural Health Monitoring, p. 8. IWSHM, Stanford (2013)
4. Bagajewicz, M., Sa, M.: Cost-optimal design of reliable sensor networks. J. Comput. Chem. Eng. **23**, 1757–1762 (2000)
5. Unnikrishnan, J., Vetterli, M.: Sampling and reconstructing spatial fields using mobile sensors. In: 2012 IEEE International Conference on Acoustics, Speech and Signal Processing (ICASSP). IEEE, Berkeley (2012). doi:10.1109/ICASSP.2012.6288742
6. Matarazzo, T.J., Pakzad, S.N.: Structural modal identification for mobile sensing with missing data. J. Eng. Mech. (2015). doi:10.1061/(ASCE)EM.1943-7889.0001046
7. Zhu, D., Yi, X., Wang, Y., Lee, K.-M., Guo, J.: A mobile sensing system for structural health monitoring: design and validation. Smart Mater. Struct. **19**(5), 1–11 (2010). doi:10.1088/0964-1726/19/5/055011
8. Guo, J., Lee, K.-M., Zhu, D., Yi, X., Wang, Y.: Large-deformation analysis and experimental validation of a flexure-based mobile sensor node. IEEE/ASME Trans. Mechatron. **17**(4), 606–616 (2012). doi:10.1109/TMECH.2011.2107579
9. Lin, C.W., Yang, Y.B.: Use of a passing vehicle to scan the fundamental bridge frequencies: an experimental verification. Eng. Struct. **27**(13), 1865–1878 (2005). doi:10.1016/j.engstruct.2005.06.016
10. Cerda, F., Garrett, J., Bielak, J., Bhagavatula, R., Kovačević, J., Need, T., Monitoring, H.: Exploring indirect vehicle-bridge interaction for bridge SHM. In: Proceedings of the Fifth International Conference on Bridge Maintenance, Safety and Management, Philadelphia, pp. 696–702 (2010)
11. Cerda, F., Garrett, J., Bielak, J., Rizzo, P., Barrera, J., Zhuang, Z., Kovačević, J.: Indirect structural health monitoring in bridges: scale experiments. In: Proceedings of the Seventh International Conference on Bridge Maintenance, Safety and Management, Lago Di Como, pp. 346–353 (2012)
12. McGetrick, P.J., González, A., OBrien, E.J.: Theoretical investigation of the use of a moving vehicle to identify bridge dynamic parameters. Insight Non-Destr. Test. Cond. Monit. **51**(8), 433–438 (2009). doi:10.1784/insi.2009.51.8.433
13. Gonzalez, A., O'Brien, E.J., McGetrick, P.J.: Identification of damping in a bridge using a moving instrumented vehicle. J. Sound Vib. **331**(18), 4115–4131 (2012). doi:10.1680/geot.2008.T.003
14. Matarazzo, T.J.: A Framework for the Use of Mobile Sensor Networks in System Identification. Dissertation, Lehigh University (2015). It is available through ProQuest here: http://gradworks.umi.com/37/18/3718513.html
15. Matarazzo, T.J., Pakzad, S.N.: STRIDE for structural identification using expectation maximization: iterative output-only method for modal identification. J. Eng. Mech. (2015). doi:10.1061/(ASCE)EM.1943-7889.0000951
16. Horner, M., Kosner, K., Korneva, K., Matarazzo, T.J., Pakzad, S.N.: A wireless mobile sensor platform for structural health monitoring. In: Proceedings of the Joint 6th International Conference on Advances in Experimental Structural Engineering (6AESE) and 11th International Workshop on Advanced Smart Materials and Smart Structures Technology (11ANCRiSST), Urbana-Champaign, pp. 1–7 (2015)
17. Matarazzo, T.J., Shahidi, S.G., Pakzad, S.N.: Exploring the efficiency of BIGDATA analyses in SHM. In: Chang, F.-K. (ed.) Proceedings of the 10th International Workshop on Structural Health Monitoring, Stanford, pp. 2981–2989 (2015)
18. Chang, M., Pakzad, S.N.: Observer Kalman filter identification for output-only systems using interactive structural modal identification toolsuite (SMIT). J. Bridg. Eng. **19**(5), 1–11 (2013). doi:10.1061/(ASCE)BE.1943-5592.0000530
19. Peeters, B., De Roeck, G.: Reference-based stochastic subspace identification for output-only modal analysis. Mech. Syst. Signal Process. **13**(6), 855–878 (1999). doi:10.1006/mssp.1999.1249
20. Matarazzo, T.J., Pakzad, S.N.: Truncated physical model for dynamic sensor networks with applications in high-resolution mobile sensing and BIGDATA. J. Eng. Mech. (2015). doi:10.1061/(ASCE)EM.1943-7889.0001022
21. Smyth, A., Wu, M.: Multi-rate Kalman filtering for the data fusion of displacement and acceleration response measurements in dynamic system monitoring. Mech. Syst. Signal Process. **21**, 706–723 (2007). doi:10.1016/j.ymssp.2006.03.005
22. Juang, J.-N., Phan, M.Q.: Identification and Control of Mechanical Systems. Cambridge University Press, Cambridge (2001)
23. Spencer, Jr., B.F.: Getting started guide for new users. Illinois Structural Health Monitoring Project. http://shm.cs.uiuc.edu/files/docs/GettingStarted_NewUsers.pdf (2011). Retrieved 4 July 2015
24. Applied Motion Products: Si Programmer™ Software Manual. http://www.applied-motion.com/sites/default/files/Si_Programmer_Software_Manual.pdf (2009). Accessed 12 May 2015
25. Juang, J.-N., Pappa, R.S.: An Eeigensystem Rrealization Algorithm for Modal Parameter Identification and Model Reduction, NASA Langley Research Center, Hampton **8**(5) 620–627 (1984)

Chapter 23
A Blind Source Separation Based Approach for Modal Parameter Estimation in Traditional Input-Output Experimental Modal Analysis Framework

Vikas Arora and Shashank Chauhan

Abstract Though Blind Source Separation (BSS) techniques have typically been applied within Operational Modal Analysis (OMA) framework, there joint diagonalization property can also be utilized within traditional input-output Experimental Modal Analysis (EMA) for the purpose of modal parameter estimation. This paper explores this possibility and suggests an approach to achieve the same. The paper presents the mathematical concepts that make it possible for Second Order Blind Identification (SOBI), a blind source separation algorithm to be applied to impulse response functions for the purpose of modal parameter estimation. It is also shown in the paper that, in its current form, the approach provides real mode shapes, irrespective of the nature of the system under investigation. In addition to demonstrating the approach by means of studies conducted on an analytical 5 degrees-of-freedom system, the real mode shapes extracted using the suggested approach are also used for model updating purposes.

Keywords Blind source separation • Modal parameter estimation • Second order blind identification • Joint-diagonalization • Model updating

23.1 Introduction

Blind Source separation (BSS) [1, 2] techniques aim at solving the problem of mixed source signals. Goal is to identify the source signals, and the mixing matrix, solely on the basis of observed mixed signals. The procedure applied to achieve this goal often involves exploitation of higher order statistics, as many techniques use mutual independence [1] as the guiding principle for source separation. However, there are several applications where second order statistics suffice. Application of BSS in the field of modal analysis is one such example.

In last few years, there has been tremendous interest in utilizing BSS techniques for modal analysis purposes [3–7]. Most of these works are oriented towards application of BSS techniques to Operational Modal Analysis (OMA). In OMA, one aims at identifying the modal parameters of a dynamic system based on only measured output responses. This is in contrast to traditional modal analysis, where knowledge of input force excitation is also available, and utilized, for modal parameter estimation. OMA lines up well with BSS and both are seemingly analogous. However, mathematically BSS can be looked upon as a decomposition, whose central idea is joint diagonalization. Thus, there is no reason why it cannot be applied to cases that are not 'blind' per se.

This paper develops this idea and explores the possibility of applying BSS to traditional modal analysis. The paper utilizes a second order BSS technique, *Second Order Blind Identification* (SOBI) for this purpose. This technique is described in Sect. 23.2.1. The mathematical basis of application of SOBI to traditional modal analysis is presented in Sect. 23.2.2. It is shown in this section how joint diagonalization of measured impulse response functions can be utilized for estimating modal parameters.

One of the salient features of the procedure explained in this paper is that irrespective of the actual system characteristics, suggested method always estimates real mode shapes. This apparent limitation of the proposed method, can however be

V. Arora (✉)

Department of Technology and Innovation, University of Southern Denmark, Campusvej 55, 5230 Odense, Denmark
e-mail: viar@iti.sdu.dk

S. Chauhan

Brüel and Kjær Sound and Vibration Measurement A/S, Skodsborgvej 307, 2850 Nærum, Denmark
e-mail: schauhan@bksv.com

exploited effectively by noting that one typically needs real mode shapes for finite element model updating purposes. Thus, even though the true mode shape is complex in nature, for model updating purposes it is first normalized such that it becomes real. This paper looks into these possibilities as well, beginning with Sect. 23.3 where a recap of natural frequency and mode shape based model-updating procedure is provided.

The ideas put forth in this paper are validated by means of studies conducted on a numerical 5 degrees-of-freedom (DOF) system, as presented in Sect. 23.4. The properties of this system are changed to investigate variety of cases and evaluate the performance of proposed technique. The section ends with the results of model updating procedure for two separate cases in which different stiffness values of the lumped mass system are updated.

23.2 BSS and Modal Analysis

Most Blind Source Separation (BSS) based Operational Modal Analysis (OMA) techniques have modal expansion theorem [8] as their foundation. Modal expansion theorem states that response of a structure can be expressed as a linear combination of the modal vectors. Mathematically, this is represented as

$$\mathbf{x}(t) = \mathbf{\Phi}\,\mathbf{\eta}(t) \tag{23.1}$$

where, $\mathbf{x}(t)$ is the response of the structure, $\mathbf{\Phi}$ is matrix of modal vectors and $\mathbf{\eta}(t)$ are modal coordinates or principal coordinates. This mathematical relationship also forms the basis of modal coordinate transformation, which uncouples the equations of motion of a multiple degrees-of-freedom system into several simpler single degrees-of-freedom equations.

As has been noted in several works [1, 2], BSS algorithms aim at finding the original source signals and the corresponding mixing matrix that generated the output response signals. The mathematical relation that BSS algorithms exploit is similar to Eq. (23.1) and is given as

$$\mathbf{x}(t) = \mathbf{A}\,\mathbf{s}(t) \tag{23.2}$$

Under certain conditions, such as when source signals have a temporal structure with different autocorrelation functions and are mutually uncorrelated, it is possible to extract the source signals $\mathbf{s}(t)$ and the mixing matrix $\mathbf{A}$, which is assumed to be real. In general, BSS techniques require source signals to be statistically mutually independent (not just mutually uncorrelated). This is what enables higher order statistics based BSS algorithms to operate on response signals, $\mathbf{x}(t)$. However, from the point of view of OMA, it suffices that they are mutually uncorrelated as this is the case with modal coordinates (which are analogous to source signals in Eq. (23.2)). Thus, most BSS based OMA algorithms are based on second order statistics.

23.2.1 Second Order Blind Identification (SOBI) Algorithm

Second Order Blind Identification (SOBI) [9] is a BSS algorithm that lends itself very well to the cause of modal parameter estimation task in OMA. This algorithm jointly diagonalizes the output response covariance matrices at various time lags in order to obtain modal vectors $\mathbf{\Phi}$ and modal coordinates $\mathbf{\eta}(t)$, which provide the estimate of the modal frequency and damping. SOBI algorithm is briefly explained below,

1. Estimate the covariance matrix of the output observations x

$$\widehat{R}_x(0) = \frac{1}{N}\sum_{k=1}^{N} x(k)x^T(k) \tag{23.3}$$

where $\widehat{R}_x(0)$ is the covariance matrix at zero time lag and N is the total number of time samples taken.
2. Compute EVD (or SVD) of $\widehat{R}_x(0)$

$$\widehat{R}_x(0) = V_x\Lambda_x V_x^T = V_s\Lambda_s V_s^T + V_N\Lambda_N V_N^T \tag{23.4}$$

where V_s is m X n matrix of eigenvectors associated with n principal eigenvalues of $\Lambda_s = diag\ (\lambda_1, \lambda_2, ..., \lambda_n)$ in descending order. V_n is m X (m-n) matrix containing the (m-n) noise eigenvectors associated with noise eigenvalues $\Lambda_n = diag\ (\lambda_{n+1}, \lambda_{n+2}, ..., \lambda_m)$. The number of sources n are thus estimated based on the n most significant eigenvalues (or singular values in case of SVD).

3. Perform pre-whitening transformation

$$\bar{x}(k) = \Lambda_s^{-1/2} V_s^T x(k) = Qx(k) \tag{23.5}$$

4. Estimate the covariance matrix of the vector $\bar{x}(k)$ for preselected time lags other than p = 0. Perform SVD on the estimated covariance matrix.

$$\widehat{R}_{\bar{x}}(p) = \frac{1}{N}\sum_{k=1}^{N} \bar{x}(k)\bar{x}^T(k-p) = U_{\bar{x}}\sum_{\bar{x}} V_{\bar{x}}^T \tag{23.6}$$

5. Perform Joint Approximate Diagonalization on the above set of covariance matrices to estimate the orthogonal matrix U that diagonalizes a set of covariance matrices.

$$\widehat{R}_{\bar{x}}(p_i) = U_{\bar{x}}\sum_{\bar{x}}(p_i)\,U_{\bar{x}}^T \tag{23.7}$$

6. The mixing matrix and source signals can be estimated as

$$\widehat{A} = Q^+ U_{\bar{x}} = V_s \Lambda_s^{1/2} U_{\bar{x}} \tag{23.8}$$

$$y(k) = \widehat{s}(k) = U_{\bar{x}}^T \bar{x}(k) \tag{23.9}$$

23.2.2 Extension of SOBI to Experimental Modal Analysis

The joint diagonalization procedure employed by SOBI, as explained above, can also be employed within the framework of traditional experimental modal analysis, where one also measures the excitation forces in addition to the output responses. In this section, SOBI is extended to traditional modal analysis.

The impulse response function, for a MDOF system, at a particular output degree of freedom (dof) p, due to excitation force applied at dof q, is expressed in terms of modal parameters, i.e. modal frequency λ_r and residue A_{pqr} as

$$h_{pq}(t) = \sum_{r=1}^{N} A_{pqr}\, e^{\lambda_r t} + A_{pqr}^*\, e^{\lambda_r^* t} \tag{23.10}$$

This can be further written in the following manner [10] (residue $A_{pqr} = \frac{R_{pqr}}{2j}$),

$$h_{pq}(t) = \sum_{r=1}^{N} R_{pqr}\, e^{\sigma_r t} \sin(\omega_r t) \tag{23.11}$$

where ω_r is the damped natural frequency of the system and σ_r is the associated damping. For the undamped/proportionally damped case, the above equation reduces to the same form as Eq. (23.1). This is also analogous to the modal expansion theorem expressed in Eq. (23.2). It is worth noting at this point that the modal expansion theorem is only applicable for undamped or proportionally damped systems. This similarity between Eq. (23.1) (and Eq. (23.2)) and Eq. (23.11) presents a possibility of applying SOBI to impulse response functions and obtain corresponding modal parameters, as long as the assumption regarding the damping are true.

For the single input multiple output (SIMO) case, the impulse response functions can be mathematically expressed as

$$\mathbf{h}(t) = \mathbf{R}\,\overline{\mathbf{\eta}}(t) \tag{23.12}$$

where $\mathbf{h}(t)$ is a vector of impulse response functions at various output dofs due to force applied at a specific input dof. $\mathbf{R}$ is then a matrix of residues, whose columns can be expressed in terms of modal vector φ_r and participation vector. For SIMO case, participation vector is essentially a scalar given as $L_{ir} = q_r \varphi_{ir}$, where q_r is the scaling factor associated with the rth mode and φ_{ir} is the modal coefficient associated with that mode at the input excitation dof i. The mode shape information can thus be extracted from the residue vector estimated using SOBI. Frequency and damping information can be estimated from $\overline{\eta}(t)$ using simple SDOF methods.

23.3 Utilizing BSS Mode Shapes for Model Updating

Equations (23.1) and (23.11) are key to utilizing SO-BSS algorithms for modal analysis purposes. They are analogous to the BSS mixing model shown in Eq. (23.2). However, the issue with this model is that it assumes the mixing matrix to be real. In terms of modal analysis, it means that the dynamic system under investigation is assumed to be undamped or proportionally damped, meaning that the modes are real normal. However, in real world, dynamic structures do not always adhere to these assumptions. Real world structures often exhibit dynamic characteristics with complex modes. This is one major limitation of the approach suggested in Sect. 23.2.2. However, this limitation can turn out to be an advantage in case of model updating. Model updating techniques often require experimentally estimated mode shapes (often complex) to be first normalized such that they are real. It is these normalized real mode shapes that are utilized for model updating purposes. Since the procedure suggested in Sect. 23.2.2 provides real mode shapes directly, one can immediately use them for model updating. In this context, it is apt to recall model updating theory.

It is well known that finite element predictions are often called into question when they are in conflict with test results [11]. Inaccuracies in finite element model, and errors in results predicted by them, can arise due to use of incorrect modeling of boundary conditions, incorrect modeling of joints, and difficulties in modeling of damping etc. This has led to the development of model updating techniques, which aim at reducing the inaccuracies present in finite element model in the light of measured dynamic test data. A number of model updating methods have been proposed in recent years, as shown in the surveys [12, 13], most of which use modal data, i.e. natural frequencies and mode shapes for the purpose of updating the finite element model.

Collins et al. [14] use the natural frequency and modeshape sensitivity for finite element model updating in an iterative framework. The updating parameters (p_i), corresponding to finite element model, are corrected to bring the analytical modal data closer to that obtained experimentally. For the rth eigenvalue, λ^r (square of the rth natural frequency in rad/s), and the rth eigenvector, $\{\Phi\}^r$ (the mode shape), linearization gives:

$$\lambda_X^r = \lambda_{FE}^r + \sum_{i=1}^{nu} \left(\frac{\partial \lambda_{FE}^r}{\partial p_i} \cdot \Delta p_i \right) \tag{23.13}$$

$$\{\Phi\}_X^r = \{\Phi\}_{FE}^r + \sum_{i=1}^{nu} \left(\frac{\partial \{\Phi\}_{FE}^r}{\partial p_i} \cdot \Delta p_i \right) \tag{23.14}$$

where subscript FE and X denote finite element model and experimental model respectively. *nu* represents number of updating parameters. The derivative of eigenvalues and mode shapes can be calculated from the following relationship given by Fox and Kapoor [15],

$$\frac{\partial \lambda_{FE}^r}{\partial p_i} = \frac{\{\varphi\}_{FE}^{rT} \left[\frac{\partial [K]}{\partial p_i} - \lambda_{FE}^r \frac{\partial [M]}{\partial p_i} \right] \{\varphi\}_{FE}^r}{\{\varphi\}_{FE}^{rT} [M] \{\varphi\}_{FE}^r} \tag{23.15}$$

$$\frac{\partial \{\Phi\}_{FE}^r}{\partial p_i} = \sum_{j=1, \neq r}^{N} \left(\frac{\{\varphi\}_{FE}^{jT} \left[\frac{\partial [K]}{\partial p_i} - \lambda_{FE}^r \frac{\partial [M]}{\partial p_i} \right] \{\varphi\}_{FE}^j}{(\lambda^r - \lambda^j)} \right) - \frac{1}{2} \{\varphi\}_{FE}^{rT} \frac{\partial [M]}{\partial p_i} \{\varphi\}_{FE}^r \tag{23.16}$$

Using the above equations, the finite element model updating for resonance frequencies and modeshapes can be written for m number of modes as:

$$\begin{Bmatrix} \lambda_X^1 - \lambda_{FE}^1/\lambda_{FE}^1 \\ \{\Phi\}_X^1 - \{\Phi\}_{FE}^1 \\ \vdots \\ \vdots \\ \vdots \\ \lambda_X^m - \lambda_{FE}^m/\lambda_{FE}^m \\ \{\Phi\}_X^m - \{\Phi\}_{FE}^m \end{Bmatrix} = \begin{bmatrix} \frac{\partial \lambda_{FE}^1}{\partial p_1}/\lambda_{FE}^1 & \frac{\partial \lambda_{FE}^1}{\partial p_2}/\lambda_{FE}^1 & \cdots\cdots & \frac{\partial \lambda_{FE}^1}{\partial p_{nu}}/\lambda_{FE}^1 \\ \frac{\partial \{\Phi\}_{FE}^1}{\partial p_1} & \frac{\partial \{\Phi\}_{FE}^1}{\partial p_2} & \cdots\cdots & \frac{\partial \{\Phi\}_{FE}^1}{\partial p_{nu}} \\ \cdots & \cdots & \cdots\cdots & \cdots \\ \cdots & \cdots & \cdots\cdots & \cdots \\ \cdots & \cdots & \cdots\cdots & \cdots \\ \frac{\partial \lambda_{FE}^m}{\partial p_1}/\lambda_{FE}^m & \frac{\partial \lambda_{FE}^m}{\partial p_2}/\lambda_{FE}^m & \cdots\cdots & \frac{\partial \lambda_{FE}^m}{\partial p_{nu}}/\lambda_{FE}^m \\ \frac{\partial \{\Phi\}_{FE}^m}{\partial p_1} & \frac{\partial \{\Phi\}_{FE}^m}{\partial p_2} & \cdots\cdots & \frac{\partial \{\Phi\}_{FE}^m}{\partial p_{nu}} \end{bmatrix} \cdot \begin{Bmatrix} \Delta p_1 \\ \Delta p_2 \\ \vdots \\ \vdots \\ \vdots \\ \Delta p_{nu} \end{Bmatrix} \tag{23.17}$$

where $\{\Delta p\}$ is a vector of change in updating parameters. It can be observed from Eq. (23.17) that values of updating parameters are mostly affected by eigenvalues as magnitude of eigenvalues is significantly higher than eigenvectors. In order to include the effect of changes in eigenvectors, the ratio of eigenvalues is considered in this problem formulation.

23.4 Investigations on an Analytical 5 DOF System

23.4.1 Modal Parameter Identification

A simple 5 DOF system as shown in Fig. 23.1 is selected to investigate the applicability of the proposed method. The associated mass and stiffness matrix for this system are listed below.

$$\mathbf{M} = \begin{bmatrix} 250 & 0 & 0 & 0 & 0 \\ 0 & 350 & 0 & 0 & 0 \\ 0 & 0 & 30 & 0 & 0 \\ 0 & 0 & 0 & 450 & 0 \\ 0 & 0 & 0 & 0 & 50 \end{bmatrix} \quad \mathbf{K} = 1000 \times \begin{bmatrix} 9000 & -5000 & 0 & 0 & 0 \\ -5000 & 11000 & -6000 & 0 & 0 \\ 0 & -6000 & 12500 & -6500 & 0 \\ 0 & 0 & -6500 & 14500 & -8000 \\ 0 & 0 & 0 & 0 & 15000 \end{bmatrix}$$

23.4.1.1 Case 1: Undamped System

To begin with, the above-mentioned system is considered undamped. Since the current version of proposed approach is formulated for SIMO scenario, the third column of the impulse response matrix, $\mathbf{h}_{:,3}$ is considered in this study. It should be noted that the algorithm was set up to jointly diagonalize the first 1500 time lags of IRFs. A comparison of estimated natural frequencies with theoretical values is provided in Table 23.5 at the end of this section. This table lists and compares the natural frequencies from various cases investigated in this study. Mode shape comparison is given in Table 23.1.

The separation using SOBI, illustrated in Fig. 23.2, shows the power spectra of decoupled SDOF systems, calculated on the basis of estimated $\bar{\eta}(t)$. It is noticeable that estimated mode shapes match very well with theoretical values. The only error noticeable, although very small, is for the fourth mode.
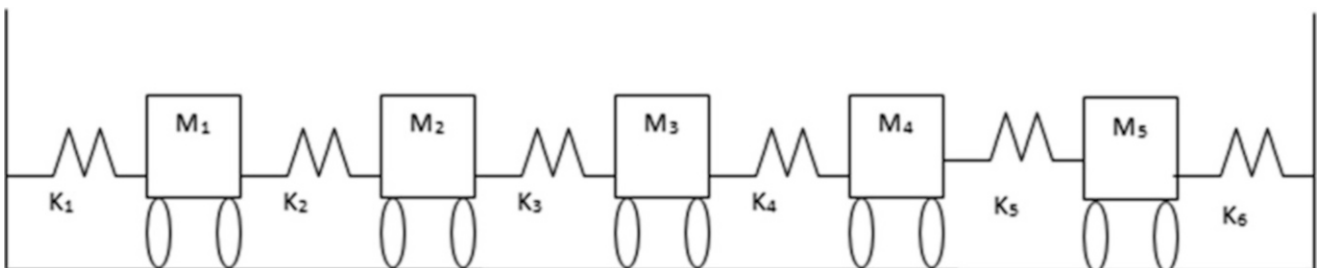
Fig. 23.1 5 DOF lumped mass system

23.4.1.2 Case 2: Light Proportional Damping

Next, damping is introduced to the above-mentioned 5 DOF system and several possibilities are considered. To begin with damping is considered as proportional, $\mathbf{C} = 1.3\,\mathbf{M} + 4e^{-6}\mathbf{K}$. Modal vectors in this case are still real and same as that listed in Table 23.2 along with estimated mode shapes. Note that modal frequency and damping for this proportionally damped case are listed in Table 23.5 and 23.6. The power spectra of estimated SDOF systems (Fig. 23.3) again shows that the system modes are decoupled satisfactorily by SOBI. The mode shape estimates compare well in this case also.

Table 23.1 Modal shape comparison for undamped system

	Mode 1		Mode 2		Mode 3		Mode 4		Mode 5	
DOF	Theo.	Est.	Theo.	Est.	Theo.	Est.	Theo.	Est.	Theo.	Est.
1	1	1	1	1	1	1	1	1	1	1
2	1.4904	1.4904	0.8376	0.8377	−0.6026	−0.6025	−13.669	−13.712	−19.872	−19.872
3	1.3608	1.3611	−0.2382	−0.2397	−0.2490	−0.2500	220.79	222.254	465.19	465.19
4	1.2022	1.2022	−1.2100	−1.2099	0.1326	0.1327	121.92	121.44	−17.687	−17.687
5	0.6547	0.6547	−0.6896	−0.6896	0.0842	0.0842	−2080.6	−2073.2	21.206	21.206
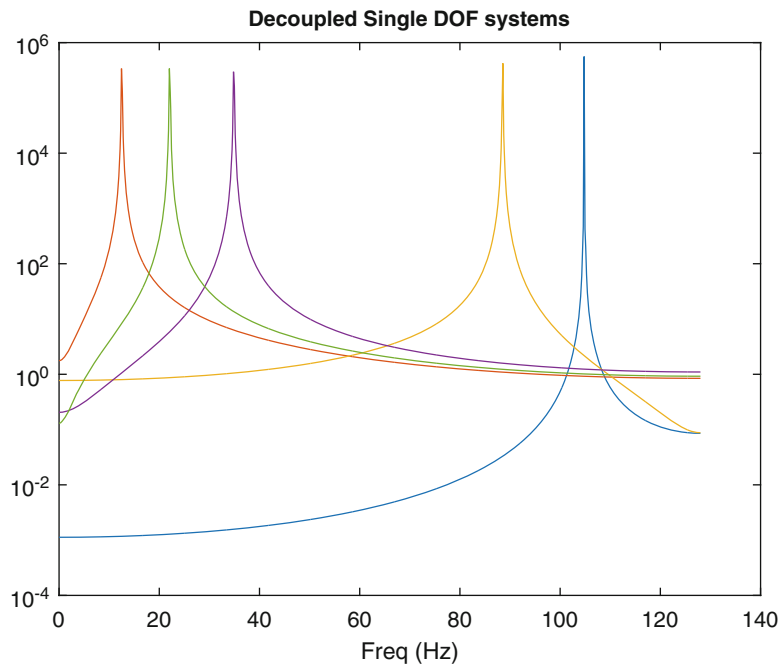
Fig. 23.2 Power spectra of decoupled modes (undamped System)

Table 23.2 Modal matrix (light proportional damping)

	Mode 1		Mode 2		Mode 3		Mode 4		Mode 5	
DOF	Theo.	Est.	Theo.	Est.	Theo.	Est.	Theo.	Est.	Theo.	Est.
1	1	1	1	1	1	1	1	1	1	1
2	1.4904	1.4906	0.8376	0.8366	−0.6026	−0.6024	−13.669	−18.247	−19.872	−19.968
3	1.3608	1.3608	−0.2382	−0.2361	−0.2490	−0.2461	220.79	279.94	465.19	467.28
4	1.2022	1.2024	−1.2100	−1.2107	0.1326	0.1326	121.92	162.58	−17.687	−17.772
5	0.6547	0.6548	−0.6896	−0.6898	0.0842	0.0843	−2080.6	−2774.8	21.206	21.298
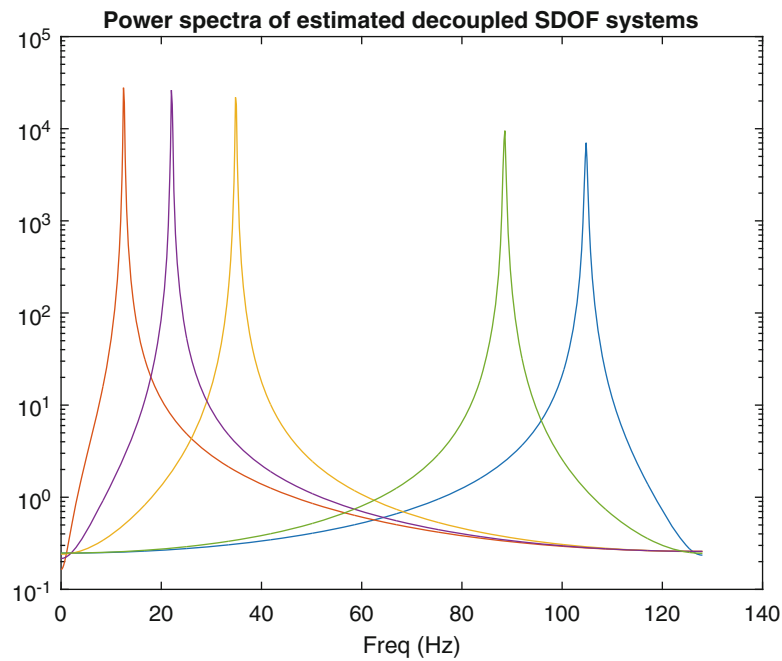
Fig. 23.3 Power spectra of decoupled modes (light proportional damping)

23.4.1.3 Case 3: Moderate Proportional Damping

In this case, damping is still considered to be proportional but it is adjusted so that the values are moderate. This is achieved by using the following value, $\mathbf{C} = 1.3\,\mathbf{M} + 9e^{-5}\mathbf{K}$. The theoretical and estimated mode shapes are listed in Table 23.3. The power spectra of separated modes, shown in Fig. 23.4, indicates that separation is not as complete as is the case with previous scenarios. This can be seen in the power spectra of 5th mode. The comparison of estimated frequency and damping is provided in Tables 23.5 and 23.6.

Table 23.3 Modal matrix (moderate proportional damping)

	Mode 1		Mode 2		Mode 3		Mode 4		Mode 5	
DOF	Theo.	Est.	Theo.	Est.	Theo.	Est.	Theo.	Est.	Theo.	Est.
1	1	1	1	1	1	1	1	1	1	1
2	1.4904	1.4907	0.8376	0.8320	−0.6026	−0.6008	−13.669	61.766	−19.872	−21.876
3	1.3608	1.3612	−0.2382	−0.2387	−0.2490	−0.2435	220.79	−1234.0	465.19	510.14
4	1.2022	1.2027	−1.2100	−1.2115	0.1326	0.1325	121.92	−71.371	−17.687	−19.351
5	0.6547	0.6549	−0.6896	−0.6900	0.0842	0.0847	−2080.6	1918.9	21.206	21.278
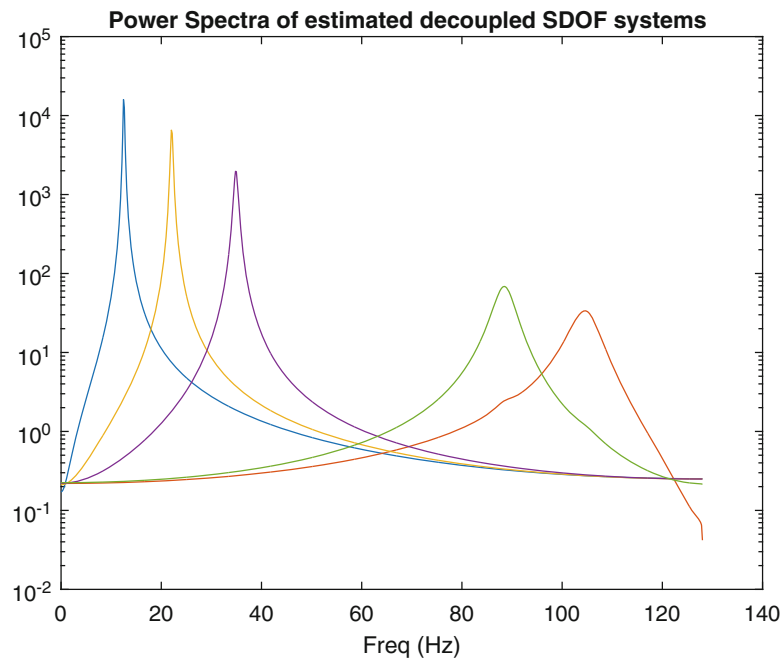
Fig. 23.4 Power spectra of decoupled modes (moderate proportional damping)

23.4.1.4 Case 4: Non-proportional Damping

Previously, damping is either neglected or considered proportional. Here, the effects of non-proportional damping are studied. The chosen damping matrix is given as

$$
\mathbf{C} = \begin{bmatrix}
3250 & -250 & 0 & 0 & 0 \\
-250 & 450 & -200 & 0 & 0 \\
0 & -200 & 320 & -120 & 0 \\
0 & 0 & -120 & 190 & -70 \\
0 & 0 & 0 & -70 & 270
\end{bmatrix}
$$

Theoretical modal parameters (frequency and damping) for the non-proportionally damped case are listed in Tables 23.5 and 23.6. Modal vectors in this case become complex and are listed in Table 23.4 along with estimated vectors, which are expectedly real. The power spectra plots (Fig. 23.5) for this case clearly show that decoupling of impulse response functions into simple SDOF system responses is not as accurate. This is expected as the method is formulated on the assumption that the system is either undamped or proportionally damped, which is not the case here.

23.4.2 Modal Frequency and Damping Comparison

Tables 23.5 and 23.6 provide the comparison of theoretical and estimated frequency and damping values for the four cases studied in last section. Results show that the estimated values compare well with theoretical parameters.

Table 23.4 Estimated modal vectors (non-proportional damping)

Mode 1		Mode 2		Mode 3		Mode 4		Mode 5	
Theo.	Est.	Theo.	Est.	Theo.	Est.	Theo.	Est.	Theo.	Est.
1.0000 + 0.0000i	1	1.0000 + 0.0000i	1	1.0000 + 0.0000i	1	1.0000 + 0.0000i	1	1.0000 + 0.0000i	1
1.4899 + 0.0382i	1.4921	0.8371 + 0.0640i	0.8167	−0.6008 + 0.0447i	−0.5942	−13.6554 + 0.5907i	14.5782	−19.8548 + 0.7166i	−21.1548
1.3601 + 0.0457i	1.3628	−0.2377 + 0.0296i	−0.2441	−0.2487 + 0.0127i	−0.2459	220.4414 − 11.8562i	−201.537	464.6472 − 19.5550i	493.378
1.2014 + 0.0505i	1.2045	−1.2086 − 0.0065i	−1.2486	0.1317 − 0.0164i	0.1111	121.8771 − 4.4640i	−112.067	−17.6589 + 0.8717i	−18.7556
0.6543 + 0.0273i	0.6559	−0.6888 − 0.0037i	−0.7105	0.0836 − 0.0099i	0.0732	−2079.5864 + 68.45084i	1917.989	21.1400 − 1.5169i	22.4043
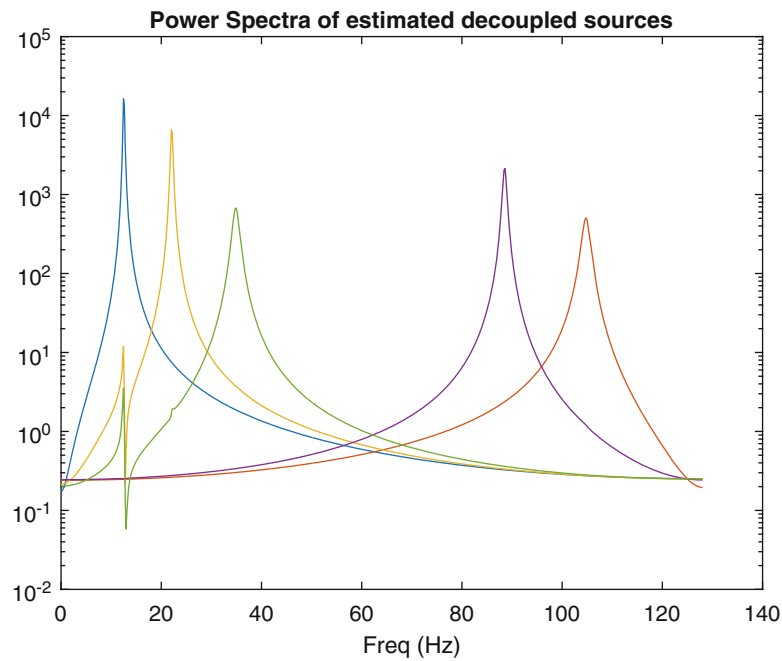
Fig. 23.5 Power spectra of decoupled modes (non-proportional damping)

Table 23.5 Comparison of modal frequencies

Undamped		Light proportional damping		Moderate proportional damping		Non-proportional damping	
Theo. (Hz)	Est. (Hz)	Theo. (Hz)	Est. (Hz)	Theo. (Hz)	Est. (Hz)	Theo. (Hz)	Est. (Hz)
12.5234	12.5672	12.5230	12.5295	12.5226	12.5336	12.5263	12.5317
22.0805	22.1070	22.0803	22.0828	22.0792	22.0900	22.0830	22.0923
34.8880	34.9054	34.8878	34.8904	34.8851	34.8931	34.8635	34.8782
88.5248	88.5651	88.5246	88.5230	88.4944	88.4275	88.5238	88.5210
104.7825	104.8246	104.7822	104.7735	104.7334	104.3835	104.7787	104.7354

Table 23.6 Comparison of modal damping

Light proportional damping		Moderate proportional damping		Non-proportional damping	
Theo. (%)	Est. (%)	Theo. (%)	Est. (%)	Theo. (%)	Est. (%)
0.8418	0.8303	1.1801	1.1874	1.1486	1.1411
0.4963	0.4928	1.0928	1.0971	1.0589	1.0643
0.3404	0.3413	1.2830	1.2809	2.1720	2.1653
0.2281	0.2278	2.6198	2.6226	0.4872	0.4876
0.2304	0.2306	3.0614	3.0748	0.8423	0.8329

23.4.3 *Investigations Related to Model Updating*

Choice of updating parameters on the basis of engineering judgment about the possible locations of modeling errors in a structure is one of the strategies to ensure that only physically meaningful corrections are made. While using the mode shapes estimated using SOBI in previous section, for model updating purposes, two different cases are considered. First, stiffness K_1 is considered as an updated parameter and later stiffness K_3. In case of 5 degrees-of-freedom lumped mass system, modeling of stiffness at the ends is expected to be a dominant source of inaccuracy in the FE model assuming that the values of material and the geometric parameters are correctly known. The modeshape and natural frequencies extracted for four different cases have been used to update the stiffness K_1. The updated values of the stiffness K_1 and corresponding

Table 23.7 Stiffness values of spring K_1 after updating

Cases	Updated values	% Error
Undamped system	4.0603×10^6	-1.5079
Lightly proportional damped	4.0303×10^6	-0.7582
Moderate proportional damped	4.0718×10^6	-1.7951
Non-proportional damping	4.0615×10^6	-1.5384

Table 23.8 Stiffness values of spring K_3 after updating

Cases	Updated values	% Error
Undamped system	6.0226×10^6	-0.3773
Lightly proportional damped	5.8769×10^6	2.0510
Moderate proportional damped	5.8988×10^6	1.6869
Non-proportional damping	5.9900×10^6	1.5384

errors are provided in the Table 23.7. It can be observed from the Table 23.7 that, after updating, the error in all the cases have been less than 2 %, which is acceptable.

Next K_3 has been considered as updated parameter. The reason for choosing K_3 is that SOBI is applied to the SIMO case where the structure is excited at location 3. It can be observed from the updated values of K_3, given in Table 23.8 that after updating the error is very small.

23.5 Discussions

Results listed in previous section show that proposed approach of applying SOBI to impulse response functions for modal parameter estimation purposes yields satisfactory results. The frequency and damping estimates compare well in most cases and the same can be said for mode shapes in general.

It is a feature of the proposed approach that mode shape matrix is estimated directly in the first step itself (mode shape matrix is analogous to mixing matrix). Expectedly, estimated mode shapes are real, irrespective of the nature of the dynamic system under investigation. There is no direct way of comparing them with theoretical mode shapes (which can be complex in certain cases). For cases such as undamped and proportionally damped system, modal coefficients compare well. It should be noted that applied algorithm is a SIMO algorithm and the chosen input DOF might not be able to excite all the modes equally. In all cases however, the modal assurance criteria (MAC) is close to 1. The biggest error in mode shapes is observed for moderately damped proportional damping case, where the mode shape associated with the fourth mode (third modal coefficient in particular) is not estimated with high accuracy. It is worth investigating if this can be improved by choosing a different excitation point. The performance with regards to non-proportional damping case is however satisfactory.

The results from finite element updating procedure show the effectiveness of this approach as the real mode shapes can be directly utilized for model updating procedure. The reported errors on the updated parameter is relatively low. However, the true measure of the advantage of this approach, for the purpose of model updating, can only be assessed by evaluating its performance vis-à-vis conventional techniques, which provide complex mode shape that are required to be normalized to obtain real mode shapes. The error on updating parameter using these two different approaches can provide more insight into the effectiveness of BSS based approach.

23.6 Conclusions

BSS algorithms have typically been employed in modal analysis domain within OMA framework. This is obvious as, like BSS, aim of OMA is to obtain modal parameters only on the basis of measured output responses. This paper treats BSS as a second order mathematical decomposition and exploits the joint diagonalization properties of SOBI to derive a new approach that is applicable to traditional experimental modal analysis framework where both input and output are known. The applicability and effectiveness of this approach is shown in this paper by means of investigations done on a numerical lumped mass system. The obtained results are satisfactory.

The suggested approach has a property that it provides real mode shapes irrespective of the nature of the dynamic system being analyzed. This is a drawback of the suggested approach but this property can be exploited for model updating purposes.

The feasibility study carried out in this paper shows promise in terms of utilizing mode shapes obtained from this approach. However, as noted earlier, a complete picture can only emerge after comparing this approach with conventional approaches, where estimated mode shapes are normalized to get real mode shapes.

References

1. Cichocki, A., Amari, S.: Adaptive Blind Signal and Image Processing. Wiley, New York (2002)
2. Hyvarinen, A., Karhunen, J., Oja, E.: Independent Component Analysis. Wiley, New York (2001)
3. Antoni, J.: Blind separation of vibration components: principles and demonstrations. Mech. Syst. Signal Process. **19**(6), 1166–1180 (2005)
4. Poncelet, F., Kerschen, G., Golinval, J.C., Verhelst, D.: Output-only modal analysis using blind source separation techniques. Mech. Syst. Signal Process. **21**(6), 2335–2358 (2007)
5. Chauhan, S., Martell, R., Allemang, R.J., Brown, D.L.: Application of independent component analysis and blind source separation techniques to operational modal analysis. In: Proceedings of the 25th IMAC, Orlando (2007)
6. Swaminathan, B., Sharma, B., Chauhan, S.: Utilization of blind source separation techniques for modal analysis. In: Proceedings of the 28th IMAC, Jacksonville (2010)
7. Antoni, J., Chauhan, S.: A study and extension of second-order blind source separation to operational modal analysis. J. Sound Vib. **332**(4), 1079–1106 (2013)
8. Allemang, R.J.: Vibrations: experimental modal analysis. UC-SDRL-CN-20-263-663/664, Structural Dynamics Research Laboratory, Department of Mechanical, Industrial and Nuclear Engineering, University of Cincinnati (1999)
9. Belouchrani, A., Abed-Meraim, K.K., Cardoso, J.F., Moulines, E.: Second order blind separation of correlated sources. In: Proceedings of International Conference on Digital Signal Processing, Cyprus, pp. 346–351 (1993)
10. Allemang, R.J.: Vibrations: analytical and experimental modal analysis. UC-SDRL-CN-20-263-662, Structural Dynamics Research Laboratory, Department of Mechanical, Industrial and Nuclear Engineering, University of Cincinnati (1999)
11. Ewins, D.J.: Modal Testing: Theory, Practice and Application. Research Studies Press, Baldock (2000)
12. Friswell, M.I., Mottershead, J.E.: Finite Element Model Updating in Structural Dynamics. Kluwer, Dordrecht (1995)
13. Imregun, M., Visser, W.J.: A review of model updating techniques. Shock. Vib. Dig. **23**, 141–162 (1991)
14. Collins, J.D., Hart, G.C., Hasselman, T.K., Kennedy, B.: Statistical identification of structures. AIAA J. **12**, 185–190 (1974)
15. Fox, R.L., Kapoor, M.P.: Rate of change of eigenvalues and eigenvectors. AIAA J. **12**, 2426–2429 (1968)

Chapter 24
Multivariate ARMA Based Modal Identification of a Time-Varying Beam

M. Bertha and J.C. Golinval

Abstract The present paper addresses the problem of modal identification of time-varying systems. The identification is based on a multivariate autoregressive moving-average model in which the time variability of the system is caught using a basis functions approach. In this approach, the time-varying regressive coefficients in the model are expended in the chosen basis functions and only the projection coefficients have to be identified. In that way, the initial time-varying problem then becomes a time-invariant one that can be solved. Because a multivariate model is used, in addition to the time-varying poles, the time-varying mode shapes may be identified too. The method is first presented and then applied on an experimental demonstration structure. The experimental structure consists of a supported beam on which a mass is travelling. The mass is chosen sufficiently large to have a significant influence on the dynamics of the primary system. This kind of problem is a classical example commonly used by many authors to test time-varying identification methods.

Keywords Modal identification • Time-varying systems • Multivariate identification • Basis functions • Autoregressive moving-average model

24.1 Introduction

Modal analysis plays a major role in the field of structure dynamics either numerically or experimentally. Concerning the analysis of linear time invariant structures, both computational and identification methods are pretty complete and robust and new challenges appear now to the extension to more complicated behaviours such as nonlinear and time-varying. This paper deals with this latter case. Some analyses of time-varying dynamic structure have already been performed. We can find for example in [1] a double identification based on wavelet transform and on a modified version of the Stochastic Subspace Identification method (SSI) applied on short successive time windows (short-time SSI). Another way to handle the time variability is to expand it on a set of Basis Functions (BF) such as explained in [2] for general time-varying processes. The method of basis function (also named Functional Series in [3, 4]) is also used to create time-varying Auto Regressive Moving-Average identification models for modal analysis purposes. A recurrent setup to test such methods consist in a simple beam on which a heavy mass is moving. A similar structure is used in this paper.

The paper is organized as follows. Section 24.2 presents the way to perform modal analysis using multivariate ARMA models in the field of linear time invariant structure dynamics along with its adaptation to the analysis in linear time-varying behaviour. In Sects. 24.3 and 24.4 the setup used in this study and its time invariant and time-varying analyses are presented with their corresponding results.

24.2 Presentation of the ARMAV Method for LTI Modal Analysis and Its Extension to Time-Varying Systems

The AutoRegressive Moving-Average (ARMA) model can be used in the field of experimental modal analysis. In its vector, or multivariate, form (ARMAV) it is possible to identify a complete modal model i.e. that the mode shapes of the system can be identified in addition to the poles (eigenfrequencies and damping ratio's). If we denote by $y[t]$ the $d \times 1$ vector

M. Bertha (✉) • J.C. Golinval
Department of Aerospace and Mechanical Engineering, University of Liège, Liège, Belgium
e-mail: mathieu.bertha@ulg.ac.be; jc.golinval@ulg.ac.be

of the output measurements the ARMAV model of order p and q for the AR and MA parts, respectively, is given as follows:

$$y[t] + \sum_{i=1}^{p} A_i y[t-i] = e[t] + \sum_{j=1}^{q} B_j e[t-j], \tag{24.1}$$

in which $e[t]$ is the innovation, the part of the signal that may not be predicted by the past values of y. If we are faced to a dynamical system of order n, driven by its motion equation

$$M \ddot{y}(t) + C \dot{y}(t) + K y(t) = f(t), \tag{24.2}$$

it may be shown that it can be represented by an ARMAV$(2, 1)$ or $(2, 2)$ in noise-free or noisy identification, respectively [5, 6]. If the output dimension d is not equal to the dimension n of the system, an order $2m$ should be considered with m equals the rounded up value of n/d.

Let us now consider the system (24.1) in a time-varying framework. In that case, the structural properties of the system (through the M, K and C matrices) are no more constant but may exhibit a variation over time (or any other varying parameter). The motion equation then becomes

$$M(t) \ddot{y}(t) + \underbrace{\dot{M}(t) \dot{y}(t)}_{\text{Negligible}} + C(t) \dot{y}(t) + K(t) y(t) = f(t) \tag{24.3}$$

in which the mass variation rate is assumed to be slow with respect to the dynamics of the system.

If the dynamic properties of the system vary with time, it will be the same for the parameters used in the identification model. The parameters in the ARMAV model (24.1) will then be time-varying too what will lead to the next model:

$$y[t] + \sum_{i=1}^{p} A_i[t] y[t-i] = e[t] + \sum_{j=1}^{q} B_j[t] e[t-j]. \tag{24.4}$$

The time-varying $A_i[t]$ and $B_j[t]$ are the parameters to be identified which is not an easy task due to their variation. A method to manage this variation is the basis functions approach [2] also named functional series approach in [3, 4]. This method does the assumption that the varying parameters can be projected on a set of preselected basis functions (polynomials, sine/cosine, etc.) and the aim of the method is to identify those projection coefficients:

$$A_i[t] = \sum_{k=1}^{r_A} A_{i,k} f_k[t] \tag{24.5}$$

$$B_j[t] = \sum_{k=1}^{r_B} B_{j,k} f_k[t], \tag{24.6}$$

in which the $A_{i,k}$ and $B_{j,k}$ are these projection coefficients and $f_k[t]$ are the known basis functions. Note that at this stage the identification problem becomes time invariant and the system is now modelled as

$$y[t] + \sum_{i=1}^{p} \sum_{k=1}^{r_A} A_{i,k} f_k[t] y[t-i] = e[t] + \sum_{j=1}^{q} \sum_{k=1}^{r_B} B_{j,k} f_k[t] e[t-j]. \tag{24.7}$$

Introducing the following generalised regressors:

$$\phi[t]^T = \left[f_1[t]y[t-1]^T, f_2[t]y[t-1]^T, \cdots, f_{r_a}[t]y[t-p]^T \right] \tag{24.8}$$

$$\psi[t]^T = \left[-f_1[t]e[t-1]^T, -f_2[t]e[t-1]^T, \cdots, -f_{r_b}[t]e[t-q]^T \right] \tag{24.9}$$

and the matrix of identification parameters

$$\boldsymbol{\Theta} = \left[\boldsymbol{A}_{1,1}, \boldsymbol{A}_{1,2}, \cdots, \boldsymbol{A}_{1,r_A}, \boldsymbol{A}_{2,1}, \cdots, \boldsymbol{A}_{p,r_A}, \boldsymbol{B}_{1,1}, \cdots, \boldsymbol{B}_{q,r_B} \right], \tag{24.10}$$

the prediction error of the model can be expressed as

$$\hat{\boldsymbol{e}}[t, \boldsymbol{\Theta}] = \boldsymbol{y}[t] - \hat{\boldsymbol{y}}[t, \boldsymbol{\Theta}]$$

$$= \boldsymbol{y}[t] + \boldsymbol{\Theta} \begin{bmatrix} \boldsymbol{\phi}[t] \\ \boldsymbol{\psi}[t] \end{bmatrix}. \tag{24.11}$$

The latter prediction error is then used to build a parameter-dependent criterion to be minimized. A commonly used function is the Sum of Squared Errors (SSE) and is defined as

$$V(\boldsymbol{\Theta}) = \frac{1}{N} \sum_{t=1}^{N} \hat{\boldsymbol{e}}[t, \boldsymbol{\Theta}]^T \hat{\boldsymbol{e}}[t, \boldsymbol{\Theta}]. \tag{24.12}$$

The parameters to identify will be those that minimize this cost function, i.e.:

$$\boldsymbol{\Theta} = \arg \min_{\boldsymbol{\Theta}} \frac{1}{N} \sum_{t=1}^{N} \hat{\boldsymbol{e}}[t, \boldsymbol{\Theta}]^T \hat{\boldsymbol{e}}[t, \boldsymbol{\Theta}]. \tag{24.13}$$

The latter minimization cannot be performed using a usual least square approach because of the nonlinear dependence of the prediction error in $\boldsymbol{\Theta}$ because the $\boldsymbol{\psi}$ contains time-lagged values of the unknown innovation. This should require nonlinear optimization schemes but they often require the evaluation of the gradient of the objective function (sometimes also the evaluation of its Hessian) that may be difficult or very time consuming if a finite difference approach is chosen. A way to bypass that difficulty is to apply another iterative method such as the Multi Stage Least Squares (MSLS) method [7]. The latter assumes that, at the iteration k, an estimate of the prediction error is known such as in Eq. (24.11). Then, the estimate of $\boldsymbol{\Theta}$ at iteration $k + 1$ can be obtained via a least squares step. It remains to initialize the iterative procedure with a first estimate of the prediction error. This can be done assuming a least square estimate of a long AR only model of the system (the MA order q is put to zero).

Once the (time-dependent) Autoregressive and Moving-average matrices are identified, the modal parameters of the system can be obtained through a modal decomposition of the companion matrix made up with the Autoregressive part of the model [6, 7]

$$\boldsymbol{C}(t) = \begin{bmatrix} -\boldsymbol{A}_1[t] & \boldsymbol{I} & \boldsymbol{0} & \cdots & \boldsymbol{0} \\ -\boldsymbol{A}_2[t] & \boldsymbol{0} & \boldsymbol{I} & \cdots & \boldsymbol{0} \\ \vdots & \vdots & \vdots & \ddots & \vdots \\ -\boldsymbol{A}_{p-1}[t] & \vdots & \vdots & & \boldsymbol{I} \\ -\boldsymbol{A}_p[t] & \boldsymbol{0} & \boldsymbol{0} & \cdots & \boldsymbol{0} \end{bmatrix} \tag{24.14}$$

24.3 Presentation of the Experimental Setup

The problem under study in that work consist in a simple beam supported at its both ends by springs. On this beam moves a steel block having a mass which is not negligible with respect to the mass of the beam. In that way, this moving mass will affect the dynamic properties of the system depending of its position along the beam. The system is excited by a random force with a shaker and twelve accelerometers (five pairs along the beam and two at the springs levels) record it time response. The whole system is show in Fig. 24.1. In addition, the position of the mass is monitored using a laser sensor.
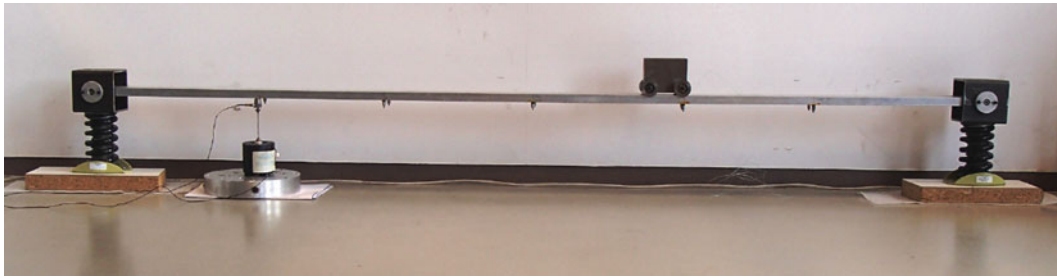
Fig. 24.1 Picture of the time-varying experimental setup
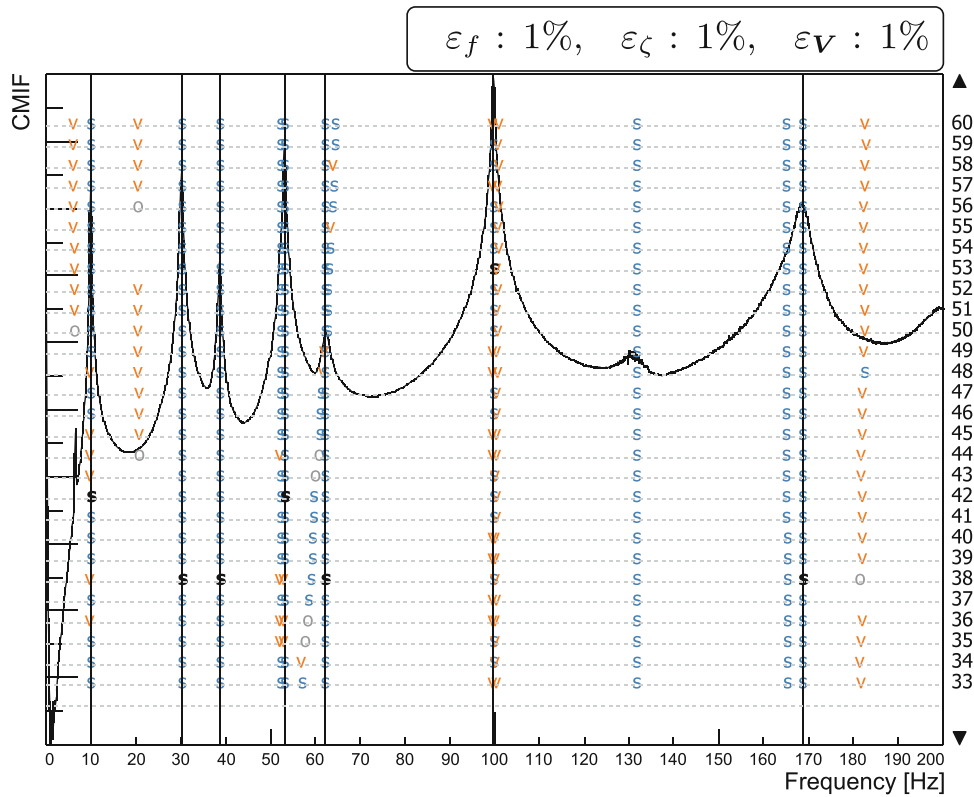
Fig. 24.2 Stabilization diagram of the time invariant subsystem. *Bold black* **s** represent the user-selected poles

24.3.1 Linear Time Invariant Identification

Before testing the structure in its time-varying behaviour, it is interesting to first test only the subsystem of the supported beam to get its modal properties. These results will further serve for comparison when the moving mass will be introduced in the system.

This LTI modal analysis is performed in LMS Test.Lab using the embedded PolyMAX method [8]. The obtained stabilization diagram is shown in Fig. 24.2 and the related results are listed in Table 24.1. The mode shapes of the subsystem are quite usual for a supported beam, let us just note the presence of stable column of poles close to 130 Hz we suspect to be a horizontal motion of the beam.

Table 24.1 Experimental modal parameters of the supported beam

Mode #	f_r (Hz)	ζ_r (%)	Type of mode
1	9.86	0.32	First bending
2	30.12	0.52	Opposite phase spring motion with small second bending
3	38.6	0.65	In phase spring motion with small first bending
4	53.14	0.27	Second bending
5	62.17	1.56	Rotation around the beam axis
6	99.70	0.28	Third bending
7	168.60	0.99	Fourth bending

24.4 Time-Varying Identification

Let us now move the mass on the beam while the latter is randomly excited by the shaker. In Fig. 24.3b, the wavelet transform of the third sensor (where the shaker is attached) is shown. This represents the evolution of the dynamics of the system through the variation of its resonance frequencies when the mass is pulled along the beam as shown in Fig. 24.3a. The interesting thing is that the resonance frequencies oscillate in ranges whose the upper value correspond to the eigenfrequencies identified in the previous LTI analysis. This is explained by the fact that when the mass is located at a node of vibration, its effect on that mode is reduced and conversely, the additional inertial effects are maximum when the mass is located at antinodes of vibration. The only exception concerns the fifth mode which is a global rotation of the beam along its axis. Because the rotation is globally the same along the beam, all its frequency line is just decreased and remains approximately constant along the time recording. Unfortunately, due to the inertia properties of the moving mass, the frequency of that mode is located at approximately the same value than the fourth one. Some frequency crossings are even observed, because of the oscillation of the fourth frequency.
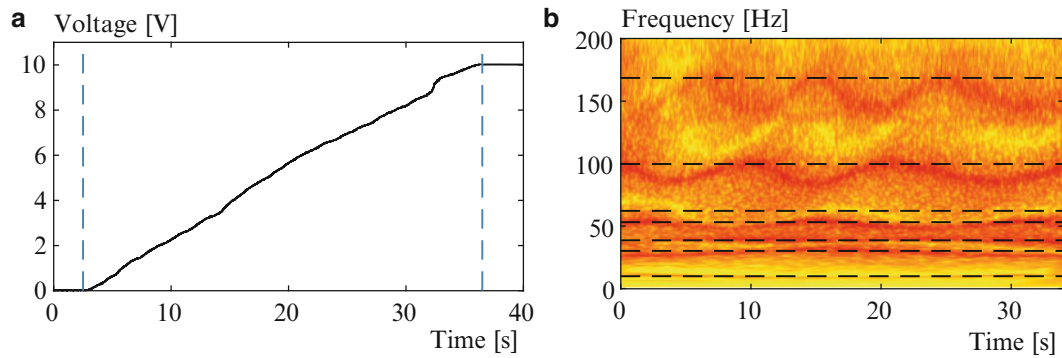
The identification of the time-varying modal properties of the system is not an easy task. As usual in most of modal identification methods, we have to select a proper structure of the model. In general the problem is solved for a series of increasing model orders and stabilization plots are used to select a good set of results. Obviously, in our case, a usual stabilization plot is not very practical due to the time dependence of our results. A second difficulty is that we do not have only a single model order but two (one for each of the AR and MA parts) and we also have to deal with the sizes of the functions bases related to the expansions of the AR and MA coefficients.

Another way to select good models rely on using some tools balancing the accuracy and complexity of identification models. The reason why the complexity of the model is took into account comes from the principle of parsimony [2] stating that the fewer the number of parameters used to explain a model, the better it is. For example, the Akaike Information Criterion (AIC) [6, 7] given by

$$AIC = N \log\left[V(\mathbf{\Theta})\right] + 2\,\delta, \tag{24.15}$$

in which δ is the number of parameters to be estimated ($d^2\,p\,r_A + d^2\,q\,r_B$) and N the number of time samples. We will then look to models close to the minimum of that criteria.

A second property of that method is that the number of modes that can be identified is related to the AR model order p but also to the number of measurement sensors d indeed, the number of identified poles (in complex-conjugated pairs) is given by the size of the companion matrix $\mathcal{C}$ in (24.14). In our case, because we want the estimation of at least seven modes, an AR model order $p = 1$ is not sufficient because with our twelve sensors, this will lead to the identification of six pairs of complex-conjugated modes. The minimal AR model order should then be two, leading to the estimation of at least twelve modes (in which spurious modes are present). Each increasing value of p will then add six modes in the identification process and the number of spurious modes dramatically increases with each increment of p because the number of structural modes remains the same. That fact adds another difficulty in the selection of the proper set of results. However this can be managed using some properties of the physical modes that are not shared with the spurious modes. In general, and it is also a property used in the selection of modes through the stabilization diagram, the physical modes of a dynamic structure exhibit low damping ratio's conversely to spurious modes that may take any value, even negative. A simple method explained in [9] that we also used in [10], is to look to the trajectory of each identified poles in the complex plane. The physical poles will then be selected by only keeping the ones whose their trajectory is the closer to the unit circle. This may give a good selection of the physical modes but in our case, we also have additional information about the time-varying modes. Because multivariate models are used, the identification of the mode shapes is also performed and the latter can also bring information about the

Fig. 24.3 Illustration of the time varying behaviour of the system. (**a**) Time varying position of the mass. The *dashed lines* show the selected time span for the identification; (**b**) wavelet transform of the third response sensor. The *dashed lines* represent the eigenfrequencies of the beam subsystem
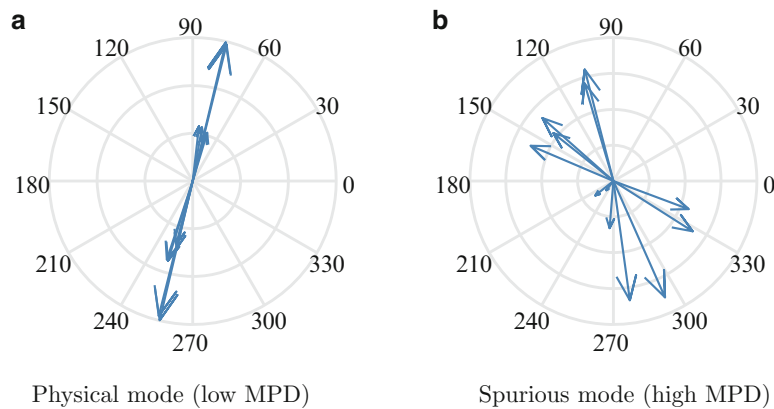
Fig. 24.4 Illustration of the mode phase dispersion in the complex plane. (**a**) and (**b**) represent mode shapes taken at $t = 4$ s. (**a**) is a physical mode at a frequency of 84.79 Hz and (**b**) is classified as a spurious one. Its frequency is 65.71 Hz

physical or spurious behaviour of any mode at any time. It is known that even if they are complex, physical mode shapes are aligned in the complex plane (each of their component are close to be in phase or antiphase with each other) conversely to spurious modes that have a more random dispersion of their components. This information can be used to select the physical modes using the Mode Phase Discrepancy (MPD) criterion that measure the spread of the components of the modes in the complex plane (Fig. 24.4).

To build our set of time-varying modal parameters, we have to compute the eigenvalue decomposition of the companion matrix for preselected time instants. Because the basis functions coefficients are calculated the results (eigenvalues/eigenvector) may be obtained for any time, not necessarily a sampled time step in the data. The eigenvalues and mode shapes are then calculated for closely spaced time instants and the mode tracking between two time instants is performed by the Modal Assurance Criterion (MAC). Once each mode trajectory is computed, their related MPD values are calculated and a preselected number of modes are retained by selecting the mode trajectories having the lowest average MPD values.

Unfortunately, there is no model (p, q, r_A, r_B) that is able to identify all the modes properly. Especially, the first mode at the lowest frequency is the most difficult to identify even if it looks not vary a lot. To perform the full identification, several models are used and the best occurrence with respect to its best average MPD value of each mode in each model is retained. This operation can be compared to the picking of modes in several model orders in stabilization diagrams.

Once this last step is performed, we obtain the result shown in Fig. 24.5.

Because a written format is not suitable to show time-varying results, let us use as example a single mode at few time instants to illustrate the identification of the time-varying mode shapes. Let us look at the sixth mode (close to 100 Hz) at five time samples corresponding to some positions of the mass close to nodes or antinodes of the sixth mode shape. It is clearly
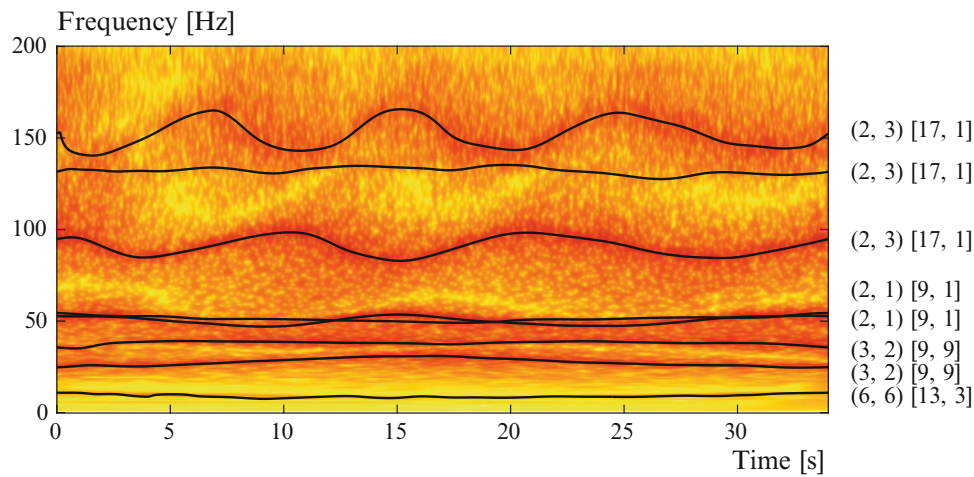
Fig. 24.5 Final set of results. Each mode comes from a TV-ARMAV model (p, q) $[r_A, r_B]$
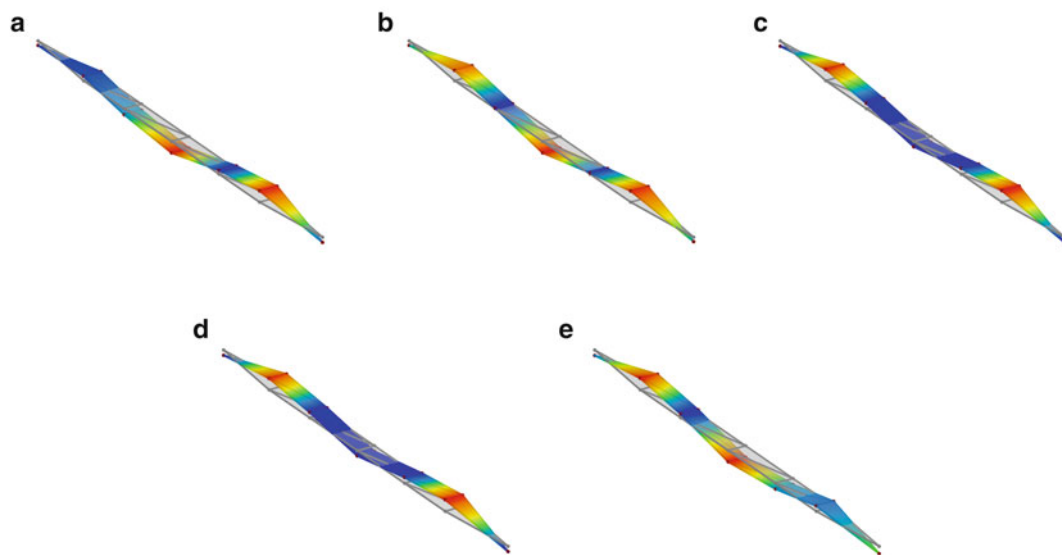
Fig. 24.6 Time-varying shape of the sixth mode at particular time spots. (**a**) Time: $t = 5$ s; (**b**) time: $t = 10$ s; (**c**) time: $t = 15$ s; (**d**) time: $t = 20$ s; (**e**) time: $t = 30$ s

visible that when the mass is located at antinodes of vibration, its amplitude decreases with respect to the other two antinodes (Fig. 24.6a, c, e). Conversely, Fig. 24.6b, d show that this mode shape is no more perturbed when the mass lies at nodes of vibration and then does not add additional inertia force on that particular mode.

24.5 Conclusion

All along this paper, a method able to perform the modal identification of time-varying systems was presented. The combination of a multivariate model and an expansion of its parameters on a set of basis functions lead to the estimation of all the modal parameters (poles and modes) with their time dependence. The results obtained with that method are in good accordance with the expected behaviour of the test structure. Because only the mass is modified in a positive manner the additional inertia forces cause the eigenfrequencies to decrease more or less depending where the mass is located. The examination of the time-varying mode shapes shows the same relation.

The selection of the final set of the modal trajectories using the MPD criteria seems to perform well even if the number of spurious modes increases.

References

1. Marchesiello, S., Bedaoui, S., Garibaldi, L., Argoul, P.: Time-dependent identification of a bridge-like structure with crossing loads. Mech. Syst. Signal Process. **23**(6), 2019–2028 (2009)
2. Niedzwiecki, M.: Identification of Time-Varying Processes. Wiley, New York (2000)
3. Spiridonakos, M., Poulimenos, A.G., Fassois, S.: Output-only identification and dynamic analysis of time-varying mechanical structures under random excitation: a comparative assessment of parametric methods. J. Sound Vib. **329**(7), 768–785 (2010)
4. Spiridonakos, M., Fassois, S.: Non-stationary random vibration modelling and analysis via functional series time-dependent ARMA (FS-TARMA) models - a critical survey. Mech. Syst. Signal Process. **47**(1–2), 1–50 (2013)
5. Andersen, P., Brincker, R., Kirkegaard, P. H.: Theory of covariance equivalent ARMAV models of civil engineering structures. In: IMAC XIV - 14th International Modal Analysis Conference, vol. 71 (1995)
6. Andersen, P.: Identification of civil engineering structures using vector ARMA models. Ph.D. thesis (1997)
7. Ljung, L.: System Identification: Theory for the User. Prentice Hall PTR, Upper Saddle River, NJ, USA (1999)
8. Peeters, B., Van der Auweraer, H.: PolyMAX: a revolution in operational modal analysis. In: 1st International Operational Modal Analysis Conference, Copenhagen (2005)
9. Beex, A., Shan, P.: A time-varying Prony method for instantaneous frequency estimation at low SNR. In: Proceedings of the 1999 IEEE International Symposium on Circuits and Systems VLSI (Cat. No.99CH36349) ISCAS'99, vol. 3, pp. 5–8 (1999)
10. Bertha, M., Golinval, J.-C.: Modal identification of time-varying systems using Hilbert transform and signal decomposition. In: Proceedings of the International Conference on Noise and Vibration Engineering, ISMA 2014, Leuven, pp. 2409–2419 (2014)

Chapter 25
Optimal Parameter Identification for Model Correlation Using Model Reduction Methods

Austin Phoenix, Dustin Bales, Rodrigo Sarlo, Thanh Pham, and Pablo A. Tarazaga

Abstract Classically, to achieve correlation between a dynamic test and a Finite Element Model (FEM), an experienced engineer chooses a small subset of input parameters and uses a model updating technique or engineering judgment to update the parameters until the error between the FEM and the test article is acceptable. To reduce the intricacy and difficulty of model correlation, model reduction methods such as the Discrete Empirical Interpolation Method (DEIM), and *dime* are implemented to reduce the scale of the problem by reducing the number of FEM parameters to its most critical ones. These model reduction methods serve to identify the critical parameters required to develop an accurate model with reduced engineering effort and computational resources. The insight gained using these methods is critical to develop an optimal, reduced parameter set that provides high correlation with minimal iterative costs. This can be seen as a particular approach to sensitivity analysis in the model updating community. The parameter set rankings derived from each method are evaluated by correlating each parameter set on five simulated test geometries. The methodology presented highlights the most valuable parameters for correlation, enabling a straightforward and computationally efficient model correlation approach.

25.1 Introduction

In an attempt to provide highly precise and representative FEMs, a correlation methodology using model reduction techniques and an iterative FEM is discussed. Classically, correlation is achieved by an experienced engineer using their judgment to iteratively modify input parameters of perceived importance. This is done until the error between the FEM and the test article is reduced and correlation is achieved. In the past few decades, many improvements have been made in model updating [1–8] in order to automate the updating process, enabling accurate correlations that were impossible to achieve previously. Parameter investigation using sensitivity methods [5–7] and methods that provide a raking of parameter importance using projection coefficient [7, 8] have been well documented. These methods provide insight into the parameters of importance however, this paper aims to investigate a novel approach with the use of reduction methods such as DEIM and *dime* (also referred to in literature as Q-DEIM) for parametric sensitivity analysis. These evaluations rank the parameters by their independence to allow for the correlation to be evaluated at an optimal number of reduced parameters that yield the greatest impact. This paper will discuss the resulting quality of the reduced parameter set as a function of the number of parameters correlated in order to define the best method for identifying critical correlation parameters.

This paper details a method to identify the parameters that have the largest impact on the dynamics of the system, and therefore should be the parameters that are correlated first. This paper details a method to define an optimal parameter list that can then be used in a model updating algorithm or other correlation method. This paper details new methods to identify the critical structural parameters required to generate a correlated model and provides insight into the parameters that can safely be ignored so that the subsequent efforts at correlation are more productive. To detail the method an introduction of the FEM model, as well as the model parameters, and error bounds associated with the geometry of interest is performed. The modeling reduction methods, SVD-DEIM, and *dime* are briefly referenced to give the reader an understanding of the different approaches. The key aspect provided herein is the identification of the number of parameters required via a SingularValue

---

A. Phoenix (✉) • T. Pham
United States Naval Research Lab, Naval Center For Space Technology, Washington, DC, USA
e-mail: aphoenix@vt.edu

D. Bales • R. Sarlo • P.A. Tarazaga
Virginia Tech, Vibrations, Adaptive Structures, and Testing Lab, 310 Goodwin Hall, Blacksburg, VA 24060, USA

Decomposition (SVD) analysis. The resulting parameter ranking development is discussed as a consequence of the SVD analysis. The resulting correlation is shown for each of the parameter reduction methods to provide a quantitative comparison of the methods. Finally, conclusions and future work are proposed.

25.2   Geometry and the Modeling Methods

The article chosen on which to perform this study is comprised of two identical 'L' shaped brackets with a length of 11.5 in. each. The full structure is joined together using a single bolt, resulting in an overall jointed beam of length equal to 23 in. The baseline article can be seen in Fig. 25.1a. The two "L" brackets are joined with a bolt, oriented in the X-direction (along the length of the beam), resulting in an unknown joint stiffness. The FEM is built to consider multiple configurations of joint stiffness as seen in Fig. 25.1b and c, where the joint stiffness is unknown. This article provides a structure representative of hard to model and validate parameters (joints) which can be modeled in a variety of methods. The approach proposed herein will develop a parameter ranking which is sensitive to these conditions and could lead to the accurate correlation of all three configurations.

This beam is modeled using a FE approach, and reasonable error bounds on the parameters have been developed to provide a design space to investigate the proposed approach. A detailed schematic of the test setup can be seen in Fig. 25.2. The parameters of interest chosen for this beam, shown in Fig. 25.3, are the six joint stiffness parameters, the system damping, local joint mass for the −X and +X side respectively, as well as the thickness, width, Young's Modulus, and density for the −X bracket and the +X bracket, respectively. These parameters do not encompass all potential FEM inputs, but provide a reasonable parameter set for this investigation. The Y-axis excitation is set 2.7 in. from the −X end of the structure. The system is excited with a random vibration loading of 1.25×10^{-4} g^2/Hz amplitude. The frequency of excitation is applied from 20 to 2000 Hz.

For this model three nodes are chosen in order to investigates the models sensitivity to parameter changes. Node 1 located at the −X edge, Node 27 at the joint location, and Node 53 at the +X end of the structure are selected. Each of the nodes in Fig. 25.2 is evaluated to obtain individual FRFs and understand the resulting dynamic response differences due to the parameter variations. These three locations were chosen to provide different optimal parameters, as would be expected in a real application where competing correlation constraints exist.

In the development of any FEM, there are parameter values that have uncertainties relative to the expected values obtained from the manufacturer (i.e., density) or provided by assembly itself (i.e., damping). For example damping is a value that can exhibit large changes due to assembly practices and density can only be known to a nominal value within a standard deviation usually provided by the manufacturer. Thus, these parameters provide a set of variables that can be updated in order to better correlate models to test results. This paper leverages this fact to develop a method that identifies the parameters that have the
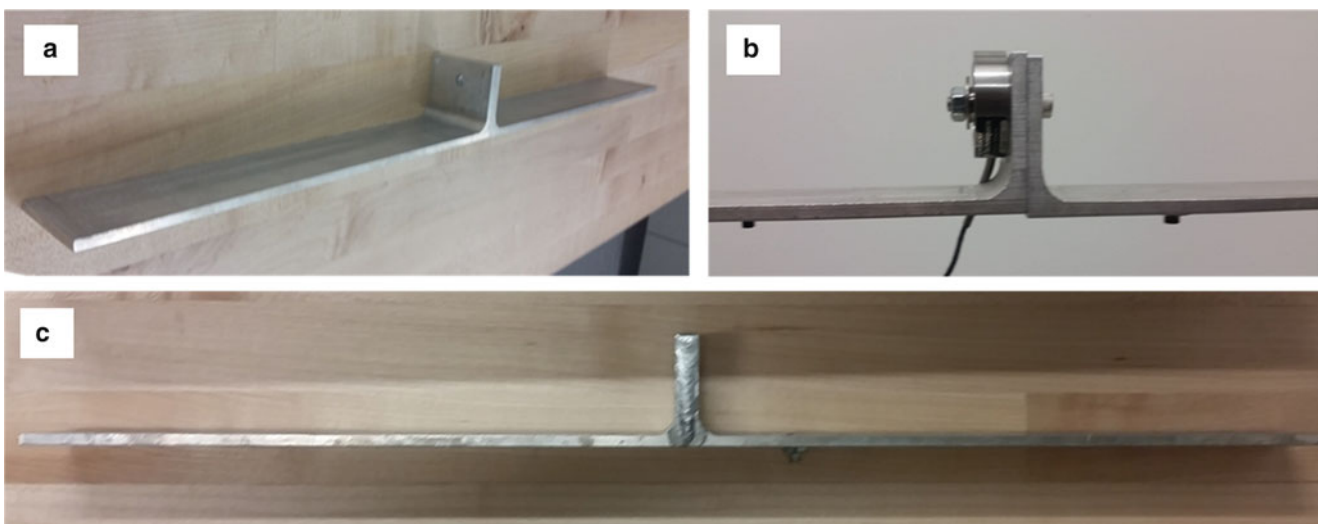
Fig. 25.1 (**a**) Test article is composed of two "L" shaped beams connected in the middle with a single bolt (bolt not shown), (**b**) Test specimen with a load cell, (**c**) Test Specimen with a welded joint
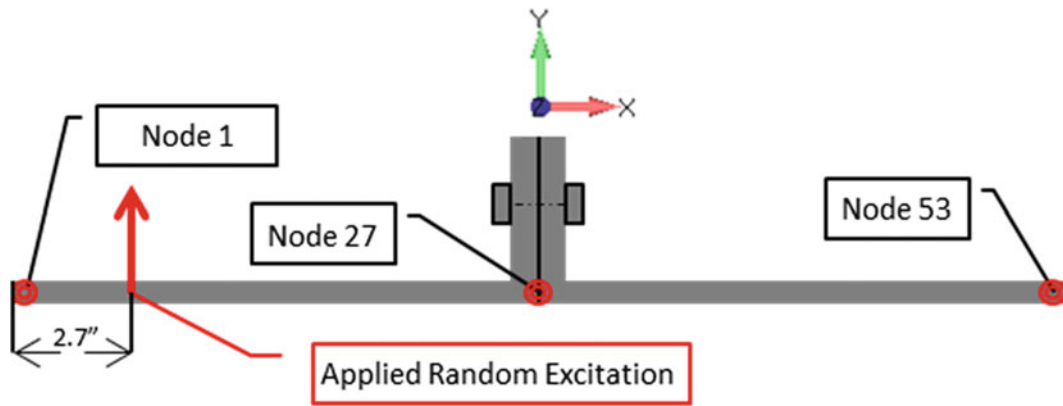
Fig. 25.2 Illustration of the nodes of interest and the geometry with the applied load
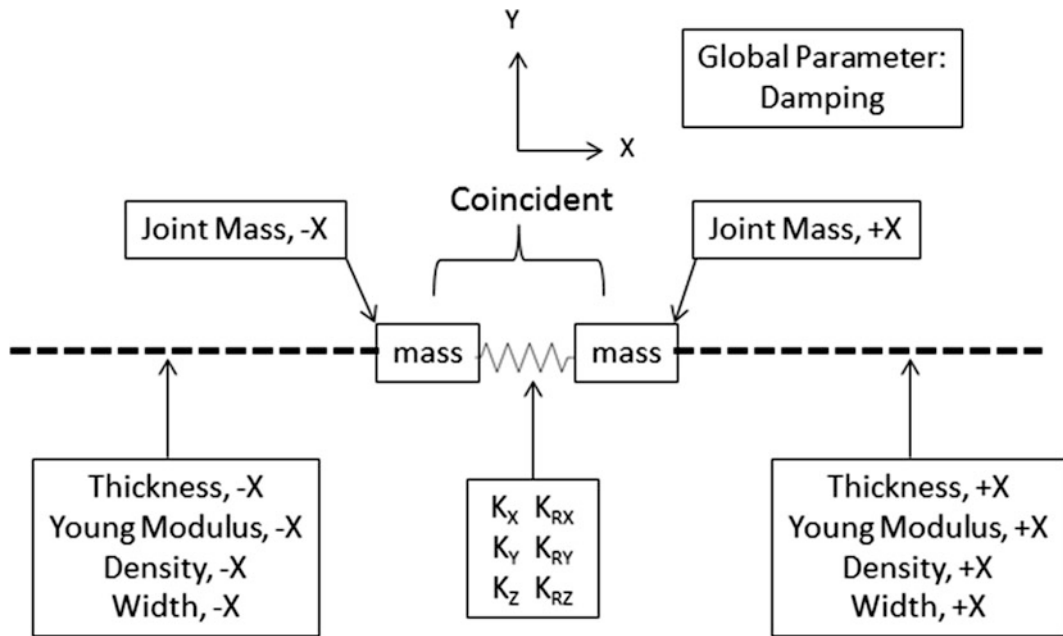
Fig. 25.3 Parameters under investigation and the location applied

largest impact on the dynamics of the system, and therefore should be the parameters that are correlated first. The key inputs from the user for this calculation are the structural parameters of interest (e.g., E, ρ, width, thickness etc.) and a reasonable error bound for those parameters. For this case, 17 parameters are used to define the system, as shown in Fig. 25.3, and the resulting error bound applied to those parameters are detailed in Table 25.1.

The jointed structure was chosen such that the estimation of several key parameters was necessary (with todays modeling capabilities monolithic components can be modeled very well). This structure is representative of a difficult to correlate part and illustrates the methodology to achieve correlation for a complex dynamic system. The error bounds are subject to manufacturing tolerances, material uncertainty, and user judgment. When calculating the parameter importance, the error bounds used have a significant effect, because the algorithm evaluates the dynamic variations due to parametric changes of the size of the error bound. This can in turn be seen as an advantage of disadvantage by the user and should be used judiciously. For this case the error bound provides a reasonable case for the development of a parameter reduction methodology.

The parameters were ranked according to the expected impact they would have on the overall dynamics of the system in order to develop the engineering judgment ranking shown in Table 25.1. This list is a good representation of engineering judgment, but by no means definitive. The resulting engineering judgement ranking is going to vary between different engineers, demonstrating a key problem with engineering judgment rankings. The range of engineering judgement and its quality as a function of experience needs to be further investigated but will be used here as a baseline comparison against the automated methods proposed.

Table 25.1 Parameter list ranked by expected importance with error bounds

Parameters	Engineering judgment order	Initial param.	Units	Error bound (%)
Damping (Q)	1	2.00E−02	in/in	50.00
+X Thickness	2	1.90E−01	in	5.00
K_{RZ}	3	1.00E+04	lbf/rad	20.00
K_Y	4	1.00E+04	lbf/in	20.00
−X Thickness	5	1.90E−01	in	5.00
+X Youngs	6	9.90E+06	psi	2.50
+X Density	7	2.54E−04	lb/in^3	2.50
−X Youngs	8	9.90E+06	psi	2.50
−X Density	9	2.54E−04	lb/in^3	2.50
+X Width	10	2.01E+00	in	5.00
K_Z	11	1.00E+04	lbf/in	20.00
K_{RY}	12	1.00E+04	lbf/rad	20.00
+X Mass	13	1.99E−04	lb	10.00
−X Mass	14	1.99E−04	lb	10.00
−X Width	15	2.01E+00	in	5.00
K_X	16	1.00E+04	lbf/in	20.00
K_{RX}	17	1.00E+04	lbf/rad	20.00

The FEM used to evaluate the system, shown in Fig. 25.3, is developed in MSC Nastran using SOL 111 for random vibration excitation from 20 to 2000 Hz in the Y-axis. The model uses 50 linear beam elements, a six degrees-of-freedom (DOF) spring element to model the joint stiffness, and two mass elements to represent the un-modeled mass of the joint (short leg of 'L' and connector), resulting in a FEM consisting of 53 nodes and 265 DOF. The mass elements used to represent the un-modeled mass are connected using a six DOF spring element with a base stiffness of 1×10^4 lbf/in. The frequency response function is recovered for Node 1, 27 and 53 for all six degrees of freedom.

To use the model reduction methods a matrix of responses (i.e., FRFs) with variations in parameter values is required to determine the parameter rank. The first step in the development of this sensitivity matrix is the generation of the sensitivity input matrix S_{input}. The sensitivity matrix is set up to evaluate the dynamic impact caused by individual parameter variations. Specifically the variations applied to generate the sensitivity input matrix are the error bounds e_i detailed earlier. The first row of the sensitivity input matrix is filled with the nominal parameter input values. The second row contains the nominal parameter input values with a reduction in the first parameter P_1 by the associated first parameter error bound e_1. The third row contains the nominal parameter input values with the second parameter P_2 reduced by the associated second parameter error bound e_2. This method is detailed by

$$S_{input} (1 : 18, :) = [P_1, P_2, \ldots, P_{17}] \quad and \ for \ i = 1 : 17 \ S_{input} (i + 1, i) = P_i (1 - e_i). \tag{25.1}$$

The visualization of the resulting difference between the parameter values in the sensitivity matrix and the nominal parameter values is shown in Fig. 25.4a and b. The plot shows the location and the absolute magnitude of the changed parameters used to develop the sensitivity matrix.

This sensitivity input matrix is used as the input parameters for the 18 FEM's developed for the parameter ranking effort. The resulting 18 FEM's outputs, for each node response, is reformatted into a $\mathbb{R}^{18 \times 1181}$ matrix S where the 1181 dimension is the frequency response function evaluated at 1181 frequencies creating the sensitivity matrix. The sensitivity matrix is used as the input for the model reduction efforts.

To better illustrate the method presented in this paper the steps to development of the correlated model are show in Fig. 25.5. The first step is to identify the parameters in the FEM that are to be investigated for correlation and identify reasonable error bounds for those parameters. The sensitivity input matrix enables the dynamic impact of each parameter to be evaluated independently by developing 18 FEM input parameter sets. These input parameter sets are designed so that each parameter can be evaluated independently. The outputs from the FEM are used to develop the sensitivity matrix S. The model reduction methods are performed on the sensitivity matrix to generate the parameter ranking. The SVD analysis is then used to determine the number of parameters to be used for an initial correlation attempt.

The sensitivity output provided by the model reduction methods are then compared by investigating five analytical test geometries that represent potential 'real' geometries. The 'real' geometries are developed using parameters that are randomly distributed within the given error bounds and could be assumed not known. This is done to simulate potential test results
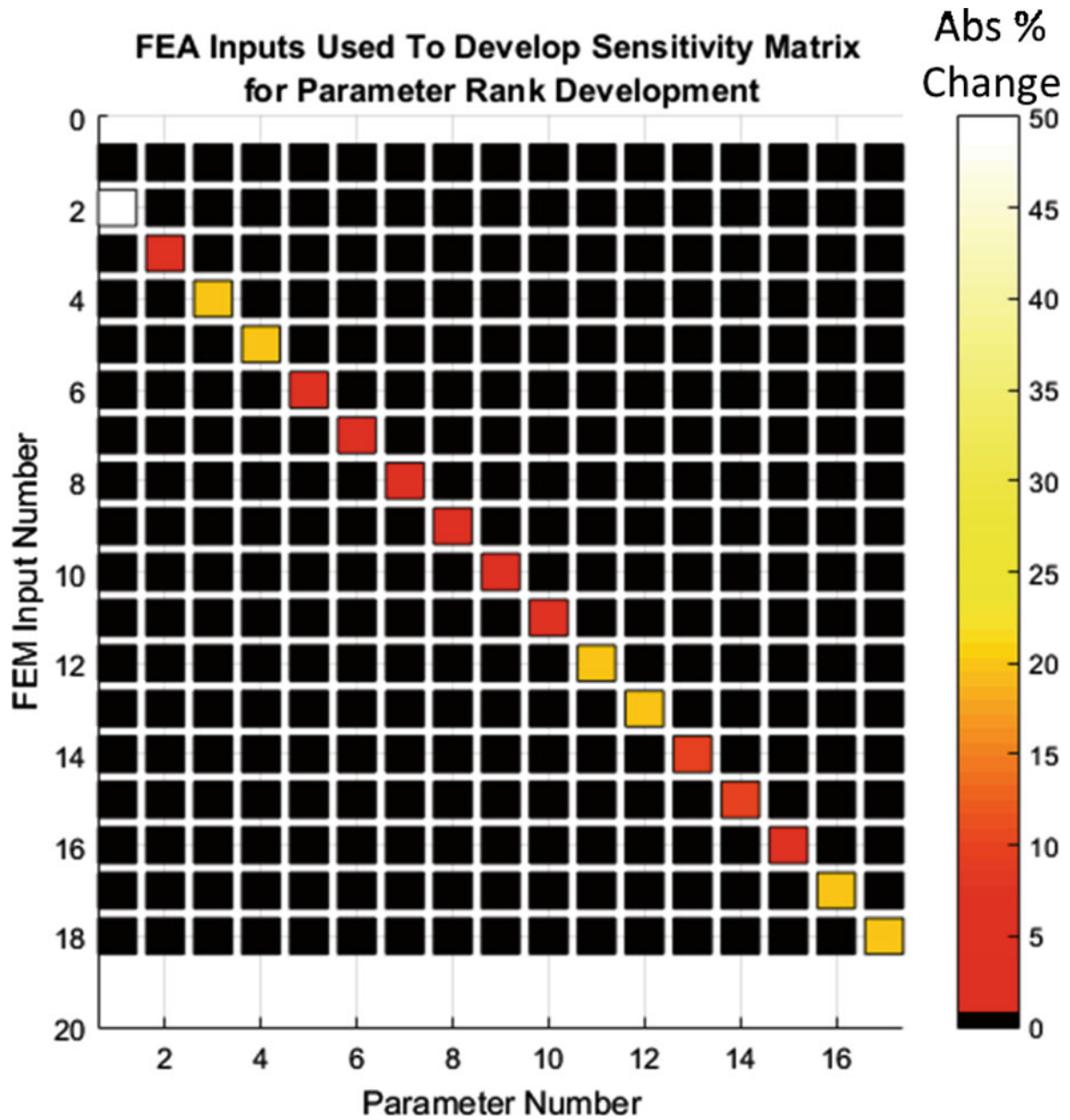
Fig. 25.4 Variations in input parameters for sensitivity matrix relative to baseline values

of real structure in order to validate the methodology without carrying out actual tests. The effectiveness of the sensitivity ranking, provided by the reduction methods, is evaluated by accurately setting the unknown parameters in the order specified by the ranking results of each method. Note that this is not a model updating scheme, but a sensitivity scheme and it is not the goal of the paper to evaluate a model updating method, but to understand which parameters need to be weighted with more importance. Normally to correlate these models a model updating scheme or using engineering judgment and iteration, is adopted to find the 'real' values. In this case, the correlated parameter values are known, thus parameter values are simply set to the correct value in the ranking order specified by each technique. The correlation is then checked and if needed, more parameters are updated.
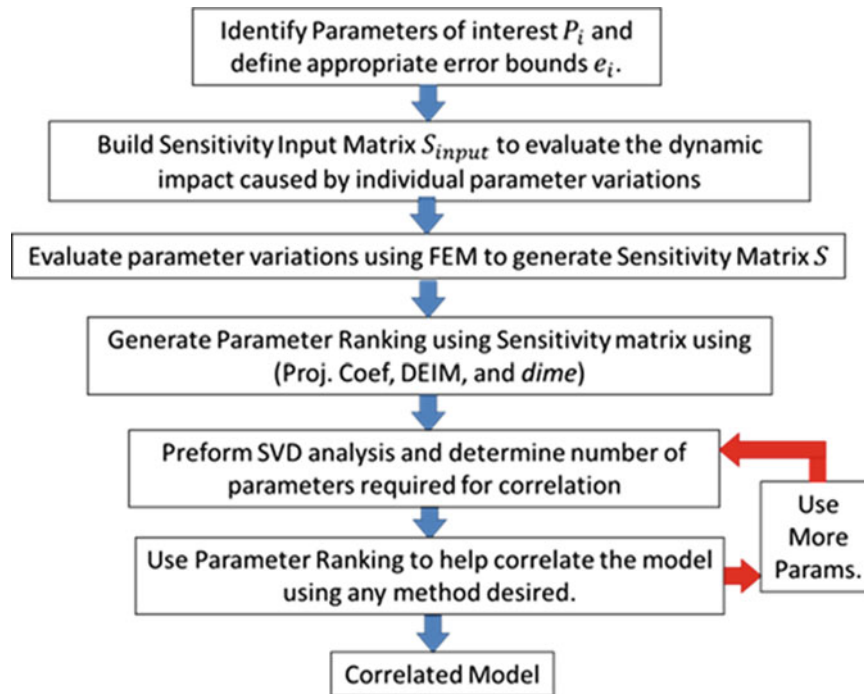
Fig. 25.5 Methodology for correlation

25.3 Model Reduction Methods

To determine the optimal method for identifying the critical parameters, classic methods such as a projection coefficient and engineering judgement are compared to two new model reduction methods known as DEIM and *dime*. The input for the projection coefficient, DEIM, and *dime* evaluations is the sensitivity matrix S developed using the FEM. The sensitivity matrix consists of 18 FEM output results for the nominal geometry and for seventeen models with one of the 17 parameters reduced by the maximum allowable amount dictated by the error bounds. This matrix is used to develop the SVD DEIM, *dime*, and projection coefficient rankings. These methods use the frequency response functions for all 18 runs to identify the critical parameters by evaluating the dynamic changes between the nominal geometry and the other parameter evaluation runs. To better understand the differences between these methods a brief discussion detailing each method is provided.

25.3.1 SVD DEIM

DEIM was proposed by Chaturantabut and Sorensen in [9] for use in the reduction of dynamical systems. Sorensen and Embree in [4] used a database search as an example similar to the proposed use in this work to find representative webpages from two geographic areas. The methodology in this work uses a SVD of the acceleration output of the parameter sweep and then a greedy search algorithm DEIM.

DEIM is an efficient method to project high dimensional, non-linear functions into a lower dimensional space for the purpose of data reduction [9]. The DEIM algorithm (found in [9]) iteratively minimizes the error of the approximation or projection onto a lower dimensional space via a selected index. The first entry is chosen by determining the index of the largest magnitude of the left eigenvector. Other entries are chosen by selecting the index associated with the largest residual error. The residual is effectively the error between the input basis and its approximation due to interpolating the basis. The SVD-DEIM methodology allows for the determination of the most independent parameters for every trial.

25.3.2   Projection Coefficient

The projection coefficient method is often used in the dynamics modeling field to determine the degree in which an experimental and analytical mode shape match. Perinpanayagam and Ewins and Chen [10, 11] show examples of using such formulation in substructural testing. This is proposed in order to determine the most relevant modes to test of the subcomponents toward the importance and relevance of the assembled structure condition. The formulation of the projection coefficients requires examining the angle between the original singular vectors (in this case, the acceleration with one parameter set to its maximum error value) and the left eigenvectors produced by the SVD.

The coefficient is calculated as the cosine of the angle between two vectors (in this case a single left eigenvector and a single vector of the sensitivity matrix). Seen in the following equation as,

$$Projection\ Coefficient = PC = \cos(\theta) = \frac{a \cdot b}{|a|\,|b|}, \tag{25.2}$$

where θ is the angle between the two vectors, a is the left eigenvector, and b is the original data vector. The coefficient varies between 1 and 0, where 1 represents a high degree of alignment of the two vectors and 0 represents orthogonality between them.

Understanding how the first left eigenvector relates to the original data, allows for an investigation of which parameters are most independent. A seemingly arbitrary selection of the first eigenvector is justified by the previously mentioned singular value decay. For this investigation, the first singular value accounts for an average of 63 % of the sum of all singular values. The first eigenvector is chosen as it represents the largest amount of the original data set, while enabling the data to be reduced to a single vector (for the purposes of angle of alignment comparison).

25.3.3   dime

The *dime* method, which is an alternate formulation of the DEIM, was developed using a QR matrix factorization for the purpose of large scale systems. Previous applications of this methodology are found in [12], where various dynamic systems are reduced as examples for comparison to the DEIM method. The *dime* method offers an improved theoretical bound on the error of the projection on a lower dimensional space compared to DEIM [12].

As stated earlier, the formulation of this method is through the QR factorization of the sensitivity matrix. The QR transformation, further explained in [13], is the factorization of a matrix, S (in our case), into the form:

$$S = QR, \tag{25.3}$$

where Q is an orthogonal matrix and R is an upper triangular matrix. The algorithm for *dime* can be found in [12, 14].

The output of these methods- projection coefficients, DEIM, and *dime* is a ranking of the 17 parameters from most independent to most redundant. The orderings of parameters were tested against the engineering judgement ranking (Table 25.1) to show the variations between each ranking process.

25.4   Parameter Ranking

Four methods were used to generate a parameter priority list, the two model reduction methods described previously, the projection coefficient approach and engineering judgment. The resulting sensitivity matrix S is used for as the basis for the reduction methods and the SVD analysis [15]. This analysis is evaluated at all three nodes of interest. The singular value decay for the nominal geometry is seen in Fig. 25.4.

By investigating the SVD results, the number of critical parameters that exist for this system can be surmised. The SVD provides a weighted analysis of which are the more sensitive parameters, as can be seen in Fig. 25.6. The SVD analysis indicates that the majority of the 17 parameters analyzed are required to achieve correlation for Node 27 and 53. There is no immediate 'drop off' in singular values until most of the parameters are included. For Node 1, the singular value reduces significantly after six parameters as is expected noting little dynamic change is expected due to changes in parameters of the +X bracket. This indicates that to correlate Node 1 six parameters should be used to maximize efficiency. For Node 53
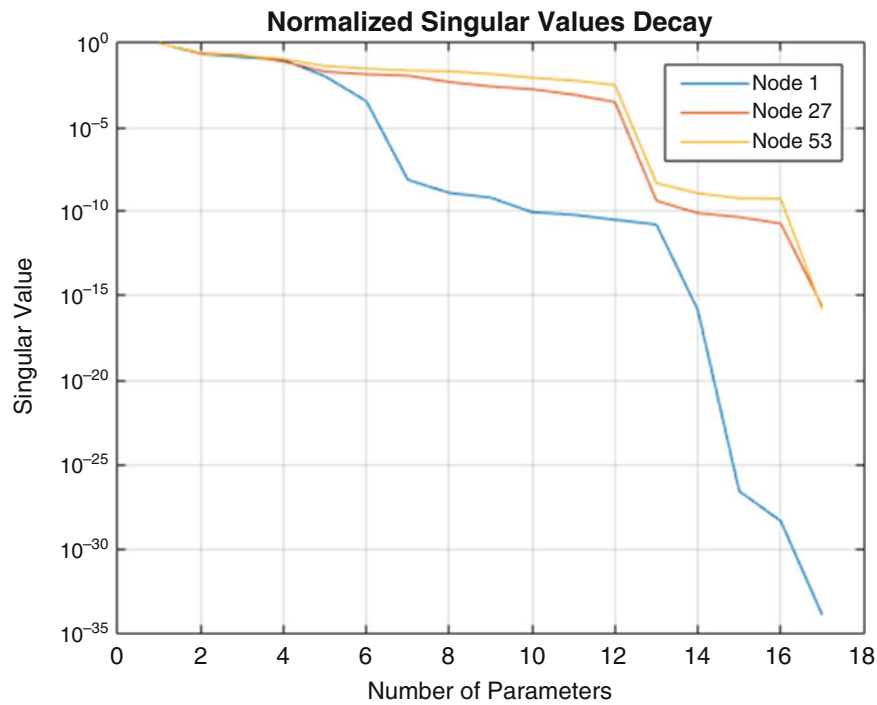
Fig. 25.6 SVD for the three nodes of interest

it can be stated that 12 parameters should be used to more effectively correlate the model, but an investigation needs to be done into the correlation of the model as a function of the number of parameters. Note that the number of parameters does not guarantee correlation but provides the most relevant parameters. If effort in matching the models is an issue for a given number of parameters, focus should be directed at the parameters that represent the higher singular values.

By running this sweep on the sensitivity matrix and developing a parameter ranked order for the projection coefficients, *dime*, and DEIM methods, we now have a basis to compare the ranking using engineering judgment. While all three nodes are evaluated, only the ranking developed for Node 53 is used for comparison in the model correlation for simplicity.

As can be seen in Table 25.2, the resulting parameter ranks vary based on the method used, but most importantly, the results vary significantly when compared to the engineering judgement case. As expected from the SVD analysis, the ranking for Node 27 and Node 53 are in strong agreement with minor variations. DEIM and *dime* are shown to produce comparable rankings due to their similar methodology. For the projection coefficients analysis, there are significant variations in the importance of the resulting parameters compared to *dime* and DEIM. To compare the resulting effectiveness of the parameter rankings, the resulting correlated accuracy needs to be computed. The correlation attempt is done using 1 through 17 correlated parameters to determine the optimal method of identifying critical parameters.

To visualize these results, all nodes with normalized rank are plotted in Fig. 25.7a and the average normalized rank for all three nodes is plotted in Fig. 25.7b. It is important to note that if the engineering judgement aligned perfectly with the other methods, the rank would linearly reduce as the parameter number increases. These plots provide insight into the variations in the methods evaluated. To credit these rankings, some type of correlation using these parameter lists needs to be completed.

25.5 Parameter Ranking Evaluation Through Test Geometry Correlation

Five test geometries are built using a nominal geometry as a reference. The test geometries are altered by applying a randomized scale factor, between -1 and 1, multiplied by the error bound and added to the nominal parameter value to achieve a representative geometry within the allowed error bounds. For example this can be applied to the modulus of elasticity for test article as,

$$Y_1 = Y_n + \alpha e_Y \tag{25.4}$$

Table 25.2 Parameter rank variations for engineering judgment, projection coefficients, DEIM, and *dime*

Parameter name	Engineering judgement order	Projection coef. rank			DEIM rank			DIME rank		
		Node 1	Node 27	Node 53	Node 1	Node 27	Node 53	Node 1	Node 27	Node 53
Damping	1	5	5	5	1	1	1	1	1	1
+X Thickness	2	9	15	15	5	5	5	5	5	5
KRZ	3	8	8	8	9	15	15	9	15	15
KY	4	1	13	14	8	13	14	8	13	14
−X Thickness	5	15	14	13	15	8	4	15	8	4
+X Youngs	6	14	1	1	3	9	6	3	9	6
+X Density	7	17	3	4	14	4	7	14	4	8
−X Youngs	8	2	7	7	4	3	8	4	3	7
−X Density	9	10	9	3	6	6	9	6	14	9
+X Width	10	11	4	6	7	14	13	7	6	13
KZ	11	12	6	9	10	7	3	11	7	3
KRY	12	16	11	2	13	17	11	13	17	11
+X Mass	13	13	2	10	17	11	16	17	11	16
−X Mass	14	6	10	12	2	12	10	10	12	2
−X Width	15	3	12	16	12	10	12	2	2	17
KX	16	7	17	17	16	16	17	16	16	12
KRX	17	4	16	11	11	2	2	12	10	10
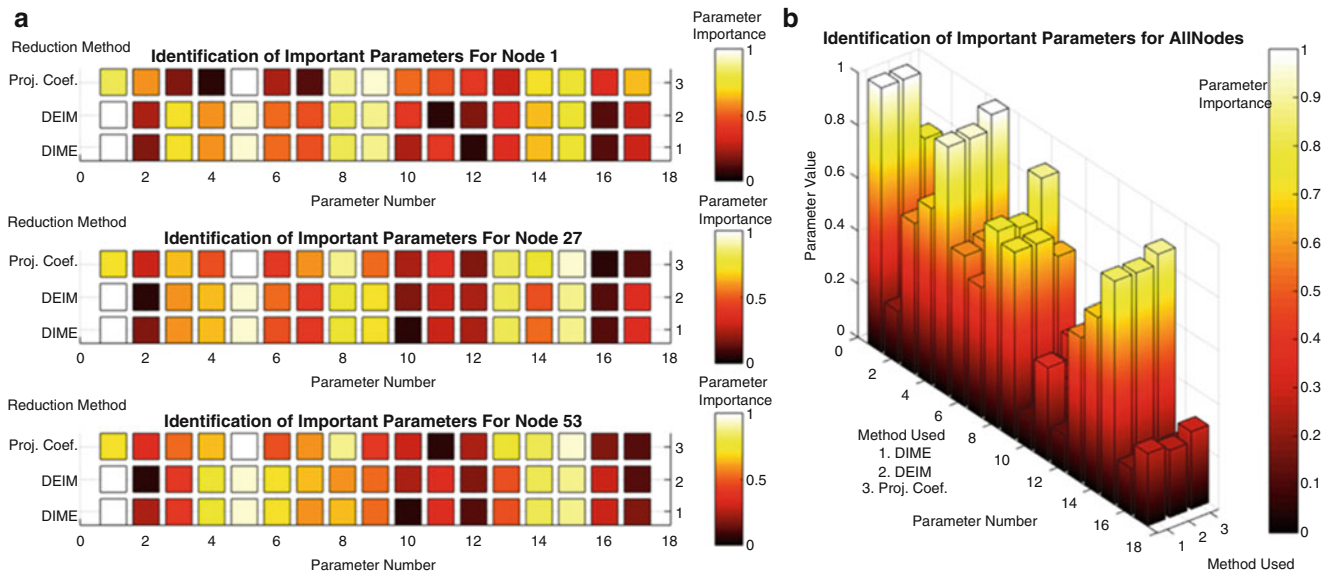
Fig. 25.7 (**a**) Parameter importance compared to engineering judgement. (**b**) Average parameter importance for all parameters and methods

where Y_n is the nominal modulus of elasticity, α is the randomized scale factor, e_Y is the error bound for the Young's modulus and Y_1 is the new randomized Young's modulus for the 1st geometry. This is extended to all parameters for each test geometry. This produces five geometries, detailed in Table 25.3, that represent a potential geometry that is built within the error bounds set for this system. To simplify the correlation attempt, the parameter lists developed for Node 1 and Node 27 were ignored and the parameter list for Node 53 was used to compare the resulting correlation developed from each method. Node 53 was used as it was determined to be slightly more independent than Node 27 as shown in Fig. 25.6. An increased number of geometries as well as nodes could be evaluated in future work to show robustness of this method.

These five test geometries were then modeled in the FEM code, and the frequency response function was calculated for the three nodes. To evaluate the methodology in this paper, the parameter rankings for engineering judgment, projection coefficient, *dime*, and DEIM, for Node 53 are applied in order and used to quantify the correlation capability of each method. A sensitivity matrix S is calculated and the rankings are calculated for each case following the method described in the previous sections.

Table 25.3 Test geometries and the applied FEM parameters

Parameters	Initial param.	Geom 1 (%)	Geom 2 (%)	Geom 3 (%)	Geom 4 (%)	Geom 5 (%)
Damping	2.00E−02	14.83	−33.08	−8.53	−4.97	−41.72
+X Thickness	1.90E−01	3.58	0.78	−4.16	−2.92	−4.59
KRZ	1.00E+04	−18.37	−1.89	14.46	14.03	9.70
KY	1.00E+04	0.41	2.18	−5.85	−8.37	−10.19
−X Thickness	1.90E−01	4.02	2.22	−0.47	−4.58	−4.65
+X Youngs	9.90E+06	−0.78	2.32	−1.75	−2.17	−0.89
+X Density	2.54E−04	−1.29	−1.22	0.54	−0.78	1.64
−X Youngs	9.90E+06	−1.03	2.34	1.12	2.27	2.01
−X Density	2.54E−04	−1.62	−0.97	0.91	−2.25	2.33
+X Width	2.01E+00	3.42	−4.71	−4.57	0.15	−3.00
KZ	1.00E+04	8.96	−7.19	−6.20	13.50	15.24
KRY	1.00E+04	−10.05	9.80	−0.24	−7.96	−15.64
+X Mass	1.99E−04	3.00	6.07	4.98	−2.32	0.53
−X Mass	1.99E−04	−6.82	4.91	−6.29	5.13	−8.59
−X Width	2.01E+00	−3.15	−4.06	3.73	−4.13	−1.32
KX	1.00E+04	2.45	4.74	−10.62	−11.81	12.53
KRX	1.00E+04	0.07	−18.39	6.38	−3.41	11.05
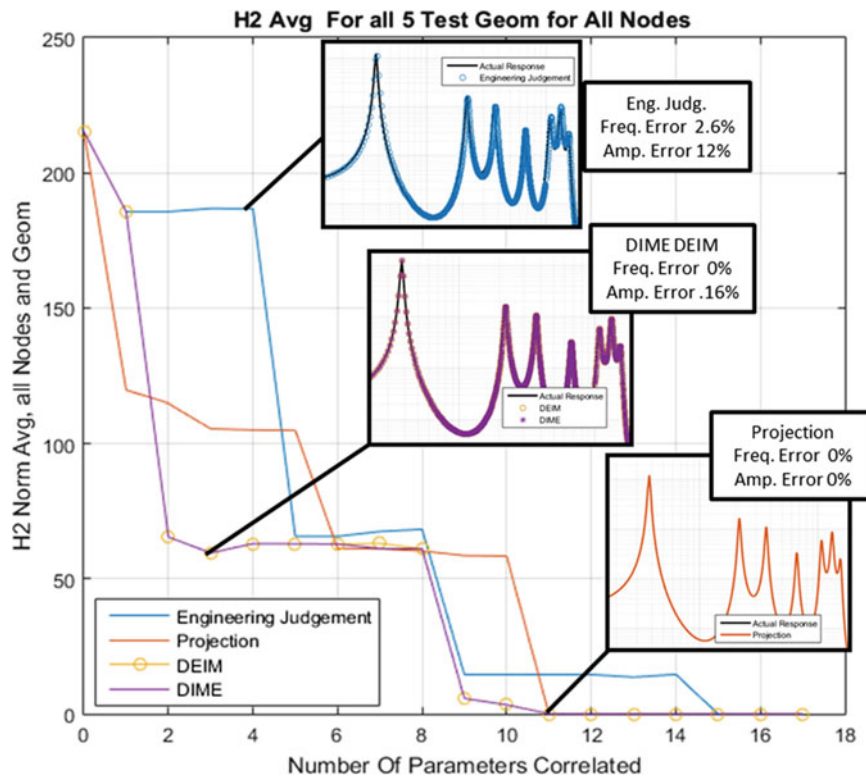
Fig. 25.8 Average correlation for all nodes evaluated at H_2 norm with representative FRF responses corresponding to the H_2 norm error

For the n parameter evaluation a model is generated for the engineering judgment, projection coefficient, *dime*, and DEIM methods. Each model exactly correlates the top n parameters defined by its assigned ranking method and a correlation is evaluated relative to the 'real' geometry. This is done for each of the five geometries and the resulting H_2 norm error is then averaged to provide one metric to compare the correlation capability. The results of the parametric sweep and the resulting peak response study can be seen in Fig. 25.8.

While the H_2 norm is not a perfect representation of the quality of the resulting model it provides a method to determine the total error between the two frequency response functions so that the resulting correlation can be evaluated. To better

compare the quantitative H_2 norm with more classical methods, Fig. 25.8 shows the frequency response function for test geometry 2 compared to the correlated model for a variety of correlation methods and parameter numbers. As shown, the frequency predictions are good for all conditions, but the amplitude error for engineering judgement with four parameters correlated is not sufficient to provide a correlated model.

The resulting parameter correlation sweep shows that overall, DEIM and *dime* produce better correlation than the projection coefficient and all methods improve on engineering judgment. Even with simple test hardware simulation, the appropriate parameters of interest are not obvious without further investigation or knowledge about the system. To better quantify the correlation associated with the H_2 norm value, the first frequency peak and frequency error is evaluated for test geometry 2 with 3 correlated parameters, resulting in a 0 % error in frequency and a 0.16 % error in amplitude. This shows that a cursory parameter sweep of those parameters would easily generate a correlated model that is within the classic correlation requirement of 5 % error in amplitude and frequency. This method provides the opportunity to drastically reduce the computational effort required to produce a highly correlated model by choosing the most relevant parameter to correlate first. This also immediately improves the quality of the resulting correlation, regardless of the experience level of the engineer preforming the analysis.

Overall, the projection coefficients method produces good results and does reduce the maximum error for the single point correlation. However, the *dime* and DEIM methods have been shown to produce higher correlation using fewer parameters for this system. Further work is needed to evaluate this comparison to other structures to better identify the relative robustness of the methods proposed. It would also beneficial to attempt a comparison to well established sensitivity analysis in the future.

25.6   Conclusion

The novel use of *dime* and DEIM have been shown to better determine critical parameters for correlation beyond engineering judgment and classic methods such as a projection coefficient approach. This methodology is shown to be valuable in providing insight into the model and the FEM parameters that are critical to achieve a more accurate model. This in turn reduces the computational time needed to run these correlation and time investment by the engineer. The *dime* and DEIM methods were able to choose the most critical parameters in order to achieve a correlated model faster for all five geometries with reduced computational and engineering time investment relative to the other methods. This efficiency is achieved by a significant reduction and optimization of the parameters to be chosen for model correlation. Future work will quantify that reduction by evaluating the correlation efforts relative to actual test hardware.

While the use of *dime* and DEIM have shown potential against these selected methods, further work is necessary to fully investigate its effectiveness and the robustness of these methods. To evaluate the robustness of the method, investigations into the impact of errors associated with the generation of the error bounds supplied by the engineer should be understood more fully as they can have a non-trivial effect on the methods. Comparison against more robust sensitivity analysis techniques should also be explored.

References

1. Tarazaga, P., Halevi, Y., Inman, D.: Model updating with the use of principal submatrices. In: Proceedings of the 22nd International Modal Analysis Conference. Springer, Berlin (2004)
2. Tarazaga, P.A., Halevi, Y., Inman, D.J.: Model updating using a quadratic form. In: ASME 2005 International Design Engineering Technical Conferences and Computers and Information in Engineering Conference. American Society of Mechanical Engineers. Springer, Berlin (2005)
3. Tarazaga, P., Halevi, Y., Inman, D.: The quadratic compression method for model updating and its noise filtering properties. Mech. Syst. Signal Process. **21**(1), 58–73 (2007)
4. Friswell, M., Mottershead, J.E.: Finite element model updating in structural dynamics, vol. 38. Springer, Berlin (1995)
5. Mottershead, J.E., Link, M., Friswell, M.I.: The sensitivity method in finite element model updating: a tutorial. Mech. Syst. Signal Process. **25**(7), 2275–2296 (2011)
6. Farhat, C., Hemez, F.M.: Updating finite element dynamic models using an element-by-element sensitivity methodology. AIAA J. **31**(9), 1702–1711 (1993)
7. Mayes, R.L.: Model correlation and calibration. In: Proceedings of the 27th International Modal Analysis Conference. Springer, Berlin (2009)
8. Mayes, R.L., et al.: A structural dynamics model validation example with actual hardware. In: Proceedings of the 27th International Modal Analysis Conference. Springer, Berlin (2009)

9. Chaturantabut, S., Sorensen, D.C.: Discrete empirical interpolation for nonlinear model reduction. In: Proceedings of the 48th IEEE Conference on Decision and Control, 2009 held jointly with the 2009 28th Chinese Control Conference (CDC/CCC 2009), pp. 4316–4321. IEEE Xplore, New York (2009)

10. Perinpanayagam, S., Ewins, D.J.: Test strategy for component modal test for model validation. In: Proceedings of the International Conference on Noise and Vibration Engineering (ISMA 2004) (2004)

11. Chen, G.: FE Model Validation for Structural Dynamics. University of London, Imperial College of Science, Technology and Medicine, London (2001)

12. Drmac, Z., Gugercin, S.: A new selection operator for the discrete empirical interpolation method – improved a priori error bound and extensions. Arxiv:1505.00370 [cs, math] (2015)

13. Francis, J.G.F.: The QR transformation—part 2. Comput. J. **4**, 332–345 (1962)

14. Sorensen, D.C., Embree, M.: A DEIM induced CUR factorization. Arxiv:1407.5516 [cs, math] (2014)

15. Golub, P.G.H., Reinsch, D.C.: Singular value decomposition and least squares solutions. Numer. Math. **14**, 403–420 (1970)

Chapter 26
A Modified Inverse Eigensensitivity Method for Large Finite Element Models

Doğuş Unlu, Ender Ciğeroğlu, and Gökhan O. Özgen

Abstract Finite element models should represent the dynamic behavior of real structures accurately to be subsequently used in design purposes. Therefore, finite element model updating methods have been developed in order to decrease the difference between analytical model and modal test results. In this paper, inverse eigensensitivity method as a sensitivity-based model updating method is summarized. Inverse eigensensitivity method with improved sensitivity computation which decreases the total calculation time of the updating procedure is introduced. A method based on the parameter sensitivities is integrated into the developed code in order to decrease the number of model updating parameters making it is possible to update large finite element models. Initially a simple plate structure is considered as an application. An aerospace structure is considered as an example where modal test is performed and modal parameters are extracted. The developed updating method is applied on the finite element model of the aerospace structure and the results of the updated model are compared with experimental ones.

Keywords Finite element model updating • Large order finite element models • Sensitivity based model updating • Computational model updating • Inverse eigensensitivity method

26.1 Introduction

The mass and stiffness properties of aerospace structures are needed to be extracted for aeroelastic analyses. Sensitivity of any aeroelastic analyses is directly affected by structural matrices generated from finite element model. Structural matrices must reflect the actual dynamic behavior of the real structure. Nonetheless, results of linear finite element models for structural dynamics studies almost never match with the real test results. This inconsistency arises from modeling errors and nonlinearities at the connection regions. These kinds of nonlinearities cannot be introduced into a linear finite element model. Incorrect modeling of boundary conditions is also a factor that affects the accuracy of the results between finite element and experimental results. Trial and error method can be applied to decrease the inconsistency between experimental and analytical results which is very time consuming and it is not adequate for large finite element models. To handle this problem, computational methods have been developed to update the parameters of finite element model by taking into account the experimental results as reference data. There are many model updating methods that can be used to update aerospace structures [1].

The model updating theory is divided into two groups with respect to the solution method: direct methods and iterative methods. Iterative methods use modal or response function methods in an iterative way; whereas direct methods use structural matrices [1].

Iterative methods are computationally effective and applicable to large finite element models [2]. Due to faster convergence properties, modal parameter-based methods are found to be more effective according to other iterative methods [3, 4].

Iterative methods which are modal parameter-based are based on the minimization of an objective function which can be constructed by including the weights of the eigenvalue and eigenvector differences. Forming the objective function, this

———————————————

D. Unlu
Middle East Technical University, 06800 Ankara, Turkey

Roketsan Missile Ind., 06780 Ankara, Turkey

E. Ciğeroğlu (✉) • G.O. Özgen
Middle East Technical University, 06800 Ankara, Turkey
e-mail: ender@metu.edu.tr

group of methods starts to work iteratively in order to decrease the difference between the experimental and analytical results. Large amount of parameters can be updated at the same time and there is an opportunity to build up an objective function with different weights given to different response values. For example, generally eigen-frequencies of analytical and experimental data are close to each other; on the other hand, eigenvectors may differ a great deal due to measurement noise and error. For that reason, initial correlation of eigenvectors should be made before updating which is explained in the following sections [4].

The analytical model parameters must be updated in each iteration. Updating the analytical model parameters, the updated analytical model must be solved again to obtain the normal modes solution, which is used in the next iteration. The value of difference of the parameters in the iteration loop shows either a divergent or convergent behavior. The procedure shows convergent manner if the parameters converge to a stationary value.

Searching the references [5–7], sensitivity based model updating methods using modal data is identified as the most efficient method that can be used to update large order finite element models owing to its computational advantage. In this paper, a sensitivity-based model updating method using modal parameters, specifically inverse eigensensitivity method is implemented using a Matlab based in-house code working with Nastran synchronously is developed to update the analytical model. In the proposed procedure, sensitivity values are obtained from Nastran according to the convergence behavior of the updating scheme. Considering the fact that calculation of sensitivity values in each iteration is time consuming, especially if the finite element model is large order; a modification is integrated into the method proposed in this paper. Sensitivity matrix is not calculated at every iteration so that the reduction in the computation time can be obtained. In the subsequent sections, first theoretical background of the inverse eigensensitivity method is explained followed by the results of the developed algorithm to simple plate structure and missile launcher.

26.2 Inverse Eigensensitivity Method

Model updating methods related to sensitivity calculation use basically Taylor Series Expansion of modal results. Experimental modal results can be formulized by using analytical eigenvectors and eigenvalues. The experimental modal results can be written as a Taylor expansion in terms of model updating parameters about analytical solution as given in Eqs. (26.1) and (26.2) [8] as follows;

$$\lambda_r^X = \lambda_r^A + \sum_{s=1}^{L} \frac{\partial \lambda_r^A}{\partial p_s} \Delta p_s + 0\left(\Delta p_s{}^2\right) + \cdots, \tag{26.1}$$

$$\{\phi_X\}_r = \{\phi_A\}_r + \sum_{s=1}^{L} \frac{\partial \{\phi_A\}_r}{\partial p_s} \Delta p_s + 0\left(\Delta p_s{}^2\right) + \cdots, \tag{26.2}$$

where subscript X indicates experimental result; subscript r indicates the rth mode, p_s is the sth design parameter and Δp_s is defined as the change in the sth design parameter and L is the total number of design parameters. λ_r and $\{\phi\}_r$ show the eigenvalue and mode shape to the rth mode, respectively. Sensitivity matrix involves first order derivatives of the modal results with respect to model updating parameters. Disregarding the effect of second and higher order terms, in Eqs. (26.1) and (26.2) can be written in an iterative matrix form as follows:

$$\{\Delta z_j\} = \left[S_j\right] \cdot \{\Delta p\} \tag{26.3}$$

where $\{\Delta z_j\}$ is the difference between the experimental and analytical modal results at the jth iteration; $\{\Delta p\}$ is the amount of change in the design parameters at the jth iteration and $[S_j]$ is the sensitivity matrix at the jth iteration. Accepting the updating procedure is based on the modal results, the sensitivity matrix describes the first order partial derivatives of natural frequencies and mode shapes with respect to the design parameters as given in Eqs. (26.1) and (26.2). It should be noted that sensitivity matrix should be calculated at each iteration which is the most time consuming part of the updating procedure. Especially for large order systems, overall updating time can be reduced considerably if the computational time spent for the calculation of the sensitivity matrix is decreased. Equation (26.3) can be written explicitly as follows:

$$\left\{\begin{array}{c} \Delta\lambda_1 \\ \{\Delta\phi\}_1 \\ \vdots \\ \Delta\lambda_m \\ \{\Delta\phi\}_m \end{array}\right\}\Bigg|_j = \left[\begin{array}{cccc} \frac{\partial\lambda_{A1}}{\partial p_1} & \frac{\partial\lambda_{A1}}{\partial p_2} & \cdots & \frac{\partial\lambda_{A1}}{\partial p_L} \\ \frac{\partial\{\phi_A\}_1}{\partial p_1} & \frac{\partial\{\phi_A\}_1}{\partial p_2} & \cdots & \frac{\partial\{\phi_A\}_1}{\partial p_L} \\ \vdots & \vdots & \ddots & \vdots \\ \frac{\partial\lambda_{Am}}{\partial p_1} & \frac{\partial\lambda_{Am}}{\partial p_2} & \cdots & \frac{\partial\lambda_{Am}}{\partial p_L} \\ \frac{\partial\{\phi_A\}_m}{\partial p_1} & \frac{\partial\{\phi_A\}_m}{\partial p_2} & \cdots & \frac{\partial\{\phi_A\}_m}{\partial p_L} \end{array}\right]_j \cdot \left\{\begin{array}{c} \Delta p_1 \\ \Delta p_2 \\ \vdots \\ \Delta p_L \end{array}\right\}, \tag{26.4}$$

where subscript j describes the terms that should be evaluated by using the design parameter values at the jth iteration. In Eq. (26.4), size of vector $\{\Delta p\}$ is $m(n+1)x1$, size of the sensitivity matrix is $m(n+1)xL$ and size of vector $\{\Delta z_j\}$ is $(Lx1)$, where n is the number of degrees of freedom obtained from the modal test; m designates the number of modes included in the updating algorithm and L is the number of design parameters to be updated. It is achievable to have an over determined problem if the number of design parameters to be updated is less than the number of equations. The parameters can be identified with the following formulation:

$$\{\Delta p_{j+1}\} = \left[S_j\right]^+ \{\Delta z_j\}, \tag{26.5}$$

where $\left[S_j\right]^+$ is the pseudo-inverse of the sensitivity matrix at the jth iteration. Using Eq. (26.4) values of the design parameters at the next iteration step can be acquired as follows:

$$\{p_{j+1}\} = \{p_j\} + \{\Delta p_{j+1}\}. \tag{26.6}$$

One of the most crucial advantages of the method is its capability of selecting the eigenvalues and eigenvectors from the full set of results extracted through modal test. Number of modes introduced into the analysis, number of measured coordinates and utilizing eigenvalues, eigenvectors or both in the analysis effects the computational time significantly; hence, they should be taken into account before an updating procedure. It should be noted that calculation of eigenvector sensitivities requires more time compared the eigenvalue sensitivities.

In application of the inverse eigensensitivity method, sensitivity calculations and normal modes analysis are made using the commercial FE software Nastran. Two different control criteria are used in the updating algorithm. In the first control criteria, the difference between experimental and analytical model results is inspected in each iteration and if this value reduces below a predefined error tolerance, algorithm ends which can be summarized as follows:

$$\{p\}^j = \left\{\begin{array}{c} \Delta\lambda_1 \\ \{\Delta\phi_1\} \\ \vdots \\ \Delta\lambda_m \\ \{\Delta\phi_m\} \end{array}\right\}^j \leq e_1. \tag{26.7}$$

where subscript j describes the terms that should be evaluated by using the design parameter values at the jth iteration, e_1 is the acceptable error limit value for the difference between experimental and analytical modal results. In the second control criteria, the rate of change of design parameters is checked. If this decrease is less than a predefined tolerance value, the sensitivity matrix is not calculated for the next iteration. The second criterion can be summarized as follows:

$$\frac{\left|\{p\}^j - \{p\}^{j-1}\right|}{L} \leq e_2, \tag{26.8}$$

where e_2 is a limiting value for the decrease in error and L is the number of design parameters. The flowchart of the developed in-house computational code which uses Matlab and Nastran simultaneously is given in Fig. 26.1.
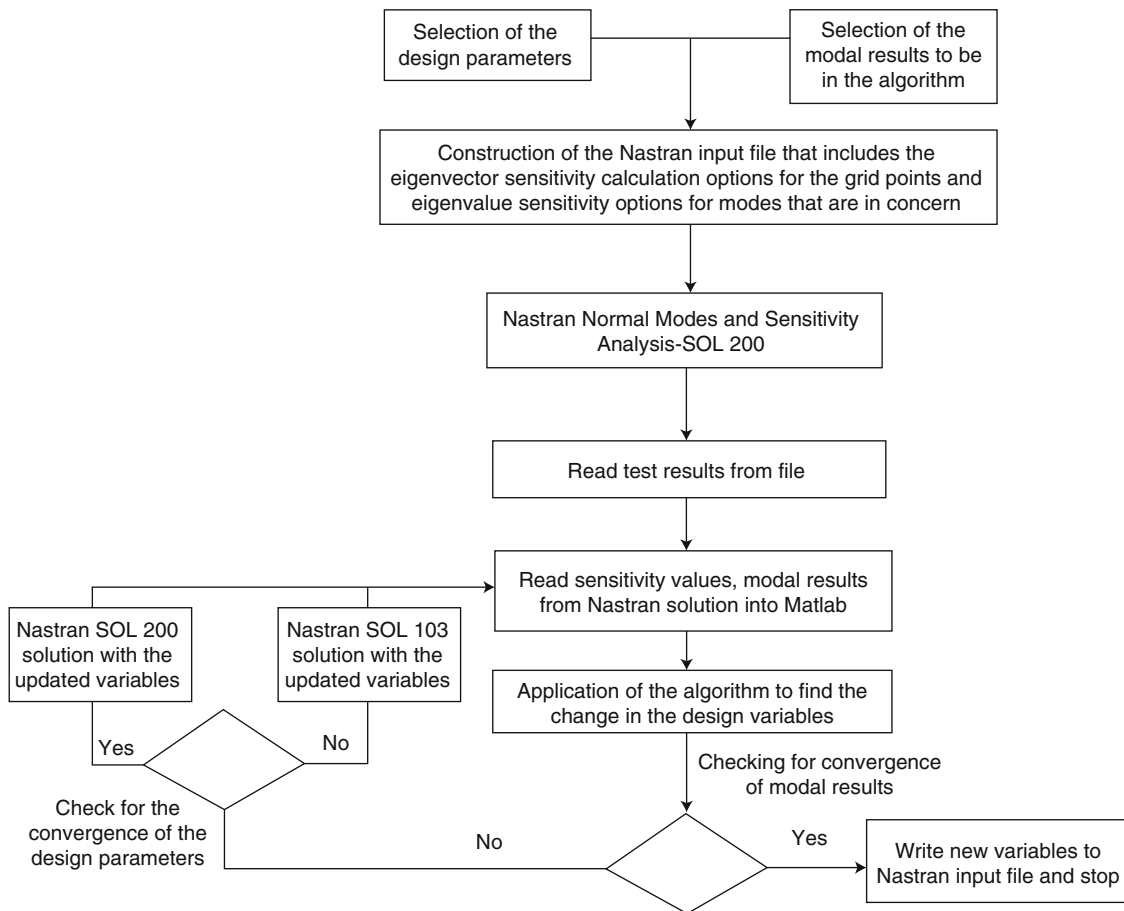
**Fig. 26.1** Flowchart of the developed algorithm

26.3 Case Studies

The developed updating procedure is first applied to a simple structure; afterwards, it is applied to a finite element of missile launcher. For the simple structure, results obtained from finite element software with different parameter values is used to simulate the test results; whereas, actual modal test is performed to extract the modal parameters of the missile launcher model.

26.3.1 Case Study 1: Simple Shell Structure

In this section, the detail of the work including the application of the developed algorithm to a simple structure as shown in Fig. 26.2 is presented. Finite element model consists of shell elements which has 6 degrees of freedom at each node. The structure is partitioned into subparts having different property identity numbers, where each property card defined in Nastran environment is updated separately. Each property has a different property card in Nastran input deck of the finite element model. Finite element model is built up with linear QUAD4 elements. There are totally 6600QUAD4 elements and 6767 nodes in the finite element model.

Five model updating variables (shell thickness values) are selected to be updated. Four natural frequency values and the first eigenvector containing the degrees of freedom of the five grid points shown in Fig. 26.2 with blue circles are used as the experimental results in the updating algorithm. There are 5 model updating parameters and totally 19 equations coming from sensitivity calculations for 4 natural frequencies and 15 values in the first eigenvector including x, y, z translations for each grid point. As the first control criteria, difference between the first 4 natural frequencies of the experimental and analytical model is taken into consideration. The number of equations (which is 19) coming from sensitivity-based calculations of
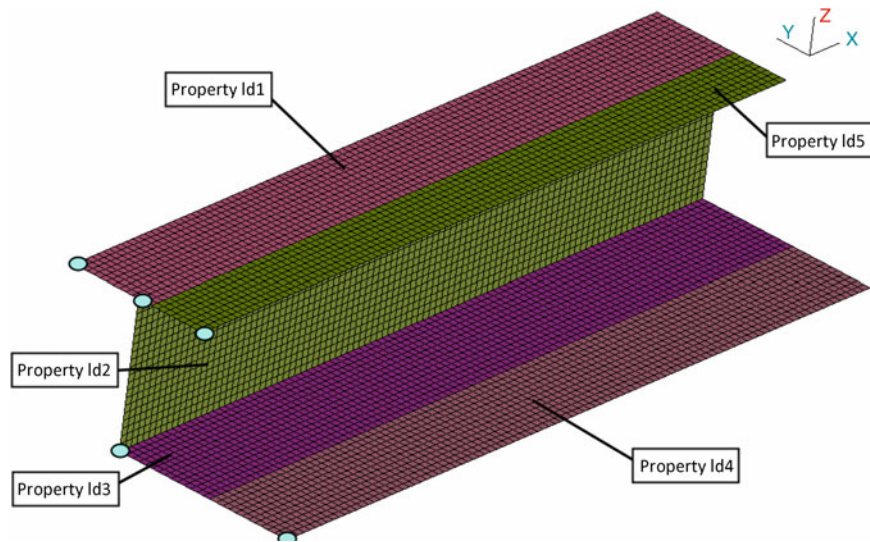
Fig. 26.2 Simple plate structure, property numbers of parts and measurement locations

Table 26.1 Simulated test and analytical model design variables

	Test values(mm)	Analytical values(mm)	% Difference
1st updating parameter	2	1	50.0
2nd updating parameter	2	2	0.0
3rd updating parameter	4	3	25.0
4th updating parameter	3	4	33.3
5th updating parameter	3	5	66.7

Table 26.2 Summary of updating procedure

	% Difference in parameters after updating						
	1st parameter	2nd parameter	3rd parameter	4th parameter	5th parameter	Number of iterations	Convergence time(s)
Case I	0.24	0.27	0.03	0.92	−0.2	8	251.7
Case II	0.42	0.47	−0.06	1.68	−0.29	7	365.3

modal parameter change for change in model updating parameters is more than the number of model updating variables (which is 5). Simulated FE analysis results are obtained by using random thickness values in the finite element software. The model updating variables for the simulated test and analytical models are compared in Table 26.1. Initially, the developed code is run with the default settings (Case I); whereas, in order to observe the effectiveness of the method developed, the same model is run by calculating the sensitivities in all iterations (Case II). Comparison of both cases including percent difference after convergence, the number of iterations needed to reach convergence and time for convergence is given in Table 26.2.

Sensitivity matrix is calculated 5 times in Case I; whereas it is calculated 7 times in Case II. The adjustment of parameters for the model with the default settings are demonstrated in Fig. 26.3; whereas, in Fig. 26.4, the change of design parameters for Case II is given. It is concluded that convergence is acquired in 8 iterations for Case I and in 7 iterations for Case II. The time elapsed for Case I is 251.7s; whereas, the time required for Case II is 365.3s. Although Case II requires less number of iterations, computational time is increased 45 % with respect to Case I. Because of the quality of the updating parameters acquired; MAC plots and natural frequency values are not presented in the paper for brevity.

26.3.2   Case Study 2: Missile Launcher Finite Element Model

In this part, Inverse Eigensensitivity method is applied to finite element model of a missile launcher which is demonstrated in Fig. 26.5. To obtain the modal parameters of the missile launcher, modal tests are carried out. Missile launcher finite element
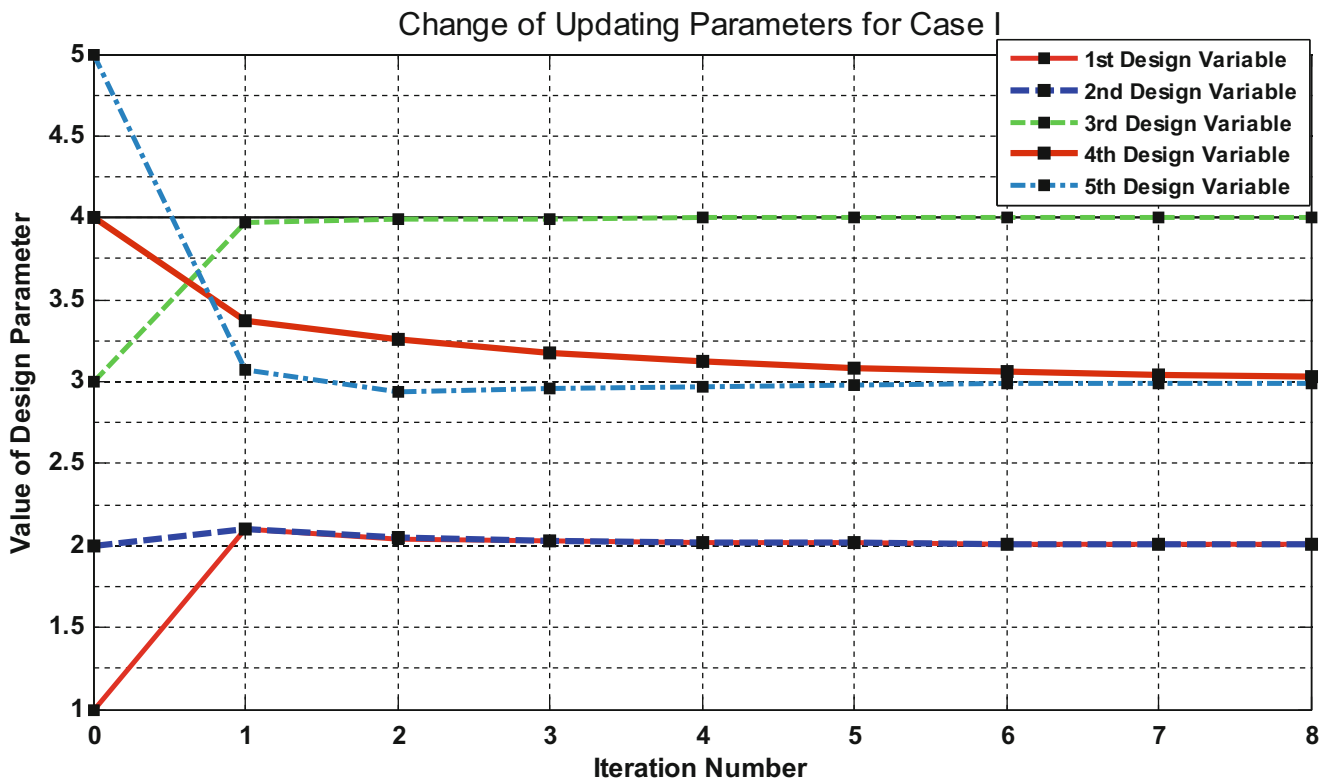
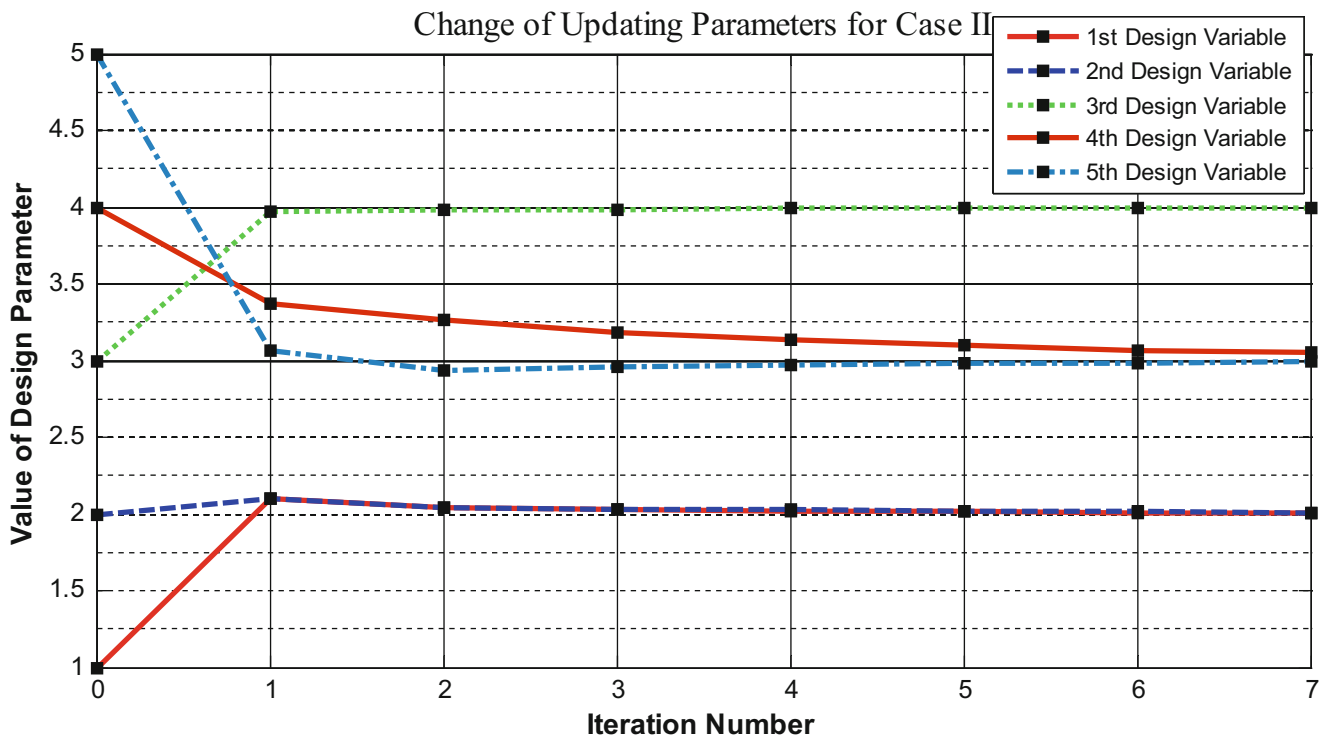**Fig. 26.3** The change of updating parameters for Case I

Fig. 26.4 The change of updating parameters for Case II

Fig. 26.5 Missile launcher
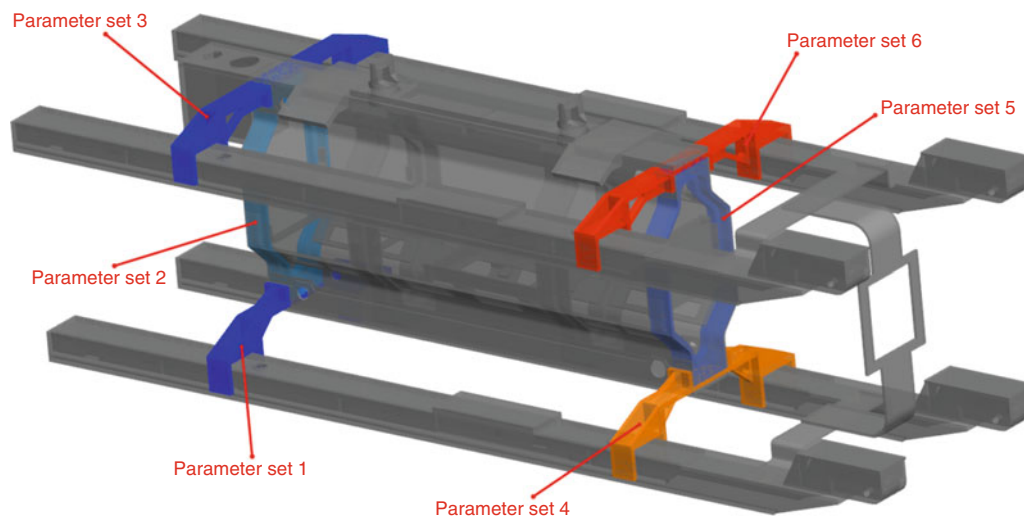
Fig. 26.6 Parameter sets defined in updating algorithm

model consists of 8 noded linear solid elements, HEX8; 10 noded quadratic linear solid elements, TET10; 4 noded linear shell elements, QUAD4; 3 noded linear shell elements, TRIA3, in Nastran. There are total number of 373630 elements, 964396 nodes and 5786376 degrees of freedom in the finite element model.

Sensitivity study is carried out to identify the dominant set of parameters on modal results. Finite element model is divided into subgroups. The selected subgroups are given in Fig. 26.6. Each subpart has its own property identity number which can be updated separately. Model updating parameters were selected as Young's Modulus of each subpart. Eigenvectors are extracted from the 26 grid points. Coordinates of the grid points are selected such that they are coincident with measurement locations in experiment. These points have the potential to move more than the other locations taking into account the first 6 mode shapes obtained from FE analysis. For proper comparison of the analytical and experimental mode shapes, each mode shape vector is normalized with respect to its element with maximum amplitude. In addition to this, MAC matrix is calculated to quantify the correlation between the analytical and experimental modes. The following formula is used to calculate the elements of MAC matrix [9]:

Fig. 26.7 MAC plot before updating

Table 26.3 MAC matrix for the missile launcher model before updating
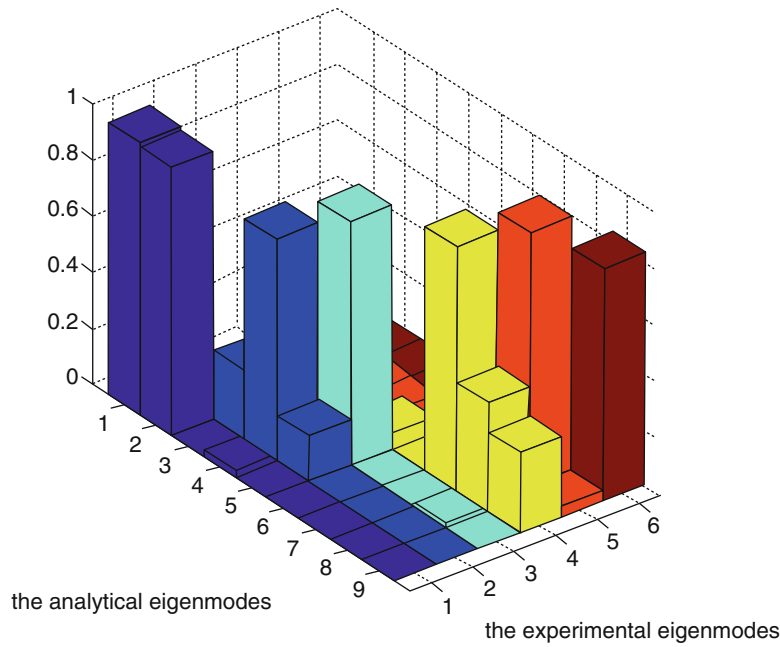
		Experimental model					
		1st mode	2nd mode	3rd mode	4th mode	5th mode	6th mode
Analytical model	1st mode	0.969	0.041	0.000	0.000	0.000	0.000
	2nd mode	0.956	0.001	0.001	0.000	0.000	0.001
	3rd mode	0.000	0.245	0.034	0.007	0.001	0.001
	4th mode	0.022	0.705	0.061	0.001	0.001	0.003
	5th mode	0.002	0.163	0.860	0.062	0.016	0.003
	6th mode	0.008	0.001	0.003	0.003	0.002	0.018
	7th mode	0.003	0.000	0.007	0.871	0.112	0.123
	8th mode	0.003	0.001	0.018	0.389	0.941	0.000
	9th mode	0.005	0.000	0.001	0.286	0.036	0.828

$$MAC\,(A, X) = \frac{\left| \{\varphi_X\}^T \{\varphi_A\} \right|^2}{\left(\{\varphi_X\}^T \{\varphi_X\} \right) \left(\{\varphi_A\}^T \{\varphi_A\} \right)}, \tag{26.7}$$

where subscripts A and X corresponds to analytical and experimental model respectively; $\{\varphi_X\}$ is normalized experimental eigenvector and $\{\varphi_A\}$ is normalized analytical eigenvector.

Initial correlation between the experimental and analytical mode shapes is shown in Fig. 26.7 by using the MAC plot, which is summarized in Table 26.3. It is observed that except the first mode, initially experimental modes are correlated with the different mode number. First 3 natural frequencies and first 3 mode shape are used in updating procedure and updating objective function is constructed to decrease the difference in the first 3 natural frequencies and increase the MAC number values.

The updating procedure is applied by considering Young's Modulus of each subpart as the updating variable. Initially, Young's modulus value is assumed as 71,000 MPa for all subparts. Density and Poisson's ratio for each subpart is taken as 2810 kg/m^3 and 0.3, respectively.

Natural frequencies and MAC values before and after updating are compared with the experimental one in Table 26.4. It is observed that the percent difference between the experimental and updated analytical natural frequencies is decreased prominently.

Table 26.4 Comparison of the natural frequencies and MAC values

		Natural frequency values		MAC values		
		% Difference before updating	% Difference after updating	MAC value before updating	MAC value after updating	Time elapsed(s)
Case I	1st mode	6.1	1.6	0.95	0.96	4120
	2nd mode	5.1	1.2	0.7	0.82	
	3rd mode	3.2	1.5	0.86	0.87	
Case II	1st mode	6.1	1.5	0.95	0.95	5520
	2nd mode	5.1	1.2	0.7	0.84	
	3rd mode	3.2	1.5	0.86	0.87	

The percent difference decreased from 6.1 to 1.6 % for the first mode; from 5.1 to 1.2 % for the second mode and from 3.2 to 1.5 % for the third mode for Case I and from 6.1 to 1.5 % for the first mode; from 5.1 to 1.2 % for the second mode and from 3.2 to 1.4 % for the third mode for Case II. Time elapsed to reach convergence is reduced 25 % in Case I.

26.4 Conclusions

An in-house computer code is improved in Matlab in order to perform model updating by using the inverse eigensensitivity method. The developed computer code uses commercial finite element software as a solver from where the modal results and sensitivities are obtained. To reduce the computational time, sensitivity matrix calculations are only executed when a specific error slope criterion is met. For the verification of the developed code and investigation of the improved sensitivity calculation approach, a simple structure composed of plates is updated, where the simulated tests are obtained exactly after updating. Furthermore large order finite element model of missile launcher is taken into account for a real case study. Experimental modal analysis of the structure is accomplished, where initially prominent difference between the analytical and experimental natural frequencies is inspected. The updating process is carried out taking into account the first 3 natural frequencies and the first 3 eigenvectors in the objective function. The results acquired showed that natural frequencies of the first 3 modes are improved prominently and MAC number of 2nd mode shape is increased. It is concluded that with the developed computer code, it is possible to analyze the sensitivity of the modal results with respect to the parameters of finite element model and large order finite element models can be updated effectively by using the subparts in the finite element model.

References

1. Friswell, M.I., Mottershead, J.E.: Finite Element Model Updating in Structural Dynamics. Kluwer Academic, Dordrecht (1995)
2. Carvalho, J., Datta, B.N., Gupta, A., Lagadapati, M.: A direct method for model updating with incomplete measured data and without spurious modes. Mech. Syst. Signal Process. **21**(7), 2715–2731 (2007)
3. Kozak, M.T., Öztürk, M., Özgüven, H.N.: A method in model updating using miscorrelation index sensitivity. Mech. Syst. Signal Process. **23**, 1747–1758 (2009)
4. Göge, D., Link, M.: Assessment of computational model updating procedures with regard to model validation. Aerosp. Sci. Technol. **7**, 47–61 (2003)
5. Göge, D.: Automatic updating of large aircraft models using experimental data from ground vibration testing. Aerosp. Sci. Technol. **7**, 33–45 (2003)
6. Schedlinski, C.: Computational model updating of large scale finite element models. In: International Modal Analysis Conference, San Antonio (2000)
7. Schedlinski, C., Göge, D., Link, M.: Parameter identification and validation of large order finite element models for industrial type structures. In: Third European Conference on Structural Control, Vienna, Austria, 12–15 July 2004
8. Maia, N.M.M., Silva, J.M.M.: Theoretical and Experimental Modal Analysis. Research Studies Press, Hertfordshire (1998)
9. Ewins, D.J.: Modal Testing: Theory, Practice and Application, 2nd edn. Research Studies Press, Hertfordshire (2000)

Chapter 27
Monte Carlo Dynamically Weighted Importance Sampling for Finite Element Model Updating

Daniel J. Joubert and Tshilidzi Marwala

Abstract The Finite Element Method (FEM) is generally unable to accurately predict natural frequencies and mode shapes (eigenvalues and eigenvectors) of structures under free or forced vibration. Engineers develop numerical methods and a variety of techniques to compensate for this misalignment of modal properties, between experimentally measured data and computed results. In this paper we compare two indirect methods of updating namely, the Adaptive Metropolis Hastings and a newly applied algorithm called Monte Carlo Dynamically Weighted Importance Sampling (MCDWIS). The approximation of a posterior predictive distribution is based on Bayesian inference of continuous multivariate Gaussian probability density functions, defining the variability of physical properties affected by dynamic behaviors. The motivation behind applying MCDWIS is in the complexity of computing higher dimensional or multimodal systems. The MCDWIS accounts for this intractability by analytically computing importance sampling estimates at each time step of the algorithm. In addition, a dynamic weighting step with an Adaptive Pruned Enriched Population Control Scheme (APEPCS) allows for further control over weighted samples and population size. The performance of the MCDWIS simulation is graphically illustrated for all algorithm dependent parameters and show unbiased, stable sample estimates.

Keywords Finite element • Finite element method • Monte Carlo dynamically weighted importance sampling • Adaptive pruned enriched population control scheme • Markov Chain Monte Carlo • Metropolis hastings • Adaptive metropolis hastings

27.1 Introduction

Physical properties, for example, areas, moments of inertia, or elasticity (Young's Modulus), all influence the outcome of eigenvalues (natural frequencies) and the eigenvectors (mode shapes) of structures, through the universally known eigenvalue problem derived from the FEM. The method of model updating discussed in this paper is of the indirect or iterative type, thus taking into account changes of physical parameters when the structure is under forced vibration or dynamic load. This result of the mass and stiffness matrices of the updated FE model has physical meaning, i.e. eigenvalues and eigenvectors [1]. In recent years, it has been well established that there exists Bayesian evidence in FE model updating of structures, [1–3]. Various MCMC sampling techniques have been applied [4], predicting uncertain i.e. stochastic parameters in order to produce realistic modal frequencies of the models under vibration.

27.2 Bayesian Inference and Gaussian Process Model

It is important to note that due to the complexity of systems, a closed form posterior distribution is not analytically available and in most cases cannot be accurately approximated. This comes about through the multi-dimensionality of the search space in multimodal systems. This multi-dimensionality of the Monte Carlo integrals causes difficulties in computation, and leads to the use of approximation methods. Thus, for the purposes of this MCDWIS simulation the normalizing constant $Z(\theta)$ of the posterior distribution is not available and is referred to as analytically intractable. In Bayesian inference, the posterior is in fact generally considered to be analytically intractable [5]. Bayesian inference is governed by Bayes Rule [6].

D.J. Joubert (✉) • T. Marwala
University of Johannesburg, Kingsway Campus, Cnr. Kingsway and University Rd, Auckland Park, South Africa
e-mail: nieljou@gmail.com

$$p\left(\boldsymbol{\theta}\middle|D\right) = \frac{f\left(D\middle|\boldsymbol{\theta}\right)\pi\left(\boldsymbol{\theta}\right)}{\pi(D)} \text{ or simply } p\left(\boldsymbol{\theta}\middle|D\right) \propto f\left(D\middle|\boldsymbol{\theta}\right)\pi\left(\boldsymbol{\theta}\right) \tag{27.1}$$

Where $\boldsymbol{\theta}$ represents the vector of updating parameters, $f\left(D\middle|\boldsymbol{\theta}\right)$ is the likelihood probability distribution function and $\pi(\boldsymbol{\theta})$, denotes the prior probability distribution function. As shown, the posterior probability can be approximated through Bayesian inference. Since we will be considering a multi-dimensional parameter search space with non-independent variables in this study, we will be using continuous multivariate probability density functions. Gaussian Processes are very popular in Bayesian estimation procedures. And in this thesis, all probability functions will be Normal. The covariance of the target distribution is unknown. These statistical parameters are approximated analytically during the burn-in stages of the simulations. However, μ_0 and Σ_0 are assumed to initialize the Gaussian process. These initializations are also known as hyper-parameters. The likelihood distribution is given as,

$$f\left(D\middle|\boldsymbol{\theta}\right) = \frac{1}{\left((2\pi)^{N_m}\left|\Sigma_f\right|\right)^{0.5}} \exp\left(-0.5\left(f_{N_m}^c - f_{N_m}^m\right)^T \Sigma_f^{-1}\left(f_{N_m}^c - f_{N_m}^m\right)\right). \tag{27.2}$$

Here N_m denotes the dimension of the frequency vector, f_i^m and f_i^c represent the measured and computed natural frequencies respectively. The determinant of the frequency covariance matrix is $\left|\Sigma_f\right|$. The Taylor expansion can be used to express the log-likelihood distribution function as,

$$\log\left(f\left(D\middle|\boldsymbol{\theta}\right)\right) = \frac{N_m}{2}\ln(2\pi) + 0.5\ln\left|\Sigma_f\right| + 0.5\left(f_{N_m}^c - f_{N_m}^m\right)^T \Sigma_f^{-1}\left(f_{N_m}^c - f_{N_m}^m\right). \tag{27.3}$$

The prior probability distribution is also chosen as a Gaussian probability density function.

$$\pi(\boldsymbol{\theta}) = \frac{1}{\left((2\pi)^d\left|\Sigma_{\theta,0}\right|\right)^{0.5}} \exp\left(-0.5(\boldsymbol{\theta} - \boldsymbol{\mu}_0)^T \Sigma_{\theta,0}^{-1}(\boldsymbol{\theta} - \boldsymbol{\mu}_0)\right) \tag{27.4}$$

Here d denotes the dimension of the variable parameter vector, $\boldsymbol{\theta}$. The process is initialized by the parameter covariance matrix, $\Sigma_{\theta,0}$ and mean vector, $\boldsymbol{\mu}_0$. Consequently, given the likelihood and prior, it is obvious to note that multiplying two Gaussian distributions yields a Gaussian distribution. Therefore these distributions are conjugate distributions. From Bayes' theorem the posterior probability distribution can be approximated as,

$$p\left(\boldsymbol{\theta}\middle|D\right) = \frac{1}{Z(\boldsymbol{\theta},D)} \exp\left(-0.5\left(f_{N_m}^c - f_{N_m}^m\right)^T \Sigma_f^{-1}\left(f_{N_m}^c - f_{N_m}^m\right) - 0.5(\boldsymbol{\theta} - \boldsymbol{\mu}_{\theta n})^T \Sigma_{\theta,n}^{-1}(\boldsymbol{\theta} - \boldsymbol{\mu}_{\theta n})\right). \tag{27.5}$$

Where the normalizing constant is described by the integral,

$$Z(\boldsymbol{\theta},D) = \int f\left(D\middle|\boldsymbol{\theta}\right)\pi(\boldsymbol{\theta})\,d\boldsymbol{\theta}. \tag{27.6}$$

Due to the multi-dimensionality of this integral, solving it is considered computationally complex. Attempts have been made to estimate reasonable normalizing constants in model updating [5, 7]. However, this is not effective given increasingly complex systems. This is to say that there is no 'one size fits all' approach in assigning normalizing constants to the posterior distribution for all structural models with varied sensitivity parameters and material properties.

27.3 Monte Carlo Dynamically Weighted Importance Sampling (MCDWIS)

A key advantage of MCDWIS is that this algorithm does not require perfect sampling. Thus, MCDWIS is interesting to consider with regard to parameter estimation in model updating of FE models. Due to the computationally expensive effort of solving to FE model at every time step during the simulation, model updating is inherently computationally very intensive. Avoiding the need for exact sampling which in itself can be very expensive or in most cases not possible, makes MCDWIS a worthwhile technique to experiment with in model updating, adopting a stochastic Monte Carlo approximation approach.

The use of the MCDWIS algorithm is thus validated in approximating unbiased estimates which is controlled within a desired reduced variance range from the originally drawn samples. Reduced variance in the system is simply achieved through the use of an importance sampling estimate. New weighted samples are then generated, referred to in literature as the new population. Through population control schemes the system becomes adaptive to the requirements of the outcome, as the posterior distribution is left invariant with respect to dynamic importance weights.

The prior distribution denoted as $\pi(\boldsymbol{\theta})$, represent the prior knowledge through observation of the previous system state. From the observed auxiliary data y the likelihood function for the statistical model is, [8]

$$f\left(y\middle|\boldsymbol{\theta}\right) = \frac{p\left(\boldsymbol{\theta},y\right)}{Z\left(\boldsymbol{\theta}\right)} \tag{27.7}$$

where $p(\boldsymbol{\theta},y)$ denotes the conditional probability density function of the state and auxiliary samples. $Z(\boldsymbol{\theta})$ is the normalizing constant which is dependent on the value of $\boldsymbol{\theta}$. The posterior probability distribution for variable $\boldsymbol{\theta}$ can thus be describe as [8],

$$p\left(\boldsymbol{\theta}\middle|y\right) = \frac{1}{Z\left(\boldsymbol{\theta}\right)}p\left(\boldsymbol{\theta},y\right)\pi\left(\boldsymbol{\theta}\right) \tag{27.8}$$

This algorithm, similar to importance sampling uses important weights to prioritize acceptance and locate the optimal search space for sampling. Each state in the Markov chain of size N is given by the joint density, $(\boldsymbol{\theta},\boldsymbol{w}) = \{\theta_1,w_1;\ldots;\theta_N,w_N\}$. Every move step of the algorithm involves two actions, namely:

1. Dynamic weighting: Where each state is updated by a dynamic weighting transition step in order to compute a new population [9].
2. Population control: Samples related to small weights with regard to updated results from the FE model are discarded while weighted samples with stronger relevance to the model objective function are duplicated in the new population. This induces biased samples but is counter balanced by assigning new weights to the samples for every new population.

Figure 27.1 below demonstrates the concept of the APEPCS in the dynamic weighting and population control stages of the algorithm [8]. The samples' weight classification residing outside of the weight control bounds W_{up} and W_{low} are scaled by the use of the control parameter d_s in the enriching stage where $w_{t,i}$ is too large and the probability density parameter q during the pruning stage ($w_{t,i} < W_{low}$), of the population control scheme. Weighting is controlled by the ratio of the upper and lower weight control bounds and can be described as, $\kappa = \frac{W_{up}}{W_{low}}$. This ratio controls the moving ability of the system and is called the freedom parameter [9]. APEPCS controls the population size within the range $[n_{min},n_{max}]$. In this fashion
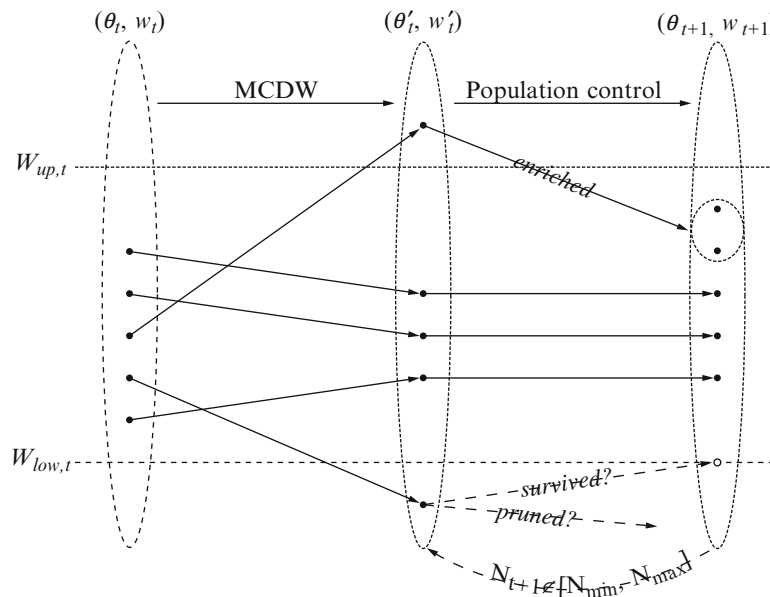

Fig. 27.1 DWIS algorithm

the algorithm constructs new populations with each run, adjusting the size according to weight assignments. These weights influence the acceptance of elements in the Markov Chain into the new population.

The details on the steps involved in the APEPCS process can be found in Liang [8]. There are two population control schemes of which for this problem the authors propose using R-scheme for simplicity of the algorithm. According to Liang [9], Scheme-R fits best with Monte Carlo simulations.

27.3.1 Scheme—R

1. Dynamic weighting: The scheme is applied to (θ_{t-1}, w_{t-1}). Where W_c denotes the dynamic move switching parameter of the value φ_t between 0 and 1 depending on the value of, $W_{up,t-1}$. In the case where $W_{up,t-1} \leq W_c$ the value, $\varphi_t = 1$. Inversely when $W_{up,t-1} \geq W_c$, φ_t is set to 0. W_c is typically chosen as an exponential expression and relates to the weight control bounds by $W_c = 10^k$. The new population is denoted as $(\boldsymbol{\theta_t}', \boldsymbol{w_t}')$. The parameter φ_t is chosen as a function of $(\boldsymbol{\theta_t}, \boldsymbol{w_t})$. It is interesting to note that, for the R-Type move, if $\varphi_t = 0$, the sampler is essentially a random walk process. And when $\varphi_t = 1$, then the sampler performs the R-Type move. Essentially, the purpose of introducing the φ_t parameter is to prevent the weighting procedure from drifting to zero or infinity.
2. Population control: Next APEPCS is applied to the new population. And the new population becomes $(\boldsymbol{\theta_t}, \boldsymbol{w_t})$.

By applying this to model updating the aim is to see the MCDWIS algorithm produce more accurate results with faster convergence and see an improvement in computational efficiency. In order to evaluate the performance of the DW process we would like to see the behavior of the switching parameter, the adaptation of $W_{up,t}$, the adaptation of the population size and the log weight of selected i^{th} states. To avoid unwanted inflation of the weighting process, it is important to implement a Weight Behavior Analysis (WBA). Further literature and proofs regarding weight behavior analysis can be found in Liang [10]. The main acceptance and rejection process can be summarized as follows:

1. Firstly a proposed sample θ^* is drawn from the proposal distribution $\pi\left(\theta^* \middle| \theta_t\right)$.
2. The auxiliary simulated state trajectories from $f\left(y \middle| \theta^*\right)$, are generated through MH a procedure $y = \{y_1, \ldots, y_M\}$. Next we compute the importance sampling (IS) estimate acting as the normalizing constant ratio $\widehat{R}_t(\theta, \theta^*) = Z(\theta) / Z(\theta^*)$ [9]

$$\widehat{R}_t\left(\theta_t, \theta^*\right) = \frac{1}{M} \sum_{j=1}^{M} \frac{p\left(y_j, \theta\right)}{p\left(y_j, \theta^*\right)} \tag{27.9}$$

3. From this the Monte Carlo dynamic weighting ratio is calculated. The conditional probability distribution can be expressed as, $p(\boldsymbol{y}, \theta_t) = p\left(\theta_t \middle| \boldsymbol{y}\right) \pi(\boldsymbol{y})$. [11]

$$r_d = r_d\left(\theta_t, \theta^*, w\right) = w\widehat{R}_t\left(\theta_t, \theta^*\right) \frac{p\left(\boldsymbol{y}, \theta^*\right)}{p\left(\boldsymbol{y}, \theta_t\right)} \frac{\pi\left(\theta_t \middle| \theta^*\right)}{\pi\left(\theta^* \middle| \theta_t\right)} \tag{27.10}$$

4. As previously discussed, the joint density is updated using a uniformly drawn random numbers $U \sim unif(0, 1)$ in the inequality, [12] From APEPCS we determine φ_t

$$\left(\boldsymbol{\theta'}, \boldsymbol{w'}\right) = \begin{cases} \left(\boldsymbol{\theta^*}, \frac{r_d}{a}\right), & if \ U \leq a, \\ \left(\boldsymbol{\theta}, \frac{w}{1-a}\right), & otherwise. \end{cases} \tag{27.11}$$

Where, $a = \frac{r_d}{r_d + \varphi_t}$.

Given the dynamic weights with associated sampled parameters, $(\theta_1, w_1), (\theta_2, w_2), \ldots, (\theta_N, w_N)$ the weighted average of the samples can be expressed as [9]

$$\widehat{\mu} = \sum_{t=burn+1}^{N} \sum_{i=1}^{n'} \left(\frac{w_{t,i} \rho\left(\theta_{t,i}\right)}{w_{t,i}}\right) \tag{27.12}$$

where $\rho(\theta_t)$ represents a state function over all the drawn samples. The mean value can be assumed to be consistent and asymptotically normally distributed. The proof for this can be found in Liang [11]. From simulating the structural model and updating the chosen sensitivity parameters behaving randomly in the system, graphs are plotted and conclusions are drawn to support the findings in performance. Various plots will test the validity of the simulation and their significance will be discussed where necessary in the coming chapters. The initial statistical parameters, constraints and initial conditions are decided upon and the various algorithm parameters are tuned by virtue of trial and error.

27.4   GARTUER SM-AG19 Simulation

The GARTEUR model is a well-known tool in the structural dynamics research field, providing researchers with common ground in testing different hypotheses in FE model updating. In this section, we simulate the MCDWIS algorithm and compare the results with an Adaptive Metropolis Hastings (AMH) algorithm. The model testbed being tested is specifically called the GARTUER SM-AG19 model, and more information can be found in papers by Degener [13] and Friswell [12]. The nominal length and width of the aero plane structure is 1.5 m and 3 m respectively. The aluminum structure has a total mass of 44 kg. A viscoelastic layer was bonded to the wings to induce an increased damping effect. The beam elements of the structure are all modelled as Euler-Bernoulli beam elements, with the materials assumed to be standard isotropic on all the elements. From Friswell [12], the natural frequencies with respect to the measured mode shapes are determined to be: 6.38, 16.10, 33.13, 33.53, 35.65, 48.38, 49.43, 55.08, 63.04, 66.52 Hz. The updating vector consists of the right wing moments of inertia and torsional stiffness ($RI_{\min}$, $RI_{\max}$, $RI_{torsional}$), the left wing moments of inertia and torsional stiffness ($LI_{\min}$, $LI_{\max}$, $LI_{torsional}$), the vertical tail moment of inertia ($VTP_{I_{\min}}$) and the overall density of the structure ρ. The updating vector is given by, $\boldsymbol{\theta} = [\rho,\ VTP_{I_{\min}},\ LI_{\min},\ L\,I_{\max},\ RI_{\min},\ RI_{\max},\ LI_{torsional},\ RI_{torsional}]$. The initial starting vector used is $\theta_0 = [2785,\ 8.34 \times 10^{-9},\ 8.34 \times 10^{-9},\ 8.34 \times 10^{-7},\ 8.34 \times 10^{-9},\ 8.34 \times 10^{-7},\ 4 \times 10^{-8},\ 4 \times 10^{-8}]$. With the maximum and the minimum bounds respectively used as, $\theta_{max} = [3500,\ 12 \times 10^{-9},\ 11.2 \times 10^{-9},\ 12 \times 10^{-7},\ 11.2 \times 10^{-9},\ 12 \times 10^{-7},\ 6 \times 10^{-8},\ 6 \times 10^{-8}]$ and $\theta_{min} = [2500,\ 6 \times 10^{-9},\ 8 \times 10^{-9},\ 6 \times 10^{-7},\ 8 \times 10^{-9},\ 6 \times 10^{-7},\ 3 \times 10^{-8},\ 3 \times 10^{-8}]$. With the diagonals of the covariance initialized as $\sigma = [5 \times 10^{2},\ 5 \times 10^{-9},\ 5 \times 10^{-9},\ 5 \times 10^{-7},\ 5 \times 10^{-9},\ 5 \times 10^{-7},\ 5 \times 10^{-8},\ 5 \times 10^{-8}]$. Fig. 27.2a–j demonstrates the mode shapes represented by the natural frequencies.

27.5   Results

A fast run of the double MH algorithm is performed, which gives the initial set of samples for the MCDWIS to start off with. From 1000 iterations, the first 200 are discarded as burn-in and 200 samples are evenly selected from the remaining 800. This initial set of samples, are allocated with weight of 1 for initialization. The algorithm parameters are given in Table 27.1.

The adaptation of the population size is given by Fig. 27.3. Figure 27.4, shows a Gaussian representation of the log weight at the 10th state. Due to the higher dimensional vector, the algorithm reacts by allocating exceptionally high weights during the first few time steps and exponentially decreases, and then fluctuates. Figure 27.5 shows the adaptation of the upper bound weight value. Figure 27.6 shows the adaptation of the R-Scheme switching parameter φ_t, during computation. When the ratio between the highest and lowest weights exceed that of the allowable ratio between the upper and lower control bounds, the algorithm reacts accordingly, by gradually drifting back into the desired range, enabling the R-Scheme procedure to take effect. Figure 27.7 shows the correlation between the new samples at the 100th state, and the symmetry over the diagonal shows that the samples are correlated.

Table 27.2 gives the values of the elements in the updated vector after the simulation. Table 27.3 gives the resultant natural frequencies corresponding to each respective mode shape. Theoretical background on the AMH algorithm implemented can be reviewed in Haario [14].
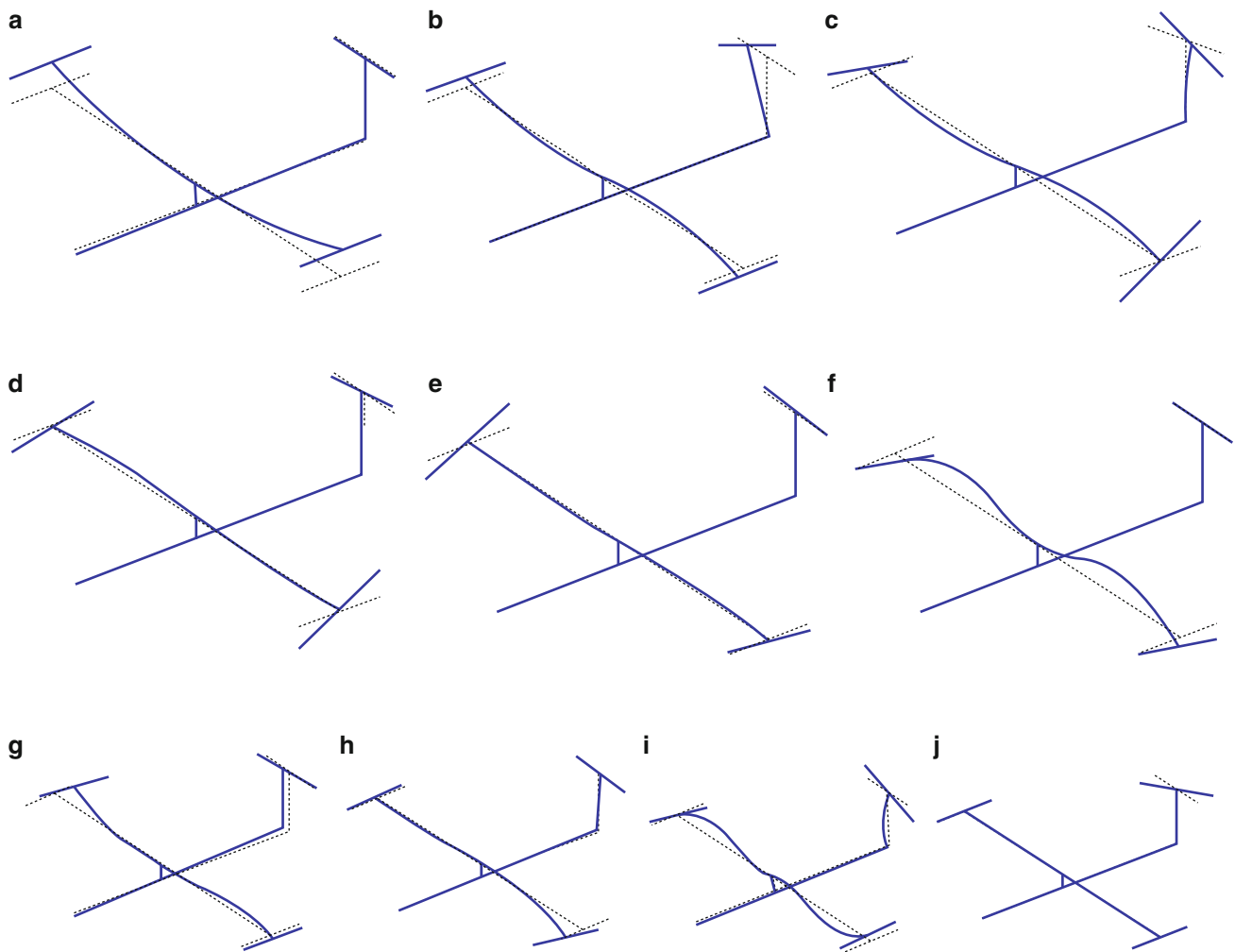
Fig. 27.2 (**a**) Mode 1 at 6.38 Hz; (**b**) Mode 2 at 16.10 Hz; (**c**) Mode 3 at 33.13 Hz; (**d**) Mode 4 at 33.53 Hz; (**e**) Mode 5 at 35.65 Hz; (**f**) Mode 6 at 48.38 Hz; (**g**) Mode 7 at 49.43 Hz; (**h**) Mode 8 at 55.08 Hz; (**i**) Mode 9 at 63.04 Hz; (**j**) Mode 10 at 66.52 Hz

Table 27.1 Algorithm parameters

| Algorithm parameter	Values
N	1000
$burn-in$	250
W_c	e^7
n_{min}	100
n_{max}	1000
n_{low}	200
n_{up}	500
λ	2
κ	$\log_{10} W_c$

27.6 Conclusion

The TME shows significantly more accurate results obtained by the MCDWIS algorithm compared to the initial frequency and the updated frequency from the AMH simulation. The consistency of the MCDWIS algorithm with higher dimensional problems and more complex models is a testament to its validity in the practice of indirect FE model updating. It is important to note that, in the MCDWIS the weighting process and importance sampling are in control. Thus, as in literature, these are presented in the plots. Additionally, the algorithm dependent parameters are relatively simple to tune by trial and error
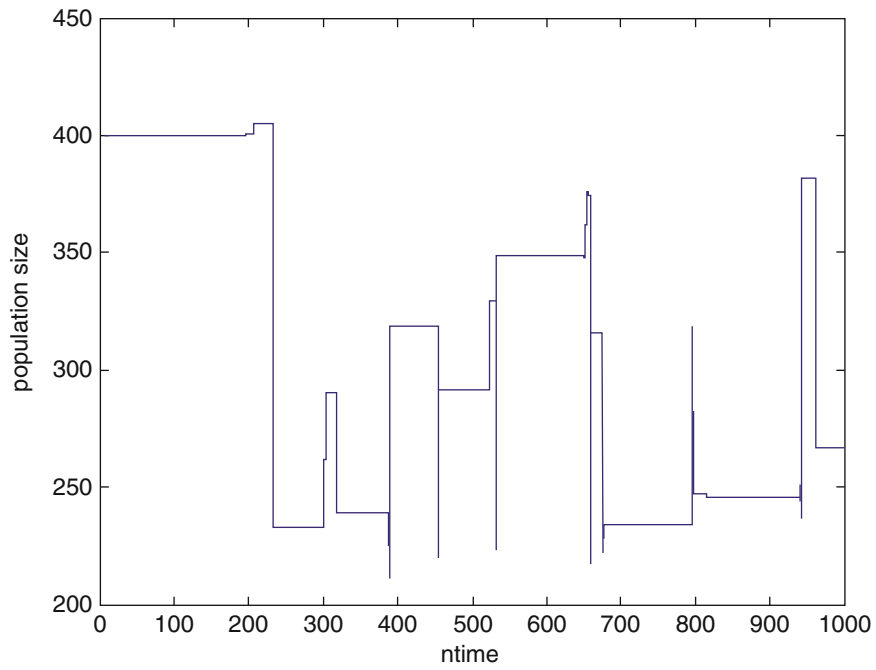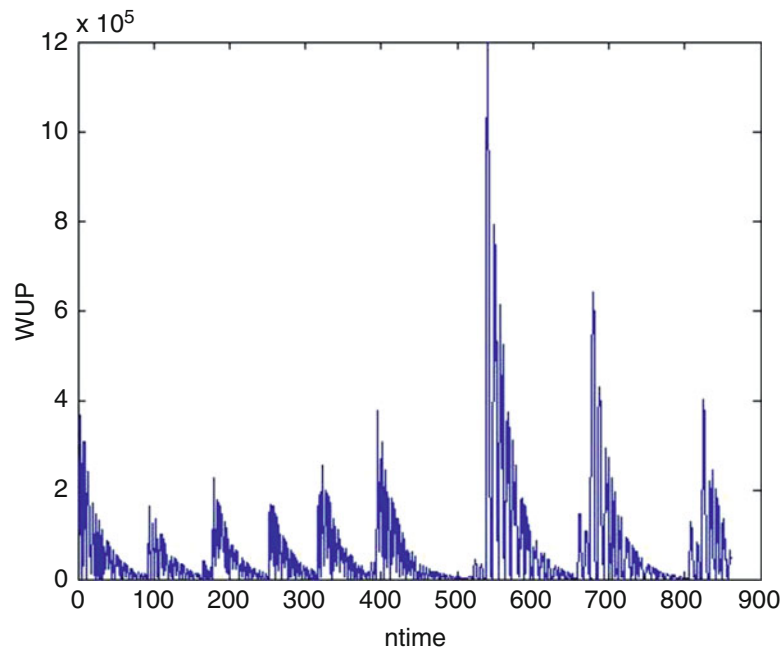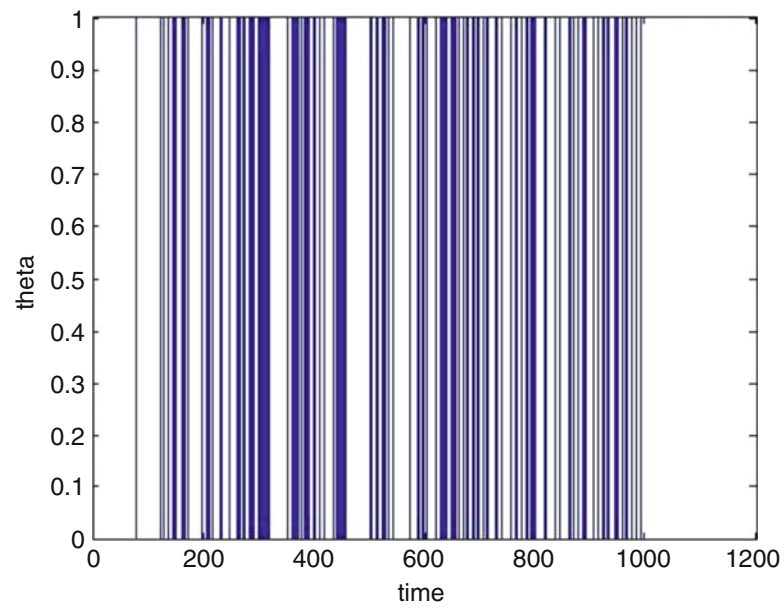
Fig. 27.3 Population size adaptation
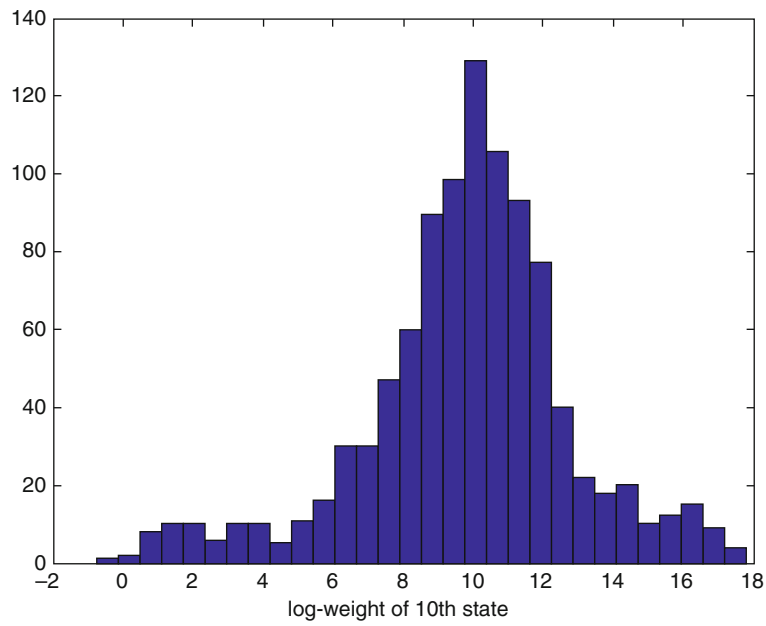
Fig. 27.4 Log weight at the 10th state

Fig. 27.5 Adaptation of WUP

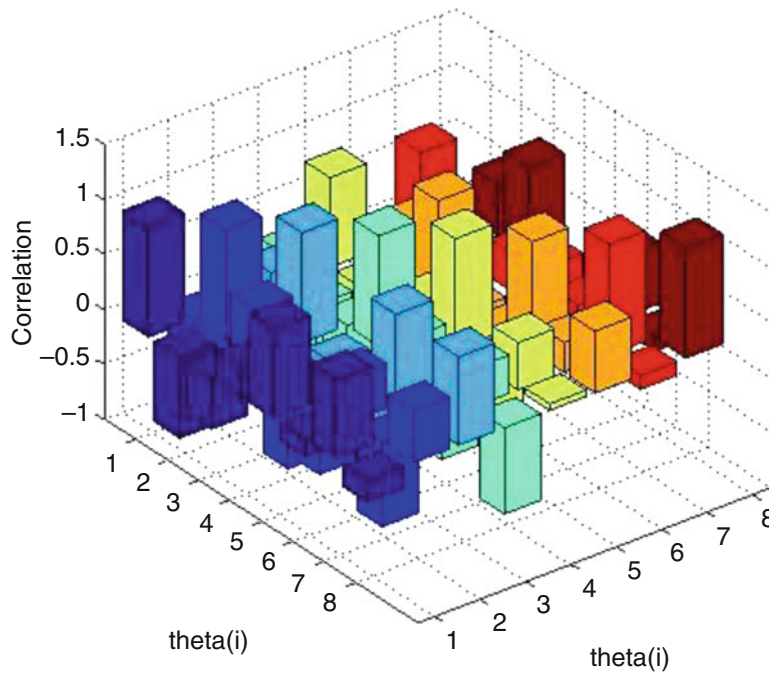**Fig. 27.6** Adaptation of the switching parameter

Fig. 27.7 Correlation

Table 27.2 Updating vector results

d	Initial $\boldsymbol{\theta}_0$	$\boldsymbol{\theta}$ vector, AMH method	$\boldsymbol{\theta}$ vector, MCDWIS method
ρ	2785	2847	2736
$VTP_{I_{min}}$	8.34×10^{-9}	9.1275×10^{-9}	7.1213×10^{-9}
LI_{min}	8.34×10^{-9}	9.2278×10^{-9}	1.0200×10^{-8}
$L\,I_{max}$	8.34×10^{-7}	7.6652×10^{-7}	7.9716×10^{-7}
RI_{min}	8.34×10^{-9}	9.6244×10^{-9}	1.0202×10^{-8}
RI_{max}	8.34×10^{-7}	8.3867×10^{-7}	6.0834×10^{-7}
$LI_{torsional}$	4×10^{-8}	4.4388×10^{-8}	4.1102×10^{-8}
$RI_{torsional}$	4×10^{-8}	3.5720×10^{-8}	3.6212×10^{-8}

Table 27.3 Natural frequency results

Mode	Measured frequency (Hz)	Initial frequency (Hz)	Err (%)	AMH frequency	Err (%)	MCDWIS frequency	Err (%)
1	6.38	5.71	10.47	6.0099	5.80	6.3021	1.22
2	16.10	15.29	5.01	16.0666	0.20	15.9326	1.04
3	33.13	32.53	1.82	32.7091	1.27	32.3035	2.49
4	33.53	34.95	4.23	34.3994	2.59	34.0557	1.57
5	35.65	35.65	0.012	37.0980	4.06	35.8587	0.58
6	48.38	45.14	6.69	46.8730	3.11	48.5070	0.26
7	49.43	54.69	10.65	52.9663	7.15	49.5125	0.17
8	55.08	55.60	0.94	54.8028	0.50	54.2495	1.51
9	63.04	60.15	4.59	62.0316	1.59	63.5583	0.82
10	66.52	67.56	1.57	67.4895	1.45	67.4334	1.37
Total mean error (TME)	–	–	4.6	–	2.7	–	1.1

and could be experimented with further, to achieve even more accurate results. The degrees of freedom of the element matrices, determines the dimensionality of the search space. The increase of dimensions of the system becomes relevant in our investigation due to the resultant increase of variable parameters in the system, and in turn this leads to Monte Carlo integration becoming computationally complex. Compared to other statistical methods, the MCDWIS algorithm is complex

however, it has been demonstrated that it works with high accuracy and given the missing data issue when dealing with multimodal and complex structures this algorithm is useful due to the fact it relieves the need for exact or perfect sampling. The dynamic weighting and population control strategies aim to increase the convergence rate to the target distribution, through the numerical approximation of unbiased importance sampling estimates.

References

1. Marwala, T.: Finite Element Updating using Computational Intelligence, pp. 40–250. Springer, London (2010)
2. Doebling, S.W., Hemez, F.M., Peterson, L.D., Farhat, C.: Improved damage location accuracy using strain energy-based mode selection criteria. AIAA J. **35**(4), 693–699 (1997)
3. Marwala, T., Sibisi, S.: Finite element updating using Bayesian framework and modal properties. J. Aircr. **42**, 275–278 (2005)
4. Wong, J.M., Mackie, K., Stojadinovic, B.: Bayesian updating of bridge fragility curves using sensordata. In: Proceedings of the 3rd International Conference on Bridge Maintenance, Safety and Management, pp. 613–614 (2006)
5. Boulkaibet, I., Mthembu, L., Marwala, T., Friswell, M., Adhikari, S.: Finite element model updating using the shadow hybrid Monte Carlo technique. Mech. Syst. Signal Process. **52–53**, 115–132 (2015)
6. Bishop, C.: Pattern Recognition and Machine Learning. Springer, New York (2006)
7. Kuss, M., Rasmussen, C.E.: Assessing approximate inference for binary Gaussian process classification. J. Mach. Learn. Res. **6**, 1679–1704 (2005)
8. Liang, F., Liu, C., Carroll, R.: Advanced Markov Chain Monte Carlo Methods (Section 6.1–6.3), pp. 165–185. Wiley, Chichester (2010)
9. Liang, F.: Dynamically weighted importance sampling in Monte Carlo computation. J. Am. Stat. Assoc. **97**(459), 807–821 (2002)
10. Wong, W.H., Liang, F.: Dynamic weighting in Monte Carlo and optimization. Proc. Natl. Acad. Sci. USA **94**, 14220–14224 (1997)
11. Liang, F.: Monte Carlo dynamically weighted importance sampling for Spatial models with intractable normalizing constants. J Phys. Conf. Ser. **197**, 1742–6596 (2009)
12. Friswell, M.I.: Generation of validated structural dynamic models – results of a benchmark study utilizing the GARTEUR SM-AG19 testbed. Mech. Syst. Signal Process. **17**(1), 9–20 (2003). COST action special issue
13. Degener, M., Hermes, M.: Ground vibration test and finite element analysis of the GARTEUR SM-AG 19 testbed, Deutshe Forschunsanstalt fur luft und Raumfahrt e.V Institut fur Aeroelastic, IB 232-96 J 08 (1996)
14. Haario, H., Saksman, E., Tamminen, J.: An adaptive Metropolis algorithm. Bernoulli **7**, 223–242 (2001)

Chapter 28
A Finite Element Model Updating Method Considering Environmental Impacts

Shanglian Zhou and Wei Song

Abstract Many researchers have observed a strong correlation between variation in structural modal properties and environmental change especially temperature fluctuation. The environmental variability of modal properties might cause uncertainties in modal properties identification. Therefore in vibration-based damage detection field, a practical issue is to discriminate temperature-induced changes in modal properties from those caused by structural damage. Currently, several techniques have been developed to help eliminate the temperature influence, such as using a linear filter to separate the temperature effects. Meanwhile, detailed studies on the influence from other environmental factors, for instance, boundary condition change, are lacking. This paper proposes a novel finite element (FE) method that can consider temperature and boundary condition change, and brings insight to how environment factors influence structural modal properties and how to consider them in the model updating process. In the proposed method, temperature and boundary condition information is incorporated into stiffness formulation of the FE model. A numerical example of damage detection on a pedestrian bridge with several damage scenarios combined with environmental variation is presented to demonstrate the effectiveness of the proposed method. Also, the sensitivity range of each updating parameter is discussed in details.

Keywords Temperature • Boundary condition • Model updating • Damage detection • Sensitivity

28.1 Introduction

Structural health monitoring (SHM) and condition assessment has been an important and popular topic for decades [1–4]. As critical level of structural damage can impair structural serviceability or even pose as a threat to general public, it is vital that structural defects and damage can be detected at early stage. Only when the initial structural damage is quickly identified and prevented through effective maintenance can the structure stay healthy as well as reliable. In damage identification field, people have developed many techniques, incorporating visual inspection, X-ray inspection, vibration-based and acoustic-based detection, etc. However, some of these methods may require visibility of the damage, accessibility to the vicinity of the damage and prior knowledge of its location. Hence their applicability and efficiency on early damage detection is limited especially when the structure has complicated details or when the damage is not directly visible or develops rapidly.

In recent years, vibration-based SHM by model updating has risen as a novel non-destructive damage detection technique and gained its worldwide popularity and sound reputation due to its wide applicability, "global" perspective, high accuracy and time efficiency [5]. The effectiveness of this technique in detecting, localizing and quantifying the structure damage has been widely demonstrated through various applications and numerical studies. Teughels and De Roeck [5] performed model updating on the Z24 Bridge, and identified the damage pattern using the natural frequencies and mode shape data obtained from ambient vibration. Jaishi and Ren [6] proposed a FE model updating method using the modal flexibility residual and demonstrated its capability of identifying the damage pattern in a simply supported concrete beam.

Because the measured modal properties of a structure are directly related to its physical properties (stiffness, mass and damping ratio), changes in the physical properties due to structural damage, such as stiffness reduction resulting from cracks formation or member disconnection, will subsequently cause changes in the structure's dynamic properties. The basic idea of vibration-based damage detection technique is to identify the structural damage through variation in modal properties (namely natural frequency, mode shape and modal damping). By comparing discrepancies in modal properties of the damaged and healthy FE model, both the damage extent and location can be identified.

S. Zhou • W. Song (✉)

Department of Civil, Construction and Environmental Engineering, The University of Alabama, Tuscaloosa, AL 35487, USA

e-mail: wsong@eng.ua.edu

One critical challenge in vibration-based damage detection method is the uncertainty in natural frequency and mode shape measurement due to environmental change. Temperature, as one of the major environmental factors, may lead to changes in dynamic properties (mostly natural frequency) up to a significant level. Sometimes, it is even comparable to those caused by medium structural damage or service level loads [7]. Researchers in Los Alamos National Laboratory [3] reported that the first natural frequency of the Alamosa Canyon Bridge varied about 4.7 % during a 24-hour period as the temperature of the bridge deck changed by approximately 22 °C. In Europe, Peeters and De Roeck [8] monitored the Z24 Bridge during one-year period and reported that the environmental changes caused 14–18 % variation of the first four natural frequencies. Xia et al. [9] performed a long term vibration monitoring on a reinforced concrete slab, and observed that the first two natural frequencies decreased by 0.23 % when temperature increased by 1 °C. In a more recent study [10] on the Tamar Bridge in England, the frequency of the first lateral symmetric mode of the deck varied by approximately 4.5 % as the temperature changed by 20 °C. In these observations, the natural frequency change caused by temperature variation is almost on the same scale as caused by medium level damage. In general, influence by temperature can be categorized into two mechanisms: one is affecting the material property (notably elastic modulus); the other is creating thermomechanical load. Both the elastic modulus variation and thermomechanical effects can induce changes in structure's stiffness, resulting in natural frequency and mode shape changes. If not properly addressed, these uncertainties in modal properties due to temperature variation will be misinterpreted as potential structural damage, thus conveying wrong message to damage identification and SHM. As a result, the efficacy and accuracy of the damage identification result will be compromised.

As another contributing environmental factor, boundary condition (more specifically, the support constraints of the structure) is usually assumed unchanged for simplicity in some studies. However, the influence from changes in boundary conditions such as support settlement and consolidation of the surrounding soil may lead to long term variation in modal properties. Several literatures implied the influences from boundary change. It is observed that in the Z24 Bridge monitoring [8] the natural frequency of the Z24 Bridge increased significantly when temperature dropped below freezing point, which may be a consequence of the surrounding frozen soil layers. Variation in boundary conditions can be modeled as stiffness change in both translational spring and rotational spring at the support. This study mainly considers support rotational stiffness change as the major form of boundary variation.

This study presents a novel FE updating method that can consider temperature induced modal property change as well as boundary condition induced change in damage identification. A numerical example of conducting damage detection on a pedestrian bridge with several damage scenarios combined with environmental variations is presented to demonstrate the effectiveness of the proposed method. Also, the sensitivity range of each updating parameter is discussed in details.

28.2 Theoretical Background

- Relationship between temperature and elastic modulus

  Elastic stiffness $\mathbf{K}_e$ is affected by temperature induced change in elastic modulus E. A linear equation between temperature and steel elastic modulus is adopted here for simplicity:

$$E(T) = E_{20\,°C}\left[1 - \theta_E\left(T - 20\right)\right] \tag{28.1}$$

  Where T is the material temperature, θ_E is the temperature coefficient of elastic modulus, $E_{20\,°C}$ is the elastic modulus at 20 °C.

- Thermoelasticity and axial loading

  Temperature change will cause thermal deformation in material. Depending on the boundary condition of the structure, material thermal deformation will generate thermomechanical load and displacement in the structure. Material thermal deformation is usually characterized by a linear relationship as:

$$\delta(T) = \theta_T \cdot \Delta T \tag{28.2}$$

  Where θ_T is coefficient of thermal expansion (CTE) and ΔT is the change of temperature.

  It is well known from structural analysis [11] that, thermal deformation in indeterminate frames generates axial forces as Eq. (28.3). The axial force N will then affect the geometric stiffness $\mathbf{K}_g$.

$$N(T) = E(T) \cdot A \cdot \delta(T) = E(T) \cdot A \cdot \theta_T \cdot \Delta T \tag{28.3}$$

- Elastic and geometric stiffness

Fig. 28.1 A structure with
rotational spring support
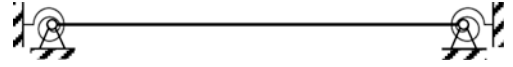
Structures are designed to experience a variety of loading conditions during their service time. The behavior of a structure is determined by not only the associated material properties and geometries but also its loading condition. In the general formulation of FE method, the (tangent) stiffness matrix **K** of a frame structure under loading can be expressed as [12, 13] (detailed formulation for each term is not provided here for simplicity):

$$
\begin{aligned}
\mathbf{K} &= \mathbf{K}_e + \mathbf{K}_L \\
&= \mathbf{K}_e + \left(\mathbf{K}_g + \mathbf{K}_d + \mathbf{K}_b \right)
\end{aligned}
\tag{28.4}
$$

In Eq. (28.4), $\mathbf{K}_e$ indicates the typical elastic stiffness matrix that is independent of loading condition; $\mathbf{K}_L = \mathbf{K}_g + \mathbf{K}_d + \mathbf{K}_b$ is the stiffness related to loading and deformation, where $\mathbf{K}_g$ is the geometric stiffness due to stress stiffening effect caused by the axial load in slender members, $\mathbf{K}_d$ is the stiffness due to large deflection (rigid-body motion) effect, and $\mathbf{K}_b$ is the stiffness due to large deformation (strain) effect. It is readily observed that all three terms contributing to $\mathbf{K}_L$ are related to loading condition of the structure. In SHM study, typically only low-level ambient vibrations will be considered. Stiffness related to large deflection and deformation ($\mathbf{K}_d$ and $\mathbf{K}_b$) is negligible in this case, and therefore only $\mathbf{K}_e$ and $\mathbf{K}_g$ will be considered. In the proposed study, the stiffness **K** of the structure under investigation can be simplified as Eq. (28.5). Two mechanisms are considered to account for the temperature influence on $\mathbf{K}_e$ and $\mathbf{K}_g$: (1) temperature T induced change in $\mathbf{K}_e(T)$; and (2) thermomechanical load caused change in $\mathbf{K}_g[N(T)]$.

$$
\mathbf{K} = \mathbf{K}_e + \mathbf{K}_g
\tag{28.5}
$$

- Boundary condition

To consider the influence from unknown varying boundary conditions, zero-length massless spring elements with rotational stiffness at each support (Fig. 28.1) are employed. The spring elemental stiffness matrix is given as:

$$
\mathbf{K}(k) = k \cdot
\begin{bmatrix}
1 & -1 \\
-1 & 1
\end{bmatrix}
\tag{28.6}
$$

Where k is the rotational stiffness; each row and column corresponds to the rotational degree of freedom (DOF) of a node.

- Vibration-based model updating method

In this study, a nonlinear optimization scheme is applied to the model updating process, for the purpose of identifying both structural damage and boundary conditions under environmental impacts. In the following session, updating parameters, objective function and optimization algorithm are discussed.

(1) Updating parameter

Stiffness reduction is usually interpreted as an indicator of damage occurrence. In the proposed FE model updating method, the stiffness matrix is a function of elemental elastic modulus, axial load, and support rotational stiffness, which are related to structural damage, thermomechanical load, and support boundary condition, respectively. The updating parameters are defined as follows:

$$
E_i = \left(1 - d_i^E \right) E_0 \quad N_i = d_i^N N_0 \quad R_j = d_j^R R_0
\tag{28.7}
$$

Where E_0 is the initial undamaged elastic modulus, N_0 is the reference axial force, and R_0 is the reference rotational stiffness. Detailed definitions on the reference values E_0, N_0 and R_0 depend on the specific cases. d_i^E and d_i^N are the updating parameters of elastic modulus and axial force for the ith beam element, respectively; d_j^R is the updating parameter of rotational stiffness for the jth spring element; E_i, N_i are the actual elastic modulus and axial force of the ith beam element; R_j is the actual rotational stiffness of the jth spring element. The lower and upper bound of the parameter set $\boldsymbol{d} = \left\{ \left[d^E \right], \left[d^N \right], \left[d^R \right] \right\}$ has to be specified prior to the updating process.

With the implementation of the updating parameter set $\boldsymbol{d} = \left\{ \left[d^E \right], \left[d^N \right], \left[d^R \right] \right\}$, the dynamic properties of the FE model are uniquely determined by $\boldsymbol{d}$. The initial parameter set of the model is denoted as $\boldsymbol{d}_{ini}$. Then a simulated damage scenario is applied to the FE model with its parameter denoted as $\boldsymbol{d}_{ref}$. The goal is to minimize the discrepancies between the updated model and the damaged model (served as reference) based on a predefined similarity criterion

referred to as the objective function and a specified nonlinear optimization scheme. As the objective function reaches its optimal value, a maximum correlation between the updated model and the simulated reference model is obtained.

(2) Objective function

Objective function depicts the discrepancy between the updated and reference FE model. Selection of the objective function for model updating can vary, although the same dynamic information is used. It is worth noting that natural frequency alone does not provide spatial information of a structure [14], therefore mode shape has to be implemented into the objective function formulation as well. Researchers have formulated various objective functions using information from both natural frequencies and mode shapes, among which the modal flexibility residual [15] has been reported to have particularly high sensitivity in terms of damage quantification [6, 16]. The modal flexibility matrix $\boldsymbol{F}$ is formulated as:

$$\boldsymbol{F} = \boldsymbol{K}^{-1} = \left(\boldsymbol{\Phi}^{-T} \boldsymbol{\Lambda} \boldsymbol{\Phi}^{-1}\right)^{-1} = \boldsymbol{\Phi} \boldsymbol{\Lambda}^{-1} \boldsymbol{\Phi}^{T} \tag{28.8}$$

Where $\boldsymbol{\Lambda}$ = eigenvalue matrix; $\boldsymbol{\Phi}$ = mass normalized mode shape matrix ($\boldsymbol{\Phi}^T \boldsymbol{M} \boldsymbol{\Phi} = \boldsymbol{I}$); $\boldsymbol{K}$ = stiffness matrix; $\boldsymbol{M}$ = mass matrix.

Several assumptions are made in the proposed method: (1) damage is directly related to stiffness reduction in the member; and (2) structural damage doesn't change the mass matrix. The modal flexibility matrix $\boldsymbol{F}$ is a function of the updating parameter set $\boldsymbol{d}$. Then the optimization problem can be stated as Eq. (28.9). As the objective function reaches minimum value, the predicted updating parameter set $\boldsymbol{d}$ will approach the reference set $\boldsymbol{d}_{ref}$.

$$\min_{\boldsymbol{d}} \boldsymbol{\Pi} \left(\boldsymbol{d}\right) = \frac{|| \boldsymbol{F} \left(\boldsymbol{d}\right) - \boldsymbol{F} \left(\boldsymbol{d}_{ref}\right) ||_{fro}^{2}}{|| \boldsymbol{F} \left(\boldsymbol{d}_{ini}\right) - \boldsymbol{F} \left(\boldsymbol{d}_{ref}\right) ||_{fro}^{2}} \tag{28.9}$$

Where $\| \cdot \|_{fro}$ denotes the Frobenius norm.

(3) Optimization algorithm

A trust region-based optimization algorithm is applied in this study to help solve the original optimization problem. The formulation at iterative step k can be written as [17]:

$$\min_{\Delta \boldsymbol{d}^k} \boldsymbol{\Pi} \left(\boldsymbol{d}^k + \Delta \boldsymbol{d}^k\right) = \boldsymbol{\Pi} \left(\boldsymbol{d}^k\right) + \nabla \boldsymbol{\Pi} \left(\boldsymbol{d}^k\right)^T \cdot \Delta \boldsymbol{d}^k + \frac{1}{2} \Delta \boldsymbol{d}^{kT} \cdot \nabla^2 \boldsymbol{\Pi} \left(\boldsymbol{d}^k\right) \cdot \Delta \boldsymbol{d}^k \tag{28.10}$$

Subject to

$$|| \Delta \boldsymbol{d}^k || \leq \delta_k \cdots \cdot \text{"trust region"} \tag{28.11}$$

In this study, the "trust region" optimization algorithm is implemented in MATLAB 2014a Optimization Toolbox.

28.3 Numerical Study

In this session, a pedestrian bridge FE model is implemented. Sensitivity of the modal flexibility matrix to the variation of each type of updating parameter is discussed. Then, a set of damage scenarios combined with temperature influence and boundary condition change is applied to the bridge model. Two numerical cases are examined: (1) when the axial force is already measured, the proposed method only updates d^E and d^R; (2) when the axial force is unknown, the proposed method updates d^E, d^R, and d^N.

- Bridge FE model implementation

Figure 28.2 shows a pedestrian bridge located at the University of Alabama campus. A corresponding FE model (Fig. 28.3) is constructed in MATLAB for damage detection purpose. The model is discretized into 67 beam elements and 2 spring elements. Detailed model properties are shown in Tables 28.1 and 28.2. Assuming the bridge was built during winter at 0 °C when no thermomechanical load was imposed, now the temperature in different members of the bridge varies from 46 to 50 °C. The ambient temperature profile of the bridge is illustrated in Fig. 28.4.

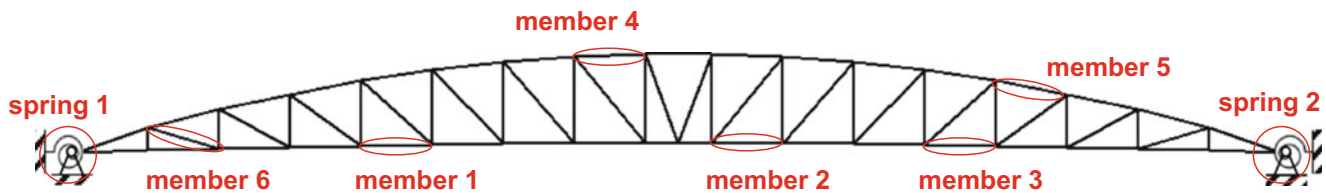**Fig. 28.2** A pedestrian bridge located at the University of Alabama campus

Fig. 28.3 Bridge FE model

Table 28.1 Section properties of the bridge model

Beam members	Horizontal members	Arch members	Vertical members	Skewed members
Steel section	HSS 8 × 6 × 3/8	HSS 8 × 8 × 3/8	HSS 8 × 6 × 3/8	HSS 4 × 2 × 3/16

Table 28.2 Material properties of the bridge model

Bridge material	Elastic modulus at 20 °C	Coefficient of thermal expansion	Temperature coefficient of elastic modulus
A36 Steel	$E_{20\,°C} = 200$ Gpa	$\theta_T = 1 \times 10^{-5}\ 1/°C$	$\theta_E = 3.6 \times 10^{-4}\ 1/°C$
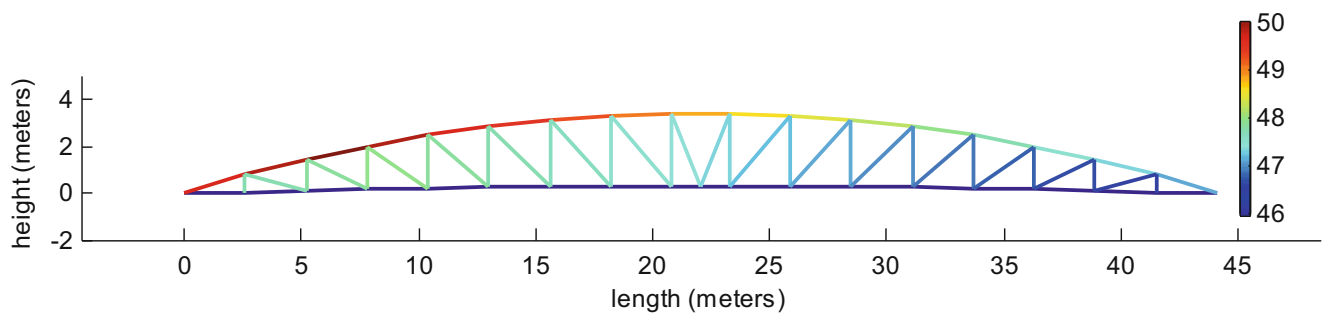
Fig. 28.4 Ambient temperature of the bridge

A set of damage scenarios combined with temperature influence and boundary condition change is applied to the bridge FE model. First ten modes are used to form the modal flexibility matrix. For simplicity, only eight elements (red circled in Fig. 28.3) are selected to participate in the optimization.

- Sensitivity range of the updating parameters

To investigate if the nonlinear optimization process will be trapped by local minimum, a sensitivity range of each type of updating parameter is examined. In other words, the proposed method will have guaranteed performance if the reference updating parameter set d_{ref} is within the sensitivity range. In this numerical study, sensitivity range of each updating parameter d is defined as a region in which the variation of d leads to significant change in the modal flexibility matrix F.

To detect the sensitivity of the modal flexibility matrix to the variation of different updating parameters, the following criterion is defined:

$$\text{sensitivity} = \frac{|| F(d) - F(d_{ref}) ||_{fro}}{|| F(d_{ref}) ||_{fro}} \tag{28.12}$$

In the sensitivity study, the reference rotational stiffness of jth spring element is the summation of the rotational stiffness from the adjacent beam member i and j, expressed as $R_0 = 4EI_i/l_i + 4EI_j/l_j$. For i^{th} beam element, the reference elastic modulus E_0 is calculated by Eq. (28.1) and the reference axial force is $N_0 = 4\pi^2 EI_i/l_i^2$. I_i and l_i denote the moment of inertia and elemental length of the ith beam element, respectively.

(1) sensitivity range of d_i^E

In order to explore the sensitivity range of d_i^E, the updating parameter set d_{ref} and d is defined as Eqs. (28.13) and (28.14):

$$d_{ref} = \left\{ \left[d^E \right], \left[d^N \right], \left[d^R \right] \right\} = \left\{ [\mathbf{0}]_{1\times6} \ [\mathbf{1}]_{1\times6} \ [\mathbf{1}]_{1\times2} \right\} \tag{28.13}$$

$$d = \left\{ \left[d^E \right], \left[d^N \right], \left[d^R \right] \right\} = \left\{ \left[0 \ 0 \ \cdots \ d_i^E \ \cdots 0 \ 0 \right]_{1\times6} \ [\mathbf{1}]_{1\times6} \ [\mathbf{1}]_{1\times2} \right\} \tag{28.14}$$

A sensitivity plot is generated for $d_i^E \in (0, 0.999)$. As shown in Fig. 28.5, a clear uprising trend of the curve along the entire region is observed, which indicates that the modal flexibility matrix F is sensitive to variation of d_i^E within the range (0, 0.999).
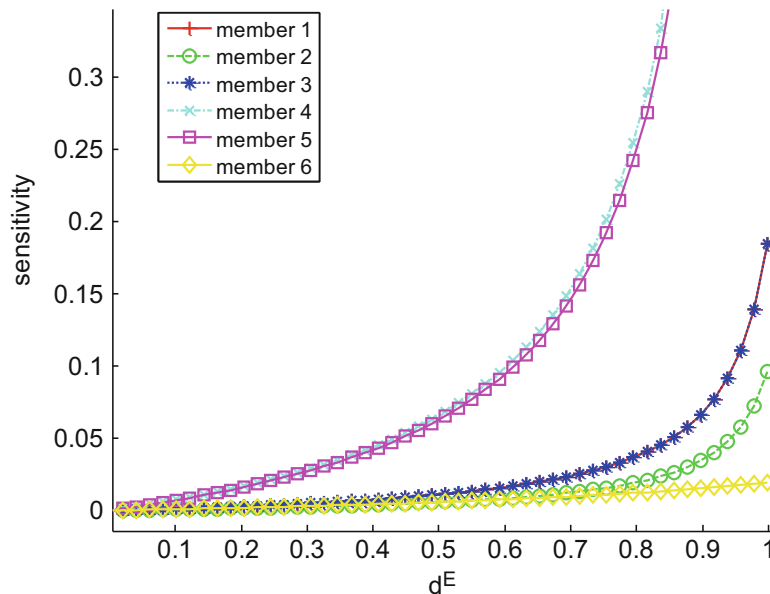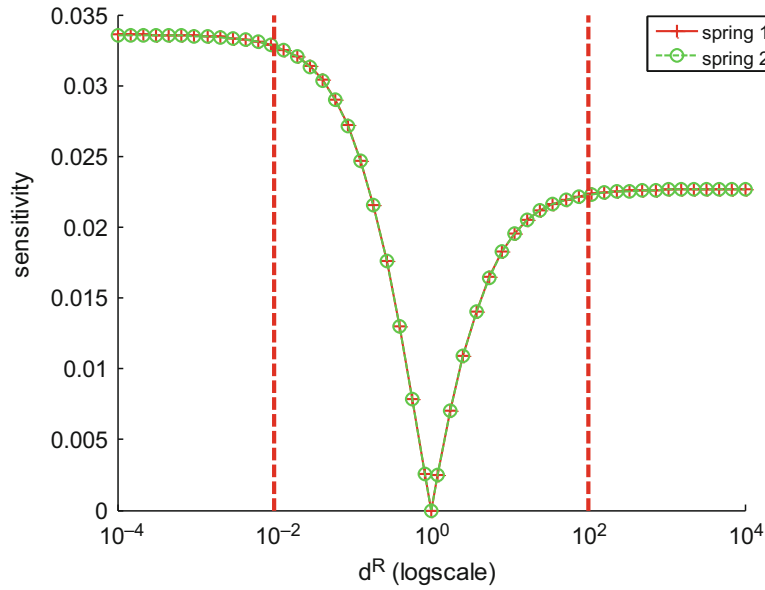

Fig. 28.5 Sensitivity plot of d_i^E

Fig. 28.6 Sensitivity plot of d_i^R

(2) sensitivity range of d_i^R

The updating parameter set is formulated as Eq. (28.15). Figure 28.6 is the corresponding sensitivity plot. It can be seen that the curve becomes flat when $d_i^R \geq 10^2$ and $d_i^R \leq 10^{-2}$, which means any change of d^R in that region will not induce significant variation in the modal flexibility matrix $\boldsymbol{F}$. Hence in the subsequent model updating, the sensitivity range of d_i^R is set as $(10^{-2}, 10^2)$. As $d_i{}^R$ increases, the end constraint pattern shifts from a hinged end to a fixed one.

$$\boldsymbol{d} = \{[d^E], [d^N], [d^R]\} = \{[\boldsymbol{0}]_{1\times6} \, [\boldsymbol{1}]_{1\times6} \, [\,1 \, \cdots \, d_i^R\,]_{1\times2}\} \tag{28.15}$$

(3) sensitivity range of d_i^N

The updating parameter set is formulated as Eq. (28.16). When $d_i^N > 0$, it is evident from Fig. 28.7 that only within $d_i^N \in (10^{-2}, 10^2)$ can the modal flexibility matrix be significantly influenced by d_i^N. When $d_i^N < 0$, the most sensitive range for detection (shown in Fig. 28.8) is $d_i^N \in (-0.9, -0.1)$.

$$\boldsymbol{d} = \{[d^E], [d^N], [d^R]\} = \{[\boldsymbol{0}]_{1\times6} \, [\,1 \, 1 \, \cdots \, d_i^N \, \cdots \, 1 \, 1\,]_{1\times6} \, [\boldsymbol{1}]_{1\times2}\} \tag{28.16}$$

- Model updating result

(1) Case I: only update d^E and d^R

If information about axial force is readily available, for instance, through strain gage measurement, then this method can directly update the elastic modulus in each member and spring rotational stiffness. In this case, the actual axial force is used to form the modal flexibility matrix. The updating parameter set consists of eight entries, as expressed in Eq. (28.17). The reference updating parameter set $\boldsymbol{d}_{ref}$ is selected such that each parameter resides in its sensitive range. The lower bound and upper bound for each type of updating parameter is set as $d_i^E \in (0, 0.999)$, $d_i^R \in (10^{-2}, 10^2)$.

$$\boldsymbol{d} = \{d_1^E \, d_2^E \, d_3^E \, d_4^E \, d_5^E \, d_6^E \, d_1^R \, d_2^R\} \tag{28.17}$$
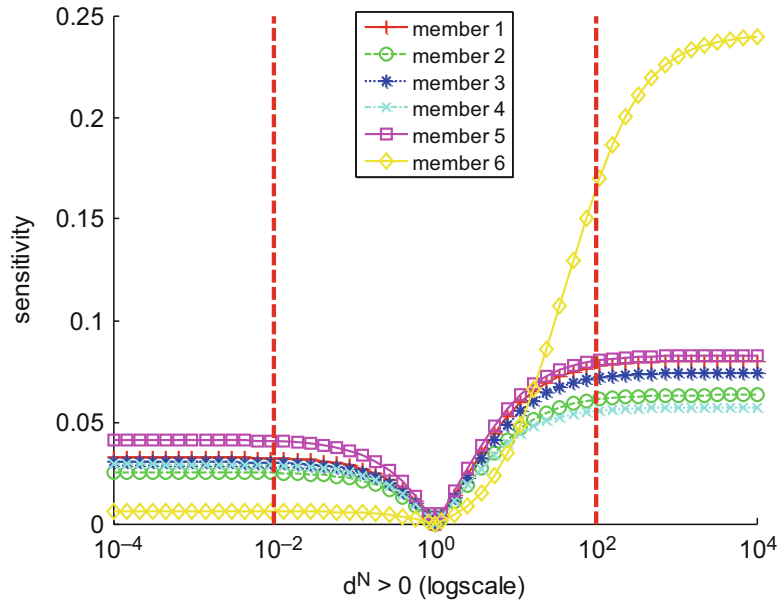
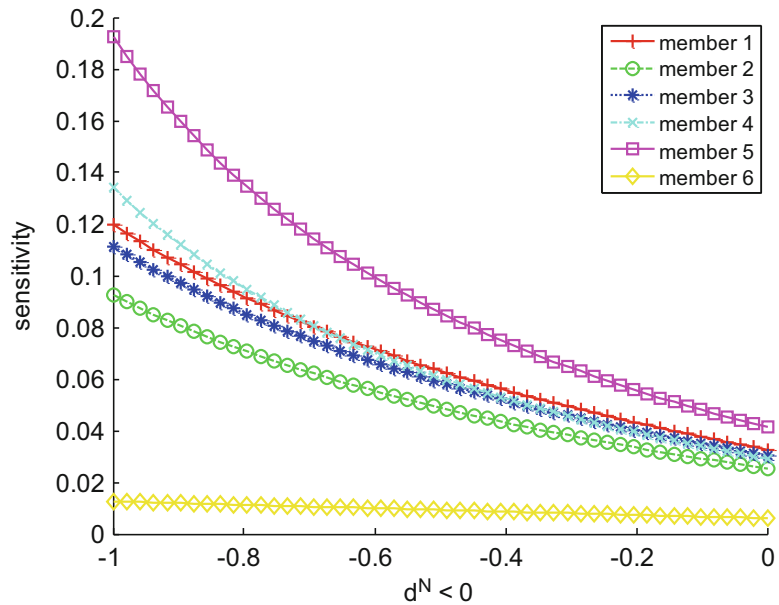**Fig. 28.7** Sensitivity plot of $d_i^N > 0$

Fig. 28.8 Sensitivity plot of $d_i^N < 0$

Equation (28.18) is used to evaluate the relative difference between each updated and reference updating parameter. Relative differences of d^E and d^R are demonstrated in Fig. 28.9. Table 28.3 provides the detailed simulation results. From Fig. 28.9, among all six damage scenarios, the maximum relative difference of the updating parameters is within 0.01 %, which indicates the damage pattern is identified with high accuracy.

$$\text{relative difference} = \frac{d - d_{ref}}{d_{ref}} \times 100\ \% \qquad (28.18)$$

(2) Case II: update d^E, d^R and d^N

Assuming only temperature data (Fig. 28.4) is available, the equilibrium condition is solved to obtain the axial force of the bridge. As six more updating parameters of axial force are introduced to the optimization, total 14
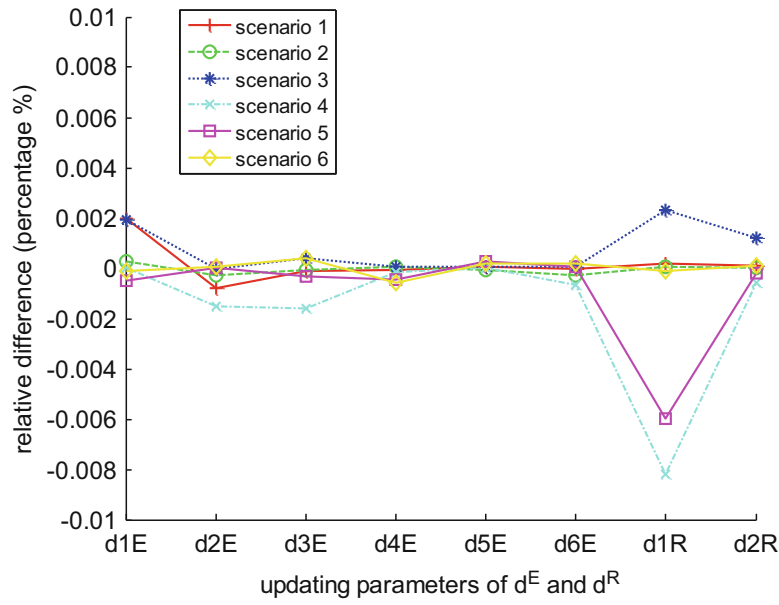
Fig. 28.9 Relative difference of d^E and d^R for case I

Table 28.3 Model updating results for case I

Scenario	d	d_1^E	d_2^E	d_3^E	d_4^E	d_5^E	d_6^E	d_1^R	d_2^R
	d_{ini}	0	0	0	0	0	0	1	1
1	d_{ref}	0.0450	0.1540	0.3350	0.0980	0.1760	0.2520	20.0000	11.5000
	$d_{updated}$	0.0450	0.1540	0.3350	0.0980	0.1760	0.2520	20.0000	11.5000
2	d_{ref}	0.1152	0.0943	0.2082	0.0634	0.0293	0.0909	20.5051	6.1691
	$d_{updated}$	0.1152	0.0943	0.2082	0.0634	0.0293	0.0909	20.5051	6.1691
3	d_{ref}	0.0287	0.3959	0.1421	0.1674	0.1158	0.0737	36.6667	23.3759
	$d_{updated}$	0.0287	0.3959	0.1421	0.1674	0.1158	0.0737	36.6675	23.3761
4	d_{ref}	0.2142	0.0810	0.1129	0.1791	0.2175	0.0805	39.8990	15.3993
	$d_{updated}$	0.2142	0.0810	0.1129	0.1791	0.2175	0.0805	39.8957	15.3992
5	d_{ref}	0.0926	0.3518	0.2487	0.0673	0.0395	0.1552	59.2929	4.4806
	$d_{updated}$	0.0926	0.3518	0.2487	0.0673	0.0395	0.1552	59.2894	4.4806
6	d_{ref}	0.1075	0.1681	0.0366	0.0160	0.0539	0.0160	10.0000	0.0261
	$d_{updated}$	0.1075	0.1681	0.0366	0.0160	0.0539	0.0160	10.0000	0.0261

updating parameters (shown in Eq. (28.19)) are updated in this case. The lower bound and upper bound of the axial updating parameter is $d_i^N \in (-0.999, 100)$. The relative differences of d^E, d^R and d^N are presented in Figs. 28.10 and 28.11, respectively. Detailed updating results are shown in Table 28.4. From Fig. 28.10, most of the relative differences of d^E and d^R are less than 1 %, meanwhile the maxima are within 5 %, which suggests the damage pattern in different scenarios is detected with good accuracy. In the axial force updating results (shown in Fig. 28.11), the fourth and fifth d_i^N parameters have more errors than others, because the corresponding axial forces are too small to cause any significant changes in the objective function. In other words, the damage detection results are barely influenced by changes in d_4^N and d_5^N parameters, because the underlying d_4^N and d_5^N are outside of the sensitivity ranges defined above. When the updating parameters are within the sensitive ranges, the performance of this damage detection method can be guaranteed.

$$d = \{d_1^E\ d_2^E\ d_3^E\ d_4^E\ d_5^E\ d_6^E\ d_1^N\ d_2^N\ d_3^N\ d_4^N\ d_5^N\ d_6^N\ d_1^R\ d_2^R\} \tag{28.19}$$
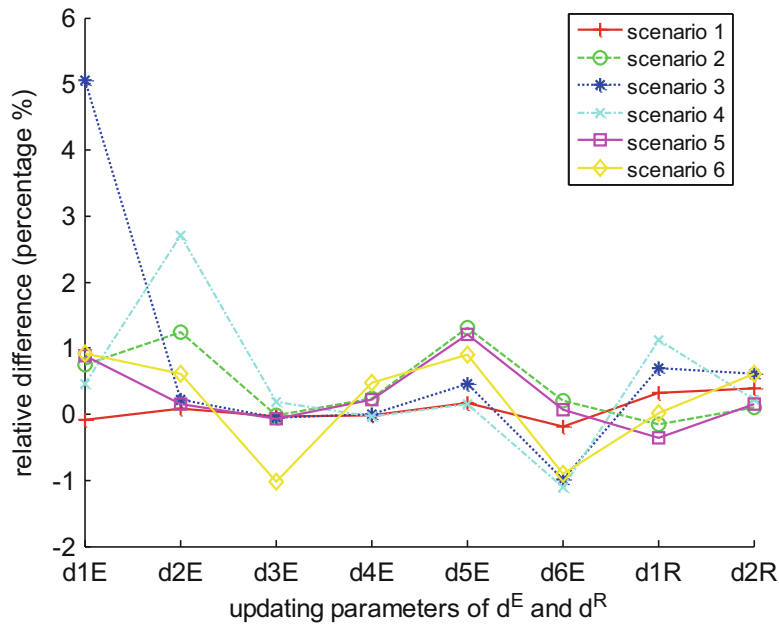
Fig. 28.10 Relative difference of d^E and d^R for case II
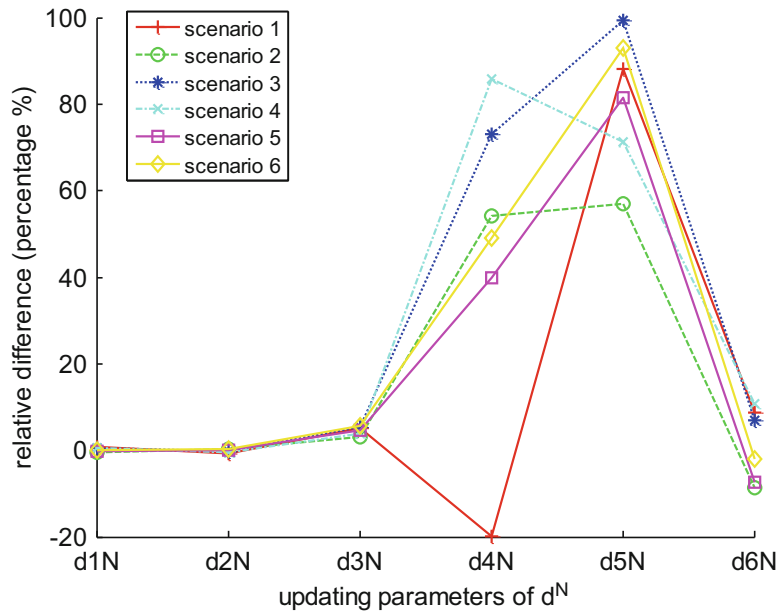

Fig. 28.11 Relative difference of d^N for case II

28.4 Conclusion

A novel FE model updating method is proposed to update FE model that can consider environmental impacts and boundary conditions. Numerical example demonstrates that the proposed method is capable of identifying the damage pattern of a pedestrian bridge while considering temperature and boundary condition influence. Also, the sensitivity range of each type of updating parameter is discussed and presented. The results have shown that successful damage identification requires an objective function which contains essential modal information, a robust optimization algorithm, and updating parameters need to reside in a range where the corresponding parameters are sensitive with respect to the objective function.

Table 28.4 Model updating results for case II

Scenario	d	d_1^E	d_2^E	d_3^E	d_4^E	d_5^E	d_6^E	d_1^N	d_2^N	d_3^N	d_4^N	d_5^N	d_6^N	d_1^R	d_2^R
	d_{ini}	0	0	0	0	0	0	0	0	0	0	0	0	1	1
1	d_{ref}	0.0450	0.1540	0.3350	0.0980	0.1760	0.2520	−0.1038	−0.0338	−0.0151	−0.0002	−0.0009	−0.0528	20.0000	11.5000
	$d_{updated}$	0.0450	0.1541	0.3349	0.0980	0.1763	0.2515	−0.1045	−0.0336	−0.0159	−0.0001	−0.0017	−0.0574	20.0651	11.5444
2	d_{ref}	0.1152	0.0943	0.2082	0.0634	0.0293	0.0909	−0.0495	−0.0634	−0.0279	0.0011	−0.0031	−0.0612	20.5051	6.1691
	$d_{updated}$	0.1161	0.0955	0.2082	0.0636	0.0297	0.0911	−0.0493	−0.0635	−0.0288	0.0017	−0.0049	−0.0560	20.4737	6.1759
3	d_{ref}	0.0287	0.3959	0.1421	0.1674	0.1158	0.0737	−0.1264	−0.0108	−0.0286	−0.0005	−0.0019	−0.0638	36.6667	23.3759
	$d_{updated}$	0.0302	0.3968	0.1420	0.1674	0.1164	0.0730	−0.1271	−0.0108	−0.0301	−0.0009	−0.0038	−0.0683	36.9235	23.5178
4	d_{ref}	0.2142	0.0810	0.1129	0.1791	0.2175	0.0805	−0.0259	−0.0703	−0.0483	0.0002	−0.0008	−0.0577	39.8990	15.3993
	$d_{updated}$	0.2152	0.0832	0.1131	0.1790	0.2179	0.0796	−0.0260	−0.0700	−0.0502	0.0004	−0.0014	−0.0640	40.3484	15.4327
5	d_{ref}	0.0926	0.3518	0.2487	0.0673	0.0395	0.1552	−0.0743	−0.0209	−0.0286	0.0019	−0.0005	−0.0668	59.2929	4.4806
	$d_{updated}$	0.0935	0.3523	0.2486	0.0674	0.0399	0.1553	−0.0741	−0.0209	−0.0300	0.0026	−0.0009	−0.0619	59.0856	4.4872
6	d_{ref}	0.1075	0.1681	0.0366	0.0160	0.0539	0.0160	−0.0335	−0.0237	−0.1044	0.0076	0.0047	−0.0518	10.0000	0.0261
	$d_{updated}$	0.1085	0.1691	0.0363	0.0161	0.0544	0.0158	−0.0335	−0.0237	−0.1102	0.0113	0.0091	−0.0507	10.0014	0.0263

References

1. Cornwell, P., Farrar, C.R., Doebling, S.W., Sohn, H.: Environmental variability of modal properties. Exp. Tech. **23**(6), 45–48 (1999)
2. Peeters, B., Maeck, J., De Roeck, G.: Vibration-based damage detection in civil engineering: excitation sources and temperature effects. Smart Mater. Struct. **10**(3), 518 (2001)
3. Sohn, H., Dzwonczyk, M., Straser, E.G., Kiremidjian, A.S., Law, K.H., Meng, T.: An experimental study of temperature effect on modal parameters of the Alamosa Canyon Bridge. Earthq. Eng. Struct. Dyn. **28**, 879–897 (1999)
4. Teughels, A., De Roeck, G.: Damage assessment of the Z24 Bridge by FE model updating. Key Eng. Mater. **245**, 19–26 (2003)
5. Teughels, A., De Roeck, G.: Structural damage identification of the highway bridge Z24 by FE model updating. J. Sound Vib. **278**(3), 589–610 (2004)
6. Jaishi, B., Ren, W.X.: Damage detection by finite element model updating using modal flexibility residual. J. Sound Vib. **290**(1), 369–387 (2006)
7. Xu, Y.L., Chen, B., Ng, C.L., Wong, K.Y., Chan, W.Y.: Monitoring temperature effect on a long suspension bridge. Struct. Control. Health Monit. **17**, 632–653 (2010)
8. Peeters, B., De Roeck, G.: One-year monitoring of the Z 24-Bridge: environmental effects versus damage events. Earthq. Eng. Struct. Dyn. **30**(2), 149–171 (2001)
9. Xia, Y., Hao, H., Zanardo, G., Deeks, A.: Long term vibration monitoring of an RC slab: temperature and humidity effect. Eng. Struct. **28**(3), 441–452 (2006)
10. Cross, E.J., Koo, K.Y., Brownjohn, J.M.W., Worden, K.: Long-term monitoring and data analysis of the Tamar Bridge. Mech. Syst. Signal Process. **35**(1), 16–34 (2013)
11. Leet, K.M., Uang, C.M., Gilbert, A.M.: Fundamentals of Structural Analysis, 4th edn. McGraw Hill, New York (2011)
12. Oran, C.: Tangent stiffness in plane frames. J Struct. Div. **99**(6), 973–985 (1973)
13. Wood, R.D., Zienkiewicz, O.C.: Geometrically nonlinear finite element analysis of beams, frames, arches and axisymmetric shells. Comput. Struct. **7**(6), 725–735 (1977)
14. Salawu, O.S.: Detection of structural damage through changes in frequency: a review. Eng. Struct. **19**(9), 718–723 (1997)
15. Aktan, A.E., Lee, K.L., Chuntavan, C., Aksel, T.: Modal testing for structural identification and condition assessment of constructed facilities. In: Proceedings of the 12th International Modal Analysis Conference, Honolulu, Hawaii, pp. 462–468 (1994)
16. Jaishi, B., Ren, W.X.: Structural finite element model updating using ambient vibration test results. J. Struct. Eng. **131**(4), 617–628 (2005)
17. Moré, J.J.: Recent developments in algorithms and software for trust region methods. In: Bachem, A., Grotschel, M., Korte, G. (eds.) Mathematical Programming, the State of the Art, pp. 256–287, Springer, New York (1983)

Chapter 29
Redundant Information Rejection in Sensor Localisation Using System Gramians

Mladen Gibanica, Thomas J.S. Abrahamsson, and Daniel C. Kammer

Abstract Sensors placement is important in vibration testing. The method of effective independence, recently extended to account for triaxial sensors, is widely used for this purpose in case a finite element model of the structure is available. In this paper a criteria is added to reject redundant information that usually arises in symmetric structures or finite element models with high candidate sensor density. A sensor placement strategy is proposed in which, initially, the method of effective independence is used to select the best sensors from a candidate set by maximising the Fisher information matrix determinant. Next, the gramians of a balanced realisation is used to compare the information between systems consisting of only previously added sensors to the final set with systems of the previous and candidate sensors. Sensors with redundant information will have negligible effect on the gramian and can be rejected. The method is fast, as gramians of systems with only one or two outputs are evaluated. It is sub-optimal in the sense that all possible sensor placement combinations are not evaluated for optimality. A test case, consisting of a rectangular plate, is presented, but the method has been used on a large scale industrial model with good results.

Keywords Sensor placement • Effective independence • Balanced realisation • System gramians • Redundant information

29.1 Introduction

With today's complex industrial components it is very important to perform a thorough pretest planning before an experimental campaign to ensure that all important system characteristics are captured by the experiment. In experimental modal analysis it is common to use accelerometers to measure the system responses, and the pretest planning stage deals with how these sensors should be localised on the test object so that they maximise some information metric. For model updating problems, a reasonably accurate finite element (FE) model is usually available and used in the sensor localisation stage. One of the most popular methods, the method of effective independence (EfI), see [1], seeks to place sensors in an optimal fashion with respect to the Fisher information matrix (FIM) determinant with respect to modal response. The method places sensors so that the mode shapes linear independence and signal strength are maximised. It was later updated by Kammer and Tinker [2] to account for triaxial sensors and by Kammer [3] to allow for a user selected initial set of positions, and increased computational efficiency by iteratively adding sensors to a final set from a candidate set instead of removing sensors from the candidate set until the amount of sensors required is satisfied. The method has also been made more computationally effective by Li, Li and Fritzen in [4, 5] by utilising the relationship between the EfI and modal kinetic energy methods, and a downdating algorithm of the QR decomposed reduced modal matrix.

Observability and controllability gramian based methods have also been considered for sensor and actuator selection. In [6], Reynier and Abou-Kandil present two methods for sensor selection where one is a gramian based method ensuring observability of the system with the selected sensors. The method allows for independence between the number of selected

M. Gibanica (✉)
Applied Mechanics, Chalmers University of Technology, Hörsalsvägen 7A, S-41296 Göteborg, Sweden

Volvo Car Corporation, S-40531 Göteborg, Sweden
e-mail: mladen.gibanica@chalmers.se

T.J.S. Abrahamsson
Applied Mechanics, Chalmers University of Technology, Hörsalsvägen 7A, S-41296 Göteborg, Sweden

D.C. Kammer
Engineering Physics, University of Wisconsin - Madison, Madison, WI 53706, USA

sensors and modes. Other gramian based methods for actuator and sensor selection are mentioned in [7–9]. There exist many more methods for optimal sensor placement, far too many to mention in this paper.

With the increased complexity of (FE) models, including very dense meshes and complex geometries, it is not only increasingly difficult to make engineering judgement of sensor placement in a vibration test, but traditional methods, such as EfI, might not produce optimal results with respect to information uniqueness. It can be especially troublesome if the candidate set is badly selected. For example, dense meshes can pose a problem if two candidate locations are chosen very close to each other. If one particular node is very important, based on the EfI metric and another node very close to it is also available as a candidate, it too will be considered important based on the EfI metric. Thus both locations will be selected as they give almost identical information. Another problem arise for symmetric structures where information duplication might occur if the candidate set contains locations that are symmetric or nearly symmetric. This follows from the fact that a symmetric structure's modal data is also symmetric. Thus, there has lately been an interest in the information uniqueness in the final sensor set. For example Trendafilova, Heylen and Brussel [10] used the mutual information concept to select sensor positions that provided independent information without any information loss by minimising the average mutual information. On the other hand Stephan [11] used a two step approach by first letting the EfI method select the best sensor from a candidate set and then remove any sensors that share the same information. The last step is performed by comparing the normalised norm of the associated Fisher information of two sensors. In [11] Stephan argues that this measure only makes sense physically if the two sensors measure in the same direction. Such co-orientations are rare for systems with complex geometries where sensors usually measure normal to the attachment surface. This becomes even more complicated for triaxial sensors.

This paper addresses the problem of information uniqueness further by utilising the idea proposed by Stephan [11]. The sensor locations are first ranked by the EfI method and then rejected, if necessary, by using balanced realisation system gramians. A system with the best ranked sensor is compared to a system with the best ranked sensor and one previously added sensors to the final set. This procedure is performed iteratively until all previously added sensors have been tested against. It is argued that no consideration for the sensor measurement direction needs to be taken because the system observability between two sensor set configurations is compared. The method works for sensors of any number of measurement directions and the new bottom-up approach proposed by Kammer [3] is used.

In Sect. 29.2 the theoretical foundation is presented and Sect. 29.3 explains the implementation of the method. A simple rectangular plate is used as an example in Sect. 29.4 to showcase the method. Section 29.5 concludes the paper.

29.2 Theory

First some general theory about mechanical systems and system theory is presented, followed by a summary of the EfI method and then the gramian rejection metric.

29.2.1 Mechanical Systems Theory

The equations of motion for a mechanically vibrating system can be written as

$$\mathbf{M}\ddot{\mathbf{q}} + \mathbf{V}\dot{\mathbf{q}} + \mathbf{K}\mathbf{q} = \mathbf{f}(t) \tag{29.1}$$

where $\mathbf{M}$, $\mathbf{V}$ and $\mathbf{K} \in \mathbb{R}^{m \times m}$ represent the mass, damping and stiffness matrices, respectively. The general displacement vector is denoted by $\mathbf{q}$ and the external force vector by $\mathbf{f}(t)$. The dot notation is used for time differentiation. The full load vector can be mapped to the input vector $\mathbf{u} \in \mathbb{R}^{n_u}$ with the Boolean transformation matrix $\mathbf{U}$ as $\mathbf{f} = \mathbf{U}\mathbf{u}$. This system on second order form can be transformed to first order form by forming the state vector as $\mathbf{x} = [\mathbf{q}^T, \dot{\mathbf{q}}^T]^T$ and using the dummy equation $\mathbf{I}\dot{\mathbf{q}} - \mathbf{I}\dot{\mathbf{q}} = 0$ which gives

$$\begin{cases} \dot{\mathbf{x}} = \mathbf{A}\mathbf{x} + \mathbf{B}\mathbf{u} \\ \mathbf{y} = \mathbf{C}\mathbf{x} + \mathbf{D}\mathbf{u} \end{cases} \tag{29.2}$$

with $\mathbf{A} \in \mathbb{R}^{n \times n}$ representing the system matrix, $\mathbf{B} \in \mathbb{R}^{n \times n_u}$ representing the input matrix, $\mathbf{C} \in \mathbb{R}^{n_y \times n}$ representing the output matrix, $\mathbf{D} \in \mathbb{R}^{n_y \times n_u}$ representing the force throughput matrix and $\mathbf{y}$ representing the system outputs. The relationship between n and m is $n = 2m$. The system matrices can be shown to be

$$\mathbf{A} = \begin{bmatrix} \mathbf{0} & \mathbf{I} \\ -\mathbf{M}^{-1}\mathbf{K} & -\mathbf{M}^{-1}\mathbf{V} \end{bmatrix} \qquad \mathbf{B} = \begin{bmatrix} \mathbf{0} \\ \mathbf{M}^{-1}\mathbf{U} \end{bmatrix} \tag{29.3}$$

where $\mathbf{C}$ and $\mathbf{D}$ are formed appropriately so that linear combinations of the system states $\mathbf{x}$ and inputs $\mathbf{u}$ form the system outputs $\mathbf{y}$. It is here assumed that the system outputs are displacements for simplicity so that $\mathbf{D} = \mathbf{0}$. While accelerations are often measured in experiments, the sensor selection method described below works for both types of system outputs.

Usually it is easier to work in modal coordinates. The undamped eigenvalue problem of Eq. (29.1) is

$$\mathbf{K}\boldsymbol{\Phi} = \mathbf{M}\boldsymbol{\Phi}\boldsymbol{\Lambda} \quad with \quad \boldsymbol{\Lambda} = \mathrm{diag}(\omega_1^2, \omega_i^2, \dots, \omega_n^2) \tag{29.4}$$

where $\boldsymbol{\Phi}$ is the modal matrix and ω^2 the system's eigenvalues. The system in Eq. (29.1) can be transformed to modal form by the coordinate transformation $\mathbf{x} = \boldsymbol{\Phi}\mathbf{q}_m$, where $\mathbf{q}_m$ represent the modal coordinates, and pre-multiplying the equation with $\boldsymbol{\Phi}^T$.

$$\mathbf{I}\ddot{\mathbf{q}}_m + \boldsymbol{\Sigma}\dot{\mathbf{q}}_m + \boldsymbol{\Lambda}\mathbf{q}_m = \boldsymbol{\Phi}^T\mathbf{f}(t) \tag{29.5}$$

The modal mass, damping and stiffness matrices are then $\mathbf{I} = \boldsymbol{\Phi}^T\mathbf{M}\boldsymbol{\Phi}$, $\boldsymbol{\Sigma} = \boldsymbol{\Phi}^T\mathbf{V}\boldsymbol{\Phi}$ and $\boldsymbol{\Lambda} = \boldsymbol{\Phi}^T\mathbf{K}\boldsymbol{\Phi}$, respectively. If proportional damping is assumed the new damping matrix is diagonal $\boldsymbol{\Sigma} = \mathrm{diag}(2\xi\omega_1, 2\xi\omega_i, \dots, 2\xi\omega_n)$, with damping ratio ξ. Thus, one possible realisation of the system in Eq. (29.3) is as follows.

$$\begin{cases} \mathbf{A} = \begin{bmatrix} \mathbf{0} & \mathbf{I} \\ -\boldsymbol{\Lambda} & -\boldsymbol{\Sigma} \end{bmatrix} \\ \\ \mathbf{B} = \begin{bmatrix} \mathbf{0} \\ \boldsymbol{\Phi}^T\mathbf{U} \end{bmatrix} \quad and \quad \mathbf{C} = \begin{bmatrix} \boldsymbol{\Phi} & \mathbf{0} \end{bmatrix} \end{cases} \tag{29.6}$$

29.2.2 System Theory

The observability $\mathcal{O}$ and the controllability $\mathcal{C}$ matrices are formed as

$$\mathcal{O} = \begin{bmatrix} \mathbf{C} \\ \mathbf{CA} \\ \mathbf{CA}^2 \\ \vdots \\ \mathbf{CA}^{n-1} \end{bmatrix} \tag{29.7}$$

$$\mathcal{C} = \begin{bmatrix} \mathbf{B} & \mathbf{AB} & \mathbf{A}^2\mathbf{B} & \cdots & \mathbf{A}^{n-1}\mathbf{B} \end{bmatrix} \tag{29.8}$$

and the system is said to be observable if $\mathcal{O}$ has full rank n and controllable if $\mathcal{C}$ also has full rank n [12]. The observability $\mathbf{W}_o$ and the controllability $\mathbf{W}_c$ gramians are obtained from the Lyapunov equations.

$$\begin{cases} \mathbf{A}^T\mathbf{W}_o + \mathbf{W}_o\mathbf{A} + \mathbf{C}^T\mathbf{C} = 0 \\ \mathbf{AW}_c + \mathbf{W}_c\mathbf{A}^T + \mathbf{BB}^T = 0 \end{cases} \tag{29.9}$$

For asymptotically stable systems a realisation of the system in Eq. (29.2) is possible where the observability and controllability gramians are equal, and diagonal with the Hankel singular values, σ_i, along the diagonal. This is called the

balanced realisation [13]. It is obtained by transforming the system in Eq. (29.9) by a transformation matrix $\mathbf{T}$, not given here, see [13],

$$\begin{cases} \dot{\mathbf{x}} = \hat{\mathbf{A}}\mathbf{x} + \hat{\mathbf{B}}\mathbf{u} \\ \mathbf{y} = \hat{\mathbf{C}}\mathbf{x} \end{cases} \tag{29.10}$$

where $\hat{\mathbf{A}} = \mathbf{T}^{-1}\mathbf{A}\mathbf{T}$, $\hat{\mathbf{B}} = \mathbf{T}^{-1}\mathbf{B}$ and $\hat{\mathbf{C}} = \mathbf{C}\mathbf{T}$, and the system gramians $\hat{\mathbf{W}} = \hat{\mathbf{W}}_o = \hat{\mathbf{W}}_c = \text{diag}(\sigma_1, \sigma_2, \ldots, \sigma_n)$. Thus, the Lyapunov equations can be written as

$$\begin{cases} \hat{\mathbf{A}}^T\hat{\mathbf{W}} + \hat{\mathbf{W}}\hat{\mathbf{A}} = -\hat{\mathbf{C}}^T\hat{\mathbf{C}} \\ \hat{\mathbf{A}}\hat{\mathbf{W}} + \hat{\mathbf{W}}\hat{\mathbf{A}}^T = -\hat{\mathbf{B}}\hat{\mathbf{B}}^T \end{cases} \tag{29.11}$$

with their solution as follows, from [13].

$$\int_0^\infty e^{\mathbf{A}t}\mathbf{B}\mathbf{B}^T e^{\mathbf{A}^T t} dt = \int_0^\infty e^{\mathbf{A}^T t}\mathbf{C}^T\mathbf{C}e^{\mathbf{A}t} dt = \hat{\mathbf{W}} \tag{29.12}$$

29.2.3 Method of Effective Independence

The EfI method seeks to maximise the Fisher information matrix (FIM), $\mathbf{Q}_c$, determinant, shown by Kammer in [3] to be formed as

$$\mathbf{Q}_c = \mathbf{\Phi}_{3c}^T \mathbf{W} \mathbf{\Phi}_{3c} \tag{29.13}$$

where $\mathbf{W}$ is a weighting matrix assumed, for simplicity, to be the identity matrix below. The target mode shapes partitioned to three translations for each triaxial location is denoted $\mathbf{\Phi}_{3c} \in \mathbb{R}^{m \times n_m}$ where n_m is the number of modes and $\mathbf{\Phi}_{3c} = [\boldsymbol{\phi}_1, \boldsymbol{\phi}_i, \ldots, \boldsymbol{\phi}_{n_m}]$ with $\boldsymbol{\phi}_i = [\phi_{1,i}^x, \phi_{1,i}^y, \phi_{1,i}^z, \phi_{2,i}^x, \phi_{2,i}^y, \phi_{2,i}^z, \ldots, \phi_{m,i}^x, \phi_{m,i}^y, \phi_{m,i}^z]^T$.

Reference [3] describes the EfI method with triaxial sensors where sensors are placed in the final set from a candidate set formed from the full FE model. Two ranking methods exist, one for a full rank FIM and one for a rank deficient FIM. For a full rank FIM the following definition is used

$$EfI3_i^+ = \frac{det(\mathbf{Q}^{+3i}) - det(\mathbf{Q}_o)}{det(\mathbf{Q}_o)} \tag{29.14}$$

where $\mathbf{Q}_0$ is the initial FIM from the user selected sensor location set, and $\mathbf{Q}^{+3i} = \mathbf{Q}_0 + \boldsymbol{\phi}_{3i}^T \boldsymbol{\phi}_{3i}$ where $\boldsymbol{\phi}_{3i}$ is the target modal matrix partitioned to the three rows of the i-th location. The rank deficient case is more complicated and a full derivation and expression is given by Kammer in [3].

29.2.4 Gramian Based Rejection

Reference [11], states that the EfI method does not account for information uniqueness. For very dense meshes where the candidate set is also very dense and give large EfI indices, the EfI method tends to select all of them. This is a consequence of the fact that usually the first few modes are of interest in experiments and they tend to exhibit global behaviour with long wavelengths. The close node locations will then have very similar modal data. The same is true when the structure is symmetric or nearly symmetric and the candidate set contains nodes that are symmetrically placed. The modal matrix will then contain multiple identical rows, depending on the number of symmetry lines. If any single one of these rows, corresponding to locations, are important from an EfI point of view all of them will be selected as no other locations are available in the candidate set that add more to the EfI metric. In both cases the EfI method will select candidates that carry similar information. It should be noted that in some situations the symmetric characteristics of a structure are of interest, for example when validating experiments or for visualisation purposes. However, there are many examples of when

sensors are limited and redundant information is not necessary, such as in model calibration where it can be argued that unique information is of greater importance and the number of sensors recording redundant information should be kept to a minimum.

In [14] it is shown that the EfI method produces a final set that is optimal from a system observability perspective. Thus, rejecting sensors that were in fact selected by EfI will result in an less optimal system observability, but this is again a consequence of the candidate set containing duplicate information. If a sensor location is deemed important and a nearly symmetric location exists in the candidate set, no other location will increase the system observability as much as the nearly symmetric position. From an information uniqueness point of view it is thus argued that these positions can safely be rejected.

In this paper, a second criteria is added to the sensor selection. First the EfI method ranks the sensors and selects the best, adding most information to the FIM determinant. The second step rejects sensors by comparing the system balanced realisation gramians of two systems. A comparison of a system with the last sensor added and a system with the last and second to the last added sensor is performed.

The criteria used for rejection is based on a normalised determinant of the gramian matrix so that all values along the diagonal are compared and the criteria is bounded. The balanced realisation gramians are diagonal meaning that the determinant can be calculated as the product of the eigenvalues of the gramian matrix. Here the matrix version will be given, for generality. Given that the output matrix is constant it can be realised from Eq. (29.12) that a system with two equal outputs will only scale the gramian matrix $\hat{\mathbf{W}}$ by a scalar. If the output matrix $\mathbf{C}_1$ contains one output and $\mathbf{C}_2$ contains the same output as in $\mathbf{C}_1$ twice, the product $\mathbf{C}_2^T\mathbf{C}_2$ is simply $\mathbf{C}_2^T\mathbf{C}_2 = \alpha\mathbf{C}_1^T\mathbf{C}_1$. Thus, a criterion that is invariant under scalar multiplication will result in the balanced realisation gramian matrix being equal for a system with one and two equal outputs. Property 3 (p3) of the matrix norm $\|\cdot\|$ definition [15] will be utilised. In the following equation $\mathbf{M}, \mathbf{N} \in \mathbb{R}^{n \times m}$ and $\alpha \in \mathbb{R}$.

$$
\begin{aligned}
&p1 \quad \|\mathbf{M}\| \geq \mathbf{0} \\
&p2 \quad \|\mathbf{M}\| = \mathbf{0} \quad iff \quad \mathbf{M} = \mathbf{0} \\
&p3 \quad \|\alpha\mathbf{M}\| = |\alpha|\,\|\mathbf{M}\| \\
&p4 \quad \|\mathbf{M} + \mathbf{N}\| \leq \|\mathbf{M}\| + \|\mathbf{N}\|
\end{aligned}
\tag{29.15}
$$

The criteria is then defined as follows:

$$
\delta_i = \frac{\left| det(\hat{\mathbf{W}})^{1/n} \right|}{\|\hat{\mathbf{W}}\|_\infty}
\tag{29.16}
$$

From this definition and p3 in Eq. (29.15) the criteria can be shown to be invariant under scalar multiplication.

$$
\delta_i(\alpha\hat{\mathbf{W}}) = \frac{\left| det(\alpha\hat{\mathbf{W}})^{1/n} \right|}{\|\alpha\hat{\mathbf{W}}\|_\infty} = \frac{\left| (\alpha^n)^{1/n} \right| \left| det(\hat{\mathbf{W}})^{1/n} \right|}{|\alpha|\,\|\hat{\mathbf{W}}\|_\infty} = \frac{\left| det(\hat{\mathbf{W}})^{1/n} \right|}{\|\hat{\mathbf{W}}\|_\infty} = \delta_i(\hat{\mathbf{W}})
\tag{29.17}
$$

It is advised that the redundant information metric be formed as follows.

$$
\gamma = \frac{|\delta_1 - \delta_2|}{|\delta_1 + \delta_2|}
\tag{29.18}
$$

Here δ_1 is for a system with the last selected sensor and δ_2 stands for a system with the last and second to last selected sensors. It can be seen that the redundancy measure γ is bound by $0 \leq \gamma \leq 1$. The metric will be zero when the two systems have equal observability characteristic, $\delta_1 - \delta_2 = 0$ and thus $\gamma = 0$, and unity when the gramian matrix of one system is singular, meaning that it is not fully observable or controllable. This might seem strange at first, but the difference in information between an observable and an unobservable system is the largest possible. Even though it is not of interest to keep a sensor that cannot observe all modes, the EfI method will not rank these highly to begin with.

The criteria chosen here, based on a normalised determinant of the balanced gramian is one of several possible criteria that can be chosen. The condition number $\kappa(\cdot)$ provides the same property of scalar multiplication invariance and it also gives a meaning to the comparison, as a small condition number indicates a system that is well observable and controllable for all modes.

The normalised norms of the FIM for each location in the candidate set are compared in [11]. Sensors are first ranked by the EfI method and one is selected. Then a ranking of the information uniqueness is performed where all non-unique

locations are deleted from the candidate set. In this paper, the EfI selected sensor system is compared to a system with the new sensor and previously added sensors to the final set. If the balanced observability gramian is equal, the location is rejected, and the next best location is chosen, as ranked by EfI and the procedure is repeated. In [1] it is stated that removing a sensor location from the candidate set and ranking the remaining locations will not necessarily rank the second best location from the previous ranking as the sensor location adding most to the EfI measure. Thus it is believed that rejecting sensor locations one at a time is a more sensible approach to find a sub-optimal sensor placement.

29.3 Implementation

The algorithm is visualised in a flowchart in Fig. 29.1. The user defines the threshold value T_s as $0 \leq T_s \leq 1$, the number of sensors in the final set N, the initial sensor vector *INIT* and the input degree of freedom *INPUT*. The modal matrix $\mathbf{\Phi}$ along with the state-space matrices are then read as input data. For gramian rejection the method must first have an input, if none was selected by the user it is proposed that the best position with respect to controllability is selected. If the initial sensor set is empty, i.e. no sensor was selected by the user it is proposed that the best position with respect to observability is selected. These two steps are only performed in the placement of the first sensor. The EfI method then ranks the positions by its metric and selects the best. If the number of sensors already in the final set, N_{fs}, is higher than the loop count i the new criteria is evaluated. If the rejection metric γ is lower or equal to the specified threshold value T_s the new sensor is rejected as no new information, or very little, is added. The algorithm then selects the next best sensor ranked by the EfI method, resets the loop counter and compares the new sensor with the previously added sensors to the final set. When the loop count exceeds the number of sensors in the final set the algorithm saves the sensor to the final set and verifies that the number of sensors in the final set is equal to the sought number N. If it is, the method has finished.

It should be noted that if the threshold value T_s is too large relative to the candidate set, the method will finish before the sought number of sensor locations are acquired as all other positions will have been rejected.

29.4 Results

The method proposed is used here on a simple clamped plate that exhibits perfect one way symmetry, see Fig. 29.1. The plate model consist of 1600 shell elements, 4920 degrees-of-freedom, elastic modulus 210 GPa, density 7850 kg/m^3 and Poissons ratio 0.3. The mesh is also very dense and every node is placed in the candidate set to point out the difference between the two methods. For a more complex structure see [16], where this method was applied to an industrial sized structure with a more realistic candidate set with good results.

For all three examples the first 10 flexible modes were selected and the algorithms were asked to find 20 triaxial sensor locations given one initial sensor location at the top right corner and one input at the same location perpendicular to the plate surface. In Fig. 29.2e the sensor location order selection is shown by colour coding. The same colours are used in all three scenarios. In Fig. 29.2a the *EfI*3$^+$ method is shown. It is seen that the final selected set is more or less symmetrical and clustered. Both the clustering of sensor locations and symmetrical behaviour were predicted from the EfI theoretical foundation. Exact sensor placement symmetry is not achieved in the middle in this example due to the very dense mesh where many nodes have very similar EfI metric values.

In Fig. 29.2b the gramian rejection method is applied with a very small threshold value $T_s = 0.05$. It is seen that the clustering disappears completely and the symmetrical positioning is also removed, but the sensor positions are still relatively close to most of the original locations seen in Fig. 29.2a. In Fig. 29.2c a more aggressive rejection threshold of $T_s = 0.1$ is applied. Here it can be seen that a larger reshuffling of the sensor locations is achieved. The second sensor location found is the top left node which can be seen to move out from the corner with a higher threshold. One location is placed at the symmetry line, which might seem strange at first, but the plate is clamped and has relatively high movement for some modes along the symmetry line. Although, other modes are poorly observed from that position, resulting in a relatively high condition number $\kappa(\hat{\mathbf{W}})$, meaning that the information content carried by the gramians will differ significantly if compared to a system with a lower condition number. This is expected. Also, the EfI method ranked this position higher than many other locations. It is also the reason for not having a too high threshold value.

Fig. 29.1 Algorithm design
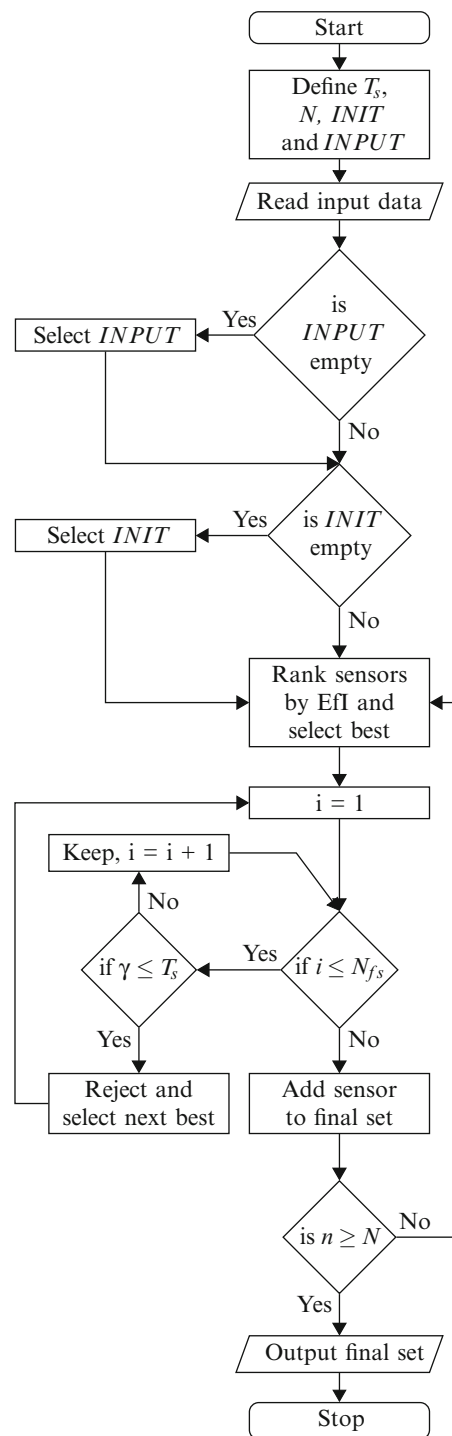
In Fig. 29.2d the FIM determinant for the three cases is shown along with the gramian condition number. It is seen that the condition number, in blue, is relatively close in all three scenarios, but the pure EfI method achieves the lowest value in the end, which was expected. For the FIM determinant the pure EfI method again achieves the highest value, although all three methods have the same order, 10^{37}, the pure EfI method has an approximately six times larger FIM determinant than the gramian rejection method with threshold $T_s = 0.05$.
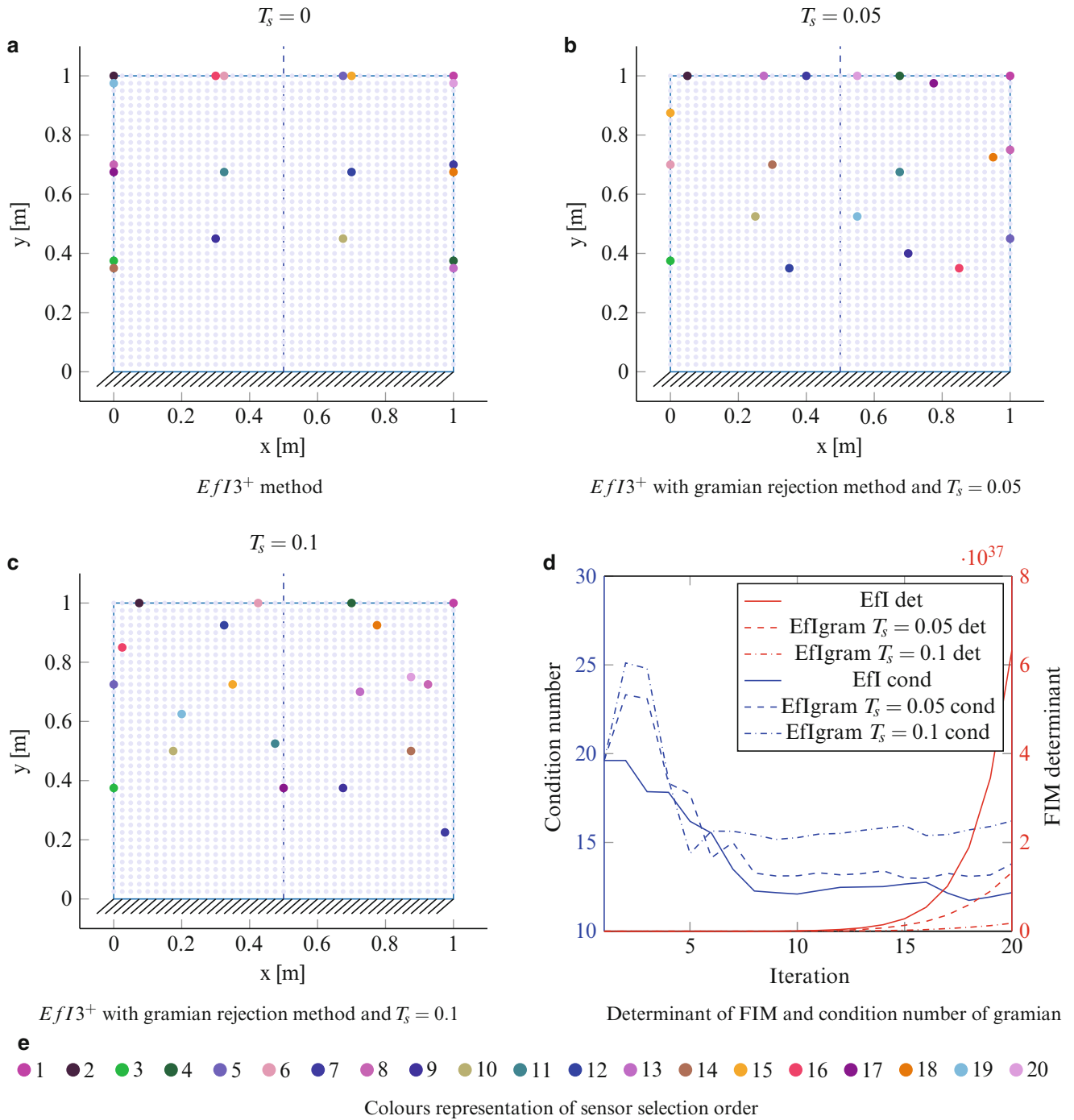
Fig. 29.2 In (**a**) the pure EfI sensor location selection is shown while (**b**) shows the selection with added gramian rejection with $T_s = 0.05$, (**c**) also shows the selection with gramian rejection added, but with $T_s = 0.1$, (**d**) shows the FIM determinant for the three selection strategies and the balanced gramian condition number and in (**e**) the selection order colours can be seen

29.5 Conclusions

A method for redundant information rejection integrated into the EfI selection strategy has been presented. It works well with the sensor set expansion method proposed in [3], and it does not need any special consideration of the sensor orientation, but can compare any sensor to any other sensor in the candidate set.

The method works by comparing two systems normalised determinant of the balanced realisation gramians. A small threshold value around $T_s = 0.1$ is found to work well for rejecting sensor position locations in a very dense plate mesh example. For more realistic candidate sets a threshold value of $T_s = 0.05$ is a more sensible option as it might be possible that all locations have been selected or rejected before the sought number of positions are found. A very high value of the threshold T_s does not guarantee large distances between sensor locations but rather that their individual observability characterisations are different. Thus a too high threshold can be counter productive.

References

1. Kammer, D.C.: Sensor placement for on-orbit modal identification and correlation of large space structures. J. Guid. Control Dyn. **14**, 251–259 (1991)
2. Kammer, D.C., Tinker, M.L.: Optimal placement of triaxial accelerometers for modal vibration tests. Mech. Syst. Signal Process. **18**, 29–41 (2004)
3. Kammer, D.C.: Sensor set expansion for modal vibration testing. Mech. Syst. Signal Process. **19**, 700–713 (2005)
4. Li, D.S., Li, H.N., Fritzen, C.P.: The connection between effective independence and modal kinetic energy methods for sensor placement. J. Sound Vib. **305**, 945–955 (2007)
5. Li, D.-S., Li, H.-N., Fritzen, C.-P.: A note on fast computation of effective independence through QR downdating for sensor placement. Mech. Syst. Signal Process. **23**, 1160–1168 (2009)
6. Reynier, M., Abou-Kandil, H.: Sensors location for updating problems. Mech. Syst. Signal Process. **13**, 297–314 (1999)
7. Gawronski, W., Lim, K.B.: Balanced actuator and sensor placement for flexible structures. Int. J. Control **65**, 131–145 (1996)
8. Hac', A., Liu, L.: Sensor and actuator location in motion control of flexible structures. J. Sound Vib. **167**, 239–261 (1993)
9. Lim, K.B.: Method for optimal actuator and sensor placement for large flexible structures. J. Guid. Control Dyn. **15**, 49–57 (1992)
10. Trendafilova, I., Heylen, W., Brussel, H.V.: Measurement point selection in damage detection using the mutual information concept. Smart Mater. Struct. **10**, 528 (2001)
11. Stephan, C.: Sensor placement for modal identification. Mech. Syst. Signal Process. **27**, 461–470 (2012)
12. Laub, A.J.: Matrix Analysis for Scientists and Engineers, p. 182. Society for Industrial and Applied Mathematics, Philadelphia (2005)
13. Moore, B.: Principal component analysis in linear systems: controllability observability, and model reduction. IEEE Trans. Autom. Control **26**, 17–32 (1981)
14. Kammer, D.C.: Optimal sensor placement for modal identification using system-realization methods. J. Guid. Control Dyn. **19**, 729–731 (1996)
15. Golub, G.H., Loan, C.F.V.: Matrix Computations, 738 pp. The Johns Hopkins University Press, Baltimore (2012). www.press.jhu.edu
16. Gibanica, M., Abrahamsson, T.J.S., Olsson, M.: Calibration, validation and cross-validation of nominally identical car subframes. In: Proceedings of the 34th IMAC, Orlando, FL, January 2016

Chapter 30
Strain-Based Experimental Modal Analysis on Planar Structures: Concepts and Practical Aspects

Fábio Luis Marques dos Santos, Bart Peeters, Wim Desmet, and Luiz Carlos Sandoval Góes

Abstract Strain modal analysis has been used for a long time as an alternative way of identifying the vibration modes of a structure, whenever the use of accelerometers is not suited (such as in aerospace applications) or when information about the dynamic strain levels in the structure is required (e.g. structural health monitoring or durability applications). However, some practical aspects of strain-based modal analysis are not always studied in such applications. For instance, how to visualize and interpret multi-directional modal strain is still an open topic. Similarly, the optimal way to correlate and distinguish these strain modes is also not usually discussed. This work will focus on clarifying some concepts related to multi-directional strain, and will show some examples on how modal strain in multiple directions can be better interpreted. For this purpose, the use of strain gauges (and strain rosettes) for modal analysis in two-dimensional structures will be introduced and some insights will be given on how to properly measure and interpret normal and shear strain modes and how to carry out modal correlation. Finally. these concepts will be applied to numerical and experimental examples.

Keywords Strain modal analysis • Dynamic strain • Strain field • Planar strain • Strain mode shape

30.1 Introduction

Experimental modal analysis methodologies can have as sensors the more commonly used accelerometers, but can also be carried out using strain gauges [1]. The use of accelerometers will lead to the identification of the displacement mode shapes, while with the strain gauges, the strain mode shapes are identified [2]. There are some small differences on the modal formulation for the use of strain gauges [3, 4], but the same modal identification techniques can be used to identify the strain mode shapes [5].

Although there is a lot of research and applications on strain modal analysis for different purposes, such as its use in structural integrity [6] evaluation and structural health monitoring [7], or the combined use of strain gauges and accelerometers [8, 9], there is still no dedicated study on the measurement, visualization and interpretation of strain modes and on modal strain measurements in more than one direction. The visual interpretation of the strain modes is something less commonly carried out and not as straight forward. While the displacement modes can be easily visualized and interpreted, the strain modes are harder to be interpreted and understood. The measurement of planar strain is however a very well studied area in solid mechanics [10, 11]. This work will focus on clarifying some concepts related to multi-directional planar strain, and will show some examples on how modal strain in multiple directions can be better interpreted or correlated.

F.L. Marques dos Santos (✉)
Siemens Industry Software, Interleuvenlaan 68, 3001 Leuven, Belgium

KU Leuven (KUL), Division PMA, Celestijnenlaan 300B, 3001 Heverlee, Belgium

Instituto Tecnológico de Aeronáutica (ITA), Praça Marechal Eduardo Gomes, 50 - Vila das Acácias, CEP 12.228-900
São José dos Campos, SP, Brazil
e-mail: fabio.m.santos@siemens.com

B. Peeters
Siemens Industry Software, Interleuvenlaan 68, 3001 Leuven, Belgium

W. Desmet
KU Leuven (KUL), Division PMA, Celestijnenlaan 300B, 3001 Heverlee, Belgium

L.C.S. Góes
Instituto Tecnológico de Aeronáutica (ITA), Praça Marechal Eduardo Gomes, 50 - Vila das Acácias, CEP 12.228-900
São José dos Campos, SP, Brazil

30.2 Strain Modal Analysis and Planar Strain

To obtain the strain modal formulation, one can start from the definition of modal analysis and define the strain modal vector, as is explained in [12] and [3]. The strain frequency response function (SFRF) matrix $\mathbf{H}^\varepsilon(j\omega)$ in the pole-residue form can be defined as:

$$\mathbf{H}^\varepsilon(j\omega) = \sum_{r=1}^{n} \left(\frac{j2\omega_r Q_r \psi_r \phi_r^T}{(\omega_r^2 - \omega^2)} \right) \tag{30.1}$$

where j is the complex unit, ω the frequency vector, ω_r the natural frequency related to the rth mode, ψ and ϕ the strain and displacement modes respectively, Q_r the scaling factor and n the number of modes taken into consideration.

The strain modal formulation shows the modal model for one given generic strain direction. However, this formulation can be extended to strain in any and more than one direction, without any loss of generality. These directions are the three normal strains and the six shear components, as shown in Fig. 30.1a. The normal strain represents relative deformation with respect to one direction, while shear strain represents an angular deformation. Figure 30.1b and c depict an element where normal and shear strain are applied to it.

These nine strain components compose the full strain tensor for a three-dimensional structure, which is a symmetric matrix—that is, $\gamma_{xy} = \gamma_{yx}$, $\gamma_{xz} = \gamma_{zx}$, $\gamma_{zy} = \gamma_{yz}$. The tensor can be represented in matrix form as:

$$E_\varepsilon = \begin{bmatrix} \varepsilon_{xx} & \gamma_{xy} & \gamma_{xz} \\ \gamma_{xy} & \varepsilon_{yy} & \gamma_{yz} \\ \gamma_{xz} & \gamma_{yz} & \varepsilon_{zz} \end{bmatrix} \tag{30.2}$$

Moreover, depending on the type of structure, the strain tensor can be reduced in dimension, as is the case for a 2D (plate-like) structure, shown in Eq. (30.3):

$$E_\varepsilon^{plate} = \begin{bmatrix} \varepsilon_{xx} & \gamma_{xy} \\ \gamma_{xy} & \varepsilon_{yy} \end{bmatrix} \tag{30.3}$$

For a 1D beam-like structure, the same strain tensor can be used as for the 2D case. To obtain the full three-dimensional strain tensor, it is necessary to measure strain in multiple directions on a structure. This can be done by measuring the two-dimensional state of strain in the three different planes.

Taking into account the strain tensor of a plate-like structure (Eq. (30.3)), one needs to measure the normal strains ε_{xx} and ε_{yy}, as well as the shear strain γ_{xy} (remembering that $\gamma_{xy} = \gamma_{yx}$) to be able to compose the full strain tensor. However, strain gauges and other strain sensors can only directly measure extensional strain (that is, ε_{xx}, ε_{yy} or a strain combination

Strain normal directions $(\varepsilon_{xx}, \varepsilon_{yy}, \varepsilon_{zz})$ and shear $(\gamma_{xy}, \gamma_{xz}, \gamma_{yx}, \gamma_{yz}, \gamma_{zx}, \gamma_{zy})$

Normal strain and linear deformation

Shear strain and angular deformation
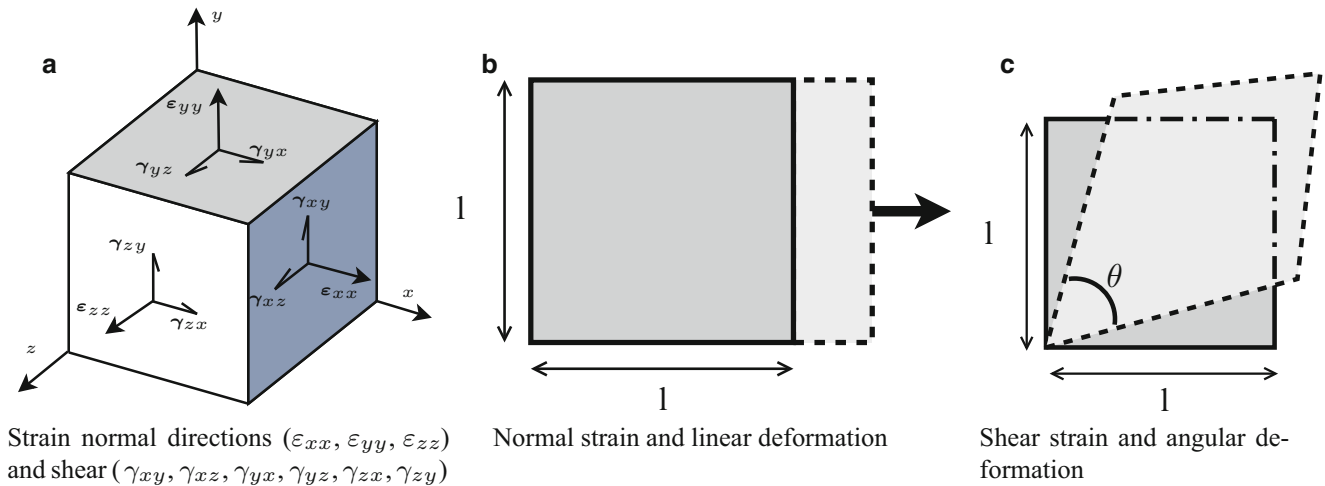
Fig. 30.1 Strain directions on element (**a**), normal (**b**) and shear strain (**c**) applied on an element

Fig. 30.2 Strain gauge oriented
with respect to a fixed axis
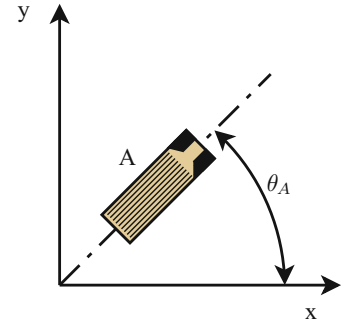
Fig. 30.3 Strain gauge rosette
aligned with xy axis
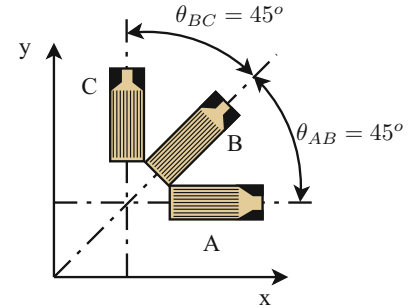
related to how the strain gauge is oriented), so there is no direct way to measure the shear strain component γ_{xy}. But this shear component can be calculated using strain transformation equations [13, 14]. Figure 30.2 shows a strain gauge oriented with respect to a fixed axis.

The elementary transformation equation that relates the strain measured on the strain gauge (ε_A) and its orientation angle θ_A with respect to the strain components ε_{xx}, ε_{yy} and γ_{xy} is:

$$\varepsilon_A = \frac{\varepsilon_{xx} + \varepsilon_{yy}}{2} + \frac{\varepsilon_{xx} - \varepsilon_{yy}}{2} \cdot \cos 2\theta_A + \frac{\gamma_{xy}}{2} \cdot \sin 2\theta_A \tag{30.4}$$

This means that if the strain gauge is aligned with one of the axes (that is $\theta_A = 0$ or $\theta_A = 90°$), it will only measure that respective axial strain (ε_{xx} or ε_{yy}). On the other hand, if the sensor is placed in any orientation within the two axes ($0 < \theta_A < 90$), then the measured strain ε_A will be a combination of ε_{xx}, ε_{yy} and γ_{xy}.

Then, if three strain gauges are positioned between each other with known angles (a configuration also known as a strain gauge rosette), then a system of equations can be used to determine the full state of planar strain. Figure 30.3 shows a case where a strain rosette with a 45° angle between sensors is placed aligned with the x and y axes.

In the case of the strain rosette in Fig. 30.3, the transformation equations deduced from (30.4) will be:

$$\varepsilon_A = \frac{\varepsilon_{xx} + \varepsilon_{yy}}{2} + \frac{\varepsilon_{xx} - \varepsilon_{yy}}{2} \cdot \cos 0 + \frac{\gamma_{xy}}{2} \cdot \sin 0 = \varepsilon_{xx} \tag{30.5}$$

$$\varepsilon_B = \frac{\varepsilon_{xx} + \varepsilon_{yy}}{2} + \frac{\varepsilon_{xx} - \varepsilon_{yy}}{2} \cdot \cos 90 + \frac{\gamma_{xy}}{2} \cdot \sin 90 = \frac{\varepsilon_{xx} + \varepsilon_{yy}}{2} + \frac{\gamma_{xy}}{2} \tag{30.6}$$

$$\varepsilon_C = \frac{\varepsilon_{xx} + \varepsilon_{yy}}{2} + \frac{\varepsilon_{xx} - \varepsilon_{yy}}{2} \cdot \cos 180 + \frac{\gamma_{xy}}{2} \cdot \sin 180 = \varepsilon_{yy} \tag{30.7}$$

Which in turn, for the known angle between the strain gauges, can be solved to yield:

$$\varepsilon_{xx} = \varepsilon_A \tag{30.8}$$

$$\varepsilon_{yy} = \varepsilon_C \tag{30.9}$$

$$\gamma_{xy} = 2\varepsilon_B - \varepsilon_A - \varepsilon_C \tag{30.10}$$

Therefore, by using a strain gauge rosette, it is possible to obtain the full planar state of strain for a measurement point.

30.3 Visualization and Interpretation of Strain Modes

The displacement modes (in multiple directions) of a structure can be easily visualized by simply setting the displacements in the x, y and z directions on the measurement points. In other words, on one point of the geometry, the three directions can be represented and visualized simultaneously. On the other hand, the same procedure cannot be done with strain modes, since they do not represent a visual displacement. Each strain component can be represented individually by a color scale—this procedure is usually done when visualizing deformations and strains in FEM software, and can also be applied to test results.

One could instead try to combine all strain components to visually represent them with only one component, that is, recombine the three components into one scalar value. A method of representing all three planar strain components (ε_{xx}, ε_{yy} and γ_{xy}) in this case is the Von Mises formulation, shown in Eq. (30.11):

$$\varepsilon_{VM} = \sqrt{\varepsilon_{xx}^2 - \varepsilon_{xx} \cdot \varepsilon_{yy} + \varepsilon_{yy}^2 + 3\gamma_{xy}} \tag{30.11}$$

The Von Mises formulation can help recombine all measured strain components into one number and in this way facilitate visualization of the strain modes. However, this method can interfere with the (already complex) interpretation of the modes—whenever a mode has one dominating direction of strain (such as the first bending mode of a plate), the Von Mises formulation does not interfere with the visualization of the modal behavior of the system, but in the case where there are similar levels of strain in more than one component, then the modal behavior in each component is mixed up, making it more difficult to be distinguished.

This mixing up of modes using the Von Mises formulation can become more clear when looking at the autoMAC of the strain modes. To visualize this, a FEM model of a plate was used (the plate properties are better described in Sect. 30.4). An autoMAC using strain from 15 points (in x, y and shear components) and 8 modes from the plate was calculated, and then the strain components were recombined in Von Mises values and the autoMAC was calculated again. The results are shown in Fig. 30.4.

It is clear from the autoMAC analysis that the Von Mises formulation makes the modes less distinguishable, and many modes get mixed up. For a better visualization of the modal behavior, the 8th strain mode of the plate is shown in Fig. 30.5. The components in x, y, shear and Von Mises combination are shown, where the coloring represents the strain values in the respective component. The mode shape using the Von Mises formulation leads to a worse interpretation of the strain in the multiple components.

Another difficulty that usually arises when dealing with strain mode shapes is to determine the mode type. This task can be made easier if the full state of strain is available, but it isn't always possible. Sometimes strain measurements are available
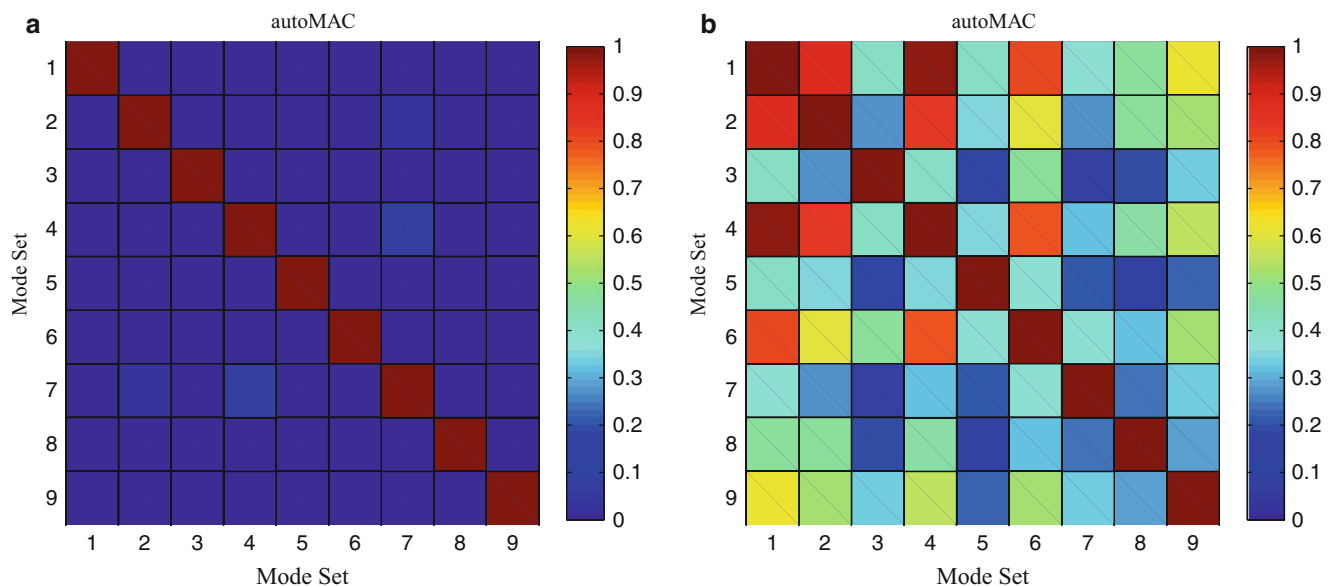
Fig. 30.4 Comparison between autoMAC using all strain components and autoMAC using strain components combined into the Von Mises formulation. (**a**) Strain autoMAC with full 2D tensor. (**b**) Strain autoMAC with 2D tensor recombined with Von Mises formulation
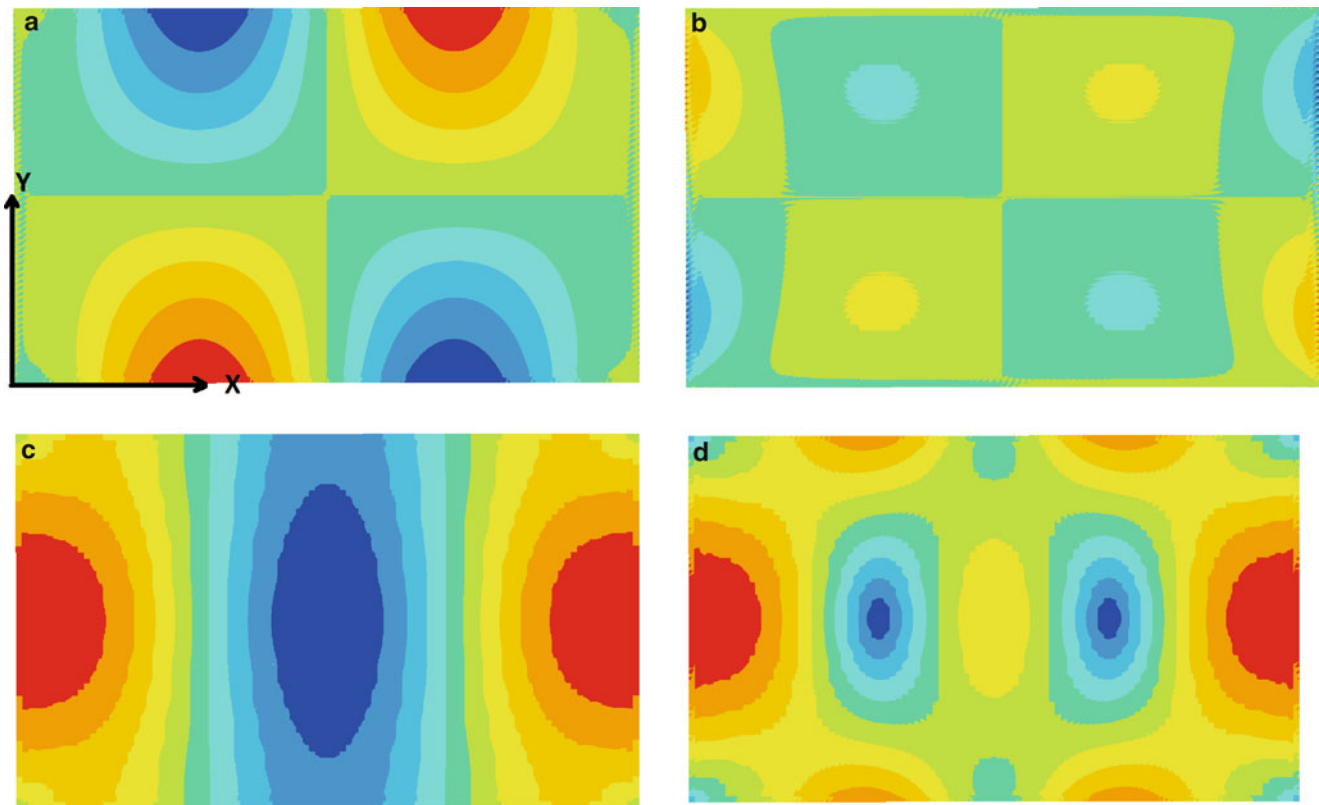
Fig. 30.5 Comparison between strain mode shape components for 8th mode of plate. (**a**) Plate 8th strain mode shape in the x direction. (**b**) Plate 8th strain mode shape in the y direction. (**c**) Plate 8th strain mode shape shear component. (**d**) Plate 8th strain mode shape Von Mises equivalent

in only one direction or only a few sensors are available. The experimental example will show planar strain measurements, as well as correlation between experimental and simulation models, measuring the planar strain directions, and how to better carry out the correlation procedure.

30.4   Experimental Modal Analysis of a Carbon Fiber Plate

To verify some procedures for interpretation of planar strain modes, an experimental modal analysis was carried out on an orthotropic composite plate. While its displacement modes can be easily visualized and interpreted, the strain modes are harder to be understood. As an example, Fig. 30.6 shows the first displacement mode and strain modes (planar x and y and shear), obtained from the finite element model of a rectangular carbon fiber composite plate (dimensions shown in Fig. 30.7). While it is easy to interpret the displacement mode, it is harder to arrive to the same conclusions when looking at the strain modes.

Similarly, one can use experimental results to understand how to interpret and correlate the identified strain mode shapes. For this purpose, a composite carbon fiber plate was manufactured to be used in the experiments. The composite plate is composed of seven plies, with a stacking sequence of [0,90,0,90,0,90,0]. Each ply is made of unidirectional carbon fiber prepreg (Hexply M10R 38% UD300 CHS) and the plate was cured using an out-of-autoclave process. The dimensions of the plate are 500 mm × 300 mm with a thickness of 2 mm. The properties of the plate are the same used for the simulation, shown in Fig. 30.6.

To investigate the full state of strain of the vibration modes, the plate was instrumented with 15 strain gauge rosettes (Micro-Measurements CEA-06-250UR-350), forming a 5 × 3 grid of sensors. Figure 30.7 shows the strain gauge rosette locations on the plate.
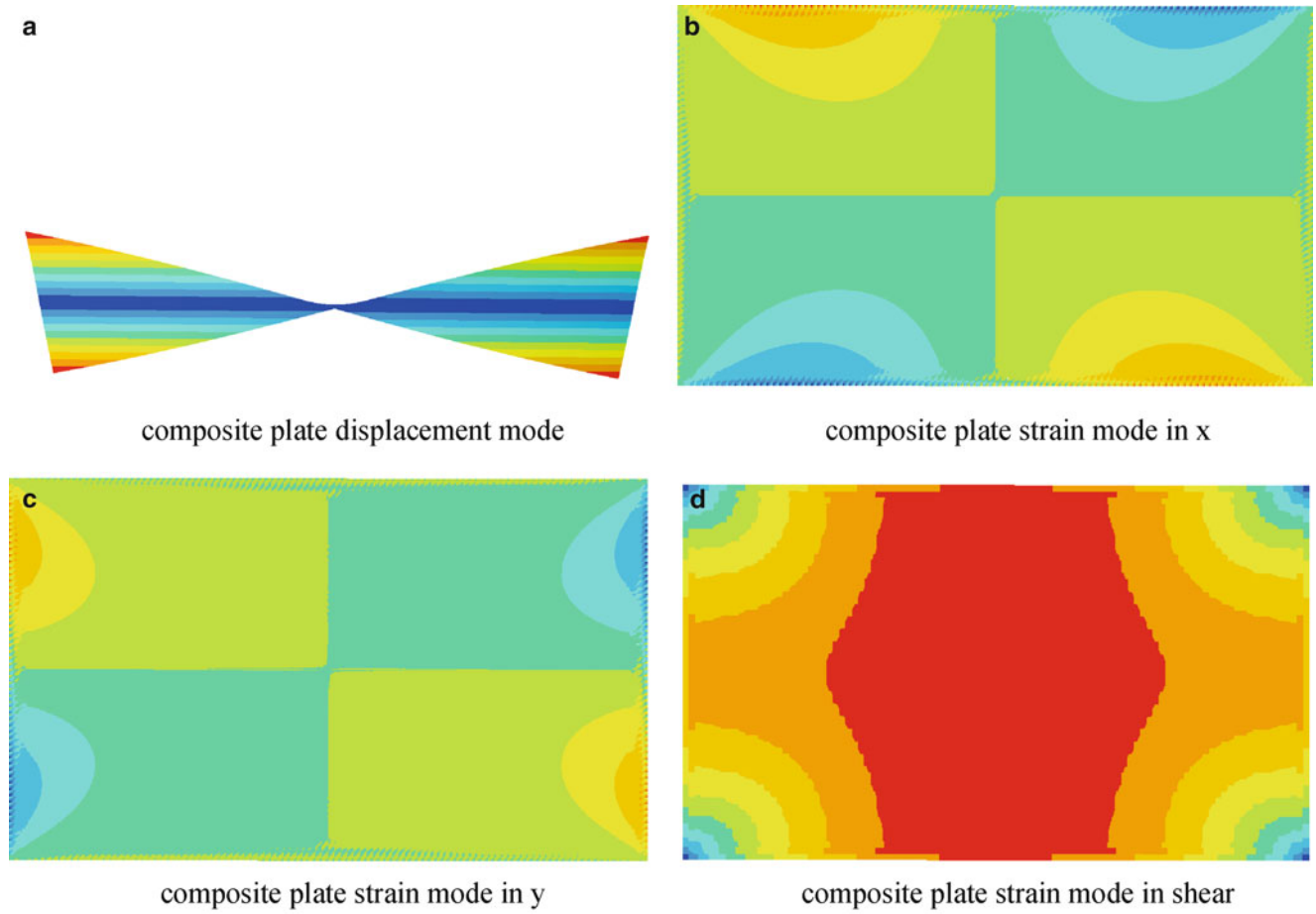
Fig. 30.6 Carbon fiber composite plate (free-free) first vibration mode (0,0): (**a**) displacement mode; (**b**) strain mode in x direction; (**c**) strain mode in y direction; (**d**) shear strain mode
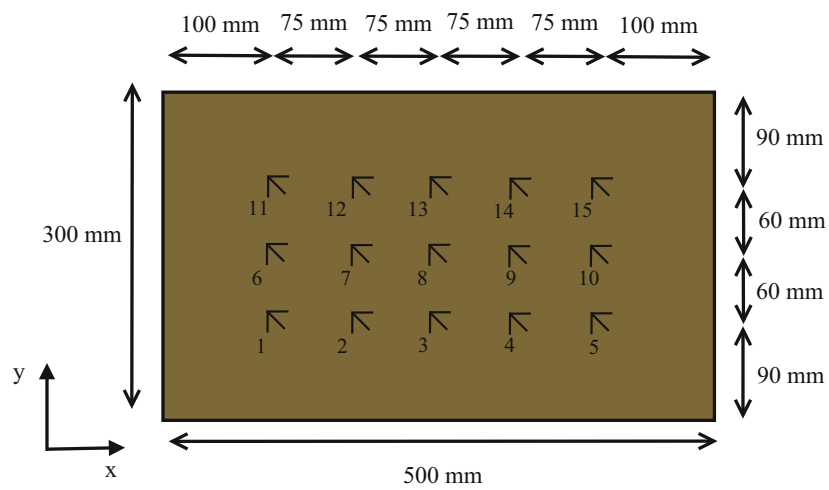
Fig. 30.7 Composite plate: strain gauge rosette locations
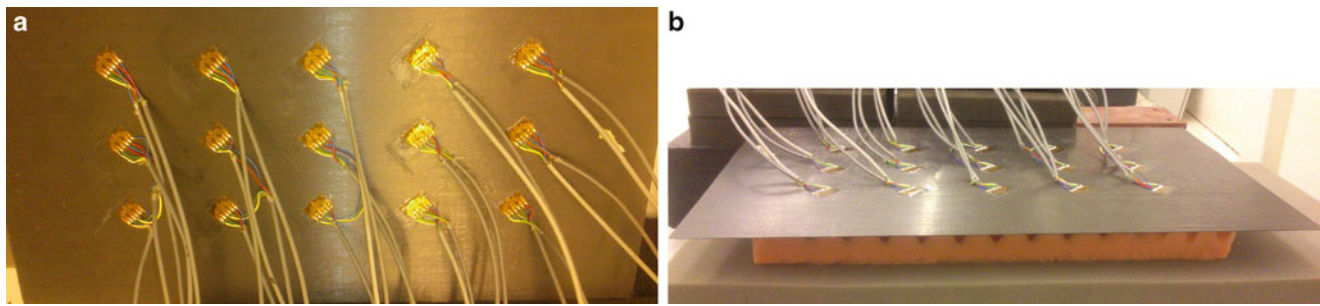
Fig. 30.8 Composite plate used for tests: strain gauge rosettes and boundary conditions. (**a**) Composite plate with sensors. (**b**) Composite plate boundary conditions

Table 30.1 Strain modes comparison—natural frequencies (ω_n) from simulation and test

Mode number	ω_n (Hz) simulation	ω_n (Hz) test	Difference %
1	29.05	33.41	13
2	62.07	61.63	0.7
3	85.41	82.60	3.4
4	112.52	116.03	3.0
5	126.46	125.31	0.9
6	171.07	168.92	1.2
7	174.46	164.82	5.8
8	191.63	185.17	3.5
9	270.08	254.12	6.3

Each individual strain gauge from the rosette was connected using a quarter-bridge configuration (resulting in 45 total measurement sensors). For the strain modal analysis, the plate was supported on polyurethane foam, to achieve a free-free boundary condition. Figure 30.8 shows the strain rosette sensor grid bonded on the plate, as well as the test set-up with the boundary conditions.

The modal analysis was carried out using impact tests. A modal impact hammer (PCB 086C03) was used to excite the structure and to acquire the data, two LMS SCADAS mobile acquisition units were used. Then, impact test data could be processed in LMS Test.Lab software, using the PolyMAX least squares technique.

A transformation has to be done to be able to calculate the shear strain from the rosette measurements, as was explained in the previous sections. In this experiment this procedure was carried out to generate a new set of SFRFs that are representative of the shear strain, and then the strain modes in x, y and shear were identified.

Moreover a comparison and correlation with a finite element model was carried out. The model was created in NX Nastran, using the ply material properties provided by the prepreg manufacturer. As expected, the plate has bending and torsional modes, as well as modes that are a combination of bending in the x and y directions. Table 30.1 shows the mode pairing between simulation and test for the first nine modes. The natural frequency differences are quite small, except for the first mode. It is believed that the foam boundary conditions had some influence on this mode, which were not modeled in the FEM model, instead being assumed perfect free-free conditions.

An autoMAC of the experimentally obtained modes was calculated, taking into account each strain component individually and then all of them together. The objective was to verify if by measuring strain on one single direction, it was possible to completely distinguish the modes from each other. Figure 30.9 shows the autoMAC comparisons. It is visible that when taking into account only one strain component, there are a lot of off-diagonal terms, indicating that those sensors by themselves are not enough to fully distinguish the modes. On the other hand, when all strain components are taken into account, then the diagonal autoMAC shows that the modes are very well distinct, meaning that by measuring multiple strain components, the strain modes are better distinguished.

Additionally, the correlation between test and simulation modes was carried out using MAC. In this way, one can also analyze the influence of the measurement in multiple strain components, and how the simulation and test modes correlate. In this case, the same method for comparison was carried out—each direction (x,y and shear xy) was compared individually, and all the directions were put together in a vector for the MAC calculation. Figure 30.10 shows these comparisons.
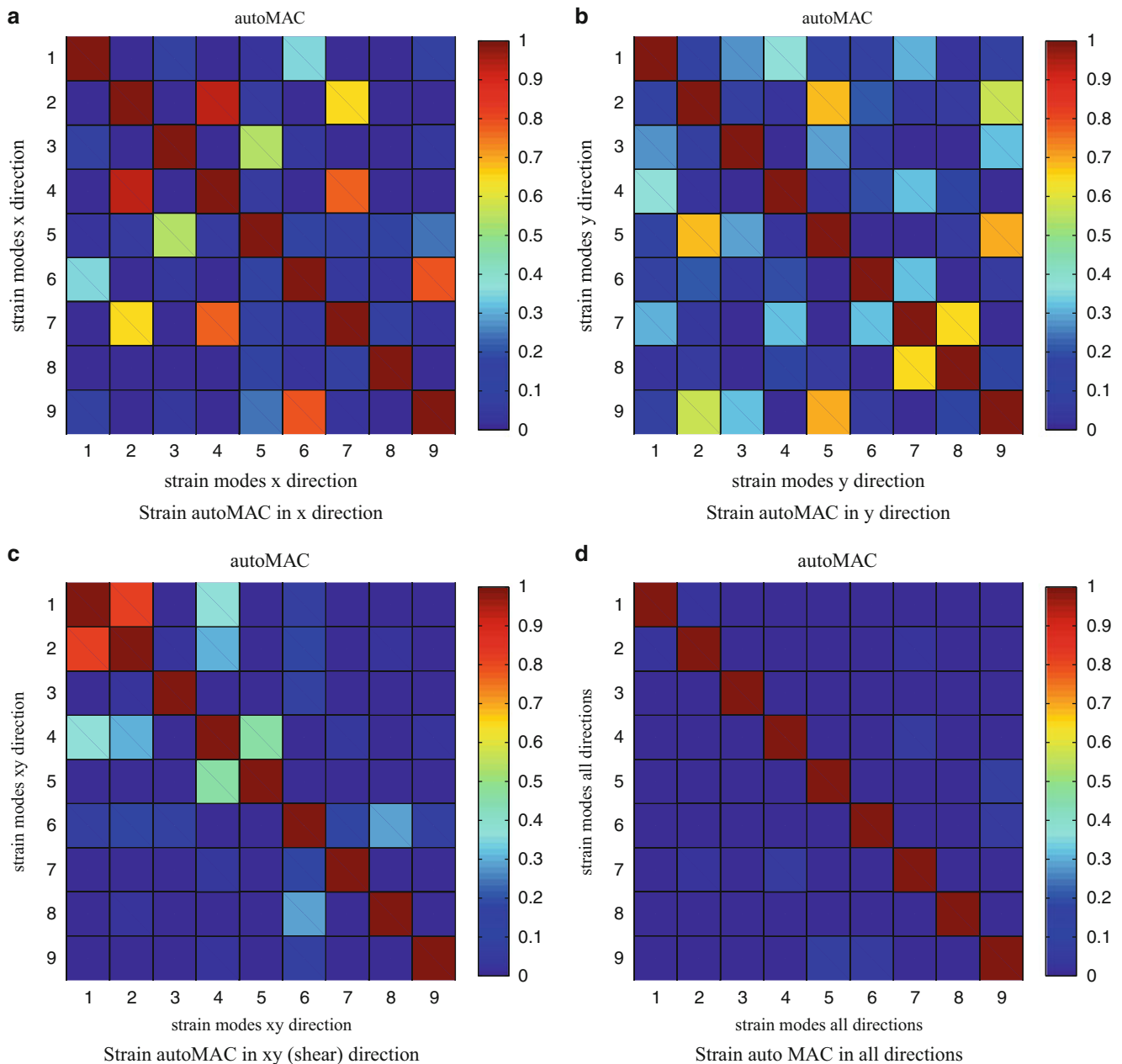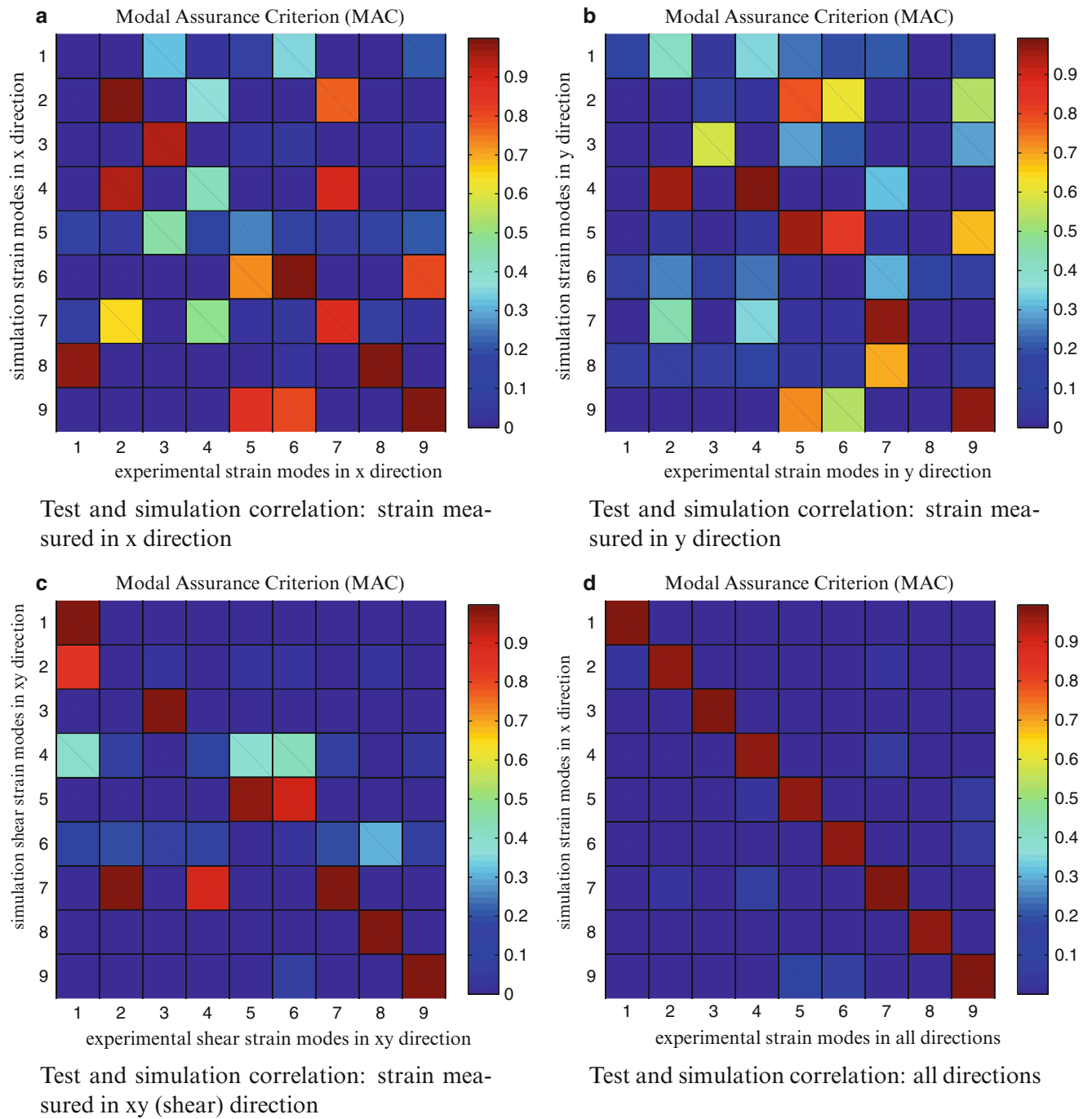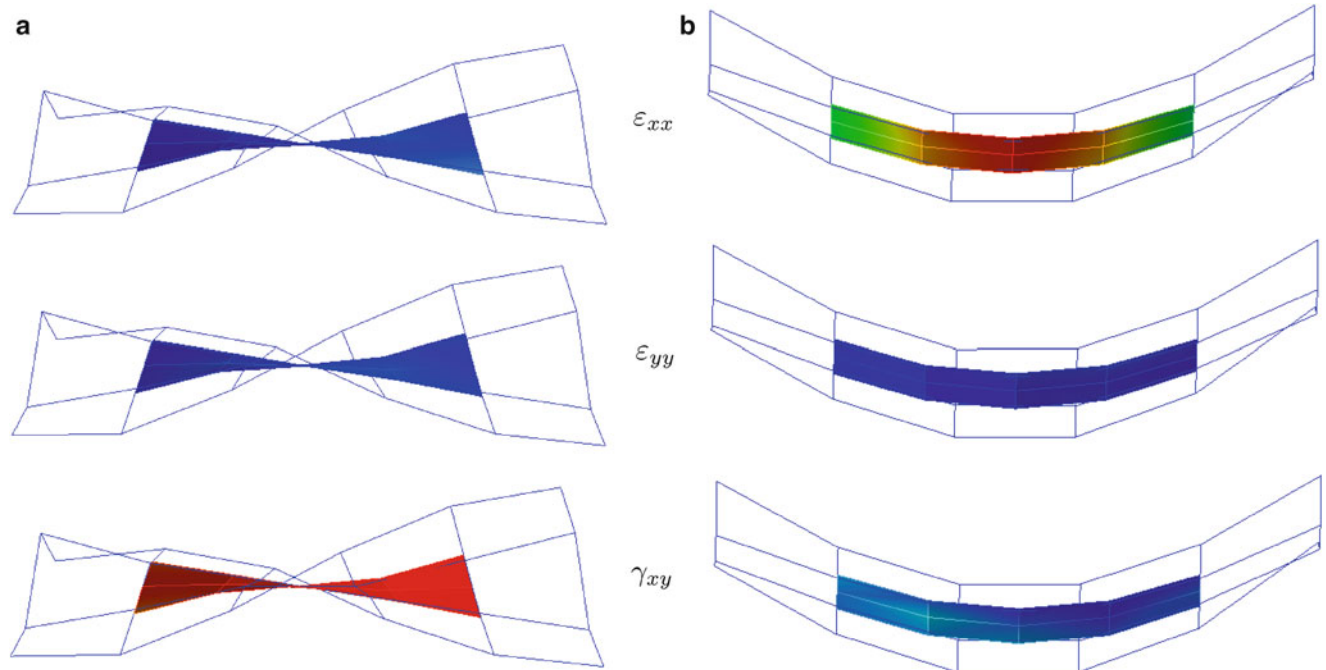
Fig. 30.9 Carbon fiber composite plate (free-free) autoMAC with strain modes: (**a**) strain modes only in x direction; (**b**) strain modes only in y direction; (**c**) strain modes only in xy (shear); (**d**) strain modes in all directions

It can be seen from Fig. 30.10 that whenever only one strain direction is taken into account, the MAC is degraded significantly. The comparison on shear shows better quality, representing the shear strain from torsion, that is almost always present, with the exception of the pure bending cases. However, once all the directions are taken into account, the MAC is drastically improved. This shows that to be able to fully represent the plate strain modes, strain measurements are required in all directions (ε_{xx}, ε_{yy} and γ_{xy}).

However, the MAC improvement in quality might also be related to the increased number of points used—when the directions are compared individually (Fig. 30.10a–c), 15 measurement points are used, while when they are put together, 45 measurement points are used. To understand whether the improvement comes from the increased number of points or not, a MAC with a reduced number of measurement rosettes was calculated—rosettes 1, 5, 8, 11 and 15 were use for the calculation, with a total of 15 measurement points (3 per rosette). Figure 30.11 shows the comparison between the MAC using all 15 sensors (45 measurements), and the MAC with a reduced sensor grid of 5 sensors (15 measurements).

Test and simulation correlation: strain measured in x direction

Test and simulation correlation: strain measured in y direction

Test and simulation correlation: strain measured in xy (shear) direction

Test and simulation correlation: all directions

Fig. 30.10 Carbon fiber composite plate test correlation with strain modes: (**a**) strain modes only in x direction; (**b**) strain modes only in y direction; (**c**) strain modes only in xy (shear); (**d**) strain modes in all directions

Comparing the results in Fig. 30.11, it can be seen that even though the quality of the correlation decreases slightly for some modes, the overall quality is very good and superior to the correlation using the individual directions, with a diagonal MAC. This proves that using a coarser grid of strain gauges, but still measuring in all directions, yields better results than using a finer sensor grid, but measuring in only one direction.

For a better visualization of the strain modes, they can be shown superimposed with the respective displacement mode. Figures 30.12 and 30.13 show the first four modes and their components in the *x*, *y* and shear (*xy*) directions. The colors represent the absolute value of strain, and the lines represent the displacement modes obtained from a roving hammer impact test.
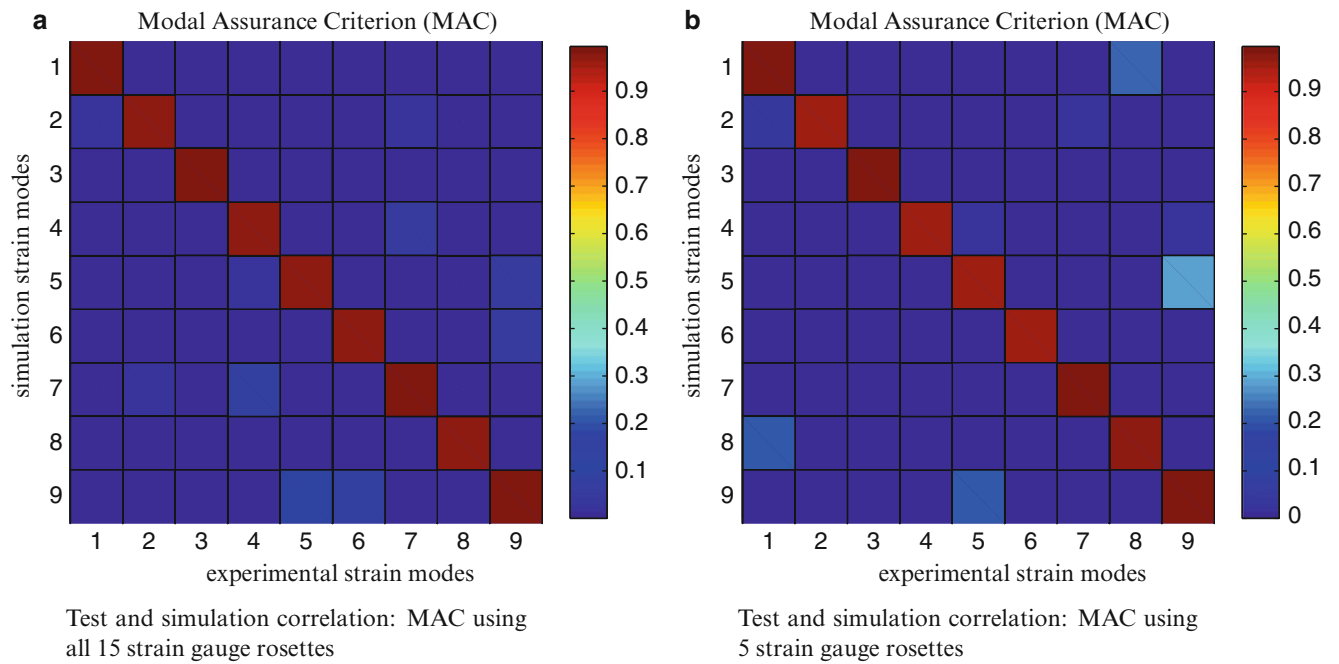
Fig. 30.11 Carbon fiber composite plate MAC with strain modes: (**a**) MAC using all 15 strain gauge rosettes; (**b**) MAC using 5 strain gauge rosettes

Fig. 30.12 Carbon fiber composite plate (free-free) first and second vibration modes: displacement modes and strain modes on ε_{xx}, ε_{yy} and γ_{xy}. (**a**) Composite plate first experimental mode—strain and displacement. (**b**) Composite plate second experimental mode—strain and displacement

30.5 Conclusions

This work presented some concepts of multi-directional modal strain, and also the equivalent strain tensor for planar strain. Then, the use of strain gauge rosettes for planar strain characterization was shown, and how the strain measurements can be decomposed to calculate shear strain and in this way measure the full strain tensor.
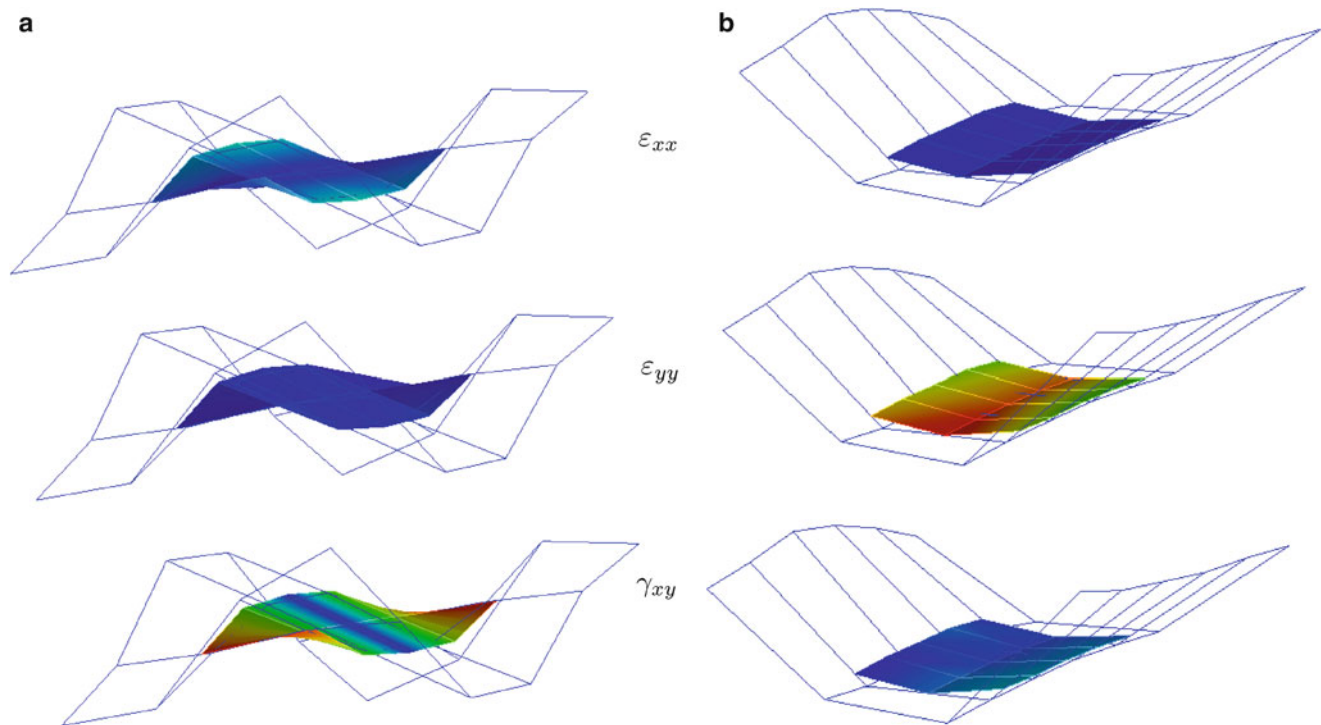
Fig. 30.13 Carbon fiber composite plate (free-free) third and fourth vibration modes: displacement modes and strain modes on ε_{xx}, ε_{yy} and γ_{xy}. (**a**) Composite plate third experimental mode—strain and displacement. (**b**) Composite plate fourth experimental mode—strain and displacement

Finally, it was seen how these planar strain measurements can be used to correlate and validate identified modes, and especially how measuring the full planar strain helps to characterize each mode as unique. Some experimental results were shown, with a carbon fiber composite plate fully instrumented with strain gauge rosettes and its strain modes were correlated with a FEM model, taking into account the individual strain components as well as the full strain tensor.

Future works include the use of different sensor technologies for strain modal analysis, as well as better methods for modal strain correlation. Moreover, the strain displacement relationship for plate-like structures will also be studied, as well as the application of strain modal analysis in structural health monitoring systems.

References

1. Suzhen, L., Zhishen, W.: Structural identification using static macro-strain measurements from long-gage fiber optic sensors. J. Appl. Mech. **8**, 943–948 (2005)
2. Kranjc, T., Slavič, J., Boltežar, M.: A comparison of strain and classic experimental modal analysis. J. Vib. Control **22**(2), 371–381 (2014)
3. Bernasconi, O., Ewins, D.J.: Modal strain/stress fields. Int. J. Anal. Exp. Modal Anal. **4**, 68–76 (1989)
4. Vári, L.M., Heyns, P.S.: Using strain modal testing. In: Proceedings of the 12th International Conference on Modal Analysis, vol. 2251, p. 1264 (1994)
5. Marques dos Santos, F.L., Peeters, B., Menchicchi, M., Lau, J., Gielen, L., Desmet, W., Góes, L.C.S.: Strain-based dynamic measurements and modal testing. In: Topics in Modal Analysis II, vol. 8, pp. 233–242. Springer, New York (2014)
6. Yam, L.H., Li, D.B., Leung, T.P., Xue, K.Z.: Experimental study on modal strain analysis of rectangular thin plates with small holes. In: Proceedings of the 12th International Modal Analysis Conference, Honolulu, HI, pp. 1415–1421 (1994)
7. Li, Y.Y., Cheng, L., Yam, L.H., Wong, W.O.: Identification of damage locations for plate-like structures using damage sensitive indices: strain modal approach. Comput. Struct. **80**(25), 1881–1894 (2002)
8. Lie, H., Kaasen, K.E.: Modal analysis of measurements from a large-scale VIV model test of a riser in linearly sheared flow. J. Fluids Struct. **22**(4), 557–575 (2006)

9. Trim, A.D., Braaten, H., Lie, H., Tognarelli, M.A.: Experimental investigation of vortex-induced vibration of long marine risers. J. Fluids Struct. **21**(3), 335–361 (2005)
10. Lubliner, J.: Plasticity Theory. Dover, Mineola (2008)
11. Rees, D.: Basic Engineering Plasticity: An Introduction with Engineering and Manufacturing Applications. Butterworth-Heinemann, London (2012)
12. Kranjc, T., Slavič, J., Boltežar, M.: The mass normalization of the displacement and strain mode shapes in a strain experimental modal analysis using the mass-change strategy. J. Sound Vib. **332**(26), 6968–6981 (2013)
13. Micro-Measurements. Plane-Shear Measurement with Strain Gages. Vishay Precision Group, document number: 11062 edition, 09 (2010)
14. Sciammarella, C.A., Sciammarella, F.M.: Strain gage rosettes: Selection, application and data reduction. In: Experimental Mechanics of Solids. Wiley, Chichester (2012)

Chapter 31
Magnetic Excitation and the Effects on Modal Frequency and Damping

B.C. Baver, A.W. Phillips, R.J. Allemang, and J. Kim

Abstract Non-contact excitation sources are critical for exciting small structures that cannot be excited by conventional means, such as electromagnetic shakers, due to the added mass and stiffness effects or by impact testing, due to potential surface damage. Magnetic excitation is one possible method of non-contact excitation. However, if the material is non-ferrous, magnetic excitation will require that a ferrous material, potentially a small magnet, be attached at a desired excitation location. The addition of the magnet will have some small effects on the modal frequency and damping. The addition of multiple magnets, combined with phased magnetic excitation to enhance bending or torsion modes, is also possible, and can cause the effects to be greater. This paper will examine the effects that the added mass has on the natural frequencies and damping of a cantilever plate. It will examine four different plate configurations; an unloaded plate (for reference), and three different mass configurations, all of which will be added to the free tip of the plate. Experimental modal analysis will be performed using two different excitation sources, an impact hammer and magnetic excitation, for comparison purposes. The natural frequencies and damping for the first five deformation modes will be compared for the two different excitation sources and between the different mass configurations. A finite element modal analysis model will be created and calibrated to the unloaded plate experimental data. Then, mass modifications (magnets) will be added into the finite element model and used to predict the natural frequencies of the various mass configurations.

Keywords Non-contact excitation • Magnetic excitation • Modal frequency estimation • Finite element analysis • Model calibration

Symbols

λ_r	Complex modal frequency
σ_r	Modal damping (rad/s)
ω_r	Damped natural frequency (rad/s)
Ω_r	Undamped natural frequency (rad/s)
ζ_r	Critical damping ratio
$[\alpha]$	Numerator polynomial matrix coefficient
$[\beta]$	Denominator polynomial matrix coefficient
$[H(\omega_i)]$	Frequency response function
$[I]$	Identity matrix
ω_i	Frequency (rad/s)

31.1   Introduction

In this paper, non-contact magnetic excitation will be examined as it pertains to exciting non-ferrous materials. In order to excite these materials, a ferrous material must be attached to the test specimen so that the magnetic source can be effective. When the structure is lightweight, these attachments can cause some effects on the modal properties. When accurately

B.C. Baver (✉) • A.W. Phillips • R.J. Allemang • J. Kim
Structural Dynamics Research Laboratory, Mechanical and Materials Engineering, University of Cincinnati,
Cincinnati, OH 45221-0072, USA
e-mail: baverbc@mail.uc.edu

predicting the natural frequencies and damping of a structure is of high importance, characterizing the effects of adding magnets to the system is critical. This section will discuss the need for non-contact excitation, background information, and provide an introduction to the test procedure used for this paper.

31.1.1 Non-contact Excitation Requirement

One of the most common types of excitation in experimental modal analysis are electrodynamic shakers. These shakers, depending on the size, have maximum operating frequencies that range from 1 to 20 kHz and force input levels from 2 to 1000 lbf [1]. However, these shakers are attached to the test specimen with a stinger, mounting pad, and a load cell. Essentially, the mounting pad is a mass between the structure and the load cell, which is detected by the load cell as added mass of the structure [1]. In structures with large mass, this connection and attachment of load cell and mounting pad does not cause any noticeable issues. However, lightweight structures will experience some effects due to the attachment.

Impact testing is another option for experimental modal analysis. This would be an ideal situation for a lightweight structure, especially if a non-contact response measurement is possible. However, this test method requires being able to reach/contact the structure, which can be difficult if the specimen is in an environment or location that is not easily accessible.

Response measurements for both of the test types mentioned above are typically measured using accelerometers attached to a structure using a wax, glue or similar adhesive material. Even the smallest accelerometers will have similar mass loading effects on a lightweight structure that adding a magnetic material would have. The accelerometer will also have a cable attached to it to transmit the acceleration signal, which will also significantly increase the damping estimate of the structure. For a lightly damped, lightweight system, this will greatly affect the damping estimate. To overcome this issue, a laser vibrometer is a non-contact response measurement method that can be used.

31.1.2 Background Information

Modal parameter estimation is the process of using experimental data (typically FRF's) to estimate the complex valued modal frequencies (frequency and associated damping) over a certain frequency range. These parameters are used to help predict how a structure will behave due to certain excitations or inputs. Predicting these properties is critical to a number of different areas of engineering. These include having information for safe and effective designs as well as failure analysis, to name a couple. These properties are more difficult to accurately predict when a system is lightly damped. The structure analyzed in this paper is an underdamped structure, so all discussion will focus on very lightly damped systems.

An underdamped system is a system that has a damping ratio less than one. This yields a complex solution to the characteristic equation, with the two roots being conjugate pairs in the form below. The real part, σ_r, is referred to as the modal damping and the imaginary part, ω_r, is the damped natural frequency. These two terms can be used to describe the undamped natural frequency, Ω_r, and the critical damping ratio, ζ_r, of a system.

$$\lambda_r = \sigma_r \pm j\omega_r{}^{[3]} \tag{31.1}$$

$$\Omega_r = \sqrt{\omega_r^2 + \sigma_r^2}{}^{[3]} \tag{31.2}$$

$$\zeta_r = -\frac{\sigma_r}{\sqrt{\omega_r^2 + \sigma_r^2}}{}^{[3]} \tag{31.3}$$

These properties are estimated using the frequency response function (FRF) data in one of the numerous modal parameter estimation (MPE) algorithms typically implemented. These solution methods have commonalities. They can be grouped into the idea of using multiple equations of motion in matrix form to find a least squares solution for the various unknowns; this method has come to be known as the Unified Matrix Polynomial Approach, or UMPA method [6]. Even though both a time domain or frequency domain solution is possible, the basic kernel of these equations remains the same, as shown below in Eqs. (31.4) and (31.5) [4] as a matrix coefficient polynomial equation in either powers of s or z.

$$\left| [\alpha_m] s^m + [\alpha_{m-1}] s^{m-1} + \cdots + [\alpha_0] \right| = 0^{[4]} \tag{31.4}$$

$$[\alpha_m] \, z^m + [\alpha_{m-1}] \, z^{m-1} + \cdots + [\alpha_0] = 0^{[4]} \tag{31.5}$$

Equation (31.5) will become the basis of the rational fraction polynomial with Z mapping (RFP-Z) algorithm that will be used throughout the course of this study. This algorithm is a high order, frequency domain based algorithm mapped into the Z-domain for numerical improvements. These high order, frequency domain algorithms utilize the FRF information at successive frequency steps until a sufficient number of equations exists to form a solution. The general equation listed in Eq. (31.6) shows one equation used in the solution to these algorithms. Equation (31.6) is an overdetermined equation (by setting α_m to unity), allowing for the alpha and beta coefficient matrices to be determined. Knowing the alpha and beta coefficient matrices allows the roots of the characteristic polynomial equation to be solved for using Eq. (31.4).

$$\begin{bmatrix} [\alpha_0] \; [\alpha_1] \ldots \; [\alpha_{m-1}] \; [\beta_0] \; [\beta_1] \ldots [\beta_n] \end{bmatrix} \begin{bmatrix} [H\,(\omega_i)] \\ (j\omega_i)^1 \, [H\,(\omega_i)] \\ (j\omega_i)^2 \, [H\,(\omega_i)] \\ \ldots \\ (j\omega_i)^{m-1} \, [H\,(\omega_i)] \\ - \, [I] \\ -(j\omega_i)^1 \, [I] \\ - \, (j\omega_i)^2 \, [I] \\ \ldots \\ - \, (j\omega_i)^n \, [I] \end{bmatrix} = -(j\omega_i)^m [H\,(\omega_i)]^{[4]} \tag{31.6}$$

31.1.3 Test Procedure

For these experiments, a test specimen with a simple geometry and boundary conditions was examined. A rectangular plate with a fixed end was used since the geometry was simple and creating the fixed free boundary condition was relatively straight forward. This specimen was made from a non-ferrous material to ensure that the magnetic excitation would require additional magnetic materials be added. Small neodymium magnets were added in three configurations. Overall, four configurations were examined. These configurations can be seen in Figs. 31.3 and 31.4 and are listed below as well.

- 0 magnets
- 2 magnets at the center of the free end of the plate, one on each side of the plate
- 4 magnets at the free end of the plate, 2 at each of the corners of the plate (1 per side at each location)
- 6 magnets, creating a combination of the first two configurations at the free end of the plate.

These configurations were tested with two different excitation sources. One of those was a tiny impact hammer. The second was magnetic excitation. The magnetic excitation used a pseudo random signal. For the configurations with sufficient magnets (more than two), phased excitation was utilized to enhance certain modes so that their effects dominate the response measurements. This was especially useful for modes that are close in frequency. For example, for the four-magnet configuration, two different phased excitations enhance the bending modes and enhance the torsion modes, respectively. This is done by reversing the polarity of the exciters on one corner of the plate. Figures 31.1 and 31.2 compares two phased excitations to a single input excitation and an impact excitation for the plate examined here. These two modes are closely spaced. As the figures shows, the torsion mode becomes more prominent when the excitation is used to enhance that mode. It should be noted that, since response measurements are being made with a laser vibrometer, there potentially will be some fallouts/irregularities in the data, as seen in Fig. 31.1, part b and Fig. 31.2, parts a and b, with examples pointed out.

31.2 Experimental Modal Analysis

Although a non-contact magnetic excitation will have less effect on the measurements than a shaker would, having a nonmetallic test specimen requires that a magnetic material be attached to the specimen at the desired point of excitation is a potential concern. The added mass will change the mass distribution of the specimen. Therefore, various tests were performed to determine what effect the mass of the added magnets would have on the natural frequency and damping of the
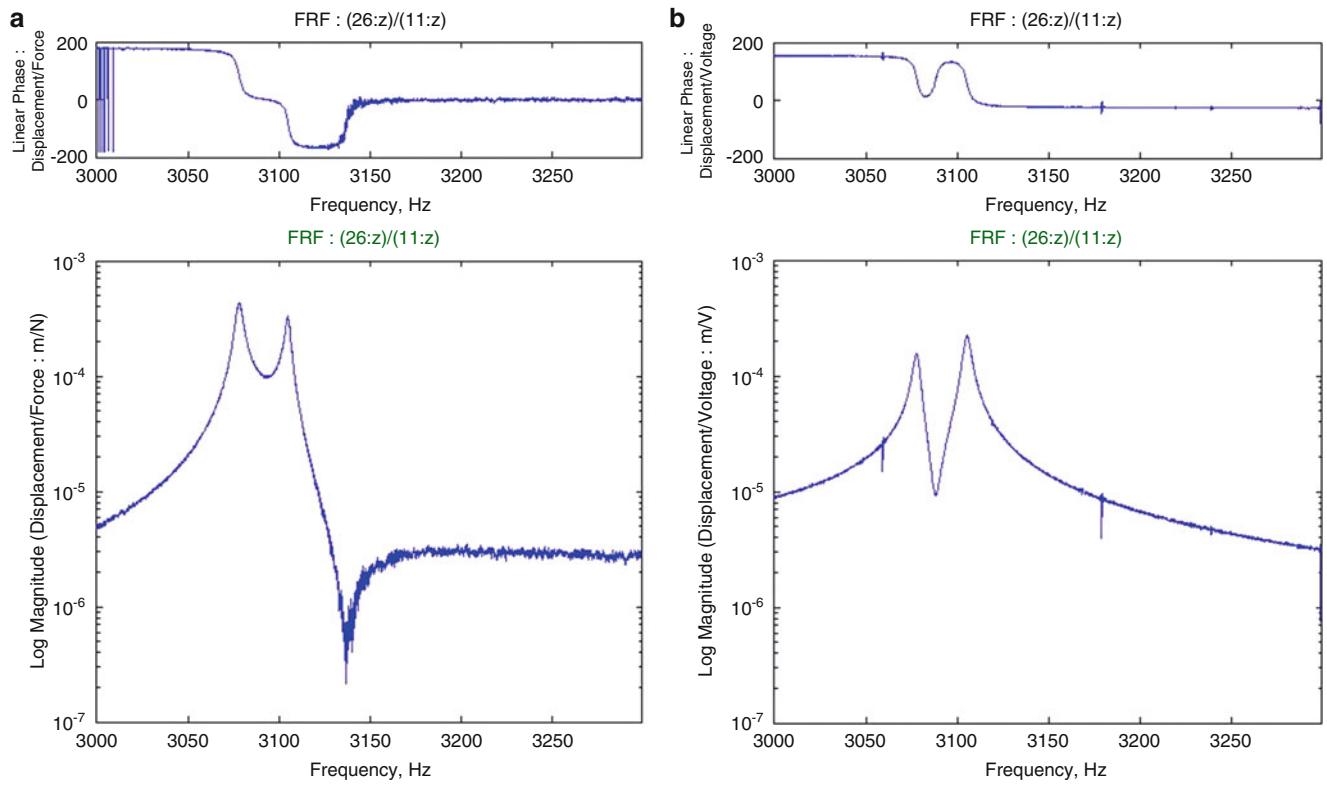
Fig. 31.1 FRF comparison for single point excitation. (**a**) Impact excitation; (**b**) Corner excitation
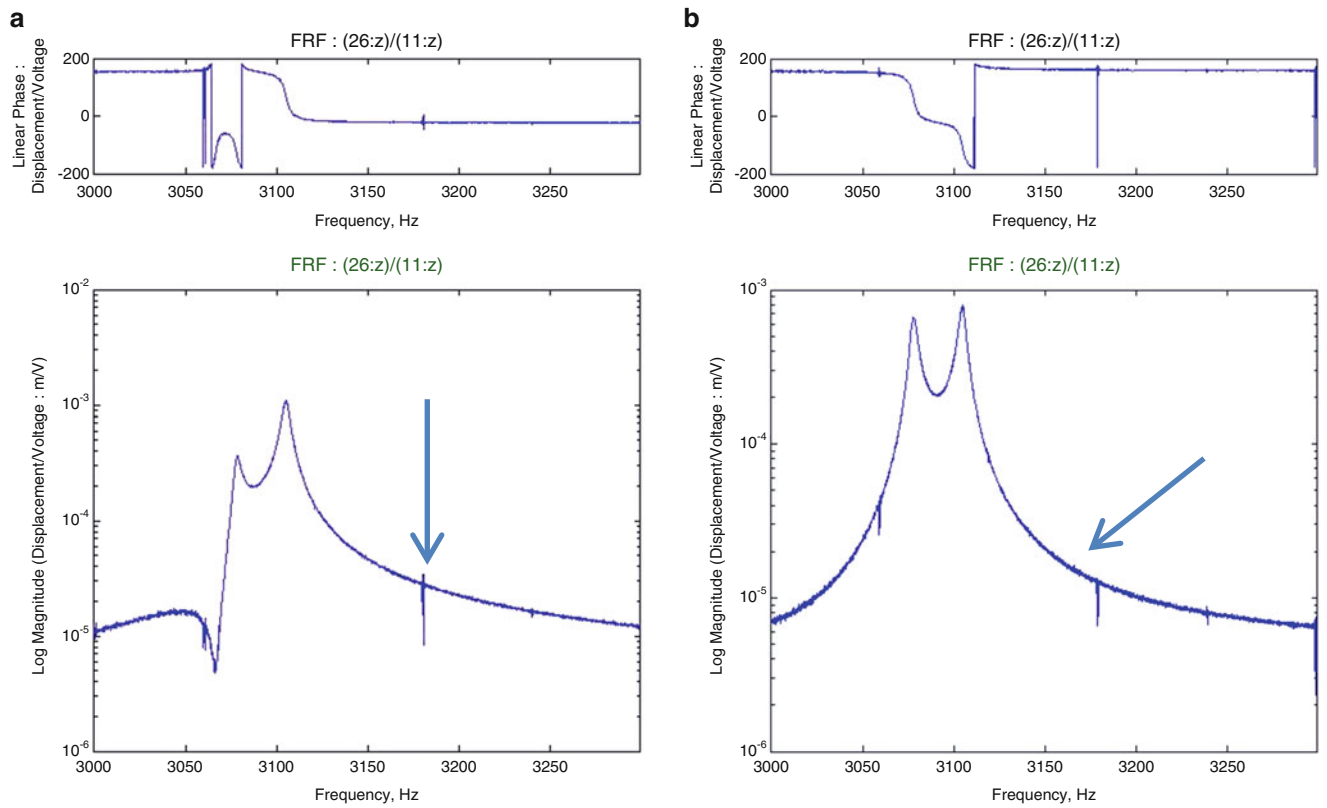
Fig. 31.2 FRF comparison for phased excitations. (**a**) Bending excitation; (**b**) Torsion excitation

Table 31.1 Natural frequency comparison for mass loaded plate, impact excitation

Mode description	0 Magnets (Hz)	2 Magnets (Hz)	4 Magnets (Hz)	6 Magnets (Hz)
1st Bend	119.8	118.5	117.2	115.9
2nd Bend	747.2	740.5	735.1	728.6
3rd Bend	2093.0	2074.3	2071.8	2054.6
1st Torsion	505.9	506.1	489.0	489.0
2nd Torsion	1651.5	1653.4	1592.1	1592.9

Table 31.2 Natural frequency comparison for mass loaded plate, magnetic excitation

Mode description	2 Magnets (Hz)	4 Magnets (Hz)	6 Magnets (Hz)
1st Bend	118.3	116.3	114.9
2nd Bend	740.4	734.9	728.2
3rd Bend	2074.4	2071.8	2054.0
1st Torsion	506.0	488.8	488.6
2nd Torsion	1653.5	1592.1	1592.1

Table 31.3 Damping comparison for mass loaded plate, impact excitation

Mode description	0 Magnets (%ζ)	2 Magnets (%ζ)	4 Magnets (%ζ)	6 Magnets (%ζ)
1st Bend	0.0317	0.0237	0.0229	0.0218
2nd Bend	0.0331	0.0291	0.0234	0.022
3rd Bend	0.0577	0.0558	0.0498	0.0463
1st Torsion	0.0279	0.0237	0.0219	0.0195
2nd Torsion	0.0361	0.0307	0.0271	0.0265

plate. First, a test of the unloaded plate with no magnets had to be performed. This was done by exciting the system with a tiny impact hammer and measuring the response with the vibrometer. Then, magnets were added along the free tip, in pairs, as described previously. These magnets were added with a bonding agent with specific application intended for magnets.

For each magnet configuration, two different excitation sources were examined. Typically, an SDOF approach is initially used for getting first estimates of the modal frequencies for a system [4]. However, these methods are limited to modes sufficiently separated in frequency. Using a MDOF approach and phased excitation allows modes close in frequency to be distinguishably identified [2, 6]. Implementing the RFP-Z algorithm allows for improved numerical conditions through the use of generalized frequency/z-mapping [4]. The frequency and damping for each configuration were compared against the excitation source as well as against each configuration. Tables 31.1 and 31.2, below, outline the natural frequency results from the mass loading tests performed with the larger of the two types of magnets.

As expected, the natural frequencies decreased with the addition of mass to the plate. It should be noted that, for the addition of two magnets to the center of the plate, the torsion modes do not change much. This is easily seen when comparing the natural frequency for the two torsion modes for the four-magnet and six-magnet test cases. This is due to the centerline of the plate being on a node line for the torsion modes, resulting in the added mass having little effect on these modes.

The excitation source does not seem to have much of an effect on the natural frequencies of the plate either. The frequencies for the modes examined are very similar for the two different excitation sources. The error associated with these differences can probably be attributed to errors due to the signal processing techniques rather than the structural properties being changed.

Damping was also examined for the four cases mentioned above to see if the addition of magnets and bonding material would provide additional damping to the system. Table 31.3 examines the effect the addition of magnets and the effect the excitation source has on the damping estimate.

As with the natural frequency, the damping ratio does reduce as the number of magnets is increased. This can be expected, since the critical damping value will decrease as the mass of the system increases.

31.3 Finite Element Analysis

Even though the magnets do not have significant mass compared to the total mass of the plate, they do have enough mass to affect the natural frequencies. In order to determine the effect, analytical modal analysis was performed on the plate in ANSYS for the various magnet configurations used in the experimental testing.

As discussed previously, the plate was analyzed four ways, one with no magnets and three with different configurations of magnets. These different configurations were modeled in ANSYS. The properties (density, Young's Modulus, Poisson's Ratio) were defined for both the plate as well as the magnets. Then, modal analysis was performed for the original plate and each of the three magnet configurations. Figures 31.3 and 31.4, below, shows each of the four models that were analyzed.

The first FE model examined was the no-magnet case. This unloaded plate model was used to calibrate the FE model to the experimental model. The calibration process is similar to the process outlined in Reference [8]. This model was evaluated with nominal properties for the material density, Young's Modulus, and Poisson's ratio. To determine the density, weights of the finite element model were compared to weights of the plate. The densities were adjusted to produce a weight that was equivalent to the physical weight. Once the density was determined, the Young's Modulus and Poisson's ratio were determined. This was done by holding one value for the material constant and changing the other to determine the effect on the modal frequencies. Typically, increasing the Young's Modulus will increase the natural frequencies of all modes, and increasing Poisson's Ratio will increase the natural frequencies of the bending modes and decrease those of the torsion modes. The changes in frequency are recorded and compared to experimental frequencies to determine what changes need to be made. The parameters are modified until the natural frequencies of the FE model are within 0.5 % of the experimental results.

The results for the first 5 deformation modes (3 bending, 2 torsion) were examined and compared to the experimental results. Both the frequency and mode shape were compared. Table 31.4 compares the natural frequencies of the FE results
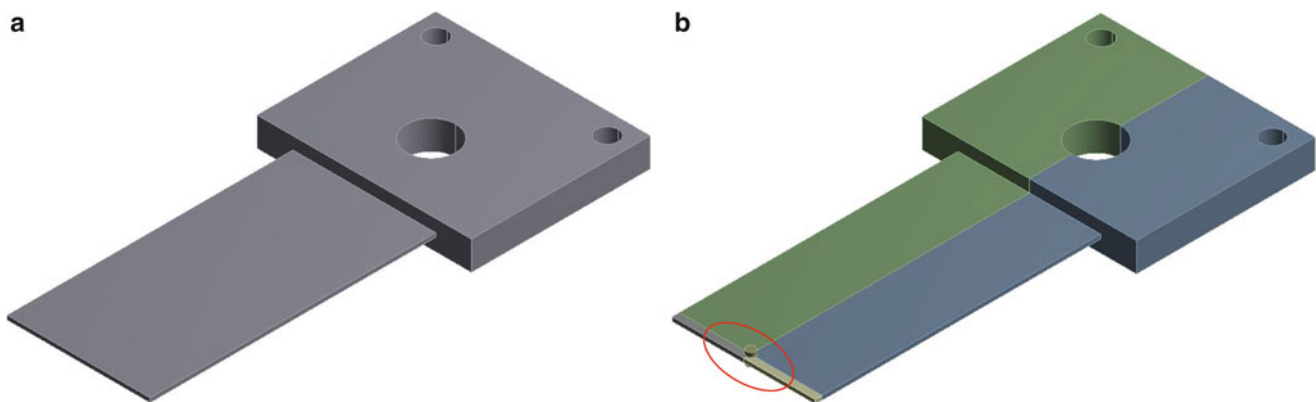
Fig. 31.3 Zero and two magnet configurations of cantilever plate. (**a**) Zero magnets; (**b**) Two magnets
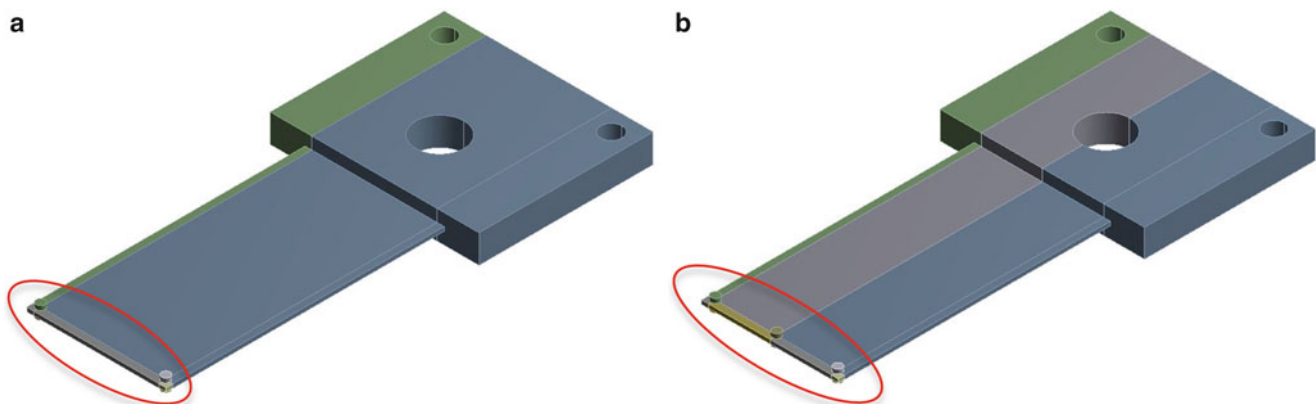
Fig. 31.4 Four and six magnet configurations of cantilever plate. (**a**) Four magnets; (**b**) Six magnets

Table 31.4 Mass loading comparison, FE vs experimental

Exp. frequency (Hz)	FE frequency (Hz)	% Diff	Mode description	# Magnets
114.9	115.3	0.35	1st Bending	6
488.6	489.8	0.25	1st Torsion	6
728.2	722.6	0.70	2nd Bending	6
1592.1	1593.2	0.06	2nd Torsion	6
2054.0	2038.1	0.77	3rd Bending	6
116.3	116.5	0.17	1st Bending	4
488.8	489.6	0.16	1st Torsion	4
734.9	728.5	0.87	2nd Bending	4
1592.1	1590.1	0.13	2nd Torsion	4
2071.8	2053.5	0.88	3rd Bending	4
118.3	117.7	0.51	1st Bending	2
506.0	505.8	0.04	1st Torsion	2
740.4	733.6	0.92	2nd Bending	2
1653.5	1649.4	0.25	2nd Torsion	2
2074.4	2073.9	0.02	3rd Bending	2
119.8	119.9	0.08	1st Bending	0
505.9	505.1	0.16	1st Torsion	0
747.2	745.4	0.24	2nd Bending	0
1651.5	1647.4	0.25	2nd Torsion	0
2093.0	2089.0	0.19	3rd Bending	0

and the experimental results and provides the percent difference between them. The small percent difference gives confidence that the FE model is calibrated to the experimental model. The description of the mode is provided as well to show that the shapes were compared.

31.4   Conclusions

Predicting the modal frequencies and damping of a lightweight, lightly damped, non-ferrous structure accurately can be difficult. First, excitation of the system is difficult. A shaker is not ideal due to the additional mass that is required to be added to the structure. An impact test is an improvement, but in difficult to reach locations is not practical. Using an accelerometer to make response measurements also causes problems similar to the shaker attachment problems, with some additional damping added to the system as well. These problems are overcome by attaching a lightweight magnetic material to the structure and using magnetic excitation to excite the source along with a non-contact response measurement system to measure the system response to the excitation.

The validity of these predictions can be determined through calibrating the finite element model with the experimental model. This is done by performing a parametric study of the density, Young's Modulus, and Poisson's Ratio of the plate in the finite element model. The density will be verified by comparing the mass of the plate to the mass of the finite element model. Once the mass is verified, Young's Modulus and Poisson's ratio will be varied one at a time to obtain natural frequencies within 1 % of the experimental model, calibrating the model to the experimental data. The final step is to make small changes to the finite element model and see if the model can predict the new properties of the structure. For the structure tested, this was done by modeling the magnet addition and using it to predict the new natural frequencies. It was shown previously how accurate the natural frequencies of the finite element model compared to the experimental model.

Overall, this paper examined the effects of adding a magnetic material to a cantilever plate has on the structures damping and modal frequencies. This was examined by comparing four different experimental datasets; this included an unloaded plate, for reference, and three different loaded conditions. Specifically, comparisons were made for both the modal frequencies and damping for the different mass loadings. A finite element model is then calibrated to the reference data and used to predict modal frequencies for the three different mass loading conditions.

References

1. The Fundamentals of Modal Testing. Agilent Technologies, Application Note 243, 66 pp (2000)
2. Ewins, D.: Modal Testing: Theory and Practice. Wiley, New York, 269 pp (1984)
3. Allemang, R.J.: Vibrations: experimental modal analysis. UC-SDRL-CN-20-263-663/664, 381 pp (2015)
4. Allemang, R.J.: Vibrations: Analytical and Experimental Modal Analysis. UC-SDRL-CN-20-263-662, 220 pp (2015)
5. Allemang, R.J., Brown, D.L.: "Modal parameter estimation" experimental modal analysis and dynamic component synthesis. USAF Technical Report, Contract No. F33615-83-C-3218, AFWAL-TR-87-3069, Vol. 3, 130 pp (1987)
6. Allemang, R.J., Brown, D.L., Fladung, W.: Modal parameter estimation: a unified matrix polynomial approach. In: Proceedings, International Modal Analysis Conference, 501–514 (1994)
7. Allemang, R.J., Phillips, A.W.: The unified matrix polynomial approach to understanding modal parameter estimation: an update. In: Proceedings, International Seminar on Modal Analysis (ISMA), 2004
8. Chang, E.: Damping identification of viscoelastic coating materials through finite element modal analysis. MS Thesis, Department of Mechanical and Materials Engineering, University of Cincinnati, 62 pp (2015)

Chapter 32
Automated Extraction of Mode Shapes Using Motion Magnified Video and Blind Source Separation

Charles J. Dorn, Tyler D. Mancini, Zachary R. Talken, Yongchao Yang, Garrett Kenyon, Charles Farrar, and David Mascareñas

Abstract Traditionally, experimental and operational modal analysis requires wired sensors that are physically attached to the structure of interest for vibration measurements. The instrumentation of these sensors on structures for long-term applications (e.g., structural health monitoring) is costly, time-consuming, and requires significant maintenance. Even if a wireless sensor network is used, there still exist substantial challenges associated with security, available bandwidth, and providing energy to the network. As a non-contact method, optics measurements from digital cameras combined with vision based algorithms have been successfully used for experimental vibration measurement and analysis. This opens the door to replacing physical sensors with remote sensing techniques, which could eliminate many of the problems associated with conventional distributed sensor networks. However, research to date has focused on simple structures that can be represented using a single edge. In this work, we propose a novel phase-based video motion magnification and Blind Source Separation (BSS) based method to perform operational modal analysis in a relatively efficient and automated manner.

Keywords Operational modal analysis • Motion magnification • Blind source separation • Video processing • Damage detection

32.1 Introduction

Traditional experimental and operational modal analysis mostly require physically-attached wired or wireless sensors, such as accelerometers that affixed to the structure. Physical instrumentation of these sensor is an expensive and time-consuming process and may have the effect of mass-loading the structure. Non-contact measurement methods such as scanning laser vibrometers can address some of these challenges; however, it is relatively expensive and can only provide sequential measurements that is likely to be time and labor consuming.

As an alternative non-contact method, video camera based measurement is relatively low-cost and agile with high spatial sensing resolution. Video camera based measurement techniques such as digital image correlation (DIC) and point-tracking methods have recently been successfully applied in experimental modal analysis [1–5]. Nevertheless, they normally require structural surface preparation such as speckle paint or high-contrast makers, which can be cumbersome when the measurement area is relatively large or inaccessible. Lately, a video processing based method using phase-based optical flow

C.J. Dorn
Department of Engineering Physics, University of Wisconsin – Madison, Madison, WI 53706, USA
e-mail: charlesjdorn@gmail.com

T.D. Mancini
Department of Mechanical and Aerospace Engineering, State University of New York at Buffalo, Buffalo, NY 14260, USA
e-mail: tylermancini@gmail.com

Z.R. Talken
Department of Mechanical and Aerospace Engineering, Missouri University of Science and Technology, Rolla, MO 65409, USA
e-mail: zrtalken@gmail.com

Y. Yang (✉) • C. Farrar • D. Mascareñas
Los Alamos National Lab – Engineering Institute, PO Box 1663, MS T001, Los Alamos, NM 87545, USA
e-mail: yyang@lanl.gov; farrar@lanl.gov; dmascarenas@lanl.gov

G. Kenyon
Los Alamos National Lab, PO Box 1663, MS D454, Los Alamos, NM 87545, USA
e-mail: gkenyon@lanl.gov

and video motion magnification technique has been proposed for operational modal analysis [6], which has the advantage of being used without paints or markers on structures. To date, this method has focused on simple structures consisting of one edge (e.g., a cantilever beam or a pipe cross-section) and relies heavily on the user for the necessary input in the modal identification implementation process. In order for video-based modal analysis methods to gain acceptance, it must be verified for more complicated structures and the user dependency must be minimized.

The objective of this study is to broaden the capabilities of video based operational modal analysis by developing an advanced computer vision and machine learning based method that is efficient requiring user supervision and without the need of surface preparation on structures. This method improves upon the previous work by automating the mode identification process and allowing for complicated geometries and motion to be analyzed. Videos of vibrating structures are first filtered using multi-scale decomposition and representation technique to extract local phase and amplitude, which is then blindly separated into individual modes by a blind source separation technique called complexity pursuit (CP) [7]. Natural frequencies are extracted from the Fourier transform of these components. By magnifying the extracted modes, the constructed video then displays a magnified operating mode shape, which can be extracted by edge detection method.

32.2 Background

32.2.1 Phase-Based Optical Flow

A method known as phase-based motion magnification of video [8] has shown promise in its ability to achieve large magnification factors without magnifying noise, leaving relatively clean video with few unwanted artifacts. This capability is extremely important for extending computer vision to modal analysis since noise can easily unravel the process.

The phase-based magnification process begins with the spatial decomposition of each video frame. A complex steerable pyramid [9] is used to decompose the image and separate the local phase and amplitude. There are multiple levels of the pyramid, corresponding to different spatial scales. The local phase is filtered temporally to isolate the frequency band specified by the user. Before the reconstruction of the video, the phases in the specified frequency band are scaled by a magnification factor.

32.2.2 Phase-Derived Vibration Motions of Structures

Video based modal analysis techniques have recently been developed utilizing phase-derived optical flow [6]. In this method, displacement signals at various regions of the structure are extracted from video. Unlike [1–5], targets are not necessary. Motion signals are extracted from the edges of a structure instead. The process begins by convolving a quadrature pair of filters with each frame of the image to determine local phase and amplitude at each pixel. Local amplitude is related to edge strength while local phase is related to velocity in at each pixel.

In [6], regions of interest are cropped from the video corresponding to where accelerometers would traditionally be placed on a structure, called 'virtual accelerometers', where velocity signals are computed from the temporal phase contours. Afterwards the peak-picking methods are used to identify the modal frequency, which is then used as inputs to the motion magnification method to magnify the specified frequency band contents and reconstruct the magnified video. This process— selection of interested region and picking the modes—needs to be supervised by modal analysis experts.

The proposed method in this study attempts to eradicate these constraints by automating the video based modal analysis process using computer vision and machine learning technique that requires little user supervision. Instead of selecting a region of interest, our method extracts the local phases and local amplitudes of each pixel of the whole video (keeping the high-resolution spatial information of the structure vibration and blindly and autonomously separates the extracted local phases into individual structural modes, which are then magnified, respectively, and reconstructed to the video containing only one mode.

32.2.3 Blind Separation of Modes

Blind source separation is a class of unsupervised learning problems that seeks to break up a set of mixed signals into the individual source signals without any knowledge of the input. The key idea of using BSS for output-only modal identification

is that modal expansion of the structural responses (local phases) has the exact same form with the linear BSS model, such that BSS can blindly and efficiently separate the structural responses into individual modes.

Filtering each frame by the complex steerable pyramid results in a set of local phase time series signals $\delta(x, t)$ for each pixel. A BSS technique called complexity pursuit (CP) can blindly separate $\delta(x, t)$ into individual modes $q(t)$ [7]

$$q(t) = W\delta(x, t) \tag{32.1}$$

Frequency and damping ratio can be identified from the time domain modal coordinates $q(t)$.

32.2.4 Motion Magnification of Individual Modes

Magnification of the blindly separated individual modes can be conducted by multiplying $q_i(t)$ (i is the mode number to be magnified) and reconstructing back to obtain the video with only the single magnified mode. Visualization of the single mode vibration is possible in the video. Edge detection can be conducted on the magnified video to obtain the mode shape with very high spatial density. The whole video processing based modal analysis process is conducted blindly and efficiently to extract the frequency and the high-resolution mode shapes with very little user supervision.

32.3 Experimental Study

A small scale model of a three story structure was used for the development of this modal analysis method. An impact hammer was used to excite the structure by striking the top floor. The base of the structure was fixed to a solid steel plate resting on the ground to eliminate the rigid body mode. For reference, the weight of the structure was 27.56 kg and the weight of the plate was 48.08 kg. The structural motion was mostly undergoing in one direction, parallel to the edge of the structure and perpendicular to the plane of the camera lens; however, no calibration is needed in the process). Modal properties measured from video were then compared to accelerometer data collected from each floor of the structure. Three uniaxial accelerometers were used to extract mode shapes for comparison and validation. One accelerometer was attached to each floor of the structure to obtain simplified three degree of freedom operating mode shapes. A single stationary camera was positioned perpendicular to the motion of the structure. Video was captured at 240 frames per second at a resolution of 1920×1080 pixels. A photo of the experimental setup is shown in Fig. 32.1 below.

32.3.1 Video Processing Procedure and Results

The proposed method uses the video measurements only to extract the natural frequency of each mode and a video containing only one single operating mode. The process begins with the spatial decomposition of each frame of the video using a complex steerable pyramid. The framework of original phase-based magnification was used to decompose and the video into spatial sub-band using a complex steerable pyramid. Each level of the pyramid is processed separately. The processing procedure for each pyramid level is as follows. A complex filter is convolved with the intensity matrix of each frame. The magnitude and argument of the complex valued filtered image correspond to the local amplitude and local phase of each pixel, respectively. The time series local phase signal for each pixel are analyzed using CP. Figure 32.2 below shows the three CP signals of the laboratory scale three story structure used in our experiment. Each signal oscillates at only one frequency, as shown by their frequency spectra which match those from the accelerometers quite well (accelerometers results are not shown here for limited space).

The output of CP is a time series signal corresponding to each active structural mode in the video. One CP signal is multiplied by a magnification factor. The CP are then reversed, reconstructing the magnified local phase matrix. Magnified local phase is then recombined with the unchanged local amplitude. This process is conducted on each level of the steerable pyramid. The collapse of the steerable pyramid constructs a magnified video with one operating mode shape strongly dominant. Figure 32.3 below shows frames (mode shapes) from the magnified videos; for limited space, only the second mode is shown here.

Fig. 32.1 Experimental setup
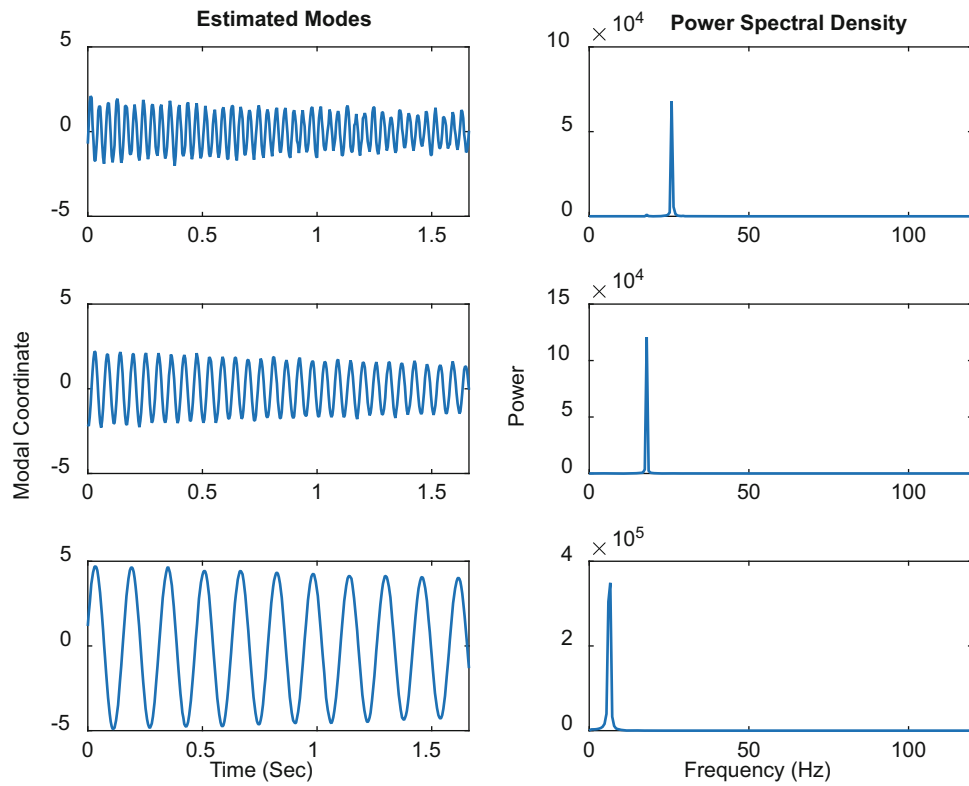
Fig. 32.2 Complexity pursuit (CP) estimated modal coordinates and their power spectral density

Fig. 32.3 A few frames from the motion magnified video (mode 2) (first row) and their corresponding mode shapes (second row) by conducting the edge detection

32.4   Conclusion

This work proposes a novel fully automated video based modal analysis technique using the advanced computer vision and machine learning techniques. Using the unsupervised blind source separation technique, this new method removes user supervision by blindly and efficiently identify and magnify mode contents from the multi-scale representation of local phases, while extending possible applications to complicated motion patterns and geometries. While inheriting the virtues of the video based measurement that is low-cost, non-contact, agile, and high spatial sensing resolution, the developed method also avoids the need of structural surface preparation that is traditionally required in image based modal analysis method. Future study can apply the proposed method on real-world structures.

References

1. Helfrick, M.N., Niezrecki, C., Avitabile, P., Schmidt, T.: 3D digital image correlation methods for full-field vibration measurement. Mech. Syst. Sig. Process. **25**(3), 917–927 (2011)
2. Wang, W., Mottershead, J.E., Ihle, A., Siebert, T., Schubach, H.R.: Finite element model updating from full-field vibration measurement using digital image correlation. J. Sound Vib. **330**(8), 1599–1620 (2011)
3. Warren, C., Niezrecki, C., Avitabile, P., Pingle, P.: Comparison of FRF measurements and mode shapes determined using optically image based, laser, and accelerometer measurements. Mech. Syst. Signal Process. **25**(6), 2191–2202 (2011)
4. Wang, W., Mottershead, J.E., Siebert, T., Pipino, A.: Frequency response functions of shape features from full-field vibration measurements using digital image correlation. Mech. Syst. Sig. Process. **28**, 333–347 (2012)
5. Baqersad, J., Niezrecki, C., Avitabile, P.: Extracting full-field dynamic strain on a wind turbine rotor subjected to arbitrary excitations using 3D point tracking and a modal expansion technique. J. Sound Vib. **352**, 16–29 (2015)
6. Chen, J.G., et al.: Modal identification of simple structures with high-speed video using motion magnification. J. Sound Vib. **345**, 58–71 (2015)
7. Yang, Y., Nagarajaiah, S.: Blind modal identification of output-only structures in time-domain based on complexity pursuit. Earthq. Eng. Struct. Dyn. **42**(13), 1885–1905 (2013)
8. Wadhwa, N.: Phase-based video motion processing. ACM Trans. Graph. **32**(4), 80 (2013)
9. Simoncelli, E., Freeman, W.T.: The steerable pyramid: a flexible architecture for multi-scale derivative computation. In: International Conference on Image Processing, Washington, DC (1995)

Chapter 33
An Alternative MIMO FRF Estimation Method Using Pneumatic Exciters

Akhil Sharma, David L. Brown, Randall J. Allemang, and Allyn W. Phillips

Abstract As an alternative to shaker and impact hammer excitation, a new method of excitation using small, single acting pneumatic cylinders is being investigated. In this method, the structure is excited by the piston of pneumatic cylinders on which a load cell and different types of impact tips can be mounted. In contrast to a shaker test, there is no mass loading of structure in this set up as the load cell is mounted on the piston of cylinder with no connection to test structure. Solenoid valves regulate air flow through the cylinders and thus control the timing and duration of impacts. An electrical circuit consisting of a transistor switch is used to actuate the solenoid valves. A system of independent, random duration and interval pulses (digital time series) is sent to each exciter system to be able to estimate Multiple Input (MI) Frequency Response Functions (FRFs). In this way, the excitation signal is more like a random input than an impact input (where only one impact per measurement ensemble is taken). Since, the random pulse sequences sent to each exciter system are uncorrelated and the cylinders and structure are not connected, it will be always possible to uncouple the forces involved. This approach can also be used for single input impact testing as there will be better repeatability in position, line of action and magnitude of impacts. This method will be validated by comparing FRFs and modal parameters obtained by it with those of traditional impact test.

Keywords Pneumatic excitation • Shaker excitation • Solenoid valve • Uncorrelated input • Frequency response function

Nomenclature

$[G_{FF}]$ Input auto power matrix
N_i Number of inputs
$[V]$ Eigenvector matrix
$[V]^H$ Eigenvector matrix Hermitian
$[\Lambda]$ Eigenvalue matrix

33.1 Introduction

FRF estimation is the first step towards finding the modal parameters of a structure. The accuracy of the obtained modal parameters relies heavily on the quality of FRF data used as an input to different Modal Parameter Estimation (MPE) methods. FRF estimation is generally done by traditional shaker or impact excitation tests. The choice of excitation technique for a particular test depends on the type of structure, purpose of test, time available for testing, equipment availability etc. Electromechanical shakers are generally used in Multiple Input Multiple Output (MIMO) excitation case. Multiple inputs ensure uniform excitation of the structure and reduce the effect of nonlinearities present in the system. But the mechanical attachment of shaker to the structure gives rise to other problems. Due to matrix inversion involved in MIMO case for estimating FRFs, it is necessary that the inputs used to excite the structure should not be perfectly correlated at any frequency. However, due to electrodynamic interaction between the shaker and structure, input forces may become partially coherent especially at resonance frequencies. As long as the forces do not become fully coherent, this generally does not cause a

A. Sharma (✉) • D.L. Brown • R.J. Allemang • A.W. Phillips
Structural Dynamics Research Laboratory, Department of Mechanical and Materials Engineering, University of Cincinnati, Cincinnati, OH 45221-0072, USA
e-mail: sharmai@mail.uc.edu

numerical problem. However, this interaction also reduces the force transmitted by the shaker to the structure causing so called force drop-off phenomenon [1]. Force transmissibility between the shaker and structure plays an important role in controlling signal to noise ratio [2]. Although, the impact excitation method by virtue of a single roving input and absence of mechanical attachment does not have these problems, repeatability of the position, magnitude and direction of input force is susceptible to human error [3]. These issues give motivation to develop a new excitation method which is free from the shortcomings of both shaker and impact excitation.

33.2 Existing Excitation Methods

33.2.1 Shaker Excitation

Shaker excitation method, particularly multiple input shaker testing, is very appealing due to shortest testing time and consistency of modal parameters obtained. Shakers are mechanically attached to the structure through stingers which are made of a material having very low stiffness in the off-axis directions. This ensures that the structure is not excited through forces which are not measured by the force transducers. Also, due to its relatively low stiffness in the on-axis direction, a stinger acts as mechanical fuse and prevents any large force from being transmitted between the shaker and structure. The procedure of computing modal parameters through multiple input excitations involves mathematical inversion of the input auto-power matrix $[G_{FF}]$.

$$[G_{FF}] = \begin{bmatrix} G_{FF_{11}} & \cdots & G_{FF_{1N_i}} \\ \vdots & \ddots & \vdots \\ G_{FF_{N_i1}} & \cdots & G_{FF_{N_iN_i}} \end{bmatrix}$$

(33.1)

There can be situations in which $[G_{FF}]$ matrix is nearly singular and therefore, its inverse may be numerically marginal. It will happen in two conditions. First, if one of the input auto power spectra is zero then the corresponding rows and columns of the $[G_{FF}]$ matrix would also be zero thus making it singular. This can be an indication of a shaker or force transducer not working. Second, if any two of the input forces are perfectly correlated at a particular frequency then the inverse of $[G_{FF}]$ matrix will not exist at that frequency. In order to make all the input forces uncorrelated, independent random signals are sent to each exciter. However, due to electrodynamic interaction between the shaker and structure, input forces may still remain partially correlated at certain frequencies. This does not generally cause a problem but is undesirable.

$$[G_{FF}] = [V] [\Lambda] [V]^{\mathrm{H}}$$

(33.2)

Principle (virtual) force analysis is done to investigate this phenomenon which involves eigenvalue decomposition of the $[G_{FF}]$ matrix at each frequency as showed in Eq. (33.2) [4]. Eigenvalues associated with the corresponding virtual inputs determine their contribution and they should be approximately same since the eigenvectors are unitary. If one eigenvalue is significantly smaller than others then either one of the inputs is not present or any two inputs are correlated.

33.2.2 Impact Excitation

Impact excitation method uses a roving impact hammer containing an embedded force transducer to excite the structure. This method works well for small as well as large structures and is attractive due to its portability, low cost and minimal equipment requirement. The frequency band of excitation is controlled by the type of tip (soft or hard), hammer's mass and the velocity of the hammer strike. A soft tip excites low frequencies pretty well while a hard tip is used for exciting higher frequencies. The impact excitation method does not suffer from typical shaker excitation problems of correlated inputs due to the application of a single impact at a time. However, it is difficult to maintain the repeatability of magnitude, direction and position of impact forces for various measurements at a degree of freedom. Also, a single impact is not capable of uniformly exciting the structure due to which the nonlinearities present in the structure can distort the measurement.

33.3   Pneumatic Excitation Experimental Set Up

A new method of excitation using single-acting pneumatic cylinders is investigated. The piston of the cylinder acts as an impact hammer with a force transducer mounted on it to measure the impact force. However, it is different from impact excitation because the structure is excited simultaneously at multiple locations (three in the existing set up). This method is more like a multiple input random excitation using continuous, randomly spaced impacts at each location to create independent random inputs. It is a sort of hybrid between shaker and impact excitation techniques, possessing the positive characteristics of both. The absence of mechanical attachment between the structure and exciter makes it possible to always uncouple the input forces. Presence of multiple inputs makes it possible to uniformly excite the structure. Also, there is high repeatability of the magnitude, direction and position of input forces as there is no direct human intervention in creating the impacts. This characteristic also makes this technique attractive for using in traditional impact excitation.

Solenoid valves are used to control the timing and duration of impacts at each location by regulating the air flow. A system of independent, random duration and interval pulses (digital time series) is sent to a simple switching circuit used to actuate the solenoid valves. The magnitude of impacts is controlled by the air-pressure and digital time series as the stroke of the cylinders is dependent on the corresponding random time delays between the pulses. As the air pressure and time delay increases, the velocities at which the exciters hit the structure also increases thus increasing the magnitude of impacts. The amount of time for which the exciter remains in contact with the structure increases with the pulse width. Flow control valves (not shown in Fig. 33.1) connected to the outlet of solenoid valves are used to control back pressure which is important for providing cushioning during the return stroke of the cylinder (Figs. 33.2 and 33.3). If enough back pressure is not applied to the cylinders then they will end their return stroke with an impact (hard seating) as can be seen in Fig. 33.4. The impact of exciter with the structure is followed by a small unwanted impact caused due to hard seating of piston on its seat. This secondary impact is not a force that is truly exciting the structure and is not present in the case of typical measurement with soft seating as shown in Fig. 33.5.
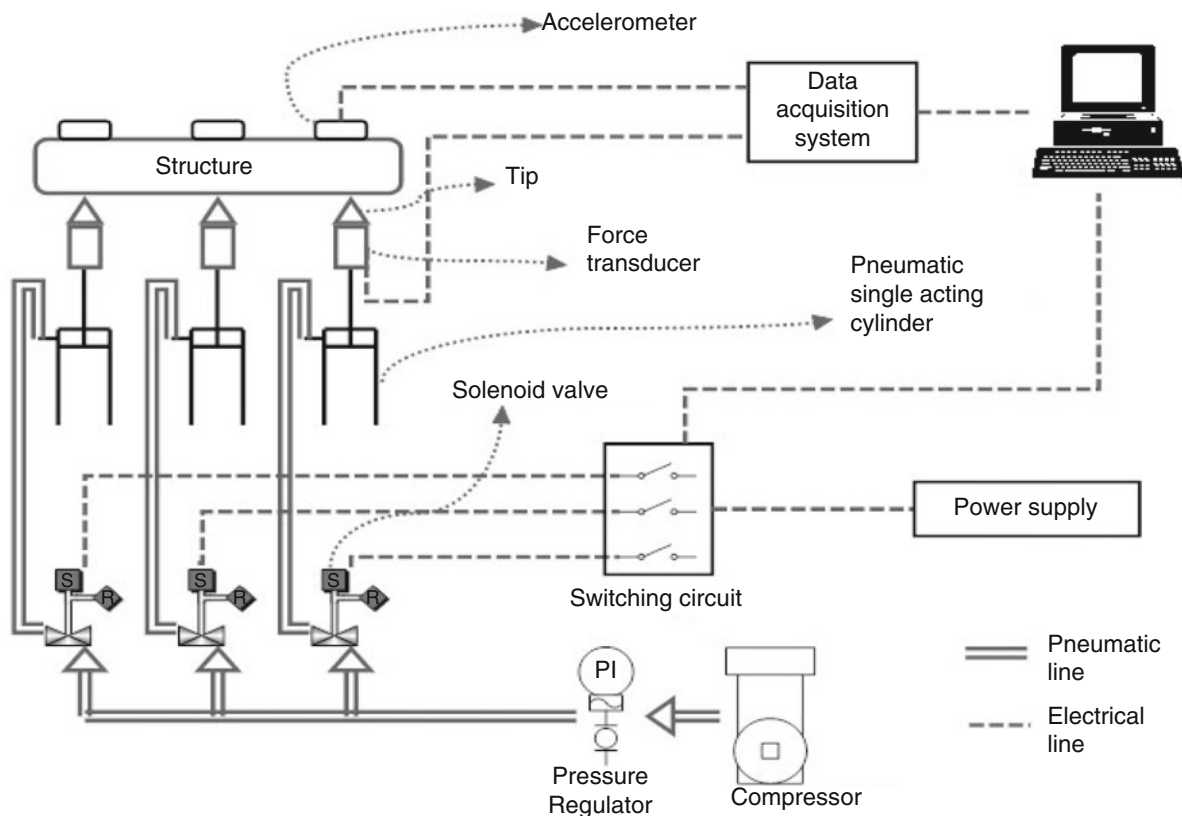
Fig. 33.1   Typical pneumatic excitation test configuration

Fig. 33.2 Physical pneumatic excitation experimental setup
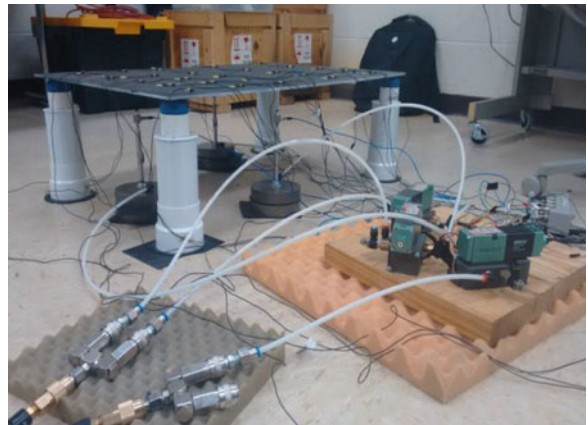
Fig. 33.3 Pneumatic exciters embedded with force transducers
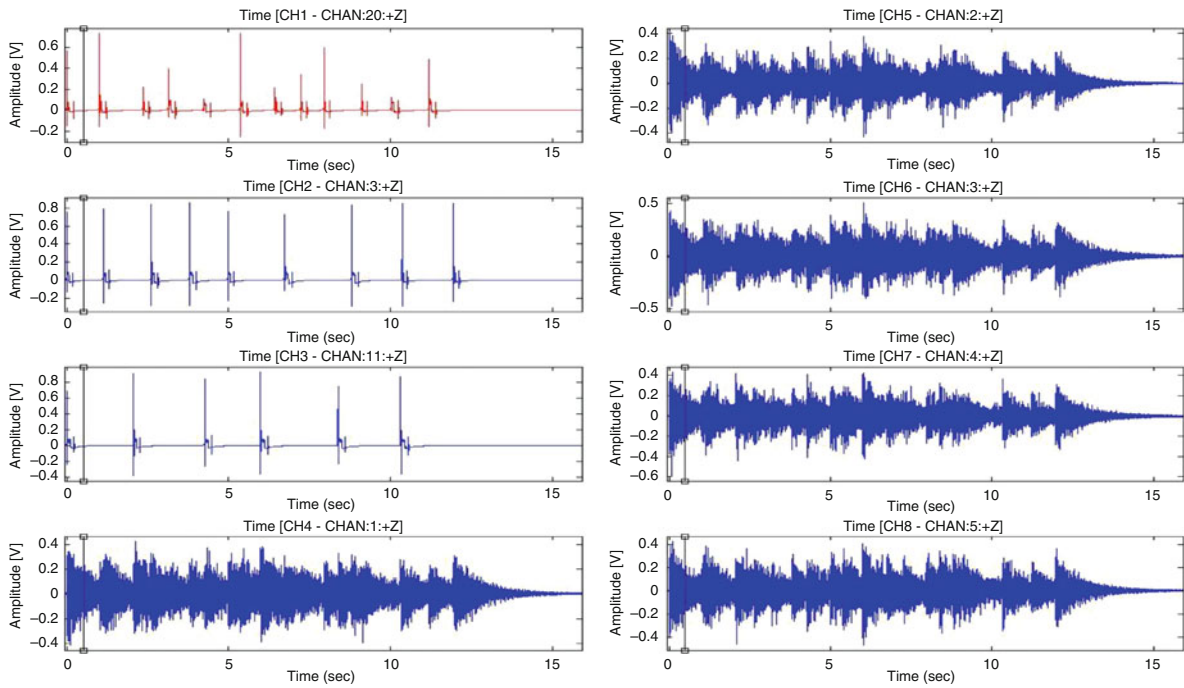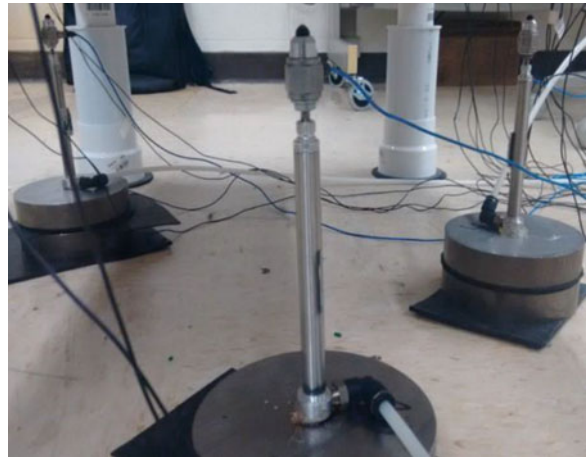
Fig. 33.4 Hard seating measurement
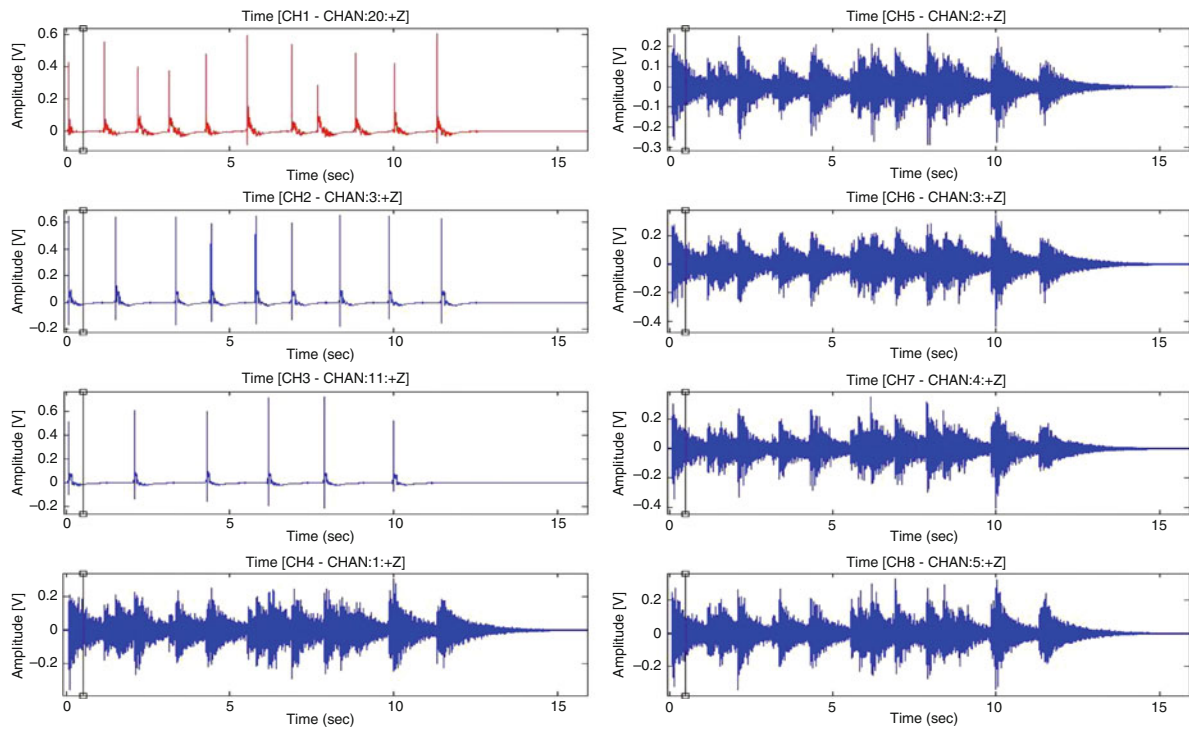
Fig. 33.5 Soft seating (typical) measurement
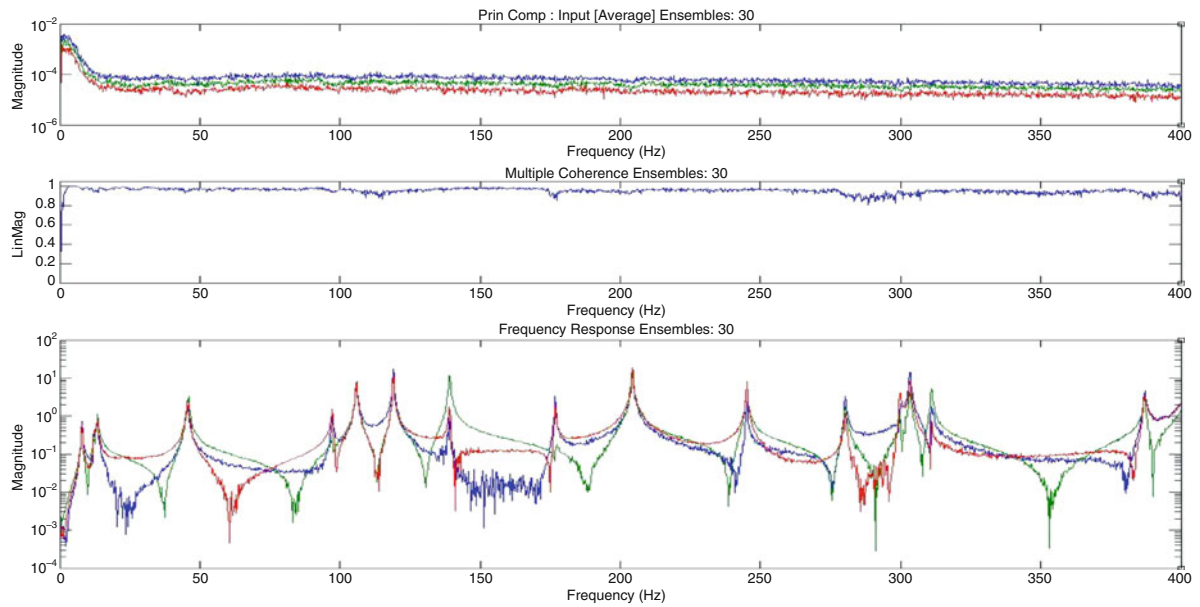
Fig. 33.6 FRF estimated during hard seating

This unwanted impact distorts the measurement as the force sensed by the load cell at this moment is not imparting any motion or energy to the structure. This violates the causal relationship between excitation and response which is very essential for experimental modal analysis. Its effect is reflected in the form of noise and coherence drops as can be seen in Fig. 33.6 and the degree of distortion can be gauged by comparing it to a measurement without hard seating while keeping other parameters same (Fig. 33.7).
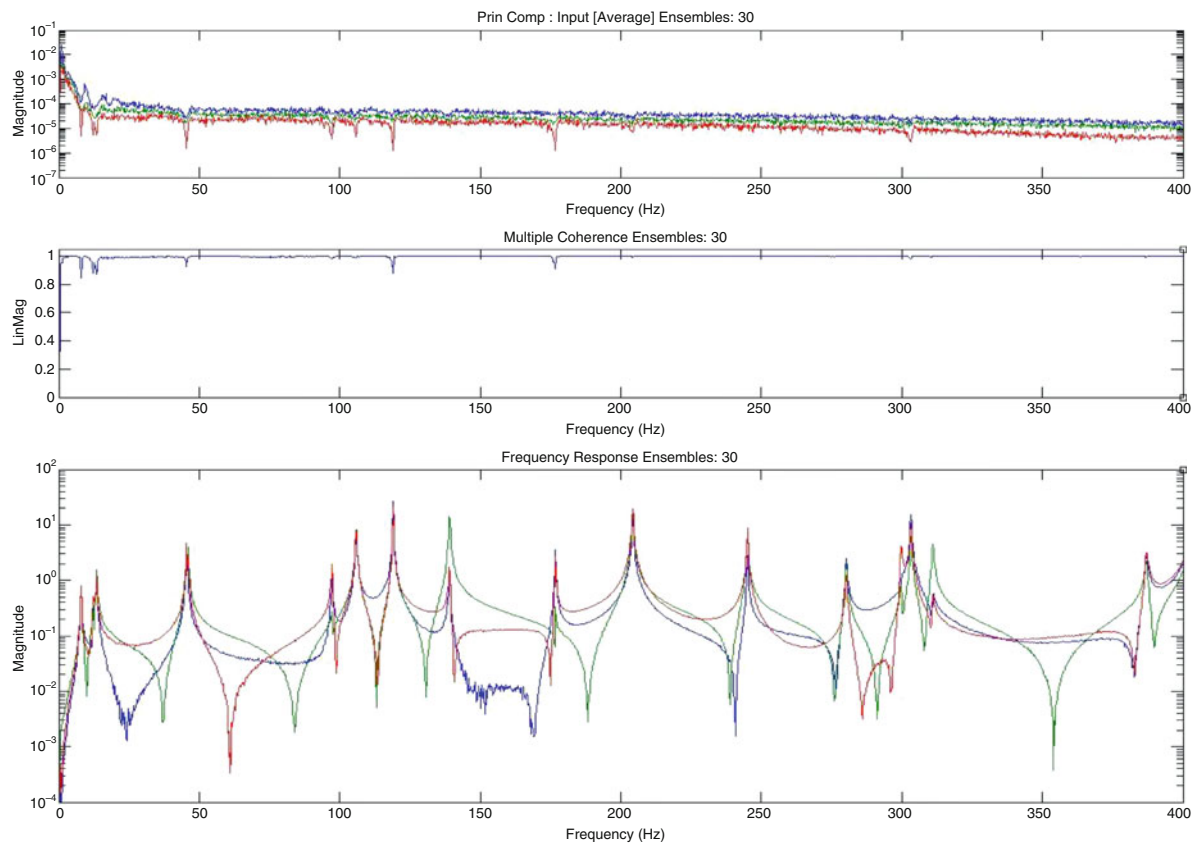
Fig. 33.7 FRF estimated during soft seating

Table 33.1 Test parameters

No. of frequency lines	1600
Maximum frequency (Hz)	400
No. of synchronous averages	30
No. of cyclic averages	–
Window function	Hanning
Trigger	Response
Data acquisition time (min)	2
Pulse width (no. of data points)	50, 70 and 80 respectively for load cells at 20, 3 and 11
Time delay (no. of data points)	200, 250 and 230 respectively for load cells at 20, 3 and 11
Pressure (psi)	20
Exciter tip	Soft

33.4 Effect of Various Parameters on the Estimated FRF

The excitation characteristics in this technique can be affected by changing several physical parameters like air pressure in the cylinder, hardness of impact tip, back-pressure and mean time delay between the successive pulses in the digital time series. The effect of these physical parameters as well as typical digital signal processing (DSP) parameters is investigated on a lightly damped structure, a rectangular plate made of steel having dimensions denoted as $34 \times 22.5 \times 0.243$ in. The number of exciters is three and the response is taken at 25 locations with driving point's degree of freedom (DOF) as 20, 3 and 11. Initially, a basic configuration is chosen which is depicted by Table 33.1 and then analysis is done by successively changing only one parameter at a time while keeping other parameters same as the last measurement so that effect only due to the currently investigated parameter can be studied.
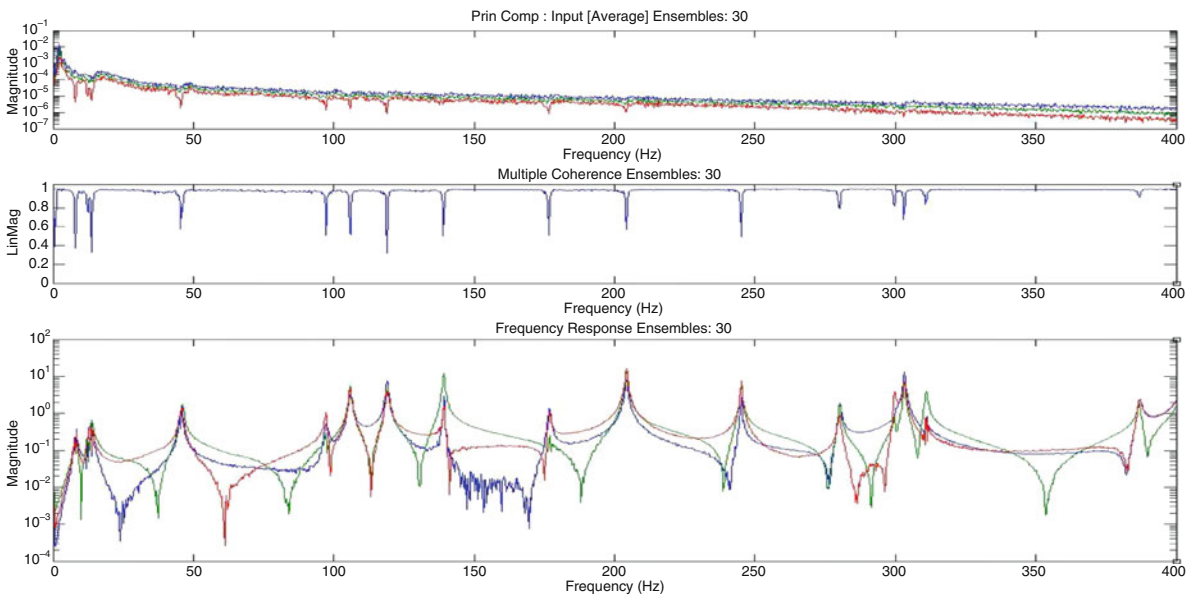
Fig. 33.8 FRF estimation without cyclic averaging
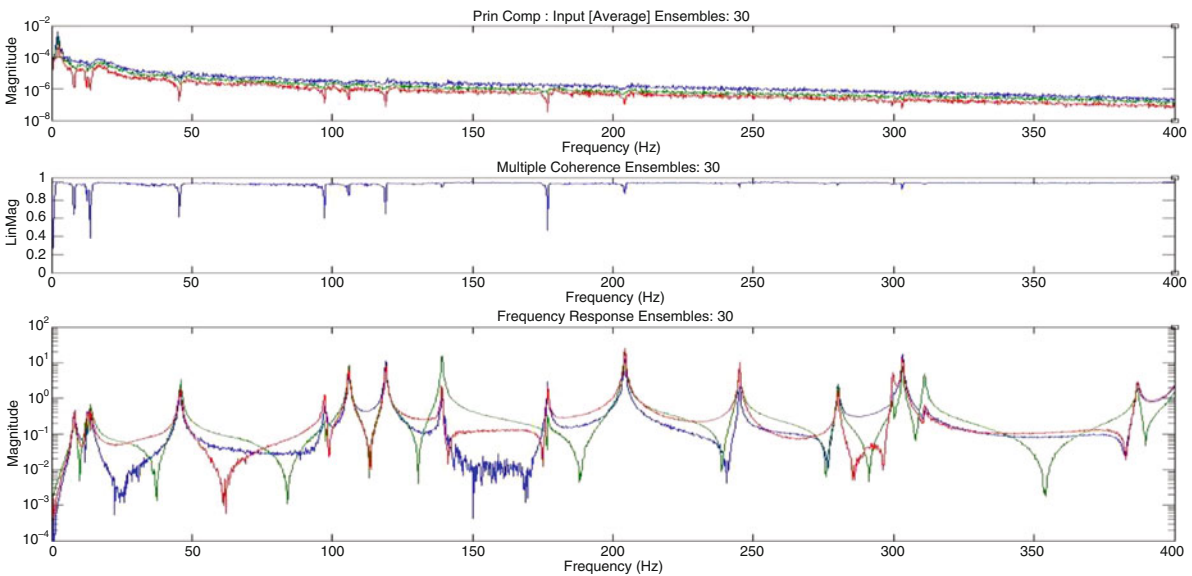
Fig. 33.9 FRF estimation with four cyclic averages

33.4.1 Effect of Cyclic Averaging

Initial FRF measurements have coherence values of almost 1 except at the peaks (modal frequencies) in the FRF as can be seen in Fig. 33.8. The drop of coherence at the peaks is often an indication of leakage which can be improved by cyclic averaging. The basic requirement of a fast Fourier transform, in order to give the best results, is that either the signal should be periodic or observed completely in the time window. Cyclic averaging makes the signal more periodic in the time window thus reducing the leakage as demonstrated by Fig. 33.9 [5]. It can be seen in the following graphs that coherence is substantially improved with cyclic averaging especially at high frequencies. However, increasing the number of cyclic averages after a point is not beneficial as improvement is marginal while testing time increases considerably. Therefore, only four (4) cyclic averages are utilized in further tests.
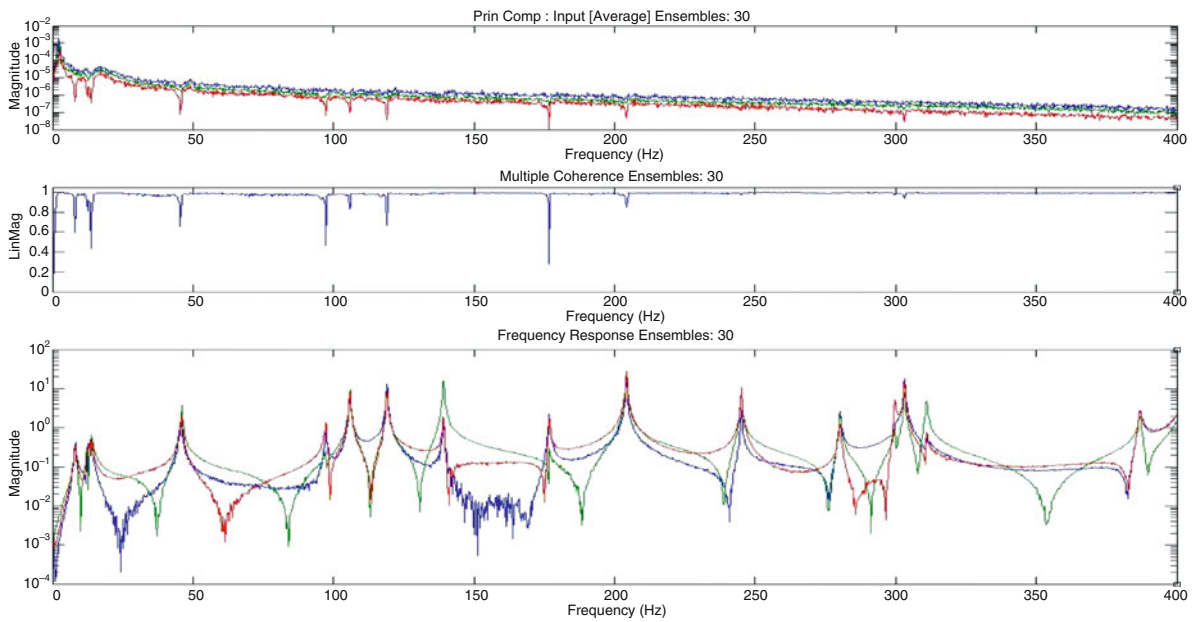
Fig. 33.10 FRF estimation with eight cyclic averages
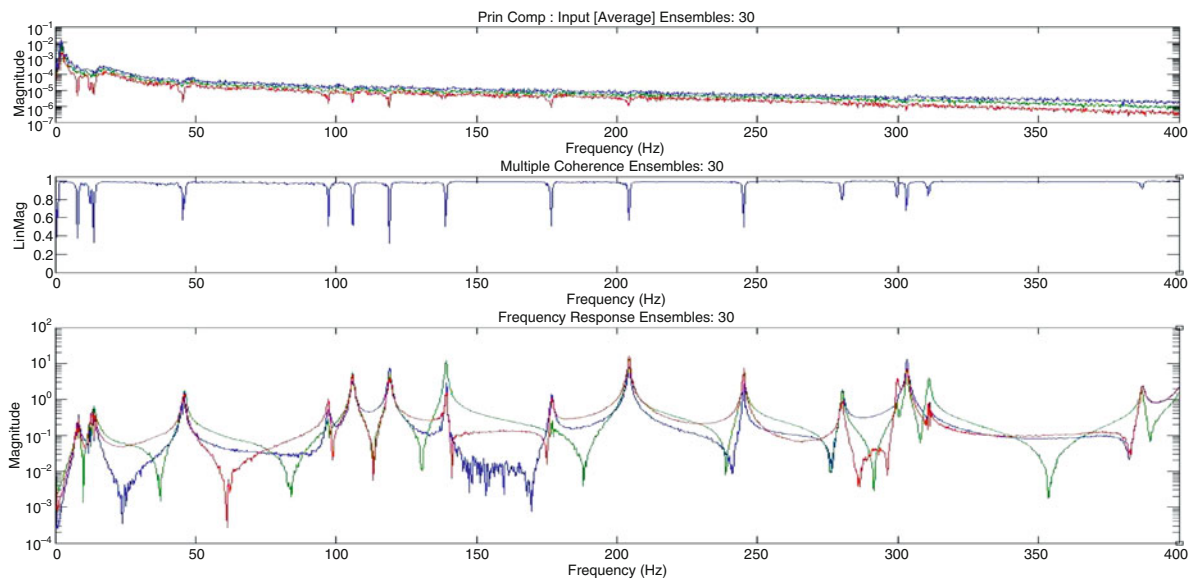
Fig. 33.11 FRF estimation with small mean time delays

33.4.2 Effect of Mean Time Delay

The mean time delay between the pulses dictates the effect of one impact on the next one and the magnitude of impact force. As the mean time delay increases, the piston has more chance of completing its return stroke and in the next stroke it strikes the structure with more velocity. With increased time delay, the structure has more time to ring down thus reducing the effect of one impact on the next one. All the three pulses have a base value of time delay (mean time delay) and they are randomized by multiplying and adding random numbers to this value. In order to study the effect of mean time delay, only the base value is changed from one measurement to the other. In the first case, the time delays are 200, 250, and 230 and in the second case, the time delays are 650, 1000 and 1500 for exciters at position 20, 3 and 11 respectively. It can be seen in the figures below that increased time delay has improved the coherence appreciably (Figs. 33.11, and 33.12).
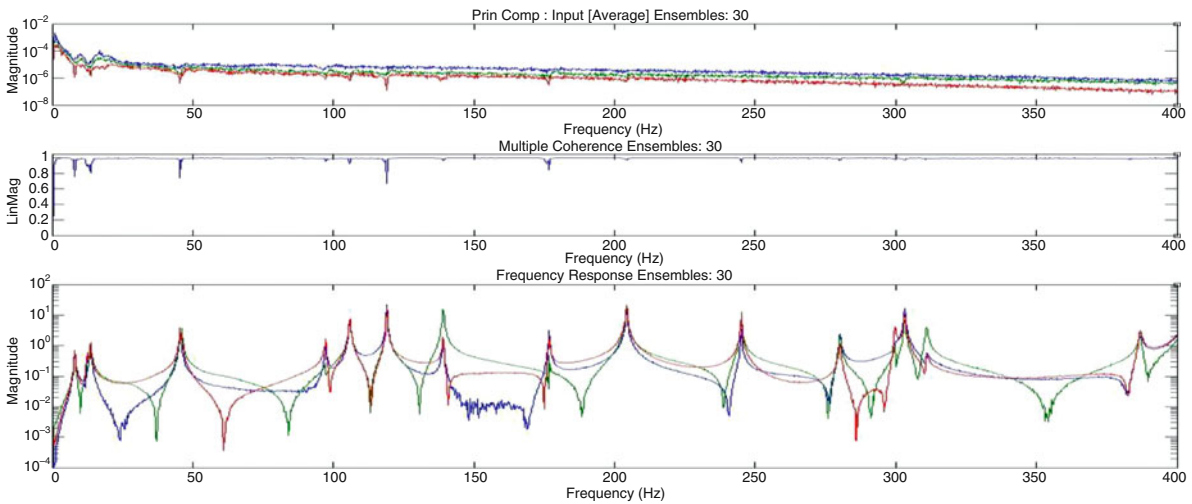
Fig. 33.12 FRF estimation with comparatively larger mean time delays
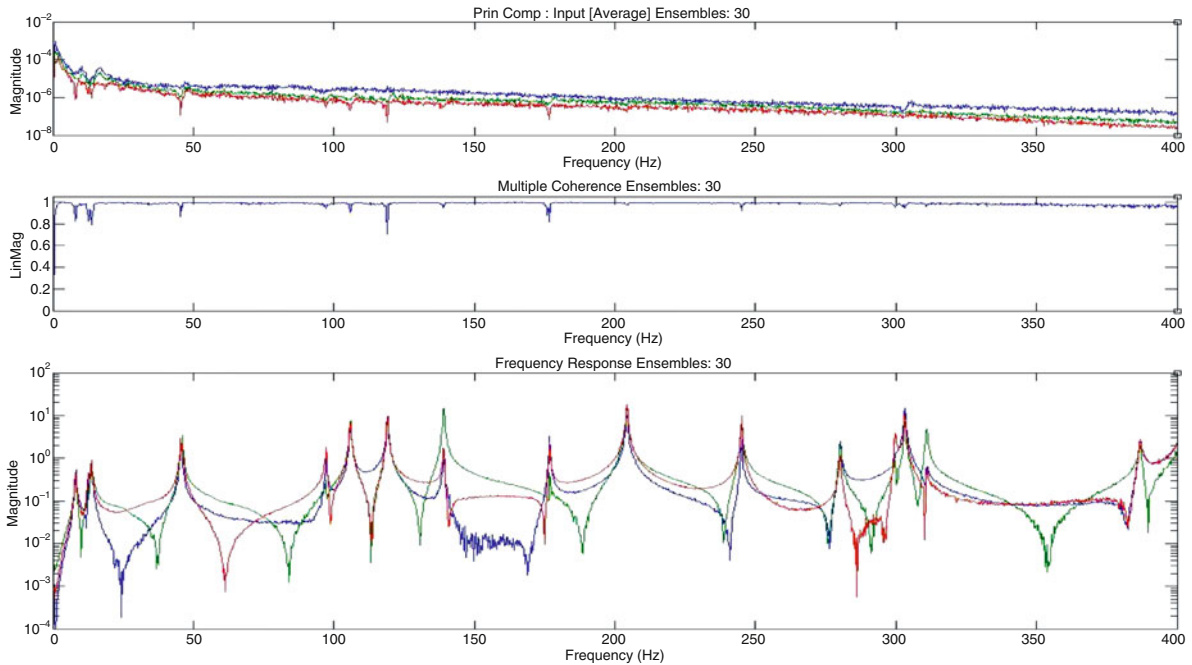
Fig. 33.13 FRF estimated at 17 psi

33.4.3 Effect of Air Pressure

The air pressure has a direct effect on the force with which the exciters hit the structure as high pressure results in high impact velocities and higher force levels. The time delay between the pulses and air-pressure can be used in conjunction to regulate the impact force. The technique is being tested at 17, 20 and 25 psi though initial intention was to use 15 psi in place of 17 psi but that much pressure is not enough for the exciters to hit the structure because of insufficient stroke. All the test cases discussed in this section up to this point are conducted at 20 psi. The FRF estimated at 17 and 25 psi are shown in Figs. 33.13 and 33.14 respectively.
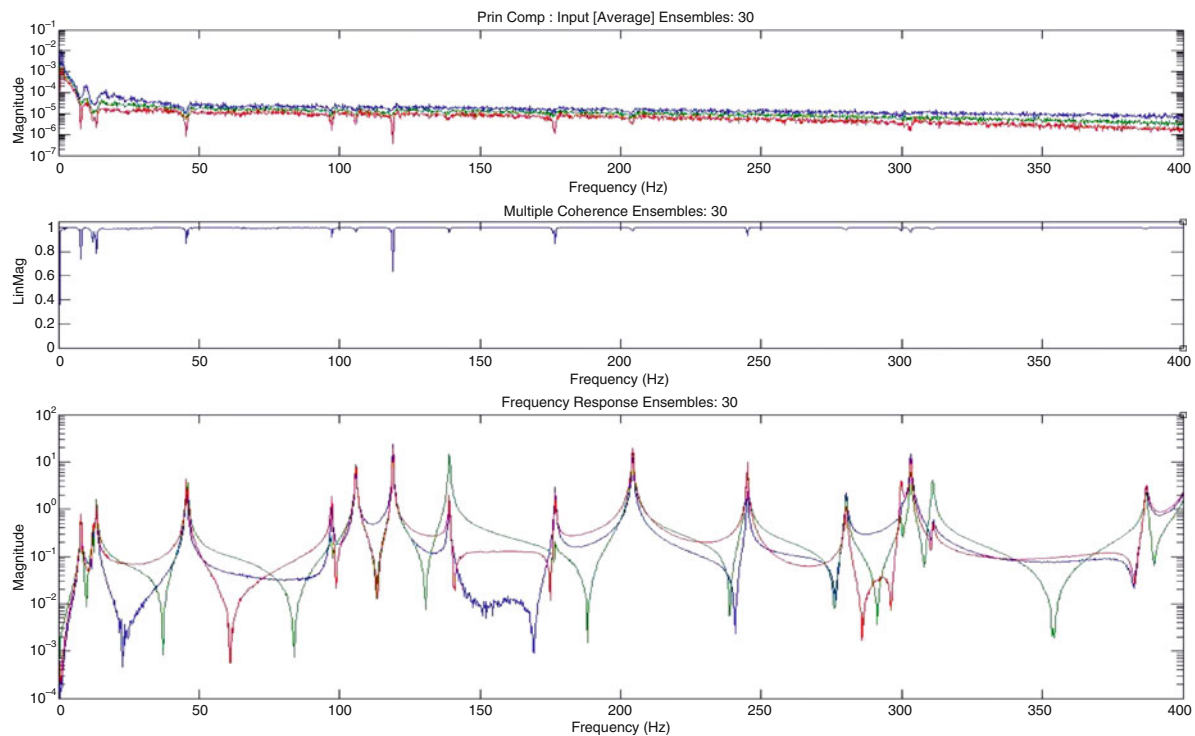
Fig. 33.14 FRF estimated at 25 psi

There is no significant change in coherence by changing the pressure from 17 to 25 psi. However, FRF and coherence are smoother at 25 psi due to the increased signal to noise ratio as can be noticed by comparing the magnitude of impacts in Figs. 33.15 and 33.16 (each row represents impact force of an exciter namely at DOF 20, 3 and 11 from top to bottom respectively).

33.4.4 Effect of Burst Random Excitation

Even after increasing the time delay and air-pressure there are still small coherence drops at peaks. Another method to reduce leakage is to allow the signals to become zero within the time window. This can be done by exciting the structure only for a limited time and is investigated at 75, 50 and 25 % of the total time window and is essentially very similar to well-known burst random excitation (Figs. 33.17, 33.18, 33.19, 33.20, 33.21, and 33.22).

It can be seen from the figures mentioned above that there is significant improvement in coherence with burst random excitation used along with cyclic averaging [6]. The impacts and responses almost diminish to zero towards the end of the time window thus tending to become completely observable. Burst lengths of 75 % gives better results as compared to 50 and 25 % burst length as can be noticed by lesser coherence drop at low frequencies with 75 % burst length as compared to others. A possible explanation for this could be the fact that high signal to noise ratio can be attained with 75 % burst length as compared to 50 and 25 %.

33.4.5 Effect of Exciter Tip

Exciter tips of different hardness also affect impact forces and frequencies at which the structure is excited due to varying stiffness at the point of contact as in normal, single input impact testing. In order to investigate this phenomenon, one softer and one harder tip as compared to the tip used until now is tested. The different types of tips used can be seen in Fig. 33.23. Though the tips have different heights, the distance between the touching point of the tip and the structure is kept same in all the cases by changing the number of rubber pads (used for vibration isolation with the floor) under the round steel fixtures.
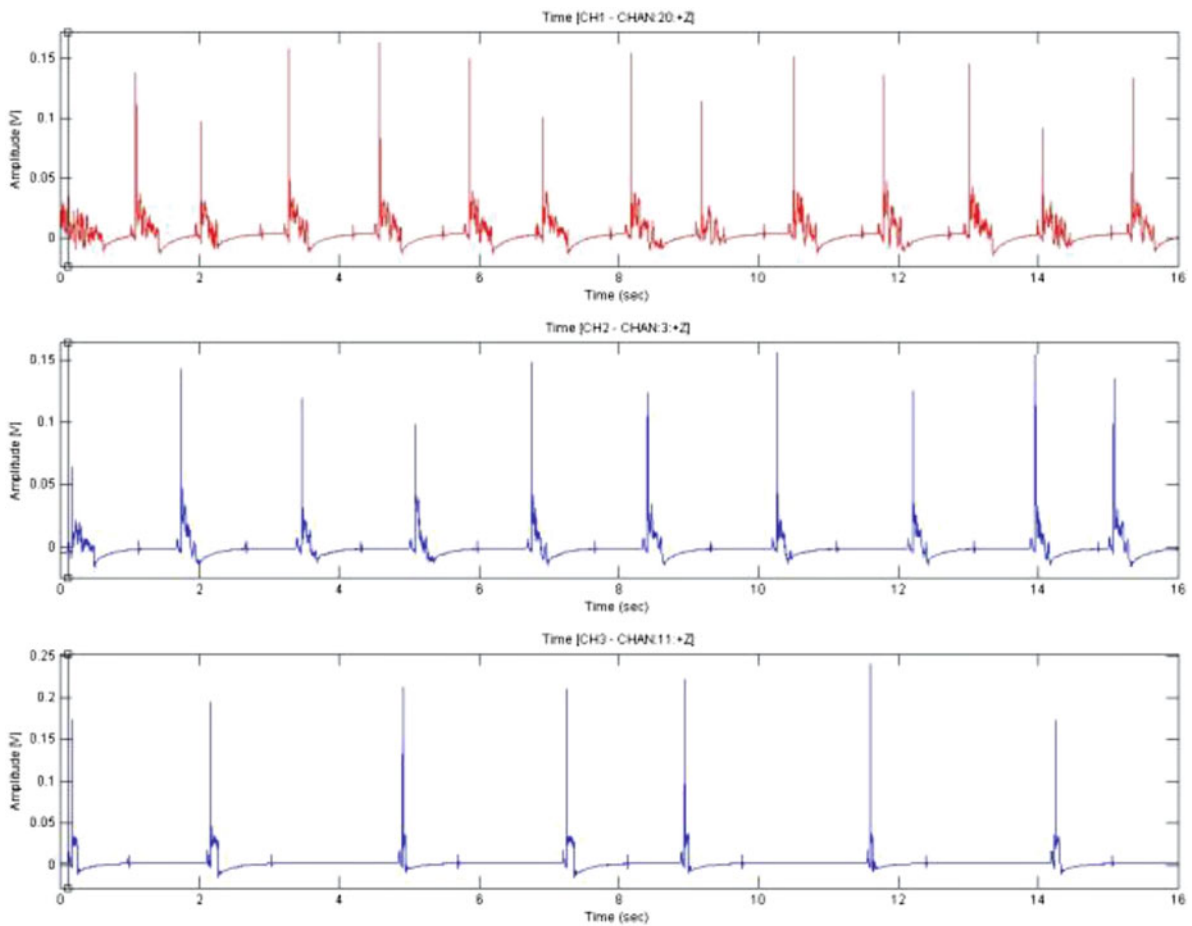
Fig. 33.15 Impact forces at 17 psi

The coherence has dropped more at the peaks in the case of the harder tip. It can be attributed to the higher energy imparted by the harder tip to the structure as compared to the softer tip since; more energy does not allow the vibration to die down within the time window. The coherence in the case of harder tip can be improved by adjusting other parameters like air pressure and burst length as they have also an effect on the energy transmitted to the structure.

33.5 Comparison of Modal Parameter Obtained with Pneumatic and Traditional Impact Test

In order to validate thismethod, it can be useful to compare the modal parameters obtained by this method to the modal parameters obtained by an established method like traditional impact test. The data from the best configuration of the pneumatic input tests (with multiple inputs) in terms of the quality of estimated FRF measurements is used for modal parameter estimation (MPE). Poly-reference time domain (PTD) method available in X-Modal (experimental data acquisition and modal analysis tool developed by UC-SDRL) is used for MPE and all the measurements for this research work are also done with the help of X-Modal. The parameters of the impact and pneumatic excitation are compared in Table 33.2.

It can be observed in Fig. 33.26 that the difference in the damping estimate of the modes obtained from the two methods is never more than 0.05 % zeta, and the frequency difference is almost negligible. In order to check the linear independence of the modal vectors, the modal assurance criterion (MAC) matrix is also estimated as can be seen in Figs. 33.27 and 33.28 where blue colour represents a MAC value of zero while the red colour represents a MAC value of one. All these results validate the pneumatic excitation as a viable method for experimental modal analysis.
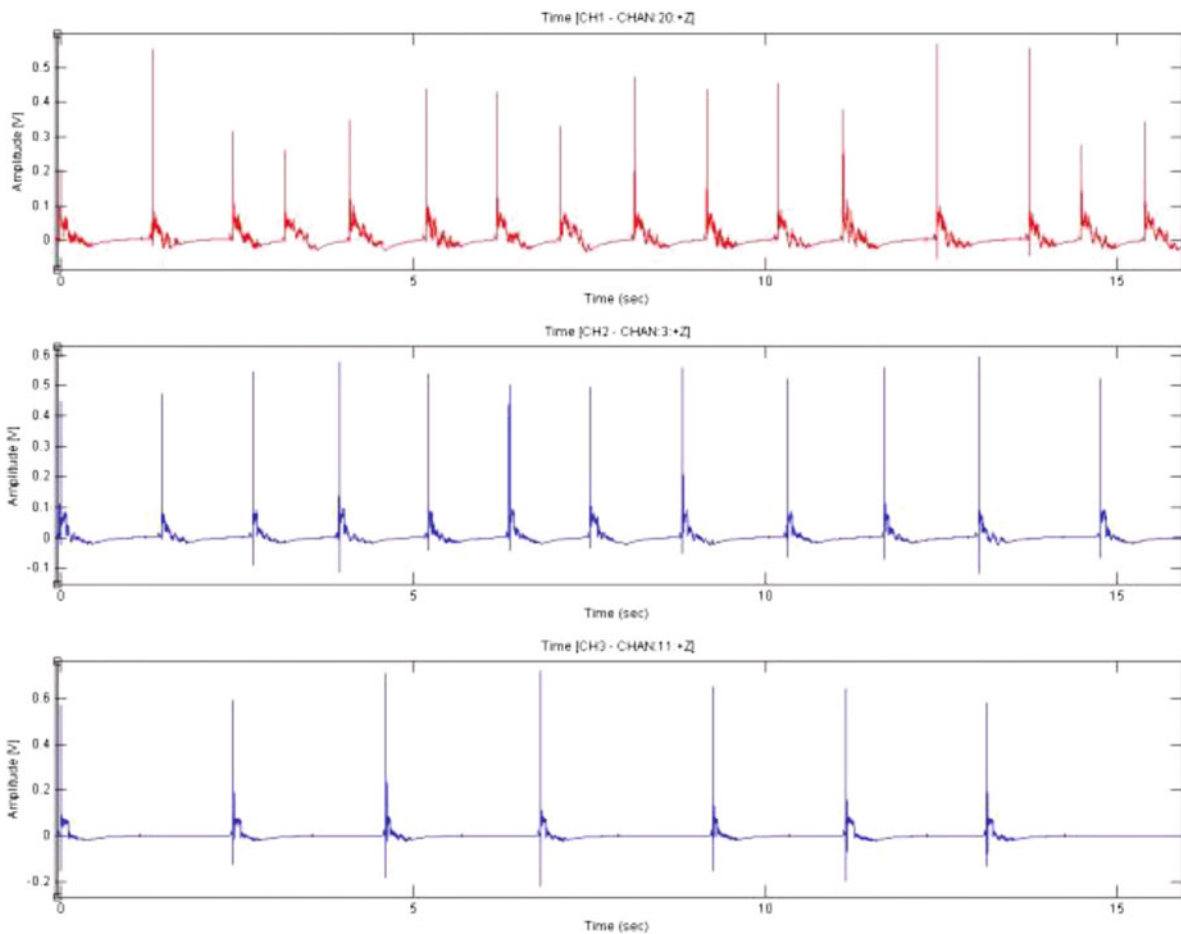
Fig. 33.16 Impact forces at 25 psi

33.6 Conclusion

Pneumatic excitation seems to be a good alternative to traditional excitation methods especially shaker excitation. The experimental setup is made up of simple components and can be easily customized (sized) for different testing requirements. Due to the compact size of pneumatic cylinders it may be possible to excite certain portions of a structure like an automobile which otherwise may be inaccessible to shakers. In order to reduce the setup time for a pneumatic excitation test, a sturdy fixture that can rotate the exciter in three dimensions as well as adjust its height (currently done by changing the number of rubber pads) could be developed. Also, it will be an interesting exercise to mathematically relate the various parameters of pneumatic excitation affecting the measurements. Another attractive feature of this technique is the low cost associated with its setup which may be a factor of 5–10 cheaper than small modal shakers. As the size and consecutively, the price of the modal shakers increase this factor will also increase. Since, the structure (rectangular plate) used in the test has a simple geometry, the next step could be to validate this method for complicated geometries such as the body of an automobile
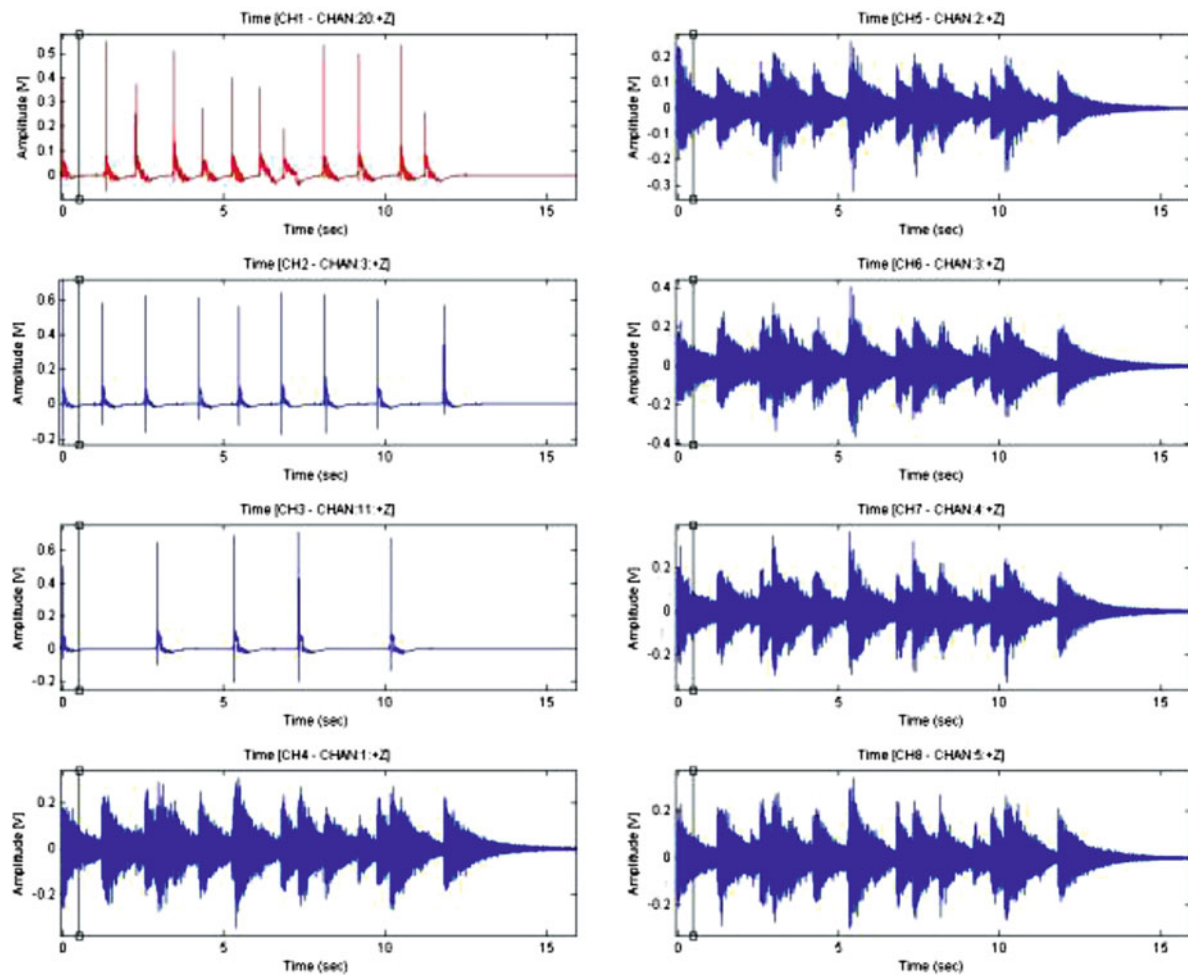
Fig. 33.17 Impact forces at 75 % burst

References

1. Varato, P.S., de Oliviera, L.P.R.: On the force drop off phenomenon in shaker testing in experimental modal analysis. Shock. Vib. **9**(4–5), 165–175 (2002)
2. Dargah, M.H.P., Allemang, R.J., Phillips, A.W.: Exciter impedance and cross-axis sensor sensitivity issues in FRF estimation. In: Proceedings of the International Modal Analysis Conference (IMAC), Jacksonville, vol. 5, pp. 535–545 (2012)
3. Brown, D.L., Allemang, R.J., Phillips, A.W.: Forty years of use and abuse of impact testing: a practical guide to making good frf measurements. In: Proceedings of the International Modal Analysis Conference (IMAC), Orlando, vol. 8, pp. 221–241 (2015)
4. Allemang, R.J., Phillips, A.W., Allemang, M.R.: Application of principal component analysis methods to experimental structural dynamics. Proceedings of the International Modal Analysis Conference (IMAC), Jacksonville, vol. 3, pp. 477–498 (2011)
5. Allemang, R.J., Phillips, A.W.: Cyclic averaging for frequency response function estimation. In: Proceedings of the International Modal Analysis Conference (IMAC), Dearborn, pp. 415–422 (1996)
6. Phillips, A.W., Allemang, R.J., Zucker, A.T.: A new excitation method: combining burst random excitation with cyclic averaging. In: Proceedings of the International Modal Analysis Conference (IMAC), Santa Barbara, pp. 891–899 (1998)
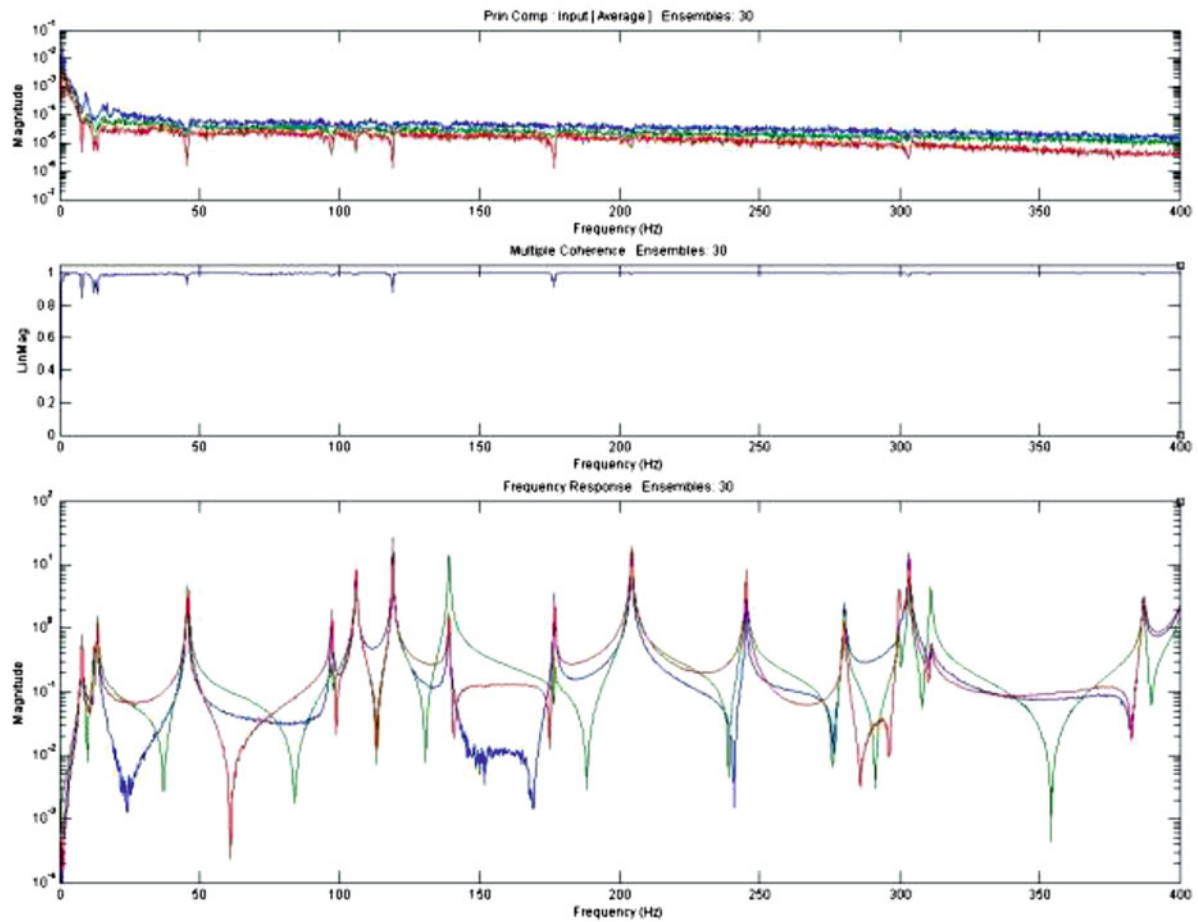
Fig. 33.18 FRF estimated at 75 % burst length

Table 33.2 Test parameters

Parameter	Impact excitation	Pneumatic excitation (best configuration)
No. of frequency lines	1600	1600
Maximum frequency (Hz)	400	400
No. of synchronous averages	10	30
No. of cyclic averages	4	4
Window function	Force-rectangular	Hanning
Burst length (percentages)	–	75
Trigger	Input	Response
Pulse width (no. of data points)	–	50, 70 and 80 respectively for load cells at 20, 3 and 11
Time delay (no. of data points)	–	650, 1000 and 1500 respectively for load cells at 20, 3 and 11
Pressure (psi)	–	25
Exciter tip	Soft	Soft
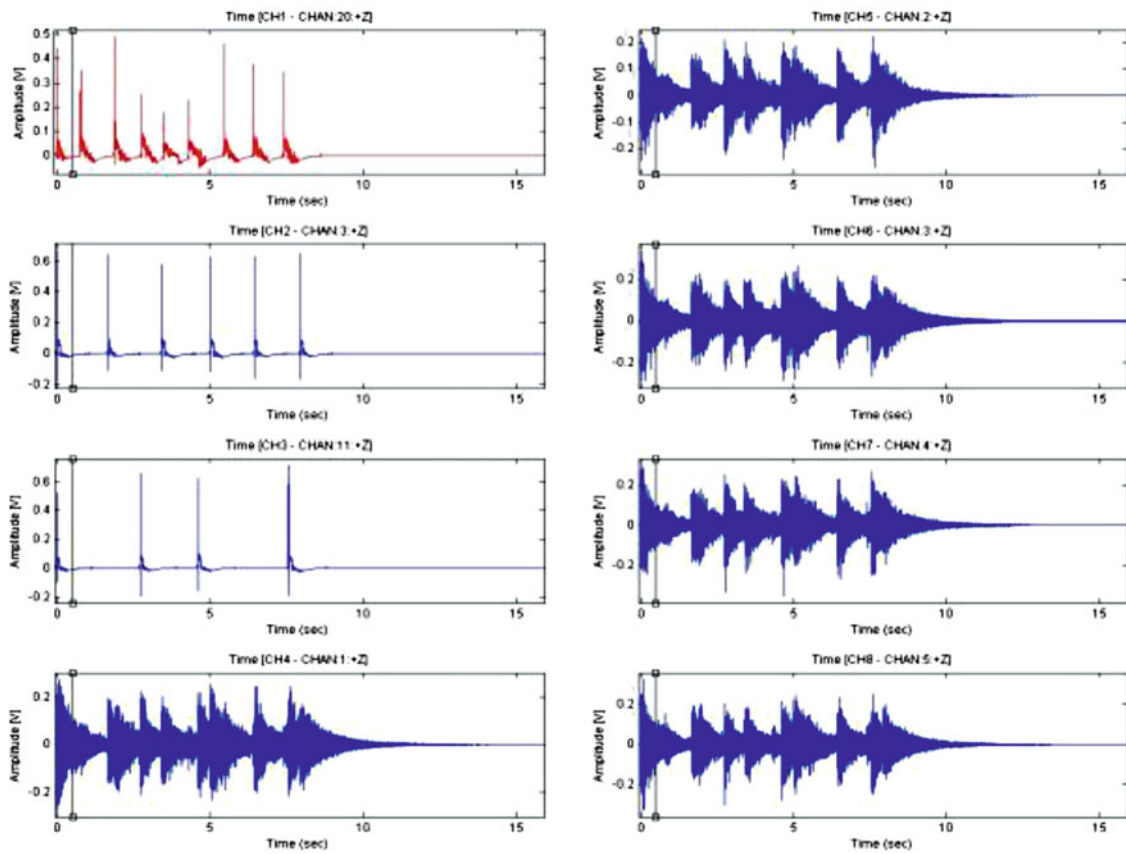
Fig. 33.19 Impact forces at 50 % burst length
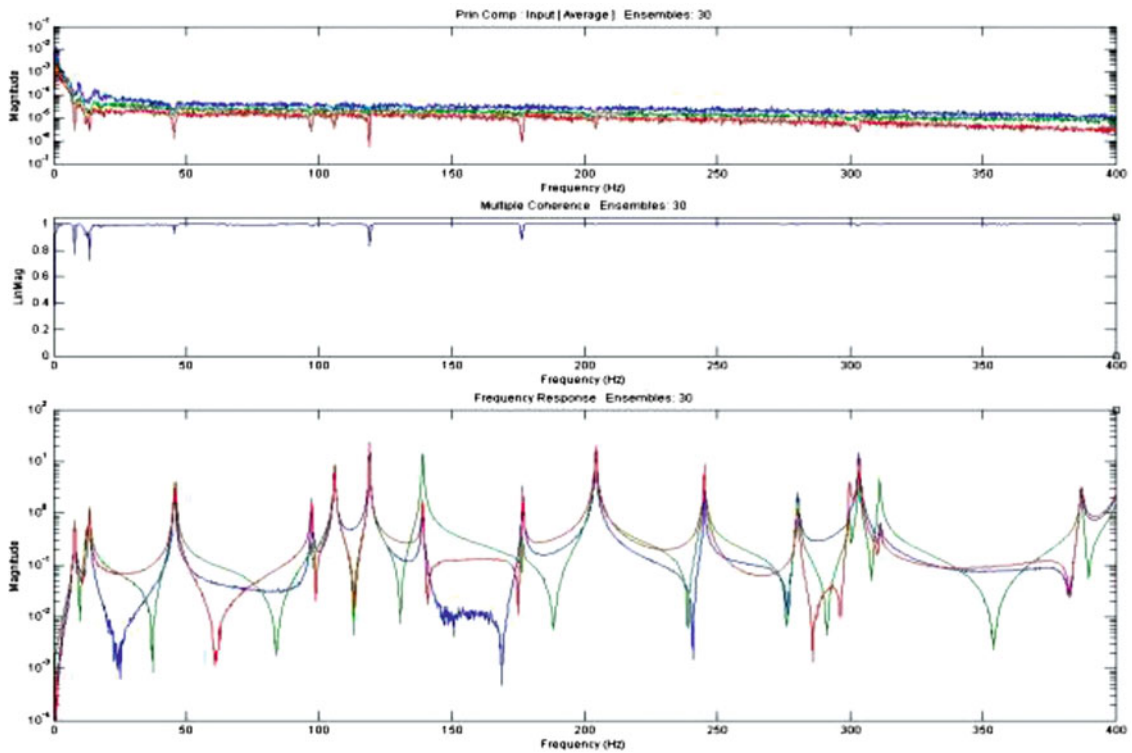
Fig. 33.20 FRF estimated at 50 % burst length
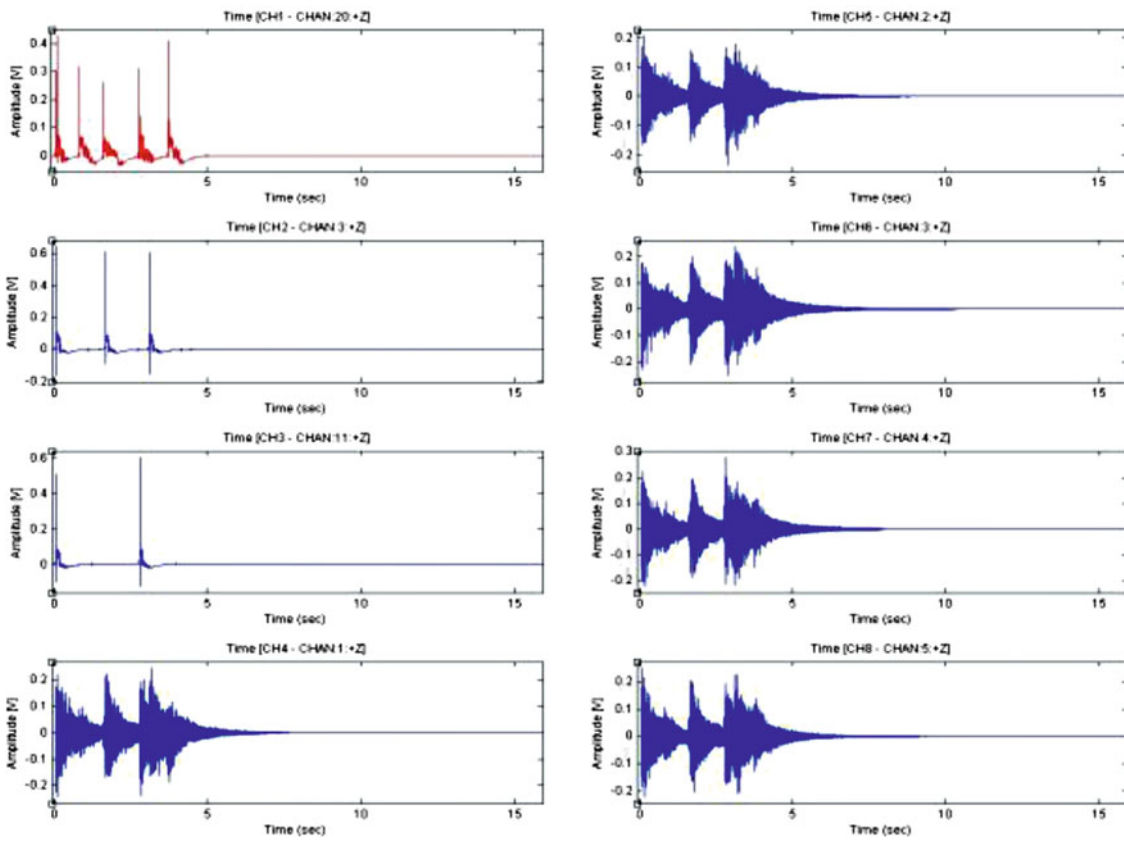
Fig. 33.21 Impact forces at 25 % burst length
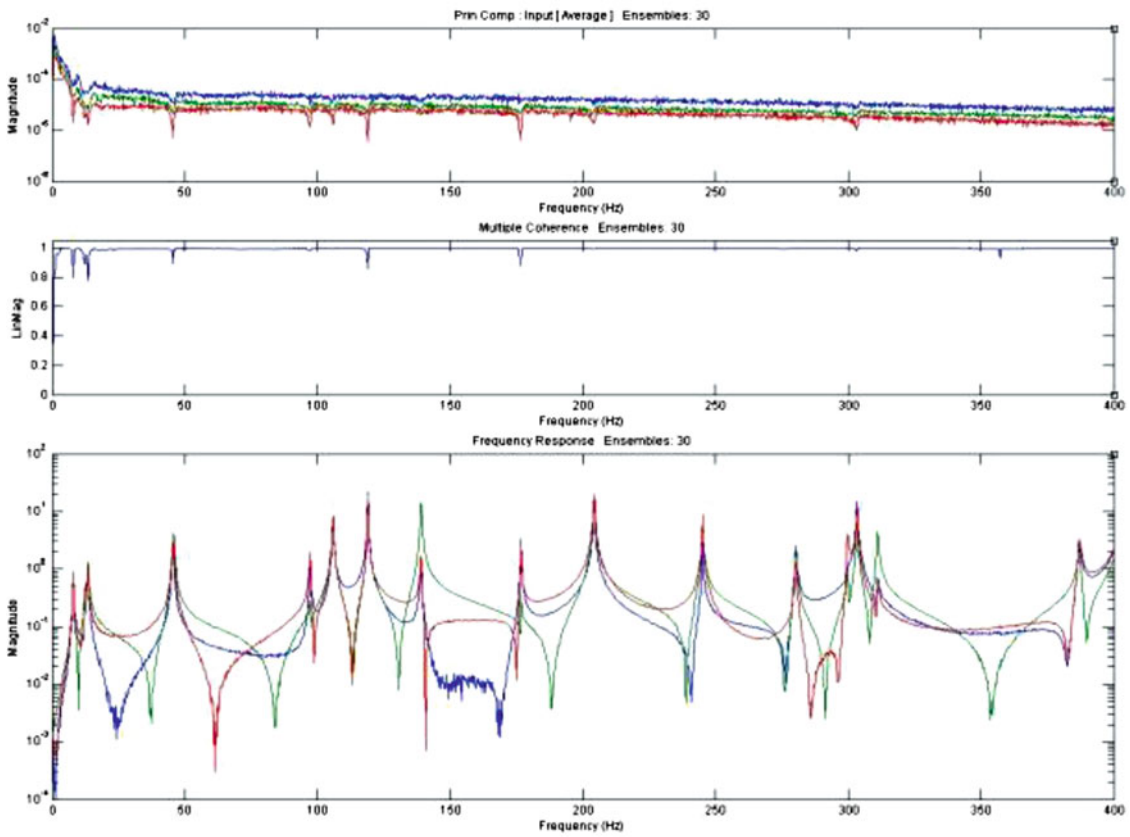
Fig. 33.22 FRF estimated at 25 % burst length
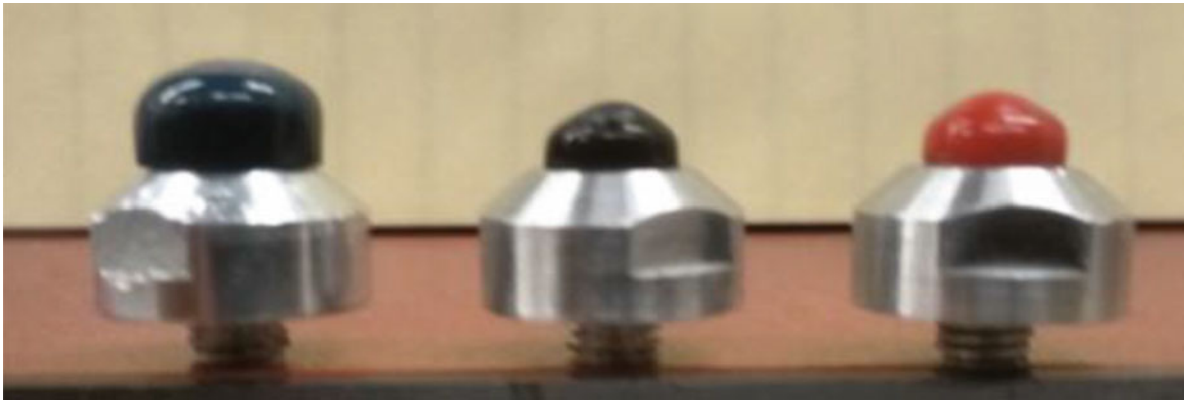
Fig. 33.23 (From *left* to *right*) Harder, soft and softer impact tip
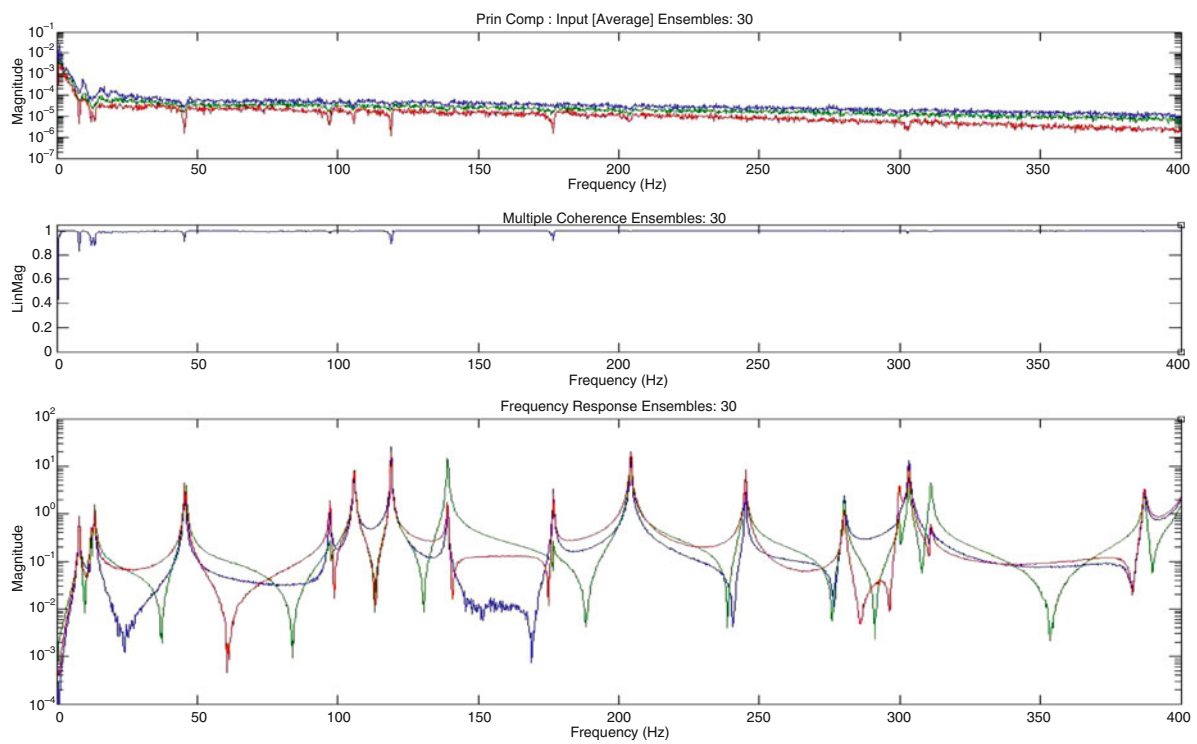
Fig. 33.24 FRF estimated with softer tip
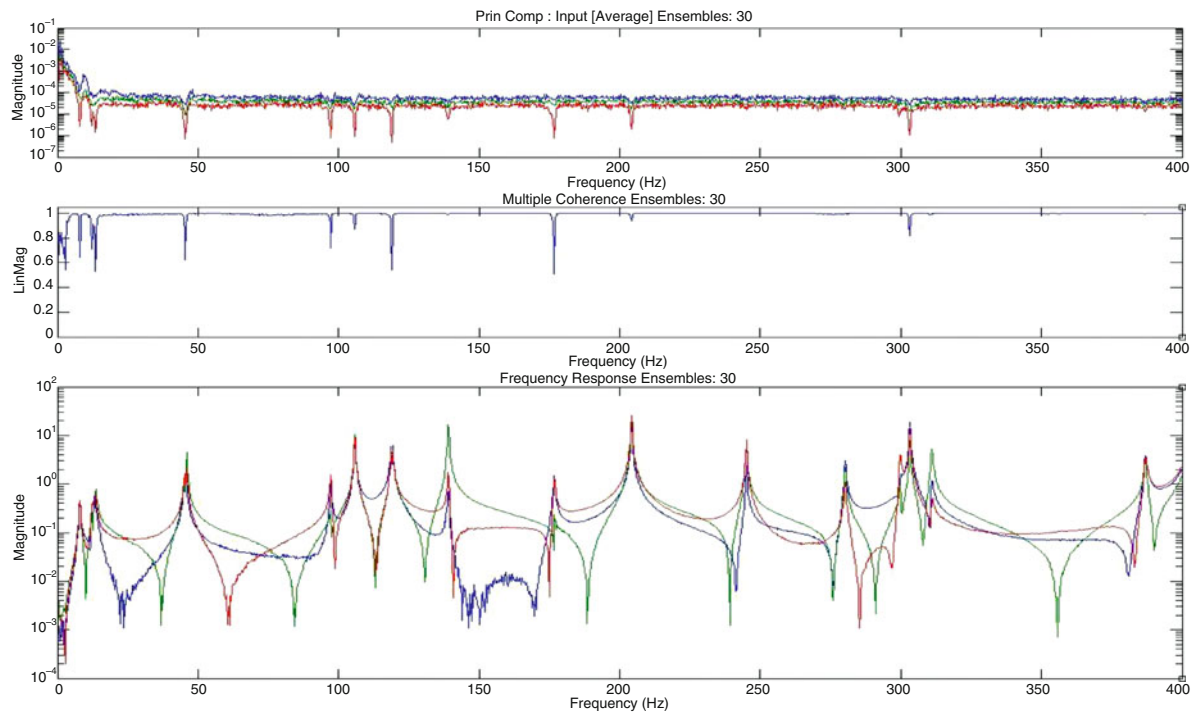
Fig. 33.25 FRF estimated with harder tip
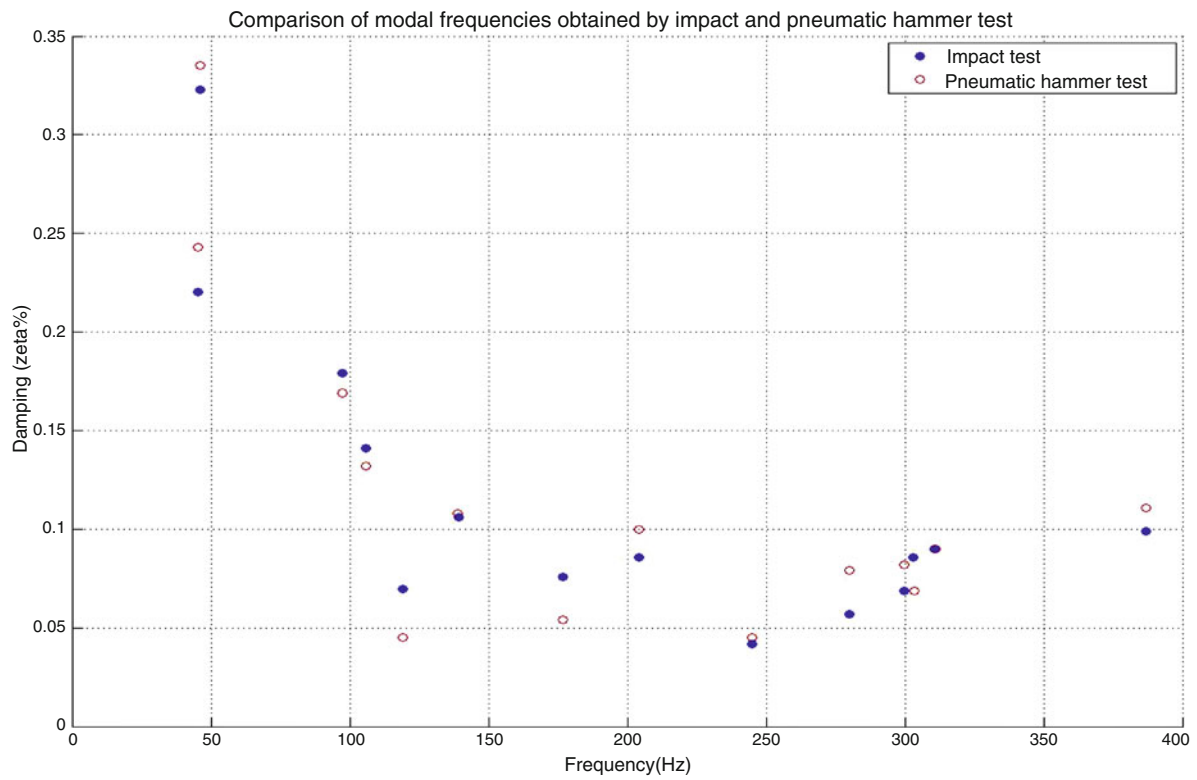
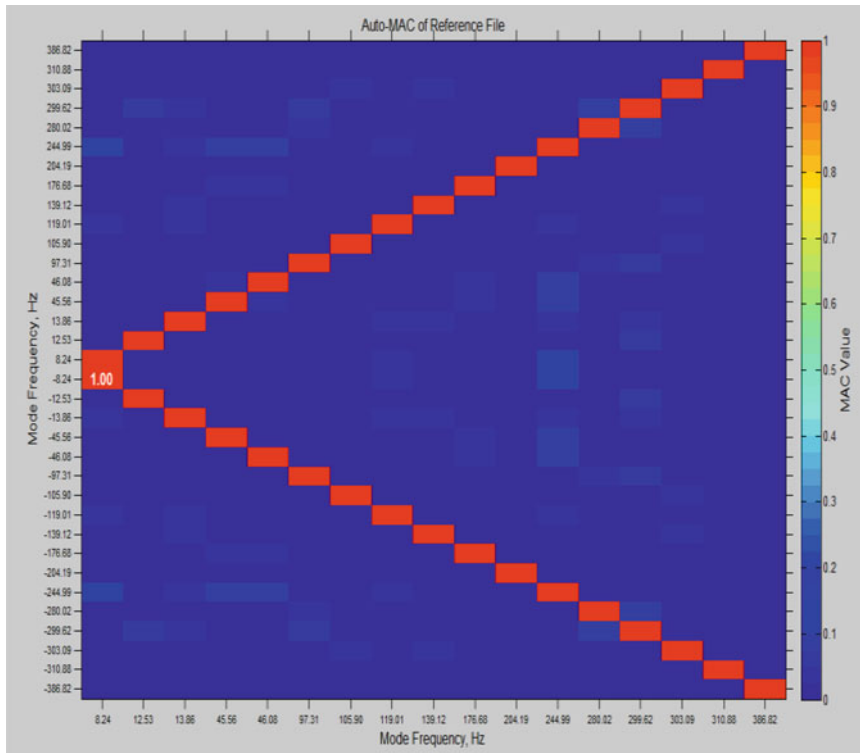**Fig. 33.26** Comparison of modal frequencies
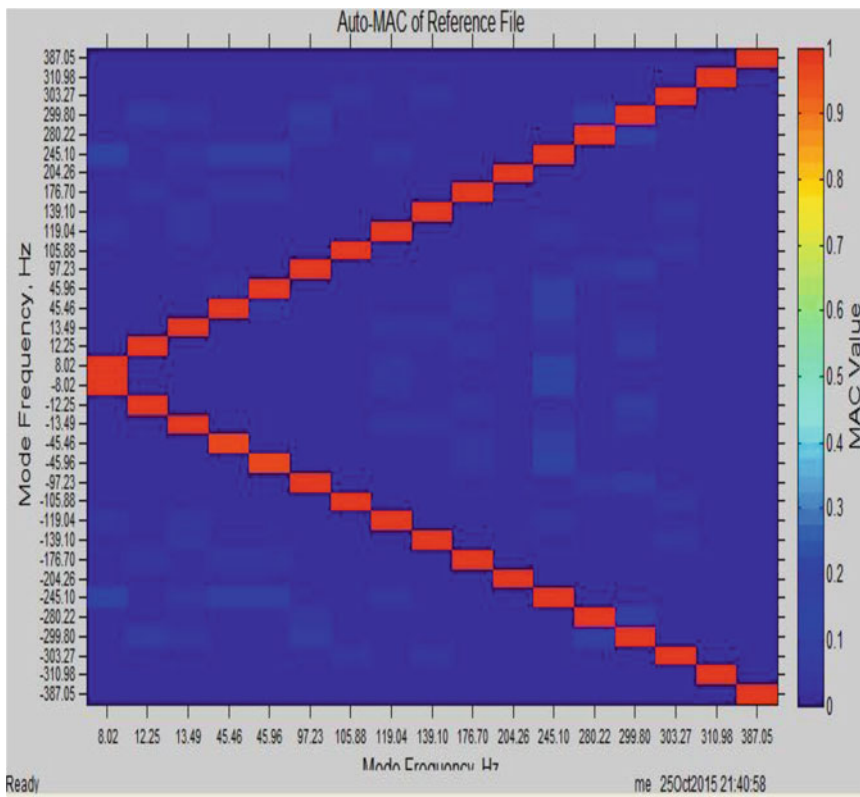
Fig. 33.27 Modal assurance criteria (impact test)

Fig. 33.28 Modal assurance criteria (pneumatic test)

Chapter 34
Estimating System Modal Parameters Using Free Decay Time Data

Alexander Young, David Brown, and Randall J. Allemang

Abstract   The response of a system following the removal of an external forcing function is known as its free decay response. Assuming that all modes of interest are excited, the free decay response data taken at various system degree-of-freedoms (DOFs) contain all the information necessary to extract eigenvalues and eigenvectors. In the 1940s, 1950s and early 1960s, it was possible to measure free decays on a strip chart or an oscilloscope, and it was also possible to measure frequency response functions (FRFs) using step sine methods. In the late 1950s and early 1960s, the introduction of 8-bit analog-to-digital convertors (ADCs) and tracking filters made it possible to measure or digitize free decays, but the technology was not available to computationally extract the eigenvectors and eigenvalues. The history of free decay testing will be reviewed along with an example demonstrating the extraction of modal parameters using time-only free decay responses and multiple input, multiple output (MIMO) methods and algorithms developed in the 1970s and 1980s.

Keywords   Free decay • Response only modal analysis • Time domain modal parameter estimation • Impact testing • Historical modal analysis

34.1   Introduction

Free decay responses have been used for hundreds of years in the tuning many musical instruments. Musical instruments which relied upon a transient input excitation were (and still are) tuned by ear by adjusting the structural properties of the instrument to achieve the desired acoustical characteristics. The response of the instrument includes all the modes of vibrations excited by the forcing function. A skilled musician or musically skilled technician could make adjustments to the instrument, its inputs or the environment to achieve the desired musical effect. Likewise, a second class of musical instruments generated sound by using a self-excitation process where an unstable interaction (self-excited vibration) exists between the external force acting on the instrument, the air column or strings, and the structural dynamics characteristics of the instrument. Again, a skilled musician could adjust (tune) the instrument or air column to achieve the desired acoustical characteristic of the instrument.

34.2   1940s–1960s

From the 1940s through the 1960s, there was significant interest in controlling two self-excitation vibration problems. The first was the problem of aerodynamic flutter where an unstable interaction arises between the air flow over the surface of an aircraft and the deformation of the aircraft structure, itself due to aerodynamic forces. The second was machine tool chatter where there is an unstable interaction between the cutting forces and the change in the structure of the work piece following the cutting process of a machine tool. Both of these problems are dependent upon the structural dynamics characteristic of the aircraft or the machine tool. Unlike the case of the musical instruments, a skilled technician could not simply observe or listen to the interaction between the forcing functions and structure and suggest modification to the structures to eliminate the self-excitation problem [1].

A. Young (✉) • D. Brown • R.J. Allemang

Structural Dynamics Research Laboratory (SDRL), Department of Mechanical and Materials Engineering,
University of Cincinnati, Cincinnati, OH 45221-0072, USA
e-mail: younap@mail.uc.edu

In the 1940s and 1950s, the aerospace community formulated the basic mathematics of the flutter problem in the frequency domain because the experimental measurements were made using a step sine excitation process which measured response due to external forcing functions at various frequencies. At the same time, the machine tool industry was investigating the cutting process using a step sine excitation process to measure FRFs between the cutting force and deformation of the work piece.

The major difference between the two cases is the nature of the input force. In the case of machine tool chatter, the excitation is transmitted into the work piece at a single point, while in the case of flutter, the forcing function acts over the entire surface of the aircraft. However, in both cases, the overall structural characteristics of the physical systems need to be considered. For example, on a machine tool the chatter problem may be eliminated by changing a structural characteristic such as a mounting point or by adding a remote tuned absorber. Obviously, modifying the aerodynamic profile or structural dynamics of an aircraft would have a significant effect on the dynamic response. By the late 1950s and early 1960s, techniques developed in the area of controls, namely methodologies for controlling the negative feedback problem, system models based upon using experimentally formulated impedance models and modal models were being studied. The impedance models and modal models were formulated from measured data using step sine, or by the early 1960s, swept sine testing methods. This testing generated FRF measurements which could be used directly in the impedance modeling case. For the case of modal modeling, however, the modal parameters had to be extracted from the measured FRFs. In the aerospace industry, there was a method known as force appropriation wherein eigenvalues and eigenvectors could be directly extracted directly during experimentation, however, no such method could be used in the machine tool industry. It was for this reason that in the 1960s a significant effort arose to mathematically extract modal parameters from measured FRFs.

To extract the modal parameters directly from FRF measurements required solving a set of non-linear equations, and there was much effort but no truly successful procedures in the 1960s. Most of the methods that were used in the mid-1960s were based upon single degree-of-freedom (SDOF) approximations. Some of these methods were commercialized and used in an effort to generate system models based upon the experimentally measured data.

In the mid-1960s, the development of Fast Fourier Transform (FFT) algorithm and its inverse made it possible to produce free decay responses directly from measured FRF data with possible signal processing errors arising during measurement due to sampling and windows, etc. However, there was still no practical computational method for extracting the modal information from the free decay data. Beginning in the late 1960s, a significant effort began to develop computational algorithms which could extract the information from the free decay data.

34.3 1970s

By chance, one author attended a meeting at Ford Motor Company where Ford was examining signal processing tools which could be used in the diagnostics of automatic transmissions. One presentation described an algorithm which could extract system eigenvalues from a free decay signal [2]. This algorithm, first developed in the late 1960s, was limited to a single measurement, but later, a least-squares (Least Squares Complex Exponential or LSCE) version was developed which could handle multiple free decays simultaneously measured on the same structure [3]. Once the eigenvalues were known, the modal contribution of each mode required solving a set of linear equations at a number of observed response points. The end result was that the eigenvalues and eigenvectors could be estimated using the free decays of the system. In the late 1960s, following to the development of the FFT, impulse, rapid sine sweeps, random, etc., excitation signals could be used in the measurements of FRFs.

In the 1970s, a major effort was employed to make the best possible FRF measurement: to minimize signal processing errors, average out the influence of non-coherent noise and minimize non-linear effects [4, 5]. Force measurements were of key importance to being able to make high quality FRFs. At this time, the data acquisition systems were limited to two to eight channels of simultaneously sampled data for most users with the exception of the aerospace industry where the cost of testing justified several hundred channels.

In the mid-to-late 1970s, transient testing techniques became popular for field testing of large structures. Two examples were tests conducted of two large windmills for NASA. The first test was in 1975 at Plumbrook, Ohio. The test was conducted with a two channel acquisition system. The windmill was excited by gently swinging a large mass suspended from a crane in order to impact a fixed point on the windmill. The impact force as well as the response from a single roving accelerometer were measured. FRFs were generated using cross power spectra and auto power spectra. A very good set of measured FRFs was made using three impacts at a single impact location (DOF). The mode shape data was extracted from the FRF's quadrature response. As a side note, this was the first test where mode shapes were animated on-site in real time.

A second larger windmill was tested in 1978 at Boone, North Carolina using a four channel HP Fourier Analyzer. The windmill was located on the top of remote hill, and it was not possible to get a crane for the test. This was the first test where a large structure was tested utilizing pure free decays data sets to determine the system eigenvalues and eigenvectors. It was tested with a step relaxation procedure [6]. A steel cable was connected to a load cell at a single input point on the windmill with the plan to measure the force due to the step relaxation event. A truck with a winch was used to apply the preload to the cable, and it was released. Unfortunately, the load cell data was completely unreliable due to the cable whip. A fall back procedure was used where a reference accelerometer was mounted near the cable attachment point to replace the load cell and three accelerometers were roved over the structure. The four free decay signals from the four accelerometers were captured and processed using the LSCE algorithm to obtain the system eigenvalues. In order to estimate the eigenvectors, the residues of the eigenvalues were estimated and the ratio of the residues for the three roving accelerometers to the reference accelerometer was used as a measure of the eigenvector at the roving points. The data from the three roving sensors were stitched together to get the complete characteristics of the system. The results from this test provided a high level of confidence in the methods used.

There were also several random decrement methods developed beginning in the late 1960s through the 1970s which attempted to process random data into the "buried" free decay contributions (autoregressive terms) [7–12]. A limitation of this method which has been addressed in recent years is the need for very high sampling capabilities to capture the precise trigger point.

34.4 1980s

In the early 1980s, the Polyreference Time Domain (PTD) algorithm, and later the Eigenvalue Realization Algorithm (ERA), were developed [13–17]. Both of these algorithms utilize an eigenvalue decomposition which can process the free decay data from MIMO data sets and extract the eigenvalues and eigenvectors of the system. In the case of free decay data, the multiple inputs would be replaced by multiple references (different free decay sets of data). It should be noted that this technique has rarely been used historically on directly measured free decay data, rather it is typically used on impulse response functions found by transforming FRFs. Some examples from the 1980s where free decays were used came primary from SDRC and UC-SDRL during field testing of machine tool, earth moving, power generation and mining equipment where it was difficult or impossible to measure the input forces. The rule of thumb, then as it is now, was to measure the excitation forces whenever possible. In the testing laboratory, the major research effort was spent on signal processing. In these cases, frequency response data was generated from measured input force and output response data. The control-distribution-measurement of the input forces were important on reducing the influence of non-coherent noise and non-linearity on the estimation of the frequency response data.

34.5 1990s: Present

In the previous 25 years, there has been an increased interest in testing large structures (bridges, dams, buildings, etc.) in order to evaluate or to detect potential damage or degradation. For smaller structures, an array of impactors, shakers and step relaxation techniques are available. For very large structures, which are subject to significant environmental inputs, various techniques utilizing cross power spectrum measurements of the responses of large arrays of sensors responding to environmental excitations are processed to obtain eigenvalues and eigenvectors. Random decrement methods have been used in civil infrastructure testing that tried to measured random data over a long period of time and then extract the free decay (autoregressive) response through averaging. This work continues today and is the basis of modern operational modal analysis (OMA) methods, sometimes called response only methods [18–20]. These methods sometimes use random decrement averaging but more often use response cross power spectra and the associated response cross covariance.

In 2003, in order to evaluate new testing equipment and procedures, the Boeing Company invited a number of vendors to evaluate new testing procedures and equipment for performing a ground vibration test of a Boeing 737 aircraft. A paper of this test was presented at the 2004 IMAC by Boeing and the vendors that participated in the test [21]. The main purpose of the test was to evaluate a new data acquisition system, the digital signal sensor (DSS) system, which was designed to significantly reduce transducer cabling. The data from 64 sensors could be transmitted over a single unshielded cable to the data acquisition unit. A number of standard excitation FRF testing procedures (sinusoidal or transient) were used. Pure free-decay data was captured using impacting and step relaxation. An impact hammer was used where a large soft tip (beach ball)

Fig. 34.1 Boeing test using step relaxation techniques

was attached to the hammer. A step relaxation procedure was also used where a 20–40 pound mass was hung at various points on the plane and free decays resulted from cutting the rope holding the mass (see Fig. 34.1). In another test, a person simply pulled down on the wings and released to trigger the free decay. This data was then processed using a standard ERA algorithm. Very encouraging results were obtained from the free decay testing.

34.6 Processing Free Decay Data

As has been noted in the previous sections that reviewed the history of free decay testing, pure free decay testing (response only) is a testing technique which has been seldom used. It was a fallback solution when it was not possible or at least impractical to measure excitation forces. The development of long dimension, low order MIMO FRF parameter estimation algorithms, such as ERA, made it a viable testing method which can now be easily extended to the multiple reference free decay testing situation [22, 23]. With the current increase in interest in testing large in-the-field test objects, it can potentially become an additional tool for extracting the complex valued modal frequencies and complex-valued modal vectors when it is not convenient or possible to measure external forces used to excite the structure.

Obtaining clear free decays requires applying an external transient forcing function to the test structure of sufficient amplitude to generate a response signal significantly greater that the ambient response of the system. It is necessary to capture a time history of the response signals which includes a pre-trigger time delay before the external force is applied and includes the response during the period when the force is being applied and the free decay response after the force is removed. The pre-free decay data is to help to identify any noise on the data which might mistakenly be identified as system characteristics (eigenvalues or eigenvectors). For example, periodic signals due to piece of rotating equipment on or near the structure could be identified by the parameter estimation process as complex-valued modal frequencies and modal vectors when they actually represent forced modes of vibrations associated with the frequencies of the rotating system. If the available number of response sensors are not sufficient to document the system characteristics, then a subset of sensors can be roved over the structure, and the eigenvectors can be stitched together to obtain the complete vector.

As mentioned previously, the free decays are the responses to the system after the external forces are removed from the system. The best results are going to be obtained for lightly damped systems. For moderate to heavily damped systems, where the free decays are very short, multiple coherent external forces must be applied and the free-decay responses averaged to remove the influence of non-coherent noise. This may be difficult, and for this condition, this can be a real limitation. It should be noted that this is a limitation currently encountered when performing standard transient testing procedures.

34.7 General Free Decay Test Procedure

1. Eliminate or reduce noise sources as much as possible:

   (a) If possible, shut down equipment which is exciting the test object.
   (b) Test at times when there is reduced environmental noise.
   (c) For periodic noise sources, process the pre-test data and synthesize and subtract the periodic noise from the free decay data.

2. In case of non-linear response:

   (a) Take a different region of the free decay signals to determine if the eigenvalues and eigenvector are stable.
   (b) For cases where the ambient noise is a minimum, process different regions of free decay data to determine if systems eigenvalues are changing as a function of the amplitude of the response.
   (c) Generate a backbone response curve which shows how the eigenvalues change as a function of amplitude of the free decay data.

3. If a finite element model (FEM) or pretest data is available:

   (a) Choose excitation signals or input excitation points which will excite or enhance critical modes of interest.

4. Excitation methods:

   (a) Step relaxation

      i. For large test items, step relaxation is often easiest method.
      ii. Connect cable or rope to or hang a mass from an input point of interest and cut or release.
      iii. Repeat process for number of points in MIMO fashion.
      iv. Use algorithm such as ERA to process data, estimate eigenvalues/eigenvectors.
      v. The main advantage of step relaxation is that it puts most energy into the low frequency range where the response sensors usually have less sensitivity, and it does not require a person swinging a hammer or directing a large impacting mass.

   (b) Impact testing

      i. Impact with a hammer or a large suspended mass to create transient excitation. Most impact hammers have built-in load cells which can be used to measure the force.
      ii. If convenient, as in the case of field or large structure testing, place a soft tip on the impact surface and simply impact the interface. This large mass may be too heavy swing, so a crane or cherry picker may be required. Large masses are also difficult to ship to the test site, so often a large massive object at the test site is used.
      iii. Procedure is fast if it is convenient to move the impacting device.
      iv. If roving the large mass is difficult, take a number of impacts at a given point to reduce noise since moving a large mass may be impractical.
      v. Use an algorithm such as ERA which is a LS estimator that weighs the data to help reduce non-coherent noise. Of course, multiple input points are still required to separate closely couple and repeated modes.
      vi. Be aware of the potential issue of overloads when using transient inputs on individual response sensors.

   (c) Periodic excitation (if noise is a problem)

      i. Use an electromechanical or hydraulic shaker and tune to the frequency of a mode of interest. Shut down the shaker (or better yet disconnect from the structure). The mode that is tuned will dominate the free decay, and the eigenvalues and eigenvector of this mode will be enhanced.
      ii. In case of a repeated root, excite the structure from two or more points so that the ERA algorithm can estimate the repeated eigenvalues and eigenvectors.
      iii. This becomes somewhat similar to the force approbation method except the modes do not have to be precisely tuned. The parameter estimation process uncouples the modes.
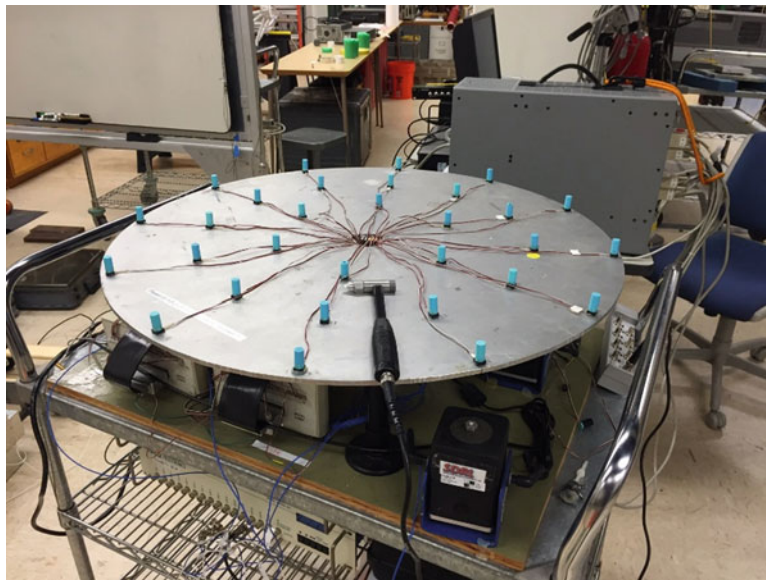
Fig. 34.2 C-plate test structure

34.8 C-Plate Example

An aluminum circular plate (C-plate) located in UC-SDRL was used as test object to demonstrate the free decay testing procedure. This is an ideal test object to evaluate the potential of the method. The plate itself is 30 inches in diameter and a quarter-inch thick. It has a number repeated modes which are lightly damped and has been used as test object to train students for 40 years or more. Thirty accelerometers are permanently mounted on the structure which is mounted on soft springs. The structure is often tested in a MIMO configuration with three electromechanical shakers (Fig. 34.2).

34.9 Test Setup

Testing was carried out by impacting a set of randomly selected points on the plate. The force was measured so that FRFs could be compared with previous tests of the same structure, and also to compare results to the method of using free decay response only data where force measurements were not used to the obtain results. An advantage of this method is that it focuses on the response in the early part of its decay where the signal-to-noise ratio (SNR) is relatively very high. As the ERA method is a long dimension, low order modal parameter estimation method, the data used in the ERA algorithm needs to be only a short sequence of time points at the beginning of the response signals, and the total number of data points used in the estimation process is equal to this sequence of points multiplied by the number of response points multiplied by the number of impacts on the structure. By having many responses and impact locations, there is an inherent averaging process to reduce the influence of measurement noise since much of the ambient noise is not coherently related to eigenvalues and eigenvectors of the system.

The C-plate was tested by impacting at a large number of points (20). This essentially results in a twenty reference, thirty response set of free decay data. Only one impact was taken at each point. The impact forces were measured but were not used when processing the free decay data. FRFs were constructed using the force signals for comparison. While randomly chosen, the large number of impact locations was meant to ensure that all modes, including repeated modes, of interest were excited. Care was taken to avoid overloading sensors. The raw data was stored initially in 3D matrix which was the size of the number of responses by the number of impacts by the length of the time histories. The lab environment has some level of ambient noise, however, and different levels of analytically generated random and periodic noise was added to the ambient noise in order to evaluate the effects of various and relatively high amounts of noise.

34.10 Processing the Data

The measured free decay responses were processed using ERA-based algorithms (both a student-generated version and the version of ERA implemented in the UC-SDRL X-Modal research software) where a state space vector of response data span the column space of the matrix, and the row space is spanned by the sampled free decay time data. For the algorithm, the sampled free decay data can be taken from different regions of the sampled data space. As mentioned, the data taken shortly after the transient input has the best SNR, however, in order to investigate non-linear effects, response data samples can be processed from different regions of the free decays. A backbone plot of the non-linear response can be generated by using the data from different regions of the free-decay response data.

The free decays were recorded at the 30 instrumented points on the C-plate due to a force generated by the impact at 20 randomly selected impact points. The data block size was 20,480 data points per free decay data record. The first 1024 points were pre-trigger information, and the remaining were the measured free decay data. A MATLAB™ script was developed based upon the ERA algorithm which processed the measured data. The analysis of the data consisted of varying the starting point of the region, the number of points in the region and the number of state space expansions used in the ERA algorithm. The number of solutions was equal to the product of the number of the data blocks selected multiplied by the number of points used in each solution multiplied by the number of state space terms. This generated a very large number of solutions. These solutions were filtered using information generated by comparing the state space eigenvectors of the solutions. The modal assurance criteria (MAC) between the estimated state space vectors for two different state space solutions was used to filter out the computational state space vectors [24, 25]. The remaining filtered data is then plotted to generate a series of cluster plots of the filtered pole data. From each cluster, the eigenvalues and the eigenvectors are estimated.

During typical impact tests, the C-plate is impacted multiple times at multiple locations, the force is measured at the impact points and the response at the 30 output points. In general, averaging is used, and impact windows are applied to the input forces and response outputs and FRFs are estimated. Time or generalized frequency domain parameter estimation algorithms are used to extract the eigenvalues, eigenvectors and modal scale factors. Typically, just a few references are used [2–6].

The results are quite similar using both the FRF and the free decay techniques. Of course, the modal scale factors are not available using the free decay procedure. The major difference is that the free decay test inputs were selected assuming no prior knowledge of the system characteristics, and, as stated, there were no measured forces used in the free decay analysis.

34.11 Results and Discussion

34.11.1 Case 1

In the first case, five input points were selected randomly from the 20 impact points taken during the free decay testing, and this set of data was processed using both a basic MATLAB™-generated ERA algorithm and a free decay capability in X-Modal's ERA implementation. The estimated eigenvalues and eigenvectors come from a large combination of different starting values, data block sizes, state space model order, etc. The very large data space of potential solutions was filtered using the modal assurance criteria (MAC) between two different least squares eigenvector normalization solutions (A_0 and A_1). Using a model vector or pole-weighted vector MAC has proven to be a very effective filter for separating system modal parameters from computational modes due to non-coherent noise.

An example of the process is shown by plotting the pole locations of a typical data processing session (Figs. 34.3, 34.4, and 34.5).

34.11.2 Case 2

In the second case the 20 impact points are used, and the data is processed in a similar process as the previous example. There is good correlation with results obtained with the five impact data. The figure of the plot of the clusters for the 20 impact case yields a nearly identical result as Case 1 (Figs. 34.6, 34.7, and 34.8).
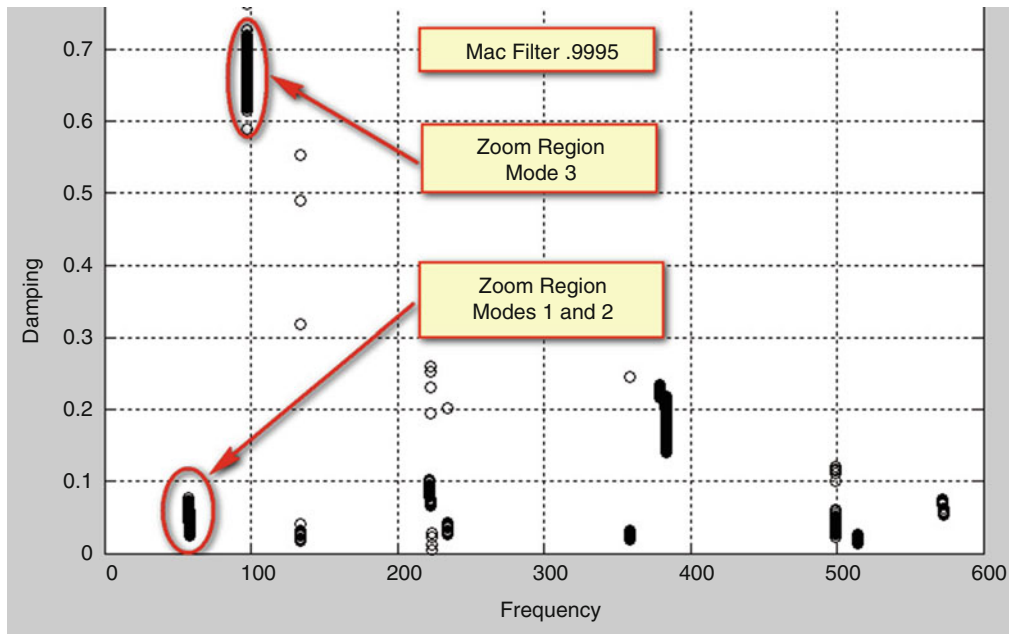
Fig. 34.3 Estimated filtered pole locations, Case 1
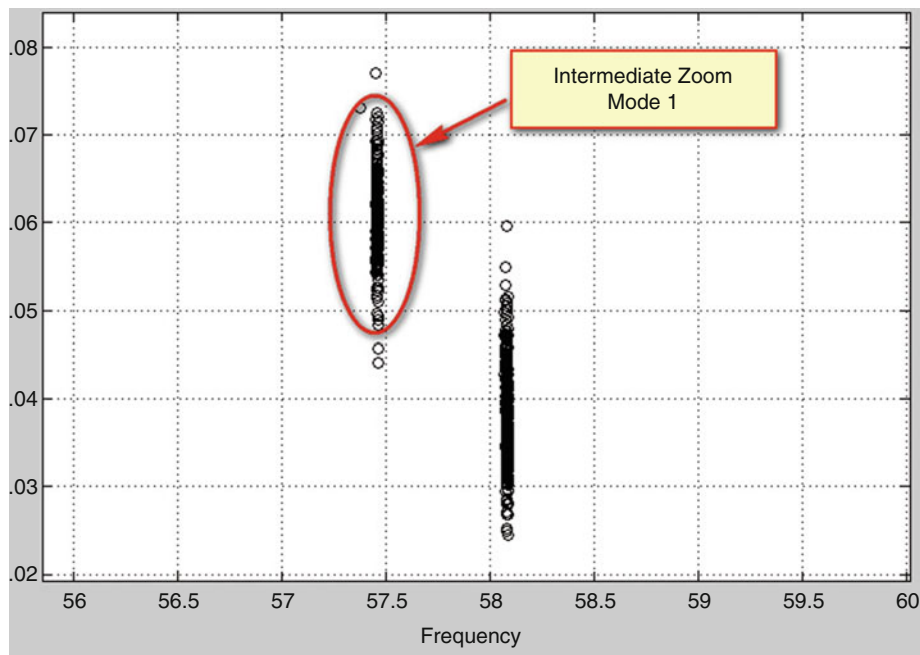

Fig. 34.4 Intermediate zoom of first cluster, Case 1

34.11.3 Case 3

In the third case, a fairly high level of non-coherent random noise is added to the test data, and the ERA processing is repeated as in Case 2. In Fig. 34.9, a typical plot of the free decay with ambient noise is shown in blue, and the additive pure random noise is overlaid in red. It is clear that the additive noise is a significant part of the data. However, the pure random data does not supply additional damped exponential component information, and the additive noise is largely filtered out by the ERA processing. In Fig. 34.10, a plot of the filtered eigenvalue clusters are shown, and the results are very similar to results shown for the case where only the ambient environmental noise was present (see Fig. 34.3). Both the environmental and additive noise are reduced by the ERA processing.
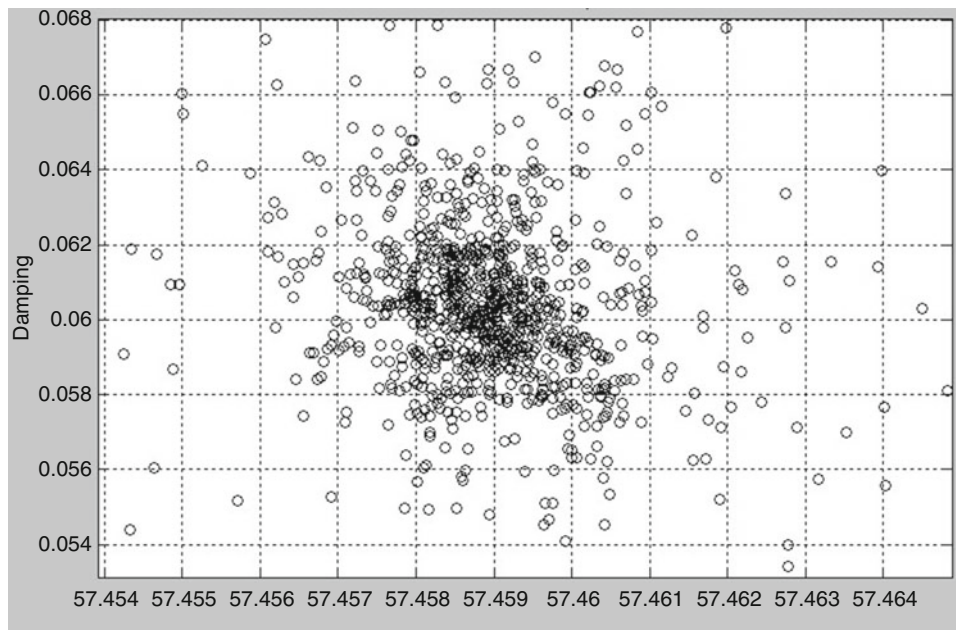
Fig. 34.5 Cluster of first mode, Case 1
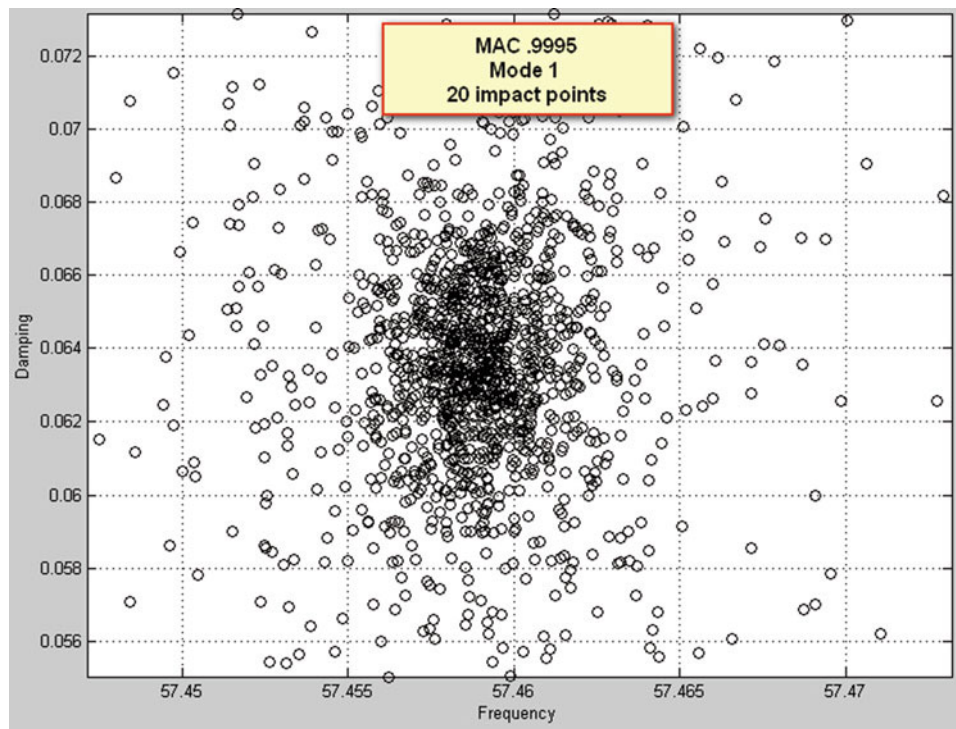
Fig. 34.6 Cluster of first mode, Case 2
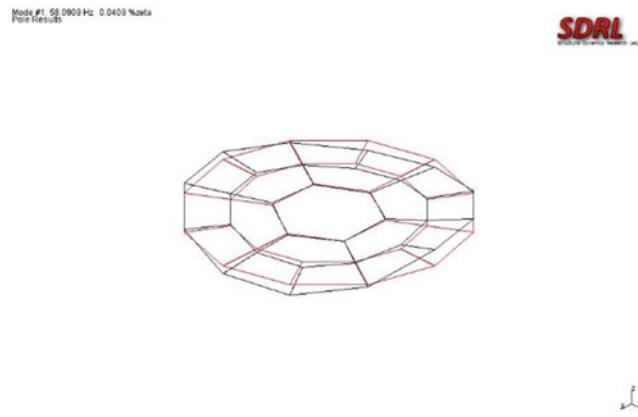
Fig. 34.7 Mode 1, repeated mode, generated using X-Modal
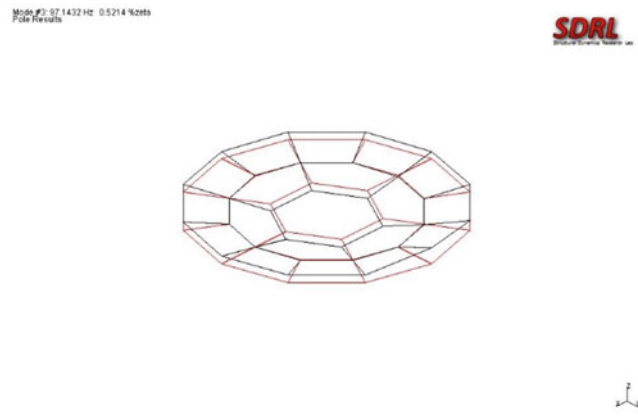
Fig. 34.8 Mode 3, generated using X-Modal
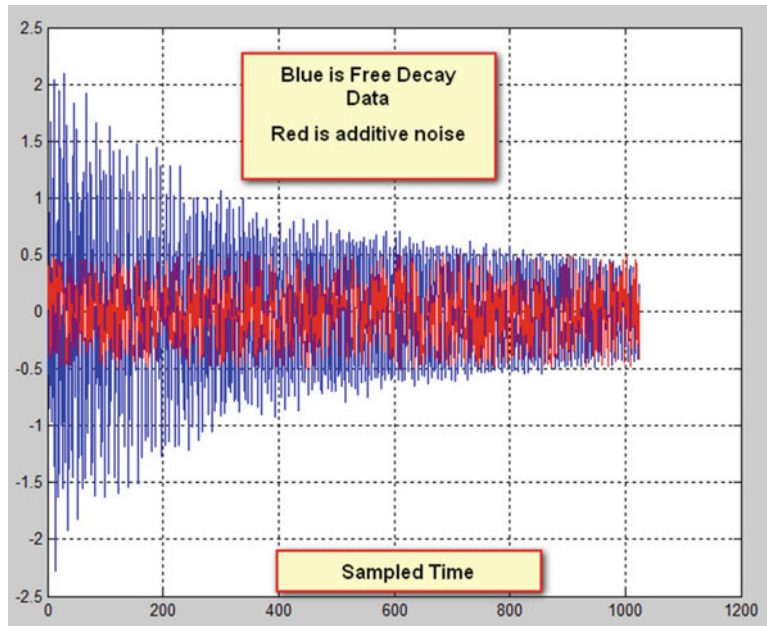
Fig. 34.9 Free decay response (*blue*) with additive noise (*red*), Case 3
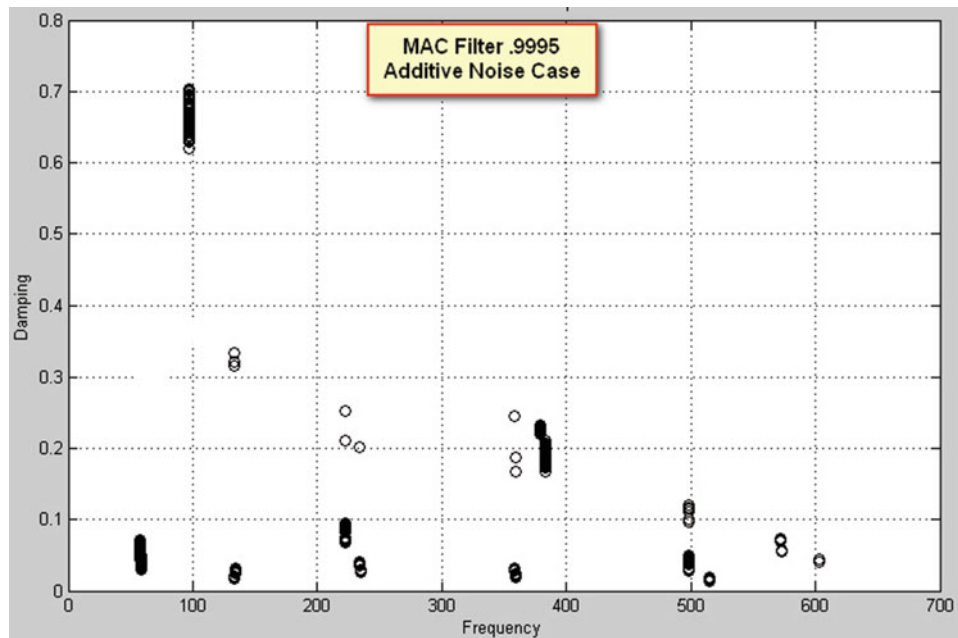
Fig. 34.10 Estimated filtered pole locations, Case 3

34.12 Conclusions

The free decay method outlined in this paper is a potential testing method which can be applied to large structures or structures where it is difficult to measure the input forces acting on the structure. An unmeasured transit force is applied to the structure, and the free decay responses of the structure are measured simultaneously at a large number of response points. The eigenvalues and eigenvectors at the measured response points can be extracted using ERA or an equivalent algorithm. This is sufficient information to check correlation with FEM by comparing the resulting eigenvalues and eigenvectors. If an experimental modal model is required, then it is necessary to measure the input(s) to derive modal scale factors. For future study, the effect of periodic or forced vibration noise on a system undergoing the test methods proposed in this paper should be explored.

References

1. Brown, D.L., Allemang, R.J.: The modern era of experimental modal analysis: one historical perspective. Sound Vib. Mag. **40**
2. Spitznogle, F.R., et al.: No. 1, 10 pp., January, 2007. Representation and analysis of sonar signals, volume 1: improvements in the complex exponential signal analysis computational algorithm. Texas Instruments, Inc. Report Number U1-829401-5, Office of Naval Research Contract Number N00014-69-C-0315, 37 pp (1971)
3. Brown, D.L., Allemang, R.J., Zimmerman, R.D., Mergeay, M.: Parameter estimation techniques for modal analysis. SAE Paper No. 790221, SAE Trans. Vol. 88, pp. 828–846 (1979)
4. Ramsey, K.: Effective measurements for structural dynamics testing: part I. Sound Vib. (1975)
5. Ramsey, K.: Effective measurements for structural dynamics testing: part II. Sound Vib. (1976)
6. Stenger, G.: Step relaxation method for structural dynamic excitation. Master of Science Thesis, Department of Mechanical Engineering, University of Cincinnati, 54 (1979)
7. Imes, R.S., Jennings, W.P., Olsen, N.L.: The use of transient testing techniques in Boeing YC-14 flutter clearance program. AIAA Paper Number 78-0505 (1978)
8. Cole, H.A. Jr.: On-the-line analysis of random vibrations. AIAA Paper Number 68-288 (1968)
9. Cole, H.A. Jr., Failure detection of a space shuttle wing flutter model by random decrement. NASA TM X-62, 041 (1971)
10. Cole, H.A. Jr.: On-line failure detection and damping measurement of aerospace structures by random decrement signatures. NASA CR-2205 (1973)
11. Hammond, C.E., Doggett, R.V. Jr.: Determination of subcritical damping by moving-block/randomdec applications. Flutter Testing Techniques, NASA-SP-415, pp. 59–76 (1975)
12. Reed, R.E.: Analytical aspects of randomdec analysis. AIAA Paper Number 79-0828, pp. 404–409 (1979)

13. Vold, H., Kundrat, J., Rocklin, T., Russell, R.: A multi-input modal estimation algorithm for mini-computers. SAE Trans. **91**(1), 815–821 (1982)

14. Vold, H., Rocklin, T.: The numerical implementation of a multi-input modal estimation algorithm for mini-computers. In: Proceedings of the International Modal Analysis Conference, pp. 542–548 (1982)

15. Juang, J.N.: Mathematical correlation of modal parameter identification methods via system realization theory. J. Anal. Exp. Modal Analysis **2**(1), 1–18 (1987)

16. Juang, J.-N., Pappa, R.S.: An eigensystem realization algorithm for modal parameter identification and model reduction. AIAA J. Guid. Control. Dyn. **8**(4), 620–627 (1985)

17. Fukuzono, K.: Investigation of multiple-reference Ibrahim Time Domain Modal parameter estimation technique. M.S. Thesis, Department of Mechanical and Industrial Engineering, University of Cincinnati, 220 pp (1986)

18. Chauhan, S., Martell, R., Allemang, R.J., Brown, D.L.: Unified matrix polynomial approach for operational modal analysis. In: Proceedings of the International Modal Analysis Conference, 13 pp (2007)

19. Chauhan S., Martell, R., Allemang, R.J., Brown, D.L.: Application of independent component analysis and blind source separation techniques to operational modal analysis. In: Proceedings of the International Modal Analysis Conference, 13 pp (2007)

20. Chauhan S., Martell, R., Allemang, R.J., Brown, D.L.: Implementation of complex frequency mapping to low order frequency domain algorithm for operational modal analysis. In: Proceedings of the International Modal Analysis Conference, 12 pp (2007)

21. Pickrel, C.R., Foss, G.C., Phillips, A.W., Allemang, R.J., Brown, D.L.: New concepts GVT. In: Proceedings of the International Modal Analysis Conference, 11 pp (2006)

22. Allemang, R.J., Brown, D.L., Fladung, W.: Modal parameter estimation: a unified matrix polynomial approach. In: Proceedings of the International Modal Analysis Conference, pp. 501–514 (1994)

23. Allemang, R.J., Phillips, A.W.: The unified matrix polynomial approach to understanding modal parameter estimation: an update. In: Proceedings of the International Conference on Noise and Vibration Engineering, Katholieke Universiteit Leuven, Belgium, 36 pp (2004)

24. Allemang, R.J., Brown, D.L.: A correlation coefficient for modal vector analysis. In: Proceedings of the International Modal Analysis Conference, pp. 110–116 (1982)

25. Allemang, R.J.: The modal assurance criterion (MAC): twenty years of use and abuse. In: Proceedings of the International Modal Analysis Conference, pp. 397–405 (2002). Sound Vib. Mag. **37**(8), 14–23 (2003)

Chapter 35
Structural-Acoustic Mode Coupling in a Bolted Aluminum Cylinder

Benjamin Pacini and Gregory Tipton

Abstract This work presents a modal test on a cylindrical bolted structure that initially appeared to be a routine model calibration experiment. However, while reviewing the test data the structure appeared to have two pairs of ovaling modes with identical shapes. Assuming this to be the result of an uninstrumented component of the test article, extensive efforts were conducted to identify this feature. When all options were exhausted, the interaction between the structure and the air contained within was investigated. Contrary to the typical assumption that the fluid-structure interactions are negligible for such a thick walled cylinder, analysis showed that for this test article the acoustic modes of the internal air significantly impacted the structural response. In this case, the acoustic and the structural modes coincided in frequency, causing the first ovaling modes to split into two pairs at different frequencies. Experimental and analytical results are presented that describe this structural-acoustic mode coupling phenomenon.

Keywords Experimental modal analysis • Analytical modal analysis • Structural-acoustics • Coupled modes

Nomenclature

|	
CMIF	Complex mode indicator function
FEM	Finite element model
FRF	Frequency response function
SMAC	Synthesize modes and correlate (computer program)
$\varnothing$	Mode shape vector
s	Subscript for structural
a	Subscript for acoustic
F	Fractional contribution to mode shape

35.1 Introduction

A typical assumption in structural dynamics is that the interaction between the test object and surrounding air is negligible. While a valid assumption in many cases, structural-acoustic interaction can have an effect on the mode shapes and frequencies of a structure. The magnitude of these interactions depends on the effective mass and stiffness contributions of the fluid to the structure. Many references exist describing such structural-acoustic interactions [1–3].

During routine modal testing of a bolted aluminum cylinder, two pairs of (2,0) ovaling modes were found at different frequencies but with identical mode shapes. Initially thought to be the result of an un-instrumented feature of the structure, it was later determined that these repeated modes were the result of acoustic coupling between the cylinder and the air inside. This was not expected due to the fact that the cylinder was fairly stiff with a relatively thick wall. Finite element analyses demonstrated the effect of the acoustic coupling on the modes of cylinder.

B. Pacini (✉) • G. Tipton

Sandia National Laboratories, Engineering Sciences Center, P.O. Box 5800 – MS0557, Albuquerque, NM 87185, USA

e-mail: brpacin@sandia.gov; dgtipto@sandia.gov

Fig. 35.1 Test hardware
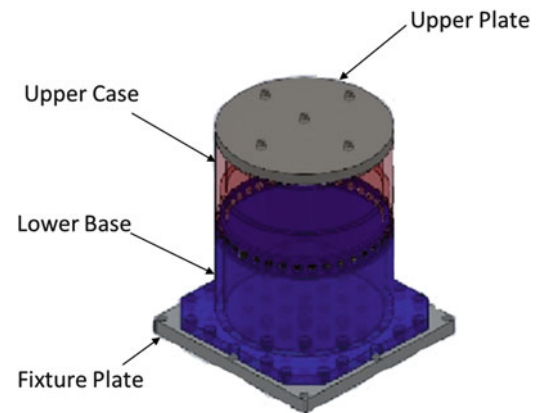
The work presented here describes both the experimental and analytical modal analysis that was performed on the cylinder. Particular attention is paid to the structural-acoustic coupling effects on the ovaling modes. Section 35.2 describes the hardware used in this study. The test setup and results of the experimental modal analysis are discussed in Sect. 35.3. In Sect. 35.4, finite element modeling results of the coupled structural-acoustic modes are presented. Section 35.5 provides conclusions.

35.2 Description of Structure

The test hardware was a hollow, cylindrical assembly consisting of an upper plate, upper case, lower base, and fixture plate, see Fig. 35.1. The upper plate was connected to the upper case via 5 bolts and the lower base to the fixture plate with 40 bolts. The upper case and lower base are hollow and fit together tightly with the former sliding over the latter. This lap joint is completed with 36 screws. The structure was approximately 25.4 cm tall with a 0.95 cm thick cylindrical wall. All pieces of the structure were made from aluminum.

35.3 Experimental Modal Analysis

35.3.1 Test Set Up

The test assembly was softly suspended using bungee cords which were looped through each of the holes on the corners of the base plate. This approximated a free-free condition which was desirable because the experimental results can be directly compared to free modes from the finite element model (FEM).

The assembly was externally instrumented with 21 uniaxial and 16 triaxial accelerometers. Figure 35.2 shows the locations of these test gages on the assembly. The global Cartesian coordinate system and one cylindrical coordinate system were defined for this test. Figure 35.2 displays the global coordinate system in black and the cylindrical coordinate system in purple. The origins of both coordinate systems are at the center of the bottom face of the fixture plate. The cylindrical coordinate system had its Z+ axis aligned with the global Z+, R+ pointing outward radially from Z+, and $\theta = 0°$ at the global X+. Nodes 311–314, 411–414, and 511–514 were located and oriented with the cylindrical coordinate system while all other nodes used the global coordinate system.

35.3.2 Test Results and Analysis

Hammer impact tests were conducted on the hardware described above for the purposes of FEM calibration. The input locations are denoted in Table 35.1. These locations and directions were selected in an attempt to excite as many modes of the structure within the bandwidth of interest (0–2500 Hz) as possible.
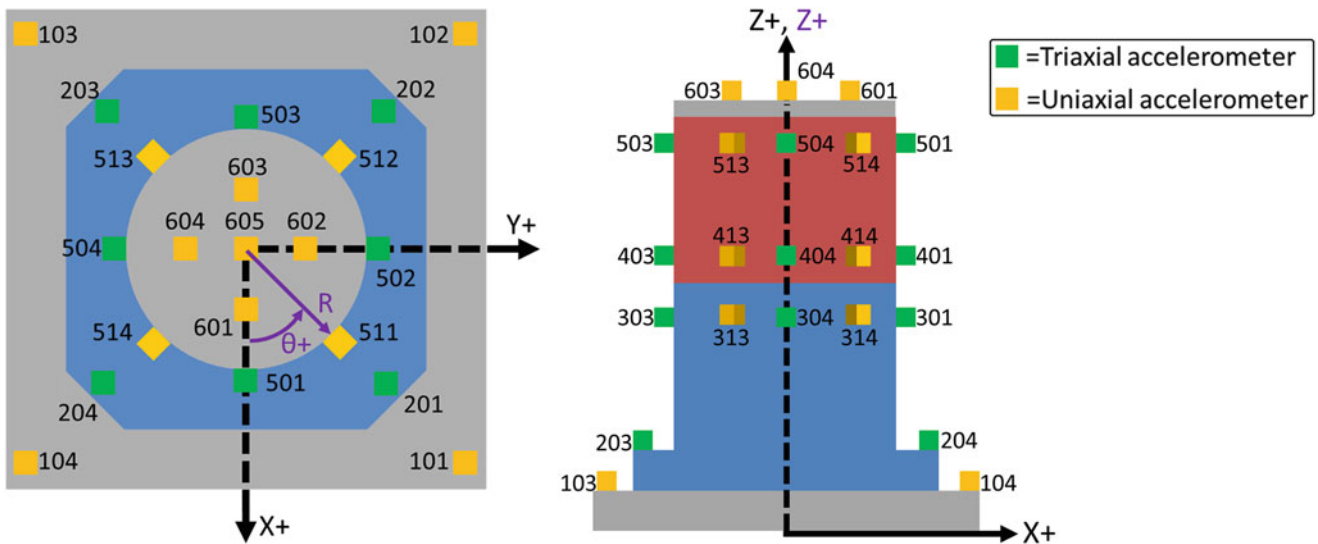
Fig. 35.2 Node locations and coordinate systems

Table 35.1 Force input locations and descriptions

Input	Description
101Z+	Vertical input on the bottom side of the fixture plate
201X−	Horizontal input on the vertical face of the flange of the lower base
301X−	Inward-radial input near the top of the lower base
414R−	Inward-radial input near the bottom of the upper case

Table 35.2 Experimentally extracted modal parameters

Mode	Frequency (Hz)	Damping (%cr)	Shape reference	Description
1	2141	0.49	414R−	(2,0) ovaling of case at 45° from X-Y axes
2	2166	0.46	301X−	(2,0) ovaling of case aligned with X-Y axes
3	2214	0.18	414R−	(2,0) ovaling of case at 45° from X-Y axes
4	2226	0.49	301X−	(2,0) ovaling of case aligned with X-Y axes

Data analysis was performed using the Synthesize Modes And Correlate (SMAC) program [4] with a real modes approximation. Due to slight nonlinearities in the data, each set of FRFs had to be analyzed separately; there were four different analyses, and then the results were sieved to extract modes from the best drive points. The resulting modal parameters are listed in Table 35.2. Note that no modes of interest for this work were extracted from the 101Z+ nor 201X− data as the other two inputs (301X− and 414R−) better excited these modes.

Figure 35.3 shows the comparison of the multi-reference Complex Mode Indicator Function (CMIF) synthesized from the extracted modal parameters (dashed) with the CMIF calculated from the measured 301X and 414R data (solid). This provides a measure of how well the extracted modal parameters represent the actual data. Given the high degree of correspondence between the synthesized and measured data, the modal parameters from Table 35.2 adequately capture the structural dynamics of the test hardware.

The modes listed in Table 35.2 appear to be identical pairs; mode shapes 1 and 3 are seemingly indistinguishable as are mode shapes 2 and 4. This is illustrated in Figs. 35.4, 35.5, and 35.6. Moreover, the modal assurance criteria (MAC) was calculated and showed that the two modes in each pair were identical at all of the measurement locations; both mode pairs each had MAC values of 0.999. This is usually an indication of either insufficient or poorly placed instrumentation. Once the instrumentation is updated, the shapes can typically be differentiated. However, after an exhaustive investigation where an accelerometer was mounted to nearly every internal and external surface, no feature was found that distinguished the shapes. This lead to the hypothesis that the air contained within the cylindrical portion of the test article was interacting with the structure. This was confirmed through structural-acoustic finite element simulations discussed in the next section.
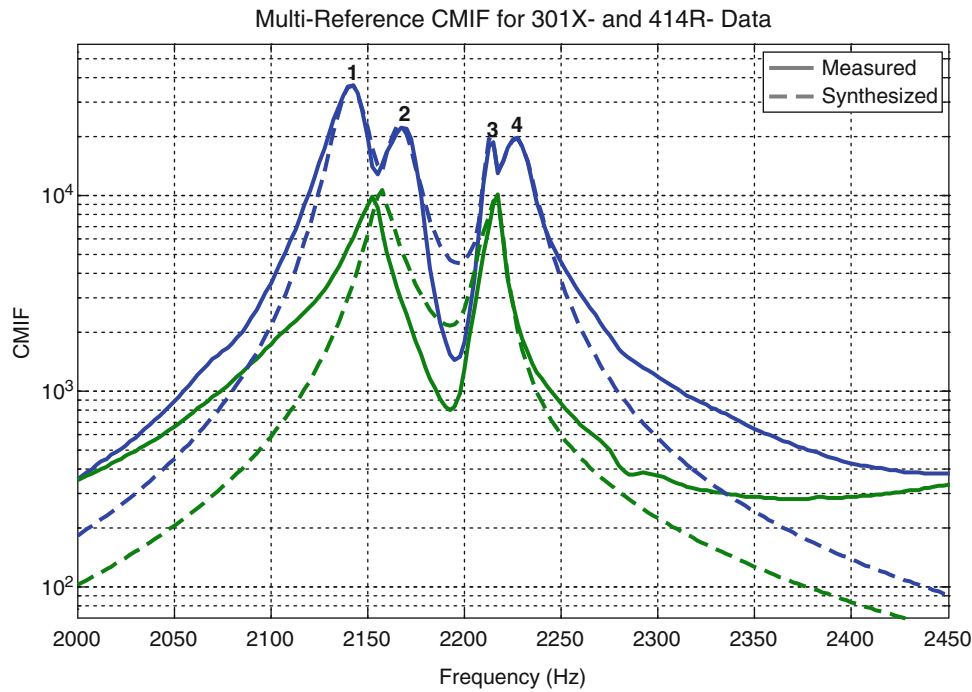
Fig. 35.3 Multi-reference CMIF, synthesized (*dashed*) versus measured (*solid*) data
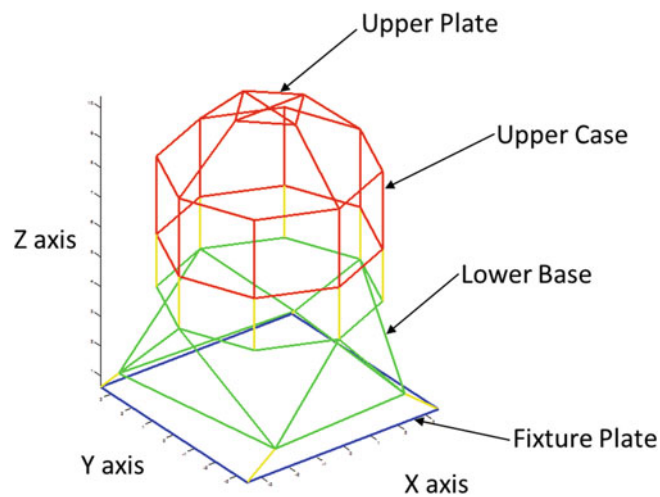

Fig. 35.4 Undeformed shape

35.4 Finite Element Analysis

35.4.1 Model Overview

A finite element model was created to investigate the modes of the structure. This finite element model included the air inside the cylindrical cavity to study the effects on the modes of the structure. Analyses were performed with the air present and with the air removed. The finite element model can be seen in Fig. 35.7 This model was designed to run in the structural dynamics module of the Sierra Mechanics software written by Sandia National Laboratories [5]. It should be noted that the model uses a slightly different coordinate system than the experiment.

Each portion of the model was meshed with solid, 8-node hexahedral elements, including the air. Each bolted joint was represented by a set of six springs (three translational and three rotational) to allow for adjustment of the local bolt stiffnesses. Tied contact was used to attach the air mesh to the structure mesh. For the pure structural simulations (no air), real eigenvalue
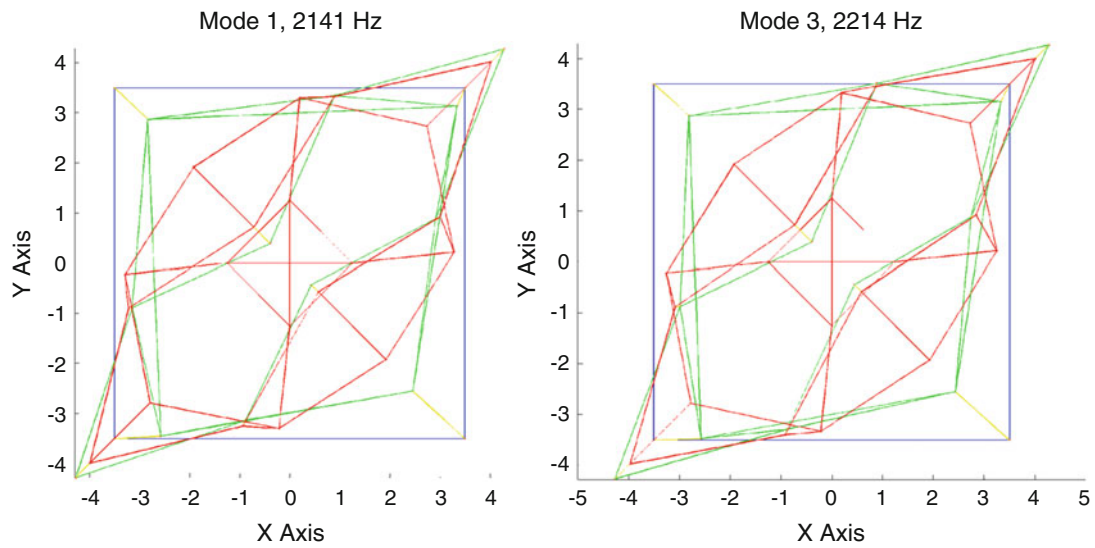
Fig. 35.5 Shapes for Modes 1 and 3
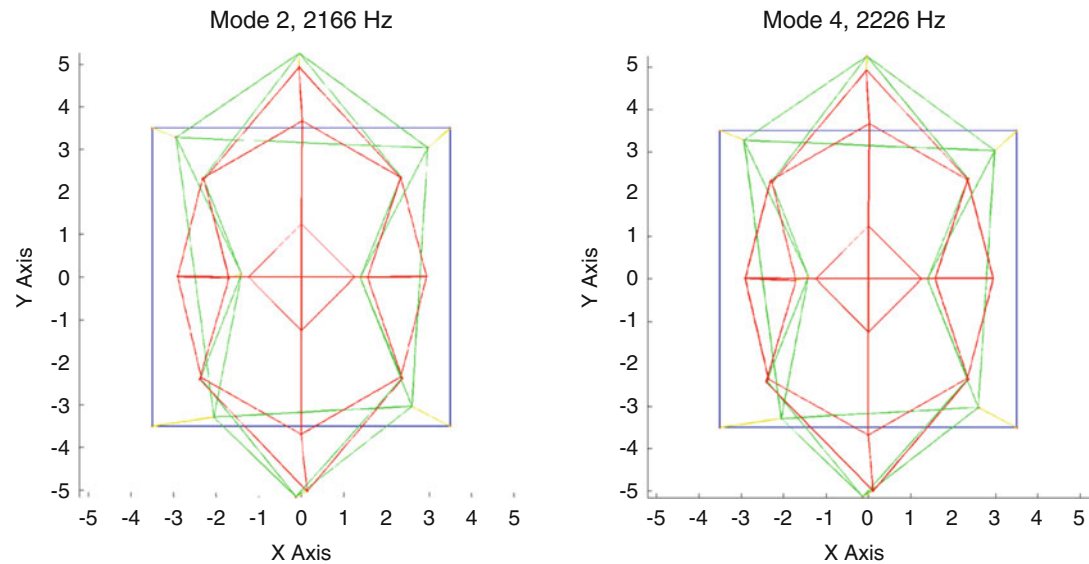
Fig. 35.6 Shapes for Modes 2 and 4

analyses were performed to compute the modes of the structure. For the coupled problem with the air present, quadratic eigenvalue analyses were performed resulting in complex natural frequencies and mode shapes. The complex eigenvalue analyses were performed using a method available in Sierra Mechanics that uses a combination of the pure-structure modes and the pure-acoustic modes to estimate the coupled-modes of the system (the sa_eigen method). In addition to eigenvalue analyses, direct frequency response simulations were performed to compute driving-point frequency response functions (FRF) of the structure with and without the air.

It should be noted that this model was not calibrated to the experimental modal data presented above. The results presented here are from the original model as first assembled. Thus, the natural frequencies do not match the experimental modes exactly. A maximum of 6 % error is seen between the subject experimental and analytical modes. Future versions of the model will have updated spring stiffnesses which should improve the correlation.
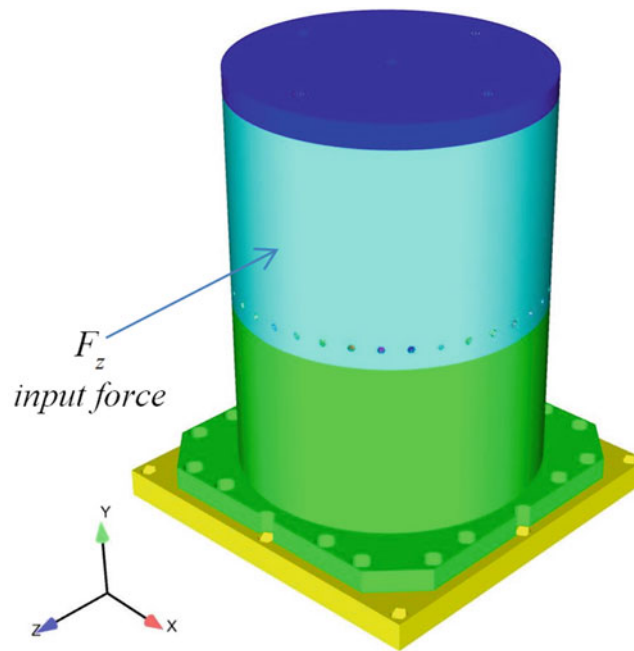
**Fig. 35.7** Finite element model of the bolted can assembly
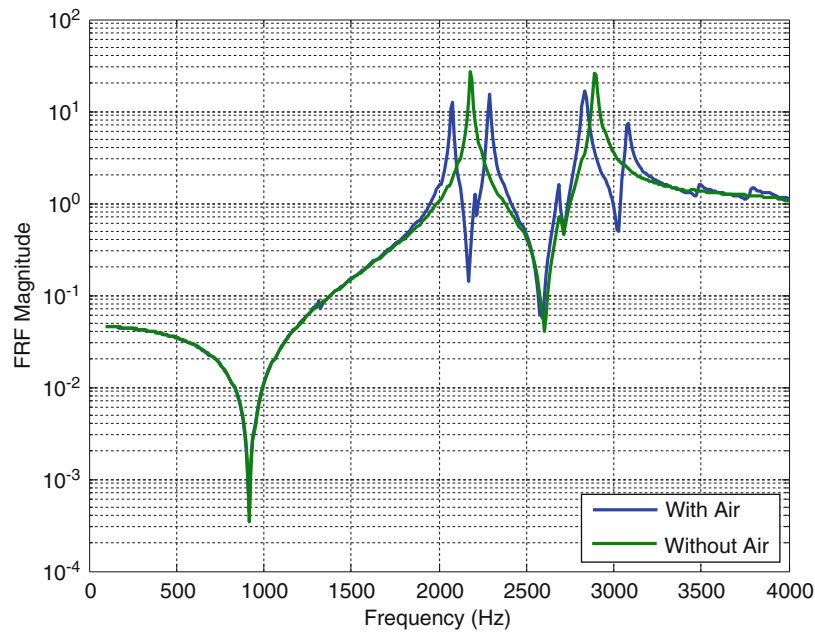
Fig. 35.8 Driving-point FRF's with and without air included in the structure

35.4.2   Model Results

Results from the direct frequency response function analyses can be seen in Fig. 35.8. In the figure it can be seen that the air within the cavity of the structure has an effect on the (2,0) ovaling modes of interest. In the pure-structural simulations, only one pair of (2,0) ovaling modes is predicted at a frequency of approximately 2200 Hz (the first peak in the green curve). With the air included in the model, this pair of modes splits into two pairs of ovaling modes. In the FRF shown in the figure, the 2200 Hz (2,0) ovaling mode split into two identical modes at 2078 and 2290 Hz. These modes are aligned with the major axis of the model and correspond to modes 2 and 4 shown in Table 35.2 above. The orthogonal pair of (2,0) modes corresponding to 1 and 3 in Table 35.2 were computed at 2006 and 2237 Hz.
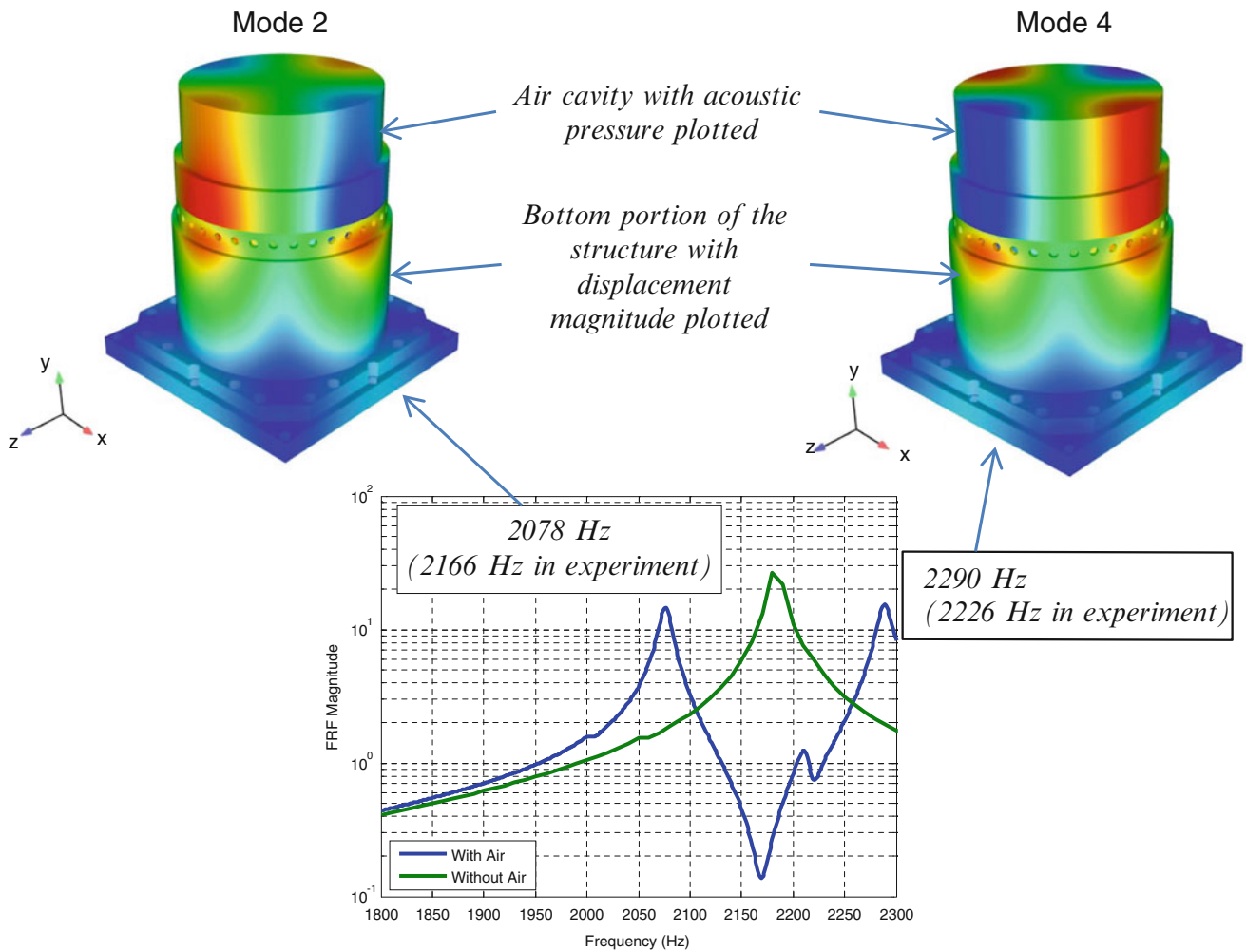
Fig. 35.9 Z-response/Z-input FRF and associated structural-acoustic mode shapes

A close-up of the driving-point FRF is shown in Fig. 35.9 along with the associated structural-acoustic mode shapes (corresponding to modes 2 and 4 from Table 35.2 above). It should be noted that the magnitude of the displacement is plotted on the structure and the acoustic pressure is plotted in the air. The top portion of the structure has been hidden to reveal the air inside the cavity. The complimentary orthogonal modes 1 and 3 are similarly shown in Fig. 35.10.

In both Figs. 35.9 and 35.10, the color contours on the structure vary from zero displacement in blue to maximum displacement magnitude in red. The color contours in the air cavity represent a negative pressure in blue and a positive pressure in red. Close examination of the model results indicated that the air and the structure are in phase for modes 1 and 2 but are out of phase for modes 3 and 4. So even though modes 1 and 3 show identical structural displacements, the air is in phase for one and out of phase for the other resulting in different modal frequencies. The similar argument can be made for modes 2 and 4. This explains the experimental results shown in Figs. 35.5 and 35.6 above. A summary of the modal results is presented in Table 35.3.

The FRF's shown in Figs. 35.9 and 35.10 additional peaks to those discussed here. These represent other modes of the structure that were not affected by the structural-acoustic coupling and are outside the scope of the research presented here.

The finite element model results also indicate that the (2,0) ovaling mode of the air cavity alone occurs at approximately the same frequency as the (2,0) ovaling mode of the structure without air. As these acoustic and structural modes grow closer together they combine and produce two pairs of nearly identical modes. It was shown above that these pairs of modes differ in whether the air is in phase or out of phase with the structure. In addition, the relative contribution from the air and the structure can be computed for each mode. Assume each mode shape can be partitioned into structural and acoustic contributions as
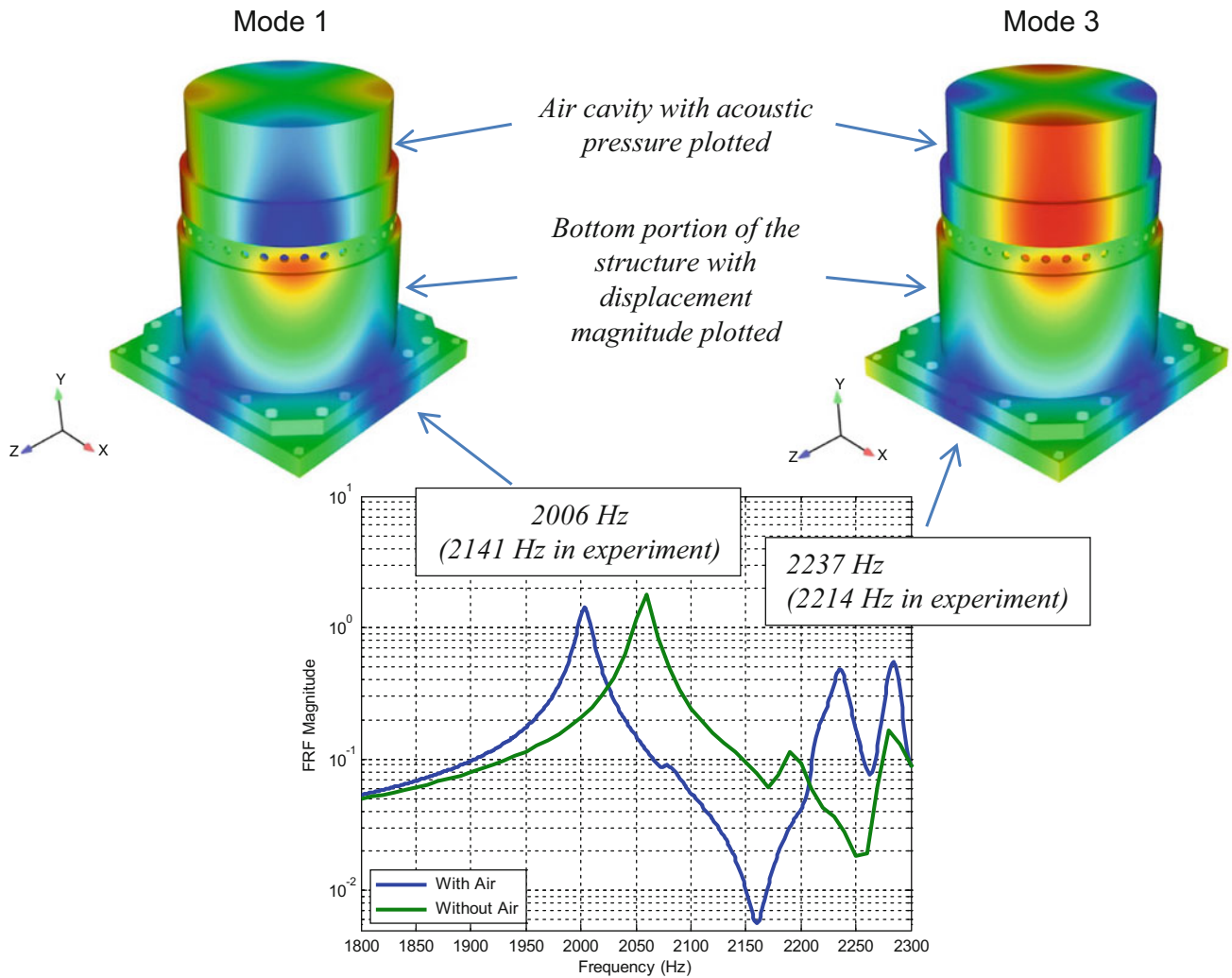
Fig. 35.10 X-response/Z-input FRF and associated structural-acoustic mode shapes

$$[\varnothing] = \begin{bmatrix} \varnothing_s \\ \varnothing_a \end{bmatrix}. \tag{35.1}$$

The structural fraction is computed as

$$F_s = \frac{\varnothing_s^* \cdot \varnothing_s}{\varnothing_s^* \cdot \varnothing_s + \varnothing_a^* \cdot \varnothing_a} \tag{35.2}$$

where the * represents the complex conjugate transpose. The acoustic fraction can be computed in a similar fashion. Computing these fractions can quantify the respective participation of the air and structure in a coupled mode shape. A summary of the computed structural and acoustic fractions is presented in Table 35.3.

The modal fraction results in Table 35.3 show that mode 1 has a higher structural fraction while mode 3 has a higher acoustic fraction. With the air present, the first (2,0) ovaling mode split into one primarily driven by the structure and one primarily driven by the fluid. On the other hand, the orthogonal mode pair (2 and 4) have essentially equal participation from both the fluid and the structure.

Table 35.3 Structural and acoustic fractions for each mode shape

Mode	Analysis frequency (Hz)	Experimental frequency (Hz)	Description	Structural fraction	Acoustic fraction
1	2006	2141	(2,0) ovaling at 45°—air in phase	0.81	0.19
2	2078	2166	(2,0) ovaling—air in phase	0.50	0.50
3	2237	2214	(2,0) ovaling at 45°—air out of phase	0.21	0.79
4	2290	2226	(2,0) ovaling—air out of phase	0.49	0.51

35.5 Conclusions

Modal test and analysis results for a bolted aluminum cylinder have been presented. Atypical for such a structure, the air inside the cylinder's cavity had a measureable influence on the modes of the structure. In particular, the first set of (2,0) ovaling modes of the structure corresponded closely in frequency with the (2,0) mode of the air cavity. The coincidence of these structure and acoustic frequencies caused the (2,0) ovaling modes to split into two separate pairs at different frequencies, but with nearly identical mode shapes. Coupled structural-acoustic finite element analyses of the hardware demonstrated the mode splitting behavior and allowed interpretation of the mode shapes that were determined experimentally. In particular, analyses showed that even though some of the modes had identical structural deformations, the air was in phase for one and out of phase for the other resulting in the different frequencies. The analyses also demonstrated that one mode pair demonstrated reciprocal structural and acoustic participation while the other mode pair had near equal structural and acoustic participation.

References

1. Blevins, R.D.: Formulas for Natural Frequency and Mode Shape. Krieger Publishing Company (2001)
2. Kinsler, L.E., Frey, A.R., Coppens, A.B., Sanders, J.V.: Fundamentals of Acoustics. 4th edn. Wiley (2000)
3. Junger, M.C., Feit, D.: Sound, Structures, and Their Interaction. 2nd edn. MIT (1986)
4. Hensley, D.P., Mayes, R.L.: Extending SMAC to multiple references. In: Proceedings of the 24th International Modal Analysis Conference, pp. 220–230 (2006)
5. Structural Dynamics Code Development Team. Sierra Structural Dynamics—User's Notes. Sandia National Laboratories, Version 4.36.1 (2015)

Chapter 36
Accurate Frequency Measurement on Small Structures with Shaker Excitation

Christopher J. Pye

Abstract Measurement of the frequency response functions of a structure is an important part of modal analysis. Excitation of the structures is often by a shaker coupled to the structure through a stinger and force transducer. The force transducer adds a small, uncompensated, mass to the system while the stinger may add additional stiffness. These can lead to errors in determining natural frequency.

Previous work, involving the model updating of small structures, had resulted in corrections to the Young's Modulus of Aluminum that put it outside the normally accepted range. This was assumed to be the result of errors in natural frequency measurement resulting from the use of a stinger and force transducer.

In this paper, this assumption is evaluated both experimentally and analytically. It demonstrates how the use of a shaker for excitation can change the measured FRF's of a structure and proposes an FE model of a stinger and force sensor that can be used to assess the changes before testing.

Keywords Modal test • Shaker • Frequency measurement

36.1 Introduction

Previous work [1] has described the determination of adhesive properties from the measurement of natural frequencies of simple adhesively bonded structures. The structure selected consisted of two Z-shaped aluminum profiles bonded together to form a closed section beam. Three different adhesives were used , referred to as soft, middle and hard adhesives which have increasingly higher elastic moduli. Finite Element (FE) models of the test specimens were built and solved to determine the natural frequencies and mode shapes. Modal tests were performed on the specimens and the results correlated with the analytical models. The adhesive modulus would then be determined using the NX FE Model Updating software using the test modes and reference.

The FE model and the test showed that there were a group of modes whose frequencies were essentially independent of the adhesive modulus. The frequencies of these modes were only affected by the properties of the modulus of the aluminum. Applying the model updating to these modes gave a Young's Modulus for the aluminum of 65.3 GPa, significantly below the nominal value of 70.5 GPa.

It was suggested that the use of a shaker, with associated stinger and force cell had led to errors in the determination of the natural frequency. Response measurement had been with a laser interferometer so mass loading by accelerometers was not an issue. This could have been verified with a simple impact test, but, unfortunately, the test specimens had already been cut up for visual inspection of adhesive thickness.

The work described here investigates the effect of using shaker excitation for the determination of natural frequencies of a lightweight structure with free-free boundary conditions.

C.J. Pye (✉)

Maya HTT Ltd, 4999 St. Catherine W, Montreal, QC, Canada H3Z 1T3

e-mail: c.pye@mayahtt.com

36.2   Approach

To determine the influence of the shaker excitation system on natural frequencies, a simple specimen was selected and drive point FRF's determined with a number of different excitation methods. The specimen is a square aluminum 6063 tube, 31.75 mm outside dimension, 3.05 mm wall thickness and 610.5 mm long.

A finite element model of the specimen was created using shell elements placed on the mid plane of the tube side. The model was solved with free-free boundary conditions and used with pre-test planning software to determine a suitable excitation point and accelerometer placement that would allow the modes to be clearly distinguished after the test. Once accelerometer locations were determined, point masses were added to the FE model to represent the accelerometers. Testing was limited to the first 5 modes to keep the number of accelerometers required to distinguish between the modes at a minimum. Six small uniaxial accelerometers were used; three had a mass of 0.9 g each and the remaining three a mass of 1.5 g each. The test specimen mass was 600 g.

Determination of an FRF requires measurement of the force applied to a structure and the resulting response. The only force applied should be at the drive point in the selected direction. The drive point FRF of the specimen was measured using the three methods listed in Table 36.1 and shown diagrammatically in Fig. 36.1.

Method 1, the impact test, adds no loading to the structure and should provide the most accurate determination of natural frequency. Method 2 is the classic excitation with a shaker. The concept is that by placing the force sensor at the structure, the applied force is measured and that by minimizing the mass of the sensor between the sensing element and the structure, the effect of the sensor is minimized. This approach assumes that the motion of the force sensor is purely axial. If there is lateral or rotational motion then additional, unmeasured, forces will be applied to the structure due to the inertia of the force sensor and the bending stiffness of the stinger. These additional forces will change the measured response. The stinger used was a 3 mm steel rod, 187 mm long, this was selected based on the principle that 'longer is more flexible and therefore better'.

Method 3, exciting the structure by impact through the mounted force sensor, will remove any effects due to the stinger bending stiffness but will still include the inertia effects of the force sensor.

Table 36.1 Excitation methods for FRF measurement

Method #	Method	Description
1	Impact test	The drive point was impacted directly with an impact hammer.
2	Shaker	Excitation from shaker via stinger and force sensor
3	Impact through force sensor	The force sensor used for the shaker test is mounted used to monitor excitation force. Excitation is by impact to the base of the force sensor
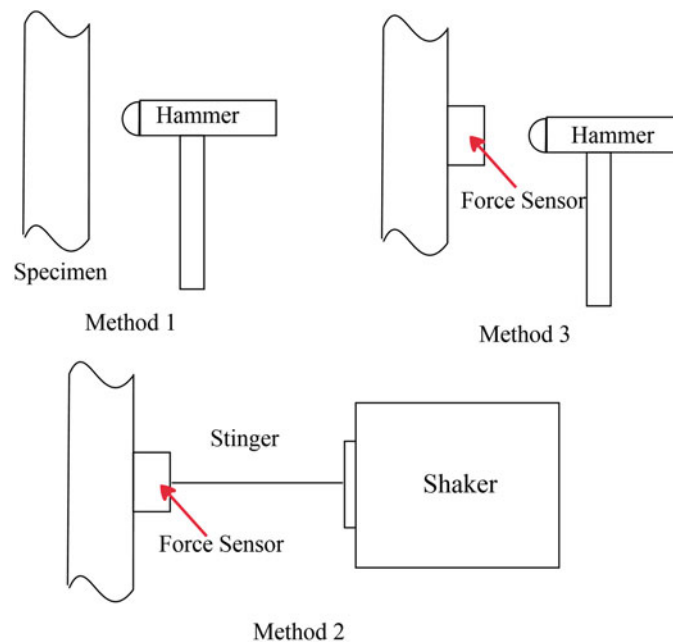
Fig. 36.1 Excitation methods

36.3 Test Results

The resulting drive point FRF's are shown in Fig. 36.2. The frequency range presented covers first and second bending modes and first torsion. The frequencies of these modes predicted by the analysis are given in Table 36.2. The slight frequency difference between the frequencies of what should nominally be identical modes, arise from the presence of the accelerometer masses. Figure 36.2 shows that there are significant changes in the FRF's between the three excitation methods, the spread of the frequency peaks for a given mode (or mode pair) increasing with modal frequency.

In order to ensure valid comparison of frequencies, modal extraction was performed for each set of test results and the resulting shapes correlated with the analytical model. The resulting frequencies are listed in Table 36.3, which shows frequencies for the test and analysis modes and, for the test modes, the percent change from the analysis modes. Note that none of the excitation methods excited mode 1, the first bending mode in the plane perpendicular to the excitation direction. The FRF peak for the first bending mode is small indicating that the excitation point was near a response node for the first bending modes, therefore excitation of the paired mode in the plane perpendicular to the applied force is difficult.
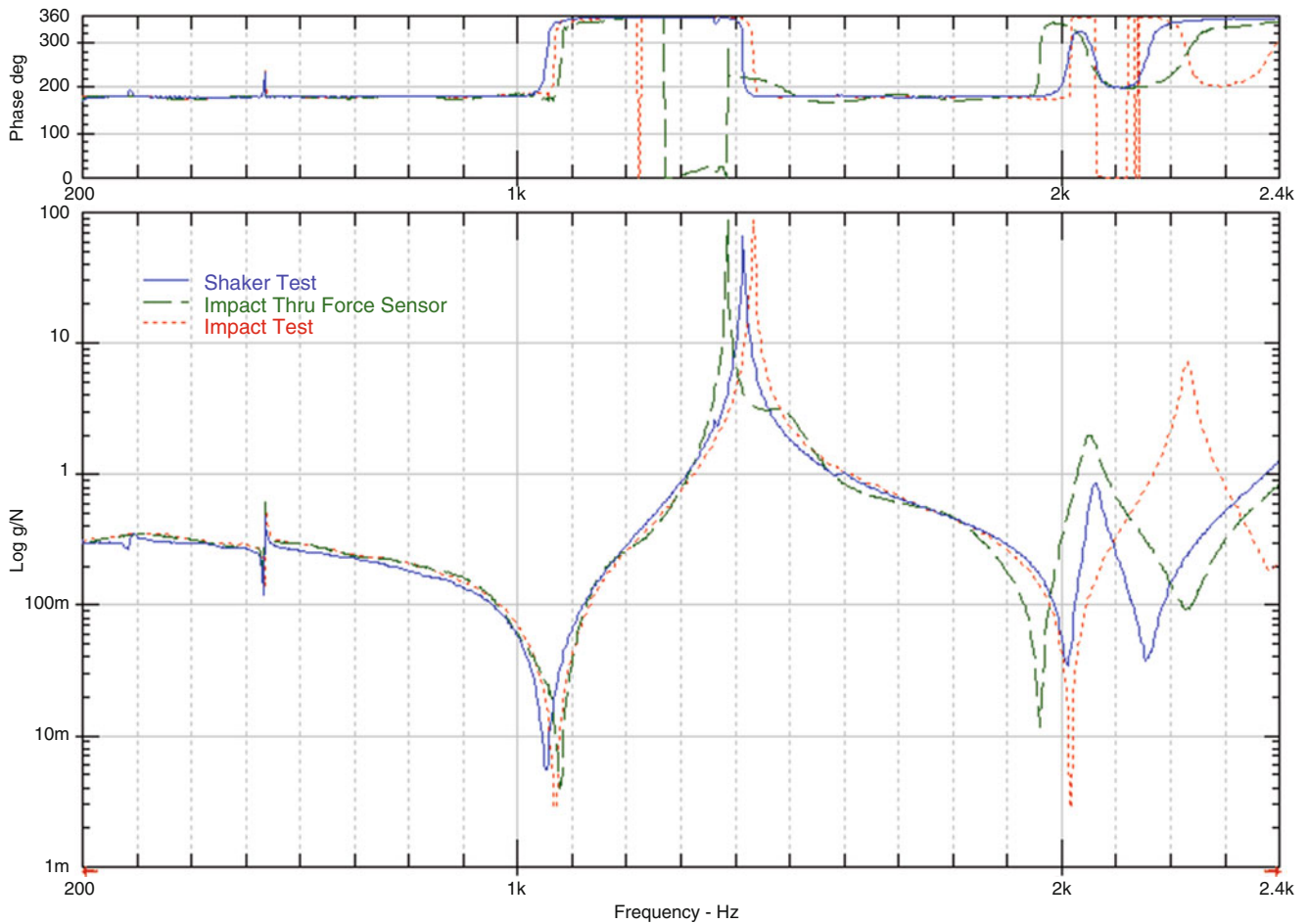

Fig. 36.2 Drive point FRF's for three excitation methods

Table 36.2 Analysis frequencies

Mode	Description	Predicted frequency (Hz)
1	First bending	544.2
2	First bending—repeated	544.3
3	Second bending	1437.4
4	Second bending—repeated	1437.7
5	First torsion	2185.6

Table 36.3 Test and analysis frequencies

Mode	Analysis Freq. (Hz)	Impact test Freq. (Hz)	% Difference	Shaker test Freq. (Hz)	% Difference	Impact thru sensor test Freq. (Hz)	% Difference
1	544.2	–		–		–	
2	544.3	538.3	−1.1 %	535.8	−1.6 %	535.4	−1.6 %
3	1437.4	1428	−0.7 %	1363	−5.2 %	1367	−4.9 %
4	1437.7	1434	−0.3 %	1417	−1.4 %	1386	−3.6 %
5	2185.6	2232	2.1 %	2048	−6.3 %	2051	−6.2 %

For the second mode, the test frequencies are close with the difference from the analysis frequencies ranging from −1.1 to −1.6 %. This is likely a result of the drive point being near a response node where motion is small. For paired modes three and four, the second bending modes, we see significant differences between the frequencies for the Shaker test and the Impact Thru Sensor test. The force sensor is introducing some asymmetry into the specimen that affects the two modes differently. For mode 3, the Shaker test and the Impact Thru Sensor give very similar frequencies, suggesting that the inertia effects are the main influence. For mode 4 there is a significant difference with the shaker test giving the higher frequency. A simplistic explanation might be that the added inertia gives the frequency drop seen in the Impact Thru Sensor test and the additional stiffness that the stinger adds in the Shaker test raises the frequency to be to that measured in the Impact test. Mode 5, the first torsion mode, shows the greatest change in frequency going from 2.1 % above the analysis frequency for the Impact test to over 6 % below it for the other two tests.

The results show that the use of a shaker/stinger/force sensor for a modal test can significantly affect the resulting frequencies. This raises the question: is it possible to assess the impact of shaker excitation before conducting a test?

36.4 Predicting Effect of Shaker System

The effect of stingers and senor mass on FRF's is discussed in [2] and extensive references made to previous work. Ashory [2] also provides a method for selecting a suitable stinger based on required force and frequency range and a discussion on mass compensation to account for sensor masses. The mass compensation is relatively easy to apply at a drive point but more difficult to apply to a cross FRF measurement. The force sensor is always mounted at a drive point, however, the added mass has an effect in all six degrees of freedom. Even if the response is measured in all three directions, the mass compensation must now be applied to the cross FRF's at the drive point, a more difficult task. The solution proposed in [2] is to make the cross FRF measurement with two different accelerometer and applying a modified mass compensation. This adds to the complexity of the test.

Modal testing is often performed for the purpose of validating an analytical model. If an FE model is available, can it be used to determine the influence of a stinger and force sensor on the response of a structure?

The basic FE model of the test specimen was modified to include the stinger and force transducer. The stinger was modeled using NASTRAN CBAR elements. The force transducer and stinger end fitting were modeled as a pair of masses connected by a CBUSH element. The CBUSH element is a generalized spring-damper element where the properties in each of the 6 degrees of freedom are individually defined. Since the force transducer is measuring axial forces, axial effects from the stinger will have no influence on the structure. The CBUSH element was therefore defined with zero stiffness in the axial direction and high stiffness in all others.

The two masses attached to the FE model are shown schematically in Fig. 36.3, note that, in the actual model, the two nodes of the CBUSH element are coincident. To determine the force transducer mass between the sensing element and the test specimen, the force transducer was placed on a shaker and driven with a sine wave. By measuring the acceleration of the shaker head and the output from the force transducer it is possible to determine the required mass value. This value is assigned to Mass 1 along with the rotary inertia properties of the force sensor and stinger end fitting.

The rotary inertia terms were estimated by creating a simple solid model of the force transducer and stinger end fitting, tuning the masses then calculating inertia properties. Mass 2 is assigned the remaining mass of the force transducer and zero values for the rotary inertia terms. The end of the stinger that attaches to the shaker was fixed in all degrees of freedom in the FE model.

The results from the shaker test and the FE model that includes the stinger and force sensor representation are shown in Table 36.4. The high MAC values confirm the correct mode pairing. Comparing the results with those listed in Table 36.3, all frequency differences are smaller. Frequency differences for modes two through four, the bending modes, have improved
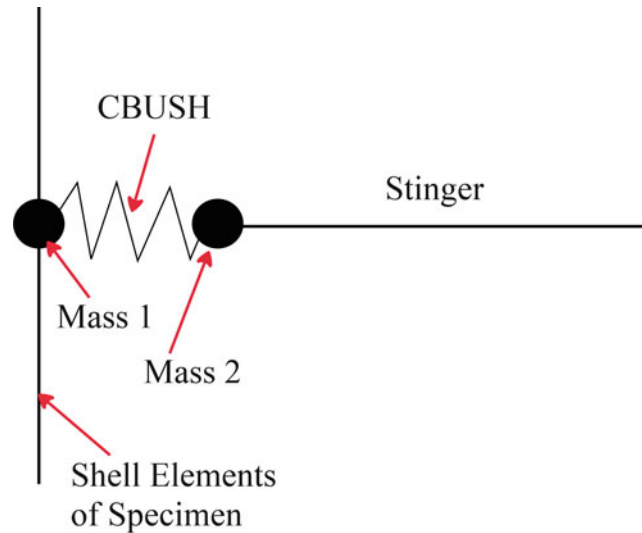
Fig. 36.3 FE representation of force transducer

Table 36.4 Comparison of shaker test and FE model results

Mode	Test freq. (Hz)	Analysis freq. (Hz)	MAC	Freq. % difference
2	535.8	543.0	0.96	1.35
3	1363.3	1341.2	0.97	−1.62
4	1416.6	1410.2	0.99	−0.44
5	2048.2	2138.5	0.99	4.40

significantly from a maximum absolute difference of 5.2 % to a maximum of 1.6 %. However, for mode 5, the first torsion mode, the frequency difference is still significant at 4.4 %, but reduced from 6.2 % in Table 36.3.

36.5   Discussion

The FE model with the force sensor and stinger show good agreement with the measured frequencies for the bending modes considered but not for the torsion mode. Table 36.3 shows that the original FE model predicted a first torsion mode frequency lower than that measured in the Impact test. The modified FE model predicts a frequency higher than that measured in the Shaker test. The FE model torsion modes are, therefore, less sensitive to the addition of the shaker and stinger than the actual structure is. This will require further investigation.

The selected stinger is significantly longer than recommended by the stinger selection methods presented in [2]. The FE model showed the first three bending modes of the stinger were in the same frequency range as the modes of the structure. The FE model also showed significant rotation of the specimen surface where the stinger end connects to it. In practice the force sensor contacts the structure over a finite area so the FE model could be improved by connecting the stinger to the structure at multiple nodes corresponding to the contact area.

The good agreement for the bending modes suggest that there is potential for modeling the effects of shaker excitation using an FE model, however, further work is required in improve agreement for the torsional modes. Confidence in the method could also be improved by investigating stingers of different lengths.

References

1. Pye, C.J., Idrisi, K.: 'Test and Analysis Correlation of Bonded Aluminum Z-profiles Using Adhesives with Widely Varying Moduli'. Schwingungsanalyse & Identifikation. VDI Wissenforum, Leonberg (2013)
2. Ashory, M.R.: High quality modal testing methods. Ph.D. Thesis, Imperial College of Science, Technology and Medicine, London (1999)

Chapter 37
Theoretical and Experimental Modal Analysis Correlation Studies for Coupled Catalytic Converter

Nandakishor Venkatesh, Roy A. Pace, and S.B. Kandagal

Abstract The main function of an exhaust system is to control the noise and to funnel exhaust fumes. The catalytic converter is designed to reduce the amount of harmful emissions products by transforming pollutants into water vapor and less harmful gases. Converter's modal parameters such as frequency, damping and mode shapes play a significant role in functioning of an exhaust system. The influence of the thermal expansion unit of the close coupled catalytic converter on the exhaust system and experimental modal analysis of catalytic converter is presented. It is observed that there is good correlation between the calculation results based on finite element analysis and the results obtained from experimental modal analysis.

Keywords Converter • Correlation • Exhaust • Modal parameters • Thermal expansion element

37.1 Introduction

The natural frequency analysis methodology is adopted to perform the structural dynamics analysis of an exhaust system's coupled catalytic converter [1]. The coupled catalyst assembly consists of a ceramic monolith brick, a mat holding and protecting the monolith, the converter shell and the thermal expansion element (TEE). The purpose of the thermal expansion element in a catalytic converter of an exhaust system is to decouple the thermal expansion induced due to the high temperature exhaust gases coming from the exhaust manifold of an engine. Thus to study the influence of thermal expansion or growth on the modal parameters this correlation study is investigated.

37.2 Correlation Study

The potential modal analysis techniques to perform the correlation study on the coupled catalytic converter with TEE are the experimental and analytical approach.

The modal assurance criterion (MAC) is chosen as the correlation parameter as it defines the relationship between the experimental and analytical mode shape. The expression for the MAC (A, X) is given by Eq. (37.1)

$$MAC\ (A, X)\ =\ \frac{\left(\{\Psi_X\}^T \{\Psi_A\}\right)^2}{\left(\{\Psi_X\}^T \{\Psi_X\}\right)\left(\{\Psi_A\}^T \{\Psi_A\}\right)} \tag{37.1}$$

N. Venkatesh • R.A. Pace (✉)
FECT, Columbus Tech Center, 950W, 450S, Columbus, IN 47201, USA
e-mail: roy.pace@faurecia.com

S.B. Kandagal
Indian Institute of Science, C V Raman Ave, Bengaluru, Karnataka 560012, India

37.3   Experimental Modal Analysis

The experimental modal analysis is performed by using the impact hammer to excite the catalytic converter at 12 measuring points. A wooden fixture was used to simulate the fixed-free boundary condition (Refer left and right photo below) and then the coupled converter was mounted on the fixture setup.

Photo Courtesy IISC: Wooden Fixture (*left*) and converter assembly on the fixture setup (*right*)

37.4   Frequency Response

At designated measuring points the component was excited and the response was captured using the FFT analyzer. The frequency response data obtained from the FFT analyzer is plotted in the rectangular coordinates and the plots are as shown in Figs. 37.1, 37.2, and 37.3 for mode 1, mode 2 and mode 3 respectively.

37.5   Logarithmic Decrement

Logarithmic decrement is used to find the damping ratio of an underdamped system in the time domain. The logarithmic decrement is the natural log of the ratio of the amplitudes of any two successive peaks. In this investigation the damping ratio is obtained referring to the logarithmic decrement plots presented in Figs. 37.4 and 37.5 for mode 1 and mode 2 respectively. The damping of real plots shows the resonating frequencies for mode 1, mode 2 and mode 3 (refer Fig. 37.6).

37.6   FEM Simulation Results

The FEM simulation was carried out by fixing the converter inlet so as to simulate a case similar to cantilever beam. The plots of the same are shown in Fig. 37.7. After carrying out the modal analysis the natural frequencies and normalized mode shapes for mode 1, mode 2 and mode 3 for X-direction, Y-direction and Z-direction respectively were extracted.
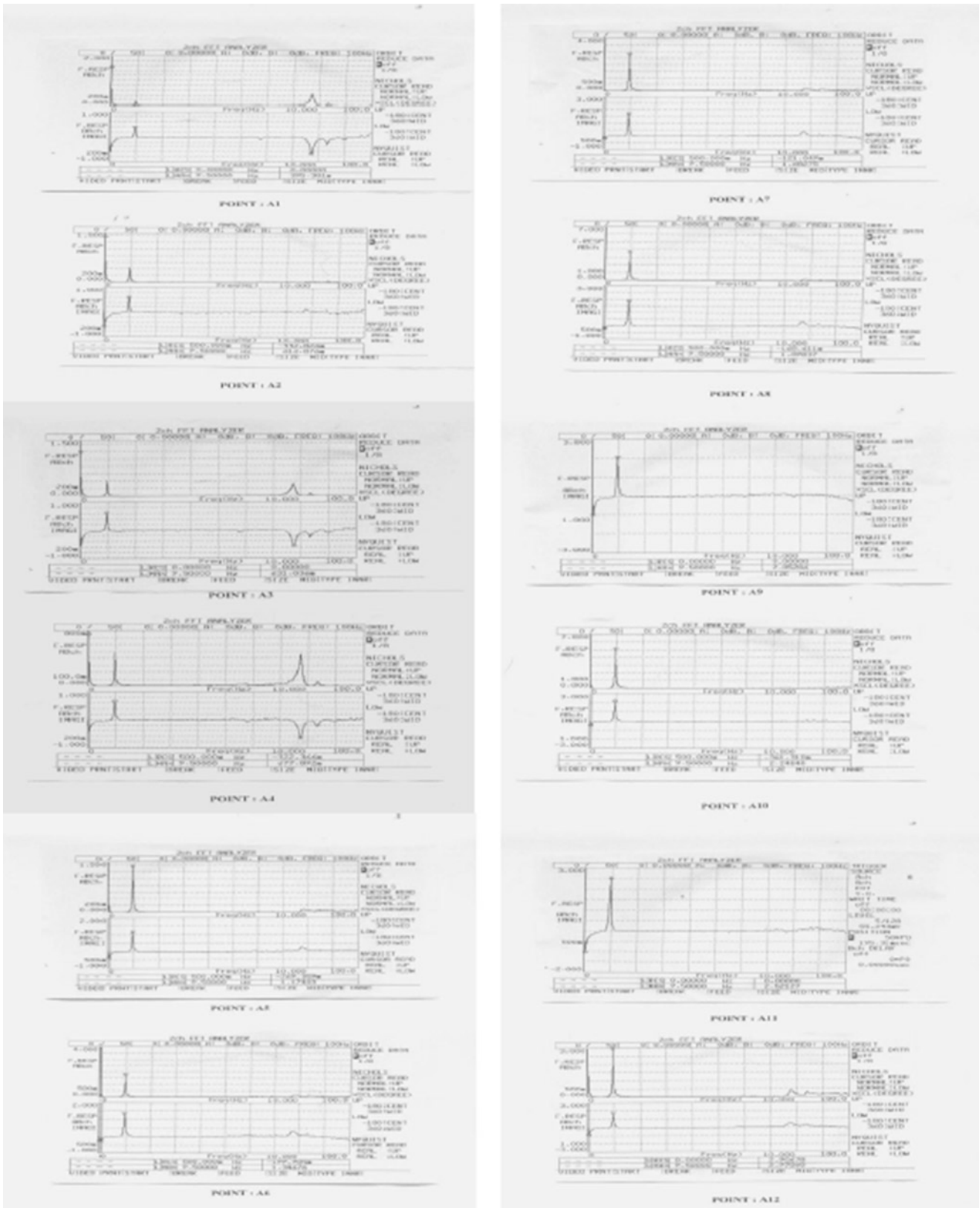
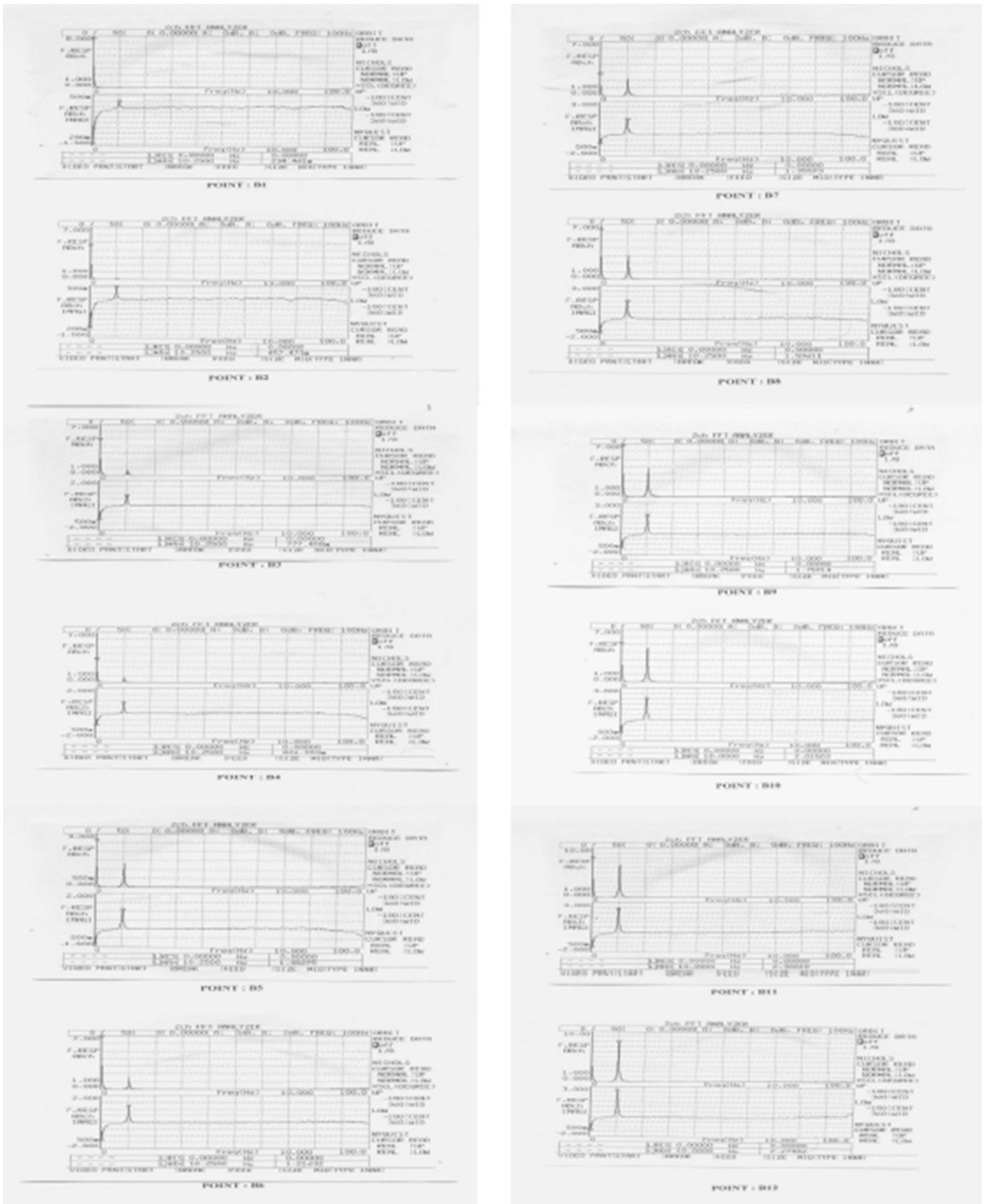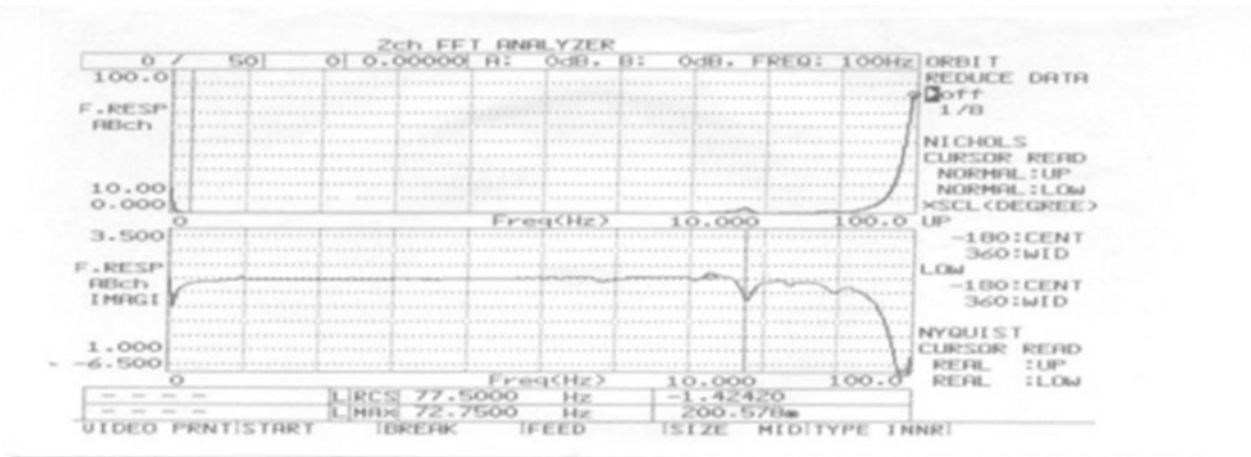**Fig. 37.1** Mode 1 Point A1 through A12 frequency response plots
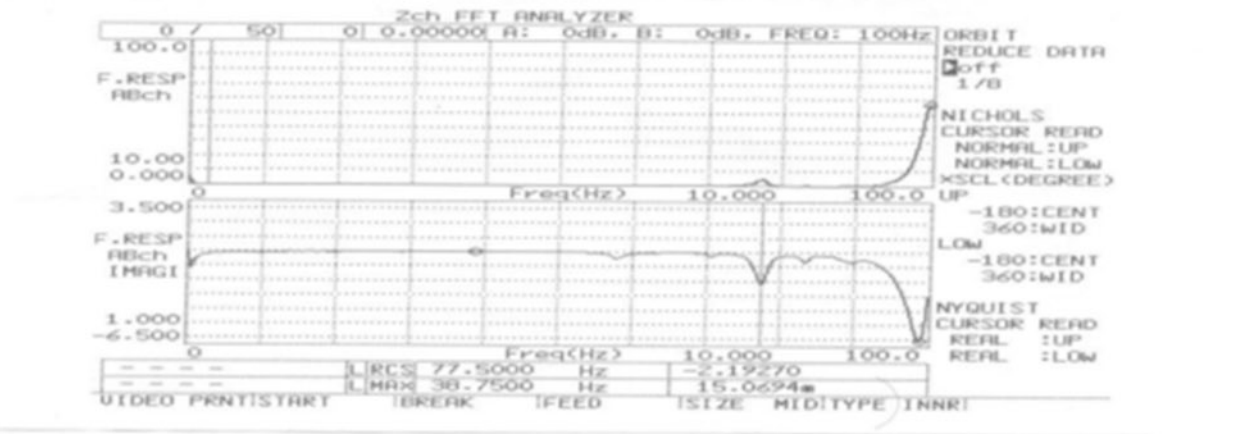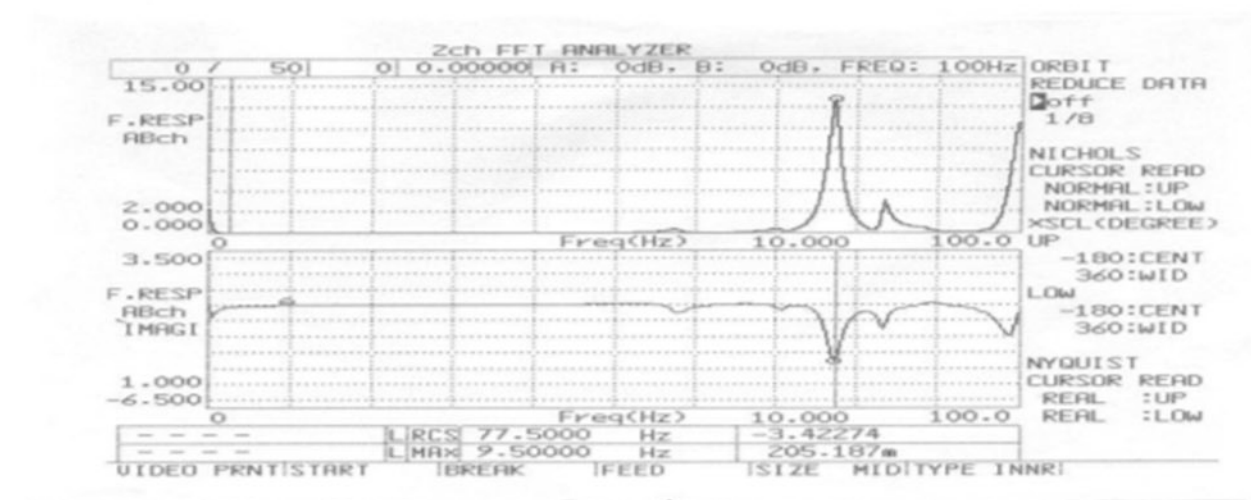
Fig. 37.2 Mode 2 Point B1 through B12 frequency response plots

POINT X1:

POINT X2:

POINT X3:

Fig. 37.3 Mode 3 Point X1 through X3 frequency response plots
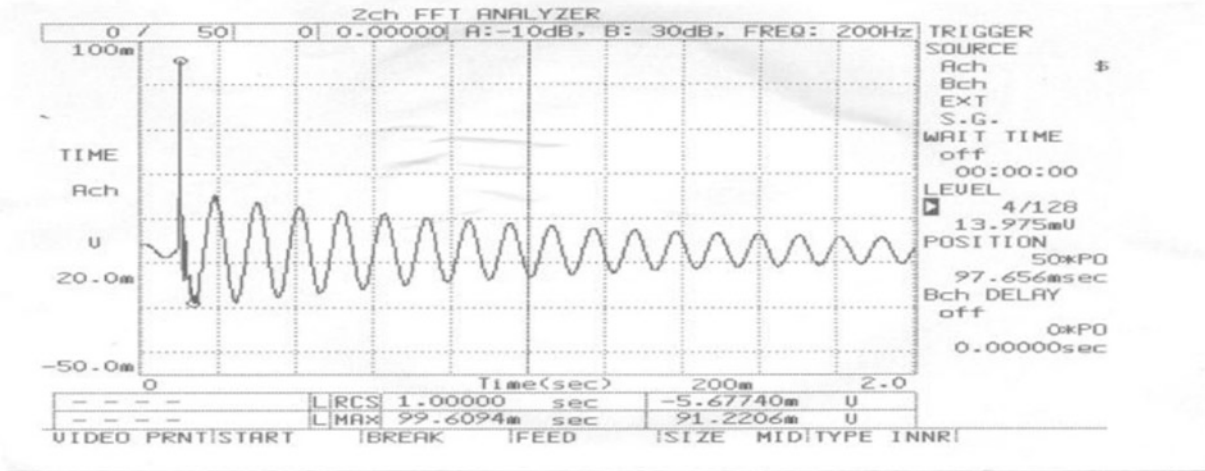
Fig. 37.4 Mode 1 Logarithmic decrement plot

37.7   MAC Evaluation

Modal assurance criterion was calculated using the Eq. (37.1). And the results are presented in the Tables 37.1, 37.2, and 37.3 for mode 1, mode 2 and mode 3 respectively

37.8   Eigen Value Variation Study

Another investigation was carried to study the effect of temperature variation from the range of 10–600 °C on the Eigen value. The results of this variation study are being presented in the Table 37.4 for mode 1, mode 2 and mode 3. Due to the lack of resources the experimental part of the investigation will be taken up in the future scope.

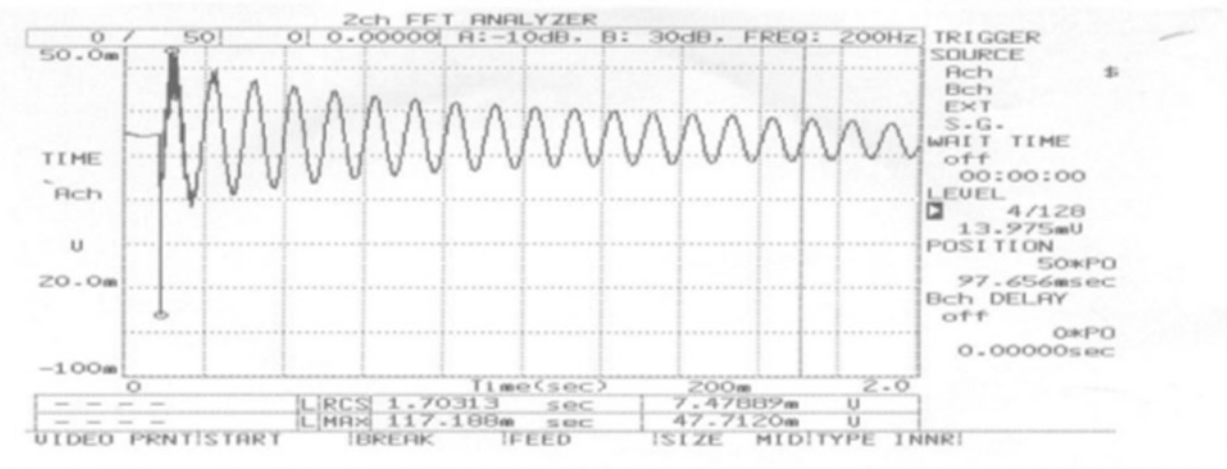**DAMPING : mode -2 (10,25Hz)** [38.32 units to 21.67 in 10 cycles]

Fig. 37.5 Mode 2 Logarithmic decrement plot

37.9 Results Summary

From correlation study we can observe that there is average 2.1 % deviation in the natural frequency from mode 1 through mode 3, which is illustrated from the Table 37.5.

And from the Eigen value variation study across the temperature range of 10–600 °C (refer Table 37.4), we can observe that there is around 12 % decrease in the Eigen values. It showed be noted that because of the presence of the TEE there was lesser stepper decrease in the Eigen values magnitude.

37.10 Conclusion

From the correlation study investigated in this paper we can concluded that the deviation obtained while evaluating the natural frequency is appreciable less, this signifies a good correlation. The modal analysis of a catalytic converter is very crucial in terms of structural and also the functional requirements such as to maintain the environment standards and noise requirements of the customer. At first stage of an analysis process the modal analysis plays a pivotal role by simulating the
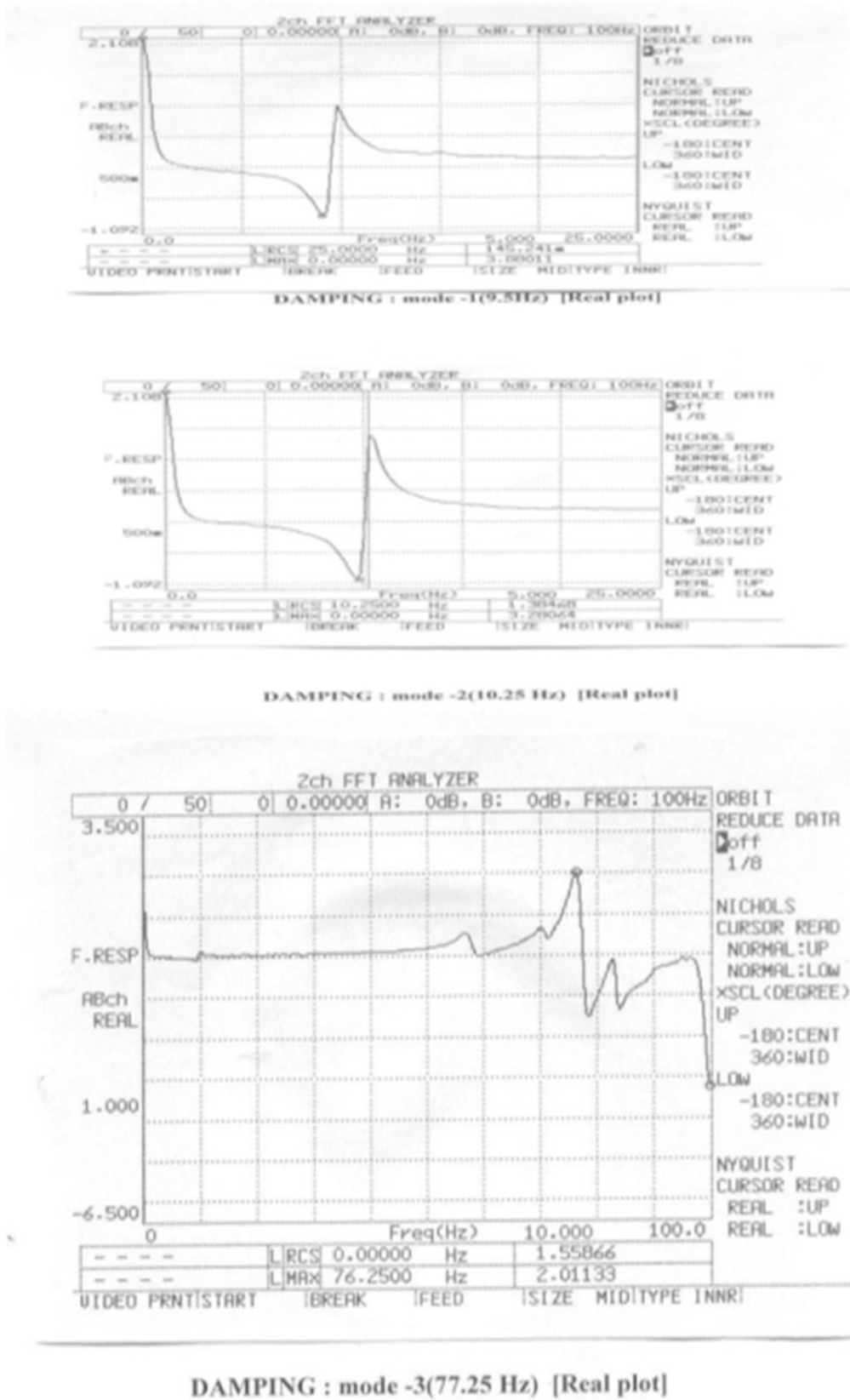
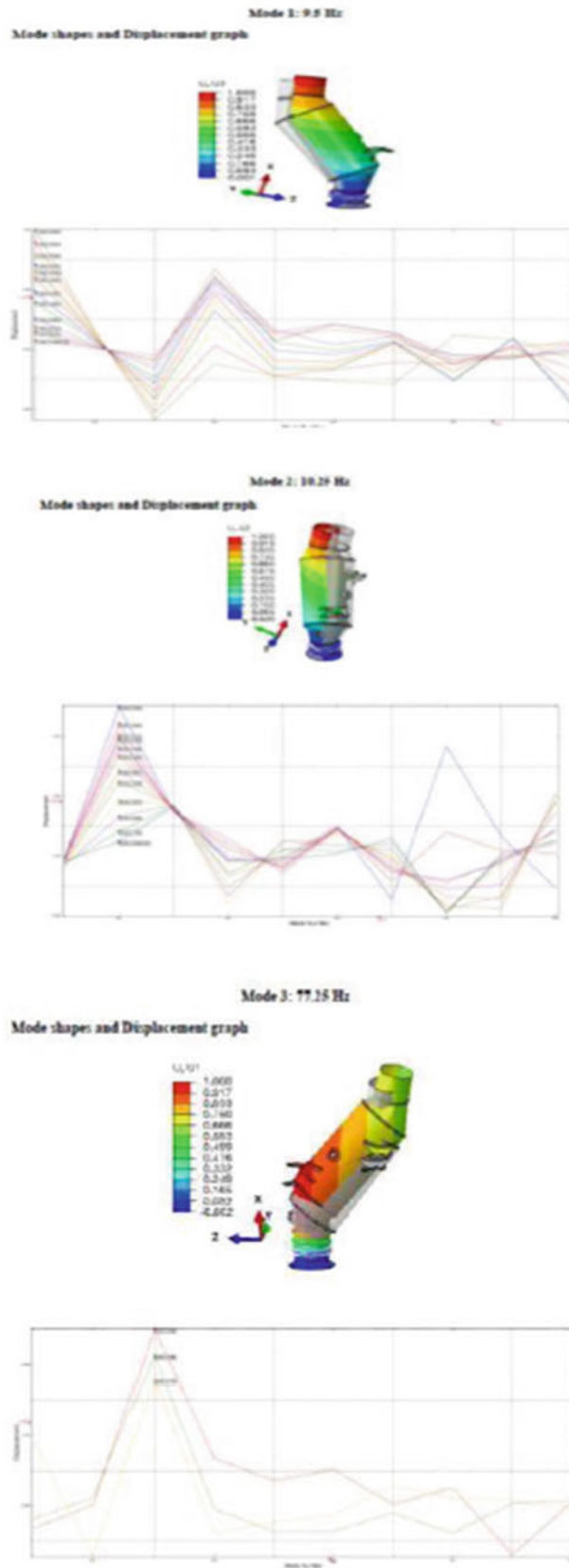**Fig. 37.6** Damping of real plot for mode 1, mode 2 and mode 3

Fig. 37.7 FEM Simulation results for Mode 1 through Mode 3

Table 37.1 Mode 1: 9.5 Hz

Point	Mode shapes amplitudes (Units) (Experiment)	Maximum amplitude normalized mode shape (Units) (Experiment) Ψ_X	Mode shape FEM Ψ_A
A12	2.970	1.000	1.000
A11	2.521	0.848	0.894
A10	2.248	0.756	0.793
A09	2.052	0.691	0.702
A08	1.898	0.639	0.649
A07	1.682	0.566	0.594
A06	1.356	0.456	0.479
A05	1.174	0.395	0.394
A04	0.677	0.228	0.254
A03	0.631	0.212	0.184
A02	0.616	0.207	0.140
A01	0.395	0.133	0.078
MAC			0.996

Table 37.2 Mode 2 = 10.25 Hz

Point	Mode shapes amplitudes (Units) (Experiment)	Maximum amplitude normalized mode shape (Units) (Experiment) Ψ_X	Mode shape FEM Ψ_A
B12	2.675	1.000	1.000
B11	2.366	0.844	0.886
B10	2.015	0.753	0.808
B09	1.769	0.657	0.784
B08	1.696	0.596	0.725
B07	1.356	0.507	0.637
B06	1.216	0.455	0.571
B05	1.083	0.405	0.495
B04	0.827	0.309	0.371
B03	0.777	0.290	0.266
B02	0.457	0.171	0.166
B01	0.234	0.087	0.098
MAC			0.994

Table 37.3 Mode 3 = 77.25 Hz

Point	Mode shapes amplitudes (Units) (Experiment)	Maximum amplitude normalized mode shape (Units) (Experiment) Ψ_X	Mode shape FEM Ψ_A
X03	−3.422	1.000	1.000
X02	−2.927	0.855	0.854
X01	−1.424	0.416	0.717
MAC			0.970

behavior of the system in the fixed free boundary condition, now depending on the definition of customer requirements, selecting a methodology is important. And it's always advisable to verify the results obtained from numerical method to that obtained from experimental method. From the correlation study it is discovered that due to the temperature effect and also due to the inclusion of TEE in the converter inlet there is around 12 % variation across mode 1, mode 2 and mode 3. Although the thermal expansion element (TEE) serves the purpose of reducing the thermal induced plastic strain, there will be certain effect it on the modal parameters.

As it was cost sensitive and more time-consuming it was quite a bit difficult to investigate it further; and hence it was proposed to implement these counter measures to be carried out in the early product development phases so as to correlate the analytical with the experimental methodology. Especially before its mass production.

Table 37.4 Eigen value variation w.r.t temperature Study using numerical approach

Sl No	Temperature in °C	Mode 1 in Hz	Mode 2 in Hz	Mode 3 in Hz
1	10	9.23	10.18	74.85
2	15	9.23	10.18	74.85
3	20	9.23	10.18	74.85
4	50	9.18	10.13	74.46
5	100	9.10	10.04	73.80
6	150	9.00	9.93	72.90
7	200	8.90	9.81	72.16
8	250	8.81	9.71	71.40
9	300	8.72	9.61	70.68
10	350	8.62	9.50	69.92
11	400	8.53	9.41	69.10
12	500	8.34	9.20	67.61
13	600	8.11	8.95	65.70

Table 37.5 Natural frequencies and damping

Mode	FEM natural frequency (Hz)	Experiment natural frequency (Hz)	% Deviation	Damping, ζ(%)
1	9.25	9.50	2.6	1.08
2	10.20	10.25	0.5	0.90
3	75.00	77.50	3.2	1.10

37.11 Future Scope

In this correlation study of theoretical and experimental modal analysis it is proposed to conduct a test to capture the temperature effect on the thermal growth of the entire exhaust system by designing the fixtures appropriately. Also the study of effect of temperature change on the damage calculation can be investigated in the near future by developing a methodology to do the hot temperature calibration of the catalytic converter. Further a thermal induced vibration fatigue analysis can be carried out to study the thermo-mechanics of an exhaust system.

Reference

1. Ekholm, H., Zettervall, B.: Modal analysis on an exhaust manifold to define a catalyst FE-model. Department of Mechanical Engineering, Blekinge Institute of Technology, Karlskrona, Sweden, ISRN:BTH-AMT-EX—2008/CI-01-SE, 11 2008